

**DOT/FAA/AR-xx/xx**

Air Traffic Organization  
NextGen & Operations Planning  
Office of Research and  
Technology Development  
Washington, DC 20591



# **Volume V: UAS Airborne Collision Severity Evaluation - Assessment of sUAS deflections due to aerodynamic interaction with a 14 CFR Part 25 Commercial Aircraft**

October 2021

Final Report

This document is available to the U.S. public  
through the National Technical Information  
Services (NTIS), Springfield, Virginia 22161.

This document is also available from the  
Federal Aviation Administration William J. Hughes  
Technical Center at [actlibrary.tc.faa.gov](http://actlibrary.tc.faa.gov).



U.S. Department of Transportation  
**Federal Aviation Administration**

## **NOTICE**

This document is disseminated under the sponsorship of the U.S. Department of Transportation in the interest of information exchange. The U.S. Government assumes no liability for the contents or use thereof. The U.S. Government does not endorse products or manufacturers. Trade or manufacturers' names appear herein solely because they are considered essential to the objective of this report. The findings and conclusions in this report are those of the author(s) and do not necessarily represent the views of the funding agency. This document does not constitute FAA policy. Consult the FAA sponsoring organization listed on the Technical Documentation page as to its use.

This report is available at the Federal Aviation Administration William J. Hughes Technical Center's Full-Text Technical Reports page: [actlibrary.tc.faa.gov](http://actlibrary.tc.faa.gov) in Adobe Acrobat portable document format (PDF).

**Legal Disclaimer:** The information provided herein may include content supplied by third parties. Although the data and information contained herein have been produced or processed from sources believed to be reliable, the Federal Aviation Administration makes no warranty, expressed or implied, regarding the accuracy, adequacy, completeness, legality, reliability, or usefulness of any information, conclusions or recommendations provided herein. Distribution of the information contained herein does not constitute an endorsement or warranty of the data or information provided herein by the Federal Aviation Administration or the U.S. Department of Transportation. Neither the Federal Aviation Administration nor the U.S. Department of Transportation shall be held liable for any improper or incorrect use of the information contained herein and assumes no responsibility for anyone's use of the information. The Federal Aviation Administration and U.S. Department of Transportation shall not be liable for any claim for any loss, harm, or other damages arising from access to or use of data or information, including without limitation any direct, indirect, incidental, exemplary, special, or consequential damages, even if advised of the possibility of such damages. The Federal Aviation Administration shall not be liable to anyone for any decision made or action taken, or not taken, in reliance on the information contained herein.

**Technical Report Documentation Page**

1. Report No. DOT/FAA/AR-xx/xx		2. Government Accession No.		3. Recipient's Catalog No.	
4. Title and Subtitle  <b>Volume V: UAS Airborne Collision Severity Evaluation - Assessment of sUAS deflections due to aerodynamic interaction with a 14 CFR Part 25 Commercial Aircraft</b>				5. Report Date <b>October 2021</b>	
				6. Performing Organization Code	
7. Author(s) <b>Gerardo Olivares, Eduardo Divo, Harsh Shah, Luis Gomez, Fardin Khalili, Nidhi Sathyanarayana.</b>				8. Performing Organization Report No.	
9. Performing Organization Name and Address  National Institute for Aviation Research Wichita State University 1845 Fairmount Wichita, KS 67260-0093				10. Work Unit No. (TRAIS)	
				11. Contract or Grant No.	
12. Sponsoring Agency Name and Address  U.S. Department of Transportation Federal Aviation Administration Office of Aviation Research Washington, DC 20591				13. Type of Report and Period Covered	
				14. Sponsoring Agency Code	
15. Supplementary Notes					
16. Abstract  The A16 Unmanned Aircraft Systems (UAS) Airborne Collision Severity Evaluation was an extension of the A3 study that focused on severity evaluation of an UAS airborne collision with a Narrow Body Commercial Aircraft and a Business Jet. The research presented in this report addresses the question of whether or not a sUAS would be deflected prior to impact with a large transport aircraft. Using Computational Fluid Dynamics (CFD) methods coupled with a six-degrees-of-freedom (6-DOF) solver, it was determined that the vertical deflections were not large enough for the sUAS to deflect away from the intended impact location for any of the three impact locations. It was also determined that the final orientation of the sUAS at impact differed slightly from the initial orientation. Based on these findings, the research team concluded that the aerodynamic interaction between a DJI Phantom III drone and a large transport category aircraft would: 1) not cause the drone to deflect away prior to impact with the wing or the horizontal stabilizer, and 2) modify the orientation of the drone at the time of impact with the wing or the horizontal stabilizer.					
17. Key Words  <b>sUAS, UAS, Deflection, Trajectory, Crashworthiness, Airborne Collision, National Institute for Aviation Research, NIAR</b>			18. Distribution Statement  This document is available to the U.S. public through the National Technical Information Service (NTIS), Springfield, Virginia 22161. This document is also available from the Federal Aviation Administration William J. Hughes Technical Center at <a href="http://actlibrary.tc.faa.gov">actlibrary.tc.faa.gov</a> .		
19. Security Classif. (of this report)  Unclassified		20. Security Classif. (of this page)  Unclassified		21. No. of Pages	22. Price

## REVISION HISTORY

Revision	Description of Modifications	Release Date
IR	Initial release	10/30/2021
	-	

## ACKNOWLEDGEMENTS

The authors would like to thank all the Federal Aviation Administration (FAA) personnel that have been involved in this research project. In particular, the authors would like to thank Sabrina Saunders-Hodge, Hector Rea, Nick Lento, Bill Oehlschlager, and Melanie Flavin for all their contributions and their valuable input throughout the research.

The authors would also like to thank Colonel Stephen P. Luxion and Hannah Thach from the FAA's Center of Excellence for Unmanned Aircraft Systems (ASSURE) for supporting this research.

The authors also acknowledge the contributions of the graduate research assistant from the National Institute for Aviation Research Virtual Engineering Laboratory, Guillermo Caro. Last but not least, thanks to all the industry participants that helped throughout the research.

## TABLE OF CONTENTS

Chapter	Page
TABLE OF CONTENTS	VII
LIST OF FIGURES	IX
LIST OF TABLES	X
LIST OF ACRONYMS	XI
LIST OF SYMBOLS	XII
EXECUTIVE SUMMARY	XIII
1. BACKGROUND	1
2. PROJECT SCOPE	1
3. OVERVIEW OF RESEARCH	2
3.1 Selection of Impact Conditions	2
3.2 Selection of Impact Locations	4
3.3 Simulation Matrix Definition	6
3.4 Methodology Overview	7
4. SUMMARY OF RESULTS	8
4.1 Validation of Aircraft Aerodynamic Performance	8
4.2 Trajectory Analysis Results	10
4.2.1 Cross-Verification Study Results	11
4.2.2 Simulation Matrix Results of Primary Impact Scenarios	16
5. KEY CONCLUSIONS AND RECOMMENDATIONS	21

6. REFERENCES

22

ANNEX A: NIAR FINAL REPORT

ANNEX A - 1

ANNEX B: ERAU FINAL REPORT

ANNEX B - 1

## LIST OF FIGURES

Figure	Page
1. Side view showing the placement of the drone with respect to (a) CRM aircraft ( $0^\circ$ AoA) (b) CRM aircraft ( $5^\circ$ AoA) (c) HL-CRM aircraft (d) CRM Horizontal Stabilizer ( $0^\circ$ AoA) and (e) CRM Horizontal Stabilizer ( $5^\circ$ AoA).	5
2. Spanwise locations at which the pressure coefficients are measured.	9
3. Pressure coefficient plots over the CRM wing at Stations 1 through 6, compared with experimental data.	10
4. The sign convention used to define the displacements of the drone.	11
5. The sign convention used to define the angular displacements of the drone.	11
6. (a) Horizontal, (b) Lateral, and (c) Vertical displacements of the drone for impact scenario IC1-IL1 and IC2-IL1 obtained by NIAR and ERAU.	13
7. (a) Roll, (b) Pitch, and (c) Yaw angular displacements of the drone for impact scenario IC1-IL1 and IC2-IL1 obtained by NIAR and ERAU.	14
8. (a) Side and (b) Top view of the pressure contour over the drone approximately at the time of impact for impact scenario IC1-IL1 obtained by (1) ERAU and (2) NIAR.	15
9. (a) Side and (b) Top view of the pressure contour over the drone approximately at the time of impact for impact scenario IC2-IL1 obtained by (1) ERAU and (2) NIAR.	16
10. (a) Horizontal, (b) Lateral, and (c) Vertical displacements of the drone at the point of impact for primary impact scenarios.	19
11. (a) Roll, (b) Pitch, and (c) Yaw angular displacements of the drone at the point of impact for primary impact scenarios.	20

## LIST OF TABLES

Table	Page
1. Impact conditions used for the study.	4
2. Primary impact locations of the drone used for the trajectory analysis.	6
3. Summary of primary impact scenarios (simulation matrix) used for the trajectory analysis.	7
4. CRM aircraft force coefficients obtained from simulation compared against experimental data.	9
5. Drone displacements for impact scenarios IC1-IL1 and IC2-IL1 obtained by NIAR and ERAU.	13
6. Drone angular displacements for impact scenarios IC1-IL1 and IC2-IL1 obtained by NIAR and ERAU.	14
7. Drone displacements at the point of impact for primary impact scenarios.	18
8. Drone angular displacements at the point of impact for primary impact scenarios.	18

## LIST OF ACRONYMS

AGL	Above Ground Level
AoA	Angle of Attack
CFD	Computational Fluid Dynamics
CFR	Code of Federal Regulations
CG	Center of Gravity
CRM	Common Research Model
DOF	Degrees-of-Freedom
ERAU	Embry-Riddle Aeronautical University
FAA	Federal Aviation Administration
HL-CRM	High Lift Common Research Model
IC	Impact Condition
IL	Impact Location
KIAS	Knots-Indicated Air Speed
MSL	Mean Sea Level
MtSU	Montana State University
NAS	National Airspace System
NASA	National Aeronautics and Space Administration
NIAR	National Institute for Aviation Research
NTSB	National Transportation Safety Board
RBD	Rigid Body Dynamics
sUAS	Small Unmanned Aircraft Systems
UAH	University of Alabama in Huntsville
UAS	Unmanned Aircraft Systems
UAV	Unmanned Aerial Vehicle
VTOL	Vertical Take-Off and Landing
WP	Working Packages
WSU	Wichita State University

## LIST OF SYMBOLS

$\text{AOA}_{\text{CRM}}$	Angle of attack of CRM aircraft
$\text{AOA}_{\text{HL-CRM}}$	Angle of attack of HL-CRM aircraft
$C_D$	Coefficient of drag
$C_L$	Coefficient of lift
$C_P$	Coefficient of pressure
$V_{\text{CRM}}$	Velocity of CRM aircraft
$V_{\text{DJI}}$	Velocity of DJI drone/sUAS
$V_{\text{HL-CRM}}$	Velocity of HL-CRM aircraft
$X, Y, \text{ and } Z$	Represents the global inertial reference frame in XYZ axes
$\Delta C_D$	Difference in drag coefficient
$\Delta C_L$	Difference in lift coefficient
$\Delta p, \Delta q, \Delta r$	Angular velocities in global inertial reference frame (XYZ)
$\Delta u, \Delta v, \Delta w$	Velocities in global inertial reference frame (XYZ)
$\Delta x, \Delta y, \Delta z$	Displacements in global inertial reference frame (XYZ)
$\Delta \phi, \Delta \theta, \Delta \psi$	Angular displacements in global inertial reference frame (XYZ)
$\eta$	Fraction of the wing semispan (y/semispan)

## EXECUTIVE SUMMARY

The A16 Unmanned Aircraft System (UAS) Airborne Collision Severity Evaluation was an extension of the A3 study that focused on severity evaluation of a UAS airborne collision with a Narrow Body Commercial Aircraft and a Business Jet. The A16 study focused on three main research areas – evaluation of deflection of a small UAS (sUAS) prior to impact with a large transport aircraft due to aerodynamic interaction, which is explained in depth in this volume, evaluation of the severity of sUAS collisions with a rotorcraft, and evaluation of the severity of sUAS collisions with a general aviation aircraft. The A16 team consisted of the National Institute for Aviation Research (NIAR) at Wichita State University (WSU), the University of Alabama in Huntsville (UAH), Montana State University (MtSU), and Embry-Riddle Aeronautical University (ERAU).

NIAR and ERAU completed the Task 1 study which addressed the question of whether or not a sUAS would be deflected prior to impact with a large transport aircraft. This study used the National Aeronautics and Space Administration (NASA) Common Research Model (CRM) aircraft model that represents a large transport category aircraft, similar to Boeing 777-200. The sUAS model used in this study was representative of the DJI Phantom III drone. The research team obtained the sUAS deflections by performing a series of trajectory analyses in which the sUAS was placed on a collision path with an aircraft at various locations. The researchers performed the trajectory analyses using Computational Fluid Dynamics (CFD) methods coupled with a six-degrees-of-freedom (6-DOF) solver, and validated the models with available experimental data. The team selected three impact locations on the aircraft to compute the deflection of the sUAS – first near mid-span of the wing, second near the root of the wing, and third near mid-span of the horizontal stabilizer. Aircraft operating speed was based on a typical holding flight pattern. The researchers performed cross-verification of their trajectory analysis for two conditions corresponding to the first impact location. The sUAS deflections obtained by both universities on the research team showed an acceptable level of agreement.

NIAR and ERAU determined that the vertical deflections were not large enough for the sUAS to deflect away from the intended impact location for any of the three impact locations. It was also determined that the final orientation of the sUAS at impact slightly differed from the initial orientation.

Based on these findings, the research team concluded that the aerodynamic interaction between a DJI Phantom III drone and a large transport category aircraft would: 1) not cause the drone to deflect away prior to impact with the wing or the horizontal stabilizer, and 2) modify the orientation of the drone at the time of impact with the wing or the horizontal stabilizer.

## 1. BACKGROUND

Unmanned Aircraft Systems (UASs) constitute an Unmanned Aerial Vehicle (UAV) and the equipment necessary to safely and efficiently operate the unmanned aircraft. The UAS industry is growing at a rapid pace and becoming a widely used system in applications such as military, security, construction and infrastructure, entertainment, and agricultural operations [1]. The large growth in the UAS industry poses many challenges regarding safety and regulations. The expansion of UAS applications can lead to drones violating the restricted national airspace, highlighting the UAS operational needs. In addition, safety concerns to the public and other manned aircraft have led the research in creating safety regulations for the safe use of UAS.

The regulation of UAS operations in the National Airspace System (NAS) ensures the appropriate level of safety for all manned and unmanned aircraft. According to the guidance on UAS operations provided by the Range of Commanders Council, the UAS must show a level of risk to human life no greater than that of a piloted aircraft in order to have an Equivalent Level of Safety [2]. The Federal Aviation Administration (FAA) recently released proposed rules for unmanned aircraft weighing less than 55 pounds and flown within visual line of sight [3]. The National Transportation Safety Board (NTSB) has defined two categories of relevant collision accident scenarios; (i) in-flight collisions with obstacles such as birds, trees, power lines, and (ii) mid-air collisions with other aircraft. UAS requirements were defined based on the latter scenario. The effects of bird impact on aircraft have been researched and are well documented. However, the probability of a mid-air collision between a rigid body such as a UAS and a manned aircraft needs to be investigated in detail.

Prior research by the A3 Airborne Collision Severity Evaluation study [4] provided an understanding of the physics of mid-air collisions between manned aircraft and UAVs. The research also identified characteristics of the UAV that influence the damage on manned aircraft. The research analyzed airborne collisions between a multi-rotor vertical take-off and landing (VTOL) quadcopter and two types of manned aircraft: a typical narrow-body commercial transport jet and a typical business jet certified under *14 Code of Federal Regulations (CFR) Part 25* requirements [5]. The A3 study [4] also identified regions on the aircraft where the impact from a UAS could cause critical damage. This research evaluated the trajectory of the multi-rotor UAS or drone as it approaches a transport category aircraft. As the UAS or drone approaches an aircraft, it could deflect away from the aircraft because of the influence of its aerodynamic forces, thereby preventing a collision. The purpose of the joint study conducted by the National Institute for Aviation Research (NIAR) and Embry-Riddle Aeronautical University (ERAU) was to determine the extent of the UAS deflection resulting from the interaction between the flow field generated by the aircraft and the UAS as the UAS approaches the aircraft.

## 2. PROJECT SCOPE

This research task intended to answer the following research questions:

- a. Can a sUAS be deflected prior to impact with a large transport aircraft due to the aerodynamic interaction between the sUAS and the aircraft?
- b. How does the impact location on the aircraft, i.e., wing and horizontal stabilizer, affect the deflections of the sUAS?
- c. How do the sUAS deflections relate to flight parameters, including relative speed and angle of attack?

The research task was broken down into fundamental steps called Working Packages (WP):

- a. WP I: Definition of the Target (Aircraft) geometry, selection of the aircraft speeds, angles of attack, and selection of impact locations on the aircraft.
- b. WP II: Definition of the Projectile (sUAS) geometry, including definitions of mass and inertia and selection of the sUAS speed.
- c. WP III: Validation of the Computational Fluid Dynamics (CFD) model of the aircraft with available experimental data.
- d. WP IV: Cross verification of sUAS deflections obtained from the trajectory analyses conducted by the National Institute for Aviation Research (NIAR) and Embry-Riddle Aeronautical University (ERAU).
- e. WP V: Trajectory Analyses of the sUAS for the impact locations on the aircraft wing.
- f. WP VI: Trajectory Analyses of the sUAS for the impact locations on the aircraft horizontal stabilizer.

The research task was completed with the following assumptions and limitations:

- a. The trajectory analyses were performed only for a single sUAS quadcopter drone model.
- b. The flow field of the quadcopter rotors was not modeled to reduce the computational time.
- c. The drone model was considered to be a rigid body in the trajectory analyses.
- d. The drone's motion was partially constrained to allow for a flight path with constant altitude, attitude, and speed, outside of the influence of the aircraft flow field.

### 3. OVERVIEW OF RESEARCH

NIAR and ERAU performed the trajectory analysis using CFD analysis coupled with a Rigid Body Dynamics (RBD) solver. The RBD solver implements six-degrees-of-freedom (6-DOF) equations to calculate the rigid body motion. The drone model used in this study was the DJI Phantom III model reverse-engineered by NIAR for the A3 study [4]. The aircraft model used in this study was the Common Research Model (CRM) developed by NASA that represents a large transport category aircraft similar to Boeing 777-200.

NASA developed the CRM aircraft geometry to help facilitate the validation of CFD methodologies against experimental data. This geometry is available as an open-source geometry to the community [6]. Several experimental investigations for the aerodynamics of the CRM aircraft exist in the literature available for CFD model validation [7] [8]. A variant of the CRM with high-lift devices is the High Lift Common Research Model (HL-CRM), which NASA also developed. The HL-CRM geometry has flaps and slats deployed. This geometry is also available to the community as an open-source geometry [9]. The research team used the HL-CRM geometry in this study to determine the effect of the deployment of high lift devices on the sUAS trajectory.

#### 3.1 SELECTION OF IMPACT CONDITIONS

The operating speeds for transport category aircraft at various altitudes are set in the FAA General Operating and Flight Rules (14 CFR Part 91) airworthiness requirements [10]. For holding conditions, the Aeronautical Information Manual paragraph 5-7-2-j.2(b) [11] indicates the following speeds in Knots-Indicated Air Speed (KIAS):

- 200 KIAS below 6,000 ft.
- 230 KIAS from 6,001 to 14,000 ft.

- 265 KIAS above 14,000 ft.

Since sUAS operations typically occur at lower altitudes, the likelihood of a sUAS colliding with a large transport category aircraft would be high in a holding, take-off, or landing scenario. §91.117(b) [10] specifies a maximum velocity of 200 KIAS at an altitude of 2,500 ft Above Ground Level (AGL) or below within 4 miles of Class C and D airspace. This velocity of 200 KIAS is equivalent to 208 kts (107 m/s) true airspeed at 2500 ft Mean Sea Level (MSL).

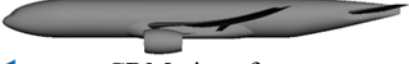
Therefore, NIAR and ERAU selected a true airspeed of 200 kts (102.89 m/s), which is less than the maximum true air speed of 208 kts (107 m/s), as the aircraft velocity in this study. In addition, the operating flight altitude was selected to be 2,500 ft (762 m) MSL in this study. These conditions typically correspond to a holding flight pattern after a missed approach. The research team also investigated the effect of a lower aircraft velocity, i.e., 170 kts (87.46 m/s) in this study for the HL-CRM configuration.

The research team selected the drone velocity based on the work performed in the A3 study [4]. In the A3 study, a relative velocity of 250 kts (128.61 m/s) was used for the impact analysis. Since the aircraft velocity was selected to be 200 kts (102.89 m/s), the drone velocity is computed to be 50 kts (25.72 m/s). This velocity is much higher than the maximum speed of the DJI Phantom III. The A3 study [4] mentions that it is realistic to assume that future sUAS models have enhanced flight capabilities with higher flight speeds. Therefore, the research team selected a true airspeed of 50 kts (25.72 m/s) as the drone velocity in this study. The research team also investigated the effect of the drone in a hover operation in this study, for which they specified the drone velocity to be zero kts.

The research team investigated the effect of high lift devices on the aerodynamic interaction between the drone and the aircraft in this study with the HL-CRM aircraft configuration. High lift devices result in larger pressure gradients over the aircraft, leading to a greater aerodynamic influence on the drone trajectory. The research team also investigated the effect of the aircraft angle of attack (AoA) in this study. Increasing the aircraft AoA results in a larger pressure gradient over the aircraft. In this study, the research team used two different aircraft AoAs, 0° and 5°.

Table 1 provides a summary of the impact conditions analyzed in this study.

Table 1. Impact conditions used for the study.

Impact Condition (IC)	Depiction		University
IC1	 Drone → $V_{Drone} = 0$ kts	 ← CRM aircraft $V_{CRM} = 200$ kts $AoA_{CRM} = 0^\circ$	NIAR, ERAU
IC2	 Drone → $V_{Drone} = 50$ kts	 ← CRM aircraft $V_{CRM} = 200$ kts $AoA_{CRM} = 0^\circ$	NIAR, ERAU
IC3	 Drone → $V_{Drone} = 50$ kts	 ← CRM aircraft $V_{CRM} = 200$ kts $AoA_{CRM} = 5^\circ$	NIAR, ERAU
IC4	 Drone → $V_{Drone} = 50$ kts	 ← HL-CRM aircraft $V_{HL-CRM} = 200$ kts $AoA_{HL-CRM} = 0^\circ$	NIAR
IC5	 Drone → $V_{Drone} = 50$ kts	 ← HL-CRM aircraft $V_{HL-CRM} = 170$ kts $AoA_{HL-CRM} = 0^\circ$	NIAR
IC6	 Drone → $V_{Drone} = 50$ kts Drone Trajectory at an Angle of $-1.27^\circ$	 ← CRM aircraft $V_{CRM} = 200$ kts $AoA_{CRM} = 5^\circ$	ERAU

### 3.2 SELECTION OF IMPACT LOCATIONS

In the A3 study [4], the impact locations selected were the aircraft wing, the horizontal and vertical stabilizers, and the windshield. In this study, NIAR and ERAU selected the wing and the horizontal stabilizer – the two most critical aircraft aerodynamic components, as the regions of interest. NIAR

and ERAU selected three impact locations – first near mid-span of the wing, second near the root of the wing, and third near mid-span of the horizontal stabilizer to compute the deflection of the sUAS at these locations.

The research team defined the impact locations to be at the leading-edge of the wing for the CRM aircraft, the leading-edge of the slat for the HL-CRM aircraft, or the leading-edge of the horizontal stabilizer of the CRM aircraft, as shown in Figure 1. The team specified the spanwise/lateral position of the impact location with respect to the fuselage symmetry plane. For the trajectory analysis, the initial release location of the drone center of gravity (CG) was aligned with the impact location, as shown in Figure 1.

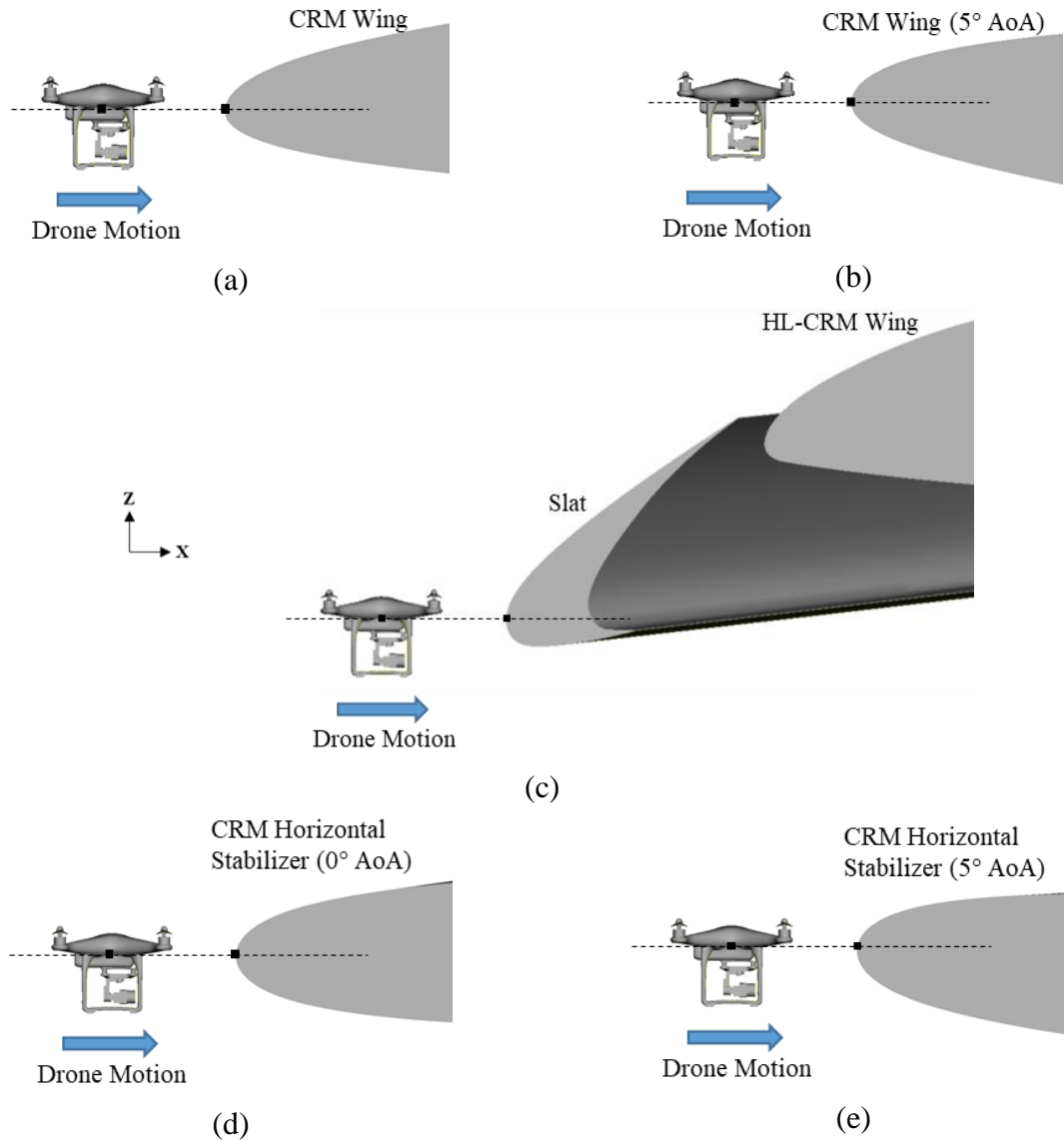


Figure 1. Side view showing the placement of the drone with respect to (a) CRM aircraft (0° AoA) (b) CRM aircraft (5° AoA) (c) HL-CRM aircraft (d) CRM Horizontal Stabilizer (0° AoA) and (e) CRM Horizontal Stabilizer (5° AoA).

The research team selected the first impact location (IL1) based on a critical case, in terms of impact severity, from the A3 study [4]. The lateral position of IL1 was specified to be at a distance of 16.8 m from the fuselage symmetry plane. The team evaluated the drone trajectory at IL1 for both the CRM and HL-CRM aircraft configurations, and utilized the drone trajectory evaluated at IL1 for their cross-verification study.

The second impact location (IL2) was located near the wing root. The lateral position of IL2 was defined at the midpoint between the nacelle centerline and the fuselage symmetry plane of the CRM aircraft, resulting in a distance of 4.89 m from the fuselage symmetry plane. This impact location was selected to analyze the effect of pressure gradients generated by the wing root and the fuselage on the drone's trajectory. The research team evaluated the drone trajectory at IL2 for both the CRM and HL-CRM aircraft configurations.

The third impact location (IL3) was located on the horizontal stabilizer. The lateral position of IL3 was defined at the midpoint on the horizontal stabilizer of the CRM aircraft, resulting in a distance of 6.25 m from the fuselage symmetry plane. The research team evaluated the drone trajectory at IL3 for the CRM aircraft configuration.

Table 2 lists the primary impact locations and the corresponding aircraft configurations that the research team utilized in this study. In addition to the primary impact locations, ERAU defined secondary impact locations that had the same lateral position as that of IL1. However, the vertical position was slightly varied above and below the wing leading-edge. Details regarding the secondary impact locations are provided in Annex B:.

Table 2. Primary impact locations of the drone used for the trajectory analysis.

<b>Impact Location</b>	<b>Aircraft Configuration</b>	<b>Aircraft Region of Interest</b>	<b>Lateral Position (m)</b>
IL1	CRM	Wing	16.80
IL1	HL-CRM	Wing	16.80
IL2	CRM	Wing	4.89
IL2	HL-CRM	Wing	4.89
IL3	CRM	Horizontal Stabilizer	6.25
IL3	CRM	Horizontal Stabilizer	6.25

### 3.3 SIMULATION MATRIX DEFINITION

The research team defined nine primary impact scenarios for which the drone trajectories were evaluated in this research. The impact scenarios are defined as a combination of the impact conditions and the impact locations. The primary impact scenarios listed in Table 3 formulate the simulation matrix used in this study. The team evaluated trajectories for the first two impact

scenarios (IC1-IL1 and IC2-IL1) as part of their cross-verification study. The trajectory results for the simulation matrix and the cross-verification study are provided in the next section.

Table 3. Summary of primary impact scenarios (simulation matrix) used for the trajectory analysis.

S No.	Impact Scenario Definition	Aircraft Configuration	Impact Location on Aircraft	Aircraft Speed (m/s)	Aircraft AoA (degrees)	Drone Speed (m/s)	Drone Lateral Location (m)	University
1	IC1-IL1	CRM	Wing	102.89	0	0.00	16.80	NIAR, ERAU
2	IC2-IL1	CRM	Wing	102.89	0	25.72	16.80	NIAR, ERAU
3	IC3-IL1	CRM	Wing	102.89	5	25.72	16.80	NIAR
4	IC4-IL1	HL-CRM	Wing	102.89	0	25.72	16.80	NIAR
5	IC5-IL1	HL-CRM	Wing	87.45	0	25.72	16.80	NIAR
6	IC3-IL2	CRM	Wing	102.89	5	25.72	4.89	NIAR
7	IC4-IL2	HL-CRM	Wing	102.89	0	25.72	4.89	NIAR
8	IC2-IL3	CRM	Horizontal Stabilizer	102.89	0	25.72	6.25	ERAU
9	IC6-IL3	CRM	Horizontal Stabilizer	102.89	5	25.72	6.25	ERAU

### 3.4 METHODOLOGY OVERVIEW

NIAR and ERAU conducted a set of trajectory analyses where the drone was placed on a collision path with selected impact locations on the CRM and HL-CRM aircrafts. The research team performed the trajectory analysis using a coupled CFD-RBD approach wherein a CFD solver is coupled with a 6-DOF solver. NIAR and ERAU utilized two different numerical solvers: Ansys® Fluent, Release 18.2 and Siemens Simcenter STAR-CCM+, Version 2020.1.1 respectively, to perform the trajectory analyses.

In the simulations, overset meshes were used to capture the drone motion. Additionally, mesh adaption was used with the motion of the drone to refine the region of interest and coarsen other regions in order to reduce the computational expense. Details regarding the mesh motion and adaption are provided in Annex A: and Annex B:.

The trajectory analysis relied on partially constrained motion of the drone to allow for a flight path with constant altitude, attitude, and speed, outside of the influence of the aircraft flow field. At the start of the simulation, the drone was placed at a sufficiently far distance from the aircraft in the numerical model. This allowed a steady flow field to develop over the drone while it was outside the influence of the aircraft flow field. The partially constrained motion of the drone was implemented by balancing the aerodynamic forces and moments experienced by the drone in the steady flow field. The drone release location, i.e., the drone's distance from the aircraft at the start of each simulation in the longitudinal direction, varied based on the impact scenario and was at least 45 m. Details regarding the force balance and drone release location for each impact scenario are provided in Annex A: and Annex B:.

NIAR and ERAU first validated the CFD solver by conducting a steady-state analysis of the aircraft. Next, the research team compared the results obtained from the simulation against experimental results for the validation study. Next, the team verified the trajectory analysis methodology by conducting a cross-verification study between the two solvers used in this study. Once the cross-verification was complete, the researchers defined the simulation matrix and evaluated drone trajectory analyses on the impact scenarios defined in the simulation matrix.

#### 4. SUMMARY OF RESULTS

This section briefly describes the results obtained from this study. This section highlights the results for the validation study of the CRM aircraft flow field, the results of the cross-verification study for the trajectory analysis methodology, and the final deflections and the drone's orientation for the primary impact scenarios defined in the simulation matrix.

##### 4.1 VALIDATION OF AIRCRAFT AERODYNAMIC PERFORMANCE

NIAR and ERAU validated the numerical model used to compute a flow field analysis over the CRM aircraft by comparing the lift, drag, and pressure coefficients obtained from the simulation against experimental results [13] [14]. The operating conditions and the boundary conditions in the steady-state CFD analysis were set to match the tunnel conditions.

To capture the aerodynamic influence of the aircraft over an object in its vicinity, it is important to determine the pressure distribution over the aircraft. The pressure near the leading-edge of the wing dictates the aerodynamic influence on a nearby object. In order to validate the pressure distribution obtained from the CFD analysis, the pressure coefficient ( $C_p$ ) was obtained at six stations along the span of the wing, shown in Figure 2, for comparison with experimental results. Figure 3 shows the comparison between the  $C_p$  distribution over the wing at these spanwise stations obtained from the experiment and the simulation. There is a good correlation between the simulation results and the experimental data, especially near the wing leading-edge.

The lift and drag coefficients of the CRM aircraft are presented in Table 10. The lift coefficient obtained from the simulation is within 2% of the experimental data. The difference in the drag coefficient obtained from the simulation is more than 30% compared to the experimental data. This is most likely due to the choice of turbulence modeling strategy used in the analysis. In order to reduce the computational time, a wall-function approach was used to compute the boundary layer flow in the CFD analysis. The wall-function approach fails to compute the skin friction drag accurately. Additionally, the experimental data available for the wing-body-nacelle-pylon configuration of the CRM was obtained on a configuration without the horizontal tail. This resulted in an over prediction of drag in the numerical model compared to the experimental data. The drone's

trajectory was largely affected by the pressure distribution over the wing and not the skin friction forces. Therefore, an accurate prediction of the drag coefficient was not consequential to this study.

Additional details on the validation study for the CRM aircraft are provided in Annex A: and Annex B: NIAR also validated the computational model for the HL-CRM aircraft. The results for the validation study of the HL-CRM aircraft are provided in Annex A:.

Table 4. CRM aircraft force coefficients obtained from simulation compared against experimental data.

Force Coefficients	Experimental Data	Simulation Results	% Difference
$C_L$	0.493	0.501	1.5
$C_D$	0.026	0.035	33.3

C <sub>p</sub> Measurement Location		
Station	$\eta$	Distance from Fuselage Centerline (m)
Station 1	0.131	3.85
Station 2	0.286	8.40
Station 3	0.502	14.75
Station 4	0.603	17.72
Station 5	0.846	24.86
Station 6	0.95	27.91

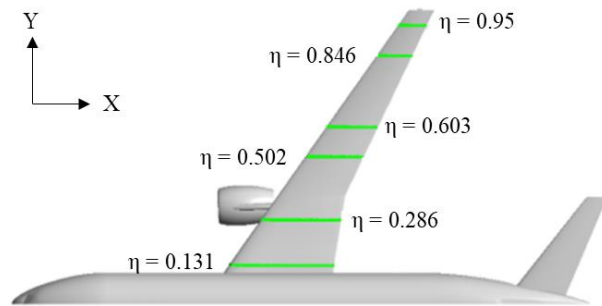


Figure 2. Spanwise locations at which the pressure coefficients are measured.

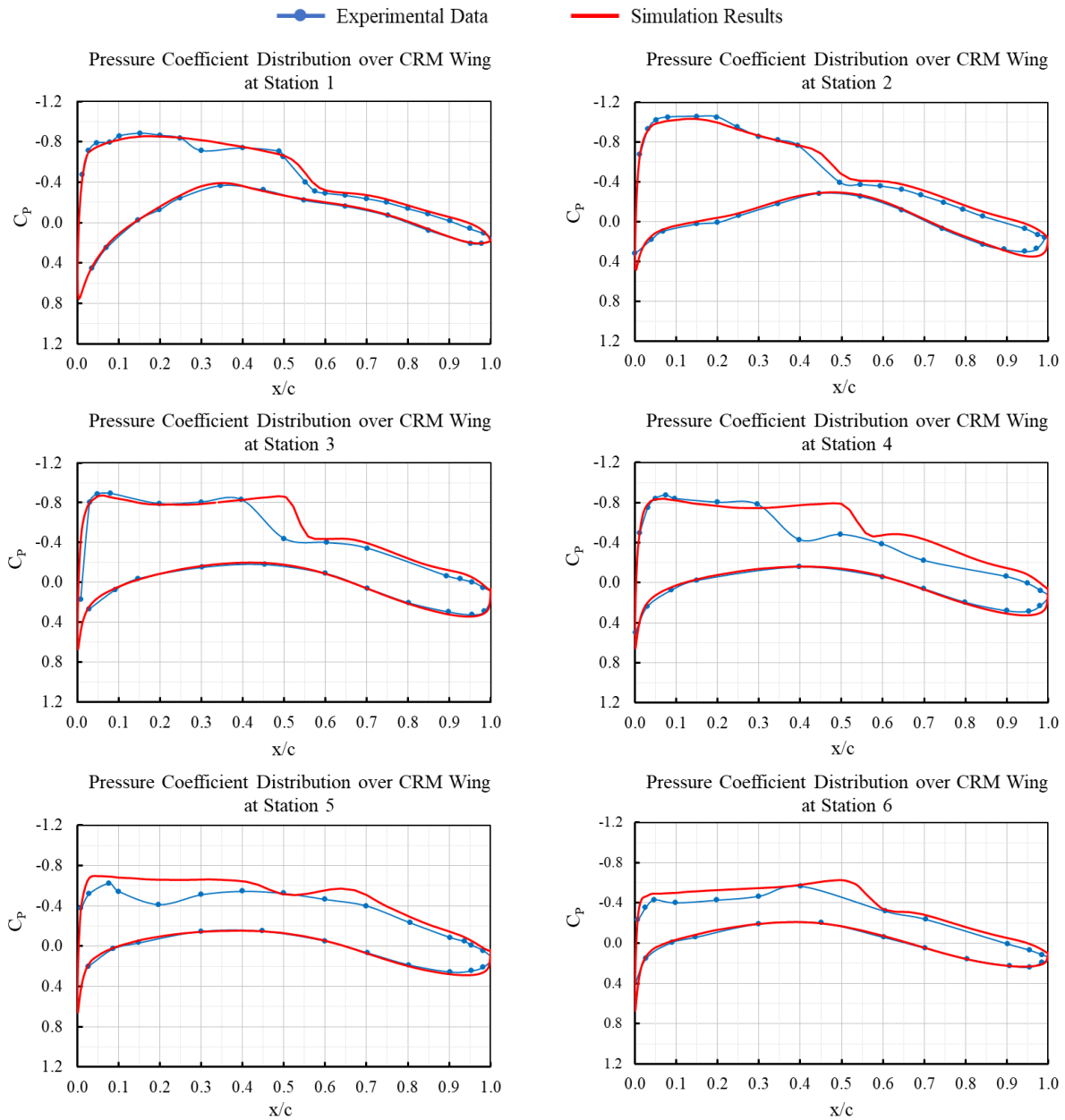


Figure 3. Pressure coefficient plots over the CRM wing at Stations 1 through 6, compared with experimental data.

#### 4.2 TRAJECTORY ANALYSIS RESULTS

Figure 4 and Figure 5 depict the sign conventions and nomenclature used to describe the results. Figure 4 shows the drone displacements about each axis and the corresponding sign convention. Along the direction of motion (X-axis), the displacement is considered positive when the drone's position is further ahead than the position from the prescribed. The displacement is considered negative when the position of the drone is further back than the position from the prescribed. The

displacement is considered positive along the Y-axis when the drone moves away from the fuselage towards the wingtip. The displacement is considered negative when the drone moves towards the fuselage. Along the Z-axis, the displacement is considered positive when the drone moves in the upward direction. The displacement is considered negative when the drone moves in the downward direction. Figure 5 shows the drone angular displacements about each axis and the corresponding sign convention. The sign convention is defined using the right-hand rule.

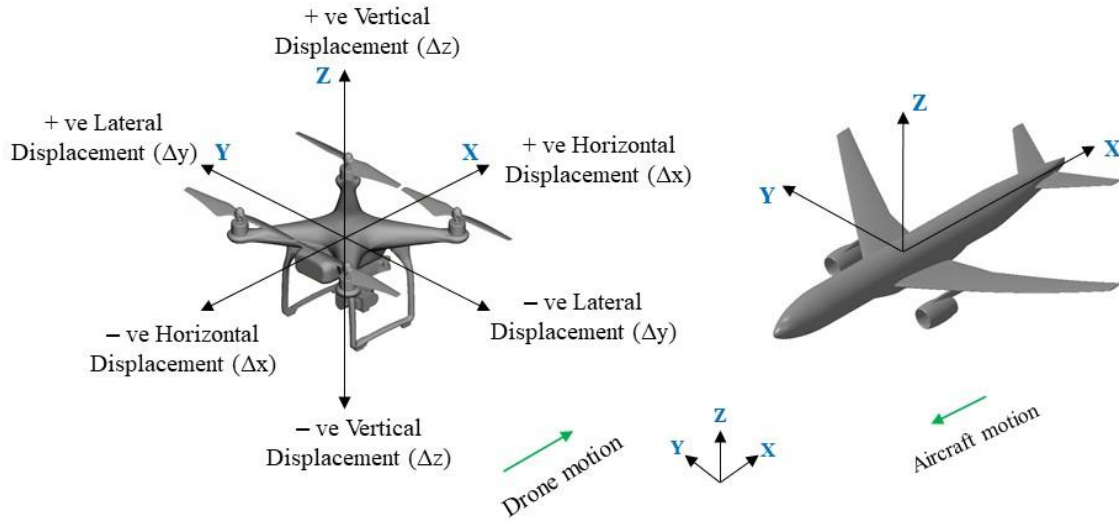


Figure 4. The sign convention used to define the displacements of the drone.

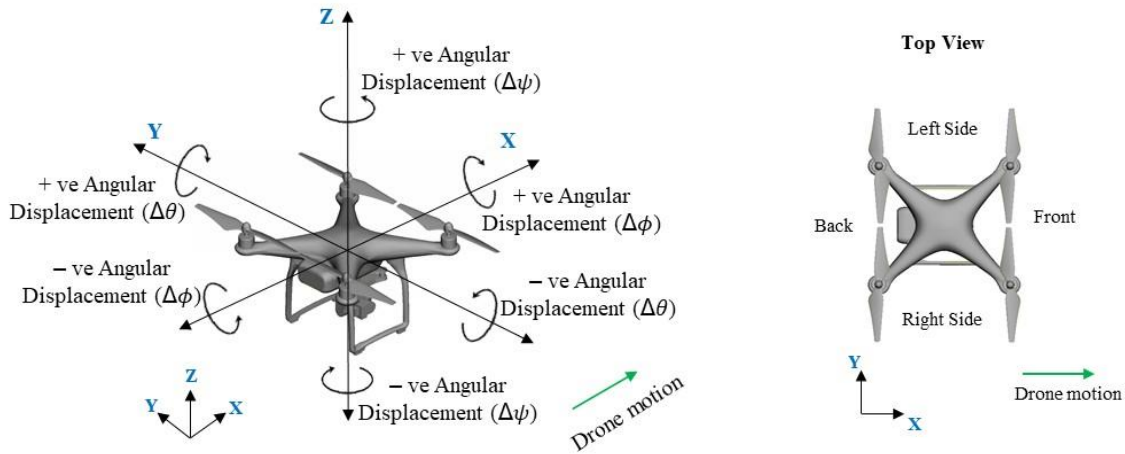


Figure 5. The sign convention used to define the angular displacements of the drone.

#### 4.2.1 Cross-Verification Study Results

NIAR and ERAU both simulated impact scenarios IC1-IL1 and IC2-IL1 for the cross-verification study. This study aimed to establish confidence in the trajectory analysis methodology and to ensure the trends established in the trajectory analysis results are independent of the solver. The final deflections of the drone and the final orientation of the drone obtained by NIAR and ERAU are compared in this section. The horizontal, lateral, and vertical displacements at the time of

impact are listed in Table 5 and graphically compared in Figure 6. The roll, pitch, and yaw angular displacements at the time of impact are listed in Table 6 and graphically compared in Figure 7. A top and side view of the pressure distribution around the drone and the aircraft at the time of impact is shown in Figure 8 and Figure 9 for the two impact scenarios.

The horizontal, lateral, and vertical displacements at the time of impact obtained by both NIAR and ERAU were small in magnitude and therefore are considered insignificant. The vertical displacement obtained by both NIAR and ERAU was less than 1 cm for the two impact scenarios. The vertical displacement of the drone needs to be at least 20 cm for the drone to deflect away from the intended impact location.

The change in orientation of the drone at the time of impact can be determined from the angular displacements. The roll, pitch, and yaw angular displacements at the time of impact obtained by NIAR and ERAU were mostly in good agreement, except for the roll angular displacement of the IC2-IL1 impact scenario. This difference was most likely due to the slight variation in the prediction of the steady-state rolling moment used in force and moment balance by the two CFD solvers.

Based on the results obtained in the cross-verification study by both NIAR and ERAU, it was observed that the drone will only slightly deflect upwards and will still impact the wing very close to the original impact location. The orientation of the drone will not remain the same compared to the original orientation at the time of impact. This change in the orientation of the drone can be observed in Figure 8 and Figure 9.

Table 5. Drone displacements for impact scenarios IC1-IL1 and IC2-IL1 obtained by NIAR and ERAU.

Drone Displacement (cm)				
	IC1-IL1		IC2-IL1	
	NIAR	ERAU	NIAR	ERAU
<b>Horizontal</b>	0.01	-0.14	0.71	0.71
<b>Lateral</b>	0.10	0.09	0.26	0.60
<b>Vertical</b>	0.13	0.17	0.25	0.89

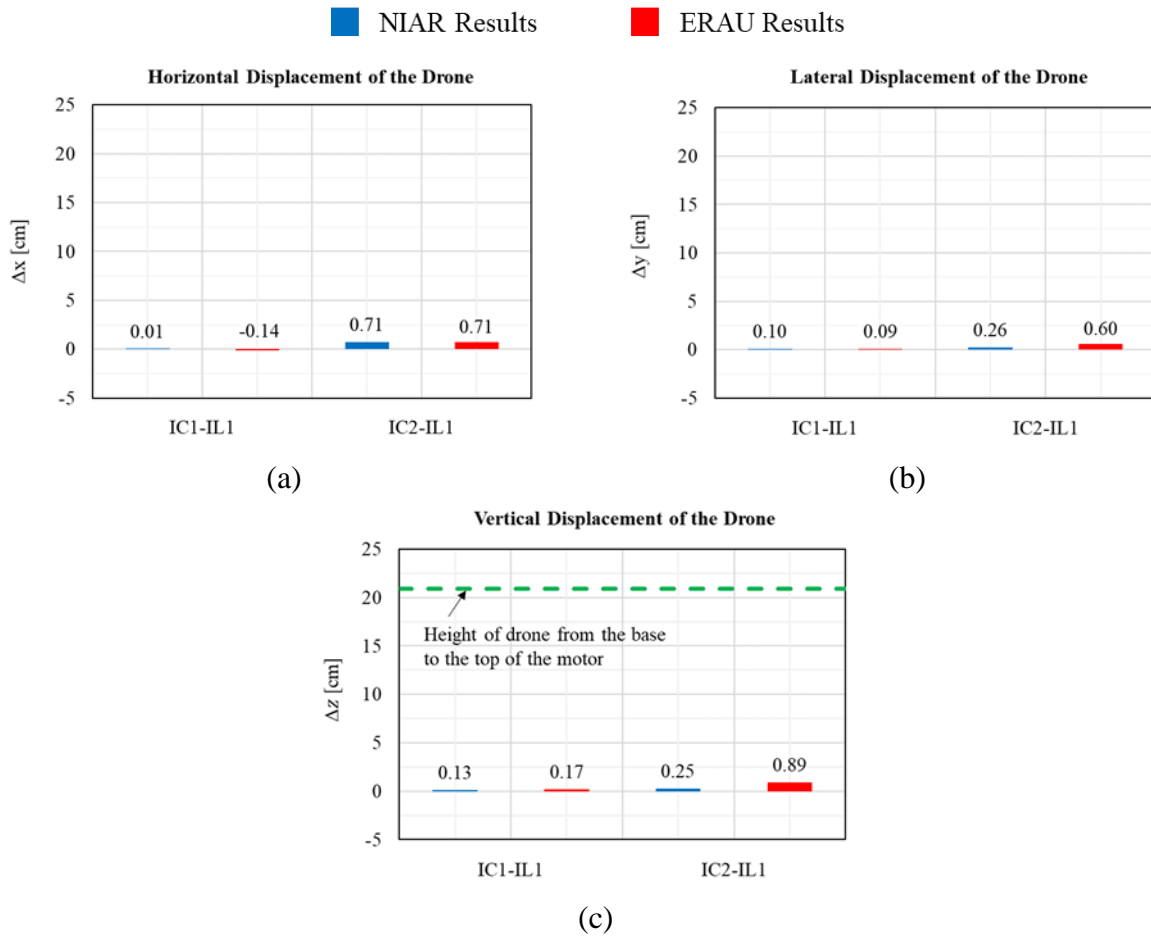


Figure 6. (a) Horizontal, (b) Lateral, and (c) Vertical displacements of the drone for impact scenario IC1-IL1 and IC2-IL1 obtained by NIAR and ERAU.

Table 6. Drone angular displacements for impact scenarios IC1-IL1 and IC2-IL1 obtained by NIAR and ERAU.

Drone Angular Displacement ( <i>degrees</i> )				
	IC1-IL1		IC2-IL1	
	NIAR	ERAU	NIAR	ERAU
<b>Roll</b>	0.13	-0.04	5.61	0.35
<b>Pitch</b>	-1.09	-0.40	-2.21	-1.50
<b>Yaw</b>	-0.28	-0.13	1.75	0.70

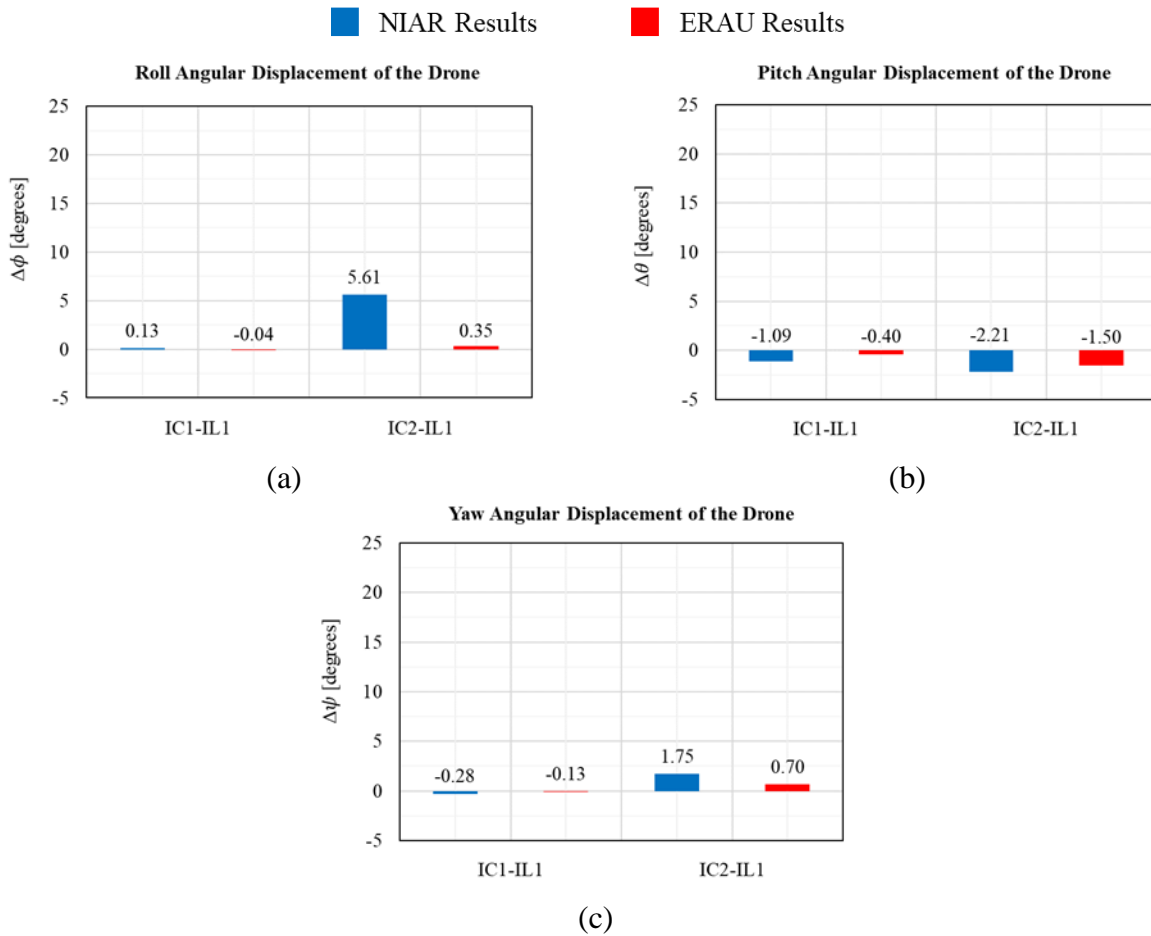


Figure 7. (a) Roll, (b) Pitch, and (c) Yaw angular displacements of the drone for impact scenario IC1-IL1 and IC2-IL1 obtained by NIAR and ERAU.



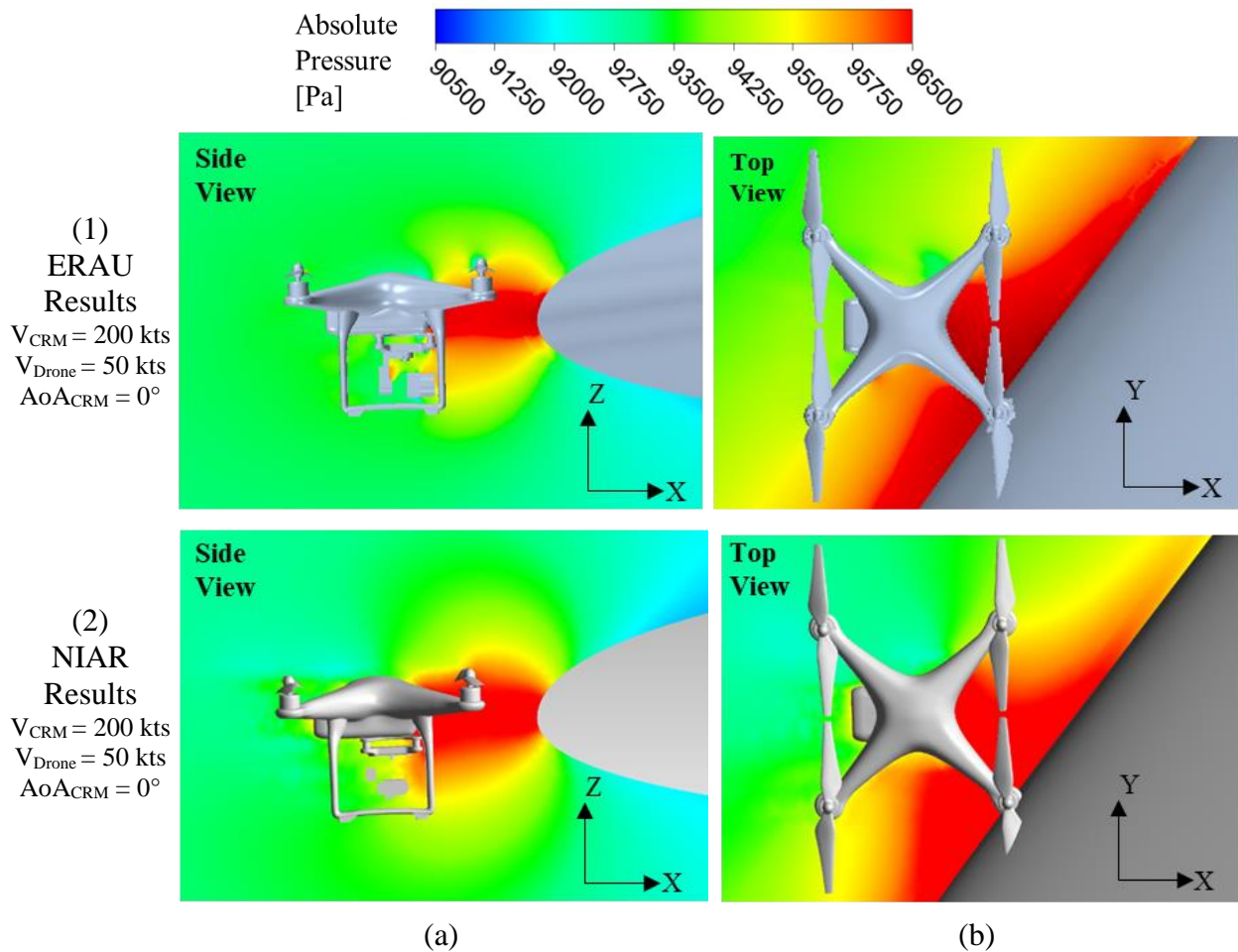


Figure 9. (a) Side and (b) Top view of the pressure contour over the drone approximately at the time of impact for impact scenario IC2-IL1 obtained by (1) ERAU and (2) NIAR.

#### 4.2.2 Simulation Matrix Results of Primary Impact Scenarios

NIAR and ERAU analyzed the drone trajectories for the simulation matrix of the primary impact scenarios listed in Table 3. The final deflections of the drone and the final orientation of the drone obtained by NIAR and ERAU for the primary impact scenarios are provided in this section. The horizontal, lateral, and vertical displacements at the time of impact are listed in Table 7 and graphically compared in Figure 10. The roll, pitch, and yaw angular displacements at the time of impact are listed in Table 8 and graphically compared in Figure 11. The complete time history of the simulated trajectory and the pressure contours at selected time steps are provided in Annex A: and Annex B: of the report.

The vertical displacement of the drone was the most relevant parameter that determined whether the drone would impact at a specified location on the aircraft or deflect away. The key findings from the results shown in this section are:

- Effect of Impact Location on Wing: The vertical displacement was higher for the impact scenario IC3-IL2, where the impact location was near the wing root, compared to IC3-IL1, where the impact location was near mid-span of the wing. The lateral displacement was also higher for IC3-IL2 compared to IC3-IL1. The impact scenario IC3-IL2 resulted in the largest yaw angular displacement out of all the primary impact scenarios. This indicates that the wing root area and the fuselage have a larger aerodynamic influence on the drone trajectory.
- Effect of Aircraft Velocity: The effect of aircraft velocity on the drone trajectories was small. The vertical displacements for the impact scenarios IC4-IL1 (aircraft velocity of 200 kts) and IC5-IL1 (aircraft velocity of 170 kts) were almost identical.
- Effect of Drone Velocity: The effect of drone velocity was evident from the trajectories obtained for impact scenarios IC1-IL1 (drone velocity of 0 kts) and IC2-IL1 (drone velocity of 50 kts). For the faster-moving drone case, the linear and angular displacements were higher.
- Effect of High Lift Devices: The vertical displacement of the drone was higher for the HL-CRM impact scenarios compared to the corresponding CRM impact scenarios. This indicates that high lift devices have a larger aerodynamic influence on the drone trajectory.
- Effect of AoA: The vertical displacement of the drone was higher for the 5° AoA impact scenarios compared to the 0° AoA impact scenarios. This indicates that the larger the AoA, the larger the aerodynamic influence on the drone trajectory.
- Horizontal Stabilizer vs. Wing: In case of the 0° AoA, the vertical displacement of the drone was smaller for the horizontal stabilizer impact location (IC2-IL3) compared to the wing impact location (IC2-IL1). However, for the 5° AoA, the vertical displacement of the drone was much higher for the horizontal stabilizer impact location (IC6-IL3) compared to the wing impact location (IC3-IL1). The angular displacements of the drone were high for both the horizontal stabilizer impact scenarios, especially the pitch angle. This is most likely due to the influence of the wing flow field on the drone trajectory as it approaches the horizontal stabilizer. Additionally, the wing downwash impacts the horizontal stabilizer flow field. The drone is in the aircraft flow field longer as it traverses the length of the aircraft prior to impacting the horizontal stabilizer.

The results for all the primary impact scenarios indicate that the drone slightly deflects upwards and still impacts the wing/horizontal stabilizer very close to the original impact location. The orientation of the drone does not remain the same compared to the original orientation at the time of impact.

Table 7. Drone displacements at the point of impact for primary impact scenarios.

Impact Scenario Definition	Aircraft Configuration	Impact Location on Aircraft	Drone Displacements ( <i>cm</i> )		
			Horizontal ( $\Delta x$ )	Lateral ( $\Delta y$ )	Vertical ( $\Delta z$ )
IC1-IL1	CRM	Wing	0.01	0.10	0.13
IC2-IL1	CRM	Wing	0.71	0.26	0.25
IC3-IL1	CRM	Wing	1.26	0.30	1.25
IC4-IL1	HL-CRM	Wing	1.13	0.16	1.93
IC5-IL1	HL-CRM	Wing	1.17	0.13	2.06
IC3-IL2	CRM	Wing	-3.93	4.93	3.30
IC4-IL2	HL-CRM	Wing	-3.46	4.82	2.49
IC2-IL3	CRM	Horizontal Stabilizer	-13.08	0.09	0.08
IC6-IL3	CRM	Horizontal Stabilizer	-0.03	6.91	3.93

Table 8. Drone angular displacements at the point of impact for primary impact scenarios.

Impact Scenario Definition	Aircraft Configuration	Impact Location on Aircraft	Drone Angular Displacements ( <i>degrees</i> )		
			Roll ( $\Delta \phi$ )	Pitch ( $\Delta \theta$ )	Yaw ( $\Delta \psi$ )
IC1-IL1	CRM	Wing	0.13	-1.09	-0.28
IC2-IL1	CRM	Wing	5.61	-2.21	1.75
IC3-IL1	CRM	Wing	1.96	-2.65	0.73
IC4-IL1	HL-CRM	Wing	1.43	-4.48	0.20
IC5-IL1	HL-CRM	Wing	1.38	-0.11	1.42
IC3-IL2	CRM	Wing	7.85	-1.76	10.61
IC4-IL2	HL-CRM	Wing	7.02	-2.92	9.68
IC2-IL3	CRM	Horizontal Stabilizer	3.83	-24.74	7.45
IC6-IL3	CRM	Horizontal Stabilizer	15.29	-20.08	-4.56

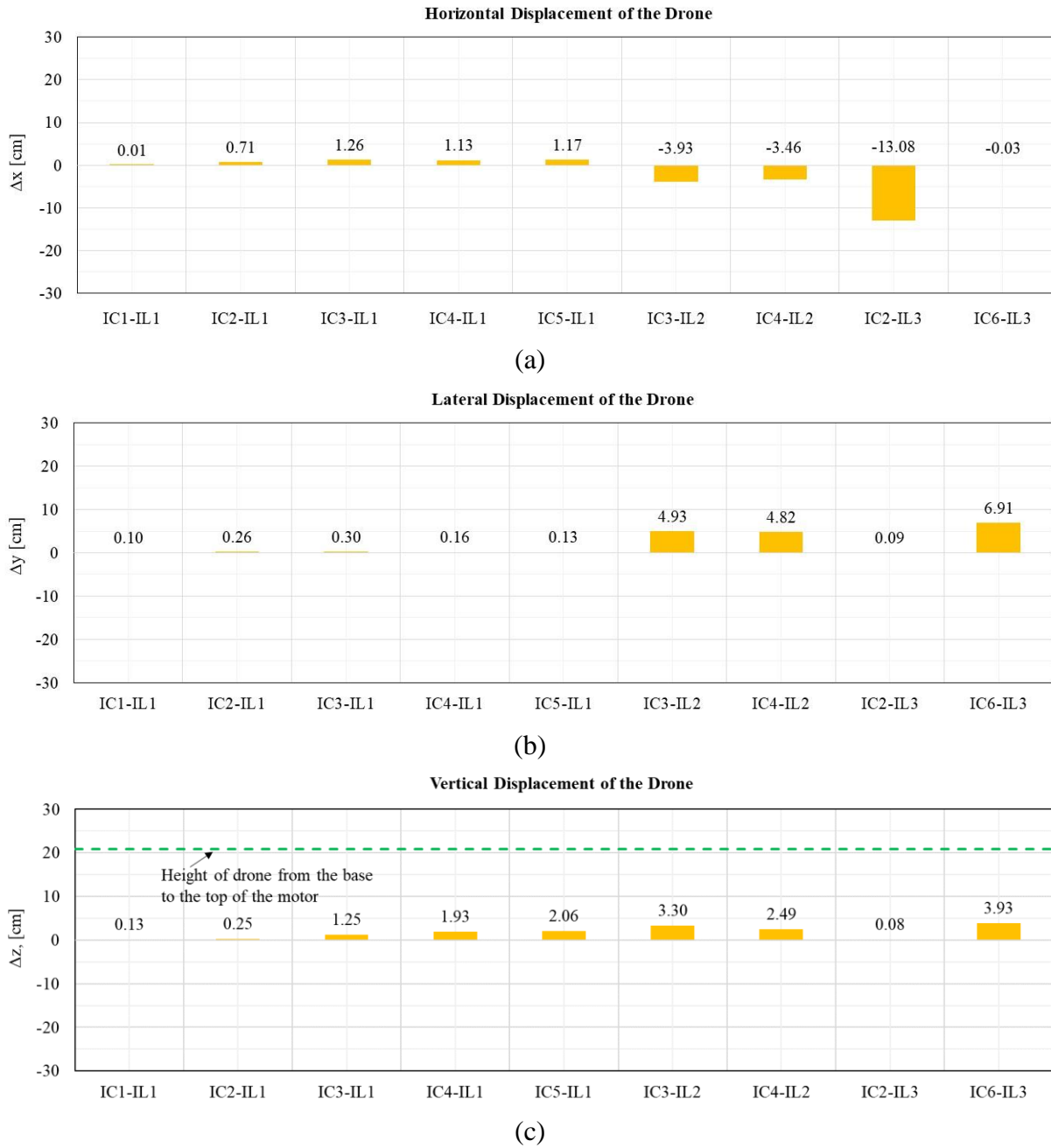
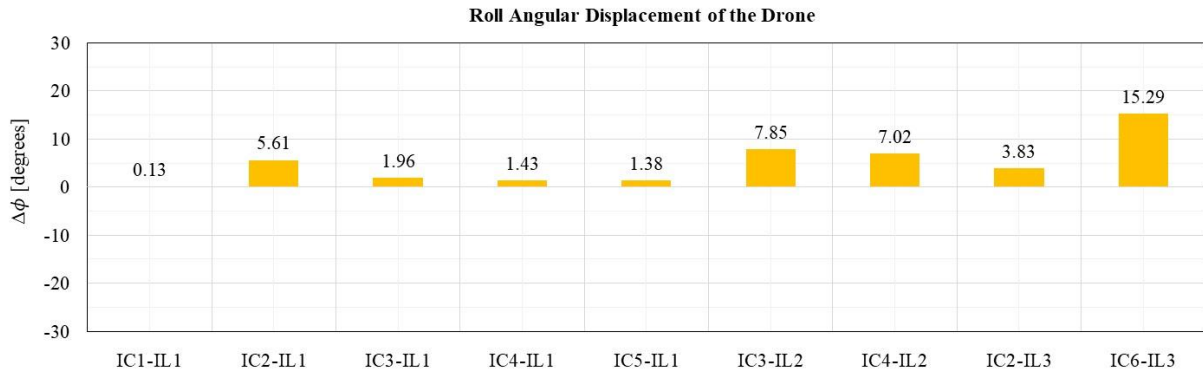
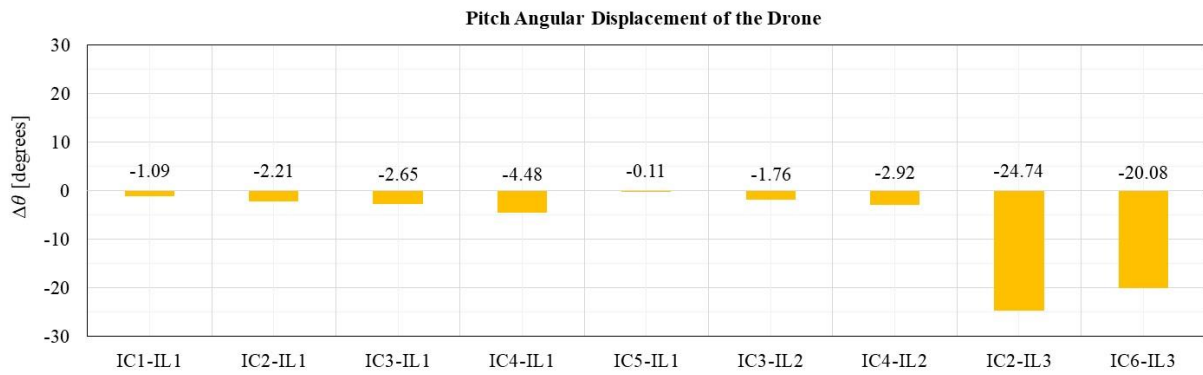


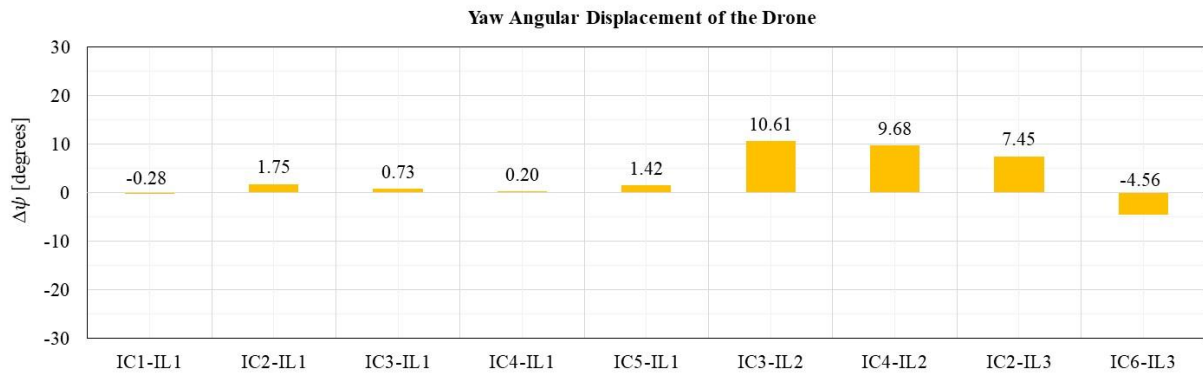
Figure 10. (a) Horizontal, (b) Lateral, and (c) Vertical displacements of the drone at the point of impact for primary impact scenarios.



(a)



(b)



(c)

Figure 11. (a) Roll, (b) Pitch, and (c) Yaw angular displacements of the drone at the point of impact for primary impact scenarios.

## 5. KEY CONCLUSIONS AND RECOMMENDATIONS

The A16 Task 1 study, conducted by NIAR and ERAU, addressed the question of whether or not a sUAS would be deflected prior to impact with a large transport aircraft. The research team performed a series of simulations varying the impact location, aircraft and drone velocities, angle of attack, and aircraft configuration.

The study investigated the differences in deflections of the sUAS on impact with a wing and a horizontal stabilizer. The vertical deflections of the sUAS were small for both the impact locations.

For the impact location at near mid span of the wing, the range of vertical deflections was 0.13 to 2.06 cm. This range corresponds to 0.2% to 2.1% of the required deflections necessary to avoid impact. For the impact location near root of the wing, the range of vertical deflections was 2.49 to 3.30 cm. This range corresponds to 1.7% to 8.2% of the required deflections necessary to avoid impact. For the impact location at near mid span of the horizontal stabilizer, the range of vertical deflections was 0.08 to 3.93 cm. This range corresponds to 0.1% to 7.5% of the required deflections necessary to avoid impact. These results indicate that the drone will only slightly deflect upwards and will not deflect away prior to impact with a large transport aircraft on both the wing and the horizontal stabilizer.

For the impact locations on the wing, the range of roll angle displacement was  $0.13^{\circ}$  to  $7.85^{\circ}$ , the range of pitch angle displacement was  $-4.48^{\circ}$  to  $-0.11^{\circ}$ , and the range of yaw angle displacement was  $-0.28^{\circ}$  to  $10.61^{\circ}$ . For the impact location on the horizontal stabilizer, the range of roll angle displacement was  $3.83^{\circ}$  to  $15.29^{\circ}$ , the range of pitch angle displacement was  $-20.08^{\circ}$  to  $-24.74^{\circ}$ , and the range of yaw angle displacement was  $-4.56^{\circ}$  to  $7.45^{\circ}$ . These results indicate that the orientation of the drone will change relative to the original orientation at the time of impact with a large transport aircraft on both the wing and the horizontal stabilizer.

The research team also investigated the relationship between flight parameters and the sUAS deflections. The research showed that higher relative speeds and higher angles of attack result in slightly higher vertical deflections of the sUAS.

The main conclusion of Task 1 was that sUAS of size and weight similar to a DJI Phantom III would not deflect away from a collision path with a large transport aircraft under only the aerodynamic influence of the aircraft.

This study did not consider additional atmospheric factors like turbulence and gusts in this study. Atmospheric turbulence or wind/gust conditions in combination with the aerodynamic interaction between a sUAS and a large transport aircraft may deflect the drone enough to avoid impact. In addition, the research team only investigated the trajectory of one quadcopter sUAS. A smaller UAS in size and weight may have a higher probability to deflect prior impact. There is a need for additional research to understand better the effect of size of the sUAS and the effect of atmospheric factors on sUAS trajectories that lead up to impact with a larger aircraft.

## 6. REFERENCES

- [1] J. Gundlach, “Overview of Unmanned Aircraft Systems”, Designing Unmanned Aircraft Systems, 2012.
- [2] Lum, C. W., and Waggoner, B., “A Risk Based Paradigm and Model for Unmanned Aerial Systems in the National Airspace”, Infotech@Aerospace Conferences, 2011-1424, AIAA, St. Louis, MO, 2011.
- [3] FAA, “Overview of Small UAS Notice of Proposed Rulemaking,” [http://www.faa.gov/regulations\\_policies/rulemaking/media/021515\\_sUAS\\_Summary.pdf](http://www.faa.gov/regulations_policies/rulemaking/media/021515_sUAS_Summary.pdf), 2015.
- [4] Olivares, G., Gomez, L., Espinosa de los Monteros, J., Baldrige, R., and Zinzuwadia, C., “Volume II – UAS Airborne Collision Severity Evaluation – Quadcopter”, Federal Aviation Administration, Report DOT/FAA/AR-XX/XX, 2017.
- [5] U.S. Code of Federal Regulations, Title 14, Part 25, “Airworthiness standards: transport category airplanes”, Washington, DC, U.S. Government Publishing Office, 2016.
- [6] The 6th AIAA CFD Drag Prediction Workshop, June 2016. <https://aiaa-dpw.larc.nasa.gov/>
- [7] M. B. Rivers and A. Dittberner, “Experimental investigations of the NASA common research model,” 2014, DOI: 10.2514/1.C032626.
- [8] Tinoco, E.N., Brodersen, O.P., Keye, S., Laflin, K.R., Feltrop, E., Vassberg, J.C., Mani, M., Rider, B., Wahls, R.A., Morrison, J.H. and Hue, D., “Summary data from the sixth AIAA CFD drag prediction workshop: CRM cases”, Journal of Aircraft, Vol. 55, No. 4, pp.1352-1379, 2018.
- [9] The 3rd AIAA CFD High Lift Prediction Workshop, April 2019. <https://hiliftpw.larc.nasa.gov/Workshop3/testcases.html>.
- [10] U.S. Code of Federal Regulations, Title 14, Part 25, “Airworthiness standards: transport category airplanes,” Washington, DC, U.S. Government Publishing Office, 2016.
- [11] U.S. Department of Transportation, Federal Aviation Administration, “Aeronautical Information Manual: Official Guide to Basic Flight Information and ATC Procedures”, Washington, DC, U.S. Government Publishing Office, 1995.
- [12] D. S. Cairns, G. Johnson, M. Edens, and F. Arnold, “Volume I – UAS Airborne Collision Severity – Projectile and Target Definitions.” [Online]. Available: <https://www.assureuas.org/projects/deliverables/a3/Volume I UAS Airborne Collision Severity Projectile and Target Definition.pdf>.
- [13] Koklu, M., Lin, J. C., Hannon, J. A., Melton, L. P., Andino, M. Y., Paschal, K. B., Vatsa V. N., “Wind Tunnel Testing of Active Flow Control on High-Lift Common Research Model”, AIAA Aviation 2019 Forum, Hampton, VA, June 2019.
- [14] Koklu, M., Lin, J. C., Hannon, J. A., Melton, L. P., Andino, M. Y., Paschal, K. B., Vatsa V. N., “Mitigation of Nacelle/Pylon Wake on the High-Lift Common Research Model Using a Nacelle Chine”, AIAA SciTech 2020 Forum, Hampton, VA, January 2020.

## Annex A: NIAR Final Report

Air Traffic Organization  
NextGen & Operations Planning  
Office of Research and  
Technology Development  
Washington, DC 20591



## **WSU/NIAR**

# **Annex A – UAS Airborne Collision Severity Evaluation: Assessment of sUAS deflections due to aerodynamic interaction with a commercial aircraft**

October 2021

Final Report

This document is available to the U.S. public through the National Technical Information Services (NTIS), Springfield, Virginia 22161.

This document is also available from the Federal Aviation Administration William J. Hughes Technical Center at [actlibrary.tc.faa.gov](http://actlibrary.tc.faa.gov).



U.S. Department of Transportation  
**Federal Aviation Administration**

## **NOTICE**

This document is disseminated under the sponsorship of the U.S. Department of Transportation in the interest of information exchange. The U.S. Government assumes no liability for the contents or use thereof. The U.S. Government does not endorse products or manufacturers. Trade or manufacturers' names appear herein solely because they are considered essential to the objective of this report. The findings and conclusions in this report are those of the author(s) and do not necessarily represent the views of the funding agency. This document does not constitute FAA policy. Consult the FAA sponsoring organization listed on the Technical Documentation page as to its use.

This report is available at the Federal Aviation Administration William J. Hughes Technical Center's Full-Text Technical Reports page: [actlibrary.tc.faa.gov](http://actlibrary.tc.faa.gov) in Adobe Acrobat portable document format (PDF).

**Legal Disclaimer:** The information provided herein may include content supplied by third parties. Although the data and information contained herein has been produced or processed from sources believed to be reliable, the Federal Aviation Administration makes no warranty, expressed or implied, regarding the accuracy, adequacy, completeness, legality, reliability or usefulness of any information, conclusions or recommendations provided herein. Distribution of the information contained herein does not constitute an endorsement or warranty of the data or information provided herein by the Federal Aviation Administration or the U.S. Department of Transportation. Neither the Federal Aviation Administration nor the U.S. Department of Transportation shall be held liable for any improper or incorrect use of the information contained herein and assumes no responsibility for anyone's use of the information. The Federal Aviation Administration and U.S. Department of Transportation shall not be liable for any claim for any loss, harm, or other damages arising from access to or use of data or information, including without limitation any direct, indirect, incidental, exemplary, special or consequential damages, even if advised of the possibility of such damages. The Federal Aviation Administration shall not be liable to anyone for any decision made or action taken, or not taken, in reliance on the information contained herein.

**Technical Report Documentation Page**

1. Report No.		2. Government Accession No.		3. Recipient's Catalog No.	
4. Title and Subtitle  <b>Volume I – UAS Airborne Collision Severity Evaluation: Assessment of sUAS deflections due to aerodynamic interaction with a commercial aircraft</b>				5. Report Date <b>October 2021</b>	
				6. Performing Organization Code	
7. Author(s) <b>Gerardo Olivares, Harsh Shah, Luis Gomez, Nidhi Sathyanarayana.</b>				8. Performing Organization Report No.	
9. Performing Organization Name and Address  National Institute for Aviation Research Wichita State University 1845 Fairmount Wichita, KS 67260-0093				10. Work Unit No. (TRAIS)	
				11. Contract or Grant No.	
12. Sponsoring Agency Name and Address  U.S. Department of Transportation Federal Aviation Administration Office of Aviation Research Washington, DC 20591				13. Type of Report and Period Covered	
				14. Sponsoring Agency Code	
15. Supplementary Notes					
16. Abstract  The A16 Unmanned Aircraft System (UAS) Airborne Collision Severity Evaluation was an extension of the A3 study that focused on severity evaluation of an Unmanned Air Systems (UAS) airborne collision with a Narrow Body Commercial Aircraft and a Business Jet. The research presented in this report addresses the question of whether or not a sUAS would be deflected prior to impact with a large transport aircraft. Using Computational Fluid Dynamics (CFD) methods coupled with a six-degrees-of-freedom (6-DOF) solver, it was determined that the vertical deflections were not large enough for the sUAS to deflect away from the intended impact location for any of the three impact locations. It was also determined that the final orientation of the sUAS at impact differed slightly from the initial orientation. Based on these findings, the research team concluded that the aerodynamic interaction between a DJI Phantom III drone and a large transport category aircraft would: 1) not cause the drone to deflect away prior to impact with the wing or the horizontal stabilizer, and 2) modify the orientation of the drone at the time of impact with the wing or the horizontal stabilizer.					
17. Key Words  <b>sUAS, UAS, Deflection, Trajectory, Crashworthiness, Airborne Collision, National Institute for Aviation Research, NIAR</b>			18. Distribution Statement  This document is available to the U.S. public through the National Technical Information Service (NTIS), Springfield, Virginia 22161. This document is also available from the Federal Aviation Administration William J. Hughes Technical Center at <a href="http://actlibrary.tc.faa.gov">actlibrary.tc.faa.gov</a> .		
19. Security Classif. (of this report)  Unclassified		20. Security Classif. (of this page)  Unclassified		21. No. of Pages	22. Price

## REVISION HISTORY

Revision	Description of Modifications	Release Date
IR	Initial release	10/30/2021
	-	

## TABLE OF CONTENTS

Chapter	Page
TABLE OF CONTENTS	VII
LIST OF FIGURES	X
LIST OF TABLES	XVII
LIST OF ACRONYMS	XIX
LIST OF SYMBOLS	XX
1. INTRODUCTION	1
1.1 Background	1
1.2 Project Scope	1
1.3 Target Definition – Commercial Transport Aircraft	2
1.4 Projectile Definition – UAS Quadcopter	3
1.5 Impact Scenario Definition	4
1.5.1 Selection of Impact Velocities	4
1.5.2 Impact Condition Definition	5
1.5.3 Impact Location Definition	7
1.5.4 Summary of Impact Scenario Definition	10
2. VALIDATION – AIRCRAFT AERODYNAMIC PERFORMANCE	11
2.1 Overview	11
2.2 Geometry	11
2.2.1 CRM Aircraft	11
2.2.2 HL-CRM Aircraft	13
2.3 CRM Aerodynamic Performance Validation	14
2.3.1 Introduction	14
2.3.2 Mesh	15

2.3.3 Numerical Model	17
2.3.4 Results	18
2.4 HL-CRM Aerodynamic Performance Validation	21
2.4.1 Introduction	21
2.4.2 Mesh	22
2.4.3 Numerical Model	24
2.4.4 Results	25
2.5 Conclusions of Aircraft Aerodynamic Performance	28
3. UAS TRAJECTORY ANALYSIS	29
3.1 Overview	29
3.2 Methodology	30
3.2.1 Computational Fluid Dynamics	31
3.2.2 Rigid Body Dynamics	31
3.2.3 Overset Mesh Method	32
3.2.4 Mesh Adaption	34
3.3 Assumptions	35
3.4 Drone Release Location	36
3.4.1 Release Location with Fuselage	37
3.4.2 Release Location without Fuselage	37
3.5 Relative Distance Definition	39
3.6 Sign Convention and Axis-System Definition	39
3.7 UAS Force and Moment Balance	41
3.8 Mesh Definition	43
3.9 Numerical Model	45
3.9.1 Boundary Conditions and Operating Conditions	45
3.9.2 Solver Setup	46
3.10 Trajectory Analysis Results	47
3.10.1 Cross-Verification Results	48
3.10.2 Summary of Simulation Matrix Results	58
4. CONCLUSIONS	67

5. REFERENCES

68

APPENDIX A – MESH PARAMETERS AND QUALITY INFORMATION..... A-1  
APPENDIX B – USER-DEFINED FUNCTION FOR CFD-RBD COUPLING.....B-1  
APPENDIX C – UAS TRAJECTORY ANALYSIS RESULTS .....C-1

## LIST OF FIGURES

Figure	Page
1. CRM aircraft geometry compared with a traditional Part 25 transport category aircraft (Boeing 777-200) [6].	3
2. The CAD model of the drone and the CG location with respect to the origin.	4
3. Drone and propeller orientation angles.	4
4. Side view showing the vertical placement of the drone with respect to (a) CRM aircraft ( $0^\circ$ AoA), (b) CRM aircraft ( $5^\circ$ AoA), and (c) HL-CRM aircraft ( $0^\circ$ AoA).	7
5. Critical impact location identified on the commercial jet aircraft wing from the A3 Airborne Collision Severity Evaluation study [3].	8
6. The lateral position of the drone at IL1 as it approaches the (a) CRM aircraft and (b) HL-CRM aircraft.	9
7. Lateral position of the drone at IL2 as it approaches the (a) CRM aircraft and (b) HL-CRM aircraft.	10
8. Isometric view of the CRM aircraft.	12
9. CRM aircraft at (a) $0^\circ$ AoA and (b) $5^\circ$ AoA.	13
10. Location of the center of gravity of the aircraft and a representation of the rotated aircraft geometry.	13
11. Isometric view of the HL-CRM aircraft.	14
12. Domain surface mesh and size boxes used for CRM aircraft wake refinement.	15
13. CRM aircraft surface mesh details.	16
14. Surface mesh element length information on the CRM aircraft.	16
15. Prism and tetrahedral volume mesh generated for CRM aircraft.	17
16. Boundary conditions used for the CRM aircraft validation study.	18
17. Lateral positions where $C_p$ is available in experimental data on the CRM wing.	19
18. Absolute pressure contours over the CRM aircraft surface from the (a) Top view and (b) Bottom view.	20
19. Pressure contours over the wing at planes located at Stations 1 and 5 lateral locations.	20
20. Pressure coefficient plots over the CRM wing at Stations 1 through 6 compared with experimental data.	21
21. Domain surface mesh and size boxes were used to define wake refinement for the HL-CRM aircraft.	22
22. HL-CRM aircraft surface mesh details.	23
23. Surface mesh element length information on the HL-CRM aircraft.	23

24. Element lengths used on the HL-CRM aircraft surfaces in proximity.	23
25. Prism and tetrahedral volume mesh generated for the HL-CRM aircraft.	24
26. Boundary conditions used for HL-CRM validation study.	25
27. Lateral positions where $C_p$ is available in experimental data on the HL-CRM wing.	26
28. Absolute pressure contours over the HL-CRM aircraft surface from the (a) Top view and (b) Bottom view.	27
29. Pressure contours over the HL-CRM wing at Stations 1 and 2.	27
30. Comparison of simulation and experimental pressure coefficient distributions over the HL-CRM wing, slat, and flap at Stations 1 and 2.	28
31. An overview of the coupling between the CFD solver and the RBD solver in Ansys <sup>®</sup> Fluent.	30
32. Overset interface definition.	33
33. Initialization process of an overset mesh in Ansys <sup>®</sup> Fluent.	33
34. Representation of the overset mesh (a) Before and (b) After the hole cutting operation.	34
35. Representation of the overset mesh (a) Without minimization and (b) With cell-based minimization.	34
36. Mesh adaption process as the drone moves through the domain.	35
37. Absolute pressure measurement locations upstream of the CRM aircraft wing leading-edge for impact scenario IC3-IL2.	36
38. Pressure field within the domain (a) With the fuselage and (b) Without the fuselage at the lateral location of the drone at IL1.	38
39. Coefficient of Pressure distribution over the wing at IL1 for the CRM with and without the fuselage.	38
40. Relative distance between the drone and the (a) CRM aircraft and (b) HL-CRM aircraft as seen from the top view.	39
41. Representation of the (a) Global inertial reference frame, $XYZ$ , (b) Drone body-fixed reference frame, $X_{DB}Y_{DB}Z_{DB}$ , (c) Translating inertial reference frame, $X_TY_TZ_T$ .	40
42. Force and moment definition for the (a) Drone and (b) Aircraft in the global axis system.	41
43. Nomenclature used to define the drone sign convention.	41
44. Aerodynamic and external forces and moments on the drone.	42
45. Force and moment balance on the drone within the UDF.	43
46. Background mesh and domain with size boxes for aircraft wake refinement.	43
47. Component volume mesh and domain generated around the drone.	44
48. Computational domain and boundary conditions.	45
49. Displacements experienced by the drone and the sign convention used.	47

50.	The sign convention used to define the angular displacements of the drone.	48
51.	Time history of (a) Displacements and (b) Angular displacements of the drone obtained by ERAU and NIAR for impact scenario IC1-IL1.	50
52.	Time history of the change in (a) Velocities and (b) Angular velocities of the drone obtained by ERAU and NIAR for impact scenario IC1-IL1.	51
53.	Time history of (a) Displacements and (b) Angular displacements of the drone obtained by ERAU and NIAR for impact scenario IC2-IL1.	52
54.	Time history of the change in (a) Velocities and (b) Angular velocities of the drone obtained by ERAU and NIAR for impact scenario IC2-IL1.	53
55.	(a) Horizontal, (b) Lateral, and (c) Vertical displacements of the drone for impact scenario IC1-IL1 and IC2-IL1 obtained by ERAU and NIAR.	54
56.	(a) Roll, (b) Pitch, and (c) Yaw angular displacements of the drone for impact scenario IC1-IL1 and IC2-IL1 obtained by ERAU and NIAR.	55
57.	(a) Side and (b) Top view of the pressure contour over the drone when the relative distance is approximately 0 m for impact scenario IC1-IL1 obtained by (1) ERAU and (2) NIAR.	56
58.	(a) Side view and (b) Top view of the pressure contour over the drone when the relative distance is approximately 0 m for impact scenario IC2-IL1 obtained by (1) ERAU and (2) NIAR.	57
59.	Representation of the vertical displacement required by the drone in order to avoid impacting the (a) CRM aircraft and the (b) HL-CRM aircraft.	58
60.	(a) Vertical and (b) Lateral displacement of the drone at the point of impact for IC1-IL1, IC2-IL1, and IC3-IL1.	60
61.	(a) Side view and (b) Top view of the pressure contour over the drone when the relative distance is approximately 0 m, for (1) IC1-IL1, (2) IC2-IL1, and (3) IC3-IL1.	61
62.	(a) Vertical and (b) Lateral displacements of the drone at the point of impact for IC4-IL1 and IC5-IL1.	62
63.	(a) Side view and (b) Top view of the pressure contour over the drone when the relative distance is approximately 0 m, for (1) IC4-IL1 and (2) IC5-IL1.	62
64.	(a) Vertical and (b) Lateral displacements of the drone at the point of impact for IC3-IL2 and IC4-IL2.	63
65.	(a) Side view and (b) Top view of the pressure contour over the drone when the relative distance is approximately 0 m, for (1) IC3-IL2 and (2) IC4-IL2.	63
66.	(a) Horizontal, (b) Lateral, and (c) Vertical displacements of the drone at the point of impact.	65
67.	(a) Roll, (b) Pitch, and (c) Yaw angular displacements of the drone at the point of impact.	66
68.	Size boxes generated around the CRM aircraft for volume mesh refinement.	A-1

69.	Size boxes generated around the HL-CRM aircraft for volume mesh refinement.	A-3
70.	Size boxes are generated within the domain to capture the aircraft wake.	A-5
71.	Background mesh and component mesh dimensions and details at release location.	A-6
72.	Surface mesh refinement on aircraft and additional size boxes created to obtain a good transition from hexahedral to tetrahedral elements.	A-7
73.	Component mesh details from an (a) Isometric view and (b) Cross-sectional view depicting the drone and prism layers.	A-8
74.	Prescribed motion portion of the UDF used in the 6-DOF solver with comments.	B-1
75.	A section of the UDF that is used during the drone prescribed motion for impact scenario IC2-IL1.	B-2
76.	The RBD motion portion of the UDF used to calculate the trajectory by the 6-DOF solver.	B-3
77.	A section of the UDF used during the RBD motion of the drone for impact scenario IC2-IL1.	B-4
78.	Representation of data filtering on drone aerodynamic forces measured about the (a) X-axis and (b) Z-axis.	C-1
79.	XY-plane created to obtain a top view of pressure contours over the drone and aircraft at the lateral stations of (a) IL1 and (b) IL2.	C-2
80.	XZ-plane created to obtain a side view of pressure contours over the drone and aircraft at the lateral stations of (a) IL1 and (b) IL2.	C-2
81.	Axis system used for the drone.	C-3
82.	CRM aircraft (a) Drag force and (b) Lift force recorded as the drone approached the aircraft.	C-3
83.	Drone aerodynamic (a) Forces and (b) Moments plotted with respect to relative distance along with average values used in the UDF for impact scenario IC1-IL1.	C-5
84.	(a) Displacements and (b) Angular displacements experienced by the drone as it traveled towards the CRM aircraft for impact scenario IC1-IL1.	C-6
85.	(a) Velocities and (b) Angular velocities experienced by the drone as it traveled towards the CRM aircraft for impact scenario IC1-IL1.	C-7
86.	Side view of flow field development over the drone as it approaches the CRM Aircraft in impact scenario IC1-IL1 at relative distances of approximately (a) 40 m (b) 20 m (c) 5 m and (d) 0 m.	C-8
87.	Top view of flow field development over the drone as it approaches the CRM Aircraft in impact scenario IC1-IL1 at relative distances of approximately (a) 40 m (b) 20 m (c) 5 m and (d) 0 m.	C-9
88.	CRM aircraft (a) drag force and (b) lift force recorded as the drone approached the aircraft.	C-10

89. Drone aerodynamic (a) Forces and (b) Moments plotted with respect to relative distance along with average values used in the UDF for impact scenario IC2-IL1. C-11
90. (a) Displacements and (b) Angular displacements experienced by the drone as it traveled towards the CRM aircraft for impact scenario IC2-IL1. C-12
91. (a) Velocities and (b) angular velocities experienced by the drone as it traveled towards the CRM aircraft for impact scenario IC2-IL1. C-13
92. Side view of flow field development over the drone as it approaches the CRM Aircraft in impact scenario IC2-IL1 at relative distances of approximately (a) 40 m (b) 20 m (c) 5 m and (d) 0 m. C-14
93. Top view of flow field development over the drone as it approaches the CRM Aircraft in impact scenario IC2-IL1 at relative distances of approximately (a) 40 m (b) 20 m (c) 5 m and (d) 0 m. C-15
94. 5° AoA CRM aircraft (a) drag force and (b) lift force recorded as the drone approached the aircraft. C-16
95. Drone aerodynamic (a) Forces and (b) Moments plotted with respect to relative distance along with average values used in the UDF for impact scenario IC3-IL1. C-17
96. (a) Displacements and (b) angular displacements experienced by the drone as it traveled towards the CRM aircraft for impact scenario IC3-IL1. C-18
97. (a) Velocities and (b) angular velocities experienced by the drone as it traveled towards the CRM aircraft for impact scenario IC3-IL1. C-19
98. Side view of flow field development over the drone as it approaches the CRM Aircraft in impact scenario IC3-IL1 at relative distances of approximately (a) 40 m (b) 20 m (c) 5 m and (d) 0 m. C-20
99. Top view of flow field development over the drone as it approaches the CRM Aircraft in impact scenario IC3-IL1 at relative distances of approximately (a) 40 m (b) 20 m (c) 5 m and (d) 0 m. C-21
100. HL-CRM aircraft (a) drag force and (b) lift force recorded as the drone approached the aircraft. C-22
101. Drone aerodynamic (a) Forces and (b) Moments plotted with respect to relative distance along with average values used in the UDF for impact scenario IC4-IL1. C-23
102. (a) Displacements and (b) angular displacements experienced by the drone as it traveled towards the HL-CRM aircraft for impact scenario IC4-IL2. C-24
103. (a) Velocities and (b) angular velocities experienced by the drone as it traveled towards the HL-CRM aircraft for impact scenario IC4-IL1. C-25
104. Side view of flow field development over the drone as it approaches the HL-CRM Aircraft in impact scenario IC4-IL1 at relative distances of approximately (a) 40 m (b) 20 m (c) 5 m and (d) 0 m. C-26
105. Top view of flow field development over the drone as it approaches the HL-CRM Aircraft in impact scenario IC4-IL1 at relative distances of approximately (a) 40 m (b) 20 m (c) 5 m and (d) 0 m. C-27

106. HL-CRM aircraft (a) drag force and (b) lift force recorded as the drone approached the aircraft. C-28
107. Drone aerodynamic (a) Forces and (b) Moments plotted with respect to relative distance along with average values used in the UDF for impact scenario IC5-IL1. C-29
108. (a) Displacements and (b) angular displacements experienced by the drone as it traveled towards the HL-CRM aircraft for impact scenario IC5-IL1. C-30
109. (a) Velocities and (b) angular velocities experienced by the drone as it traveled towards the HL-CRM aircraft for impact scenario IC5-IL1. C-31
110. Side view of flow field development over the drone as it approaches the HL-CRM Aircraft in impact scenario IC5-IL1 at relative distances of approximately (a) 40 m (b) 20 m (c) 5 m and (d) 0 m. C-32
111. Top view of flow field development over the drone as it approaches the HL-CRM Aircraft in impact scenario IC5-IL1 at relative distances of approximately (a) 40 m (b) 20 m (c) 5 m and (d) 0 m. C-33
112. CRM aircraft (a) Drag force and (b) Lift force recorded as the drone approached the aircraft. C-34
113. Drone aerodynamic (a) Forces and (b) Moments plotted with respect to relative distance along with average values used in the UDF for impact scenario IC3-IL2. C-35
114. (a) Displacements and (b) Angular displacements experienced by the drone as it traveled towards the CRM aircraft for impact scenario IC3-IL2. C-36
115. (a) Velocities and (b) Angular velocities experienced by the drone as it traveled towards the CRM aircraft for impact scenario IC3-IL2. C-37
116. Side view of flow field development over the drone as it approaches the CRM Aircraft in impact scenario IC3-IL2 at relative distances of approximately (a) 40 m (b) 20 m (c) 5 m and (d) 0 m. C-38
117. Top view of flow field development over the drone as it approaches the CRM Aircraft in impact scenario IC3-IL2 at relative distances of approximately (a) 40 m (b) 20 m (c) 5 m and (d) 0 m. C-39
118. HL-CRM aircraft (a) Drag force and (b) Lift force recorded as the drone approached the aircraft. C-40
119. Drone aerodynamic (a) Forces and (b) Moments plotted with respect to relative distance along with average values used in the UDF for impact scenario IC4-IL2. C-41
120. (a) Displacements and (b) Angular displacements experienced by the drone as it traveled towards the HL-CRM aircraft for impact scenario IC4-IL2. C-42
121. (a) Velocities and (b) Angular velocities experienced by the drone as it traveled towards the HL-CRM aircraft for impact scenario IC4-IL2. C-43
122. Side view of flow field development over the drone as it approaches the HL-CRM Aircraft in impact scenario IC4-IL2 at relative distances of approximately (a) 40 m (b) 20 m (c) 5 m and (d) 0 m. C-44

123. Top view of flow field development over the drone as it approaches the HL-CRM Aircraft in impact scenario IC4-IL2 at relative distances of approximately (a) 40 m (b) 20 m (c) 5 m and (d) 0 m. C-45

## LIST OF TABLES

Table	Page
1. Drone properties used for trajectory analysis.	3
2. Summary of impact conditions.	6
3. Summary of impact scenarios.	11
4. CRM aircraft reference parameters.	12
5. Location of the center of gravity of the CRM aircraft.	12
6. HL-CRM aircraft reference parameters.	14
7. Location of the center of gravity of the HL-CRM aircraft.	14
8. Volume mesh information for the CRM aircraft and domain.	17
9. Operation condition and other relevant parameters used for the CRM validation study.	18
10. CRM aircraft force coefficients obtained from simulation compared against experimental data.	19
11. Lateral positions at which the pressure coefficients are measured.	19
12. Volume mesh information for the HL-CRM aircraft and domain.	24
13. Operating conditions and other relevant parameters for the HL-CRM validation study.	25
14. HL-CRM aircraft force coefficients obtained from simulation compared against experimental data.	26
15. Lateral positions at which the pressure coefficients are measured.	26
16. Change in local pressure from operating pressure at the drone release location for impact scenarios at IL2.	37
17. Change in local pressure from operating pressure at the drone release location for impact scenarios with IL1.	39
18. Sign convention for the drone forces and moments.	41
19. Background volume mesh details used in impact scenario IC3-IL2.	44
20. Component mesh details used for all the impact scenarios.	45
21. Fluid properties and operating conditions within the domain for trajectory analysis.	46
22. Aircraft and drone reference lengths and areas.	46
23. Drone displacements for impact scenarios IC1-IL1 and IC2-IL1 obtained by ERAU and NIAR.	54
24. Drone angular displacements for impact scenarios IC1-IL1 and IC2-IL1 obtained by ERAU and NIAR.	55

25. Vertical deflection of the drone necessary to avoid collision with the CRM and HL-CRM aircraft at each impact location.	59
26. Drone displacements at the point of impact for all impact scenarios.	64
27. Drone angular displacements at the point of impact for all impact scenarios.	64
28. Maximum element lengths used within the size boxes.	A-1
29. Surface mesh quality of the CRM aircraft and domain.	A-2
30. Volume mesh quality of the CRM aircraft volume mesh.	A-2
31. Maximum element lengths used within the HL-CRM size boxes.	A-3
32. Surface mesh quality of the HL-CRM aircraft and domain.	A-4
33. Volume mesh quality of the HL-CRM aircraft volume mesh.	A-4
34. Maximum element lengths used within the aircraft wake refinement size boxes.	A-5
35. Element lengths used to obtain a smooth transition from hexa- to tetra- elements.	A-7
36. Layer parameters used to generate boundary layer mesh over the aircraft.	A-7
37. Layer parameters used to generate boundary layer mesh over the drone.	A-8
38. Surface mesh quality of component and background meshes.	A-9
39. Volume mesh quality of component and background meshes.	A-9

## LIST OF ACRONYMS

AIAA	American Institute of Aeronautics and Astronautics
AoA	Angle of Attack
AUVSI	Association for Unmanned Vehicles International
CAD	Computer-Aided Design
CFD	Computational Fluid Dynamics
CFR	Code of Federal Regulations
CG	Center of Gravity
CRM	Common Research Model
DOF	Degrees-of-Freedom
DPW	Drag Prediction Workshop
ERAU	Embry-Riddle Aeronautical University
FAA	Federal Aviation Administration
HL-CRM	High Lift Common Research Model
HLPW	High Lift Prediction Workshop
IC	Impact Condition
IL	Impact Location
KIAS	Knots-Indicated Air Speed
MAC	Mean Aerodynamic Chord
NAS	National Airspace System
NASA	National Aeronautics and Space Administration
NIAR	National Institute for Aviation Research
NTF	National Transonic Facility
RANS	Reynolds-Averaged Navier-Stokes
RBD	Rigid Body Dynamics
sUAS	Small Unmanned Aircraft Systems
UAS	Unmanned Aircraft Systems
UAV	Unmanned Aerial Vehicle
UDF	User-Defined Function
VTOL	Vertical Take-Off and Landing
WP	Working Packages

## LIST OF SYMBOLS

$\text{AOA}_{\text{CRM}}$	Angle of attack of CRM aircraft
$\text{AOA}_{\text{HL-CRM}}$	Angle of attack of HL-CRM aircraft
$C_D$	Coefficient of drag
$C_L$	Coefficient of lift
$C_P$	Coefficient of pressure
$F_{DX}, F_{DY}, F_{DZ}$	Aerodynamic forces of the drone in XYZ directions
$F_{\text{ext}DX}, F_{\text{ext}DY}, F_{\text{ext}DZ}$	External forces added to the drone using the UDF in XYZ directions
$\vec{f}_G$	Forces acting on the body
$L$	Inertia tensor
$\vec{M}_B$	Moment vector of the body
$M_{DX}, M_{DY}, M_{DZ}$	Aerodynamic moments of the drone in XYZ directions
$M_{\text{ext}DX}, M_{\text{ext}DY}, M_{\text{ext}DZ}$	External moments added to the drone using the UDF in XYZ directions
$m$	Mass of the body
Re	Reynolds number
$S_\phi$	Source term of $\phi$
$\vec{u}$	Flow velocity vector
$(u_g)^\rightarrow$	Mesh velocity of the moving mesh
$V_{\text{CRM}}$	Velocity of CRM aircraft
$V_{\text{Drone}}$	Velocity of drone
$V_{\text{HL-CRM}}$	Velocity of HL-CRM aircraft
$\dot{\vec{v}}_G$	Translational acceleration of the body
$W$	Weight of the drone
$X, Y, \text{ and } Z$	Represents the global inertial reference frame in XYZ axes
$X_{DB}, Y_{DB}, Z_{DB}$	Represents the drone body-fixed reference frame in XYZ axes
$X_T, Y_T, Z_T$	Represents the translating inertial reference frame in XYZ axes
$C_x$ and $S_x$	Denotes $\cos x$ and $\sin x$
$\Delta C_D$	Difference in drag coefficient
$\Delta C_L$	Difference in lift coefficient
$\Delta p, \Delta q, \Delta r$	Angular velocities in global inertial reference frame ( $X_G Y_G Z_G$ )
$\Delta u, \Delta v, \Delta w$	Velocities in global inertial reference frame ( $X_G Y_G Z_G$ )

$\Delta x, \Delta y, \Delta z$	Displacements in global inertial reference frame ( $X_G Y_G Z_G$ )
$\Delta \phi, \Delta \theta, \Delta \psi$	Angular displacements in global inertial reference frame ( $X_G Y_G Z_G$ )
$\eta$	Fraction of the wing semispan (y/semispan)
$\Gamma$	Diffusion coefficient
$\phi, \theta, \psi$	Rotation about X, Y, and Z axes
$\rho$	Fluid density
$\vec{\omega}_B$	Angular velocity of the body
$\dot{\vec{\omega}}_B$	Angular acceleration of the body

#### Subscripts

$G$	denotes the global inertial reference frame
$B$	denotes the body-fixed reference frame
$T$	denotes the translating inertial reference frame

## 1. INTRODUCTION

### 1.1 BACKGROUND

Unmanned Aircraft Systems (UASs) are one of the fastest-growing sectors of the aviation industry today. A UAS constitutes of an Unmanned Aerial Vehicle (UAV) and equipment necessary to operate the aircraft safely and efficiently. The Association for Unmanned Vehicles International (AUVSI) estimated that more than 70,000 jobs would be created in the US by 2019 with an economic impact of more than \$13.6B [1]. The large growth in UAVs necessitates the safety, regulatory, social, and technological challenges to be addressed before being widely accepted by the public.

The primary goal of regulating UAS operations in the National Airspace System (NAS) is to assure the appropriate level of safety. National aviation agencies quantify this goal as an “Equivalent Level of Safety.” According to the guidance on UAS operations provided by the Range of Commanders Council, the UAS must show a level of risk to human life no greater than that of a piloted aircraft in order to have an Equivalent Level of Safety [2]. The National Transportation Safety Board (NTSB) has defined two categories of relevant collision accident scenarios; (i) in-flight collisions with obstacles such as birds, trees, power lines, and (ii) mid-air collisions with other aircraft. The effects of bird impact on aircraft have been researched and well documented. However, the probability of a mid-air collision between a rigid body like a UAS and an aircraft and the effects of the rigid body collision and damage has not been studied in detail.

The A3 Airborne Collision Severity Evaluation research [3] focused on understanding the physics of airborne collisions between UAVs and manned aircraft and identifying the UAV characteristics that influence the damage on the manned aircraft. The research analyzed airborne collisions of a multi-rotor vertical take-off and landing (VTOL) quadcopter, with a typical narrow-body commercial transport jet and a typical business jet, certified under *14 Code of Federal Regulations (CFR) Part 25* requirements [10]. The severity of airborne collisions between UAVs, commercial transport jets, and business jets on the windshield, wing, horizontal stabilizer, and vertical stabilizer was evaluated and classified to different severity levels. It was concluded that a UAS collision causes more damage than a bird strike for the same kinetic energy. Additionally, on commercial transport jet wings, the locations CQW1 and CQW3 between rib structures (representing target: commercial aircraft, C, projectile: quadcopter, Q, impact area: wing, W, and impact location: 1 and 3 located between ribs on the wing) were found to be more vulnerable. CQW1 was found to be the more critical case. While the A3 study [3] assessed the collision damage of a UAS, the possibility of collision between the UAS and the aircraft was not assessed.

The current research evaluates the trajectory of a UAS as it approaches a Part 25 transport category commercial jet aircraft and whether or not the UAS will deflect away from the aircraft due to the aircraft flow field. The purpose of the study is to determine the extent of the UAS deflection and the change in orientation as the UAS approaches the aircraft due to the interaction between the UAS and the aircraft flow field.

### 1.2 PROJECT SCOPE

The preceding work of the A3 study [3] was focused on understanding the extent of damage caused by an impact between a UAS and a narrow-body commercial aircraft or a business jet operating

under Part 25 requirements. The current research aims to determine whether or not the UAS could deflect prior to impacting a commercial transport aircraft.

In order to determine whether a sUAS could deflect prior to impact with a transport category aircraft, a series of trajectory analyses was completed. The trajectory of a body submerged in a fluid flow undergoing partially constrained motion can be predicted using coupled Computational Fluid Dynamics (CFD) and Rigid Body Dynamics (RBD) simulations with six-degrees-of-freedom (6-DOF). This research was completed utilizing the resources and personnel available at the National Institute for Aviation Research (NIAR) and the Embry-Riddle Aeronautical University (ERAU). The trajectory analysis was conducted using two commercially available solvers: Ansys® Fluent software, Release 18.2 by NIAR, and Siemens Simcenter STAR-CCM+, Version 2020.1.1 by ERAU.

The following research approach, divided into Working Packages (WP), was used to conduct the investigation:

- WP I: Definition of the Target (Aircraft) geometry, selection of the aircraft speeds, angles of attack, and selection of impact locations on the aircraft.
- WP II: Definition of the Projectile (UAS) geometry, including definitions of mass and inertia and selection of the UAS speed.
- WP III: Validation of the CFD model of the aircraft with available experimental data.
- WP IV: Cross verification of UAS deflections obtained from the trajectory analyses conducted by NIAR and ERAU.
- WP V: Trajectory Analyses of the UAS for the impact locations on the aircraft wing.
- WP VI: Trajectory Analyses of the UAS for the impact locations on the aircraft horizontal stabilizer.

For the investigation, the analysis was conducted using the DJI Phantom III Standard Computer-Aided Design (CAD) model developed by NIAR for the A3 study [3] for the projectile and the Common Research Model (CRM), and the High Lift Common Research Model (HL-CRM) CAD developed by the National Aeronautics and Space Administration (NASA), representing a transport aircraft for the target.

The main intent of this research study was to establish whether a UAS approaching a transport category aircraft will deflect significantly in the vicinity of the aircraft due to the interaction between the drone and the aircraft flow field and avoid the collision.

### 1.3 TARGET DEFINITION – COMMERCIAL TRANSPORT AIRCRAFT

The A3 study [3] conducted the analysis with a narrow-body commercial jet. The narrow body commercial jet CAD model was developed based on the Boeing 737 and Airbus A320 aircraft models to represent a Part 25 aircraft. Extensive aerodynamic data is unavailable for the aforementioned aircraft models. Therefore, the current research uses the CRM developed by NASA to represent a Part 25 transport category aircraft. Extensive aerodynamic data, both simulated and experimental, is available for the CRM aircraft.

The CRM is available as an open-source geometry to the community [7] and was developed by NASA to validate CFD methodologies. Because of this, extensive wind tunnel data is available for

the CRM aircraft. The CRM aircraft geometry represents a transonic wide-body twin-engine jet similar to a Boeing 777 [6] family aircraft (Figure 1).

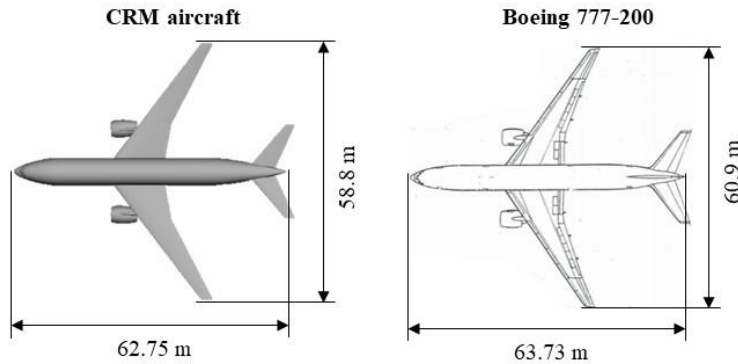


Figure 1. CRM aircraft geometry compared with a traditional Part 25 transport category aircraft (Boeing 777-200) [6].

To study the effect of high lift devices on the trajectory of the UAS, a high lift variant of the CRM called the High Lift Common Research Model (HL-CRM) was used. The HL-CRM was developed by NASA as an open-source geometry for CFD analysis [8]. The flaps and slats are deployed for the HL-CRM aircraft geometry. Detailed information regarding the individual geometries of the CRM and HL-CRM is provided in Section 2.2.

#### 1.4 PROJECTILE DEFINITION – UAS QUADCOPTER

NIAR developed the CAD model of a quadcopter (DJI Phantom III) for the A3 study [3]. The same CAD model of the DJI Phantom III drone was used as the UAS for the current research to determine the trajectory as it approached the aircraft. Figure 2 shows the UAS model used for this research and the center of gravity (CG) location. The UAS is referred to as a drone throughout the rest of the report. The drone properties used for the trajectory analysis are provided in Table 1.

The drone orientation angle is defined as  $0^\circ$  when it is facing the aircraft. For a  $0^\circ$  drone orientation angle, longitudinal and lateral axes of the drone are parallel to the X and Y global axes, respectively (Figure 3). The orientation angles are considered to be positive when the drone rotates clockwise about the vertical axis. The propeller orientation angle is  $0^\circ$  when the propellers are oriented as seen in Figure 3. For the current study, the drone was set to approach the aircraft at a  $0^\circ$  orientation angle with a  $0^\circ$  propeller orientation angle.

Table 1. Drone properties used for trajectory analysis.

<b>Mass (kg)</b>	1.2161
<b>Inertia Tensor (<math>kg\cdot m^2</math>)</b>	$\begin{bmatrix} 0.0081 & & & \\ -2.38 \times 10^{-5} & 0.0086 & & \\ 1.40 \times 10^{-5} & -3.27 \times 10^{-5} & 0.0123 & \end{bmatrix}$

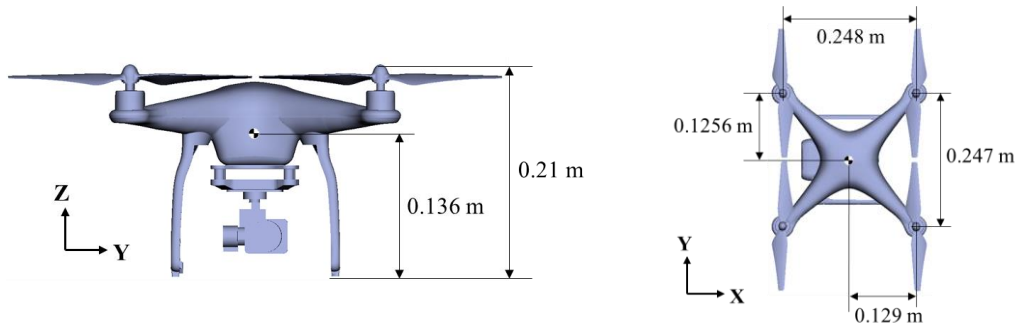


Figure 2. The CAD model of the drone and the CG location with respect to the origin.

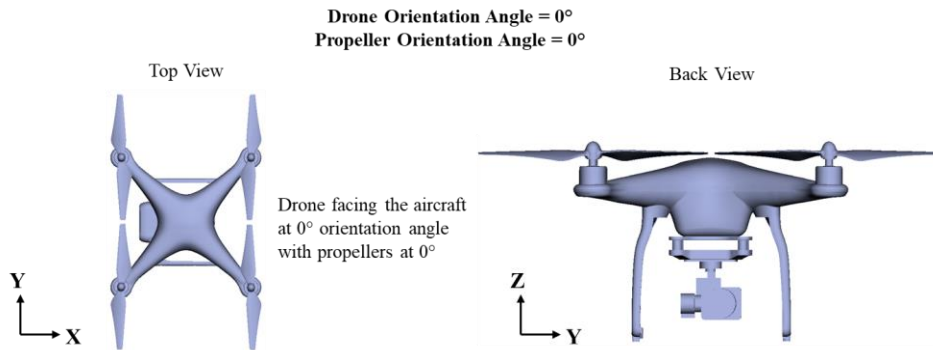


Figure 3. Drone and propeller orientation angles.

## 1.5 IMPACT SCENARIO DEFINITION

This section describes the impact conditions (IC) being studied and the lateral impact locations at which the drone was released for impact. A combination of the impact conditions and the impact locations defines each impact scenario. A total of seven impact scenarios were simulated for this investigation by NIAR. The impact conditions, locations, and scenarios are explained in detail in the following sections.

### 1.5.1 Selection of Impact Velocities

The operating speeds for transport category aircraft at various altitudes are set in the FAA General Operating and Flight Rules (14 CFR Part 91) airworthiness requirements [10]. For holding conditions, the Aeronautical Information Manual paragraph 5-7-2-j.2(b) [5] indicates the following speeds in Knots-Indicated Air Speed (KIAS):

- 200 KIAS below 6,000 ft.
- 230 KIAS from 6,001 to 14,000 ft.
- 265 KIAS above 14,000 ft.

Typical small UAS (sUAS) operations occur at low altitudes. This increases the likelihood of a collision occurring between a sUAS and an aircraft during holding, take-off, or landing conditions. Therefore, a maximum velocity of 200 KIAS is specified in §Part 91.117(b) at an altitude of 2,500 ft (762 m) AGL or below within 4 miles of Class C and D airspace. Considering that most high-velocity impact scenarios occur during holding or take-off, or landing conditions, the speed of

200 kts (102.889m/s) was selected for the aircraft velocity. Therefore, a speed of 200 kts (102.889m/s) and a flight altitude of 2,500 ft (762 m) MSL were selected as operating conditions for the aircraft. These conditions are generally typical for a holding flight pattern after a missed approach.

The specifications of the DJI Phantom III drone used for the trajectory analysis provide a maximum UAS speed of 31.1 kts (16 m/s) and a service ceiling of 19,685 ft (6,000 m). However, in the preceding work (A3 Airborne Collision Severity Evaluation study [3]), it was found that newer, similar type sUAS models had enhanced flight capabilities with maximum speeds of 38.3 kts (20 m/s). Therefore, the A3 Airborne Collision Severity Evaluation study [3] selected a relative impact velocity of 250 kts (128.6 m/s) for frontal impacts on the aircraft surfaces. The aircraft velocity was set to be 200 kts (102.889m/s), and the UAS velocity was calculated to be 50 kts (25.722 m/s). Therefore, a UAS velocity of 50 kts (25.722 m/s) was selected for the trajectory analyses conducted in the current study.

### 1.5.2 Impact Condition Definition

Five impact conditions were used for the study. A list of the factors that were analyzed is summarized below:

- Effect of drone in hover (Impact Condition 1)
- Effect of drone with velocity (Impact Condition 2)
- Effect of aircraft angle of attack (Impact Condition 3)
- Effect of high lift devices (Impact Condition 4)
- Effect of aircraft velocity (Impact Condition 5)

#### 1.5.2.1 Impact Condition 1: Effect of Drone in Hover

The drone velocity was set to zero while the CRM aircraft approached the drone at a fixed speed of 200 kts (102.889 m/s). The aircraft approached the drone at a 0° angle of attack (AoA).

#### 1.5.2.2 Impact Condition 2: Effect of Drone with Velocity

The drone approached the aircraft at a velocity of 50 kts (25.722 m/s) while the aircraft flew at a velocity of 200 kts (102.889 m/s). The CRM aircraft was used to represent the aircraft, and the AoA was set to 0°.

#### 1.5.2.3 Impact Condition 3: Effect of Aircraft Angle of Attack

Impact Condition 3 refers to the study of the effect of aircraft AoA on the drone trajectory. The drone approached the aircraft at 50 kts (25.722 m/s). The CRM aircraft approached the drone with a speed of 200 kts (102.889 m/s) while flying at an AoA of 5°.

#### 1.5.2.4 Impact Condition 4: Effect of High Lift Devices

The effect of high lift devices on the trajectory of the drone was studied. The HL-CRM aircraft was used for the investigation. The drone approached the aircraft at a velocity of 50 kts (25.722 m/s) while the aircraft approached the drone with a velocity of 200 kts (102.889 m/s). The aircraft was at 0° AoA.

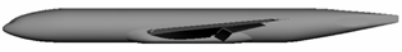
### 1.5.2.5 Impact Condition 5: Effect of Aircraft Velocity

The HL-CRM aircraft was used to investigate the effect of lower aircraft velocity on the drone trajectory. The drone approach velocity was set to 50 kts (25.722 m/s), while the aircraft approach velocity was set to 170 kts (87.455 m/s). The aircraft was at 0° AoA.

### 1.5.2.6 Summary of Impact Conditions

The impact conditions are summarized in Table 2. In addition, the drone and aircraft velocities, the aircraft AoA, and the type of aircraft geometry used are provided in detail. The impact conditions were used in combination with impact locations to create the impact scenarios for the investigation.

Table 2. Summary of impact conditions.

Impact Condition (IC)	Depiction of Impact Condition	
IC1	 Drone → $V_{Drone} = 0$ kts	 ← CRM aircraft $V_{CRM} = 200$ kts $AoA_{CRM} = 0^\circ$
IC2	 Drone → $V_{Drone} = 50$ kts	 ← CRM aircraft $V_{CRM} = 200$ kts $AoA_{CRM} = 0^\circ$
IC3	 Drone → $V_{Drone} = 50$ kts	 ← CRM aircraft $V_{CRM} = 200$ kts $AoA_{CRM} = 5^\circ$
IC4	 Drone → $V_{Drone} = 50$ kts	 ← HL-CRM aircraft $V_{HL-CRM} = 200$ kts $AoA_{HL-CRM} = 0^\circ$
IC5	 Drone → $V_{Drone} = 50$ kts	 ← HL-CRM aircraft $V_{HL-CRM} = 170$ kts $AoA_{HL-CRM} = 0^\circ$

### 1.5.3 Impact Location Definition

The location of possible impact of the drone on the aircraft was defined by the lateral distance of the drone away from the fuselage centerline at the time of release. The details of the two different impact locations used in this study are provided in this section. The CG of the drone was aligned with the leading-edge of the wing (CRM aircraft) or the leading-edge of the slat (HL-CRM aircraft) regardless of the lateral location, as seen in Figure 4.

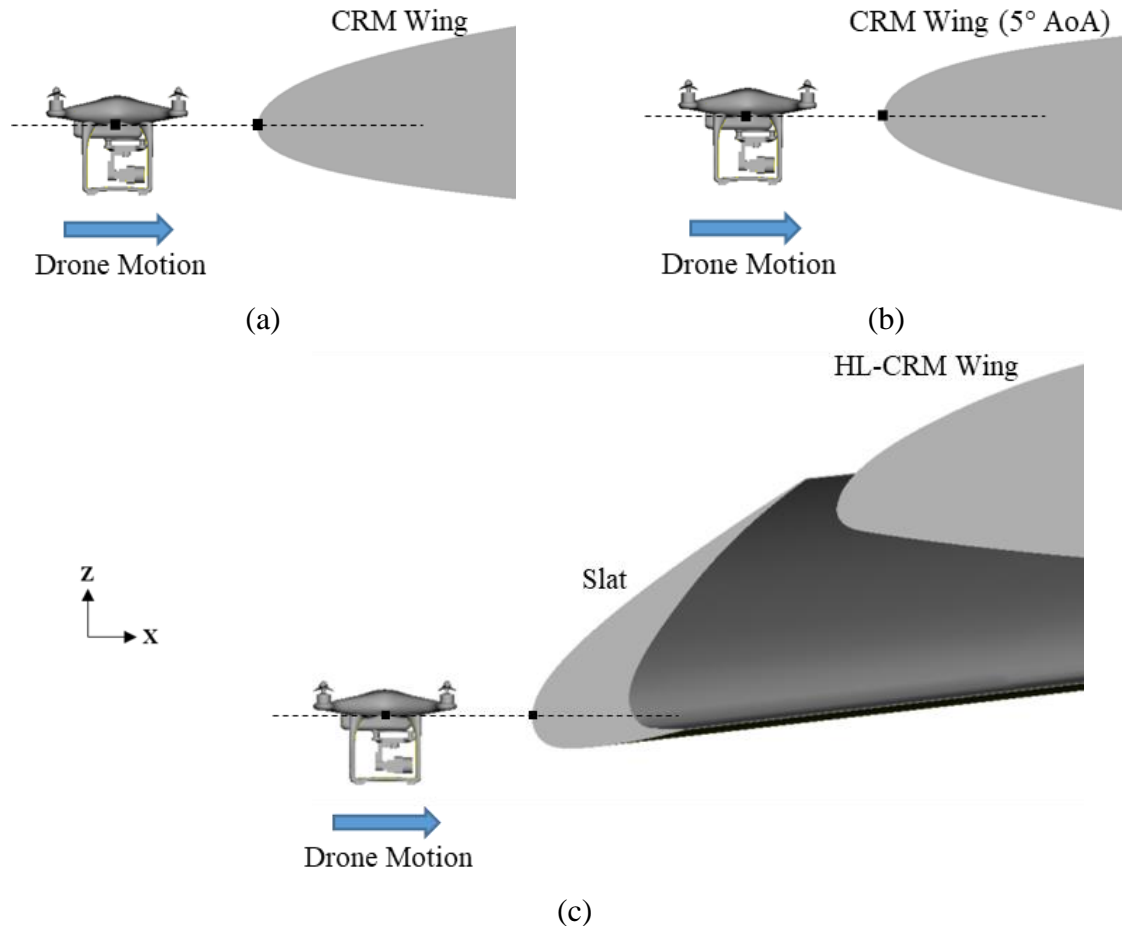


Figure 4. Side view showing the vertical placement of the drone with respect to (a) CRM aircraft ( $0^\circ$  AoA), (b) CRM aircraft ( $5^\circ$  AoA), and (c) HL-CRM aircraft ( $0^\circ$  AoA).

#### 1.5.3.1 Impact Location 1

The first impact location (IL1) was based on one of the critical impact cases identified in the A3 Airborne Collision Severity Evaluation study [3], CQW1. The CQW1 impact was based on a drone's collision on the wing of a commercial transport jet modeled based on the Boeing 737 and Airbus A320 aircraft.

Figure 5 shows the lateral location of the drone on the commercial jet wing and the critical impact case selected for the current investigation. The lateral location of the drone impact on the commercial jet aircraft wing for the critical case, CQW1, was measured, and a proportionate

distance on the CRM and HL-CRM geometry is used to determine the first impact location for this study. Therefore, for IL1, the drone was placed at a distance of 16.8 m away from the fuselage centerline for both CRM aircraft and HL-CRM aircraft as shown in Figure 6.

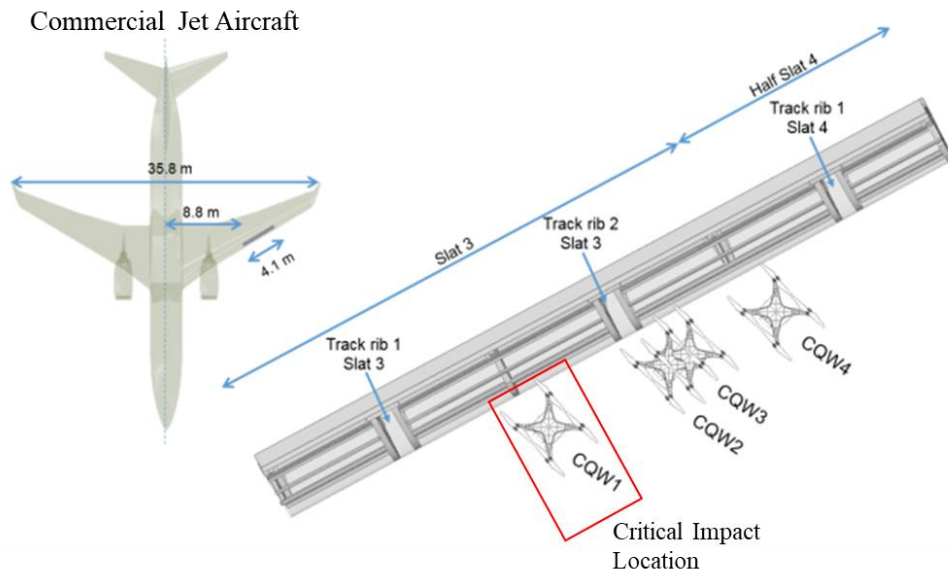
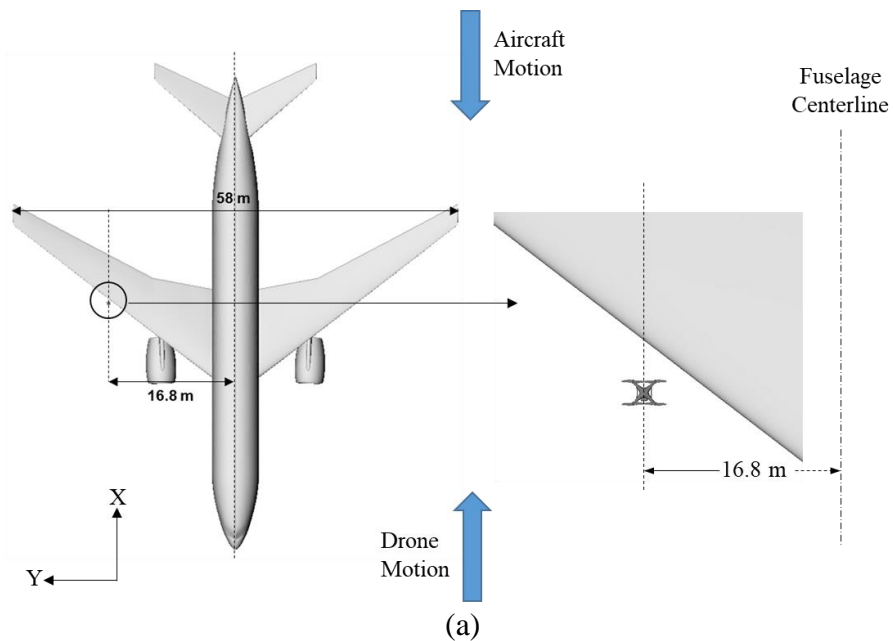


Figure 5. Critical impact location identified on the commercial jet aircraft wing from the A3 Airborne Collision Severity Evaluation study [3].

The impact studies were conducted on the left-wing of the aircraft in the preceding work. However, the CRM and HL-CRM models used for the current investigation are right symmetric half models. Therefore, the drone location from the left side was reflected to the right side of the aircraft. For the current investigation, as mentioned in Section 1.4, the drone orientation and propeller orientation were set to be 0°.



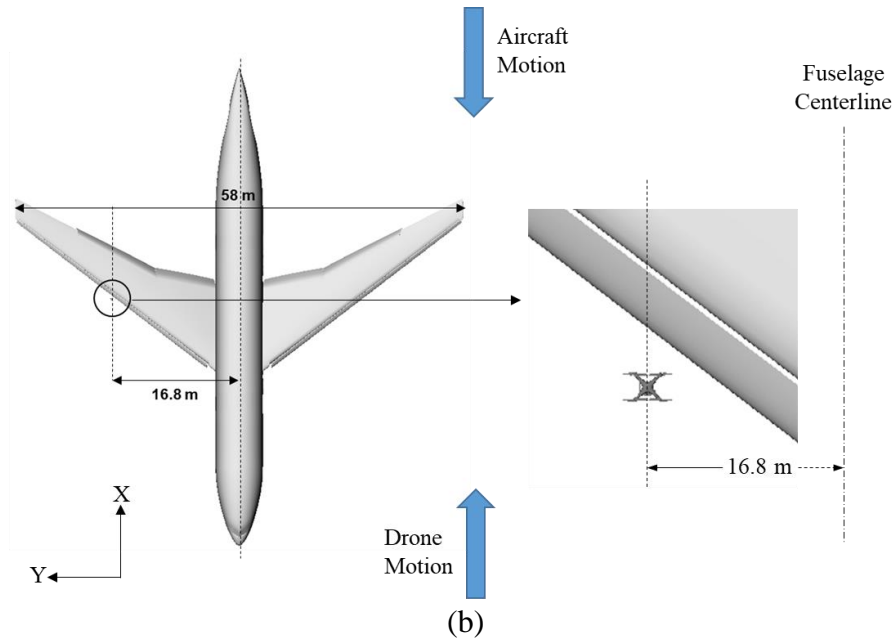


Figure 6. The lateral position of the drone at IL1 as it approaches the (a) CRM aircraft and (b) HL-CRM aircraft.

### 1.5.3.2 Impact Location 2

For the second impact location (IL2), the drone was released midway between the nacelle center and the fuselage centerline. The pressure gradients are higher near the wing root of the aircraft. The location near the root of the wing was selected to investigate the effect of these higher pressure gradients on the drone trajectory. The drone's proximity to the fuselage flow field opens up the possibility of the drone trajectory being affected in the lateral direction to a greater extent. To observe the effects of the wing root and the fuselage flow field on the drone's trajectory, the second impact location was selected. IL2 was set to be 4.89 m away from the fuselage centerline. This location for drone impact was used for both geometries with and without high lift devices, as shown in Figure 7.

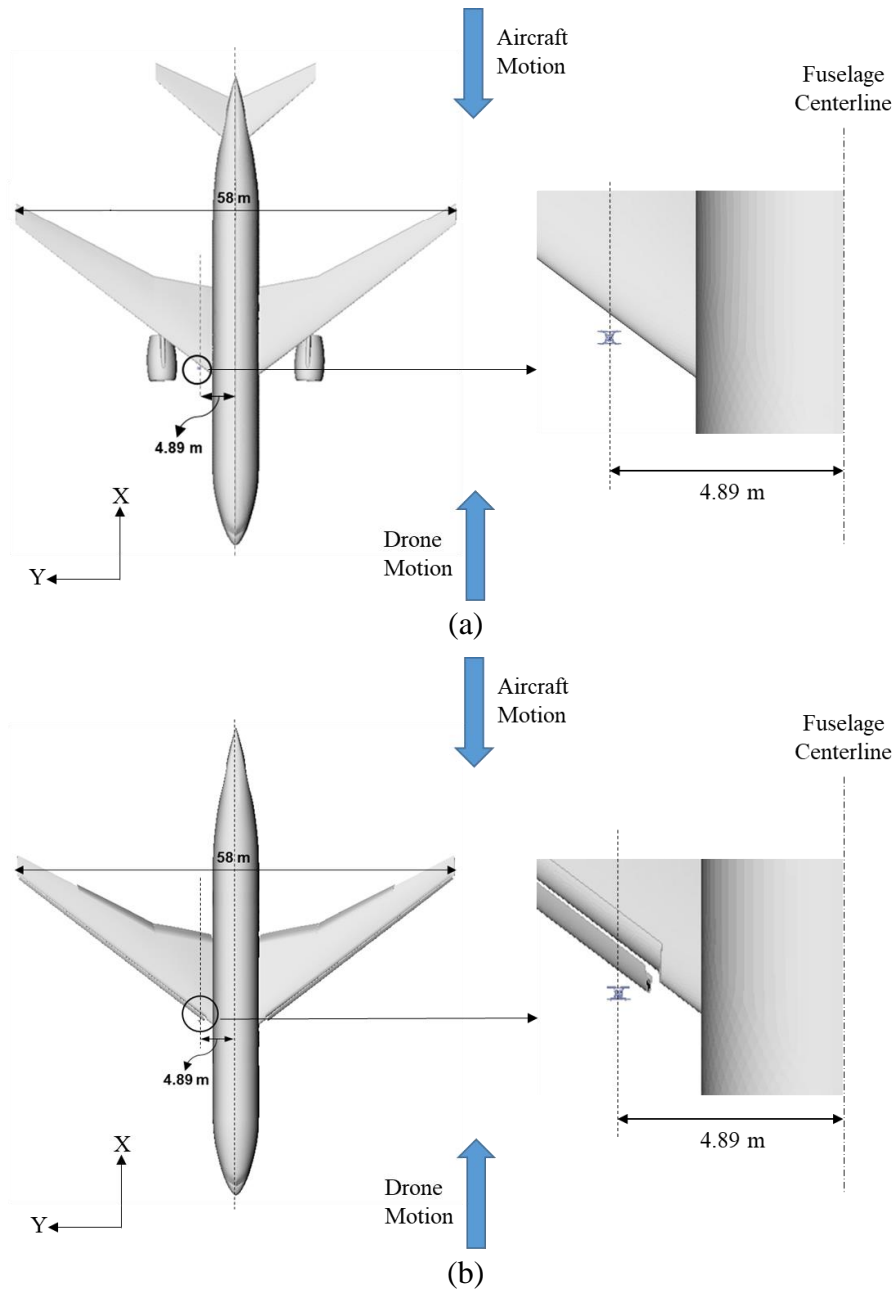


Figure 7. Lateral position of the drone at IL2 as it approaches the (a) CRM aircraft and (b) HL-CRM aircraft.

#### 1.5.4 Summary of Impact Scenario Definition

The impact conditions (IC), in combination with the impact locations (IL), define the seven impact scenarios that were simulated to determine the extent to which the drone would deflect away from the aircraft. Table 3 provides the details of each impact scenario.

Table 3. Summary of impact scenarios.

<b>Impact Scenario</b>	<b>Impact Scenario Definition</b>	<b>Aircraft Configuration</b>	<b>Impact Location on Aircraft</b>	<b>Aircraft Speed (m/s)</b>	<b>Aircraft Angle of Attack (degrees)</b>	<b>Drone Speed (m/s)</b>	<b>Drone Lateral Position (m)</b>
1	IC1-IL1	CRM	Wing	102.89	0	0.00	16.80
2	IC2-IL1	CRM	Wing	102.89	0	25.72	16.80
3	IC3-IL1	CRM	Wing	102.89	5	25.72	16.80
4	IC4-IL1	HL-CRM	Wing	102.89	0	25.72	16.80
5	IC5-IL1	HL-CRM	Wing	87.45	0	25.72	16.80
6	IC3-IL2	CRM	Wing	102.89	5	25.72	4.89
7	IC4-IL2	HL-CRM	Wing	102.89	0	25.72	4.89

## 2. VALIDATION – AIRCRAFT AERODYNAMIC PERFORMANCE

### 2.1 OVERVIEW

This section describes the aircraft geometries used in the investigation and the validation methodology used for each geometry. The CRM and HL-CRM aircraft geometries, mesh, and numerical models were validated against available wind tunnel testing data. The geometry and surface mesh generated for the validation was subsequently used for the trajectory analysis study.

### 2.2 GEOMETRY

#### 2.2.1 CRM Aircraft

The CRM geometry was developed by NASA to represent a wide-body commercial aircraft with a supercritical transonic wing [9]. The CRM aircraft has been used in the AIAA Drag Prediction Workshops (DPW) [10][11][12] as the benchmark geometry to determine best practices in CFD. In addition, the CRM geometry has been used to simulate and analyze the overall aircraft drag and the contributions to drag from the nacelle, pylon, and tail. The CRM aircraft geometry from the Sixth DPW [7] [12] is used in the current study.

The CRM aircraft configuration with nacelle, pylon, and horizontal tail was selected for this study because it most closely modeled a commercial aircraft. Figure 8 depicts the CRM aircraft geometry used for the study. The horizontal tail in this configuration is fixed at 0° incidence. The wing and horizontal planform and sectional designs are described in the workshop summary publications [10][11][12]. The reference parameters of the aircraft are provided in Table 4, and the center of gravity location with respect to the aircraft nose coordinates is provided in Table 5. The negative

direction along the Z-axis indicates that the center of gravity is located below the nose in the vertical direction.

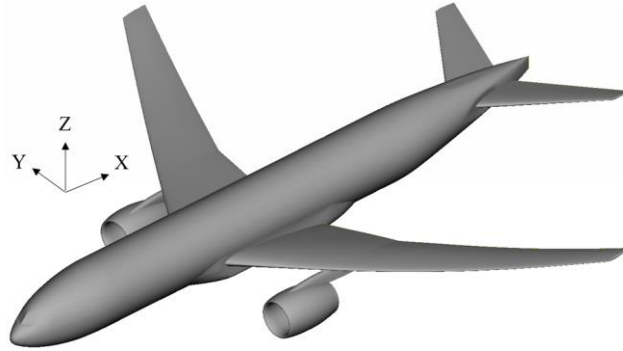


Figure 8. Isometric view of the CRM aircraft.

Table 4. CRM aircraft reference parameters.

<b>Length</b>	62.8 m
<b>Wingspan</b>	58.8 m
<b>Wing Area</b>	383.7 m <sup>2</sup>
<b>MAC</b>	7.005 m

Table 5. Location of the center of gravity of the CRM aircraft.

<b>Direction</b>	<b>Distance from Aircraft Nose (m)</b>
<b>Along the positive X-axis</b>	33.67
<b>Along the Y-axis</b>	0.00
<b>Along the negative Z-axis</b>	0.97

#### 2.2.1.1 Geometry Rotation

In traditional CFD studies, the operating AoA is commonly defined as a velocity vector while the aircraft's orientation is maintained constant (typically at 0° AoA). However, future aircraft-drone interaction simulations required the aircraft to be rotated to the desired angle for the current investigation. Using this method allowed the drone to experience freestream air parallel to the X-axis, independent of the aircraft's AoA. Therefore, for steady-state analyses, the aircraft geometry was rotated to the required AoA while maintaining the velocity vector parallel to the horizontal axis.

The CRM aircraft was rotated about the axis parallel to the Y-axis and with a rotation point defined about the aircraft CG, shown in Table 5. Figure 9 shows the CRM at an AoA of 0° and 5°, with

the freestream velocity parallel to the X-axis. Figure 10 represents the CRM aircraft after rotation and the CG and the aircraft nose coordinates before rotation.

Steady-state analysis was conducted using both the rotated geometry and the more traditional, rotated velocity vector method. A comparison between the two sets of results showed that the resultant forces and moments from the rotated aircraft were consistent with that of the velocity vector analysis. Therefore, the rotated geometry was used in trajectory analysis for impact scenarios IC3-IL1 and IC3-IL2.

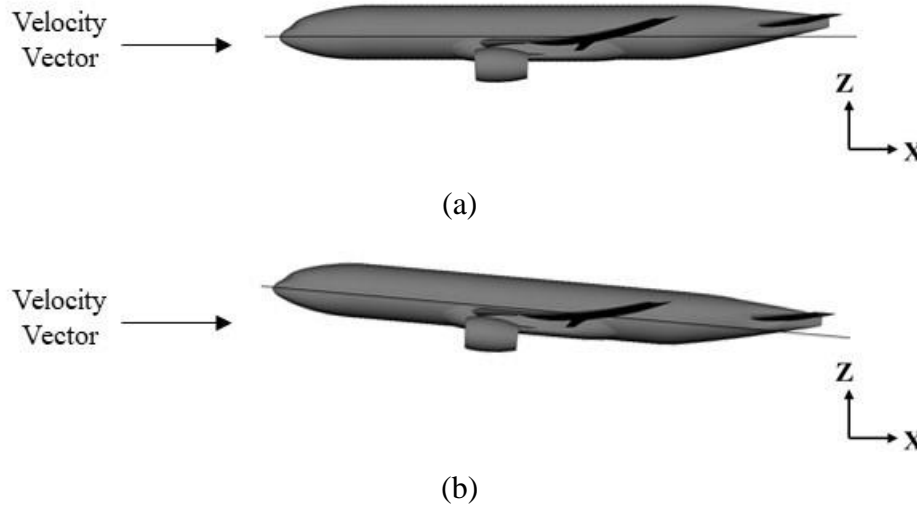


Figure 9. CRM aircraft at (a) 0° AoA and (b) 5° AoA.

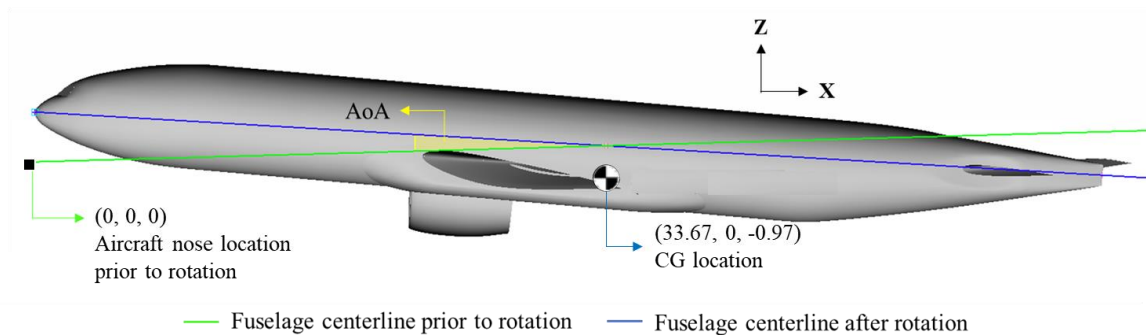


Figure 10. Location of the center of gravity of the aircraft and a representation of the rotated aircraft geometry.

### 2.2.2 HL-CRM Aircraft

The HL-CRM aircraft geometry was designed to represent a high-lift transonic commercial aircraft [13]. The HL-CRM aircraft is used in the CFD community to improve methods for predicting aerodynamic behavior through workshops such as the High Lift Prediction Workshop (HLPW). The HL-CRM wing design was based on the CRM wing, with modifications to represent takeoff and landing wing-loading by adding leading-edge slats and trailing edge flaps [13]. The HL-CRM aircraft geometry used in the current study was acquired from the 3<sup>rd</sup> HLPW [8].

Figure 11 shows the HL-CRM aircraft configuration used for the current investigation. Due to the availability of experimental data [14][15], the aircraft configuration with wing, body, flaps, and slats was selected. The HL-CRM aircraft's reference parameters are provided in Table 6, and the location of the center of gravity is specified in Table 7. The negative direction along the Z-axis indicates that the center of gravity is located below the nose in the vertical direction.

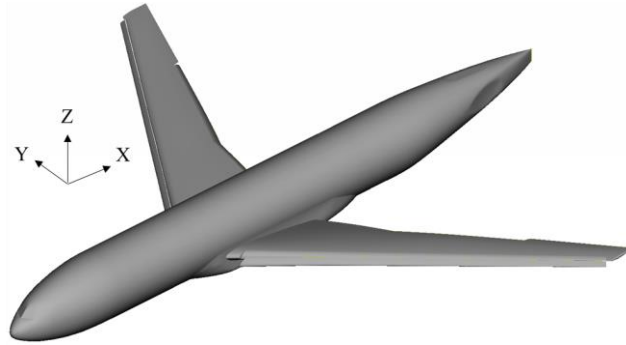


Figure 11. Isometric view of the HL-CRM aircraft.

Table 6. HL-CRM aircraft reference parameters.

<b>Length</b>	62.8 m
<b>Wingspan</b>	58.8 m
<b>Wing Area</b>	383.7 m <sup>2</sup>
<b>MAC</b>	7.005 m

Table 7. Location of the center of gravity of the HL-CRM aircraft.

<b>Direction</b>	<b>Distance from Aircraft Nose (m)</b>
<b>Along the positive X-axis</b>	31.33
<b>Along the Y-axis</b>	0.00
<b>Along the negative Z-axis</b>	0.51

## 2.3 CRM AERODYNAMIC PERFORMANCE VALIDATION

### 2.3.1 Introduction

The numerical model used to obtain the steady-state results of the CRM aircraft was validated by comparing the simulation results with experimental data from wind tunnel tests conducted by NASA at the NASA Langley National Transonic Facility (NTF) [16][17] for the NASA Drag Prediction Workshops. A steady-state, freestream analysis was conducted using the commercial Ansys® Fluent, Release 18.2 software at tunnel conditions of 0.85 Mach and a Reynolds number

of 5 million based on the mean aerodynamic chord (MAC) to validate the numerical model. Additional information about the wind tunnel testing and experimental results can be found in the literature [16][17]. In this study, the experimental data for the wing-body-nacelle-pylon configuration of the CRM was used to validate the numerical model. The experimental data available for the wing-body-nacelle-pylon configuration of the CRM was obtained on a configuration without the horizontal tail. This would result in an over prediction of drag and a slight under prediction of lift in the numerical model.

### 2.3.2 Mesh

BETA CAE Systems' commercial mesh generation software, ANSA, was used to create the numerical grid of the domain and the aircraft. The mesh was composed of an unstructured surface mesh of triangular elements and a hybrid-unstructured volume mesh consisting of prism layers and tetrahedral elements. Since the CRM aircraft is symmetric about the fuselage centerline, a half model was used to conduct the validation study. First, a hemispherical domain was created around the aircraft with a radius equal to 100 times the MAC of the aircraft. Next, size boxes were used to define refinement regions around the aircraft to better capture the flow field. The domain and the refinement regions created using the size boxes are visualized in Figure 12.

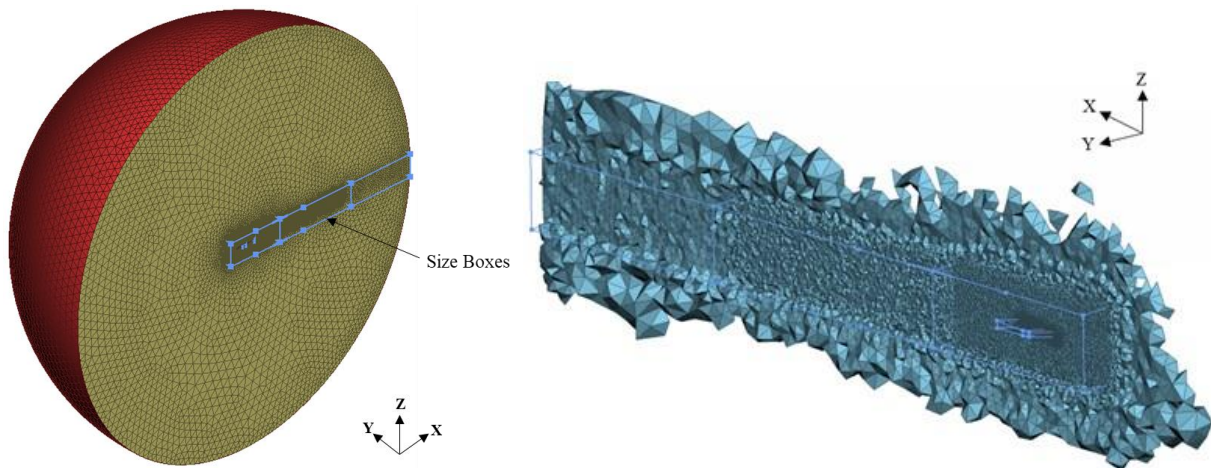


Figure 12. Domain surface mesh and size boxes used for CRM aircraft wake refinement.

Size boxes were used around the aircraft to better capture the flow field. The surface mesh was created using element sizes ranging from  $5.12E-05$  m to 0.05 m on the leading and trailing edge of the wing and horizontal tail. The surface mesh elements of the fuselage were created using element sizes ranging from  $2.4E-04$  m to 0.34 m. Figure 14 provides the element length distribution over the aircraft surface.

The prism boundary layers over the aircraft were generated with a first layer height of 0.0178 m calculated based on a target  $y^+$  value of 500. Seven layers were generated with a growth ratio of 1.16 and a final aspect ratio of 0.5. The rest of the volume mesh was generated using tetrahedral elements. Surface and volume mesh details are shown in Figure 15.

The total volume mesh size, broken down into prism layers and tetrahedral domain, is provided in Table 8. Information regarding the mesh and the mesh quality is available in Appendix A.1.

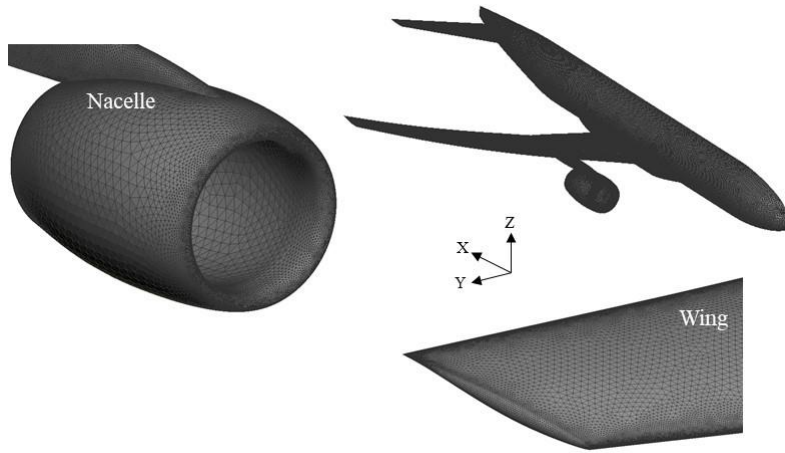


Figure 13. CRM aircraft surface mesh details.

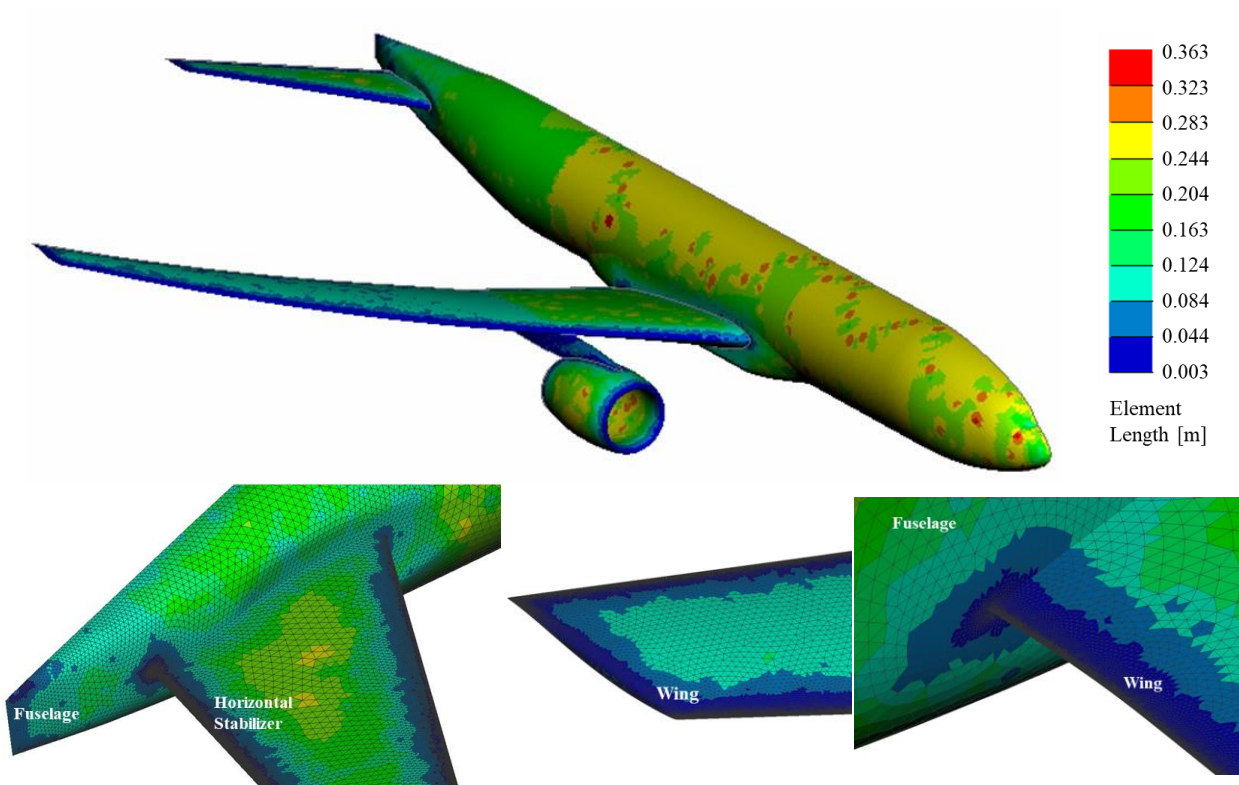


Figure 14. Surface mesh element length information on the CRM aircraft.

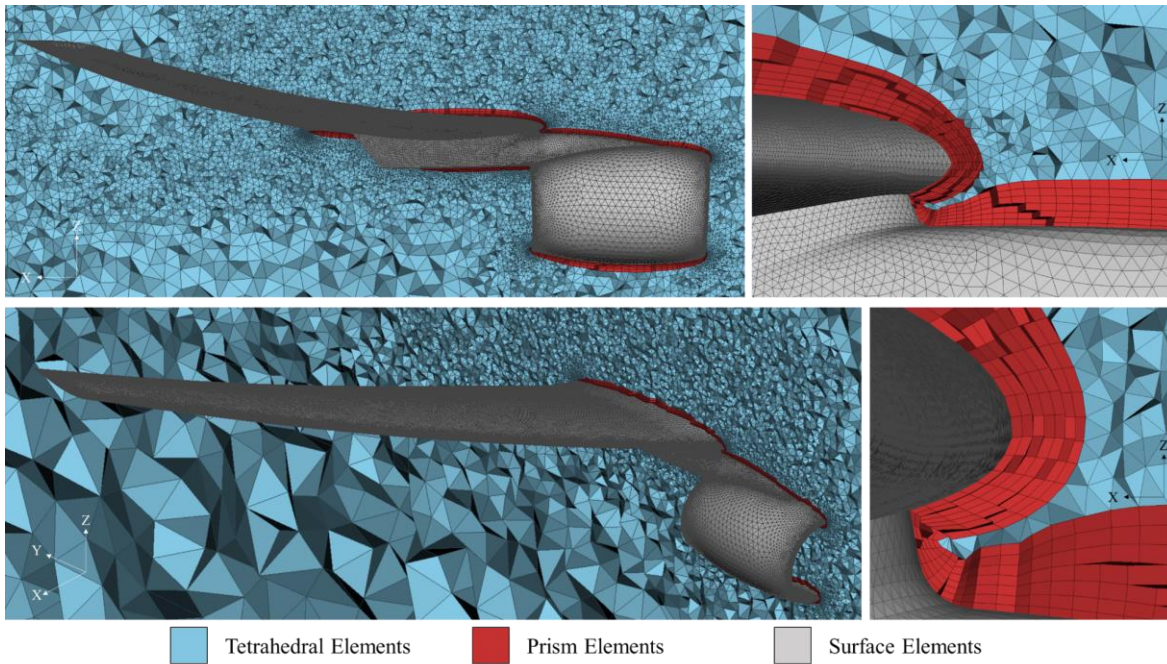


Figure 15. Prism and tetrahedral volume mesh generated for CRM aircraft.

Table 8. Volume mesh information for the CRM aircraft and domain.

Name	Volume Mesh Size ( <i>millions</i> )
Prism Layers on Aircraft	$\approx 4.87$
Tetrahedral Volume	$\approx 23.41$

### 2.3.3 Numerical Model

The operating conditions for the steady-state simulation of the CRM aircraft replicated the wind tunnel conditions used during the drag prediction workshop. The commercial Ansys® Fluent software, Release 18.2, was used to conduct the steady-state analysis.

The domain's boundary was set to pressure far-field, and a symmetry plane was defined for the aircraft half model as shown in Figure 16. The aircraft surfaces were modeled as no-slip adiabatic walls. The fluid within the domain was modeled as compressible, dry air, with the density being calculated using the ideal gas equations within Fluent. The gauge pressure and Mach number were 4194.95 Pa and 0.85 respectively for the pressure far-field boundary.

A steady-state, pressure-based, coupled algorithm with second-order spatial discretization was used to solve the flow field. A realizable k- $\epsilon$  turbulence model was used with turbulence intensity and viscosity ratio set to 1 % and 2, respectively. Since the prism mesh was generated with a target  $y^+$  value greater than 30, the standard wall function approach was used in the numerical setup. The

domain boundary conditions are shown in Figure 16. The operating conditions were selected to match the wind tunnel conditions and are summarized in Table 9.

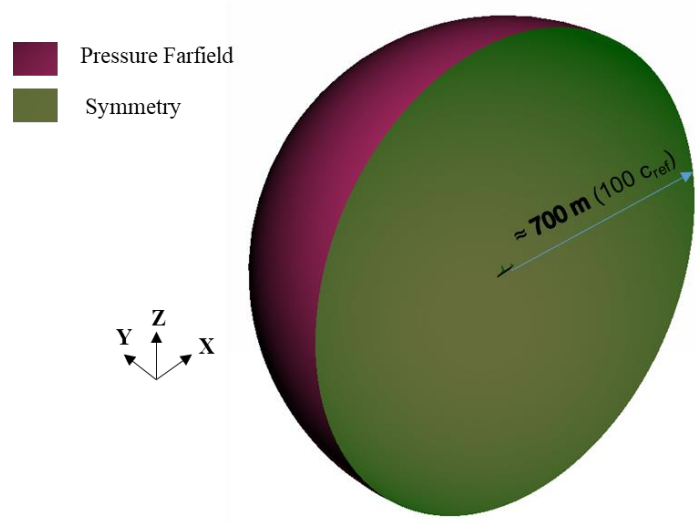


Figure 16. Boundary conditions used for the CRM aircraft validation study.

Table 9. Operation condition and other relevant parameters used for the CRM validation study.

<b>Mach Number</b>	0.85
<b>Reynolds Number</b>	$5.0 \times 10^6$
<b>Angle of Attack</b>	$2.75^\circ$
<b>Temperature</b>	311 K
<b>Pressure</b>	4,194.95 Pa
<b>Density</b>	$0.047 \text{ kg/m}^3$
<b>Viscosity</b>	$1.897\text{E-}05 \text{ N-s/m}^2$
<b>Freestream Velocity</b>	300.48 m/s

#### 2.3.4 Results

The resultant lift and drag coefficients are compared with the available experimental data [15] in Table 10. The difference in lift coefficient between the experimental data and simulation results was less than 2%. The higher drag coefficient obtained from the simulation results compared to the experimental data could be attributed to the choice of wall-modled turbulence modeling approach as well as the presence of the horizontal tail in the simulation model. Since the drone trajectory depends on the pressure distribution over the wing and the contribution of aircraft drag to the drone's trajectory is not significant, the large variation in drag coefficient between the experiment and simulation was not considered to be of consequence for the current study.

Table 10. CRM aircraft force coefficients obtained from simulation compared against experimental data.

Force Coefficients	Experimental Data	Simulation Results	% Difference from Expt. Data
$C_L$	0.493	0.501	1.5
$C_D$	0.026	0.035	33.3

The experimental data for pressure coefficient over the wing at various lateral locations were also available for comparison. The lateral stations are specified by the fraction of semispan,  $\eta$ . Table 11 provides information regarding the various lateral locations where the pressure coefficient ( $C_P$ ) was measured. Refer to Figure 17 for a representation of the lateral stations highlighted using green lines.

Table 11. Lateral positions at which the pressure coefficients are measured.

$C_P$ Measurement Location		
Station	$\eta$	Distance from Fuselage Centerline (m)
Station 1	0.131	3.85
Station 2	0.286	8.40
Station 3	0.502	14.75
Station 4	0.603	17.72
Station 5	0.846	24.86
Station 6	0.95	27.91

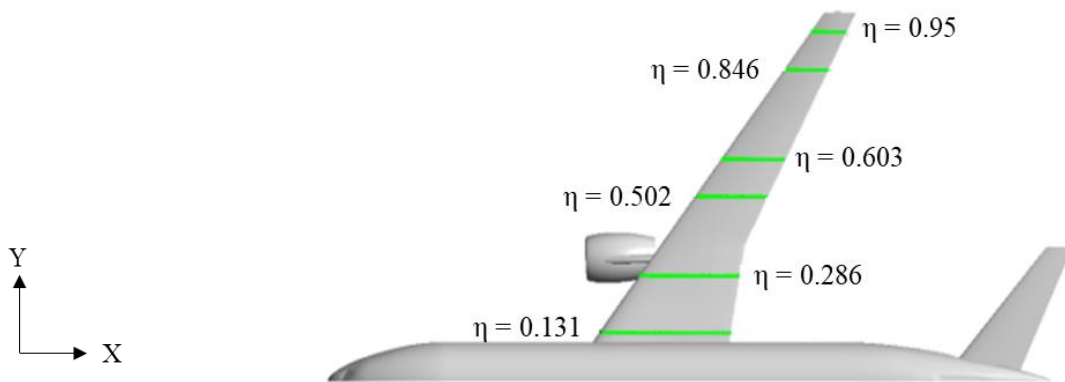


Figure 17. Lateral positions where  $C_P$  is available in experimental data on the CRM wing.

The absolute pressure contours over the CRM aircraft surface are provided in Figure 18. The pressure contour over the wing at plane locations at Stations 1 and 5 is provided in Figure 19. The  $C_P$  on the wing surfaces at the six lateral stations specified in Table 11 is compared with available experimental data in Figure 20. The simulated  $C_P$  distributions are similar to experimental data at most lateral stations. The location of the shockwave was slightly different; however, the leading-edge pressure distribution that directly affects the drone trajectory shows a good correlation with experimental data. Additionally, the trajectory simulations were conducted at aircraft holding conditions under subsonic conditions. The simulation shows a good correlation to experimental data in the low-speed regions.

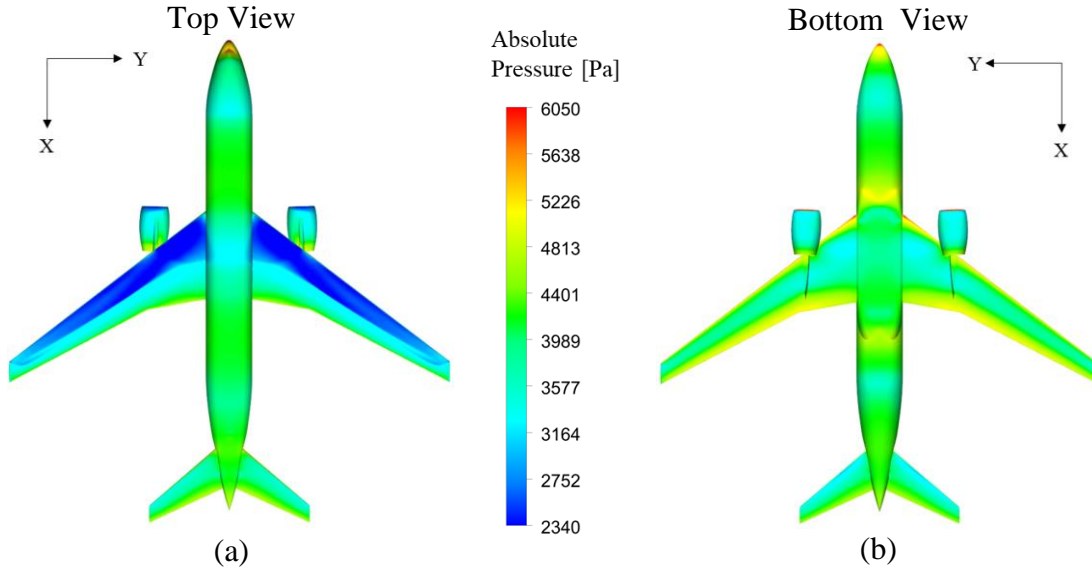


Figure 18. Absolute pressure contours over the CRM aircraft surface from the (a) Top view and (b) Bottom view.

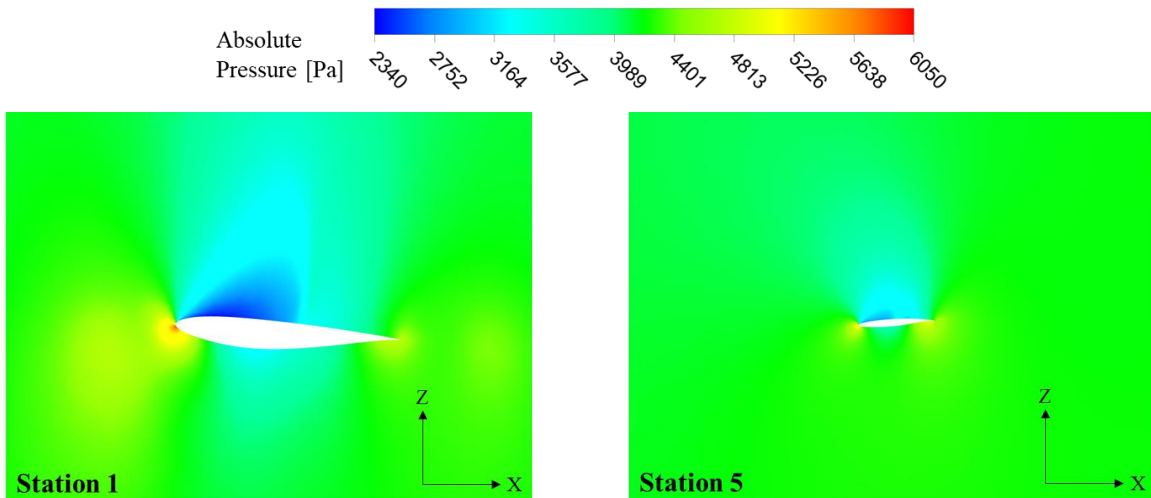


Figure 19. Pressure contours over the wing at planes located at Stations 1 and 5 lateral locations.

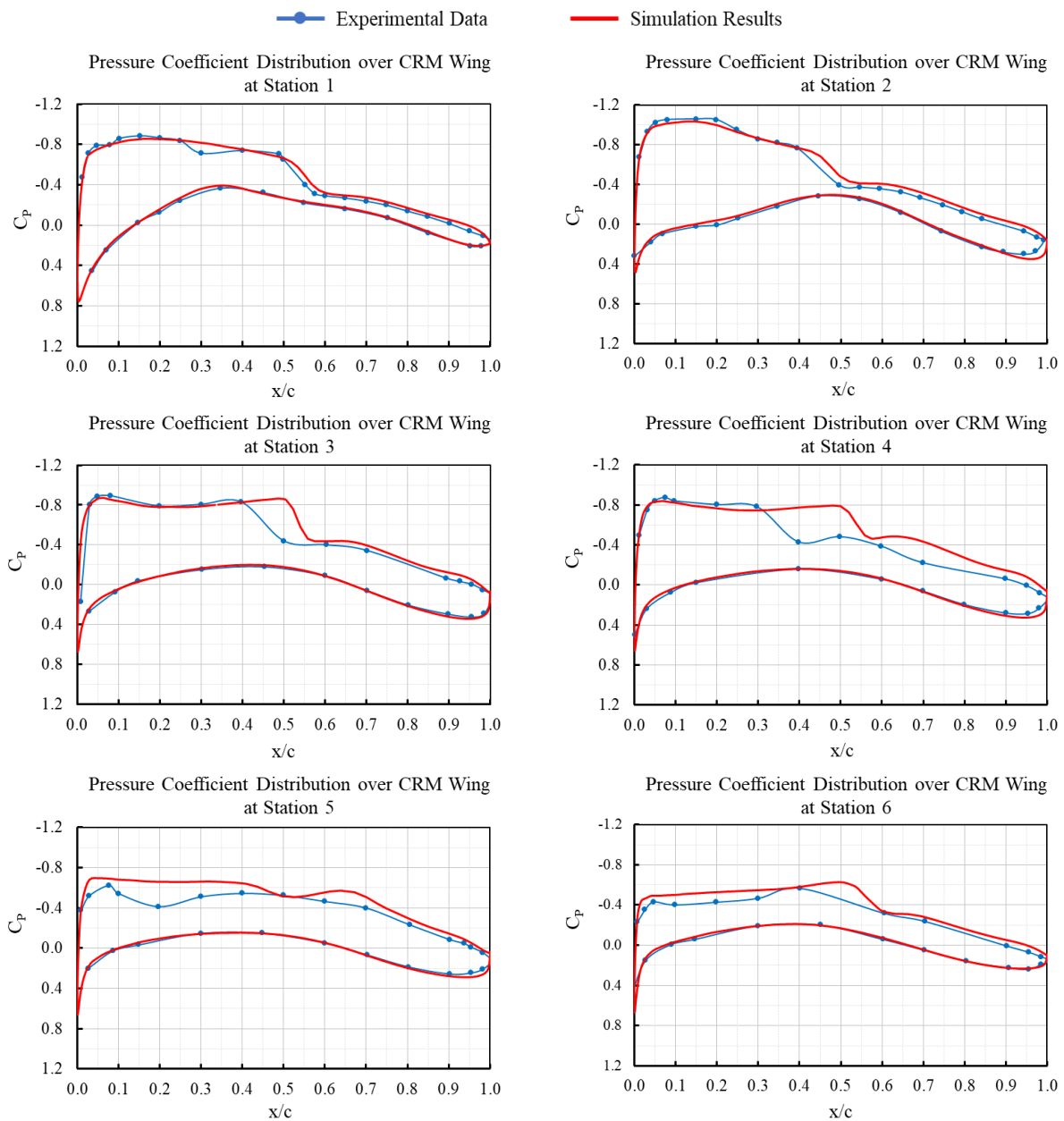


Figure 20. Pressure coefficient plots over the CRM wing at Stations 1 through 6 compared with experimental data.

## 2.4 HL-CRM AERODYNAMIC PERFORMANCE VALIDATION

### 2.4.1 Introduction

The numerical model used in Ansys<sup>®</sup> Fluent software, Release 18.2, to conduct the steady-state analysis on the HL-CRM geometry was validated by comparing the results with experimental data. Wind tunnel conditions obtained from the experimental investigations conducted by Koklu et al.

[14] were used to define the operating conditions for the simulation. The steady-state analysis used a Mach number of 0.2, a Reynolds number of 3.27 million, and a dynamic pressure of 2,870 Pa. The HL-CRM aircraft was simulated at an AoA of  $8^\circ$ . The lift and drag obtained from the simulation were compared with the experimental data. The  $C_p$  distribution over the wing was compared at 24% and 55.2% of the semispan.

### 2.4.2 Mesh

The HL-CRM aircraft mesh was generated using BETA CAE's commercial software, ANSA. The mesh was composed of an unstructured A.2.

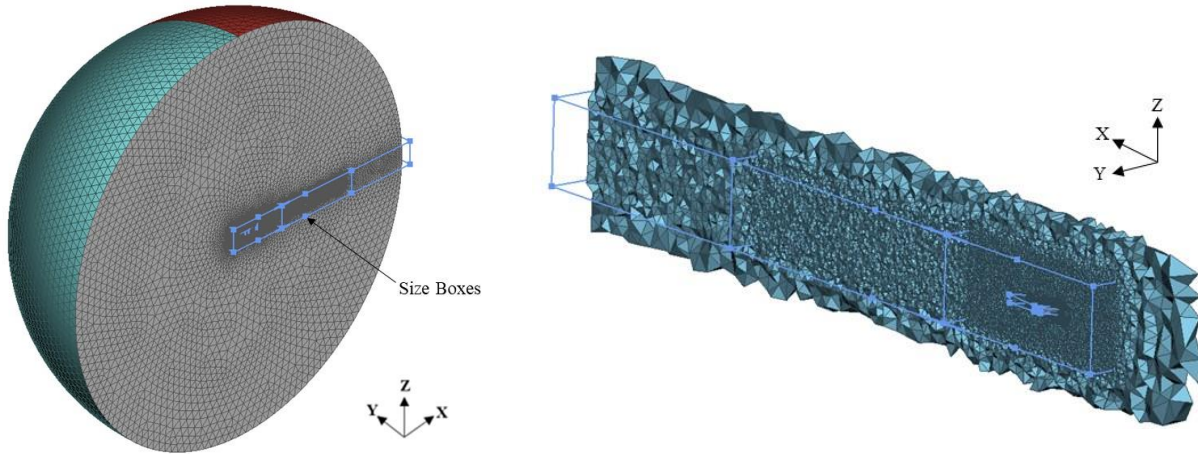


Figure 21. Domain surface mesh and size boxes were used to define wake refinement for the HL-CRM aircraft.

Special attention was paid to surfaces and edges in close proximity, such as slat and flap surfaces while generating the surface mesh as shown in Figure 22. The surface mesh for surfaces in proximity was created with equal element sizes to prevent skewness in the prism and tetrahedral volume elements during volume mesh generation. Figure 23 and Figure 24 show element lengths used to generate the surface mesh over the entire aircraft and regions where the surfaces are in close proximity: the inboard flap and fuselage surfaces and the slat and wing surfaces.

Boundary layers consisting of prism elements were generated over the aircraft with a target  $y^+$  value of 500. The first layer height was calculated to be 0.027 m. Seven boundary layers were generated with a growth factor of 1.15 and a final aspect ratio of 0.4. Tetrahedral elements were used to generate the rest of the volume mesh.

Figure 25 shows the prism layers and the tetrahedral elements generated around the aircraft. The effect of size boxes can be observed over the wing and fuselage in the tetrahedral elements. The resultant prism layers in the regions with surfaces in close proximity are also depicted in Figure 25. The total volume mesh size is provided in Table 12. Additional information regarding the mesh quality is provided in Appendix A.2.

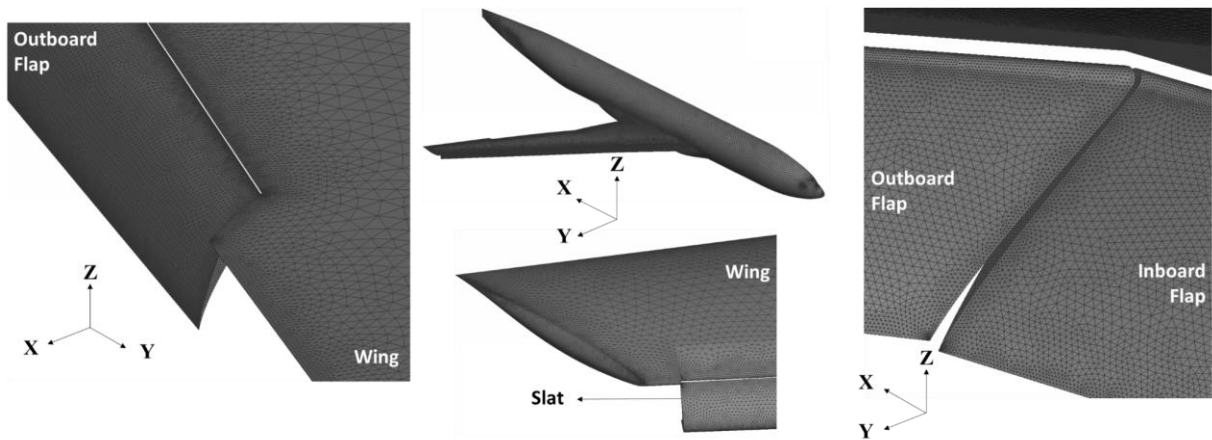


Figure 22. HL-CRM aircraft surface mesh details.

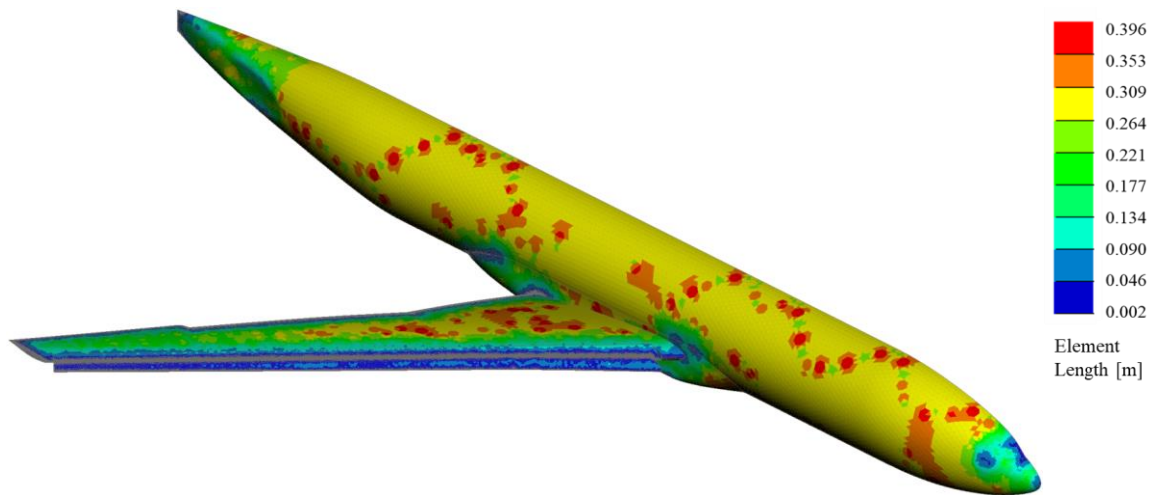


Figure 23. Surface mesh element length information on the HL-CRM aircraft.

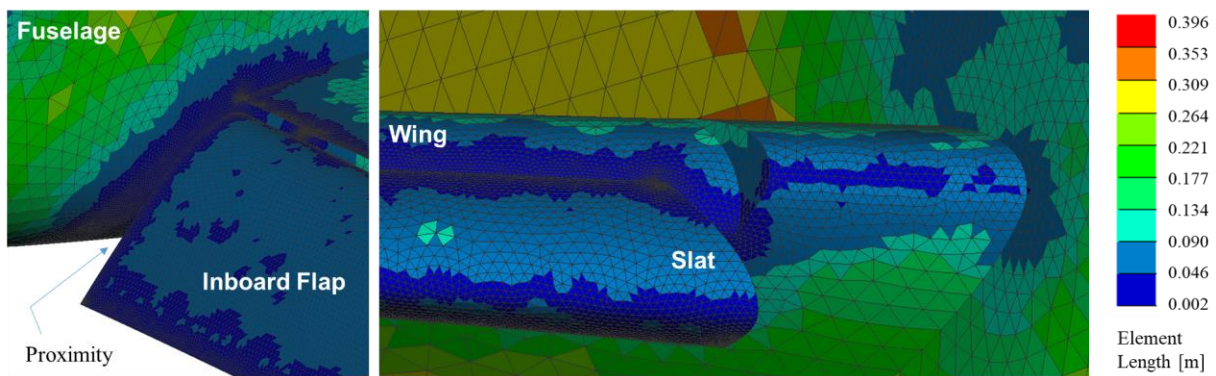


Figure 24. Element lengths used on the HL-CRM aircraft surfaces in proximity.

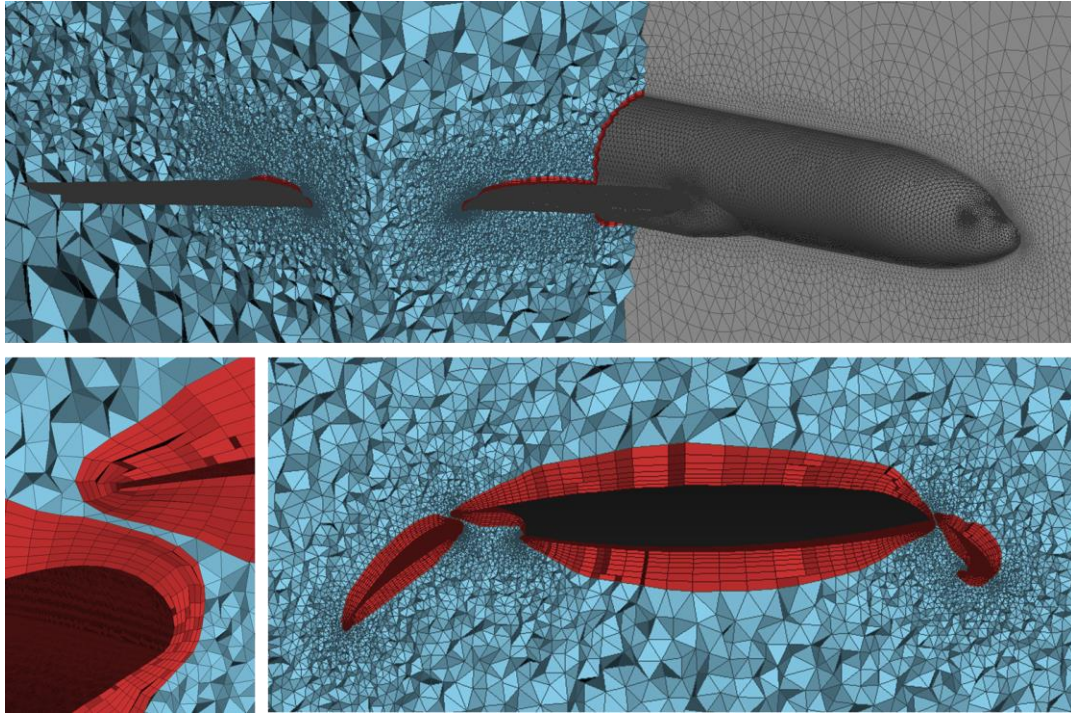


Figure 25. Prism and tetrahedral volume mesh generated for the HL-CRM aircraft.

Table 12. Volume mesh information for the HL-CRM aircraft and domain.

<b>Name</b>	<b>Volume Mesh Size (<i>millions</i>)</b>
Prism Layers on Aircraft	$\approx 4.7$
Tetrahedral Volume	$\approx 15.5$

### 2.4.3 Numerical Model

Steady-state CFD simulations were set up using Ansys<sup>®</sup> Fluent, Release 18.2, to match the wind tunnel operating conditions [14]. The wind tunnel tests for the HL-CRM were conducted at subsonic speeds. Since the simulation was conducted at subsonic speeds with incompressible gas, the boundary conditions of the domain were set to velocity inlet and pressure outlet with the XZ plane modeled using symmetry conditions as seen in Figure 26. A velocity of 68.6 m/s was defined at the velocity inlet, while a pressure outlet was defined with 0 Pa gauge pressure. The aircraft surfaces were modeled as no-slip adiabatic walls.

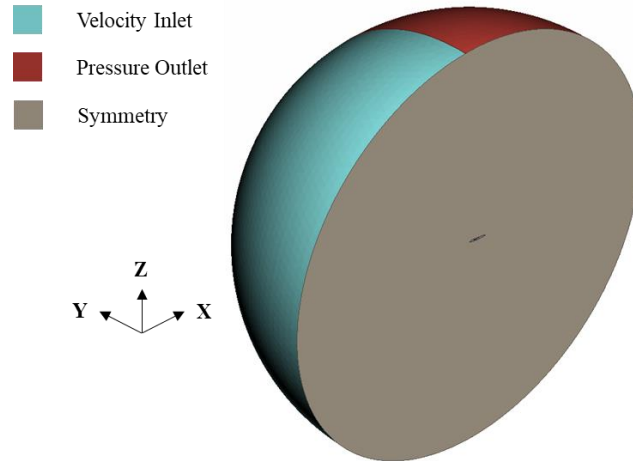


Figure 26. Boundary conditions used for HL-CRM validation study.

A pressure-based coupled solver with double precision available within Ansys<sup>®</sup> Fluent, Release 18.2, was used to solve the flow over the aircraft. The realizable k- $\epsilon$  turbulence model with turbulence intensity and viscosity ratio parameters set to 1 and 2% respectively was used. The boundary layer was resolved using standard wall functions since the wall  $y^+$  was greater than 30.

Standard sea-level atmospheric conditions were selected for pressure, temperature, and density to match tunnel conditions. Viscosity was increased to  $1.79\text{E-}04 \text{ N-s/m}^2$  to match the wind tunnel Reynolds number. The angle of attack was set to  $8^\circ$  by providing the velocity components to air at the inlet, and the simulation results were compared with the available experimental data. The operating conditions are summarized in Table 13.

Table 13. Operating conditions and other relevant parameters for the HL-CRM validation study.

<b>Mach Number</b>	0.2
<b>Reynolds Number</b>	$3.27 \times 10^6$
<b>Angle of Attack</b>	$8.0^\circ$
<b>Temperature</b>	288 K
<b>Pressure</b>	101,325 Pa
<b>Density</b>	$1.225 \text{ kg/m}^3$
<b>Viscosity</b>	$1.79\text{E-}04 \text{ N-s/m}^2$
<b>Freestream Velocity</b>	68.6 m/s

#### 2.4.4 Results

The steady-state simulation results were compared with the experimental data available in the literature [14]. The lift and drag coefficients of the HL-CRM aircraft obtained from the simulation

are compared with the experimental data in Table 14. The lift coefficient is within 10% of the experimental value. The drag coefficient was over predicted; however, it was not considered to be of consequence to this study.

Table 14. HL-CRM aircraft force coefficients obtained from simulation compared against experimental data.

<b>Force Coefficients</b>	<b>Experimental Data</b>	<b>Simulation Results</b>	<b>% Difference from Expt. Data</b>
$C_L$	1.803	1.646	-8.7
$C_D$	0.166	0.193	16.3

The experimental investigations conducted by Koklu et al. [14] contained pressure coefficient information at two lateral locations along the HL-CRM wing that were used for comparison to simulation results. The two lateral locations for which experimental  $C_P$  data is available are provided in Table 15. The green lines in Figure 27 highlight the locations.

Table 15. Lateral positions at which the pressure coefficients are measured.

<b><math>C_P</math> Measurement Location</b>		
<b>Station</b>	<b><math>\eta</math></b>	<b>Distance from Fuselage Centerline (m)</b>
Station 1	0.240	7.06
Station 2	0.552	16.23

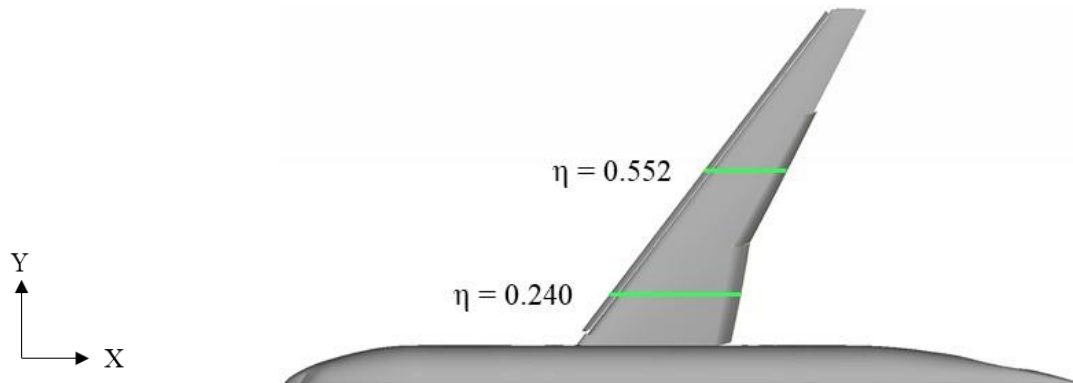


Figure 27. Lateral positions where  $C_P$  is available in experimental data on the HL-CRM wing.

The absolute pressure contours over the HL-CRM aircraft are presented in Figure 28. The pressure contours of the flow field over the wing at each lateral location are provided in Figure 29.  $C_P$  extracted from the simulation over the HL-CRM aircraft wing, slat, and flap surfaces are compared with available experimental data in Figure 30. The pressure coefficients over a larger portion of

the wing obtained from simulation are similar to experimental data. The under-predicted suction peaks provided a conservative value when proceeding to the drone trajectory analysis.

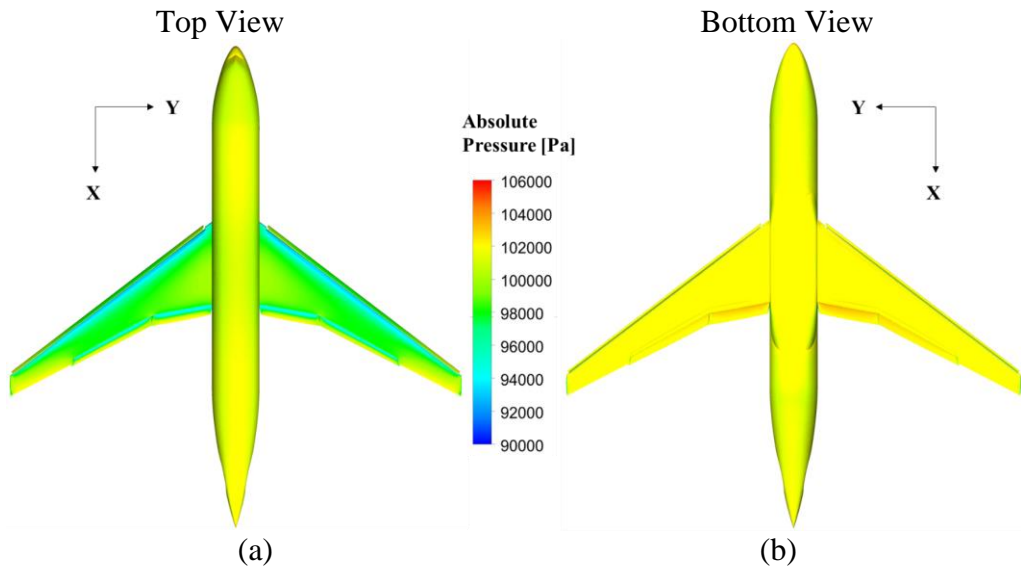


Figure 28. Absolute pressure contours over the HL-CRM aircraft surface from the (a) Top view and (b) Bottom view.

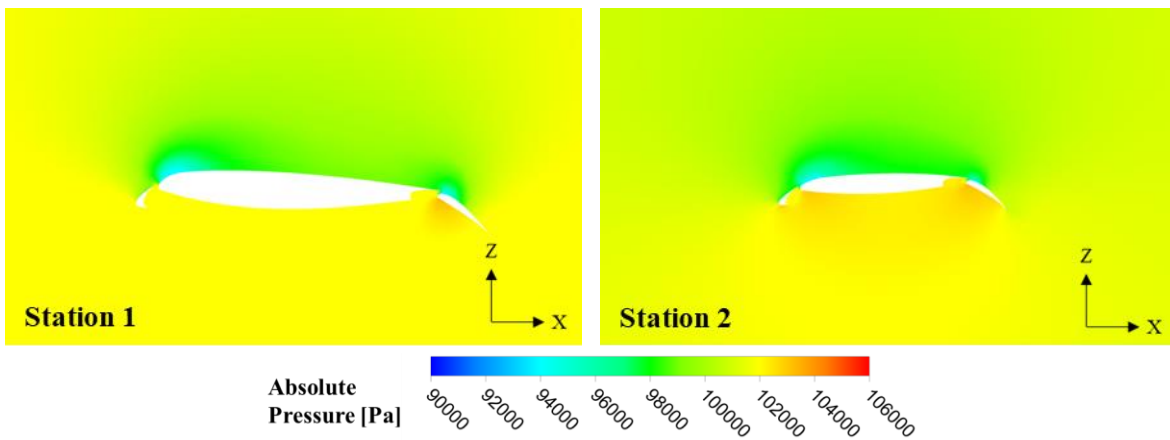


Figure 29. Pressure contours over the HL-CRM wing at Stations 1 and 2.

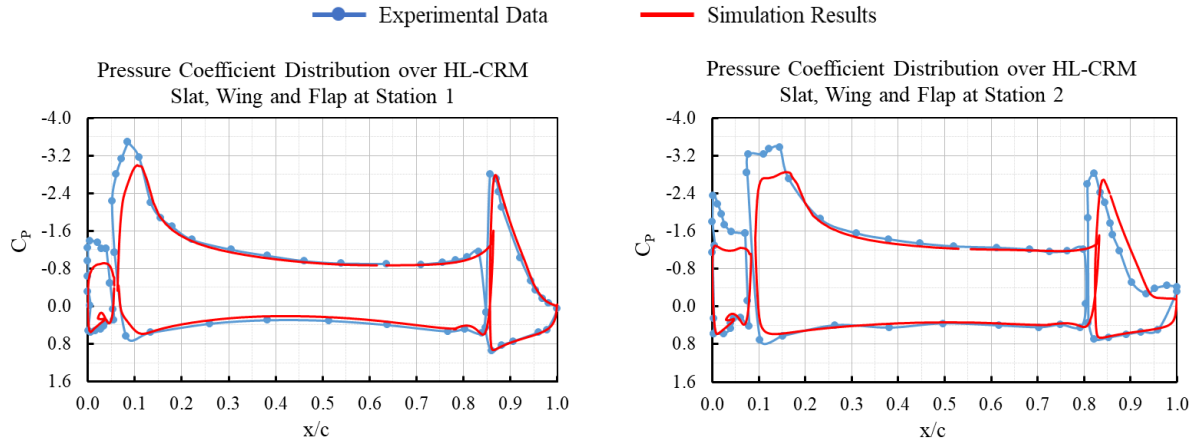


Figure 30. Comparison of simulation and experimental pressure coefficient distributions over the HL-CRM wing, slat, and flap at Stations 1 and 2.

## 2.5 CONCLUSIONS OF AIRCRAFT AERODYNAMIC PERFORMANCE

The mesh and numerical methodology used to run the steady-state analysis of the CRM and HL-CRM aircraft were validated against experimental data. At low speeds, the grid spacing used for the aerodynamic performance evaluation of the aircraft produced similar results as the experimental data. In addition, the wall function approach with a realizable  $k-\epsilon$  turbulence model provided satisfactory results for both aircraft. Therefore, the grid spacing for the CRM and HL-CRM aircrafts and the numerical methodology used for the validation was used in the drone trajectory analysis simulations.

### 3. UAS TRAJECTORY ANALYSIS

#### 3.1 OVERVIEW

The current research effort aims to evaluate whether or not a UAS/drone will collide with a transport category aircraft when the flow field interaction between the drone and the aircraft is taken into consideration. To assess the possibility of drone collision, it is important to establish if the interaction between the drone and the aircraft flow field will cause the drone to deflect away from the oncoming aircraft. The simulation of drone trajectory requires the precise prediction of forces and moments on the drone as well as the aircraft and the prediction of the change in forces and moments of the drone due to the interaction between the drone and aircraft flow fields. The predicted aerodynamic forces and moments need to be applied to the object, in this case, the drone, in real-time to predict the object's trajectory.

Traditionally, analytical [18] [19], uncoupled, and coupled approaches have been used to model the trajectory of an object in a given flow field. A database of aerodynamic forces and moments with various object orientations is first created using wind tunnel testing or CFD for the uncoupled approach. A vast number of data points need to be generated. These loads and moments are later used in the rigid body equations of motion to calculate the object's location, orientation, and trajectory. Trajectories of store separation [20] [21] and ice particles [22] [23] were modeled using this approach. In recent years, with the advancement in CFD and high-performance computing, the coupled CFD-RBD approach has proved to be more feasible. This method is widely used to model trajectories of objects.

Store separation [24] [25], projectile behavior during flight [26] [27] [28], and tracking of plate-type windborne debris [29] [30] are modeled using the coupled approach. In these applications, the aerodynamic forces and moments obtained using CFD are coupled with 6-DOF rigid body dynamics techniques to obtain a time-accurate trajectory simulation of the objects under study. For store separation problems [18] [31], the simulations are validated with wind tunnel [32] and flight test data. The CFD-RBD approach is generally used with overset grids [25] [26], unstructured tetrahedral meshes [18], Cartesian [31], and 2<sup>n</sup> tree [28] meshes to perform trajectory calculations for the prior mentioned applications. The commercial Ansys<sup>®</sup> Fluent software with dynamic meshing (smoothing and local remeshing) [18] [29] and overset meshing [25] has been used to solve for the trajectory of objects in the literature. The commercial CFD++ software with unstructured mesh [26] and hybrid structured-unstructured mesh [27] has also been used to solve coupled CFD-RBD problems in the literature.

The current trajectory simulation study differs slightly from the aforementioned ice particle, store separation, and projectile problems. For the current study, the drone's trajectory needs to be modeled by taking into consideration the flow field interaction between the aircraft and the drone. Since the drone and the aircraft are moving towards each other, the drone's trajectory changes due to the effect of the pressure field around the aircraft. This situation cannot be easily recreated in a wind tunnel to obtain test data, and it is not possible to obtain a database of aerodynamic loads on the drone due to the dynamic nature of the flow field. Since the traditional methods for trajectory tracking cannot be used for the current study, the time-accurate coupled CFD-RBD approach was used to obtain the drone trajectory as it approached a transport category aircraft. Thus helping analyze the possibility of collision.

For the current study, due to the availability of the solver, the coupled CFD-RBD approach available in the Ansys® Fluent, Release 18.2 solver was used. Additionally, a hybrid structured-unstructured overset mesh was generated using BETA CAE’s ANSA software to model the drone’s motion within the fluid volume created around the drone and aircraft.

### 3.2 METHODOLOGY

A coupled CFD-RBD method, available with Ansys® Fluent Release 18.2, was used to simulate the drone’s trajectory as it approached the aircraft. This coupled CFD-RBD method solves for aerodynamic forces and moments of the rigid body using the Reynolds-averaged Navier-Stokes (RANS) equations for each discretized time step. These aerodynamic forces and moments are used as input to the RBD solver within Ansys® Fluent called the 6-DOF solver that solves the rigid body equations of motion. In addition to the RANS computed aerodynamic forces and moments, the user can input any additional external forces and moments to the solver using User-Defined Functions (UDFs). The 6-DOF solver computes the displacement and the change in orientation of the rigid body based on these inputs. The software loops back the new object location and orientation to the RANS solver. The mesh updates to the new position, and aerodynamic forces and moments are computed based on this object’s location and orientation. The process repeats for the specified number of time steps to obtain the trajectory. The process flow is provided in Figure 31.

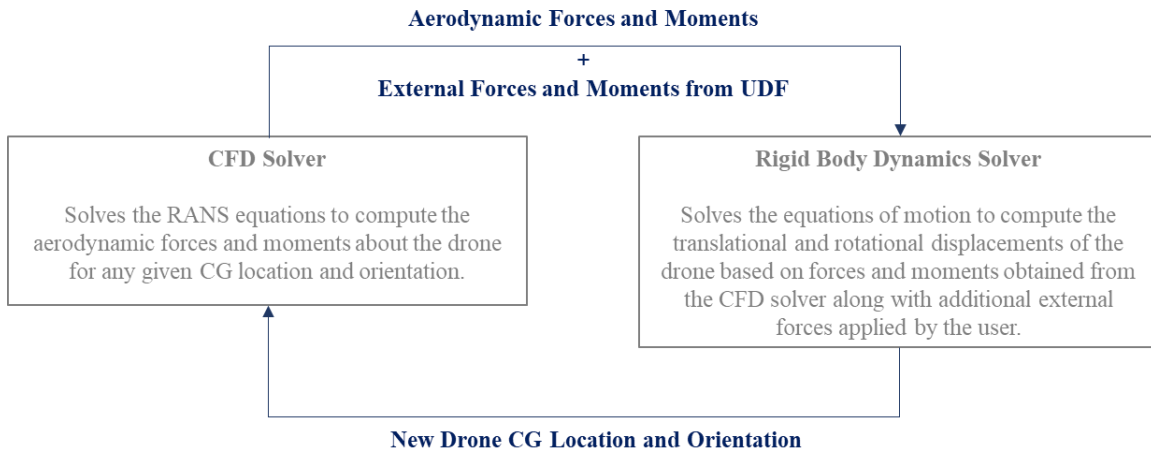


Figure 31. An overview of the coupling between the CFD solver and the RBD solver in Ansys® Fluent.

In the current study, the drone was subjected to two types of motion: prescribed motion and rigid body motion (unprescribed motion). During the prescribed motion, the drone, modeled as a rigid body, was constrained in all but one direction: the direction of motion (along the X-axis). A constant velocity value was assigned to the drone along the direction of motion for prescribed motion. During the 6-DOF rigid body motion (unprescribed motion), the drone was unconstrained in all six-degrees-of-freedom (3 translational and 3 rotational) within the solver, and additional external forces and moments were added using the UDF to partially constrain the rigid body motion according to the requirements of the investigation.

The motion of the drone through the domain was captured using Chimera/overset grid scheme. To ensure that at the start of the simulation, the drone was outside the influence of the aircraft flow

field, the simulation was started with the drone situated at a large distance away from the aircraft. This significantly increased the total mesh size. Therefore, adaptive mesh refinement was used to maintain a total mesh size of less than 40 million, thereby reducing memory usage and computational time. Details regarding the solvers and the mesh are provided in the following sections.

### 3.2.1 Computational Fluid Dynamics

The aerodynamic forces and moments experienced by the drone and the aircraft were obtained using transient, incompressible RANS equations available in Ansys® Fluent, Release 18.2. A pressure-based coupled solver was used with first-order transient formulation and second-order spatial discretization.

For the CFD-RBD coupling within the software, the 6-DOF solver was used. The conservation equations capture the flow over the moving boundaries and obtain the drone aerodynamic forces and moments. For a dynamic mesh with moving boundaries, the conservation equation is:

$$\frac{d}{dt} \int_V \rho \phi dV + \int_{\partial V} \rho \phi (\vec{u} - \vec{u}_g) \cdot d\vec{A} = \int_{\partial V} \Gamma \nabla \phi \cdot d\vec{A} + \int_V S_\phi dV \quad (3.1)$$

Where,

$\rho$  is the fluid density

$\vec{u}$  is the flow velocity vector

$\vec{u}_g$  is the mesh velocity of the moving mesh

$\Gamma$  is the diffusion coefficient

$S_\phi$  is the source term of  $\phi$

### 3.2.2 Rigid Body Dynamics

The drone was modeled as a rigid body, and the 6-DOF solver available in the software was used to track the drone's motion through the domain as it approached the aircraft. In addition, the overset mesh method was used to update the fluid volume mesh as the drone moved through the domain.

The Ansys® Fluent solver inputs the aerodynamic forces and moments obtained from the RANS solver into the 6-DOF at each time step. These forces and moments are used to calculate the translational motion of the CG of the rigid body and the orientation of the rigid body. The following equations are used to calculate the translational (Equation (3.2)) and angular (Equation (3.3)) accelerations of the CG of the rigid body.

$$\dot{\vec{v}}_G = \frac{1}{m} \sum \vec{f}_G \quad (3.2)$$

$$\dot{\vec{\omega}}_B = L^{-1} \left( \sum \vec{M}_B - \vec{\omega}_B \times L \vec{\omega}_B \right) \quad (3.3)$$

Where,

$\vec{v}_G$  is the translational acceleration of the body

$\dot{\vec{\omega}}_B$  is the angular acceleration of the body

Subscript 'G' denotes the global (inertial) reference frame

Subscript 'B' denotes the body-fixed reference frame

$m$  is the mass of the body

$\vec{f}_G$  represents the forces acting on the body

$\vec{M}_B$  represents the moment vector of the body

$\vec{\omega}_B$  is the angular velocity of the body

$L$  is the inertia tensor

The moments of the rigid body are transformed from inertial frame to body-fixed reference frame using the following transformation matrix:

$$\vec{M}_B = R \vec{M}_G \quad (3.4)$$

$$R = \begin{bmatrix} C_\theta C_\psi & C_\theta S_\psi & -S_\theta \\ S_\phi S_\theta C_\psi - C_\phi S_\psi & S_\phi S_\theta S_\psi + C_\phi C_\psi & S_\phi C_\theta \\ C_\phi S_\theta C_\psi + S_\phi S_\psi & C_\phi S_\theta S_\psi - S_\phi C_\psi & C_\phi C_\theta \end{bmatrix} \quad (3.5)$$

Where,

$C_x$  and  $S_x$  represent  $\cos x$  and  $\sin x$

$\phi$  represents rotation about X-axis

$\theta$  represents rotation about Y-axis

$\psi$  represents rotation about Z-axis

The accelerations are integrated to obtain the rates of motion, which are then used to update the position and orientation of the rigid body in the fluid domain.

The 6-DOF solver allows the user to constrain various degrees-of-freedom and add additional external forces to the rigid body using UDFs. For this study, a prescribed motion was used for the first few meters of motion (depending on the impact scenario) to allow the numerical variations in the forces and moments to stabilize. Once stability was achieved, the rigid body was partially constrained based on user-defined external forces and moments (see Section 3.7 for more information), and the trajectory was monitored.

### 3.2.3 Overset Mesh Method

An overset mesh, otherwise known as Chimera mesh, was used to model the drone moving in the fluid volume. The overset mesh consists of a component mesh created around the moving drone and a background mesh representing the rest of the volume, including the volume around the apparently stationary aircraft. An overset interface was defined at the component mesh level as seen in Figure 32.

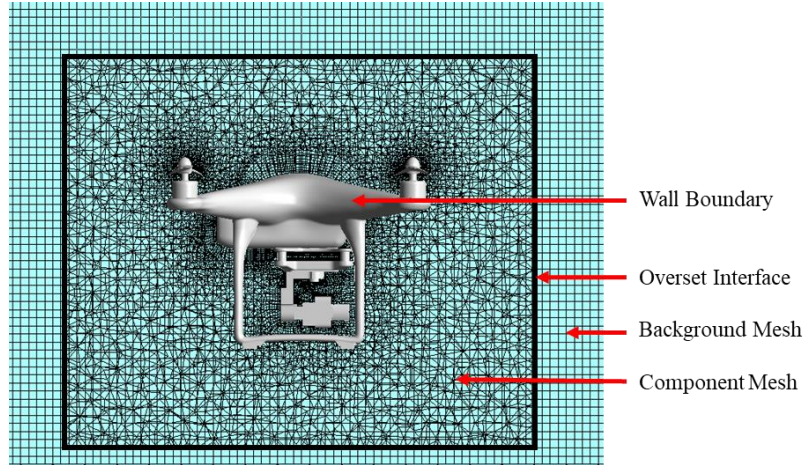


Figure 32. Overset interface definition.

Within Ansys® Fluent, when an overset interface is initialized, the solver completes three steps to establish the connection between the background and component mesh.

- Hole Cutting
- Overlap minimization
- Donor search

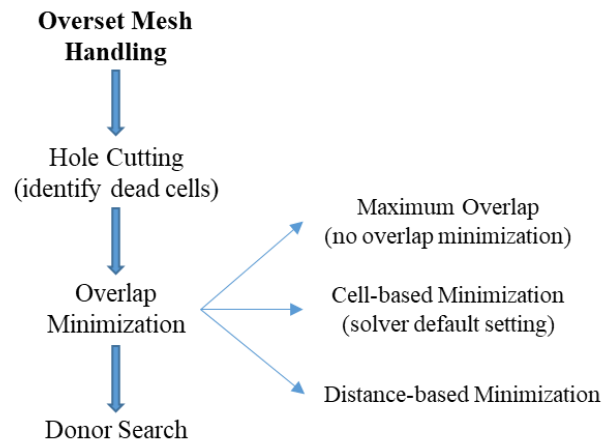


Figure 33. Initialization process of an overset mesh in Ansys® Fluent.

During the hole cutting operation, the solver identifies the cells located outside the flow field and deletes the unnecessary cells creating a hole. For the current study, the solver automatically cut the region of the background mesh that was located within the drone walls when the overset interface was initialized for all the simulations as seen in Figure 34.

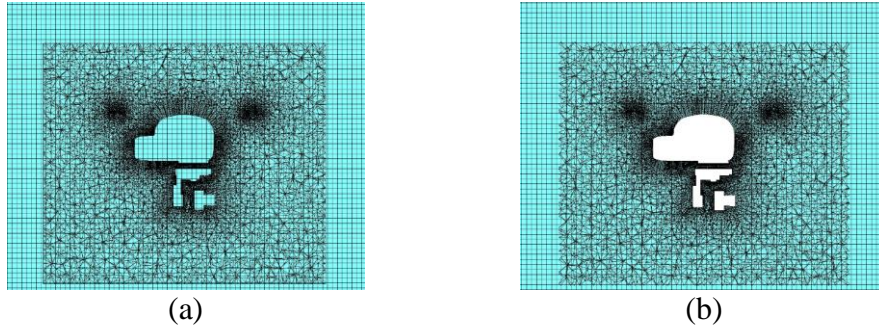


Figure 34. Representation of the overset mesh (a) Before and (b) After the hole cutting operation.

During the overlap minimization step, the solver attempts to minimize the overlap between the background cells and the component cells. The user can choose between three different methods of minimization: maximum overlap, cell-based minimization, and distance-based minimization as shown in Figure 35. Based on preliminary analysis, the maximum overlap approach was used for all the simulations in this study in order to provide sufficient cells for information exchange between component mesh and background mesh. In this method, the solver does not minimize the overlap between the component and background meshes.

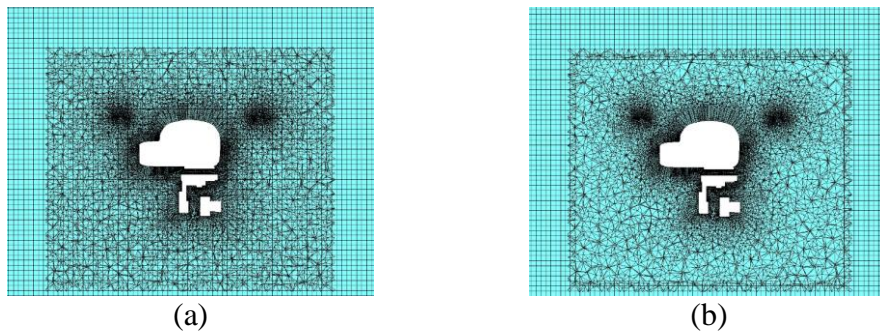


Figure 35. Representation of the overset mesh (a) Without minimization and (b) With cell-based minimization.

The final step is the donor search. This step creates a valid overlap between the background and component by identifying cells through which an exchange of information can occur between the background and component meshes and their respective flow fields. For more information on the overset interface initialization process in Ansys® Fluent, refer to the Fluent 18.2 User’s Guide [33]. Unusable cells, called orphan cells, are occasionally created during the donor search step. Orphan cells occur when the overset interface initialization does not create a valid overlap between background and component cells. The orphan cell count was kept to a minimum to prevent the solution from diverging.

### 3.2.4 Mesh Adaption

Ansys® Fluent provides a mesh adaption option where the existing mesh can be refined and coarsened during the simulation. Fluent uses the hanging node adaption process as the default mesh adaption algorithm. This default adaption process was used for the simulations conducted in this study. The hanging node adaption process divides each cell for each refinement step based on

a predefined template for every cell type. Hexahedral elements are used for this study, and the adaption process divides each hexahedral cell into 8.

The mesh adaption process was carried out by marking the cells within a specific hexahedral region to be refined or coarsened. Once the cells with centroids within the specified region were marked, the mesh was refined and coarsened to two levels to achieve the required refinement in the background mesh.

For this study, the refinement and subsequent coarsening of cells were carried out every 5 m. The refinement region was specified to encompass the component mesh of the drone along with the drone. To account for any change in the drone's velocity as it moved towards the aircraft and consequent change in the distance traveled for a given time, a 0.5 m overlap was set to occur between a coarsened region behind the drone and the next refinement region as shown in Figure 36. In addition, the refined region was extended above the drone to capture any upward deflection that may occur.

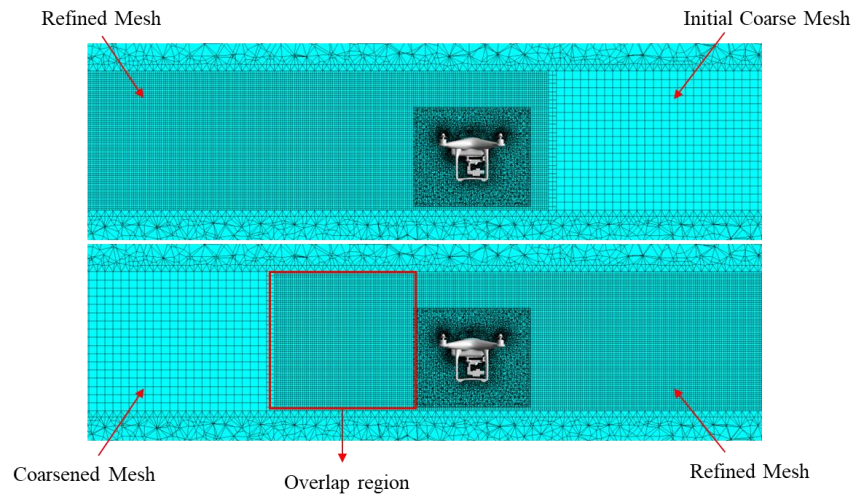


Figure 36. Mesh adaption process as the drone moves through the domain.

This approach allowed the simulation to begin with the drone initially located at a significant distance away from the aircraft without drastically increasing the total mesh size. The reduction in total mesh size decreased the total memory requirement and reduced the overall computational time for each simulation.

### 3.3 ASSUMPTIONS

The following simplifications and assumptions were made to the drone motion as it approached the aircraft:

- The drone was considered a rigid body for the trajectory analysis.
- The effect of the rotation of the propellers was not considered to reduce the computational time. Therefore, the propellers were modeled as stationary.
- The orientation of the drone was set to be  $0^\circ$  as the drone approached the aircraft. Typically, when a quadcopter drone such as the one used in this study moves, it tilts in the direction of motion. However, for the current trajectory analyses, the drone orientation was set to be  $0^\circ$ .

- The drone's motion was partially constrained using external forces and moments to allow for a flight path with constant altitude, attitude, and speed, outside of the influence of the aircraft flow field.
- The pilot did not have sufficient time to react to the change in forces and moments experienced by the drone as it approached the aircraft. Therefore, as the drone moved close to the aircraft, the external forces and moments were not modified to compensate for the changing forces and moments.

### 3.4 DRONE RELEASE LOCATION

The distance at which the drone is situated at the start of the simulation plays an important role in determining its trajectory. The drone needs to be placed at a point sufficiently far away from the aircraft to ensure that the drone is not under the influence of the aircraft's pressure field at the start of the simulation. This large distance guarantees that as the drone initially travels towards the aircraft, the forces and moments are purely due to its motion and not due to the influence of the aircraft's flow field. These forces and moments can be balanced such that the drone can maintain a constant altitude, attitude, and velocity as per the assumptions made for the investigation.

The release location is defined as the point in the domain along the X-axis of the global reference frame where the drone is located at the start of the simulation. It is measured from the drone's center of gravity to the aircraft wing leading-edge (CRM aircraft) or slat leading-edge (HL-CRM aircraft) for each lateral impact location.

The absolute pressure was measured at various points away from the aircraft to determine the release location for the drone as shown in Figure 37. The difference between the absolute pressure and operating pressure of 92,500 Pa was measured in increments of 5 m from the leading-edge of the aircraft wing at the lateral impact location. A difference of less than 10 Pa was considered small enough to establish that the drone was outside the influence of the aircraft at the beginning of the simulation.

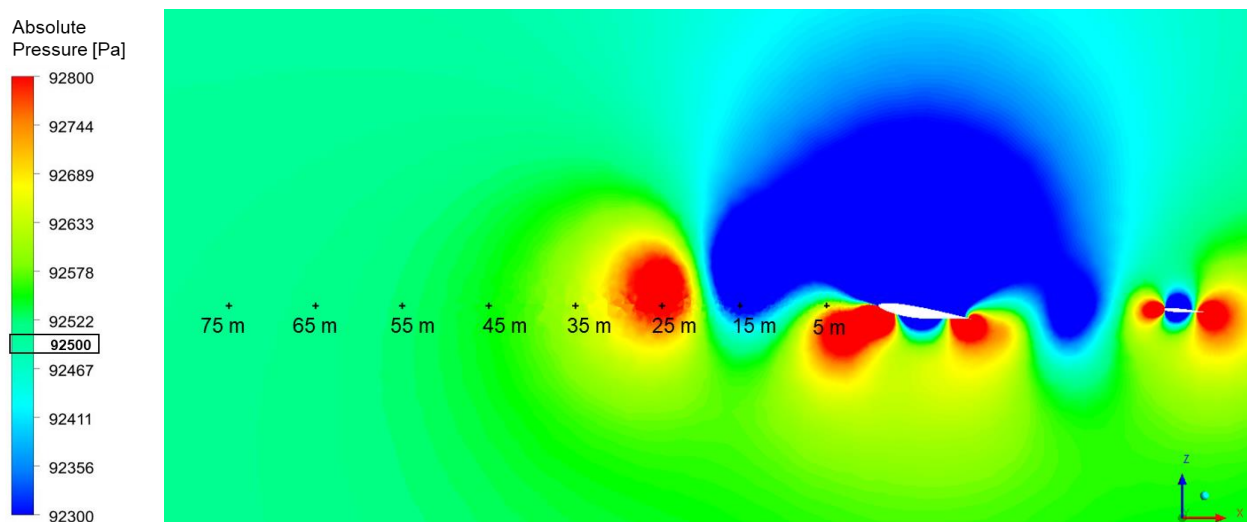


Figure 37. Absolute pressure measurement locations upstream of the CRM aircraft wing leading-edge for impact scenario IC3-IL2.

### 3.4.1 Release Location with Fuselage

Impact scenario IC3-IL2 and impact scenario IC4-IL2 require the respective CRM and HL-CRM fuselages to be included in the simulations due to the proximity of the impact location (IL2) to the fuselage. The flow field of the fuselage could potentially influence the drone trajectory. The absolute pressure at various points upstream of the aircraft was measured at IL2 and compared with the operating pressure of 92,500 Pa. The release location at which the difference between the measured absolute pressure and the operating pressure was acceptable was found to be 75 m away from the aircraft for both impact scenarios. The absolute pressure values obtained at this location for the two impact scenarios are given in Table 16.

Table 16. Change in local pressure from operating pressure at the drone release location for impact scenarios at IL2.

<b>Impact Scenario</b>	<b>Aircraft AoA (degrees)</b>	<b>Release Location (m)</b>	<b>Absolute Pressure (Pa)</b>	<b>Difference from Operating Pressure (Pa)</b>
<b>IC3-IL2</b>	5	75	92509.1	9.1
<b>IC4-IL2</b>	0	75	92509.5	9.5

### 3.4.2 Release Location without Fuselage

Impact scenarios 1 through 5 were simulated using a simplified aircraft geometry with the aircraft fuselage removed and the wing extended up to the symmetry plane. This simplification reduced the total mesh size, computational time, and resources required to run the simulation. Since the impact scenarios in question were simulated at IL1, away from the fuselage, the effect of the fuselage in the flow field at this location was investigated and found to be negligible.

Steady-state simulations were conducted at holding conditions with the aircraft flying at 102.889 m/s. The solver was configured to be similar to the trajectory prediction simulations but without the drone. Two comparisons were made to determine the flow similarity of the simplified model. The absolute pressure of the domain at the impact location at the time of release was assessed to verify the release location was still appropriate, and  $C_P$  distribution over the wing was assessed for similarity of the generated flow field.

Figure 38 shows the pressure flow field of the domain obtained at IL1 simulated with and without the fuselage. The absolute pressure was measured at the point of release with and without the fuselage, and the difference was found to be about 30 Pa which was considered negligible.

The pressure coefficient over the wing at a cross-section obtained at IL1, 16.8 m away from the fuselage symmetry plane, is plotted in Figure 39. The pressure coefficients over the wing, when simulated with and without the fuselage (Figure 39 (a) and Figure 39 (b), respectively), were nearly identical, implying a similar impact on the flow field.

The pressure contour and pressure coefficient plots show that the effect of the presence of the fuselage is negligible at the lateral location where the drone would be released when comparing the simulations with and without the fuselage. Since this difference in pressure between the drone

being released with and without the fuselage is relatively small, the CRM and HL-CRM aircraft geometries were simplified to remove the fuselage.

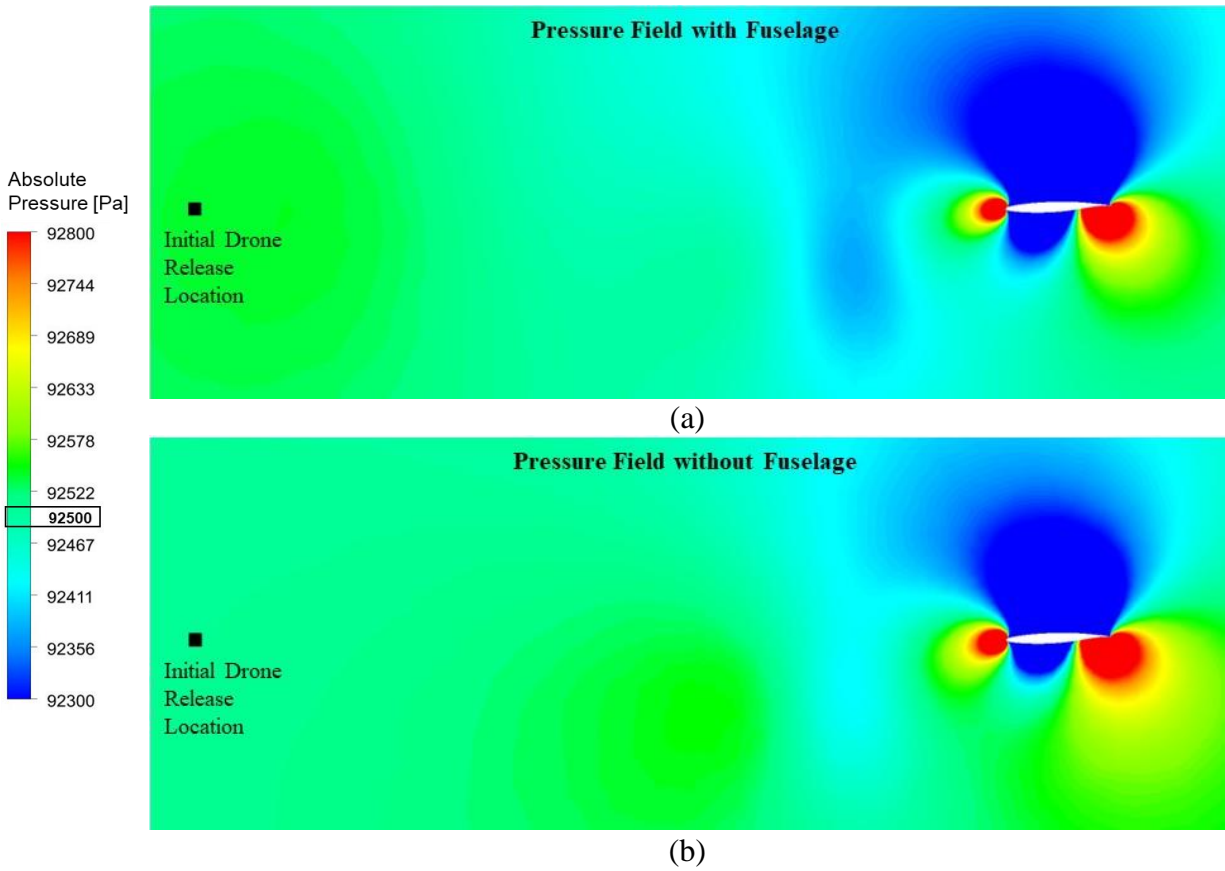


Figure 38. Pressure field within the domain (a) With the fuselage and (b) Without the fuselage at the lateral location of the drone at IL1.

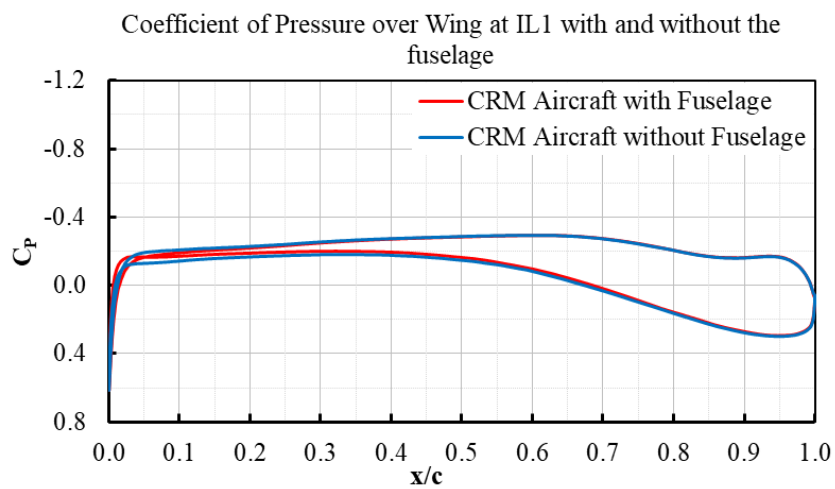


Figure 39. Coefficient of Pressure distribution over the wing at IL1 for the CRM with and without the fuselage.

The release location of the drone was determined by examination of the simplified aircraft steady-state flow field for each scenario, as seen in Table 17. The release location for impact scenarios 1 through 5 was found to be 45 m away from the aircraft leading-edge (wing or slat leading-edge) at IL1.

Table 17. Change in local pressure from operating pressure at the drone release location for impact scenarios with IL1.

<b>Impact Scenario</b>	<b>Aircraft AoA (degrees)</b>	<b>Release Location (m)</b>	<b>Absolute Pressure (Pa)</b>	<b>Difference from Operating Pressure (Pa)</b>
<b>IC1-IL1</b>	0	45	92506.2	6.2
<b>IC2-IL1</b>	0	45	92506.2	6.2
<b>IC3-IL1</b>	5	45	92506.5	6.5
<b>IC4-IL1</b>	0	45	92506.6	6.6
<b>IC5-IL1</b>	0	45	92504.4	4.4

### 3.5 RELATIVE DISTANCE DEFINITION

The results are presented in terms of the relative distance between the drone and the aircraft. The relative distance is measured from the foremost point on the drone chassis to the leading-edge point on the wing (CRM aircraft) or the slat (HL-CRM aircraft) at the lateral location corresponding to the foremost point of the drone chassis, as seen in Figure 40.

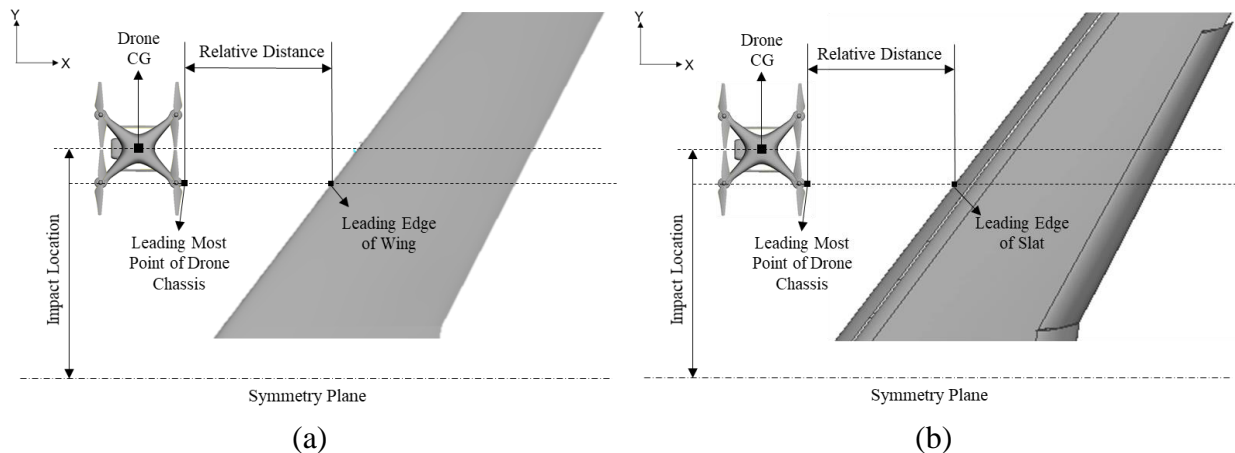


Figure 40. Relative distance between the drone and the (a) CRM aircraft and (b) HL-CRM aircraft as seen from the top view.

### 3.6 SIGN CONVENTION AND AXIS-SYSTEM DEFINITION

There are three different reference frames to consider when dealing with the movement of a rigid body in a fluid domain: the global inertial reference frame, the body-fixed reference frame, and

the translating inertial reference frame as shown in Figure 41. The global inertial reference frame is a fixed reference frame represented by  $X$ ,  $Y$ , and  $Z$ . The forces and moments of the aircraft are specified in terms of the global inertial reference frame.

The drone's location in the domain is provided by specifying its position relative to the fixed global inertial reference frame. The translating inertial reference frame specified at the CG of the drone moves along with the drone through the domain. The translating inertial reference frame, denoted by  $X_T$ ,  $Y_T$ , and  $Z_T$ , does not rotate with the drone.

The body-fixed reference frame, denoted by  $X_{DB}$ ,  $Y_{DB}$ , and  $Z_{DB}$ , specified at the CG of the drone, is used to describe the drone's orientation relative to the global inertial reference frame measured using the translating inertial reference frame. The rotation in the body-fixed reference frame is depicted using the Euler angles ( $\phi$ ,  $\theta$ ,  $\psi$ ). In Figure 41 (c), the rotation is specified based on the Tait–Bryan ZYX rotation convention where the axis system is first rotated about the positive  $Z$ -axis ( $\psi$ ), then about the positive  $Y$ -axis ( $\theta$ ) and finally about the positive  $X$ -axis ( $\phi$ ).

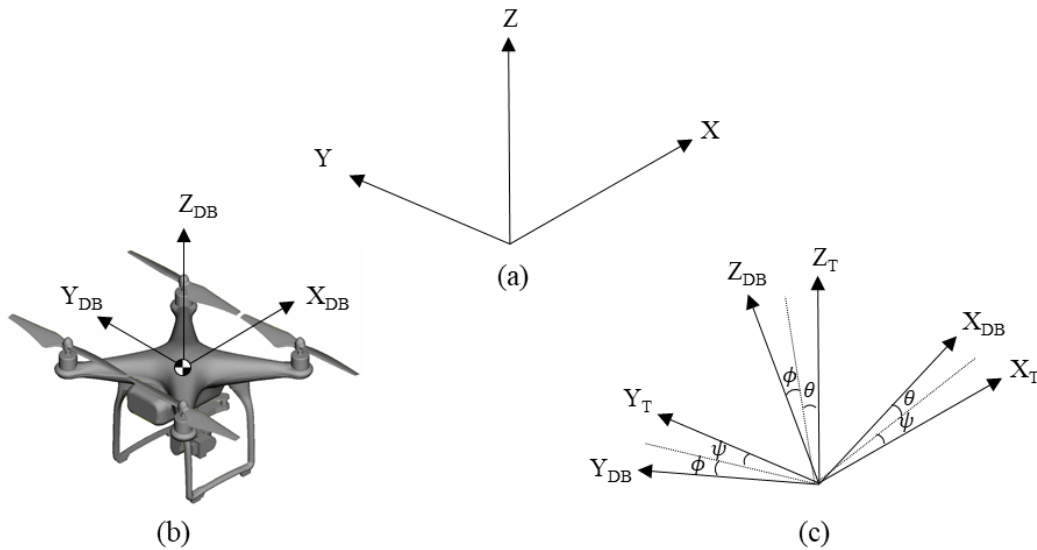


Figure 41. Representation of the (a) Global inertial reference frame,  $XYZ$ , (b) Drone body-fixed reference frame,  $X_{DB}Y_{DB}Z_{DB}$ , (c) Translating inertial reference frame,  $X_TY_TZ_T$ .

During the simulation global axis system translates along with the drone through the domain without undergoing any rotation. This allowed the drone forces and moments to be measured about the global axis system despite the rotations experienced by the drone and its body-fixed reference frame. As mentioned in Section 3.2.2, Fluent automatically converts the moments from the global inertial reference frame to the body-fixed reference frame for the necessary calculations and provides the translated locations, rotations, forces, and moments experienced by the drone in terms of the global inertial reference frame. As a result, the drone and aircraft aerodynamic forces and moments are obtained about the global inertial axis system, as seen in Figure 42. The sign convention used for the drone forces and moments in the global inertial reference frame are listed in Table 18 and shown in Figure 43.

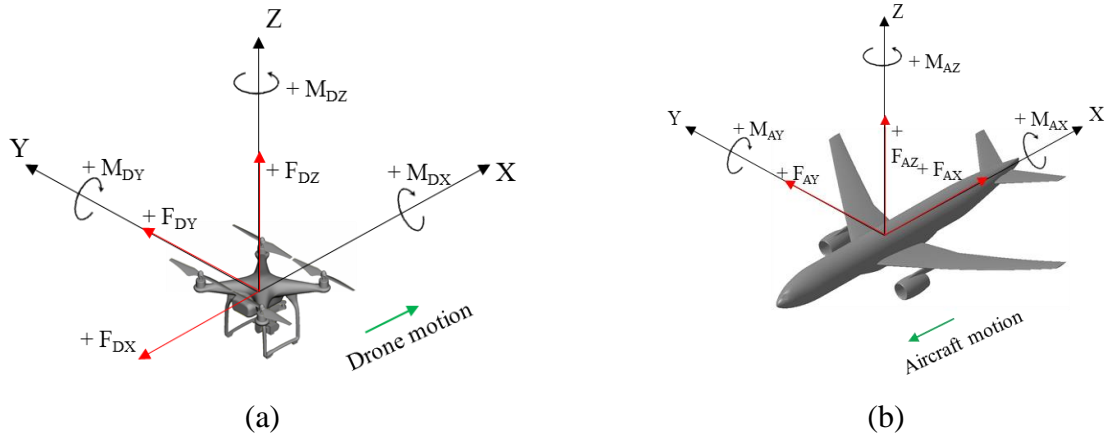


Figure 42. Force and moment definition for the (a) Drone and (b) Aircraft in the global axis system.

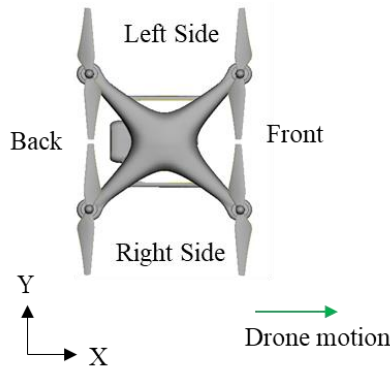


Figure 43. Nomenclature used to define the drone sign convention.

Table 18. Sign convention for the drone forces and moments.

<b>Positive Aero. Force along X-Axis:</b>	Negative X-direction
<b>Positive Aero. Force along Y-Axis:</b>	Positive Y-direction
<b>Positive Aero. Force along Z-Axis:</b>	Positive Z-direction
<b>Positive Aero. Moment about X-Axis:</b>	Right side of drone down
<b>Positive Aero. Moment about Y-Axis:</b>	Front of drone down
<b>Positive Aero. Moment about Z-Axis:</b>	Right side of drone forward

### 3.7 UAS FORCE AND MOMENT BALANCE

A UDF was applied in the Ansys<sup>®</sup> Fluent simulations to maintain the assumptions that (a) the drone approached the aircraft at a constant speed, altitude, and attitude and (b) the pilot and hence

the drone could not react to any additional changes in forces and moments experienced due to the aircraft pressure field.

To maintain a constant velocity, altitude, and attitude (when the drone was away from the influence of the aircraft flow field), the aerodynamic forces and moments experienced by the drone as a result of its independent movement within the domain and the weight of the drone were balanced using external forces and moments within the UDF. These forces and moments were set to be constant throughout the simulation, and the UDF did not compensate for any variation in the forces and moments experienced by the drone as it neared the aircraft. This allowed the drone's trajectory to be calculated purely based on the additional forces and moments due to the aircraft flow field. The weight of the drone,  $W$ , the aerodynamic forces and moments experienced by the drone, denoted by  $F_{DX}$ ,  $F_{DY}$ ,  $F_{DZ}$ ,  $M_{DX}$ ,  $M_{DY}$ , and  $M_{DZ}$ , and the external forces and moments added using the UDF, denoted by  $F_{extDX}$ ,  $F_{extDY}$ ,  $F_{extDZ}$ ,  $M_{extDX}$ ,  $M_{extDY}$ , and  $M_{extDZ}$  are shown in Figure 44.

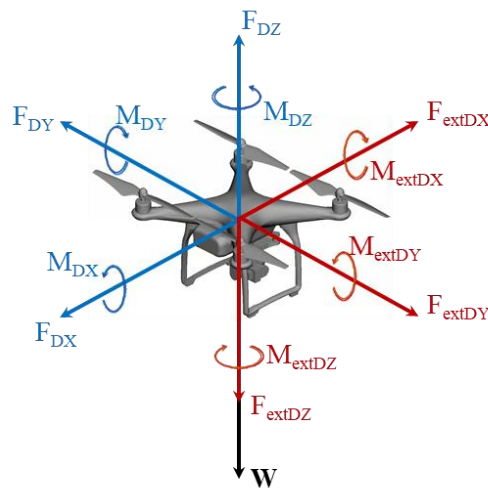


Figure 44. Aerodynamic and external forces and moments on the drone.

All the forces and moments shown in Figure 44 are considered in the global axis. During the simulation, the first 10 m of drone motion (for release location without fuselage) and the first 20 m of drone motion (for release location with fuselage) was modeled as prescribed motion for two reasons: to allow the transient aerodynamic forces and moments to wash out and to obtain average values to use in the force and moment balance equation within the UDF. The drone aerodynamic forces and moments' average value were obtained from the final 5 m of prescribed motion in both cases. These values constitute the steady-state values of the drone aerodynamic forces and moments before the RBD motion. Therefore, these values were used as external forces and moments in the UDF as shown in Figure 45. Refer to APPENDIX B for details regarding the UDF used.

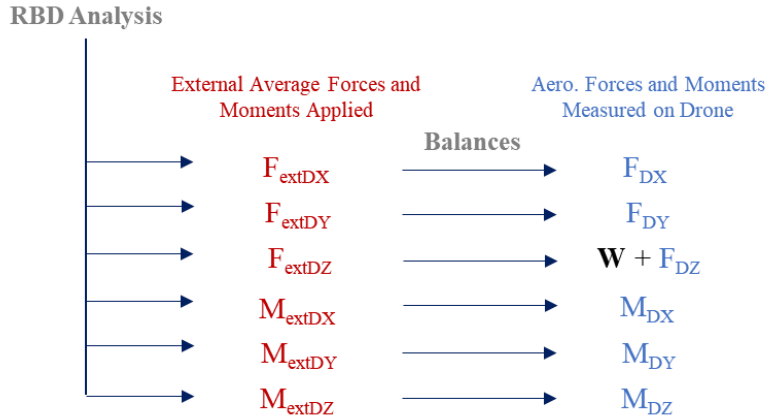


Figure 45. Force and moment balance on the drone within the UDF.

### 3.8 MESH DEFINITION

BETA CAE’s commercial mesh generation tool, ANSA, was used to generate the surface and volume meshes. The overset mesh created for the impact scenarios consists of two components: background and component mesh. The component mesh was created around the drone and moves with the drone through the stationary background mesh.

The simulation domain was hemispherical, with a radius of 100 times the MAC of the half model of the aircraft as shown in Figure 46. A coarse, structured hexahedral mesh was created within the background mesh to encompass the region expected to be traversed by the drone to establish a good overset interface upon initialization. This hexahedral mesh was refined and coarsened through the course of the simulation using mesh adaption.

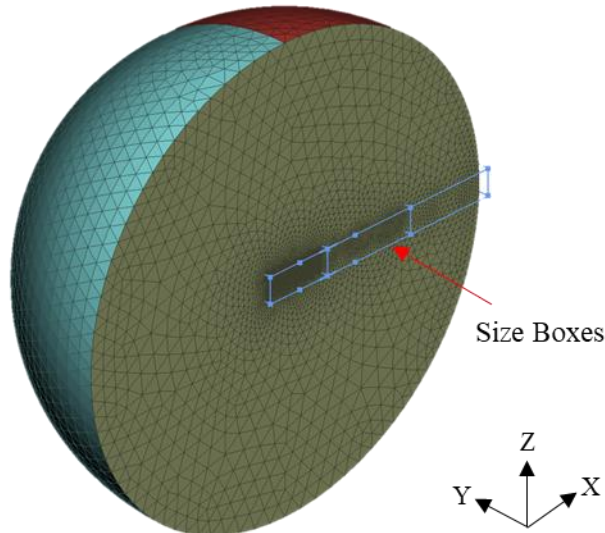


Figure 46. Background mesh and domain with size boxes for aircraft wake refinement.

For both CRM and HL-CRM aircrafts, the surface mesh was obtained from the validation study. Size boxes were created for aircraft wake refinement. A target wall  $y^+$  value of 500 was used to

obtain the first cell height, and a total of 9 prism layers were generated over the aircraft surface to capture the boundary layer. The rest of the domain volume was constructed using unstructured tetrahedral mesh. The details of a typical background mesh around a CRM aircraft before the hexahedral mesh refinement is given in Table 19. These values are similar to the HL-CRM aircraft background mesh. The total mesh size decreased when the drone was released within the domain in the absence of the aircraft fuselage.

Table 19. Background volume mesh details used in impact scenario IC3-IL2.

Name	Volume Mesh Size ( <i>millions</i> )
Prism Layers on Aircraft	≈ 6.45
Hexahedral Volume	≈ 0.73
Tetrahedral Volume	≈ 20.61

The component mesh was created as a cuboid around the drone as shown in Figure 47. The overall element length in the component domain was set to be similar to the element length of the refined hexahedral background mesh to obtain a good interface between the two.

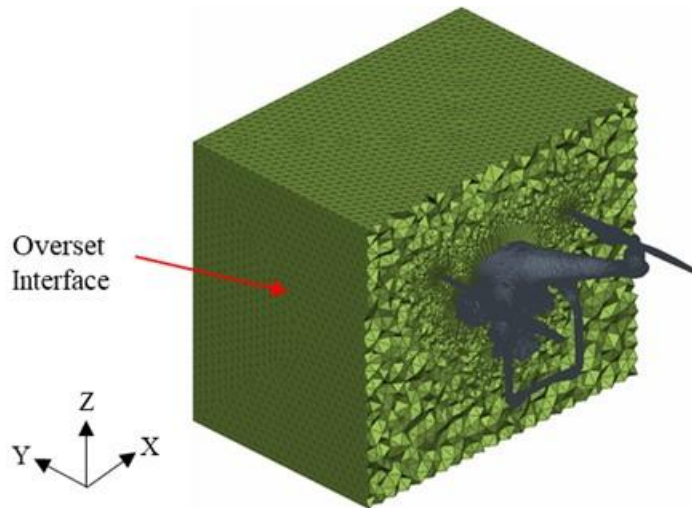


Figure 47. Component volume mesh and domain generated around the drone.

Eight prism layers were generated over the drone, with the first cell height calculated from a wall  $y^+$  value of 300. Figure 47 shows the drone within the unstructured tetrahedral component mesh domain. The details of the component mesh used for all simulations are presented in Table 20. For detailed information on the component and background meshes, the refinement regions, and the surface and volume mesh quality, refer to Appendix A.3.

Table 20. Component mesh details used for all the impact scenarios.

Name	Volume Mesh Size ( <i>millions</i> )
DJI / Prism Layers	≈ 1.58
Tetrahedral Volume	≈ 1.99

### 3.9 NUMERICAL MODEL

The operating conditions for the current study were based on the aircraft flying a holding pattern due to the low flight ceiling of the drone. Therefore, the altitude and speed for this operating condition were set as 762 m above ground and 102.889 m/s, respectively. The following sections will outline the simulation parameters used within the Ansys® Fluent solver.

#### 3.9.1 Boundary Conditions and Operating Conditions

Figure 48 presents the background domain and the boundary conditions used for the impact scenarios. The aircraft surfaces were modeled as no-slip adiabatic walls with a symmetry plane defined along the global XZ plane. The inlet velocity was set to be 102.889 m/s to simulate the aircraft's motion. The aircraft Reynolds number, based on the MAC, was calculated to be 46.5 million.

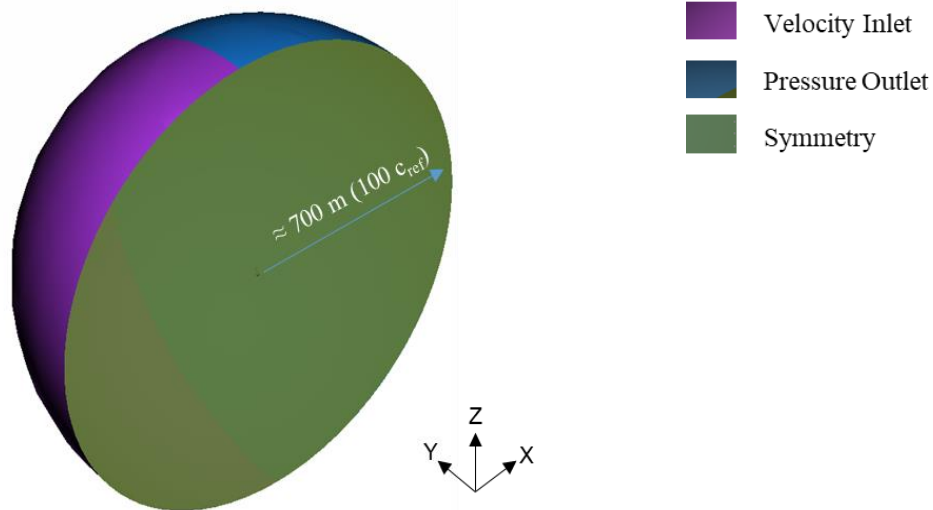


Figure 48. Computational domain and boundary conditions.

For the current scenarios, the aircraft was assumed to be flying at an altitude of 762 m. The fluid properties within the domain were set to match that of standard air at an altitude of 762 m and are provided in Table 21.

Table 21. Fluid properties and operating conditions within the domain for trajectory analysis.

<b>Temperature</b>	283.2 K
<b>Pressure</b>	92500 Pa
<b>Density</b>	1.138 kg/m <sup>3</sup>
<b>Dynamic Viscosity</b>	1.76E-05 N-s/m <sup>2</sup>
<b>Freestream Velocity</b>	102.889 m/s

An overset interface was defined at the component mesh level, and the interface was initialized without minimization. The drone surfaces were modeled as no-slip adiabatic walls. The translational drone velocity was set such that the relative velocity between the aircraft and drone was 25.722 m/s for all the relevant impact scenarios. As such, the translational drone velocity was calculated to be 128.611 m/s except for impact scenario IC5-IL1, where the aircraft velocity is 87.455 m/s, resulting in a drone velocity of 113.177 m/s. The drone Reynolds number was calculated from the relative velocity and found to be 0.41 million based on the drone characteristic length of 0.248 m (Drone length from front motor center to back motor center). The aircraft and drone reference parameters used in this study are provided in Table 22.

Table 22. Aircraft and drone reference lengths and areas.

<b>Aircraft MAC</b>	7.005 m
<b>Aircraft Span</b>	58.80 m
<b>Aircraft Reference Area</b>	383.69 m <sup>2</sup>
<b>Drone Reference Length</b>	0.248 m
<b>Drone Reference Area</b>	0.062 m <sup>2</sup>

### 3.9.2 Solver Setup

The transient pressure-based coupled algorithm available with Ansys<sup>®</sup> Fluent was used to solve the flow over the drone and the aircraft. The realizable k-ε turbulence model was used to model the flow field with the turbulence intensity and viscosity ratio set to 1 % and 2, respectively. The domain was initialized using the aircraft's steady-state flow field to reduce the overall computation time associated with the flow development over the aircraft. A time step size of 1E-04 seconds was used to run the transient simulations.

The 6-DOF solver was enabled to calculate the trajectory of the drone. First, the drone was modeled as a rigid body. Next, the initial location of the drone CG, along with the initial velocity and orientation of the drone in the inertial reference frame, were entered in the dynamic mesh solver. This allowed the solver to update the drone location and orientation at each time step and update the volume mesh around the drone using overset meshing. Finally, the UDF was compiled with the inertial properties of the drone and additional external forces and moments.

### 3.10 TRAJECTORY ANALYSIS RESULTS

The trajectory analysis was conducted in two steps. The numerical methodology was first verified by comparing the drone trajectories obtained from the different solvers used by the two participating universities (NIAR and ERAU). Once the methodology was verified, and the resulting trajectories were similar, the same solvers and numerical methodology were used to conduct simulations on other impact scenarios mentioned in Table 3.

Before presenting the results, it is necessary to mention the sign conventions used to describe the results. Figure 49 shows the drone displacements along each axis, including the sign definitions for each. Along the direction of motion (X-axis), the displacement was measured by comparing the location of the CG of the drone with rigid body motion to the location of the CG if the drone had been moving without the influence of any forces or moments. Therefore, if the drone slowed down from its initial speed, the drone experienced negative horizontal displacements, whereas if the drone sped up as it approached the aircraft, it experienced positive horizontal displacements. Along the Y-axis, positive lateral displacements indicated that the drone moved toward the aircraft's wingtip as it approached the aircraft. Negative lateral displacements indicated drone movement towards the fuselage. Likewise, positive vertical drone displacements indicated that the drone would move towards the top of the wing, while negative displacements indicated that the drone would move towards the bottom of the wing.

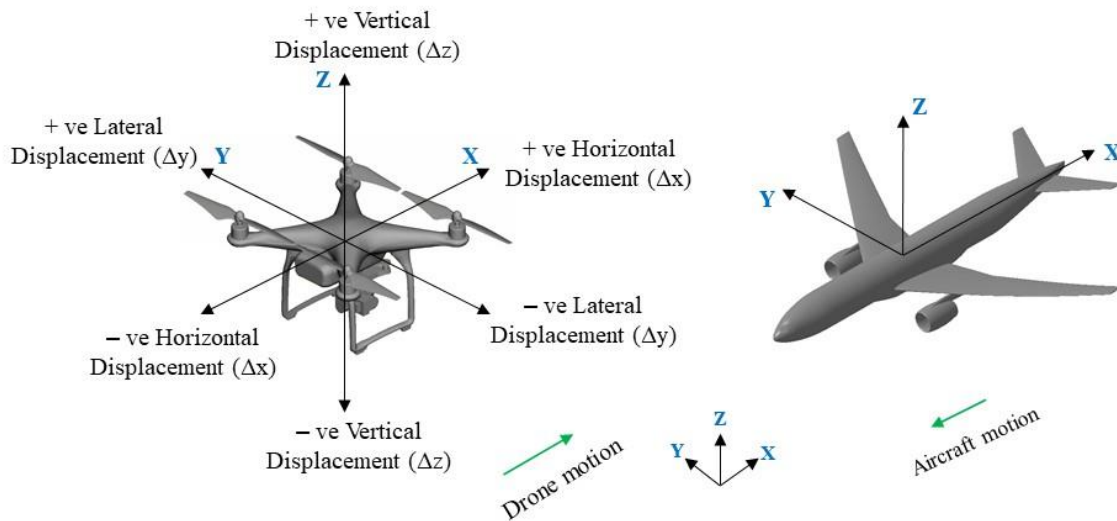


Figure 49. Displacements experienced by the drone and the sign convention used.

Figure 50 shows the sign convention used to define the angular displacements on the drone as it approaches the aircraft. The sign convention is defined by using the right-hand rule.

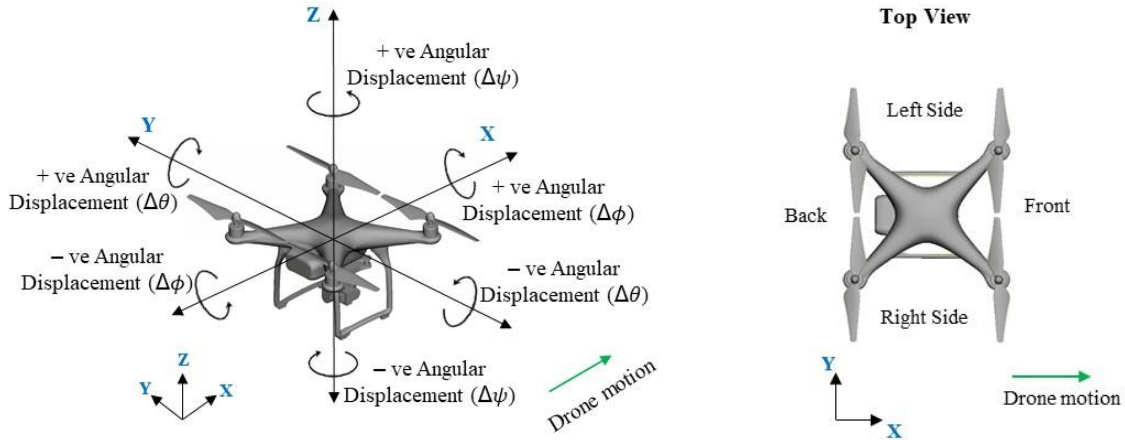


Figure 50. The sign convention used to define the angular displacements of the drone.

### 3.10.1 Cross-Verification Results

To establish confidence in the methodology used for this study, two impact scenarios were simulated by the universities participating in the study: NIAR and ERAU, with each university using a different numerical solver. The first impact scenario, IC1-IL1, and the second impact scenario, IC2-IL1, where the drone was released in the presence of the CRM aircraft at 0 m/s, and 25.722 m/s velocities, respectively, were used for the comparison.

The impact scenario IC1-IL1 was simulated by ERAU and NIAR for comparison. The drone was placed at different distances away from the aircraft by ERAU and NIAR. The 6-DOF solver was enabled when the drone was at a distance of approximately 60 m by ERAU and when it was at a distance of approximately 35 m by NIAR. The trajectory of the drone obtained by the two universities was compared. The time history of the displacements,  $\Delta x$ ,  $\Delta y$ , and  $\Delta z$ , and angular displacements,  $\Delta\phi$ ,  $\Delta\theta$ , and  $\Delta\psi$ , of the drone for impact scenario, IC1-IL1 obtained by ERAU and NIAR is provided in Figure 51. The time history of the change in velocity of the drone along the horizontal (X), lateral (Y), and vertical (Z) axes represented by  $\Delta u$ ,  $\Delta v$ , and  $\Delta w$ , respectively is shown in Figure 52 (a) for impact scenario IC1-IL1. The change in angular velocity of the drone,  $\Delta p$ ,  $\Delta q$ , and  $\Delta r$ , along the roll (X), pitch (Y), and yaw (Z) axes respectively is shown in Figure 52 (b) for impact scenario IC1-IL1.

The impact scenario IC2-IL1, where the drone approached the aircraft with a velocity of 25.72 m/s, was simulated by ERAU and NIAR, and the results were compared to verify the methodology used. While the drone was initially placed at different distances away from the wing, the 6-DOF was enabled when the drone was at a distance of 45 m by both ERAU and NIAR. The time history of the displacements,  $\Delta x$ ,  $\Delta y$ , and  $\Delta z$ , and angular displacements,  $\Delta\phi$ ,  $\Delta\theta$ , and  $\Delta\psi$ , of the drone as it approaches the aircraft is shown in Figure 53 (a) and Figure 53 (b) respectively. The change in velocity of the drone along with the horizontal, lateral, and vertical directions represented by  $\Delta u$ ,  $\Delta v$ , and  $\Delta w$ , respectively is shown in Figure 54 (a) for impact scenario IC2-IL1. The change in angular velocity of the drone,  $\Delta p$ ,  $\Delta q$ , and  $\Delta r$ , along the roll, pitch, and yaw respectively, as it approaches the aircraft for impact scenario IC2-IL1 is shown in Figure 54 (b).

The displacements,  $\Delta x$ ,  $\Delta y$ , and  $\Delta z$ , of the drone obtained by the two universities at the point of impact for impact scenarios IC1-IL1 and IC2-IL1, are shown in Figure 55. The drone

displacements at the point of impact for impact scenarios IC1-IL1 and IC2-IL1 obtained by ERAU and NIAR are provided in Table 5. The angular displacements,  $\Delta\phi$ ,  $\Delta\theta$ , and  $\Delta\psi$ , of the drone at the point of impact for impact scenarios IC1-IL1 and IC2-IL1 obtained by ERAU and NIAR are shown in Figure 7. The angular displacement values are also tabulated for comparison in Table 6.

The pressure contours over the drone at the point of impact when the relative distance between the drone and the aircraft wing is approximately 0 m was obtained about two planes: XZ plane for the side view and XY plane for the top view. For more information about the planes and their location, refer to Appendix C.2. The pressure contour from the side view and top view for impact scenario IC1-IL1 by ERAU and NIAR is provided in Figure 8. The side and top view of the pressure contours by ERAU and NIAR are provided in Figure 9 for impact scenario IC2-IL1 at the point of impact.

The drone's trajectory obtained by the two universities is similar for impact scenario IC1-IL1 with the drone at a hover velocity of 0 m/s. However, for impact scenario IC2-IL1 with the drone approaching the aircraft at a 25.72 m/s velocity, the drone's trajectory obtained by ERAU and NIAR varies slightly. This slight variation in the drone trajectory between the two data sets could be attributed to the difference in the resulting aerodynamic forces and moments for the drone and the aircraft because of the difference in mesh and solver. Additionally, the values used to balance the forces and moments on the drone in order to maintain the assumptions specified in Section 3.3 may also cause the differences observed in the drone trajectory.

Despite the slight variation in vertical displacement of the drone observed between ERAU and NIAR results, both data sets show less than 1 cm of deflection from the prescribed path. This signifies that the drone will collide with the CRM wing in both impact scenarios simulated by ERAU and NIAR. Thus, it provides sufficient confidence in the methodology used to conduct the investigation. The following section will detail the trajectory investigation carried out by NIAR.

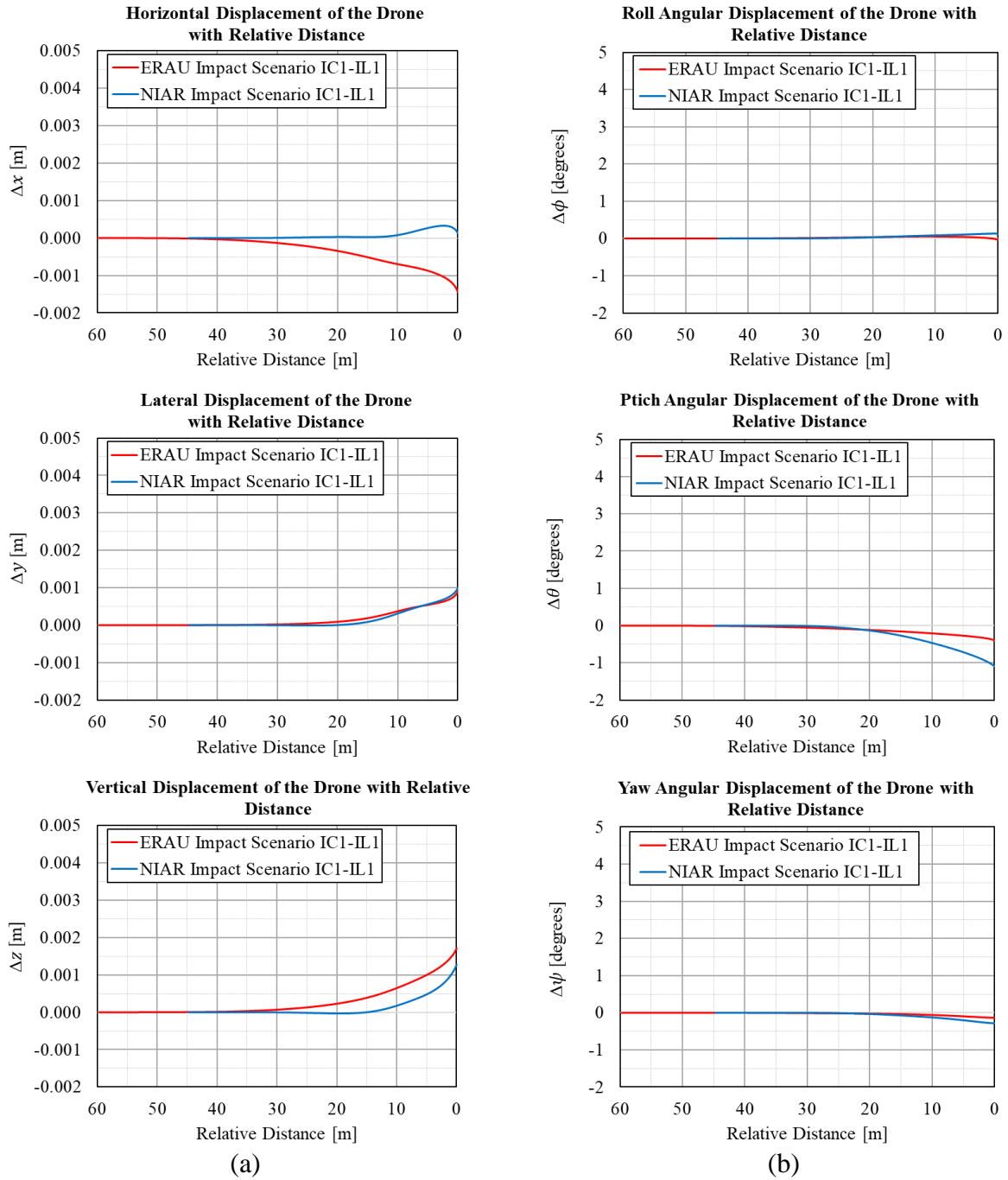


Figure 51. Time history of (a) Displacements and (b) Angular displacements of the drone obtained by ERAU and NIAR for impact scenario IC1-IL1.

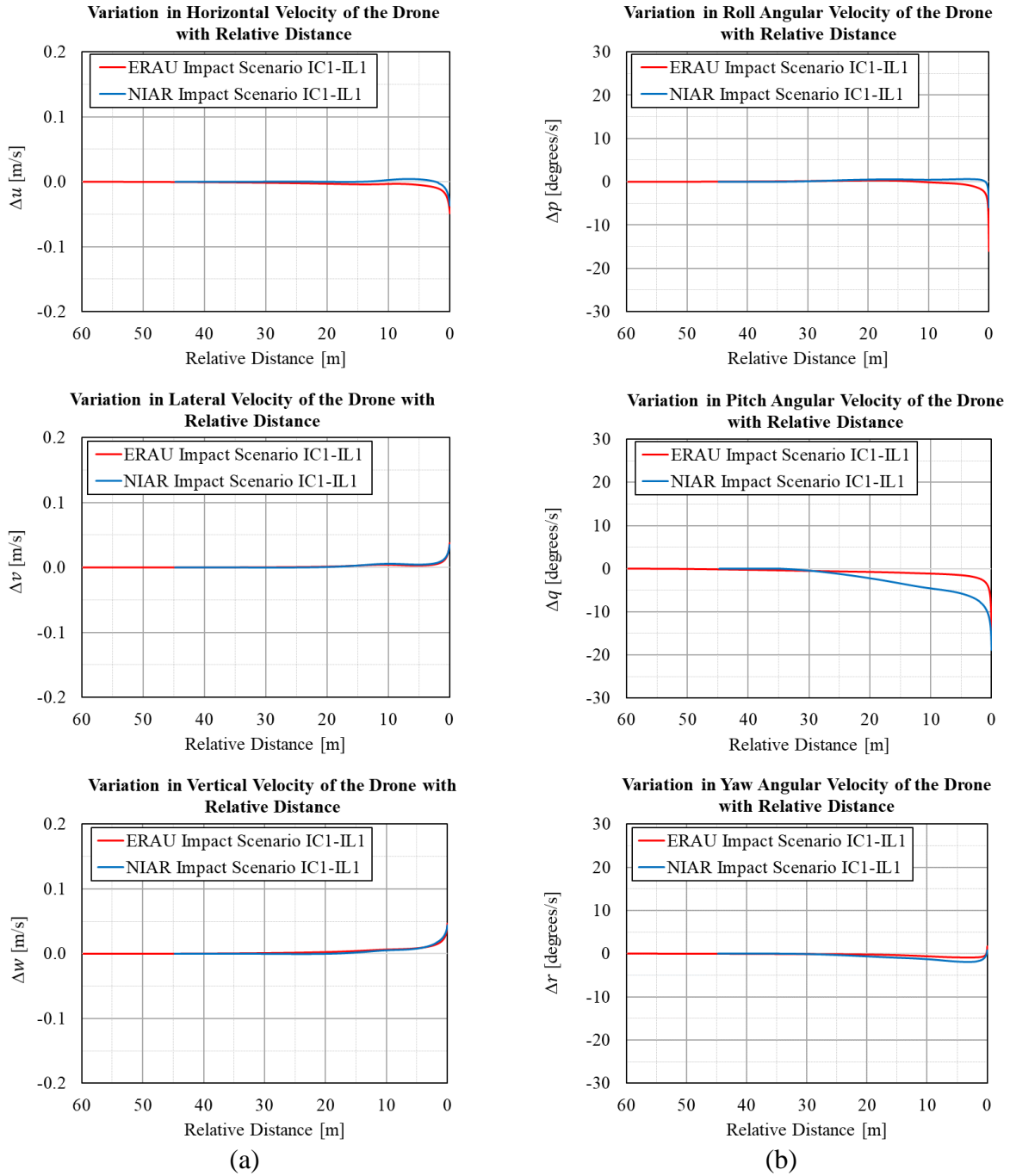


Figure 52. Time history of the change in (a) Velocities and (b) Angular velocities of the drone obtained by ERAU and NIAR for impact scenario IC1-IL1.

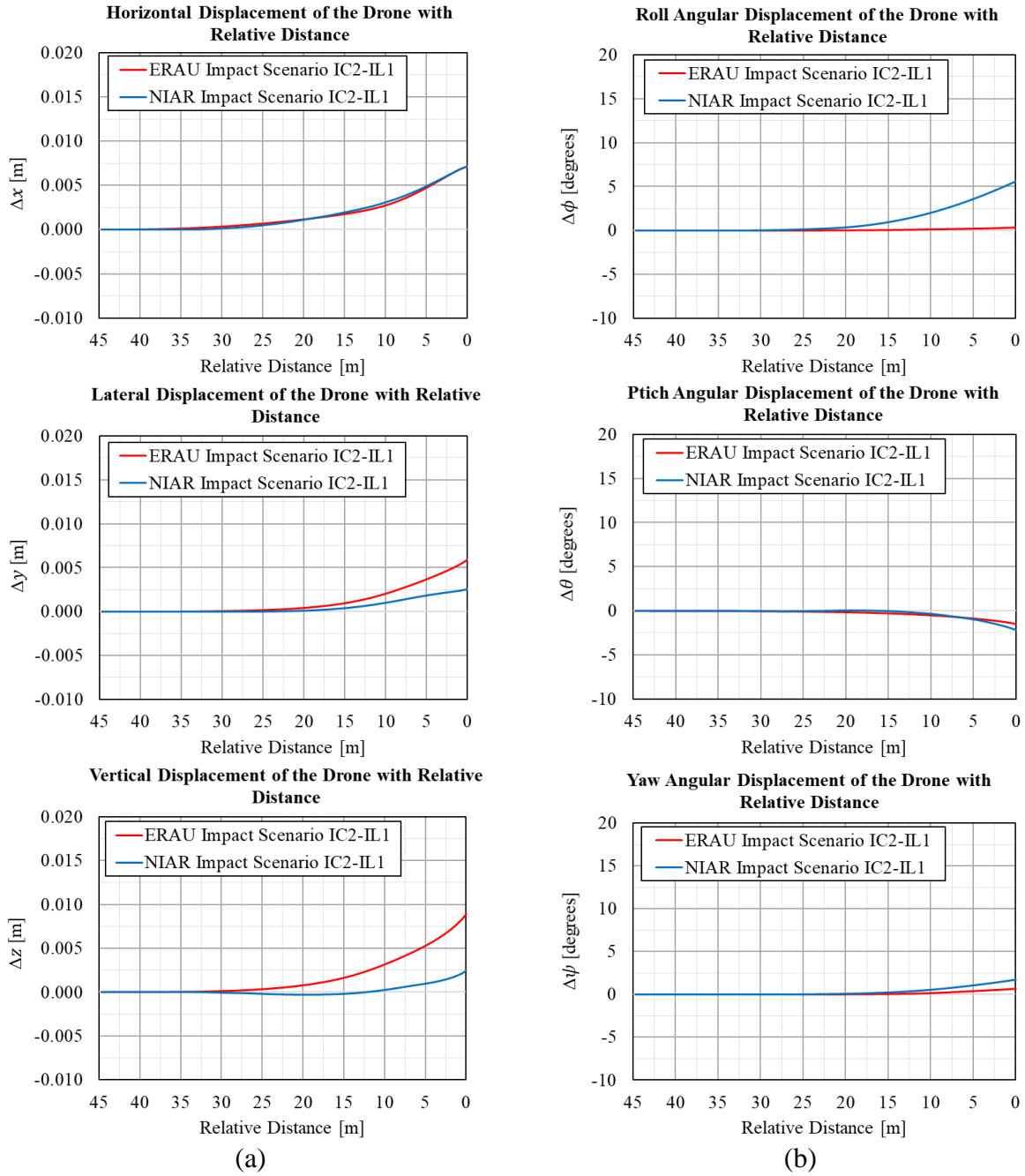


Figure 53. Time history of (a) Displacements and (b) Angular displacements of the drone obtained by ERAU and NIAR for impact scenario IC2-IL1.

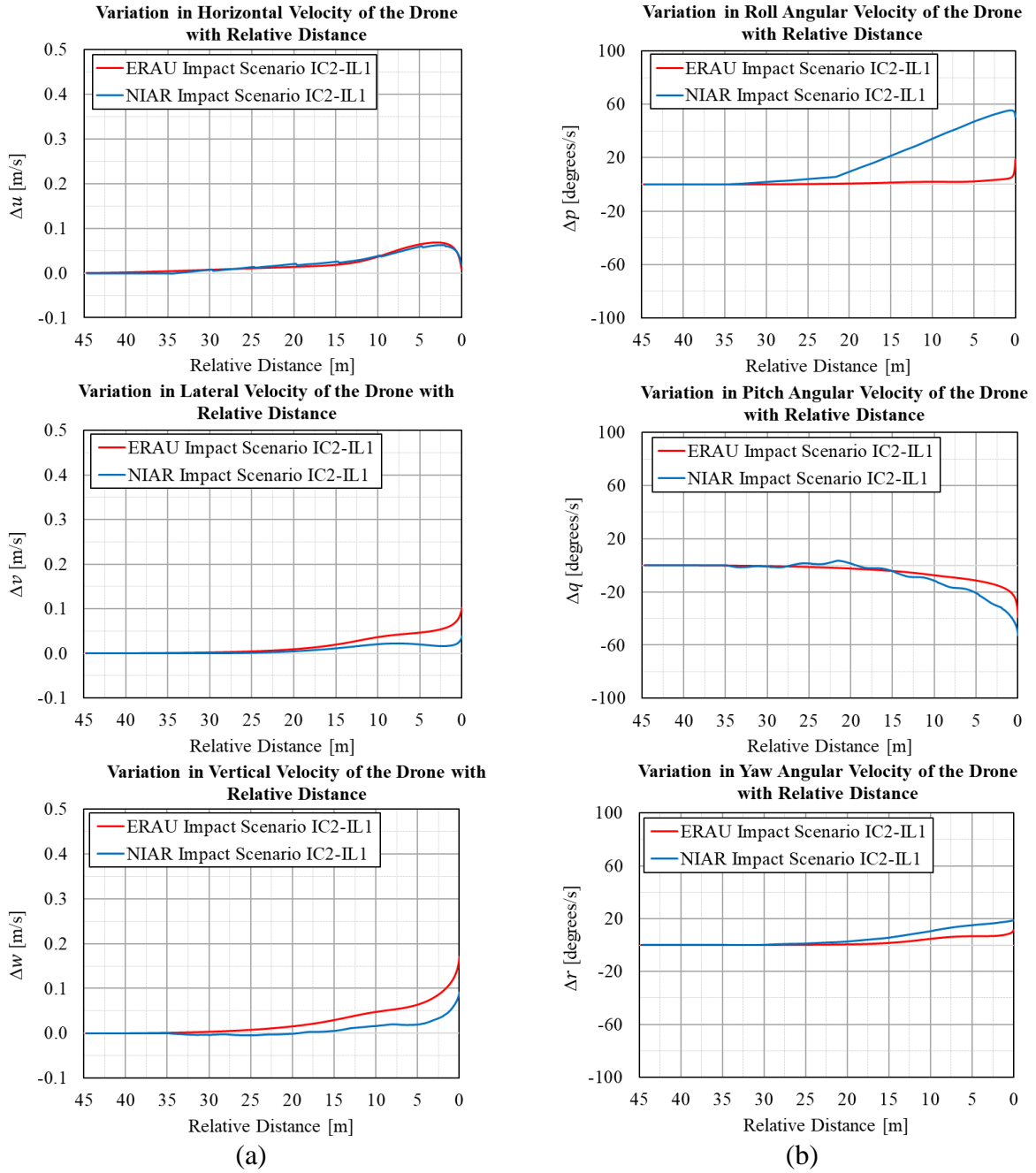


Figure 54. Time history of the change in (a) Velocities and (b) Angular velocities of the drone obtained by ERAU and NIAR for impact scenario IC2-IL1.

Table 23. Drone displacements for impact scenarios IC1-IL1 and IC2-IL1 obtained by ERAU and NIAR.

Drone Displacement (cm)				
Direction	IC1-IL1		IC2-IL1	
	NIAR	ERAU	NIAR	ERAU
Horizontal	0.01	-0.14	0.71	0.71
Lateral	0.10	0.09	0.26	0.60
Vertical	0.13	0.17	0.25	0.89

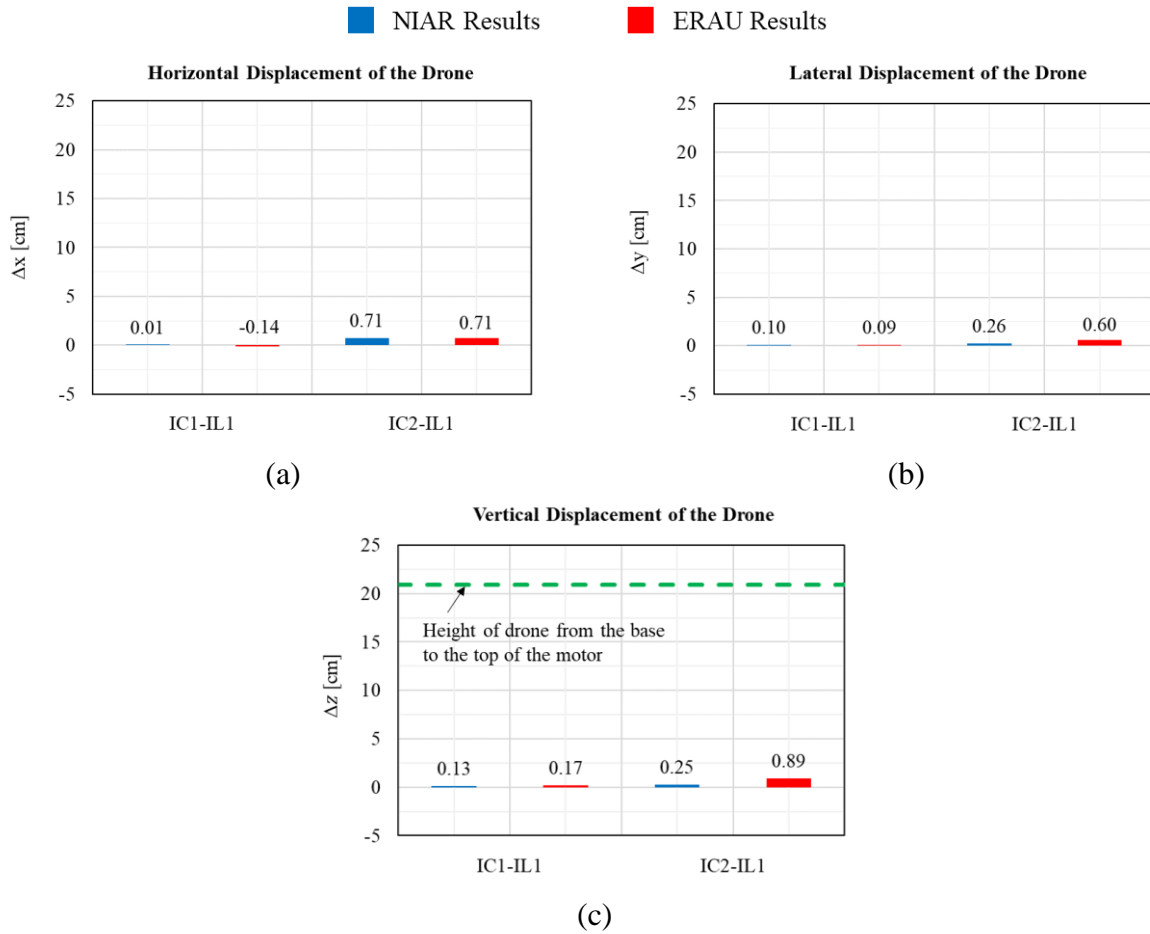


Figure 55. (a) Horizontal, (b) Lateral, and (c) Vertical displacements of the drone for impact scenario IC1-IL1 and IC2-IL1 obtained by ERAU and NIAR.

Table 24. Drone angular displacements for impact scenarios IC1-IL1 and IC2-IL1 obtained by ERAU and NIAR.

<b>Drone Angular Displacement (degrees)</b>				
<b>Direction</b>	<b>IC1-IL1</b>		<b>IC2-IL1</b>	
	<b>NIAR</b>	<b>ERAU</b>	<b>NIAR</b>	<b>ERAU</b>
<b>Roll</b>	0.13	-0.04	5.61	0.35
<b>Pitch</b>	-1.09	-0.40	-2.21	-1.50
<b>Yaw</b>	-0.28	-0.13	1.75	0.70

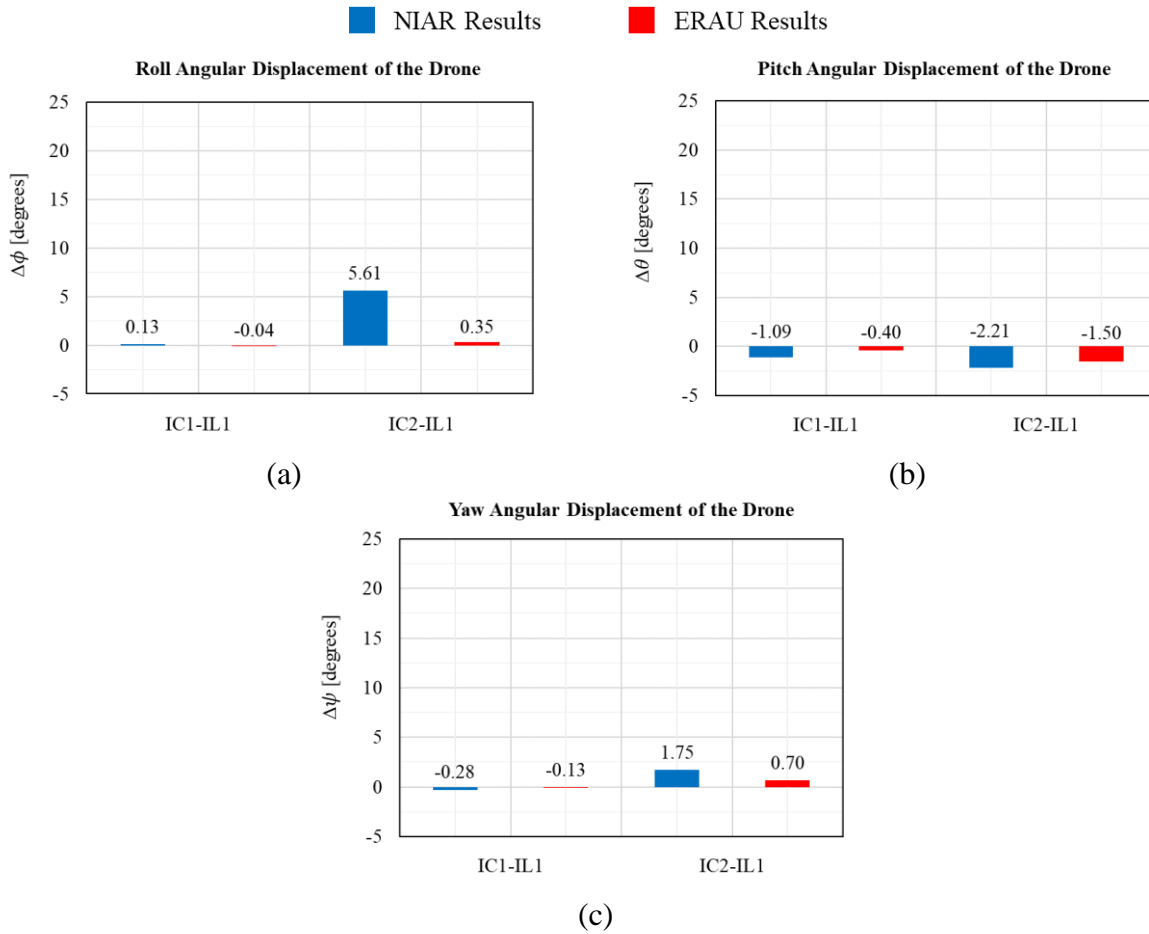


Figure 56. (a) Roll, (b) Pitch, and (c) Yaw angular displacements of the drone for impact scenario IC1-IL1 and IC2-IL1 obtained by ERAU and NIAR.

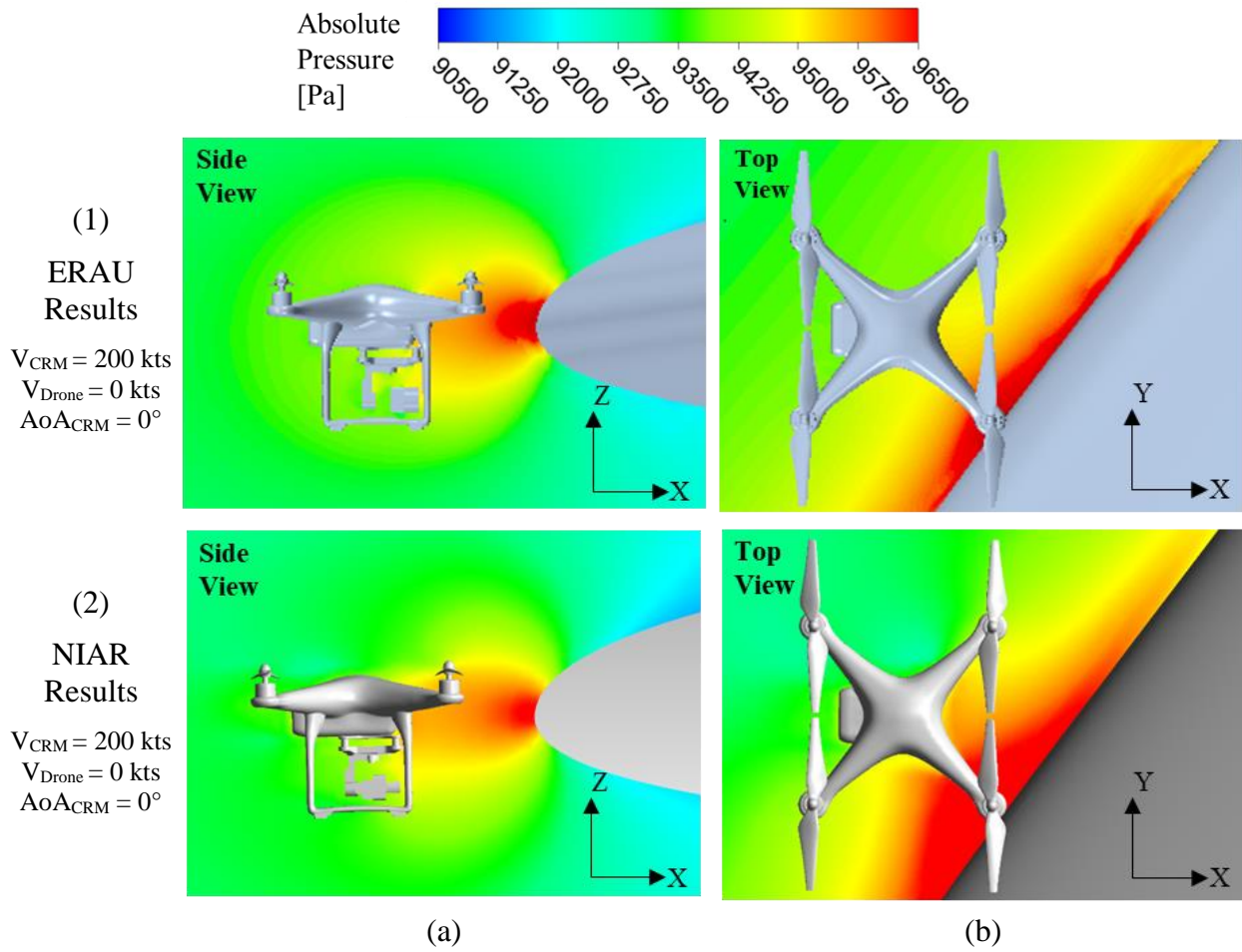


Figure 57. (a) Side and (b) Top view of the pressure contour over the drone when the relative distance is approximately 0 m for impact scenario IC1-IL1 obtained by (1) ERAU and (2) NIAR.

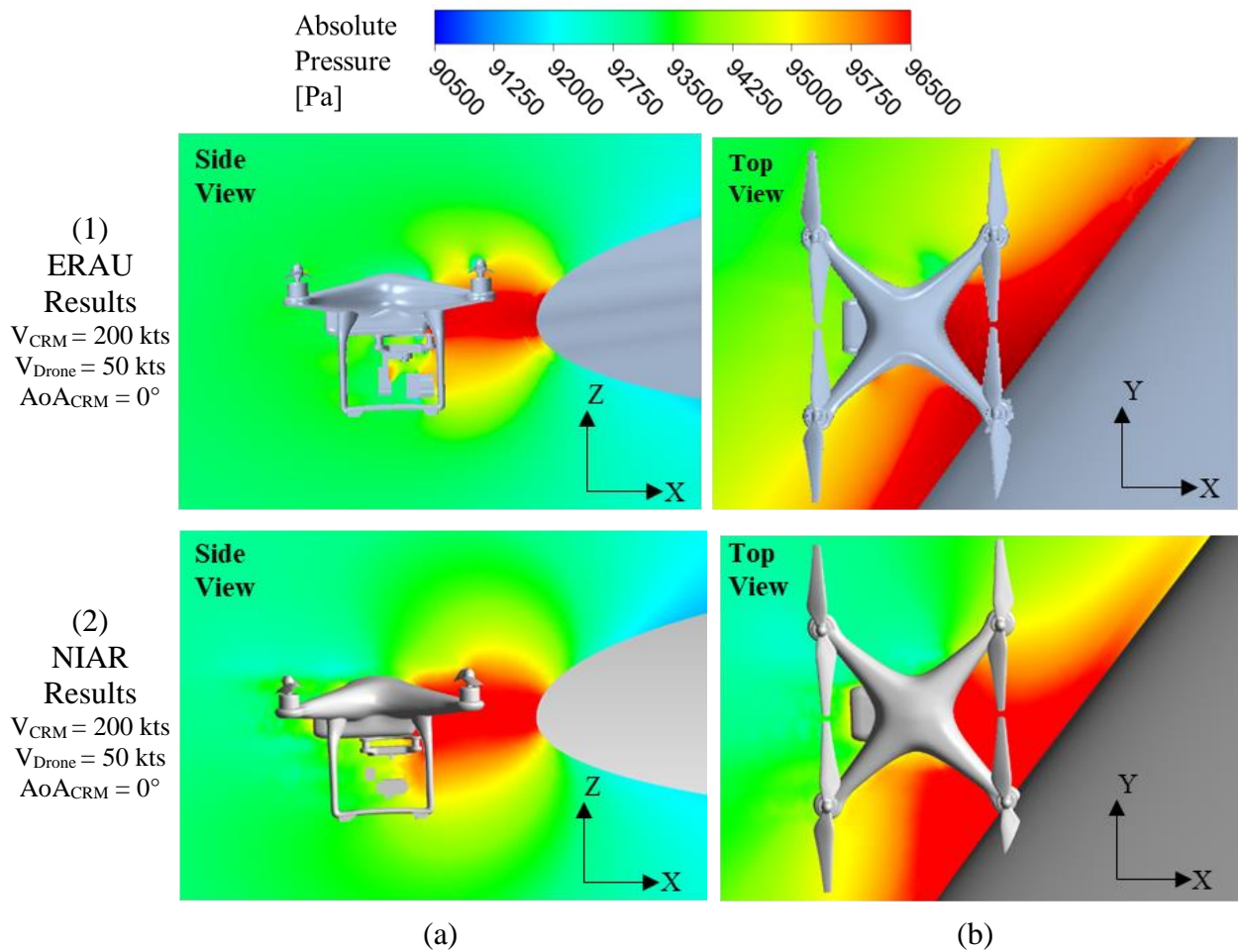


Figure 58. (a) Side view and (b) Top view of the pressure contour over the drone when the relative distance is approximately 0 m for impact scenario IC2-IL1 obtained by (1) ERAU and (2) NIAR.

### 3.10.2 Summary of Simulation Matrix Results

The Ansys® Fluent, Release 18.2, was used to simulate a drone flying towards a transport category aircraft represented by the CRM aircraft. The study's goal was to investigate the possibility of the drone colliding with the aircraft at specific impact locations. The drone's trajectory as it approached the aircraft was obtained for 5 different impact conditions and at 2 separate impact locations. The results for all 7 impact scenarios are presented in this section in terms of the horizontal displacements (X), lateral displacements (Y), and vertical displacements (Z) and the angular displacements about the X-axis ( $\phi$ ), Y-axis ( $\theta$ ), and Z-axis ( $\psi$ ).

The drone trajectory trends indicate that the drone moves upward as it approaches the aircraft for all impact scenarios. For the drone to completely deflect and avoid collision with the aircraft wing/slat, the drone CG needs to displace vertically such that the base of the drone clears the aircraft wing, in case of the CRM aircraft, and both the slat and wing, in case of the HL-CRM aircraft. Figure 59 demonstrates the deflection necessary for the drone to clear both the CRM aircraft and the HL-CRM aircraft at the point where the drone CG is aligned with the leading-edge of the wing (Figure 59 (a)) and slat (Figure 59 (b)) respectively. Table 25 provides the values of the drone vertical deflections necessary to avoid collision in either scenario.

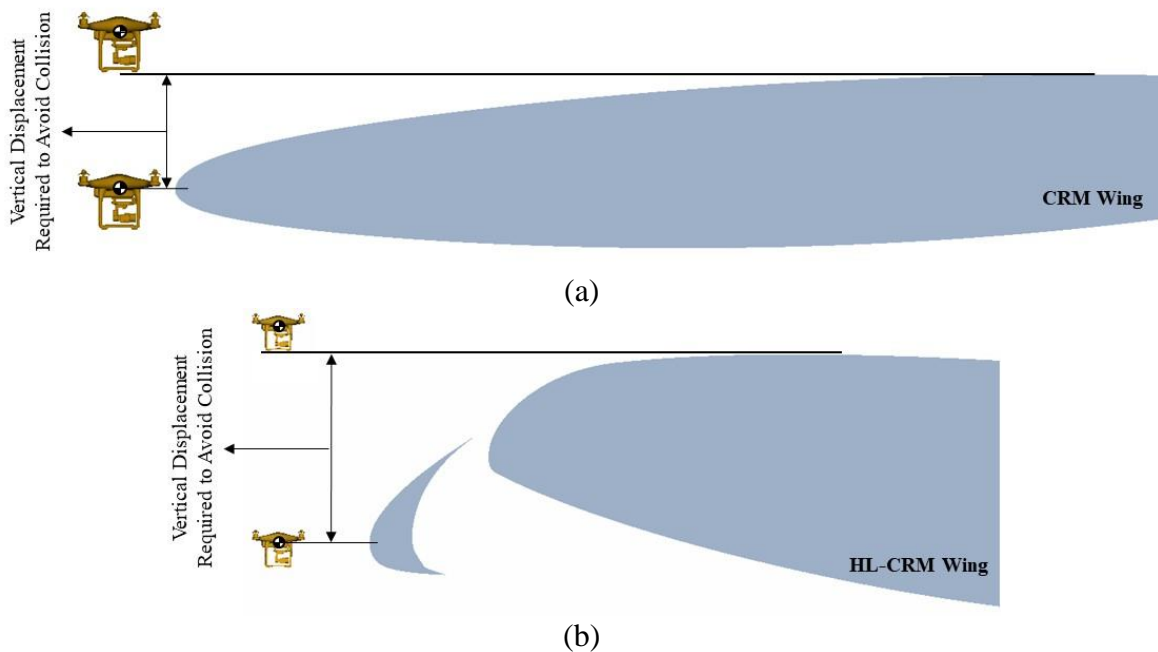


Figure 59. Representation of the vertical displacement required by the drone in order to avoid impacting the (a) CRM aircraft and the (b) HL-CRM aircraft.

Table 25. Vertical deflection of the drone necessary to avoid collision with the CRM and HL-CRM aircraft at each impact location.

<b>Aircraft Geometry</b>	<b>Impact Location</b>	<b>Aircraft Angle of Attack (<i>degrees</i>)</b>	<b>Required Vertical Displacement (<i>cm</i>)</b>
CRM	IL1	0	53.72
CRM	IL1	5	33.06
CRM	IL2	5	40.41
HL-CRM	IL1	0	99.83
HL-CRM	IL2	0	114.21

The results are presented below at the time of impact, determined by the point where the relative distance between the drone chassis and the aircraft wing/slat leading-edge was approximately 0 m. Refer to APPENDIX C for a more detailed time history of the forces, moments, displacements, and velocities experienced by the drone as it moved through the domain. The vertical displacement of the drone determined the possibility of collision of the drone with the aircraft at the time of impact. Note that the placement of the propeller at the time of impact was not considered. When the drone experienced greater angular displacements in certain scenarios, the propeller impacted the wing before the chassis was close enough. The results are presented at a time when the distance between the foremost point on the chassis and the aircraft wing (CRM aircraft) or slat (HL-CRM aircraft) was approximately 0 m to maintain consistency. This decision did not impact the conclusions drawn from these simulations, as will be presented below.

The final displacements of the drone in the vertical and lateral direction for scenarios involving the CRM aircraft with the drone released at IL1 are provided in Figure 60. The maximum vertical displacement was 1.3 cm, and the maximum lateral displacement was 0.3 cm, both of which occurred for the impact scenario where the CRM aircraft was at an angle of attack of 5° (IC3-IL1).

The pressure contours over the drone and the CRM aircraft for impact scenarios IC1-IL1, IC2-IL1, and IC3-IL1 are provided in Figure 61. The pressure contours were obtained about planes created along the XZ-plane (side view) and the XY-plane (top view) passing through the drone CG at the time of release (Appendix C.2).

As seen in Figure 61, the drone was still in the path of the CRM aircraft wing with a slight change in the vertical displacement and orientation at the time of impact. The trajectory of the drone with unconstrained motion (RBD motion) and the trajectory that the drone would have taken if it had moved without being influenced by the flow field (prescribed motion) are shown by the grey and orange lines, which are difficult to tell apart due to the similarity of the paths in these cases.

To study the effect of high lift devices and the effect of reduced aircraft velocity, impact scenarios IC4-IL1 and IC5-IL1 were investigated using a simplified HL-CRM aircraft. The deployment of the high lift devices produced slightly larger final displacements in the vertical direction, as seen in Figure 62. In addition, a vertical displacement of 2.1 cm is seen in impact scenario IC5-IL1, where the aircraft velocity was 87.455 m/s.

The pressure contours over the drone as it reaches the HL-CRM aircraft slat are shown in Figure 63. Figure 63 shows the displacements and the orientation of the drone at the point of impact. The paths taken by the drone as it approaches the aircraft with RBD motion and prescribed motion are also depicted in Figure 63.

The displacements experienced by the drone when released from IL2 in the vicinity of the aircraft with and without high lift devices are plotted in Figure 64. A vertical displacement of 3.3 cm was seen with impact scenario IC3-IL2, where the drone approached the CRM aircraft at 5° AoA (without high lift devices). It can also be observed that when the drone was released at IL2, closer to the fuselage, the drone experienced larger lateral displacements during both scenarios.

Figure 65 shows the pressure contours over the drone and aircraft wing/slat and the drone's trajectory. In both scenarios, the drone had positive displacements in the lateral direction and positive vertical displacement. Positive yaw is also visible for both scenarios.

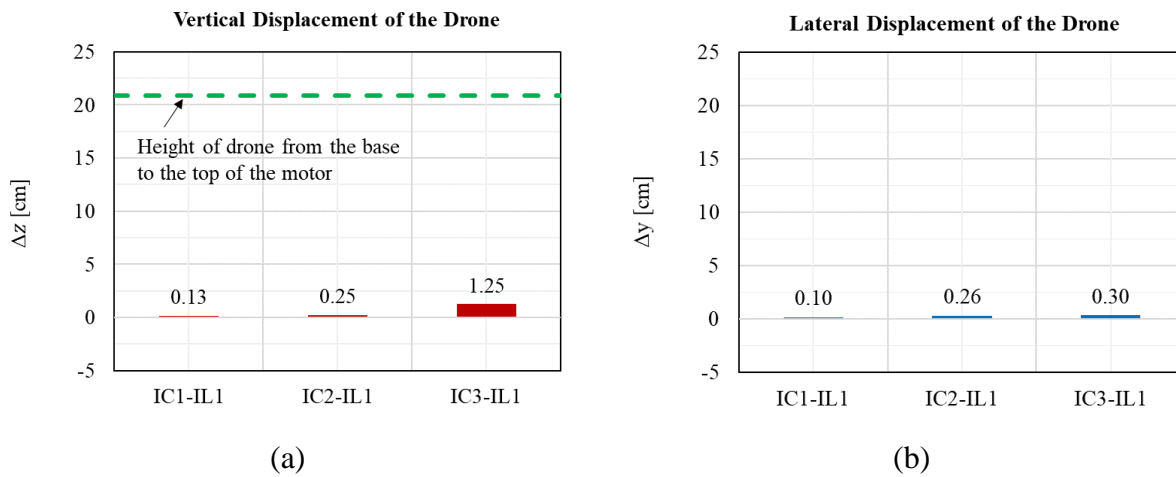


Figure 60. (a) Vertical and (b) Lateral displacement of the drone at the point of impact for IC1-IL1, IC2-IL1, and IC3-IL1.

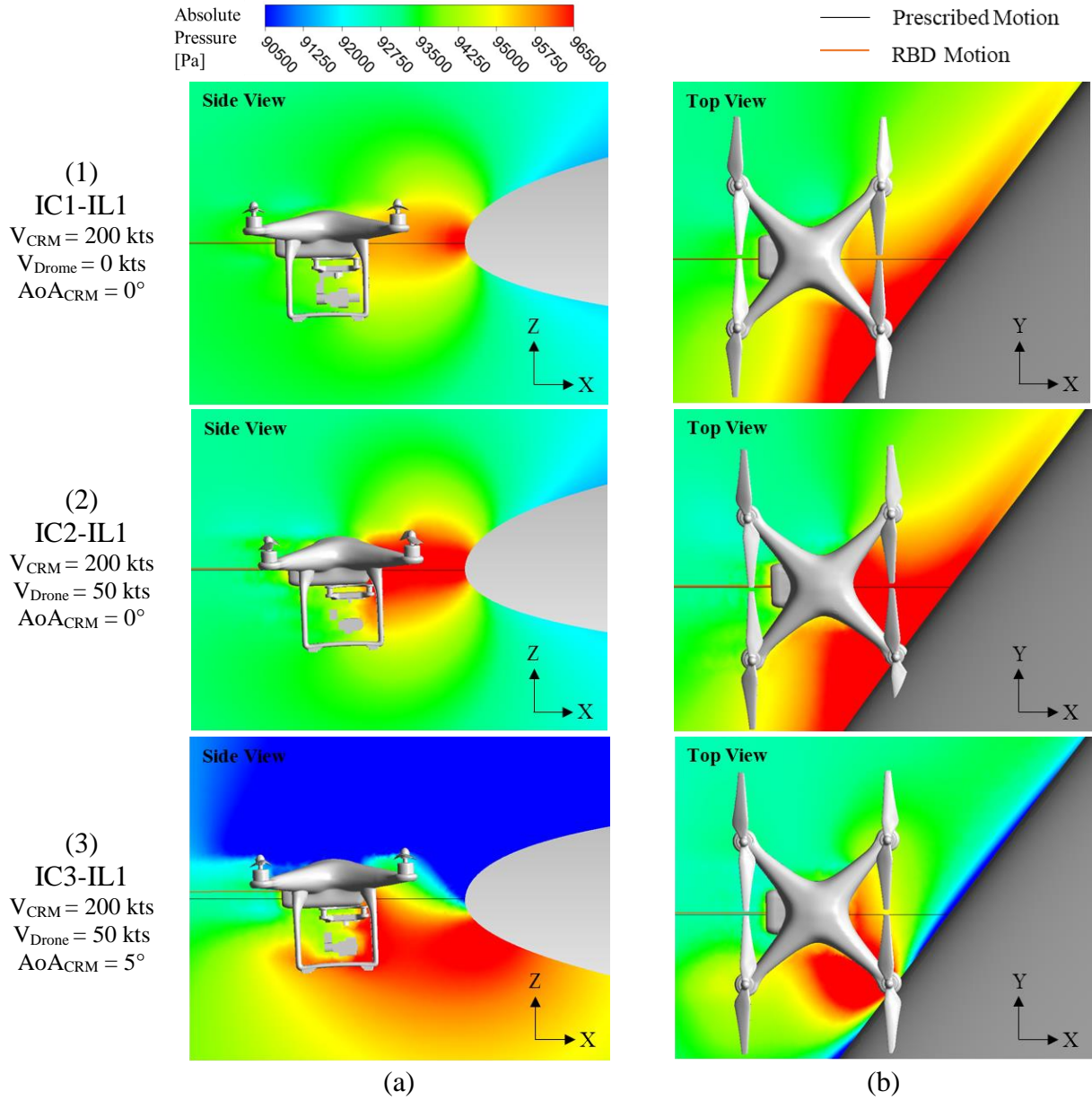


Figure 61. (a) Side view and (b) Top view of the pressure contour over the drone when the relative distance is approximately 0 m, for (1) IC1-IL1, (2) IC2-IL1, and (3) IC3-IL1.

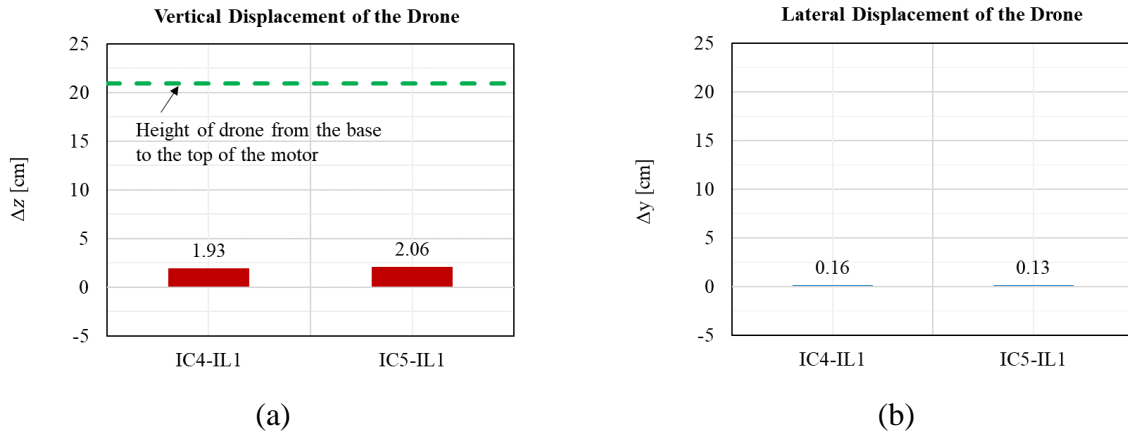


Figure 62. (a) Vertical and (b) Lateral displacements of the drone at the point of impact for IC4-IL1 and IC5-IL1.

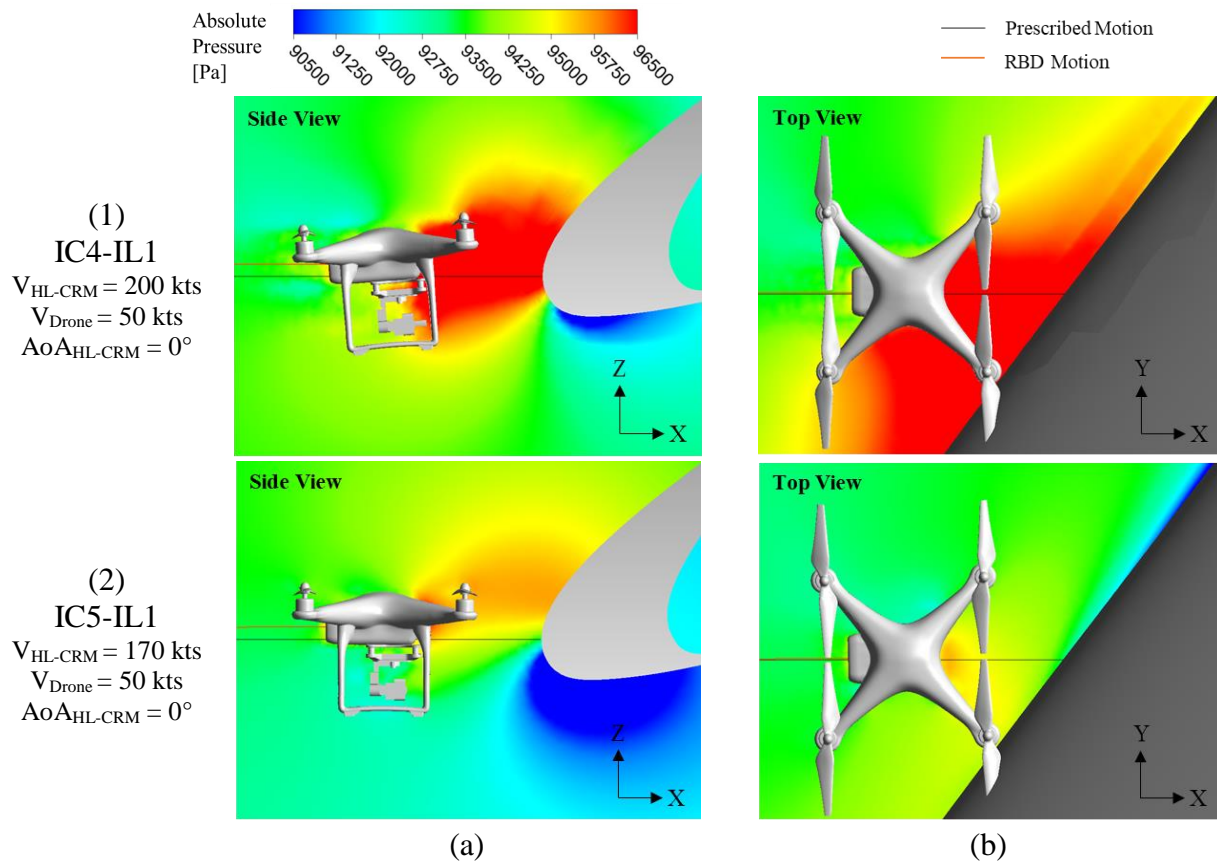


Figure 63. (a) Side view and (b) Top view of the pressure contour over the drone when the relative distance is approximately 0 m, for (1) IC4-IL1 and (2) IC5-IL1.

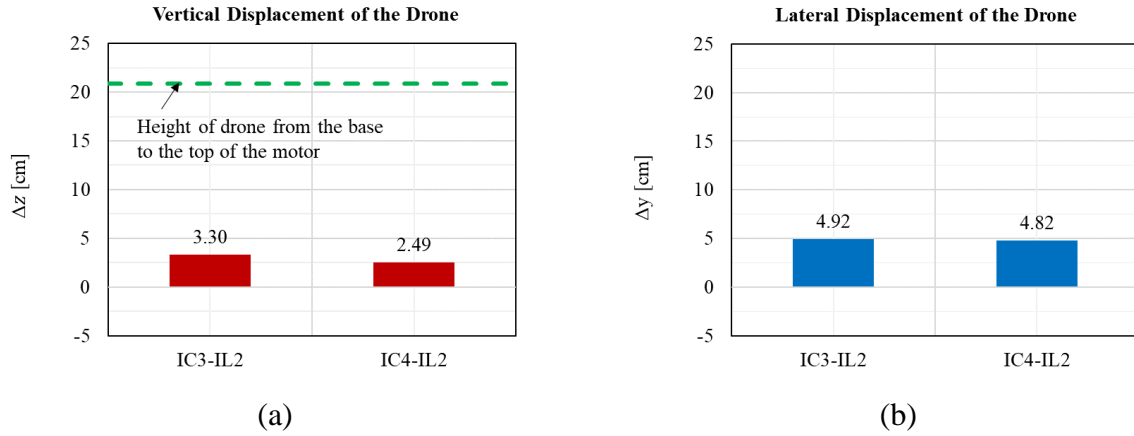


Figure 64. (a) Vertical and (b) Lateral displacements of the drone at the point of impact for IC3-IL2 and IC4-IL2.

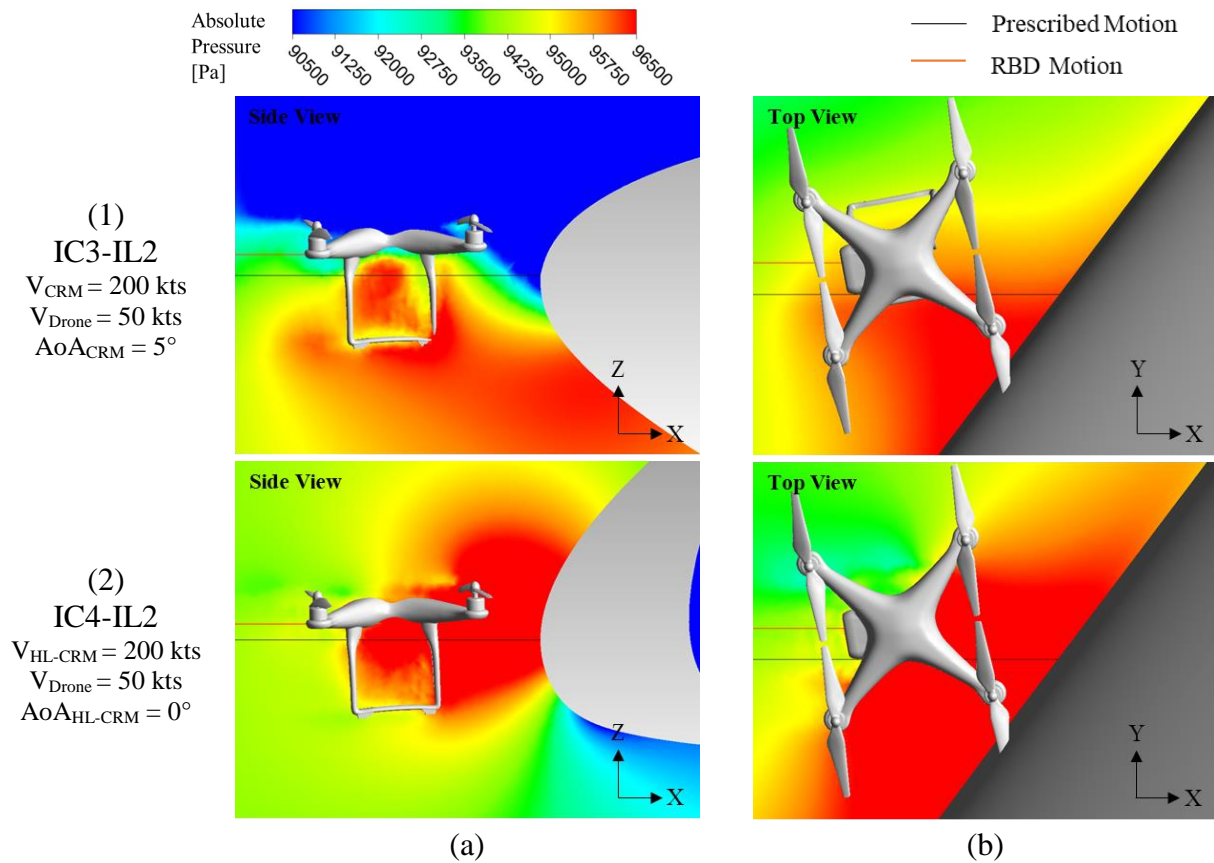


Figure 65. (a) Side view and (b) Top view of the pressure contour over the drone when the relative distance is approximately 0 m, for (1) IC3-IL2 and (2) IC4-IL2.

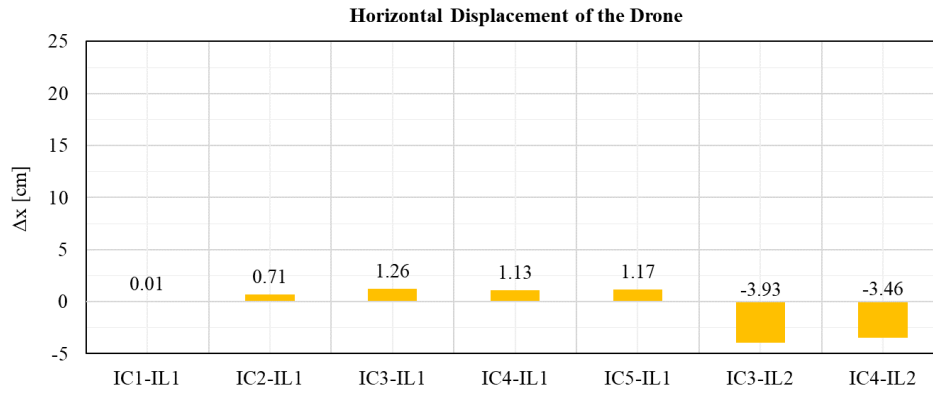
Table 26 provides the drone's horizontal, lateral, and vertical displacements for each impact scenario at the point of impact. These are presented graphically in Figure 66. The negative horizontal displacement indicates that the drone slowed down as it approached the aircraft. The largest vertical displacements were observed when the drone was released at IL2, between the nacelle and the fuselage. The largest vertical displacement occurred with the impact scenario IC3-IL2 when the aircraft was at an angle of attack of  $5^\circ$  without high lift devices deployed. The angular displacements experienced by the drone for each impact scenario are given in Table 27 and depicted in Figure 67. Slight changes in the orientation were observed in the drone as it reached the aircraft.

Table 26. Drone displacements at the point of impact for all impact scenarios.

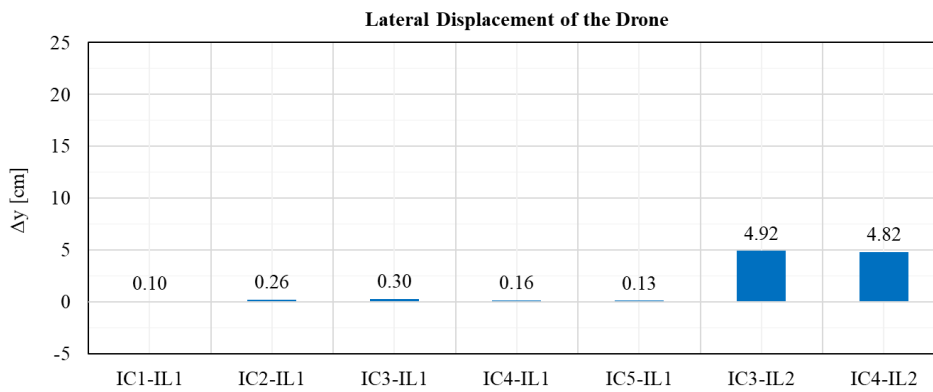
Impact Scenario	Drone Displacement ( <i>cm</i> )		
	Horizontal ( $\Delta x$ )	Lateral ( $\Delta y$ )	Vertical ( $\Delta z$ )
IC1-IL1	0.01	0.10	0.13
IC2-IL1	0.71	0.26	0.25
IC3-IL1	1.26	0.30	1.25
IC4-IL1	1.13	0.16	1.93
IC5-IL1	1.17	0.13	2.06
IC3-IL2	-3.93	4.93	3.30
IC4-IL2	-3.46	4.82	2.49

Table 27. Drone angular displacements at the point of impact for all impact scenarios.

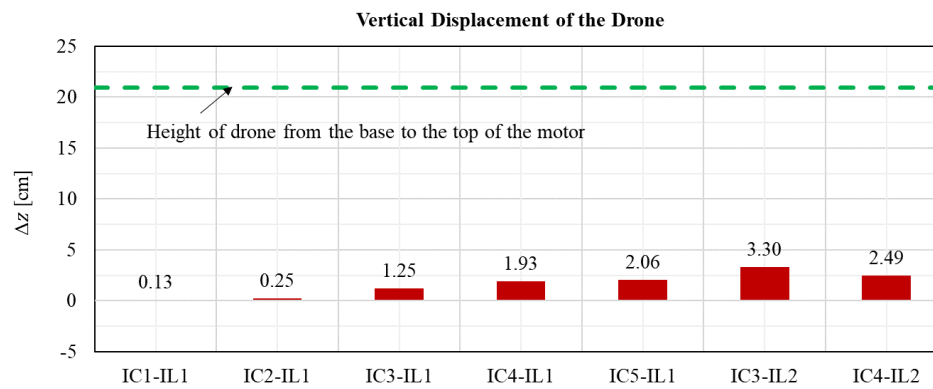
Impact Scenario	Drone Angular Displacement ( <i>degrees</i> )		
	Roll ( $\Delta\phi$ )	Pitch ( $\Delta\theta$ )	Yaw ( $\Delta\psi$ )
IC1-IL1	0.13	-1.09	-0.28
IC2-IL1	5.61	-2.21	1.75
IC3-IL1	1.96	-2.65	0.73
IC4-IL1	1.43	-4.48	0.20
IC5-IL1	1.38	-0.11	1.42
IC3-IL2	7.85	-1.76	10.61
IC4-IL2	7.02	-2.92	9.68



(a)



(b)



(c)

Figure 66. (a) Horizontal, (b) Lateral, and (c) Vertical displacements of the drone at the point of impact.

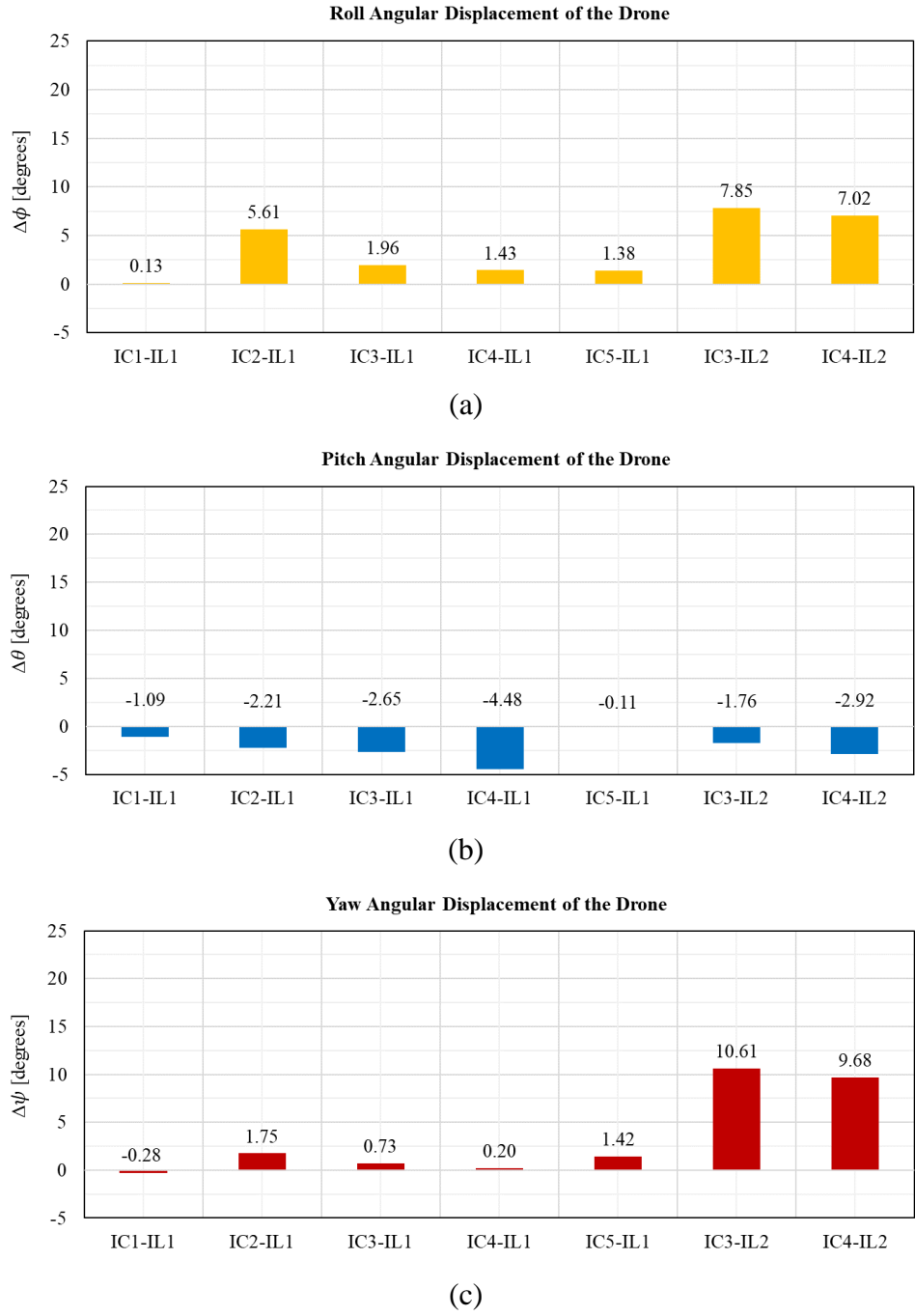


Figure 67. (a) Roll, (b) Pitch, and (c) Yaw angular displacements of the drone at the point of impact.

Comparing the drone vertical displacements across all the scenarios, the largest displacement was observed when the drone was released at IL2 with the CRM aircraft flying at an AoA of  $5^\circ$  (impact scenario IC3-IL2). A maximum vertical displacement of 3.3 cm was seen. The vertical displacement was 8.2% of the required vertical displacement and was the largest percentage of the simulated vertical displacement obtained. Therefore, the observed maximum vertical displacement

of 3.3 cm was much smaller than the required vertical displacement of 40.41 cm in order for the drone to avoid collision with the aircraft.

#### 4. CONCLUSIONS

The A16 Task 1 study, conducted by NIAR and ERAU, addressed the question of whether a sUAS would be deflected prior to impact with a large transport aircraft. The research team performed a series of simulations varying the impact location, aircraft and drone velocities, angle of attack, and aircraft configuration.

NIAR investigated the differences in deflections of the sUAS on impact with a wing in this study. The vertical deflections of the sUAS were small for both the impact locations on the wing.

For the impact location at near mid span of the wing, the range of vertical deflections was 0.13 to 2.06 cm. This range corresponds to 0.2% to 2.1% of the required deflections necessary to avoid impact. For the impact location near root of the wing, the range of vertical deflections was 2.49 to 3.30 cm. This range corresponds to 1.7% to 8.2% of the required deflections necessary to avoid impact. These results indicate that the drone will only slightly deflect upwards and will not deflect away prior to impact with a large transport aircraft on the wing.

For the impact locations on the wing, the range of roll angle displacement was  $0.13^{\circ}$  to  $7.85^{\circ}$ , the range of pitch angle displacement was  $-4.48^{\circ}$  to  $-0.11^{\circ}$ , and the range of yaw angle displacement was  $-0.28^{\circ}$  to  $10.61^{\circ}$ . These results indicate that the orientation of the drone will change relative to the original orientation at the time of impact with a large transport aircraft on the wing.

NIAR also investigated the relationship between flight parameters and the sUAS deflections. The research team showed that higher relative speeds and higher angles of attack resulted in slightly higher vertical deflections of the sUAS.

The main conclusion of the A16 Task 1 study was that sUAS of size and weight similar to a DJI Phantom III would not deflect away from a collision path with a large transport aircraft under only the aerodynamic influence of the aircraft.

This study did not consider additional atmospheric factors like turbulence and gusts in this study. Atmospheric turbulence or wind/gust conditions in combination with the aerodynamic interaction between a sUAS and a large transport aircraft may deflect the drone enough to avoid impact. The research team investigated the trajectory of only one quadcopter sUAS. A smaller UAS in size and weight may have a higher probability of deflecting prior impact. There is a need for additional research to understand better the effect of size of the sUAS and the effect of atmospheric factors on sUAS trajectories that lead up to impact with a larger aircraft.

## 5. REFERENCES

- [1] “Rise of the Drones. Managing the Unique Risks Associated with Unmanned Aircraft Systems”, Alliance Global Corporate & Specialty, 2016.
- [2] Lum, C. W., and Waggoner, B., “A Risk Based Paradigm and Model for Unmanned Aerial Systems in the National Airspace”, Infotech@Aerospace Conferences, 2011-1424, AIAA, St. Louis, MO, 2011.
- [3] Olivares, G., Gomez, L., Espinosa de los Monteros, J., Baldrige, R., and Zinzuwadia, C., “Volume II – UAS Airborne Collision Severity Evaluation – Quadcopter”, Federal Aviation Administration, Report DOT/FAA/AR-XX/XX, 2017.
- [4] U.S. Code of Federal Regulations, Title 14, Part 25, “Airworthiness standards: transport category airplanes”, Washington, DC, U.S. Government Publishing Office, 2016.
- [5] U.S. Department of Transportation, Federal Aviation Administration, “Aeronautical Information Manual: Official Guide to Basic Flight Information and ATC Procedures”, Washington, DC, U.S. Government Publishing Office, 1995.
- [6] Tipps, D. O., Skinn, D. A., Rustenburg, J. W., Jones T., and Harris, D. A., “Statistical Loads Data for the Boeing 777-200ER Aircraft in Commercial Operations”, Federal Aviation Administration, Report DOT/FAA/AR-06/11, 2006.
- [7] The 6th AIAA CFD Drag Prediction Workshop, June 2016. <https://aiaa-dpw.larc.nasa.gov/>
- [8] The 3<sup>rd</sup> AIAA CFD High Lift Prediction Workshop, April 2019. <https://hiliftpw.larc.nasa.gov/Workshop3/testcases.html>.
- [9] Rivers, M. B., “NASA Common Research Model: A History and Future Plans”, AIAA Aviation Forum, AIAA 2019-3725, June 2019.
- [10] Vassberg, J., Tinoco, E., Mani, M., Rider, B., Zickuhr, T., Levy, D., Brodersen, O., Eisfeld, B., Crippa, S., Wahls, R. and Morrison, J., “Summary of the fourth AIAA CFD drag prediction workshop”, 28th AIAA Applied Aerodynamics Conference, AIAA 2010-4547, June 2010. <https://doi.org/10.2514/6.2010-4547>
- [11] Levy, D.W., Laflin, K.R., Tinoco, E.N., Vassberg, J.C., Mani, M., Rider, B., Rumsey, C.L., Wahls, R.A., Morrison, J.H., Brodersen, O.P. and Crippa, S., “Summary of data from the fifth computational fluid dynamics drag prediction workshop”, *Journal of Aircraft*, Vol. 51, No. 4, pp.1194-1213, 2014.
- [12] Tinoco, E.N., Brodersen, O.P., Keye, S., Laflin, K.R., Feltrop, E., Vassberg, J.C., Mani, M., Rider, B., Wahls, R.A., Morrison, J.H. and Hue, D., “Summary data from the sixth AIAA CFD drag prediction workshop: CRM cases”, *Journal of Aircraft*, Vol. 55, No. 4, pp.1352-1379, 2018.
- [13] Lacy, D. S., Scalfani, A. J., “Development of the High Lift Common Research Model (HL-CRM): A Representative High Lift Configuration for Transonic Transports”, 54th AIAA Aerospace Sciences Meeting, AIAA 2016-0308, January 2016. <https://doi.org/10.2514/6.2016-0308>

- [14] Koklu, M., Lin, J. C., Hannon, J. A., Melton, L. P., Andino, M. Y., Paschal, K. B., Vatsa V. N., “Wind Tunnel Testing of Active Flow Control on High-Lift Common Research Model”, AIAA Aviation 2019 Forum, Hampton, VA, June 2019.
- [15] Koklu, M., Lin, J. C., Hannon, J. A., Melton, L. P., Andino, M. Y., Paschal, K. B., Vatsa V. N., “Mitigation of Nacelle/Pylon Wake on the High-Lift Common Research Model Using a Nacelle Chine”, AIAA SciTech 2020 Forum, Hampton, VA, January 2020.
- [16] Rivers, M. B., Quest, J., and Rudnik, R., “Comparison of the NASA Common Research Model European Transonic Wind Tunnel Test Data to NASA Test Data”, 53rd AIAA Aerospace Sciences Meeting, AIAA 2015-1093, January 2015. <https://doi.org/10.2514/6.2015-1093>
- [17] Rivers, B. R., Dittberner, A., “Experimental Investigations of the NASA Common Research Model”, *Journal of Aircraft*, Vol. 51, No. 4, 2014
- [18] Kohlman, D., and Winn, R., "Analytical Prediction of Trajectories of Ice Pieces after Release in an Airstream," 39th Aerospace Sciences Meeting and Exhibit, 2001.
- [19] Santos, L.D.C., Papa, R., and Ferrari, M. D. A., “A Simulation Model for Ice Impact Risk Evaluation,” 41st Aerospace Sciences Meeting and Exhibit, 2003.
- [20] Unal, K., and Baran, O. U., "A Modeling and Simulation Tool for Safe Store Separation Envelope Generation Using Monte Carlo Simulations," 2018 AIAA Modeling and Simulation Technologies Conference, 2018.
- [21] Sickles, W. L., Hand, T. L., Morgret, C. H., Masters, J. S., and Denny, A. G., “High-Fidelity, time-accurate CFD Store Separation Simulations from a B-1B Bay with Comparisons to Quasi-Steady Engineering Methods”, 46th AIAA Aerospace Sciences Meeting and Exhibit, AIAA 2008-186, January 2008.
- [22] Yeong, H.W., Papadakis, M., and Shimoï, K., "Ice Trajectory and Monte Carlo Analyses for a Business Jet," 1st AIAA Atmospheric and Space Environments Conference, 2009.
- [23] Murman, S., Aftosmis, M., and Nemec, M., "Automated Parameter Studies Using a Cartesian Method," 22nd Applied Aerodynamics Conference and Exhibit, 2004.
- [24] Osman A. A., and Bayoumy A.M., “Numerical Analysis of an External Store Separation from an Airplane”, AIAA Modeling and simulation technologies conference, AIAA 2016-2143, January 2016.
- [25] Naveed A., and Javed A., “Effects of Variation in Flow Field on Store Separation”, 15th International Bhurban Conference on Applied Sciences & Technology, Pakistan, January 2018.
- [26] Sahu J., “Flight Behaviors of a Complex Projectile using a Coupled CFD-based Simulation Technique: Free Motion”, 33rd AIAA Applied Aerodynamics Conference, AIAA 2015-2585, June 2015.
- [27] Sahu J., “Time-Accurate Numerical Prediction of Free-Flight Aerodynamics of a Finned Projectile”, *Journal of Spacecraft and Rockets*, Vol. 45, No. 5, pp. 946–954, September 2008.

- [28] Luu, V. T., Plourde, F., and Grignon, C., “Toward a CFD/6 DOF Coupled Model Enhancing Projectile Trajectory Prediction”, 21st AIAA Computational Fluid Dynamics Conference, AIAA 2013-2591, June 2013.
- [29] Hargreaves, D. M., Kakimpa, B., and Owen, J. S., “The Computational Fluid Dynamics Modelling of the Autorotation of Square Flat Plates”, Journal of Fluids and Structures, Vol. 46, pp. 111-133, April 2014.
- [30] Kakimpa, B., Hargreaves, D. M., and Owen, J. S., “An investigation of Plate-type Windborne Debris Flight using Coupled CFD–RBD Models. Part I: Model Development and Validation”, Journal of Wind Engineering and Industrial Aerodynamics, Vol. 111, pp. 95-103, December 2012.
- [31] Murman, S. M., Aftosmis, M. J., and Berger, M. J., “Simulations of 6-DOF Motion with a Cartesian Method”, 41st Aerospace Sciences Meeting and Exhibit, AIAA 2003-1246, January 2003.
- [32] Cenko, A., “F/A–18C/JDAM CFD Challenge Wind Tunnel and Flight Test Results”, 37<sup>th</sup> AIAA Aerospace Sciences Meeting and Exhibit, AIAA 99-0120, January 1999.
- [33] Ansys® Fluent, Release 18.2, Help System, User’s Guide, ANSYS, Inc.

## APPENDIX A – MESH PARAMETERS AND QUALITY INFORMATION

### A.1 CRM AERODYNAMIC PERFORMANCE VALIDATION

The mesh generated for the CRM validation study was created with two sets of size boxes as shown in Figure 68. The first set of size boxes was created for a refined volume region over the wing and to capture the wing wake (size boxes 1 and 2). The second set of size boxes was created around the aircraft as a general refinement region for aircraft wake capture (A, B, and C). The element lengths defined within the size boxes are specified in Table 28.

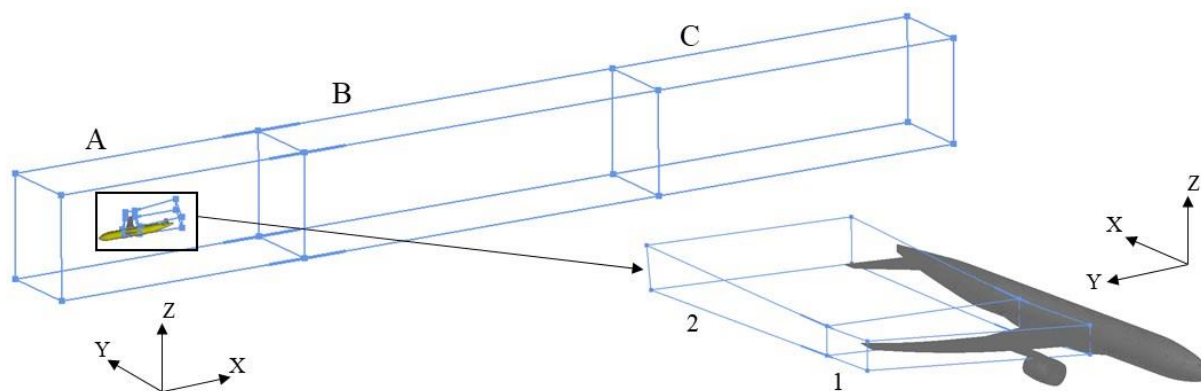


Figure 68. Size boxes generated around the CRM aircraft for volume mesh refinement.

Table 28. Maximum element lengths used within the size boxes.

Size Box	Max. Surface and Volume Element Length ( <i>m</i> )
A	2.0
B	4.0
C	8.0
1	0.2
2	0.6

The CRM aircraft surface mesh and volume mesh quality information are provided in Table 29 and Table 30, respectively. The number of 2D elements does not include the top cap elements created over the prism boundary layers.

#### A.1.1 Mesh Quality

The criteria used to determine the mesh quality for both the surface mesh and the volume mesh is provided in Table 29 and Table 30.

Table 29. Surface mesh quality of the CRM aircraft and domain.

<b>Surface Mesh</b>		<b>CRM</b>
<b>Total number of 2D elements</b>		<b>746,247</b>
<b>Surface Mesh Quality</b>		
<b>Quality Criteria</b>	<b>Target</b>	<b>% Elements Failed</b>
Aspect Ratio	< 10	0.133
Skewness	< 0.8	0.003
Maximum Angle	< 120°	0.010

Table 30. Volume mesh quality of the CRM aircraft volume mesh.

<b>Volume Mesh</b>		<b>CRM</b>
<b>Total Number of 3D Elements</b>		<b>28,282,965</b>
<b>Total Number of Prism Elements</b>		<b>4,868,074</b>
<b>Volume Mesh Quality</b>		
<b>Quality Criteria</b>	<b>Target</b>	<b>% Elements Failed</b>
Aspect Ratio – Tetrahedral, Pyramid, and Hexahedral Elements	< 15	0.0004
Aspect Ratio – Prism Elements	< 1500	0
Skewness	< 0.95	0.0001
Minimum Angle	> 20°	0.0010
Maximum Angle	< 165°	
Non-Orthogonality	> 0.01	0
No. of Negative Volume Elements	0	0

## A.2 HL-CRM AERODYNAMIC PERFORMANCE VALIDATION

Similar to the CRM validation mesh, the HL-CRM mesh was created with two sets of size boxes. Figure 69 and Table 31 detail the size box information. The surface mesh and volume mesh quality information are provided in Table 32 and Table 33, respectively.

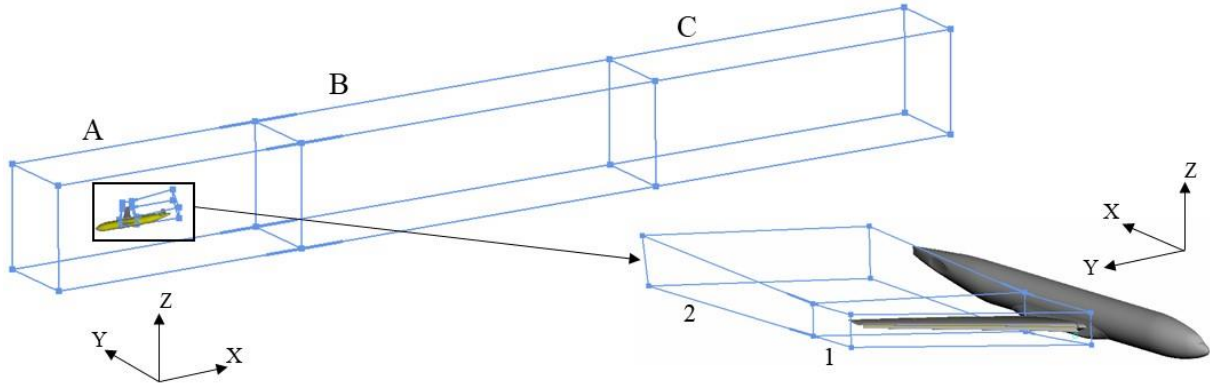


Figure 69. Size boxes generated around the HL-CRM aircraft for volume mesh refinement.

Table 31. Maximum element lengths used within the HL-CRM size boxes.

Size Box	Max. Surface and Volume Element Length ( <i>m</i> )
A	2.0
B	4.0
C	8.0
1	0.2
2	0.6

### A.2.1 Mesh Quality

The criteria used to determine the mesh quality for both the surface and volume mesh are provided in Table 32 and Table 33.

Table 32. Surface mesh quality of the HL-CRM aircraft and domain.

<b>Surface Mesh</b>		<b>HL-CRM</b>
<b>Total number of 2D elements</b>		<b>676,822</b>
<b>Surface Mesh Quality</b>		
<b>Quality Criteria</b>	<b>Target</b>	<b>% Elements Failed</b>
Aspect Ratio	< 10	0.0001
Skewness	< 0.8	0.0460
Maximum Angle	< 120°	1.586

Table 33. Volume mesh quality of the HL-CRM aircraft volume mesh.

<b>Volume Mesh</b>		<b>HL-CRM</b>
<b>Total Number of 3D Elements</b>		<b>18,651,247</b>
<b>Total Number of Prism Elements</b>		<b>4,737,710</b>
<b>Volume Mesh Quality</b>		
<b>Quality Criteria</b>	<b>Target</b>	<b>% Elements Failed</b>
Aspect Ratio – Tetrahedral, Pyramid, and Hexahedral Elements	< 15	0.0072
Aspect Ratio – Prism Elements	< 1500	0
Skewness	< 0.95	0.0045
Minimum Angle	> 20°	0.0229
Maximum Angle	< 165°	
Non-Orthogonality	> 0.01	0
No. of Negative Volume Elements	0	0

### A.3 UAS TRAJECTORY ANALYSIS

The overset mesh used to predict the drone's trajectory was created using BETA CAE's commercial mesh generation software, ANSA. The overset mesh consists of two sections: component mesh and background mesh. The component mesh consists of the objects that move within the stationary domain that makes up the background mesh.

The background mesh was generated around the CRM and HL-CRM aircraft depending on the impact condition. The domain extents were set to be 100 times the aircraft MAC of 7.005 m. Size boxes were created around the aircraft to define refinement regions for wake capture, as seen in Figure 70. The element lengths used within the refinement regions created to capture the aircraft wake are given in Table 34.

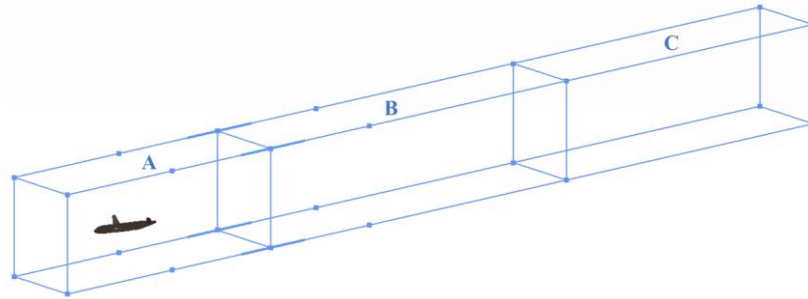


Figure 70. Size boxes are generated within the domain to capture the aircraft wake.

Table 34. Maximum element lengths used within the aircraft wake refinement size boxes.

<b>Size Box</b>	<b>Max. Surface and Volume Element Length (<i>m</i>)</b>
A	3.5
B	7.0
C	12.0

The background mesh was created in two parts: a tetrahedral volume region and a hexahedral volume region. The hexahedral volume was generated across the domain where the component mesh and hence the drone was expected to travel. The hexahedral mesh region was extended in the vertical direction, as seen in Figure 71. The vertical extension above the drone was created to capture the positive vertical displacements experienced by the drone, as observed in preliminary investigations. The background hexahedral mesh region was extended by about a meter behind the drone. The dimensions of the hexahedral background mesh region and the component mesh volume are provided in Figure 71 for the mesh generated to simulate the IC3-IL2 impact scenario.

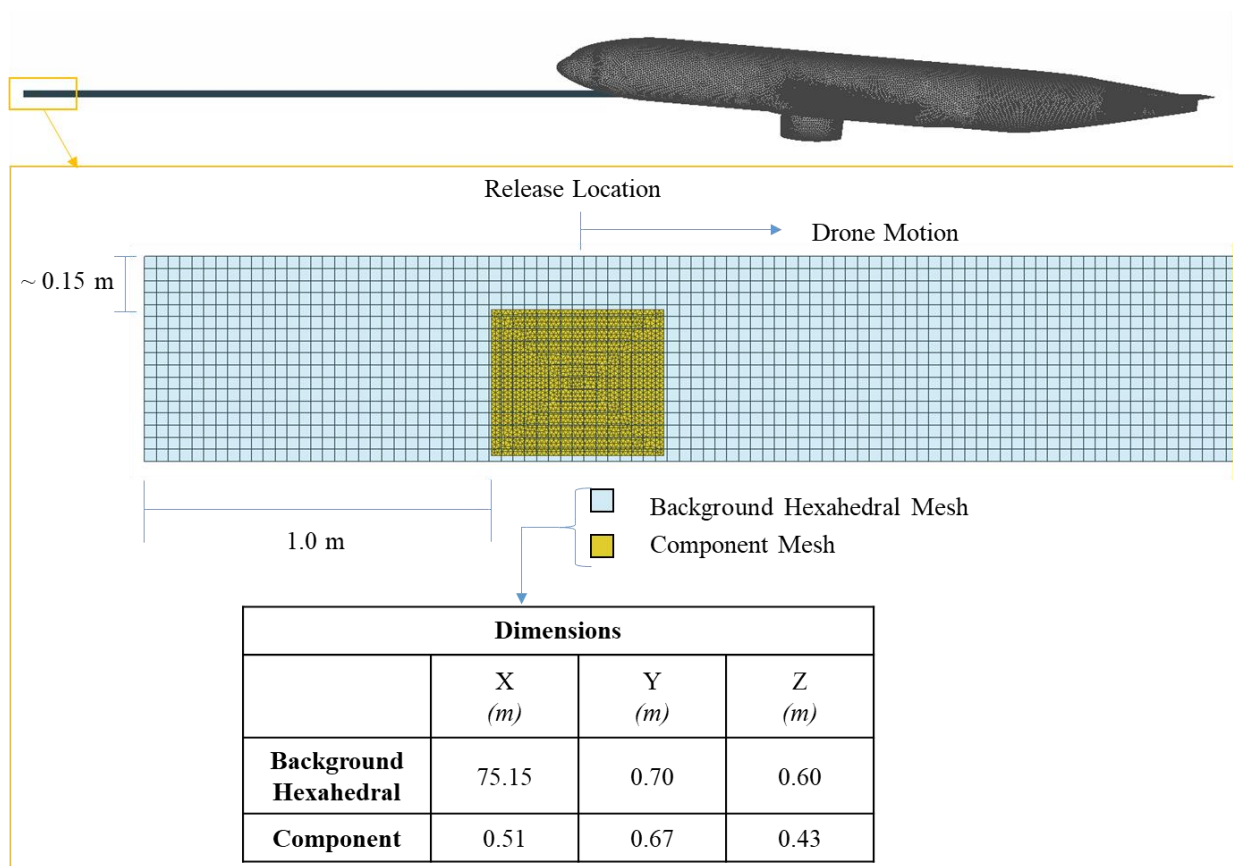


Figure 71. Background mesh and component mesh dimensions and details at release location.

In addition to the size boxes generated around the aircraft, three size boxes were created at the end of the hexahedral background region to create a smooth transition from hexahedral (hexa-) elements to tetrahedral (tetra-) elements as the drone moved closer to the aircraft wing/slat as shown in Figure 72. The surface mesh on the wing was also refined to obtain a good overlap between the small component mesh elements and the background mesh elements. Refer to Table 35 for details on the element length used within the size boxes.

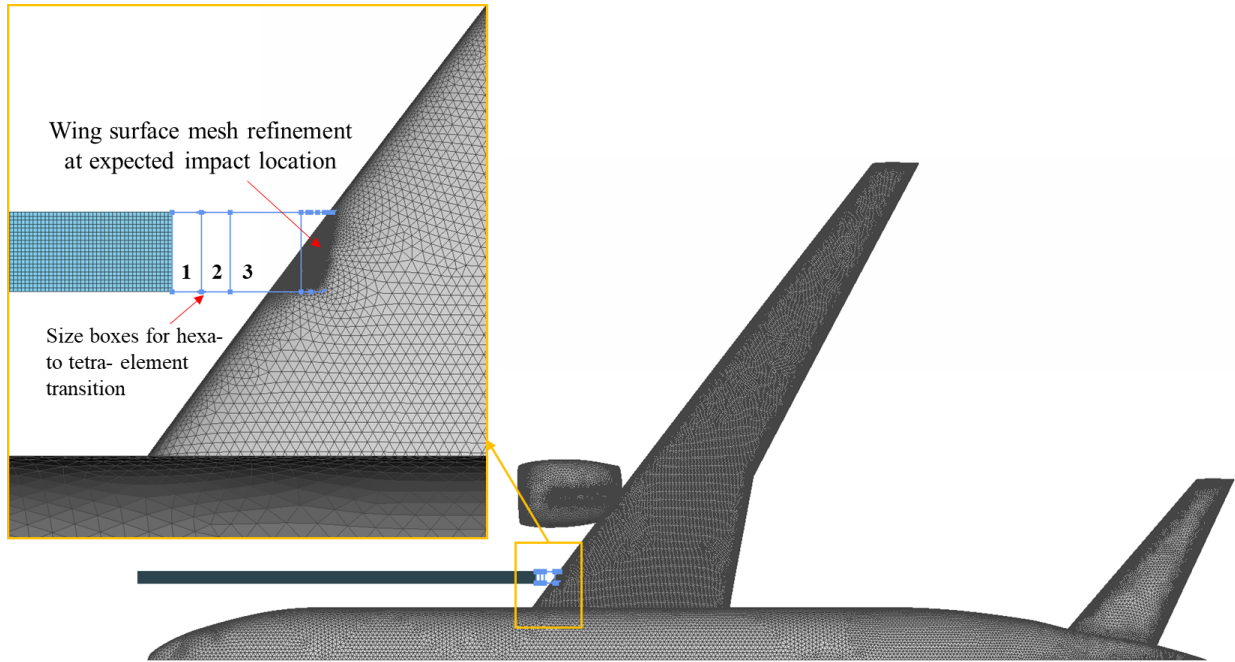


Figure 72. Surface mesh refinement on aircraft and additional size boxes created to obtain a good transition from hexahedral to tetrahedral elements.

Table 35. Element lengths used to obtain a smooth transition from hexa- to tetra- elements.

Size Box	Max. Surface and Volume Element Length ( <i>m</i> )
1	0.0348
2	0.0174
3	0.0087

The prism layers on the aircraft geometry were created based on a target  $y^+$  of 500. The first layer height was set to 0.0023 m, and the mesh to capture the boundary layer over the aircraft was generated based on the parameters listed in Table 36.

Table 36. Layer parameters used to generate boundary layer mesh over the aircraft.

Aircraft Prism Layers: $y^+ \approx 500$				
First Layer Height ( <i>m</i> )	Growth Factor	Number of Layers	Number of Additional Layers	Total Number of Layers
0.0023	1.25	4	5	9

The component mesh domain was generated around the drone to capture the drone's flow and the aerodynamic forces and moments experienced by the drone as it moved through the domain towards the aircraft. The component mesh domain dimensions are given in Figure 71. The volume mesh was generated around the drone consisting of prism and tetrahedral elements, as seen in Figure 73. The overall element size of the component volume was kept similar to the refined element size of the background hexahedral elements (0.0087 m).

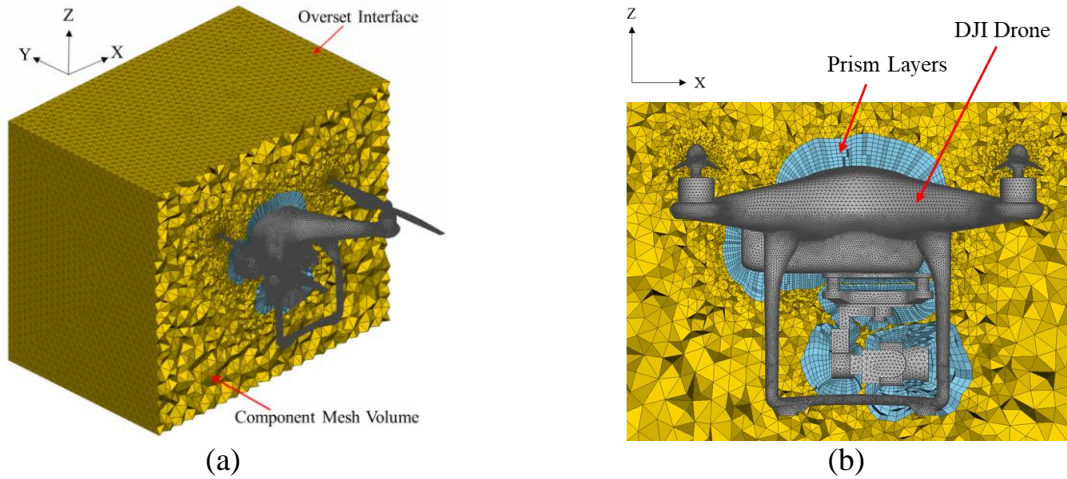


Figure 73. Component mesh details from an (a) Isometric view and (b) Cross-sectional view depicting the drone and prism layers.

The prism elements used to capture the boundary layer development over the drone were generated with a first layer height set to 0.0038 m calculated from a target wall  $y^+$  of 300. Table 37 provides details about the prism layers generated over the drone. The same component mesh was used for all impact scenarios.

Table 37. Layer parameters used to generate boundary layer mesh over the drone.

<b>Drone Prism Layers: <math>y^+ \approx 300</math></b>				
First Layer Height (m)	Growth Factor	Number of Layers	Number of Additional Layers	Total Number of Layers
0.0038	1.20	5	3	8

### A.3.1 Mesh Quality

The surface and volume meshes for both the component and background mesh were generated to ensure good mesh quality. The mesh was generated to ensure the quality failure of less than 10 % of the total elements. The criteria used to determine the mesh quality for both the surface mesh and the component volume mesh are provided, along with the quality information for both the component and background meshes for the surface mesh in Table 38 and the volume mesh in Table 39.

Table 38. Surface mesh quality of component and background meshes.

<b>Surface Mesh Size</b>			
		<b>Component</b>	<b>Background</b>
<b>Total number of 2D elements</b>		<b>221,938</b>	<b>717,653</b>
<b>Surface Mesh Quality</b>			
<b>Quality Criteria</b>	<b>Target</b>	<b>% Elements Failed</b>	
Aspect Ratio	< 10	0.000	0.000
Skewness	< 0.8	0.038	0.000
Maximum Angle	< 120°	0.996	8.361E-04

Table 39. Volume mesh quality of component and background meshes.

<b>Volume Mesh Size</b>			
		<b>Component</b>	<b>Background</b>
<b>Total Number of 3D Elements</b>		<b>3,569,993</b>	<b>27,804,634</b>
<b>Total Number of Hexahedral Elements</b>		<b>-</b>	<b>732,020</b>
<b>Total Number of Prism Elements</b>		<b>1,580,163</b>	<b>6,458,877</b>
<b>Volume Mesh Quality</b>			
<b>Quality Criteria</b>	<b>Target</b>	<b>% Elements Failed</b>	
Aspect Ratio – Tetrahedral, Pyramid, and Hexahedral Elements	< 15	0.213	4.966E-04
Aspect Ratio – Prism Elements	< 1500	0.002	0.000
Skewness	< 0.95	0.085	2.158E-05
Minimum Angle	> 20°	0.048	1.187E-04
Maximum Angle	< 165°		
Non-Orthogonality	> 0.01	0.002	0.000
No. of Negative Volume Elements	0	0.000	0.000

## APPENDIX B – USER-DEFINED FUNCTION FOR CFD-RBD COUPLING

A UDF was created and used within Ansys® Fluent to aid in the trajectory calculations. The user-defined function provided the solver with relevant information regarding the drone properties such as weight and mass moment of inertia during prescribed motion and additional information regarding the number of degrees-of-freedom provided and any external forces used in the force balance during unconstrained motion.

For this study, a compiled UDF was created with predefined macros and functions available within Ansys® Fluent to access solver data and facilitate the exchange of information between the UDF and the solver.

The DEFINE\_SDOF\_PROPERTIES macro, available within the predefined dynamic mesh DEFINE macro, was used in the UDF to pass drone properties to the 6-DOF solver. A sample UDF used for impact scenario IC2-IL1 is provided below.

The UDF was split into two sections. The first section was used to define the drone properties for prescribed motion as shown in Figure 74 and Figure 75. No external forces were added in the UDF, and the option for ‘Passive’ was enabled within the solver to indicate to the solver that the forces and moments were not be used in determining the trajectory of the drone. This portion of the UDF was primarily used to assign drone properties and to record the drone location, orientation, velocity, angular velocity, and aerodynamic forces and moments.

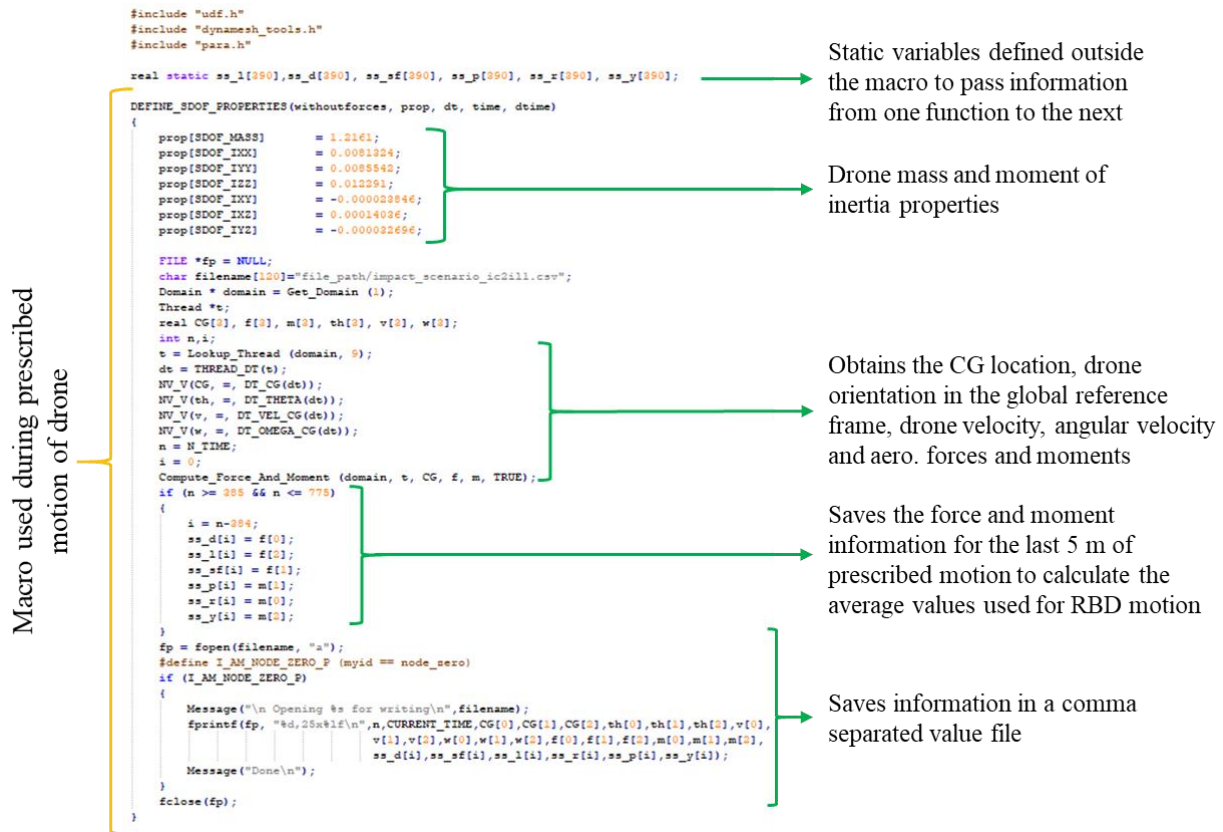


Figure 74. Prescribed motion portion of the UDF used in the 6-DOF solver with comments.

```

#include "udf.h"
#include "dynamesh_tools.h"
#include "para.h"

real static ss_l[390],ss_d[390], ss_sf[390], ss_p[390], ss_r[390], ss_y[390];

DEFINE_SDOF_PROPERTIES(withoutforces, prop, dt, time, dtime)
{
    prop[SDOF_MASS]      = 1.2161;
    prop[SDOF_IXX]      = 0.0081324;
    prop[SDOF_IYY]      = 0.0085542;
    prop[SDOF_IZZ]      = 0.012291;
    prop[SDOF_IXY]      = -0.000023846;
    prop[SDOF_IXZ]      = 0.00014036;
    prop[SDOF_IYZ]      = -0.000032696;

    FILE *fp = NULL;
    char filename[120]="/file_path/impact_scenario_ic2ill.csv";
    Domain * domain = Get_Domain (1);
    Thread *t;
    real CG[3], f[3], m[3], th[3], v[3], w[3];
    int n,i;
    t = Lookup_Thread (domain, 9);
    dt = THREAD_DT(t);
    NV_V(CG, =, DT_CG(dt));
    NV_V(th, =, DT_THETA(dt));
    NV_V(v, =, DT_VEL_CG(dt));
    NV_V(w, =, DT_OMEGA_CG(dt));
    n = N_TIME;
    i = 0;
    Compute_Force_And_Moment (domain, t, CG, f, m, TRUE);
    if (n >= 385 && n <= 775)
    {
        {
            i = n-384;
            ss_d[i] = f[0];
            ss_l[i] = f[2];
            ss_sf[i] = f[1];
            ss_p[i] = m[1];
            ss_r[i] = m[0];
            ss_y[i] = m[2];
        }
        fp = fopen(filename, "a");
        #define I_AM_NODE_ZERO_P (myid == node_zero)
        if (I_AM_NODE_ZERO_P)
        {
            Message("\n Opening %s for writing\n",filename);
            fprintf(fp, "%d,25x%lf\n",n,CURRENT_TIME,CG[0],CG[1],CG[2],th[0],th[1],th[2],
            v[0],v[1],v[2],w[0],w[1],w[2],f[0],f[1],f[2],m[0],m[1],m[2],
            ss_d[i],ss_sf[i],ss_l[i],ss_r[i],ss_p[i],ss_y[i]);
            Message("Done\n");
        }
        fclose(fp);
    }
}

```

Figure 75. A section of the UDF that is used during the drone prescribed motion for impact scenario IC2-IL1.

The second portion of the UDF was used to calculate the drone's trajectory while the drone was under the influence of external forces and moments. These external forces and moments constitute the drone's weight, inertia, and aerodynamic forces and moments due to the drone's independent motion and due to the presence of the aircraft. Figure 76 and Figure 77 show the steps used within the UDF to calculate the average forces and moments experienced by the drone and assign them as external loads to balance the aerodynamic loads experienced by the drone due to its own motion.

The difference in the various UDF's used for the impact scenarios occurs in the time step value that was used to calculate the average forces and moments. Appropriate changes were made to the time step values used within the UDF to account for the change in drone velocity and release location to calculate the average force and moment values based on the final 5 m of prescribed motion for each impact scenario. The UDF remained the same across all impact scenarios aside from the time step values used to calculate the average forces and moments.

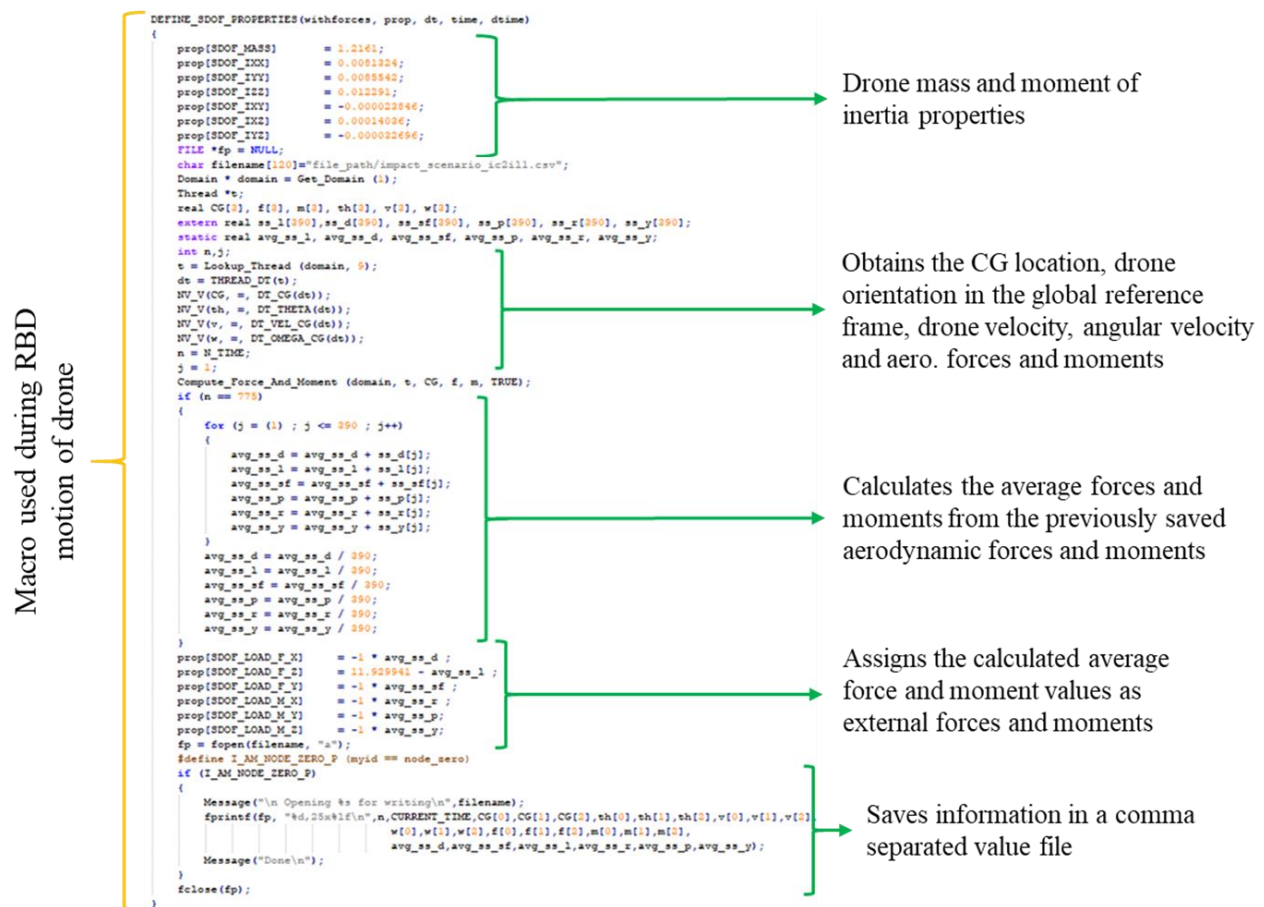


Figure 76. The RBD motion portion of the UDF used to calculate the trajectory by the 6-DOF solver.

```

DEFINE_SDOF_PROPERTIES(withforces, prop, dt, time, dtime)
{
    prop[SDOF_MASS]          = 1.2161;
    prop[SDOF_IXX]          = 0.0081324;
    prop[SDOF_IYY]          = 0.0085542;
    prop[SDOF_IZZ]          = 0.012291;
    prop[SDOF_IXY]          = -0.000023846;
    prop[SDOF_IXZ]          = 0.00014036;
    prop[SDOF_IYZ]          = -0.000032696;
    FILE *fp = NULL;
    char filename[120]="/file_path/impact_scenario_ic2ill.csv";
    Domain * domain = Get_Domain (1);
    Thread *t;
    real CG[3], f[3], m[3], th[3], v[3], w[3];
    extern real ss_l[390],ss_d[390], ss_sf[390], ss_p[390], ss_r[390], ss_y[390];
    static real avg_ss_l, avg_ss_d, avg_ss_sf, avg_ss_p, avg_ss_r, avg_ss_y;
    int n,j;
    t = Lookup_Thread (domain, 9);
    dt = THREAD_DT(t);
    NV_V(CG, =, DT.CG(dt));
    NV_V(th, =, DT.THETA(dt));
    NV_V(v, =, DT.VEL.CG(dt));
    NV_V(w, =, DT.OMEGA.CG(dt));
    n = N_TIME;
    j = 1;
    Compute_Force_And_Moment (domain, t, CG, f, m, TRUE);
    if (n == 775)
    {
        for (j = (1) ; j <= 390 ; j++)
        {
            avg_ss_d = avg_ss_d + ss_d[j];
            avg_ss_l = avg_ss_l + ss_l[j];
            avg_ss_sf = avg_ss_sf + ss_sf[j];
            avg_ss_p = avg_ss_p + ss_p[j];
            avg_ss_r = avg_ss_r + ss_r[j];
            avg_ss_y = avg_ss_y + ss_y[j];
        }
        avg_ss_d = avg_ss_d / 390;
        avg_ss_l = avg_ss_l / 390;
        avg_ss_sf = avg_ss_sf / 390;
        avg_ss_p = avg_ss_p / 390;
        avg_ss_r = avg_ss_r / 390;
        avg_ss_y = avg_ss_y / 390;
    }
    prop[SDOF_LOAD_F_X]      = -1 * avg_ss_d ;
    prop[SDOF_LOAD_F_Z]      = 11.929941 - avg_ss_l ;
    prop[SDOF_LOAD_F_Y]      = -1 * avg_ss_sf ;
    prop[SDOF_LOAD_M_X]      = -1 * avg_ss_r ;
    prop[SDOF_LOAD_M_Y]      = -1 * avg_ss_p;
    prop[SDOF_LOAD_M_Z]      = -1 * avg_ss_y;
    fp = fopen(filename, "a");
    #define I_AM_NODE_ZERO_P (myid == node_zero)
    if (I_AM_NODE_ZERO_P)
    {
        Message("\n Opening %s for writing\n",filename);
        fprintf(fp, "%d,25x%lf\n",n,CURRENT_TIME,CG[0],CG[1],CG[2],th[0],th[1],th[2],v[0],v[1],v[2],
        w[0],w[1],w[2],f[0],f[1],f[2],m[0],m[1],m[2],
        avg_ss_d,avg_ss_sf,avg_ss_l,avg_ss_r,avg_ss_p,avg_ss_y);
        Message("Done\n");
    }
    fclose(fp);
}

```

Figure 77. A section of the UDF used during the RBD motion of the drone for impact scenario IC2-IL1.

## APPENDIX C – UAS TRAJECTORY ANALYSIS RESULTS

The time history of the force, moment, displacement, velocity, angular displacement, and angular velocity of the drone are documented for each impact scenario. The domain was initialized with the aircraft steady-state flow field, and the transient simulation progressed with a time step size of 1E-04 seconds. The results are documented in terms of the relative distance measured between the drone chassis and the aircraft wing/slat leading-edge. Refer to Section 3.5 for details on the definition of relative distance.

### C.1 NUMERICAL DATA FILTERING

Due to the mesh adaption process used in Ansys<sup>®</sup> Fluent to refine and coarsen the mesh with the drone's movement through the domain, a numerical spike was observed at every mesh adaption step. The numerical spike lasted for about 25 to 30 data points each time the background mesh was refined ahead of the drone and coarsened behind the drone. To filter out the numerical spike from the data, a median method of data filtering wherein each output value was obtained by calculating the median of a specific set of raw data was used for all the forces and moments recorded for the aircraft and as well as the drone. Figure 78 depicts the simulation data with and without the filtering obtained for the drone in the X and Z-axes for impact scenario IC3-IL1. The X and Z-axes represent horizontal and vertical directions, with the drone moving horizontally as it approaches the aircraft. To ensure that the filtering method did not skew the original data, the filtered data was plotted against the original data. It can be observed that the filtered data remains unaltered from the original data in regions without the numerical spike.

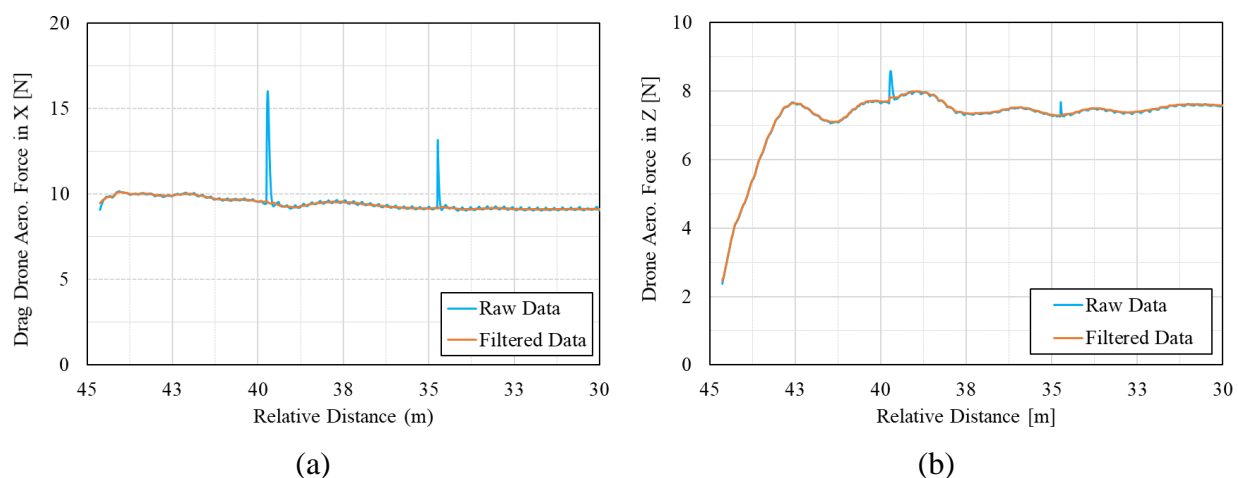


Figure 78. Representation of data filtering on drone aerodynamic forces measured about the (a) X-axis and (b) Z-axis.

For all impact scenarios, the force and moment information of the aircraft and drone are provided post-filtering. However, the displacements and velocities of the drone were not filtered.

### C.2 LOCATION OF PLANES FOR VISUALIZATION

The pressure contours of the flow field over the drone and the aircraft are obtained about the XY plane and the XZ plane for the top and side view, respectively. For the top view, an XY plane was created with the Z location placed at the initial CG location of the drone. Therefore, the XY plane

(top view) was placed such that it intersected the leading-edge of the wing in case of the CRM aircraft and the leading-edge of the slat in the case of the HL-CRM aircraft at the lateral station corresponding to IL1 and IL2 as seen in Figure 79. On the other hand, the side view was obtained by creating an XZ-plane at the Y locations corresponding to lateral stations of IL1 and IL2, as seen in Figure 80.

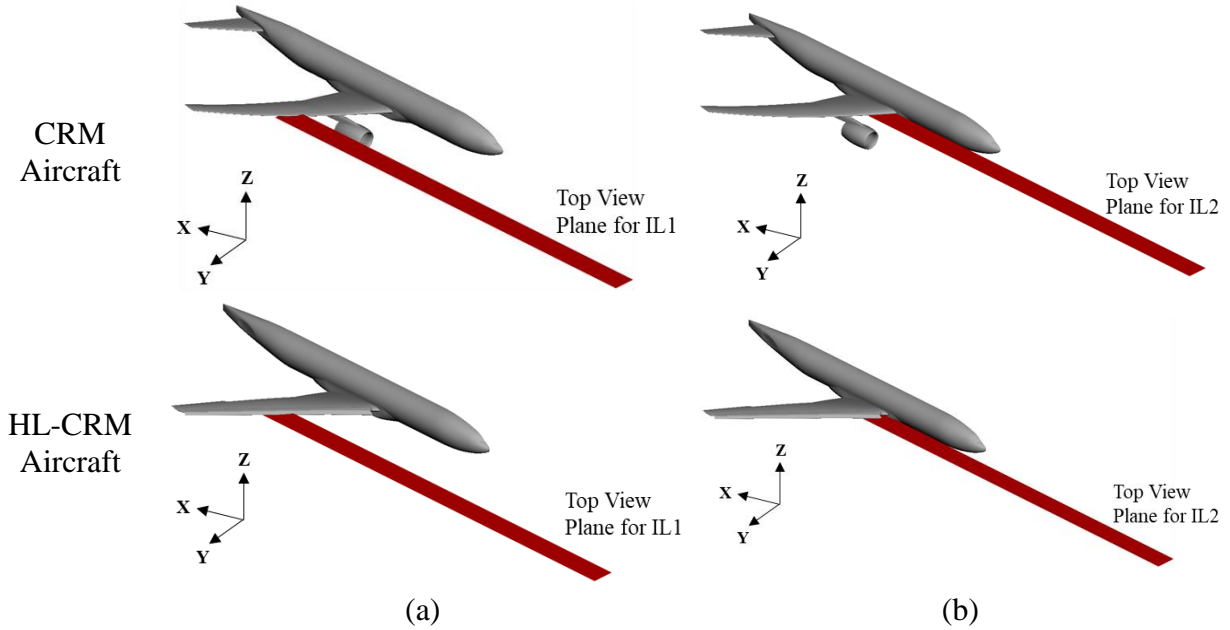


Figure 79. XY-plane created to obtain a top view of pressure contours over the drone and aircraft at the lateral stations of (a) IL1 and (b) IL2.

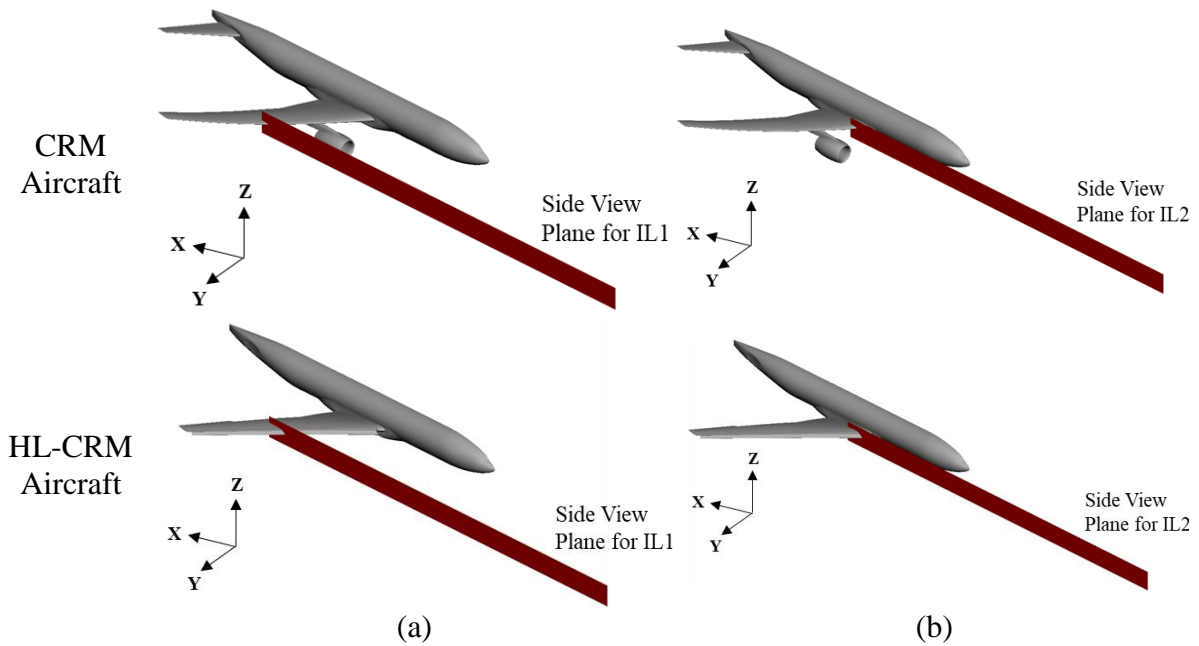


Figure 80. XZ-plane created to obtain a side view of pressure contours over the drone and aircraft at the lateral stations of (a) IL1 and (b) IL2.

### C.3 MOTION HISTORY OF SIMULATION MATRIX RESULTS

Figure 81 references the axis systems used for the motion history plots for all impact scenarios.

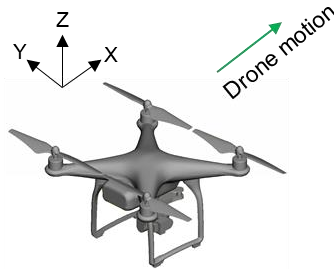


Figure 81. Axis system used for the drone.

#### C.3.1 Impact Scenario 1 – IC1-IL1

The results were obtained for the impact scenario IC1-IL1 based on releasing the drone in the domain with the CRM aircraft. Since the drone was released at impact location 1, the CRM geometry without the fuselage and tail was used for this impact scenario. The drone was released 45 m ahead of the wing's leading-edge at 16.8 m from the fuselage symmetry plane. Once released, the drone was allowed to move without the influence of forces and moments for 10 m. The steady-state force and moment values used as external forces and moments in the UDF were calculated from the last 5 m of the 10 m of prescribed motion.

The forces experienced by the aircraft during the transient simulation were compared with the forces obtained from the steady-state simulation of the CRM aircraft in the domain. Figure 82 shows an acceptable level of correlation between the steady-state and the transient simulation results for the CRM aircraft.

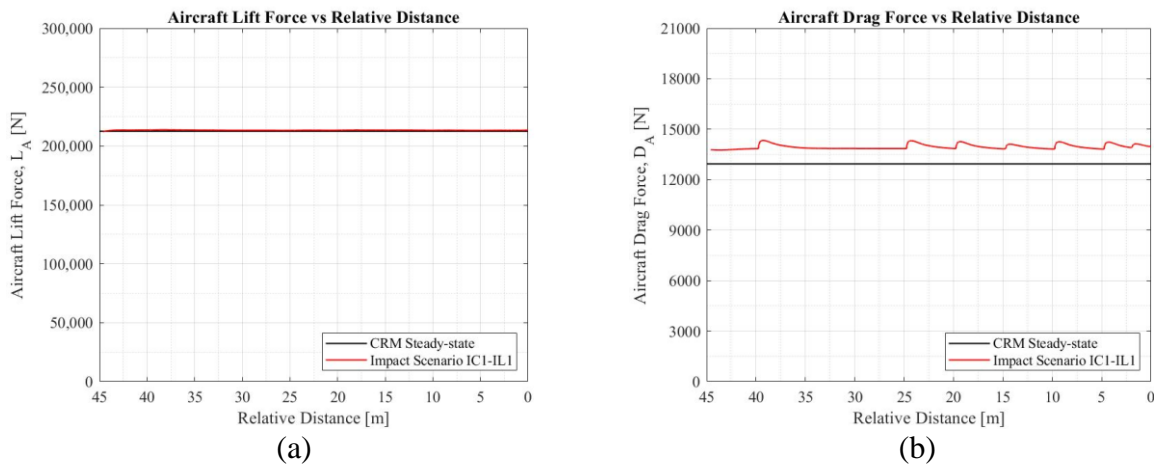
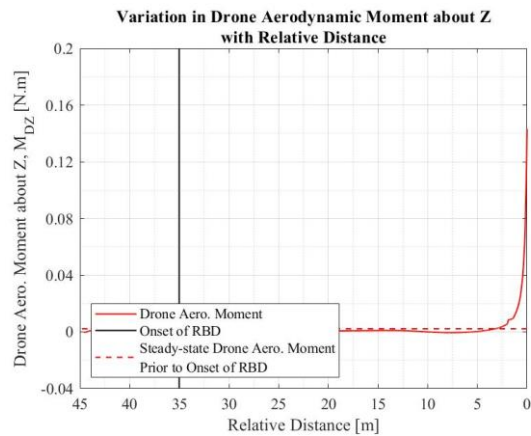
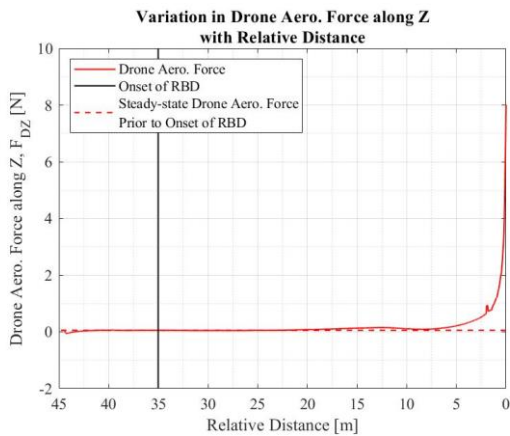
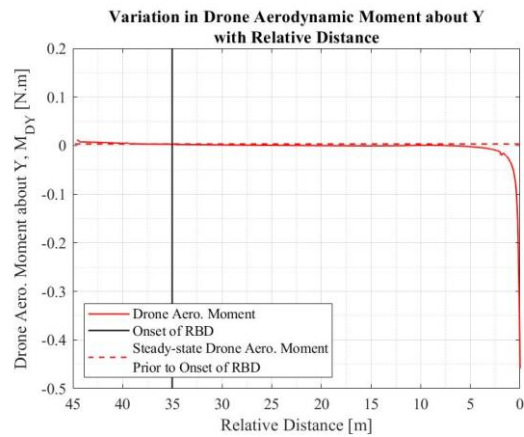
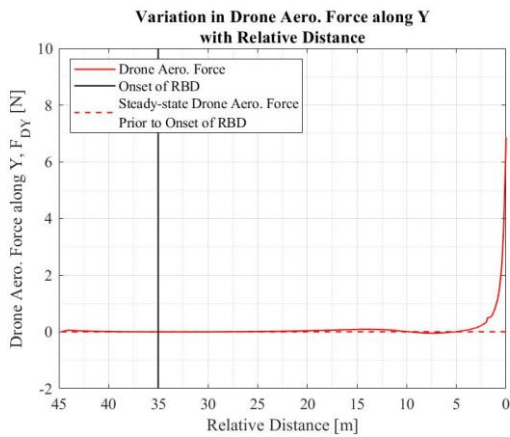
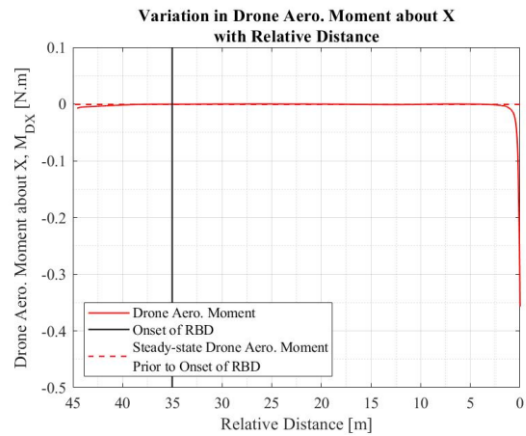
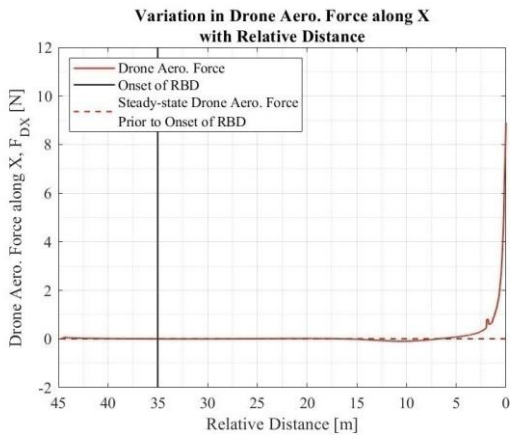


Figure 82. CRM aircraft (a) Drag force and (b) Lift force recorded as the drone approached the aircraft.

The drone forces and moments were plotted with the steady-state forces and moments used in the UDF. As the drone approached the CRM aircraft, the change in forces and moments can be seen in Figure 83 (a) and Figure 83 (b), respectively.

The linear and angular displacements experienced by the drone as it approached the CRM aircraft for impact scenario IC1-IL1 are shown in Figure 84 (a) and Figure 84 (b), respectively. The drone's linear and angular velocities as it approached the CRM aircraft for impact scenario IC1-IL1 are shown in Figure 85 (a) and Figure 85 (b), respectively.

Figure 86 and Figure 87 show the flow field development over the drone at 4 locations away from the CRM aircraft from the side view and top view, respectively. The pressure contour at the initial time of release can be viewed with the CRM aircraft wing. The pressure contour over the drone at relative distances of approximately 40 m, 20 m, 5 m, and 0 m are also provided.



(a)

(b)

Figure 83. Drone aerodynamic (a) Forces and (b) Moments plotted with respect to relative distance along with average values used in the UDF for impact scenario IC1-IL1.

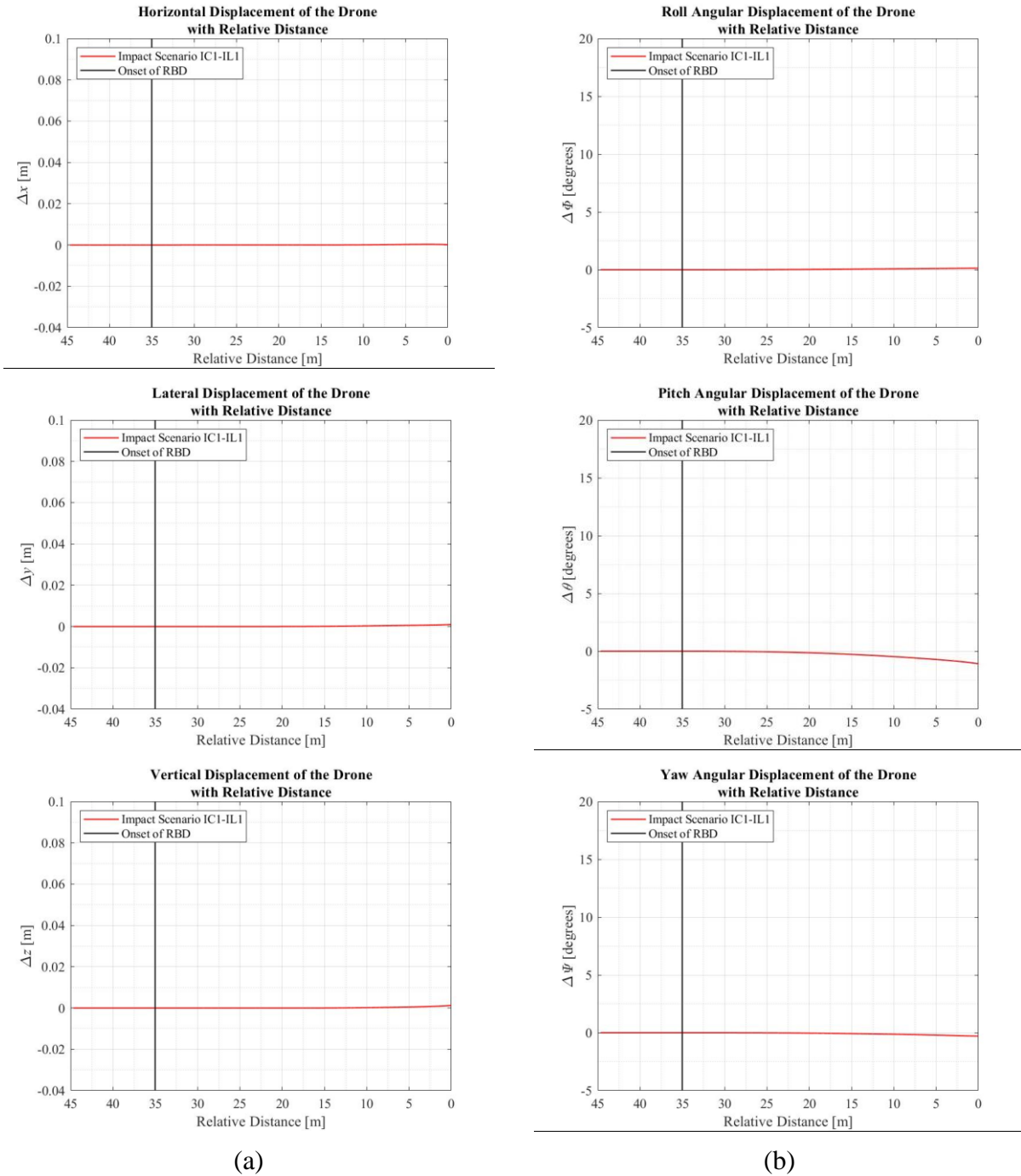


Figure 84. (a) Displacements and (b) Angular displacements experienced by the drone as it traveled towards the CRM aircraft for impact scenario IC1-IL1.

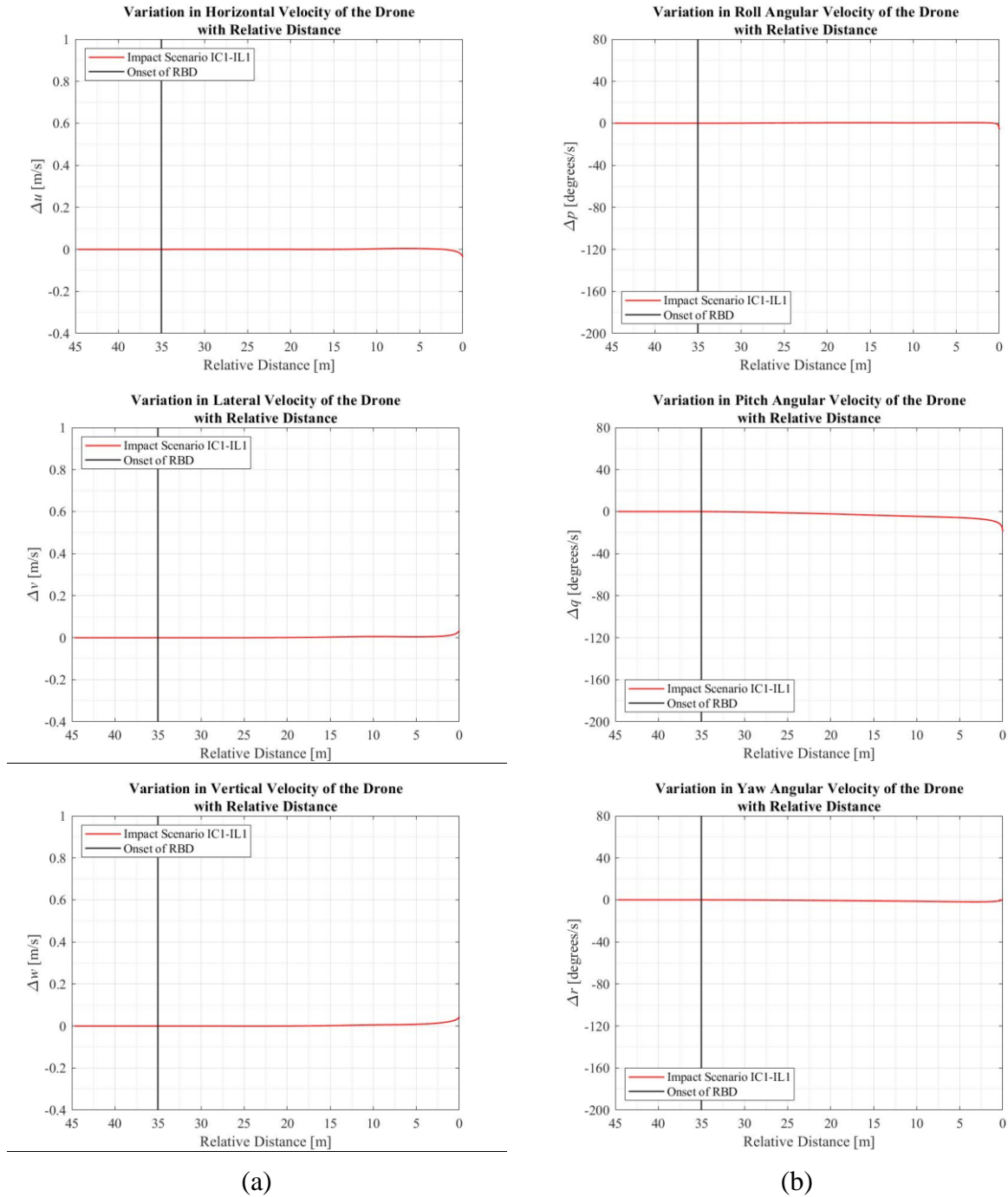


Figure 85. (a) Velocities and (b) Angular velocities experienced by the drone as it traveled towards the CRM aircraft for impact scenario IC1-IL1.

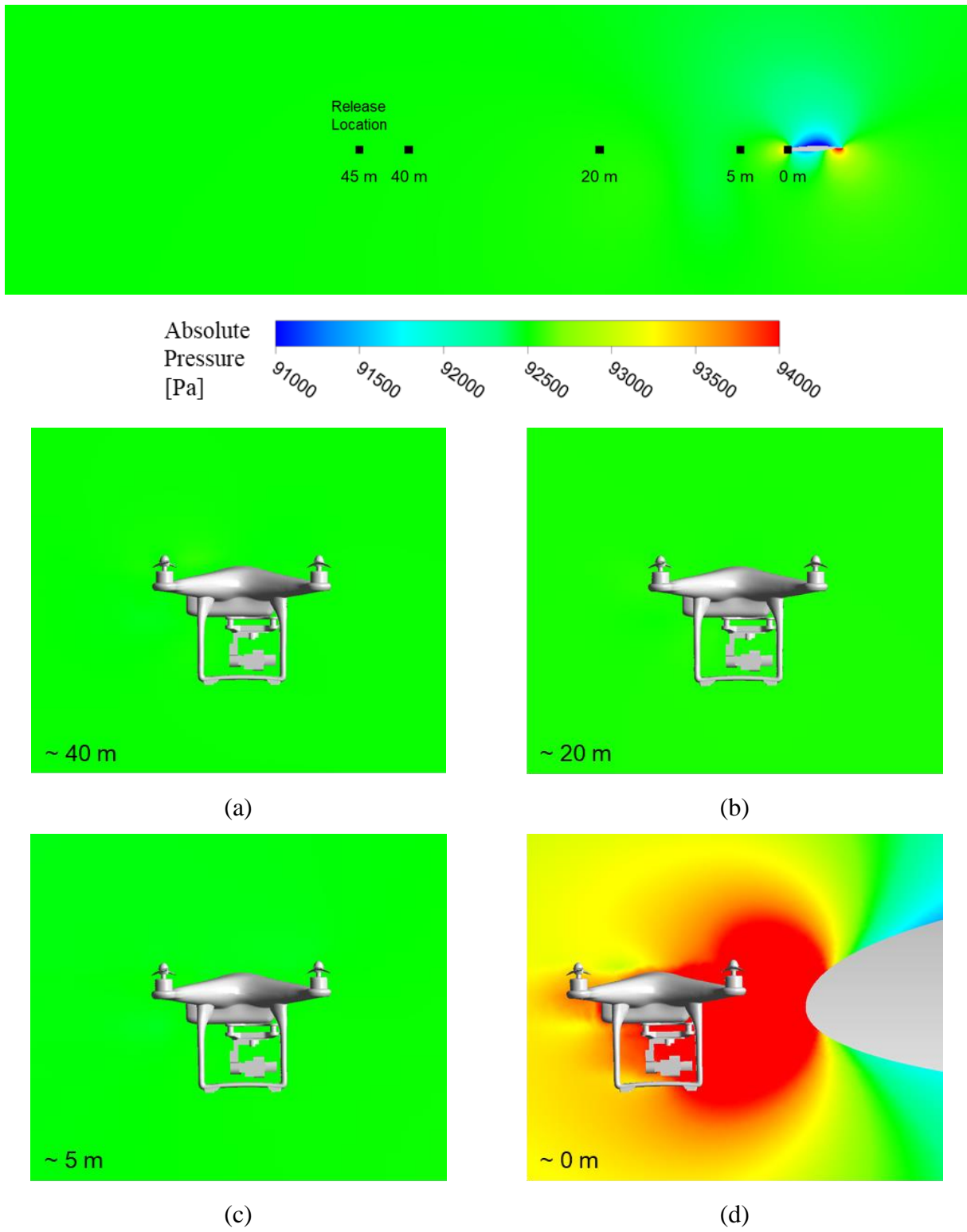


Figure 86. Side view of flow field development over the drone as it approaches the CRM Aircraft in impact scenario IC1-IL1 at relative distances of approximately (a) 40 m (b) 20 m (c) 5 m and (d) 0 m.

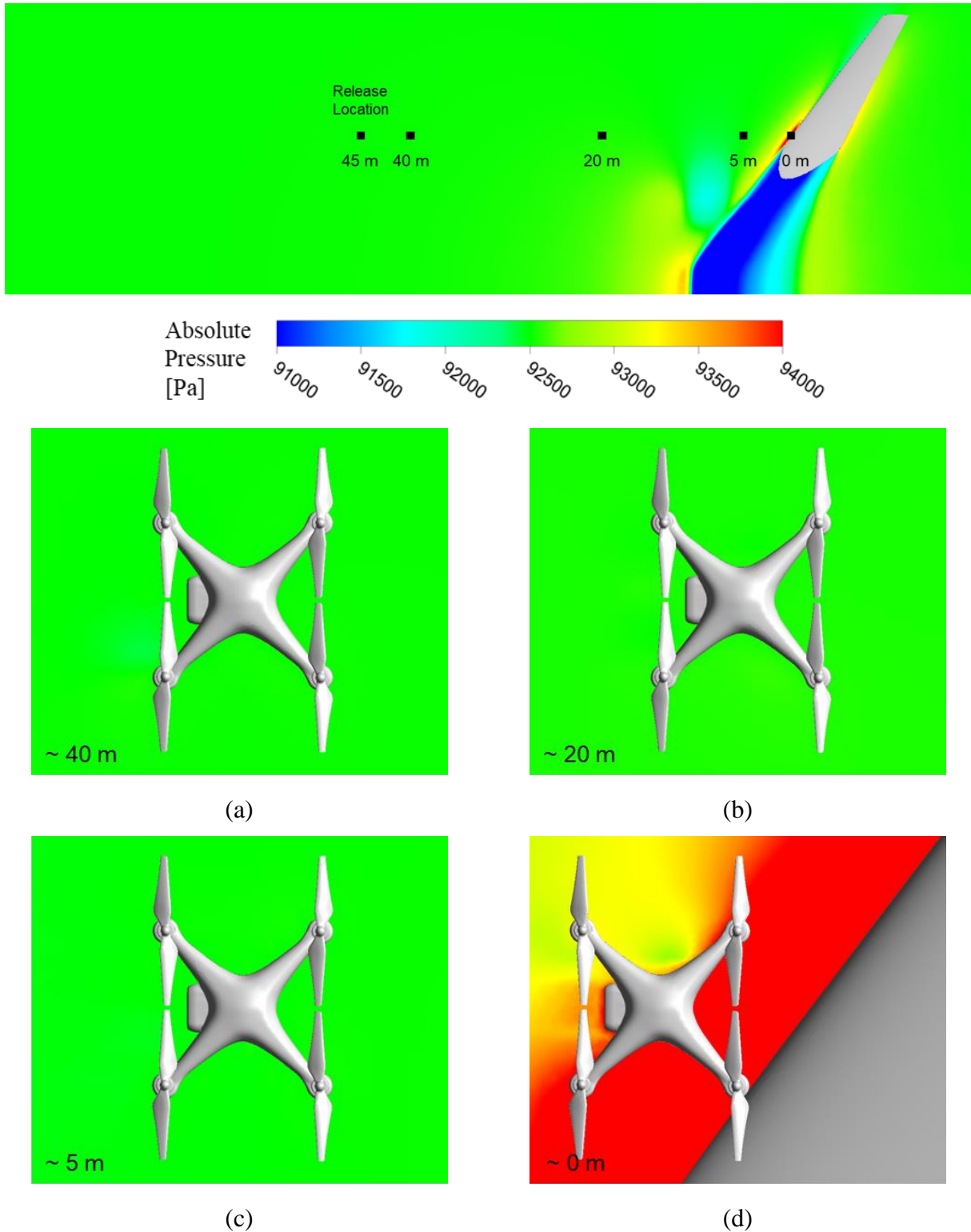


Figure 87. Top view of flow field development over the drone as it approaches the CRM Aircraft in impact scenario IC1-IL1 at relative distances of approximately (a) 40 m (b) 20 m (c) 5 m and (d) 0 m.

### C.3.2 Impact Scenario 2 – IC2-IL1

The results were obtained for the impact scenario IC2-IL1 based on releasing the drone in the domain with the CRM aircraft. Since the drone was released at impact location 1, the CRM geometry without the fuselage and tail was used for this impact scenario. The drone was released 45 m ahead of the wing's leading-edge at 16.8 m from the fuselage symmetry plane. Once released, the drone was allowed to move without the influence of forces and moments for 10 m. The steady-state force and moment values used as external forces and moments in the UDF were calculated from the last 5 m of the 10 m of prescribed motion.

The forces experienced by the aircraft during the transient simulation were compared with the forces obtained from the steady-state simulation of the CRM aircraft in the domain. Figure 88 shows an acceptable level of correlation between the steady-state and the transient simulation results for the CRM aircraft.

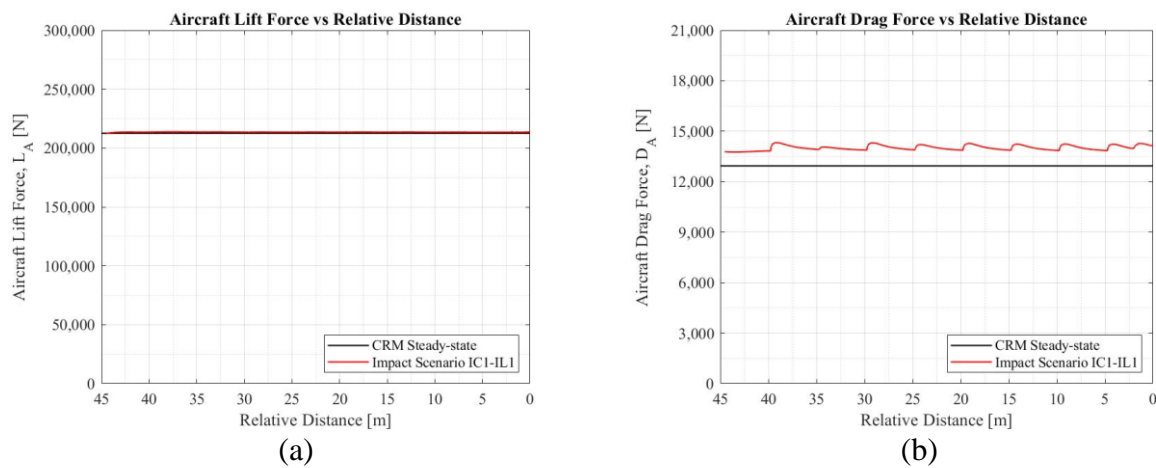
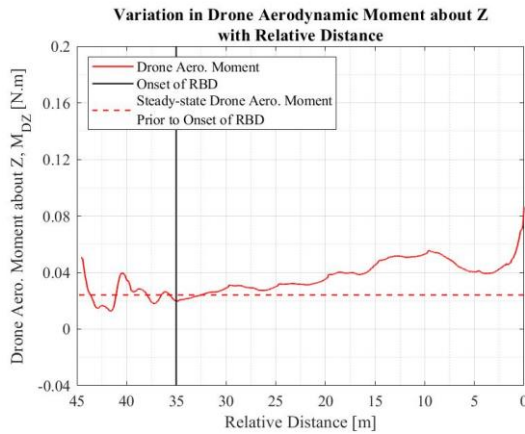
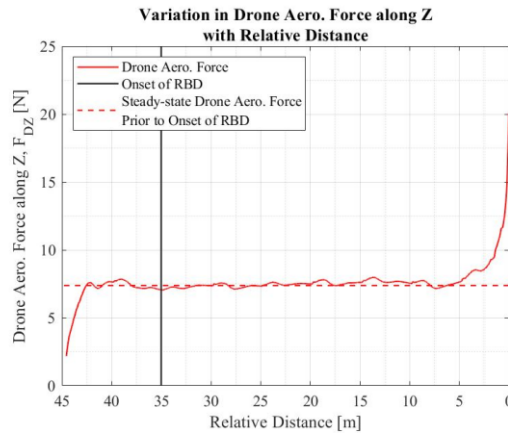
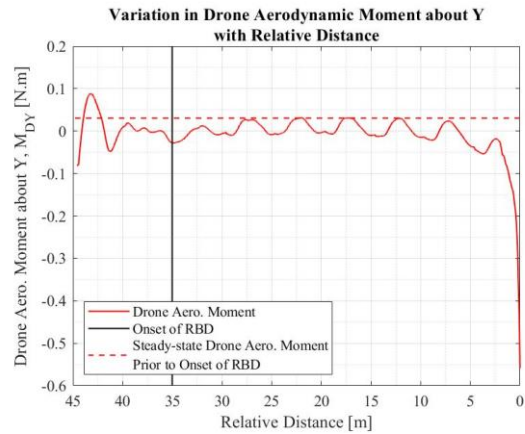
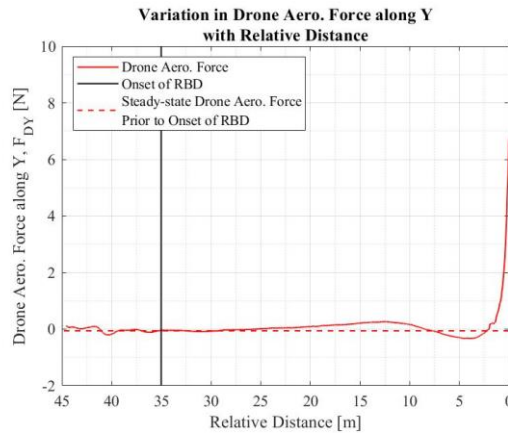
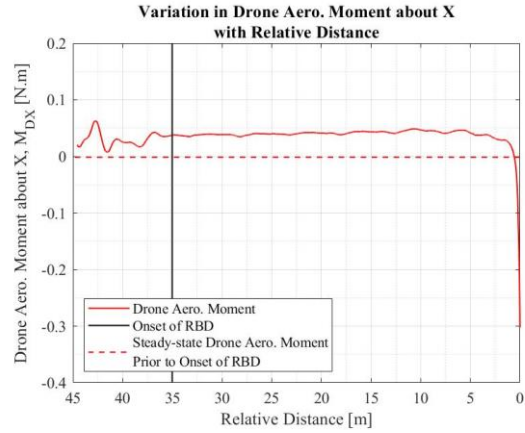
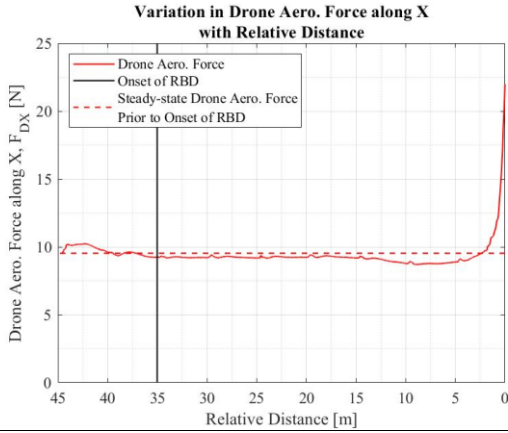


Figure 88. CRM aircraft (a) drag force and (b) lift force recorded as the drone approached the aircraft.

The drone forces and moments were plotted with the steady-state forces and moments used in the UDF. As the drone approached the CRM aircraft, the change in forces and moments can be seen in Figure 89 (a) and Figure 89 (b), respectively.

The linear and angular displacements experienced by the drone as it approached the CRM aircraft for impact scenario IC2-IL1 are shown in Figure 90 (a) and Figure 90 (b), respectively. The drone's linear and angular velocities as it approached the CRM aircraft for impact scenario IC2-IL1 are shown in Figure 91 (a) and Figure 91 (b), respectively.

Figure 92 and Figure 93 show the flow field development over the drone at 4 locations away from the CRM aircraft from the side view and top view, respectively. The pressure contour at the initial time of release can be viewed with the CRM aircraft wing. The pressure contour over the drone at relative distances of approximately 40 m, 20 m, 5 m, and 0 m are also provided.



(a)

(b)

Figure 89. Drone aerodynamic (a) Forces and (b) Moments plotted with respect to relative distance along with average values used in the UDF for impact scenario IC2-IL1.

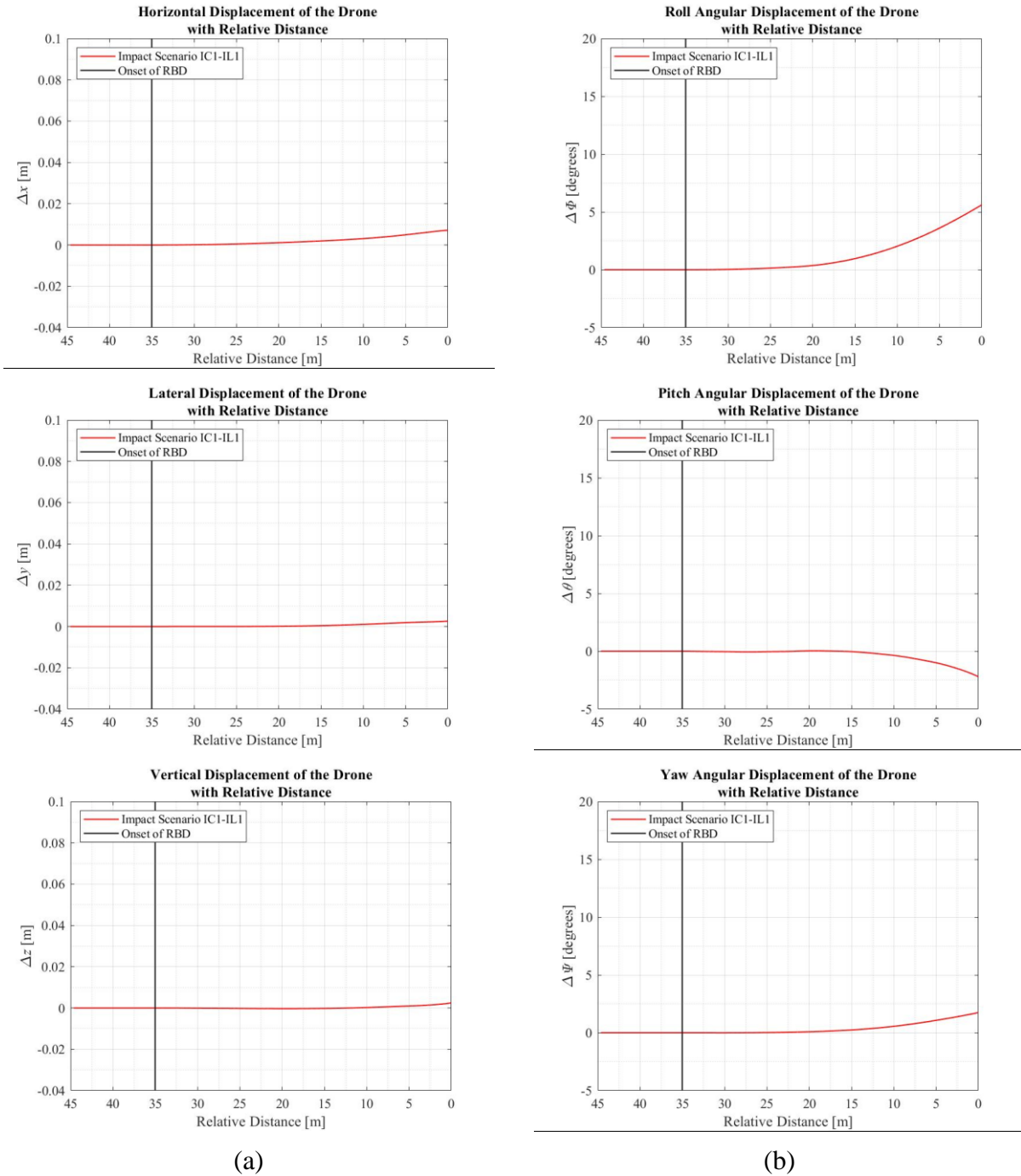
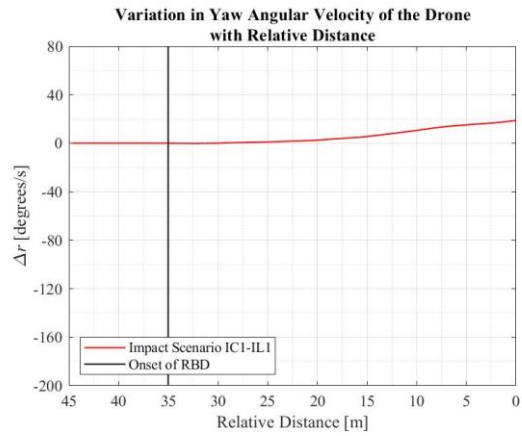
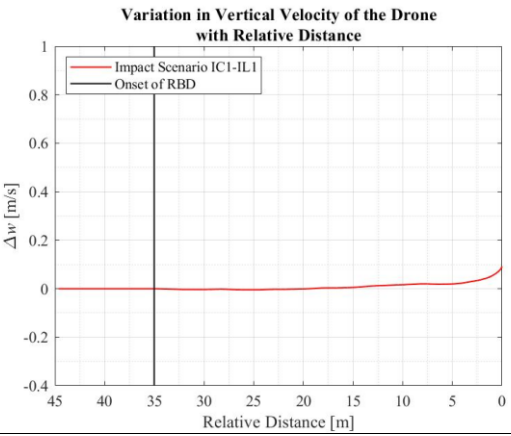
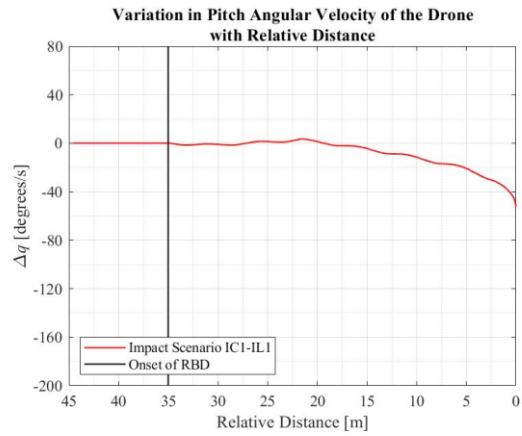
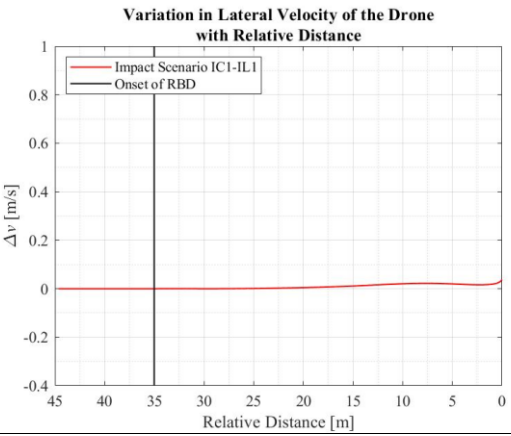
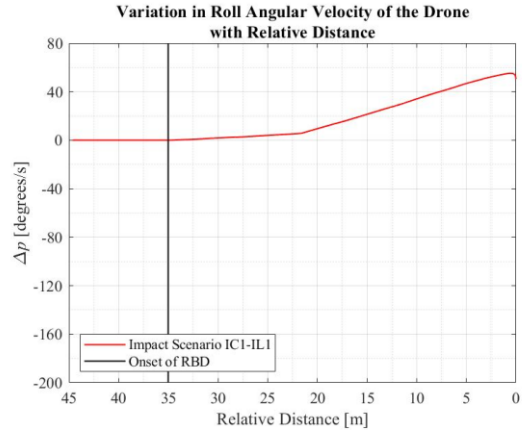
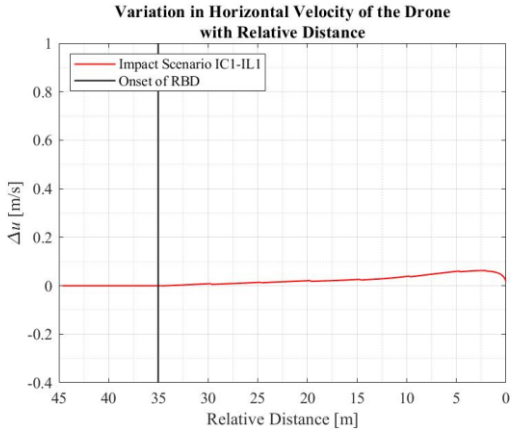


Figure 90. (a) Displacements and (b) Angular displacements experienced by the drone as it traveled towards the CRM aircraft for impact scenario IC2-IL1.



(a)

(b)

Figure 91. (a) Velocities and (b) angular velocities experienced by the drone as it traveled towards the CRM aircraft for impact scenario IC2-IL1.

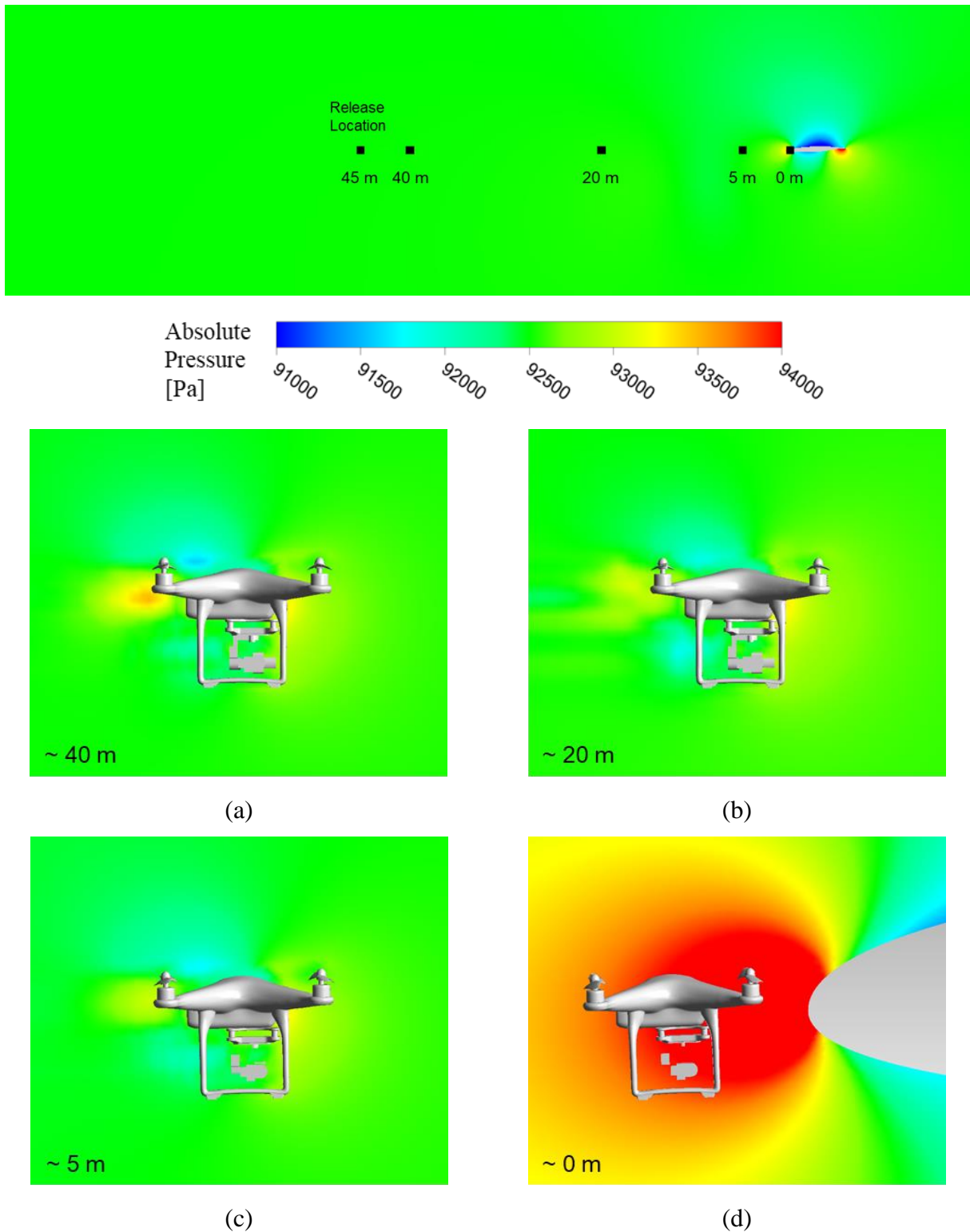


Figure 92. Side view of flow field development over the drone as it approaches the CRM Aircraft in impact scenario IC2-IL1 at relative distances of approximately (a) 40 m (b) 20 m (c) 5 m and (d) 0 m.

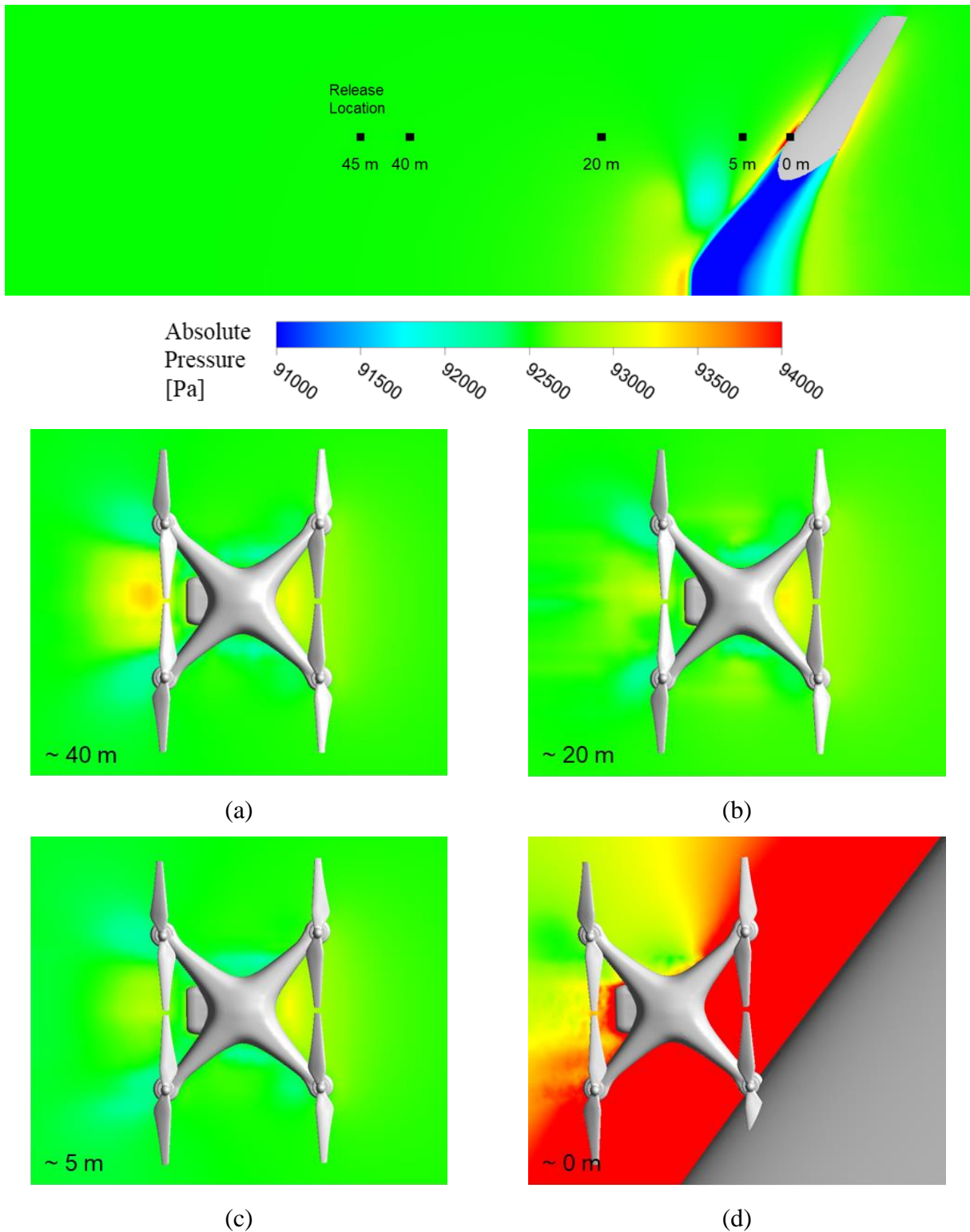


Figure 93. Top view of flow field development over the drone as it approaches the CRM Aircraft in impact scenario IC2-IL1 at relative distances of approximately (a) 40 m (b) 20 m (c) 5 m and (d) 0 m.

### C.3.3 Impact Scenario 3 – IC3-IL1

The results were obtained for the impact scenario IC3-IL1 based on releasing the drone in the domain with the CRM aircraft. Since the drone was released at impact location 1, the CRM geometry without the fuselage and tail was used for this impact scenario. The CRM aircraft geometry was rotated to  $5^\circ$  AoA. The drone was released 45 m ahead of the wing's leading-edge at 16.8 m from the fuselage symmetry plane. Once released, the drone was allowed to move without the influence of forces and moments for 10 m. The steady-state force and moment values used as external forces and moments in the UDF were calculated from the last 5 m of the 10 m of prescribed motion.

The forces experienced by the aircraft during the transient simulation were compared with the forces obtained from the steady-state simulation of the CRM aircraft in the domain. Figure 94 shows an acceptable level of correlation between the steady-state and the transient simulation results for the CRM aircraft.

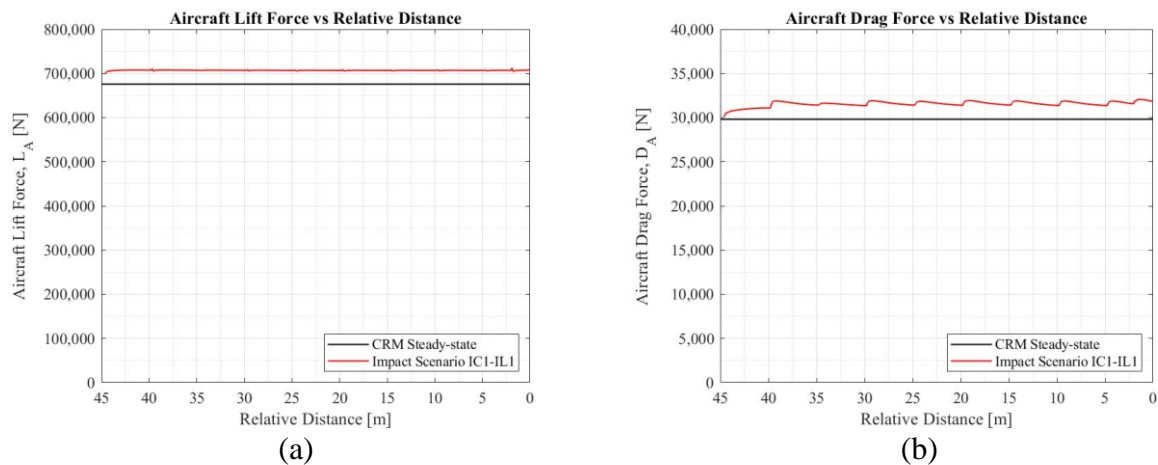


Figure 94.  $5^\circ$  AoA CRM aircraft (a) drag force and (b) lift force recorded as the drone approached the aircraft.

The drone forces and moments were plotted with the steady-state forces and moments used in the UDF. As the drone approached the CRM aircraft, the change in forces and moments can be seen in Figure 95 (a) and Figure 95 (b), respectively.

The linear and angular displacements experienced by the drone as it approached the CRM aircraft for impact scenario IC3-IL1 are shown in Figure 96 (a) and Figure 96 (b), respectively. The drone's linear and angular velocities as it approached the CRM aircraft for impact scenario IC3-IL1 are shown in Figure 97 (a) and Figure 97 (b), respectively.

Figure 98 and Figure 99 show the flow field development over the drone at 4 locations away from the CRM aircraft from the side view and top view, respectively. The pressure contour at the initial time of release can be viewed with the CRM aircraft wing. The pressure contour over the drone at relative distances of approximately 40 m, 20 m, 5 m, and 0 m are also provided.

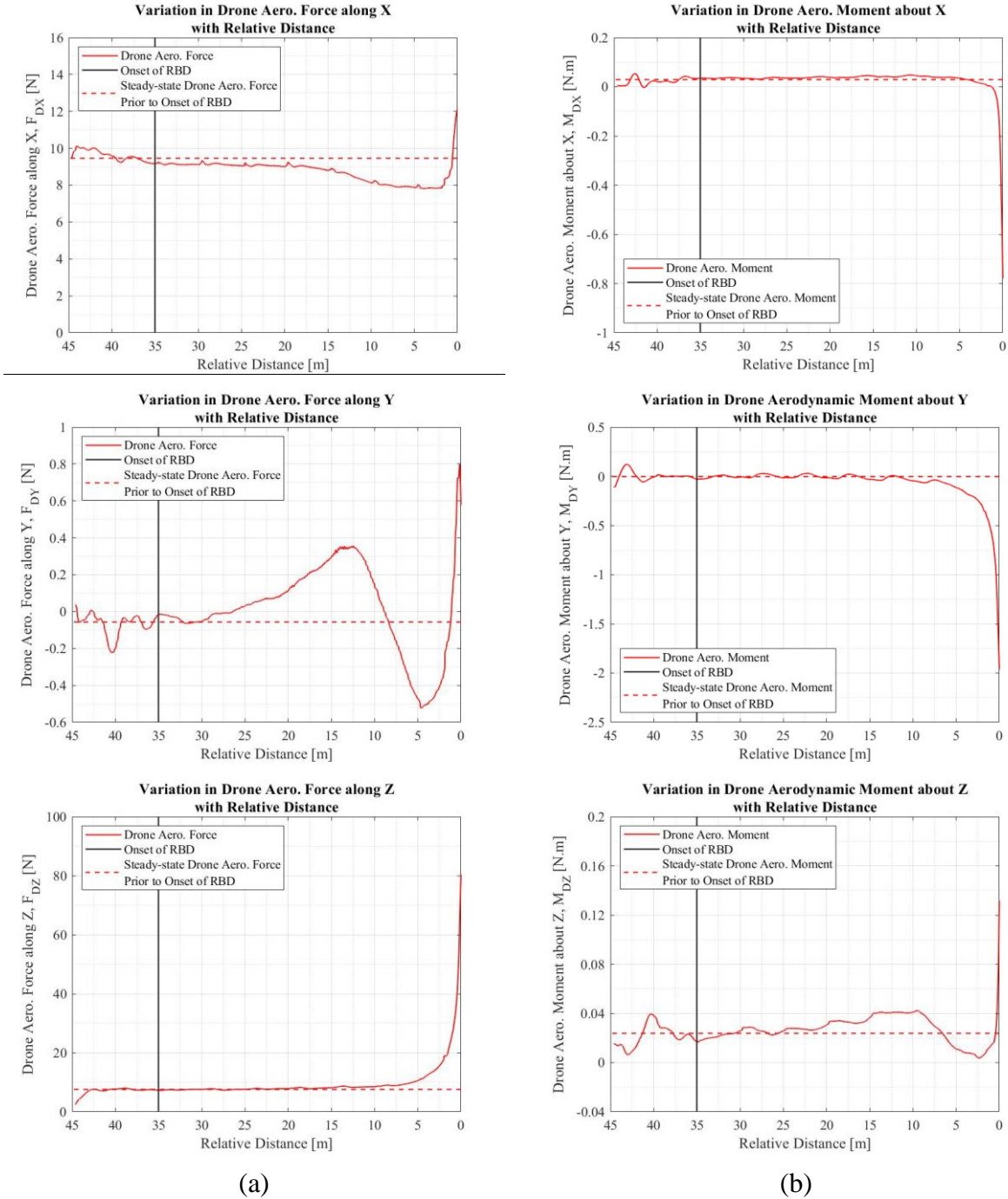


Figure 95. Drone aerodynamic (a) Forces and (b) Moments plotted with respect to relative distance along with average values used in the UDF for impact scenario IC3-IL1.

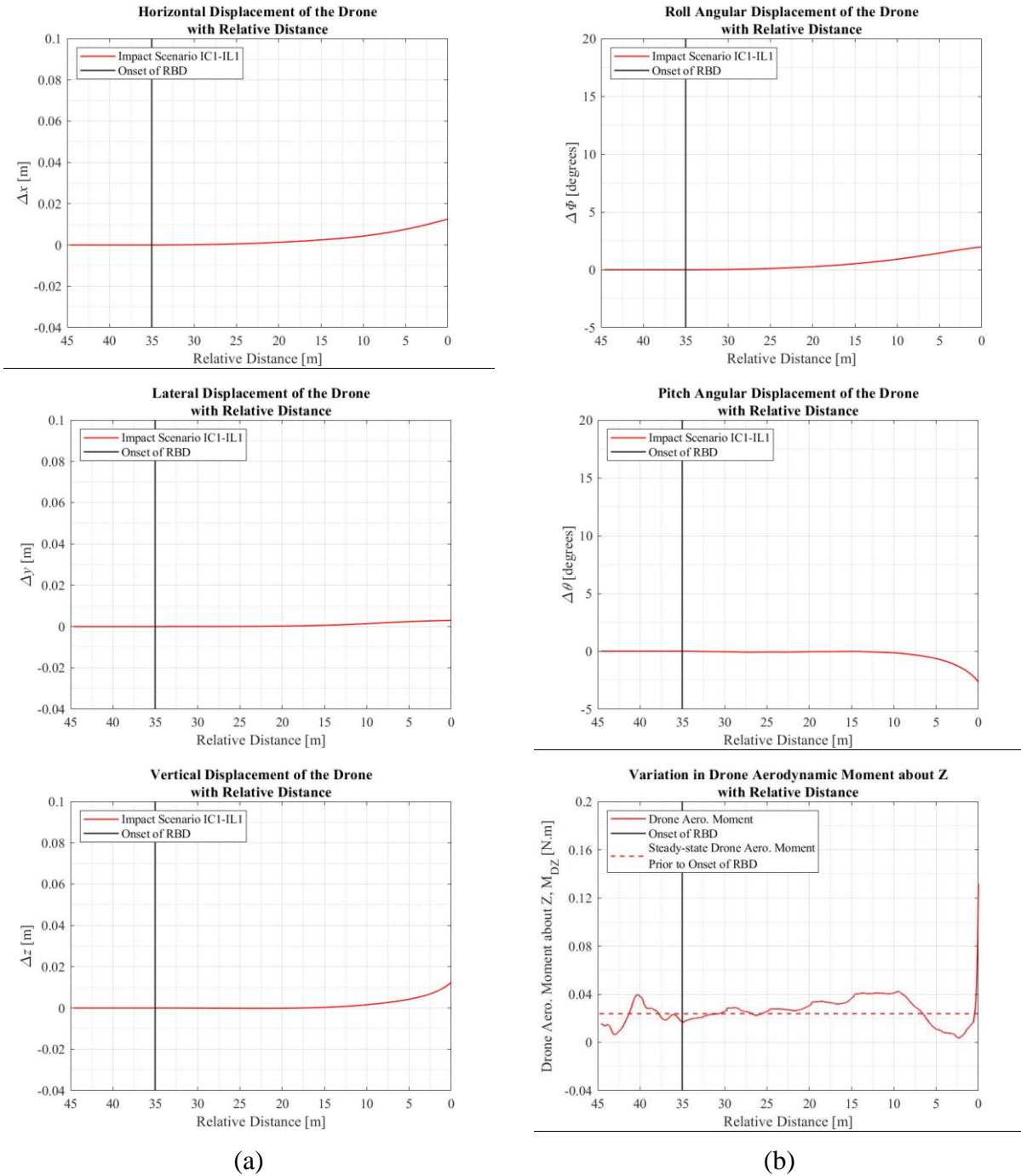
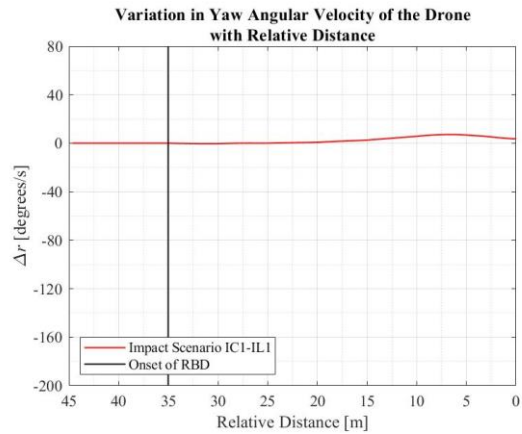
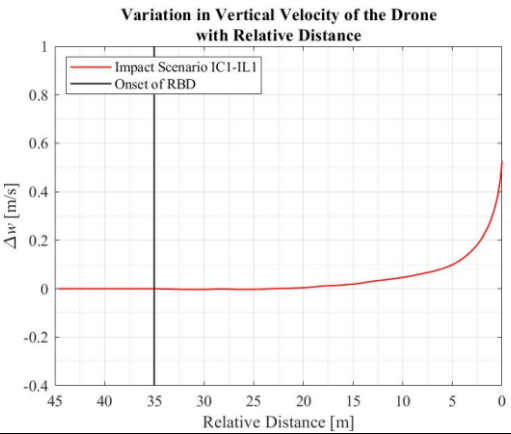
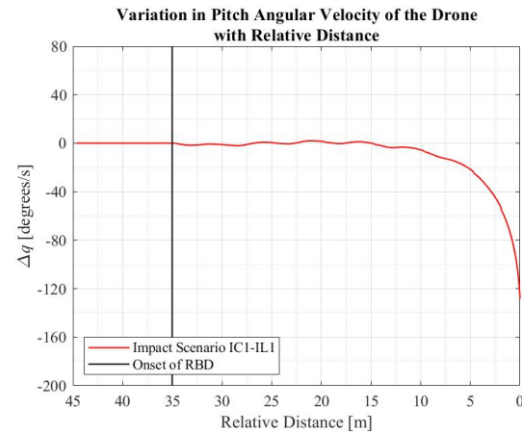
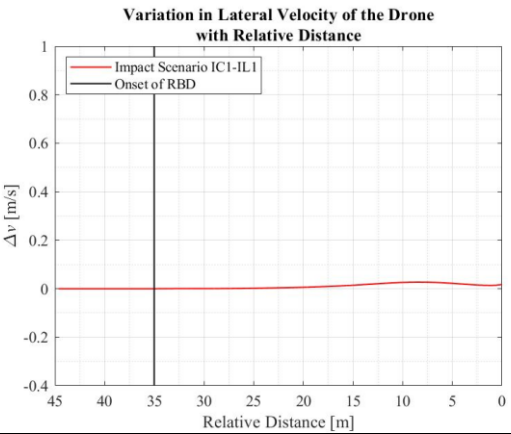
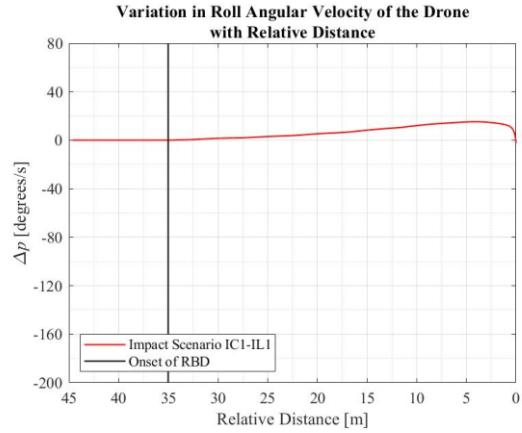
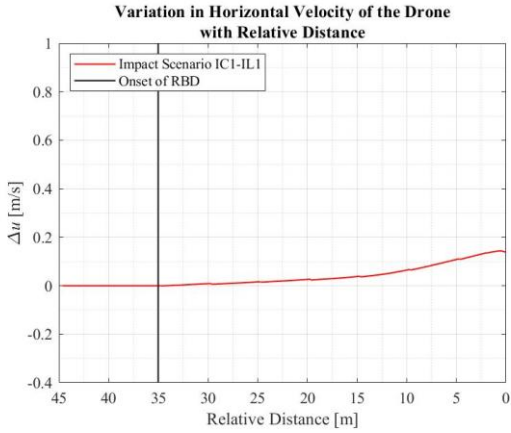


Figure 96. (a) Displacements and (b) angular displacements experienced by the drone as it traveled towards the CRM aircraft for impact scenario IC3-IL1.



(a)

(b)

Figure 97. (a) Velocities and (b) angular velocities experienced by the drone as it traveled towards the CRM aircraft for impact scenario IC3-IL1.

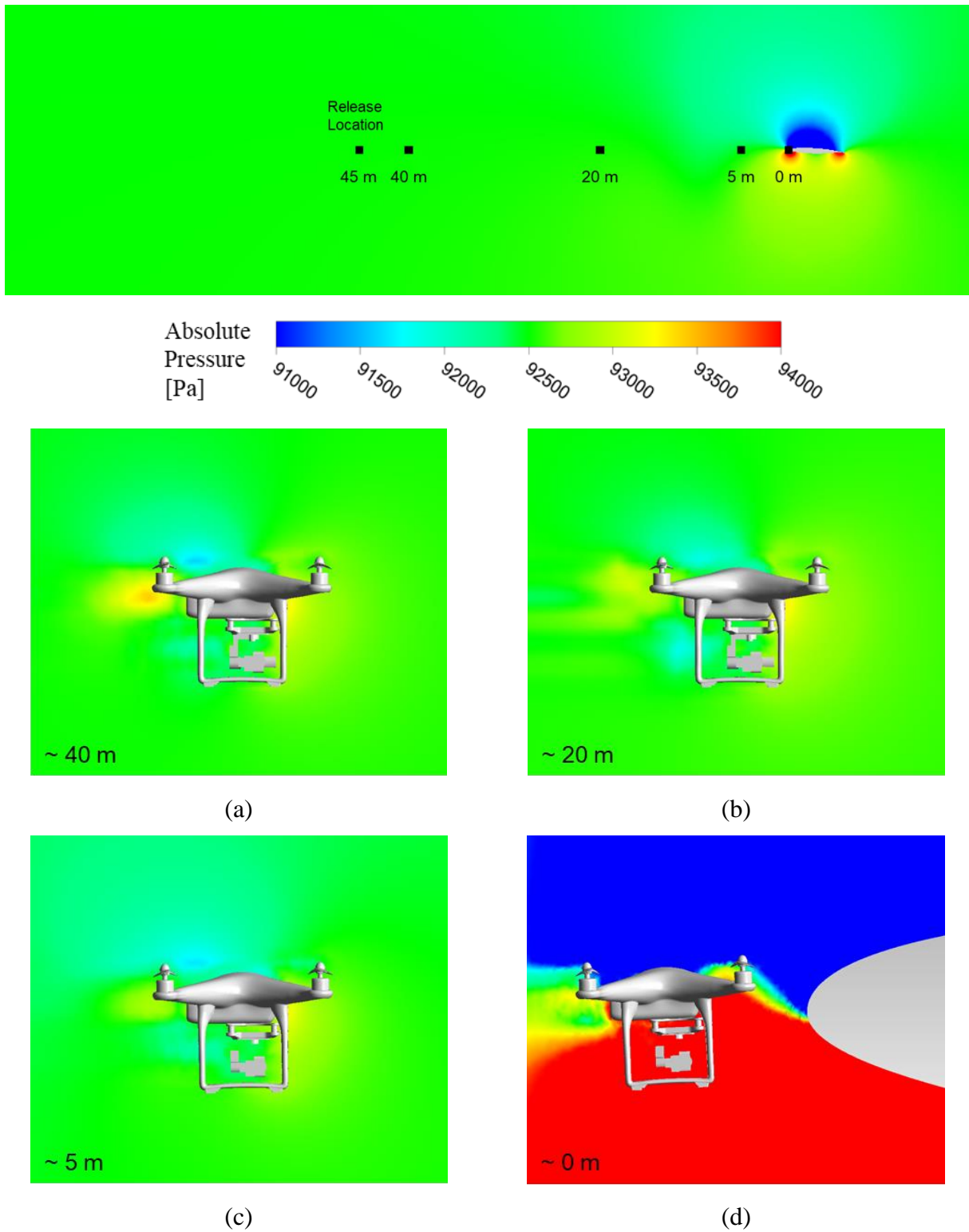


Figure 98. Side view of flow field development over the drone as it approaches the CRM Aircraft in impact scenario IC3-IL1 at relative distances of approximately (a) 40 m (b) 20 m (c) 5 m and (d) 0 m.

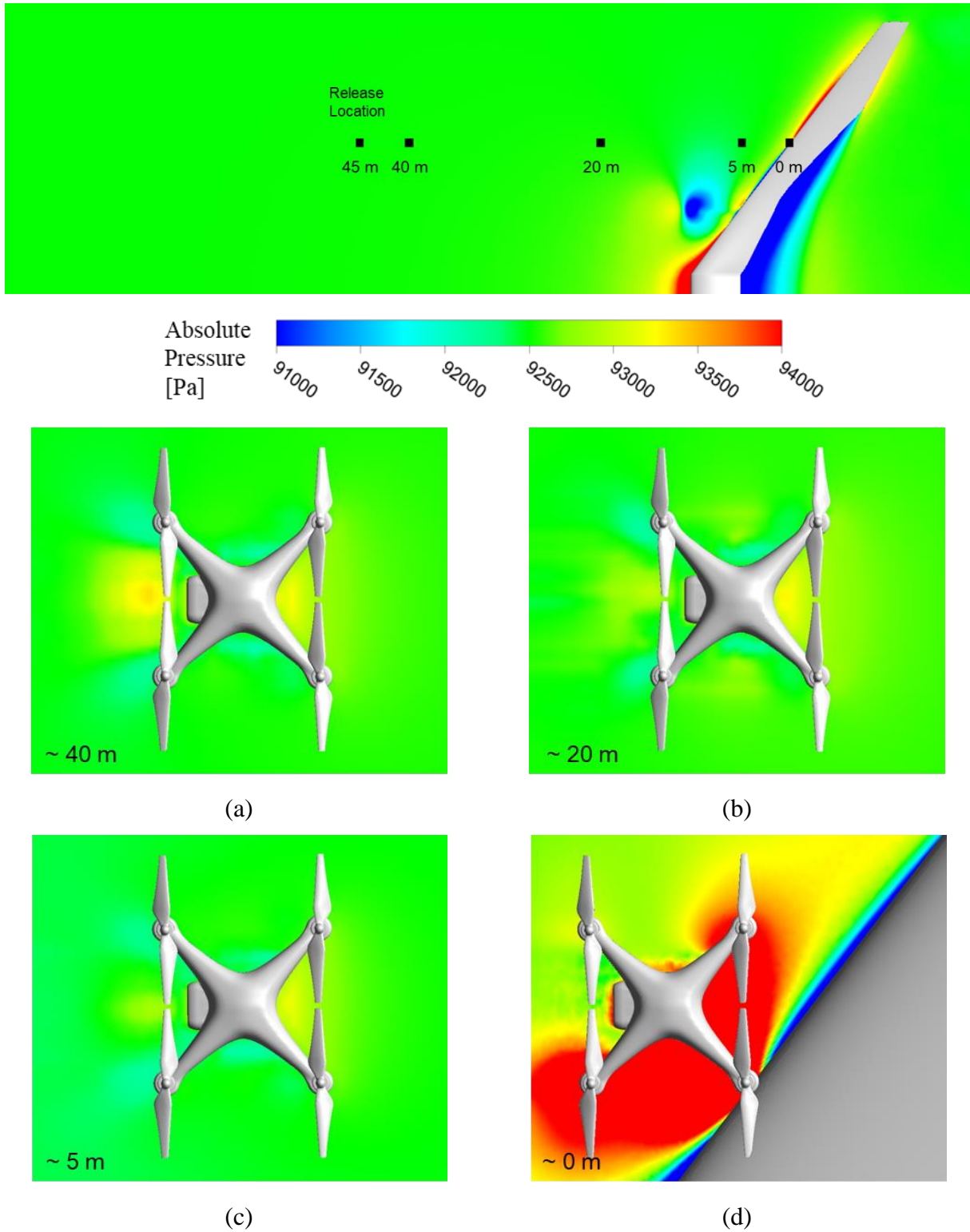


Figure 99. Top view of flow field development over the drone as it approaches the CRM Aircraft in impact scenario IC3-IL1 at relative distances of approximately (a) 40 m (b) 20 m (c) 5 m and (d) 0 m.

### C.3.4 Impact Scenario 4 – IC4-IL1

The results were obtained for the impact scenario IC4-IL1 based on releasing the drone in the domain with the HL-CRM aircraft. Since the drone was released at impact location 1, the HL-CRM geometry without the fuselage was used for this impact scenario. The drone was released 45 m ahead of the leading-edge of the slat at 16.8 m from the fuselage symmetry plane. Once released, the drone was allowed to move without the influence of forces and moments for 10 m. The steady-state force and moment values used as external forces and moments in the UDF were calculated from the last 5 m of the 10 m of prescribed motion.

The forces experienced by the aircraft during the transient simulation were compared with the forces obtained from the steady-state simulation of the HL-CRM aircraft in the domain. Figure 100 shows an acceptable level of correlation between the steady-state and the transient simulation results for the HL-CRM aircraft.

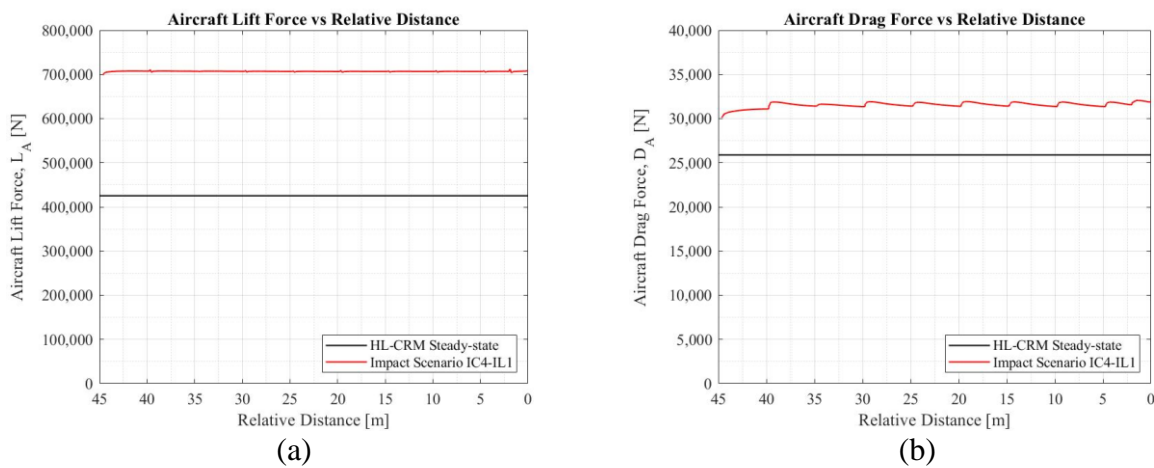
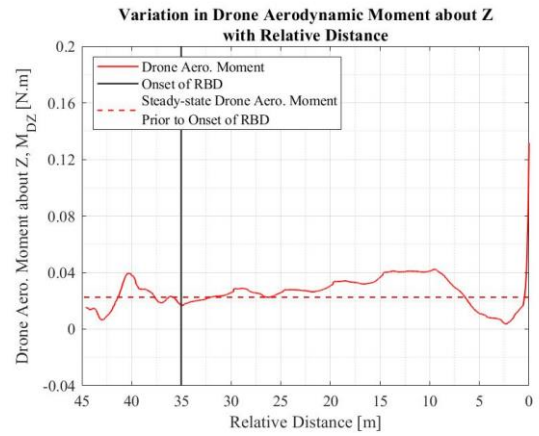
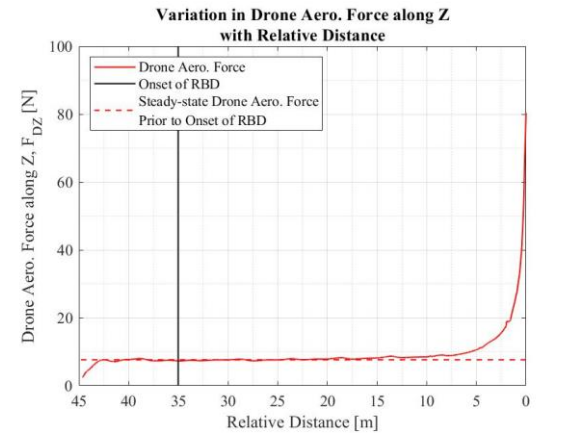
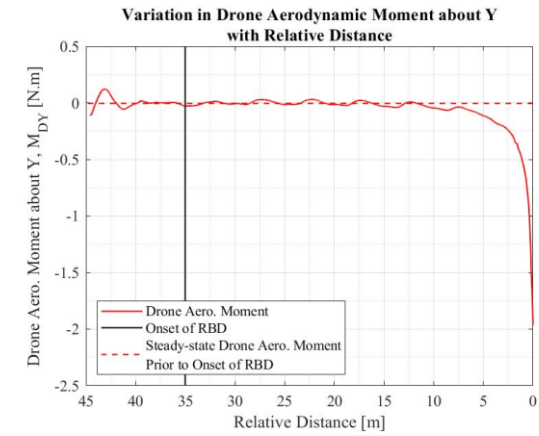
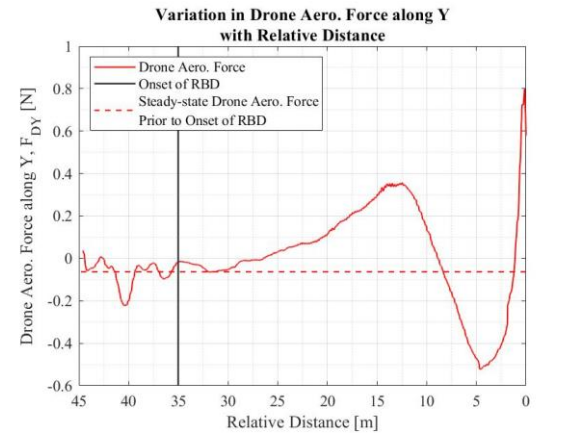
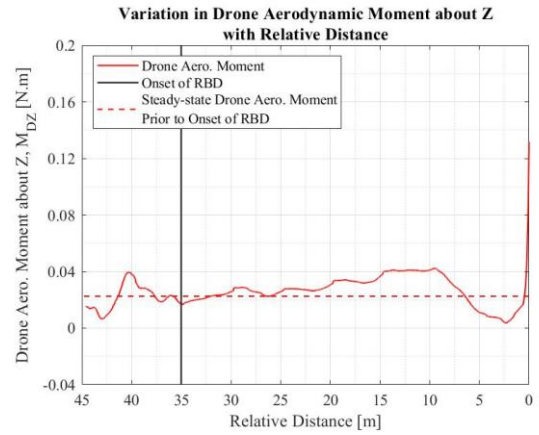
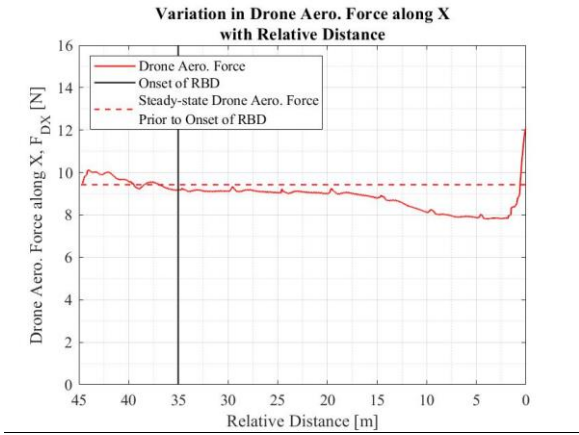


Figure 100. HL-CRM aircraft (a) drag force and (b) lift force recorded as the drone approached the aircraft.

The drone forces and moments were plotted with the steady-state forces and moments used in the UDF. As the drone approached the HL-CRM aircraft, the change in forces and moments can be seen in Figure 101 (a) and Figure 101 (b), respectively.

The linear and angular displacements experienced by the drone as it approached the HL-CRM aircraft for impact scenario IC4-IL1 are shown in Figure 102 (a) and Figure 102 (b), respectively. The drone's linear and angular velocities approaching the HL-CRM aircraft for impact scenario IC4-IL2 are shown in Figures 103 (a) and (b), respectively.

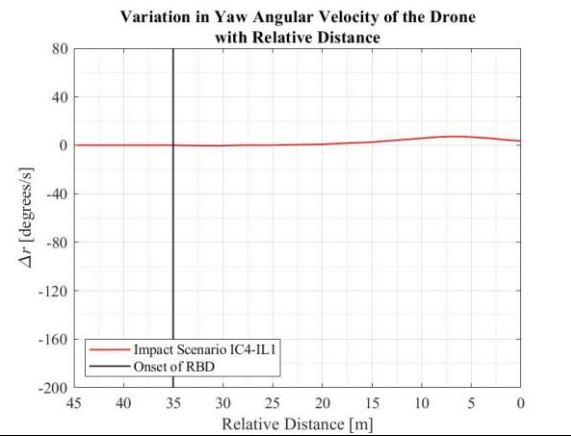
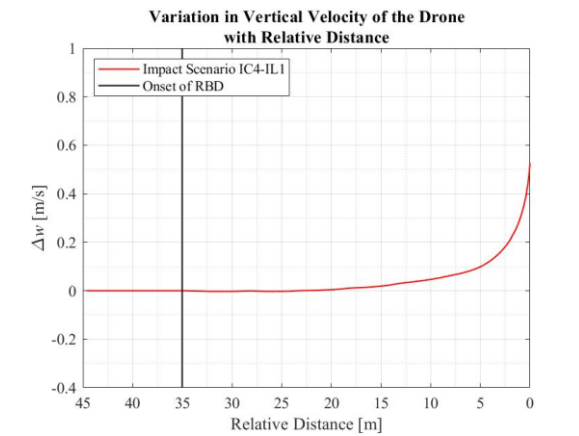
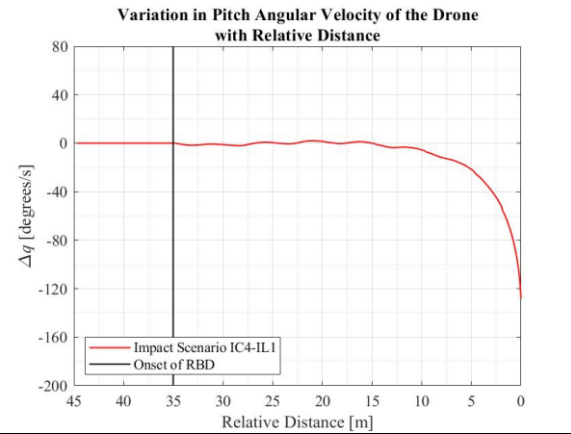
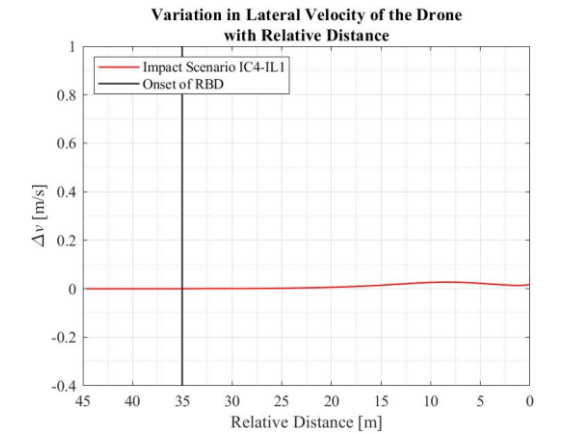
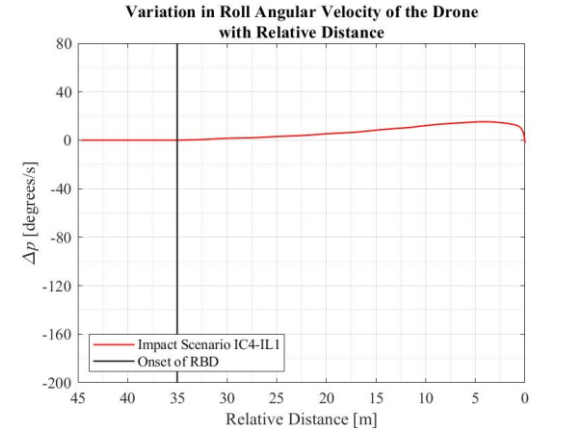
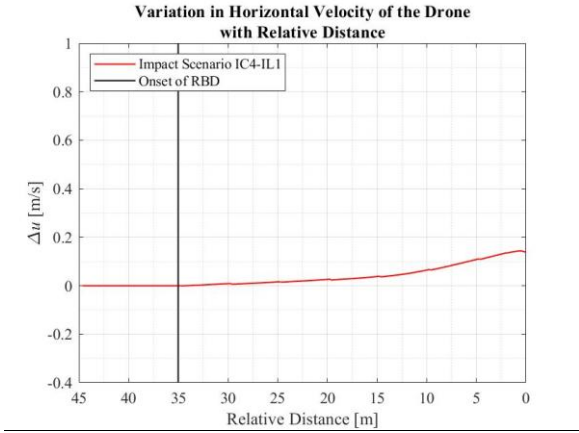
Figure 104 and Figure 105 show the flow field development over the drone at 4 locations away from the HL-CRM aircraft from the side view and top view, respectively. The pressure contour at the initial time of release can be viewed with the HL-CRM aircraft slat. The pressure contour over the drone at relative distances of approximately 40 m, 20 m, 5 m, and 0 m are also provided.



(a)

(b)

Figure 101. Drone aerodynamic (a) Forces and (b) Moments plotted with respect to relative distance along with average values used in the UDF for impact scenario IC4-IL1.



(a)

(b)

Figure 102. (a) Displacements and (b) angular displacements experienced by the drone as it traveled towards the HL-CRM aircraft for impact scenario IC4-IL2.

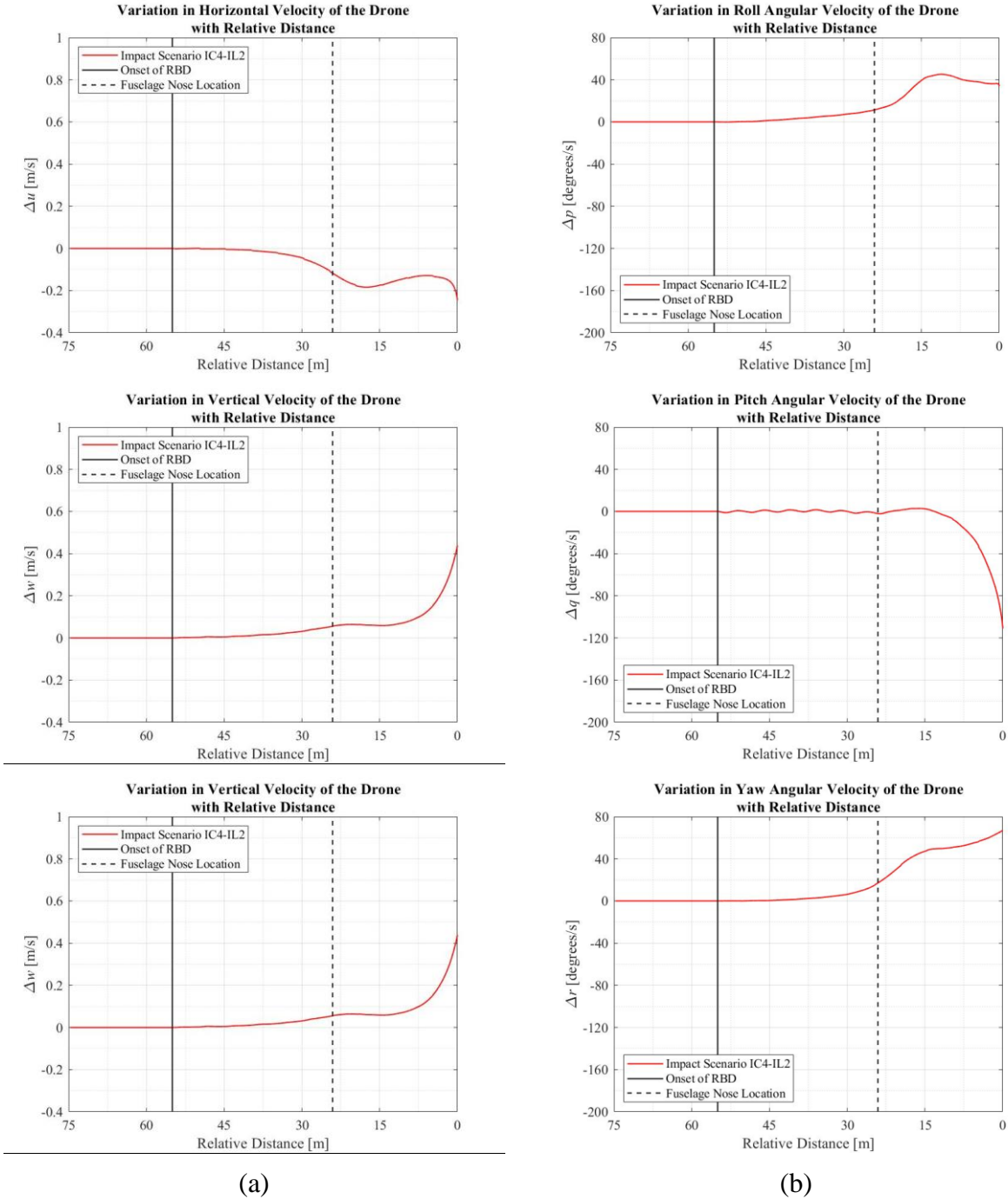
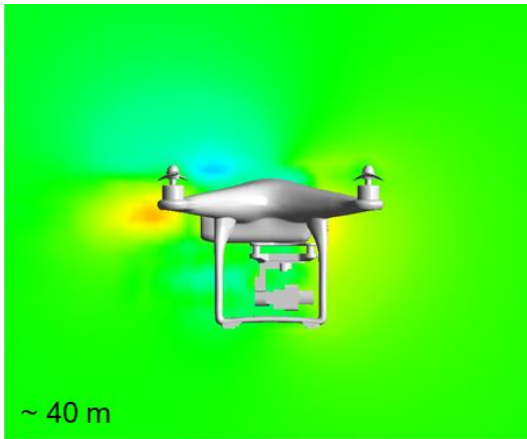
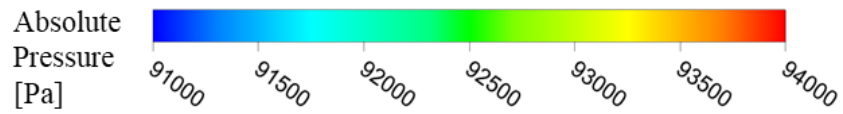
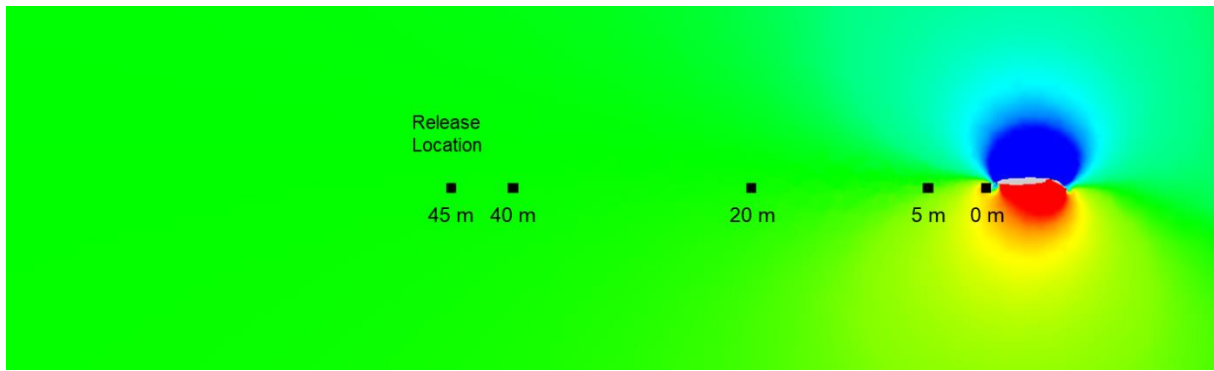
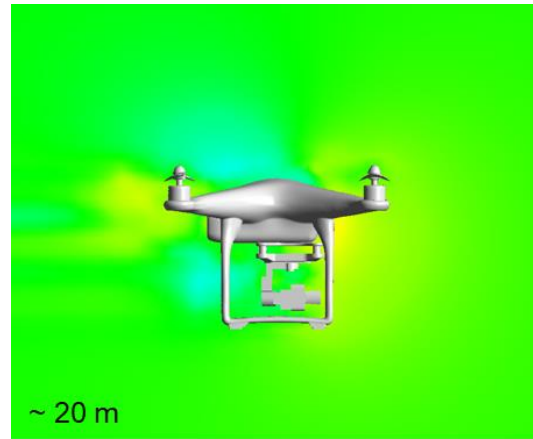


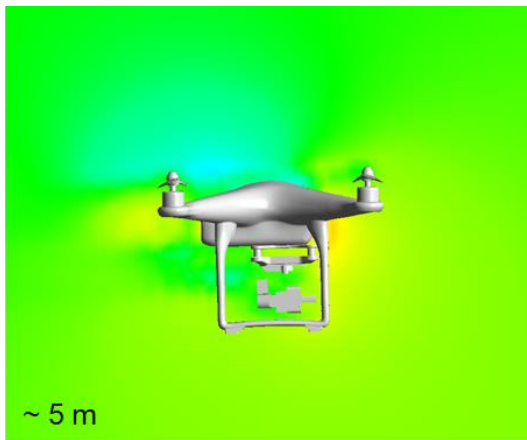
Figure 103. (a) Velocities and (b) angular velocities experienced by the drone as it traveled towards the HL-CRM aircraft for impact scenario IC4-IL1.



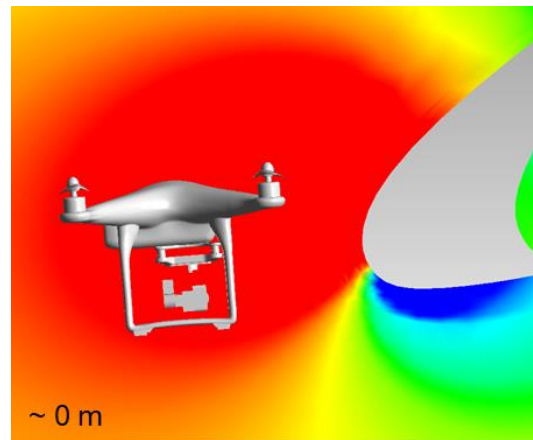
(a)



(b)



(c)



(d)

Figure 104. Side view of flow field development over the drone as it approaches the HL-CRM Aircraft in impact scenario IC4-IL1 at relative distances of approximately (a) 40 m (b) 20 m (c) 5 m and (d) 0 m.

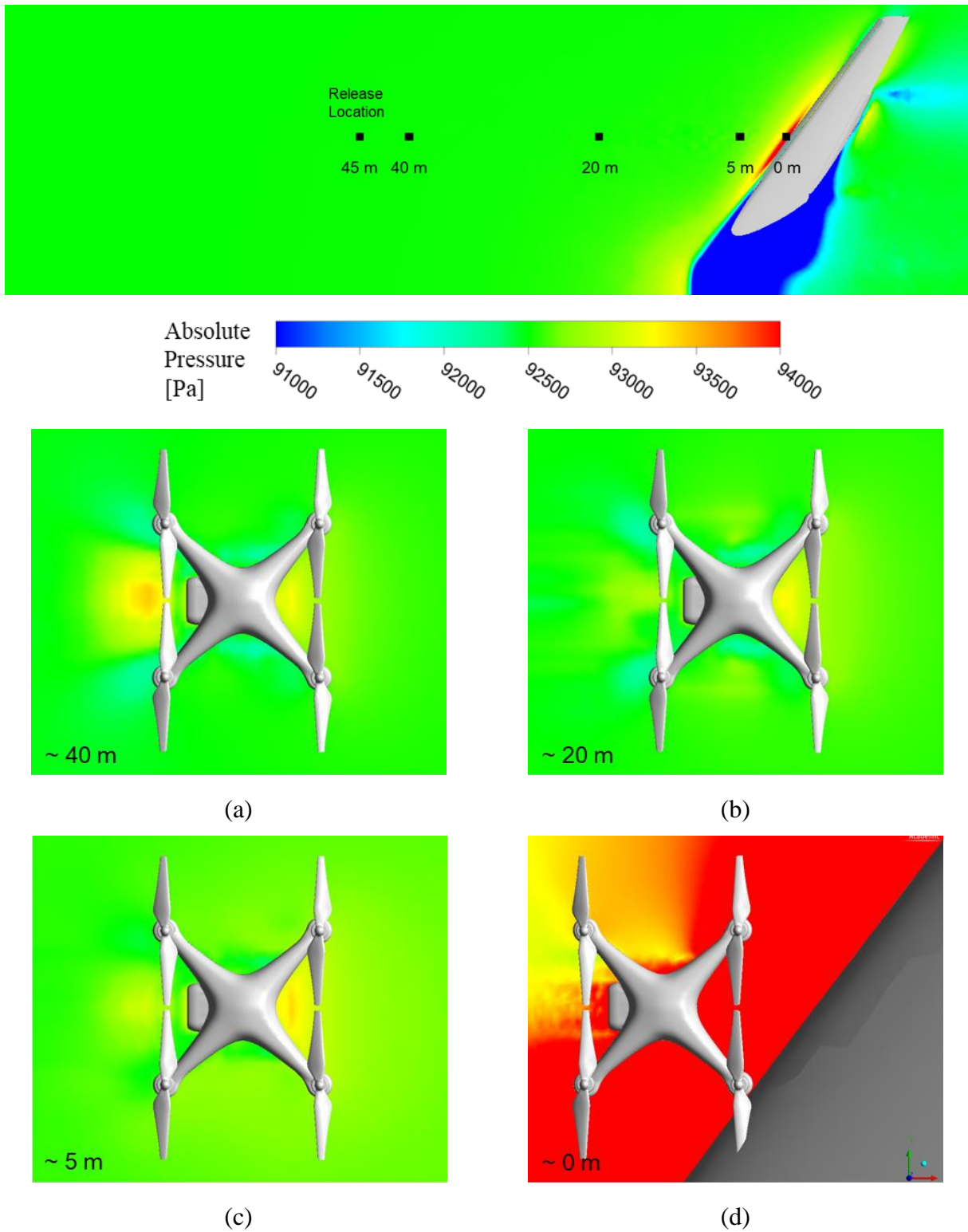


Figure 105. Top view of flow field development over the drone as it approaches the HL-CRM Aircraft in impact scenario IC4-IL1 at relative distances of approximately (a) 40 m (b) 20 m (c) 5 m and (d) 0 m.

### C.3.5 Impact Scenario 5 – IC5-IL1

For the impact scenario IC5-IL1, the results were obtained based on releasing the drone in the domain with the HL-CRM aircraft. Since the drone was released at impact location 1, the HL-CRM geometry without the fuselage was used for this impact scenario. The HL-CRM aircraft velocity was reduced to 87.455 m/s. The drone was released 45 m ahead of the leading-edge of the slat at 16.8 m from the fuselage symmetry plane. Once released, the drone was allowed to move without the influence of forces and moments for 10 m. The steady-state force and moment values used as external forces and moments in the UDF were calculated from the last 5 m of the 10 m of prescribed motion.

The forces experienced by the aircraft during the transient simulation were compared with the forces obtained from the steady-state simulation of the HL-CRM aircraft in the domain. Figure 106 shows an acceptable level of correlation between the steady-state and the transient simulation results for the HL-CRM aircraft.

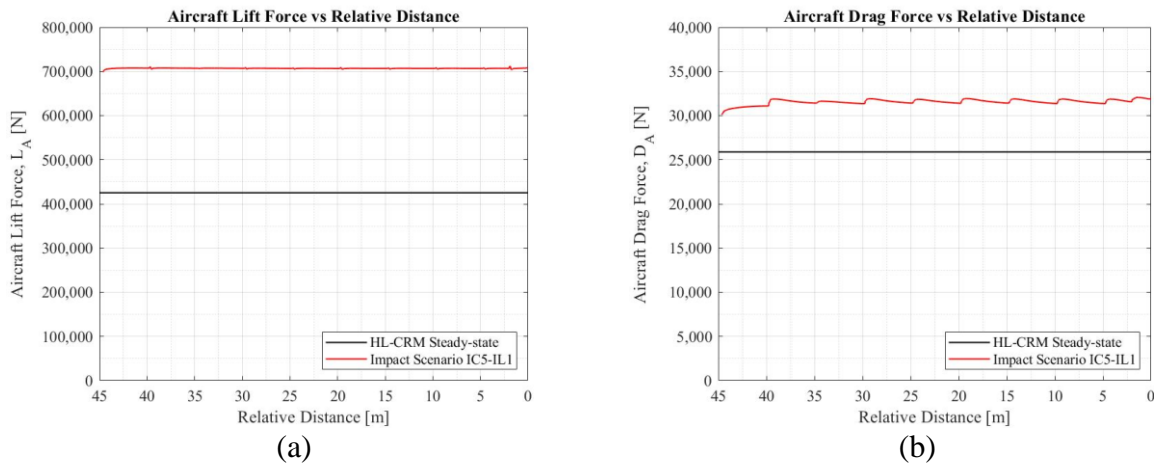
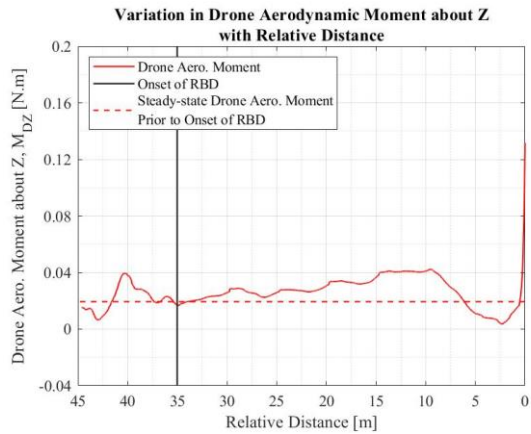
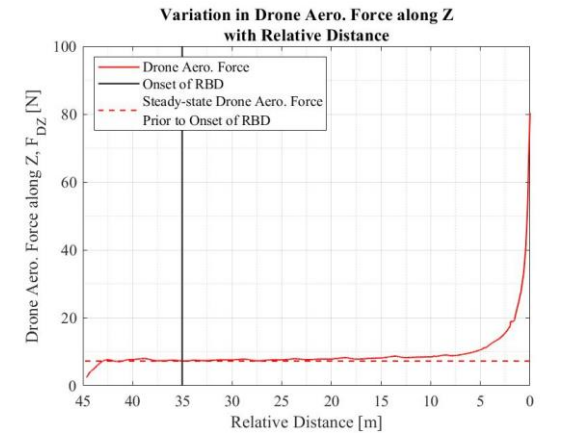
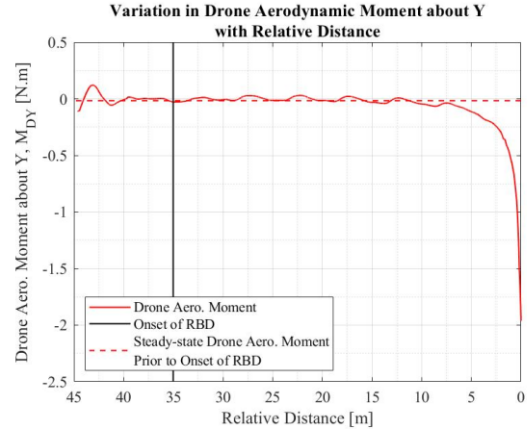
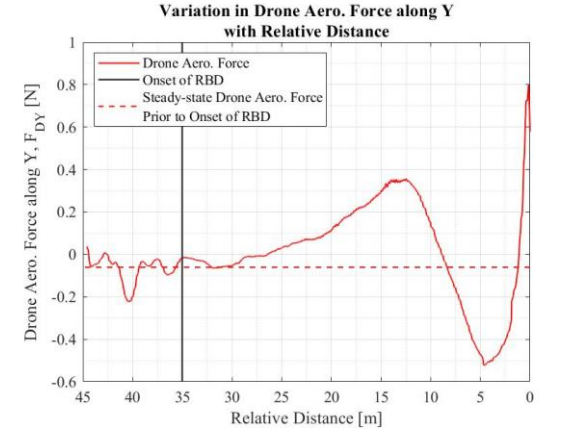
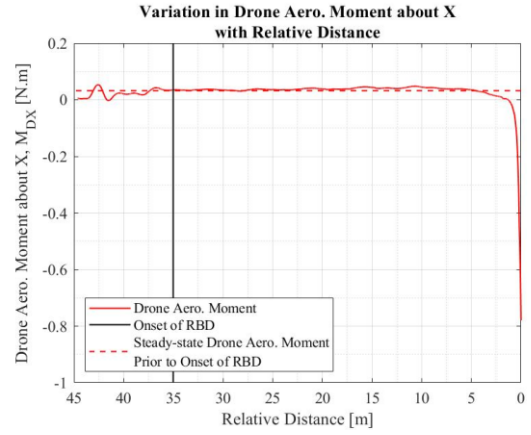
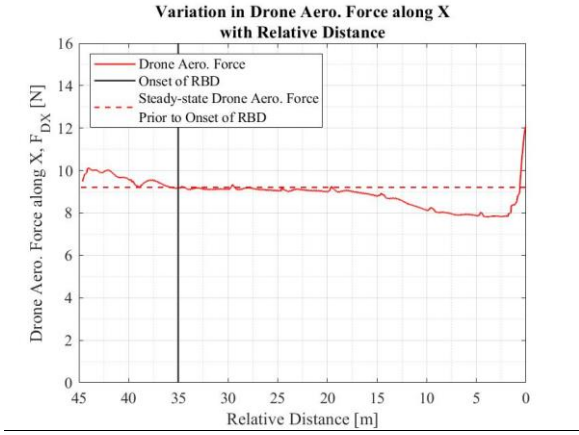


Figure 106. HL-CRM aircraft (a) drag force and (b) lift force recorded as the drone approached the aircraft.

The drone forces and moments were plotted with the steady-state forces and moments used in the UDF. As the drone approached the HL-CRM aircraft, the change in forces and moments can be seen in Figure 107 (a) and Figure 107 (b), respectively.

The linear and angular displacements experienced by the drone as it approached the HL-CRM aircraft for impact scenario IC5-IL1 are shown in Figure 108 (a) and Figure 108 (b), respectively. The drone's linear and angular velocities approaching the HL-CRM aircraft for impact scenario IC5-IL1 are shown in Figures 109 (a) and (b), respectively.

Figure 110 and Figure 111 show the flow field development over the drone at 4 locations away from the HL-CRM aircraft from the side view and top view, respectively. The pressure contour at the initial time of release can be viewed with the HL-CRM aircraft slat. The pressure contour over the drone at relative distances of approximately 40 m, 20 m, 5 m, and 0 m are also provided.



(a)

(b)

Figure 107. Drone aerodynamic (a) Forces and (b) Moments plotted with respect to relative distance along with average values used in the UDF for impact scenario IC5-IL1.

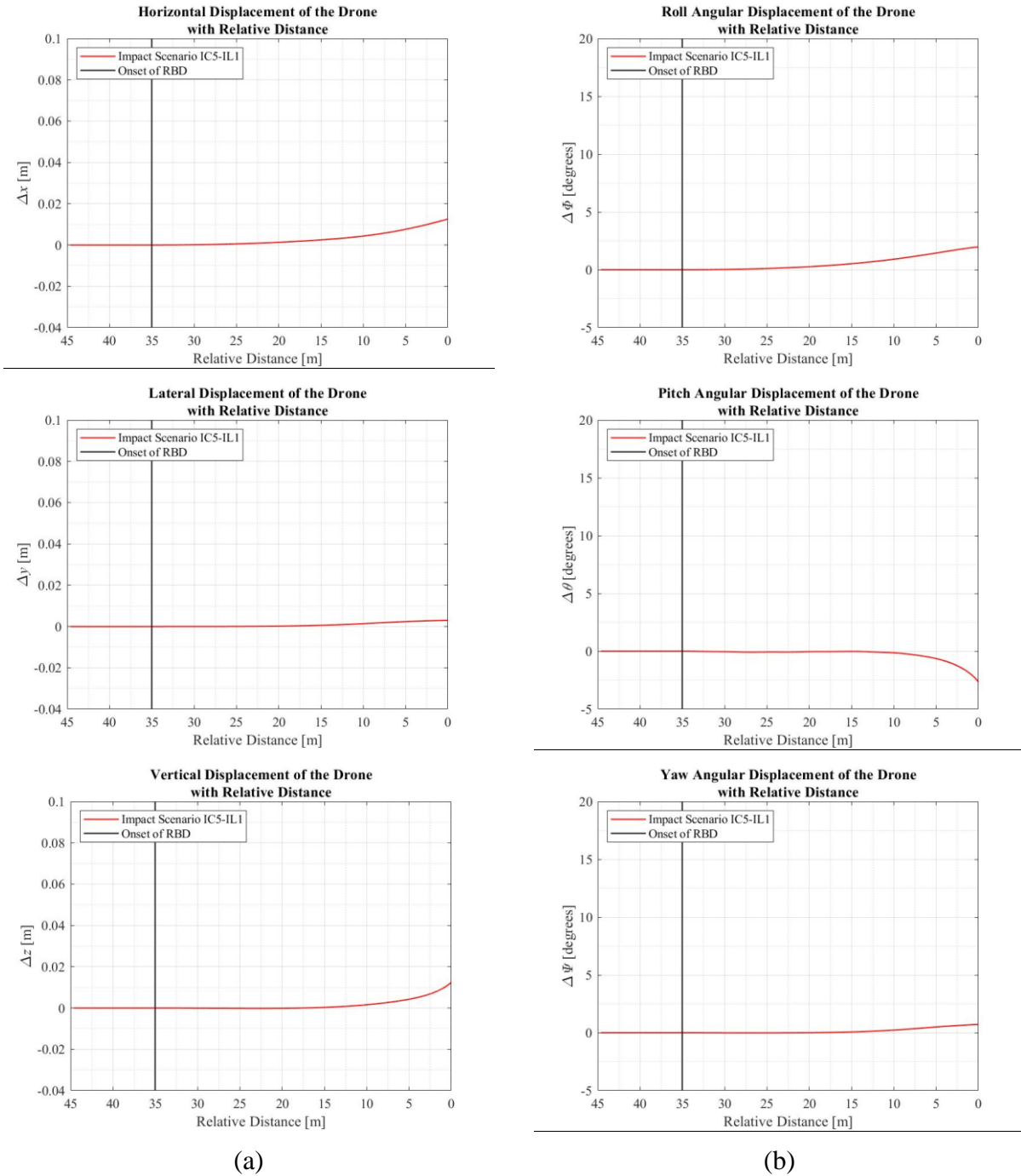


Figure 108. (a) Displacements and (b) angular displacements experienced by the drone as it traveled towards the HL-CRM aircraft for impact scenario IC5-IL1.

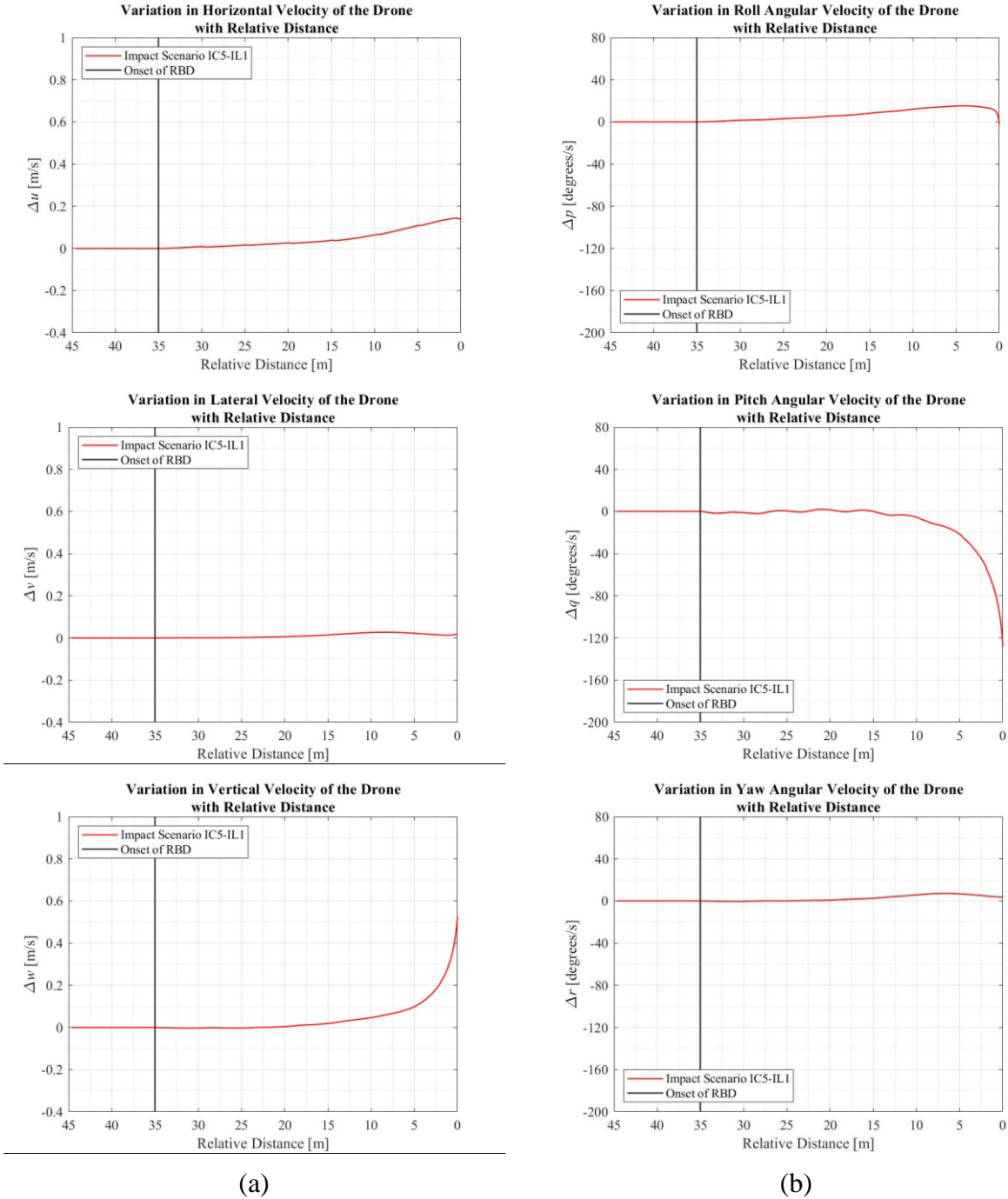


Figure 109. (a) Velocities and (b) angular velocities experienced by the drone as it traveled towards the HL-CRM aircraft for impact scenario IC5-IL1.

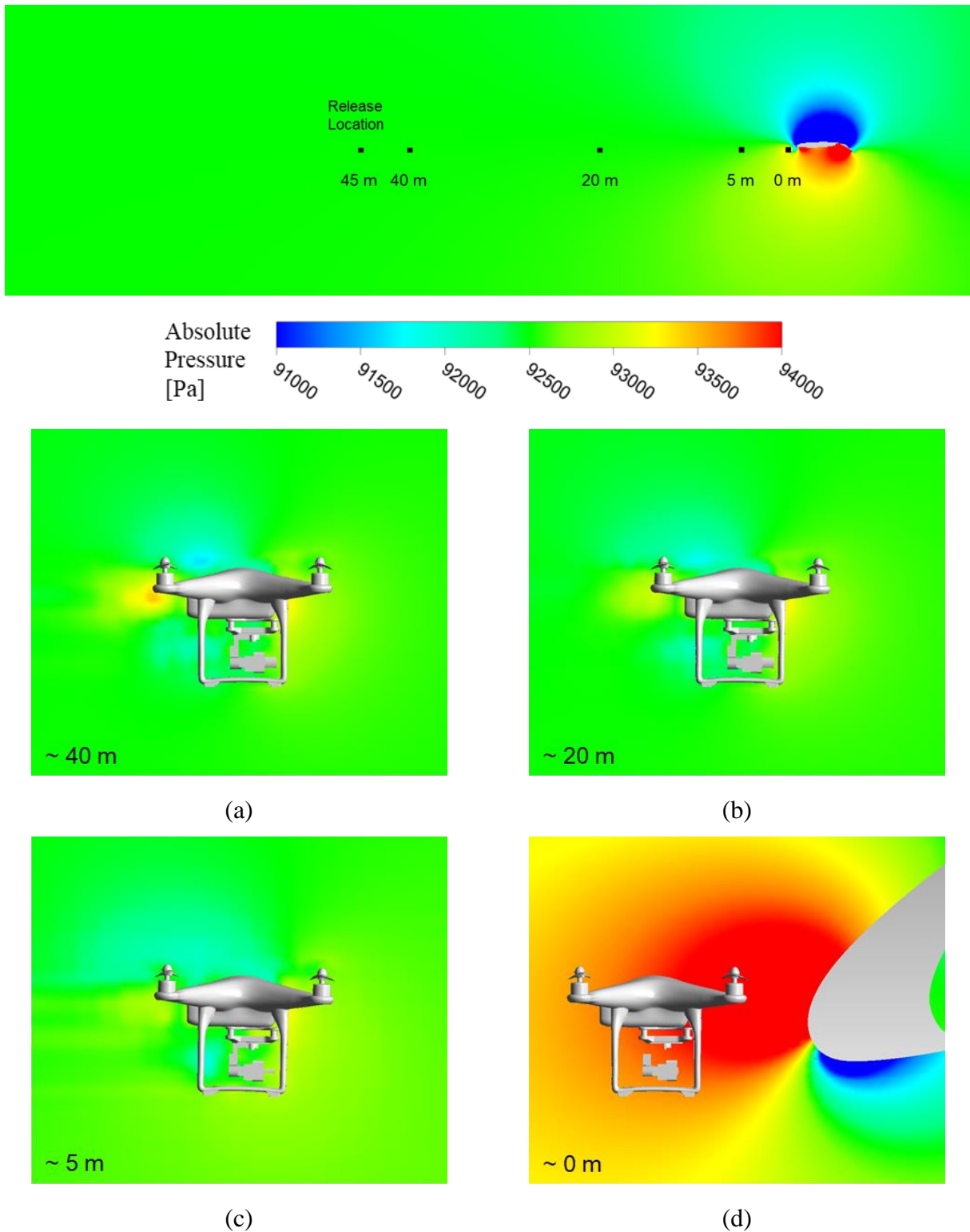


Figure 110. Side view of flow field development over the drone as it approaches the HL-CRM Aircraft in impact scenario IC5-IL1 at relative distances of approximately (a) 40 m (b) 20 m (c) 5 m and (d) 0 m.

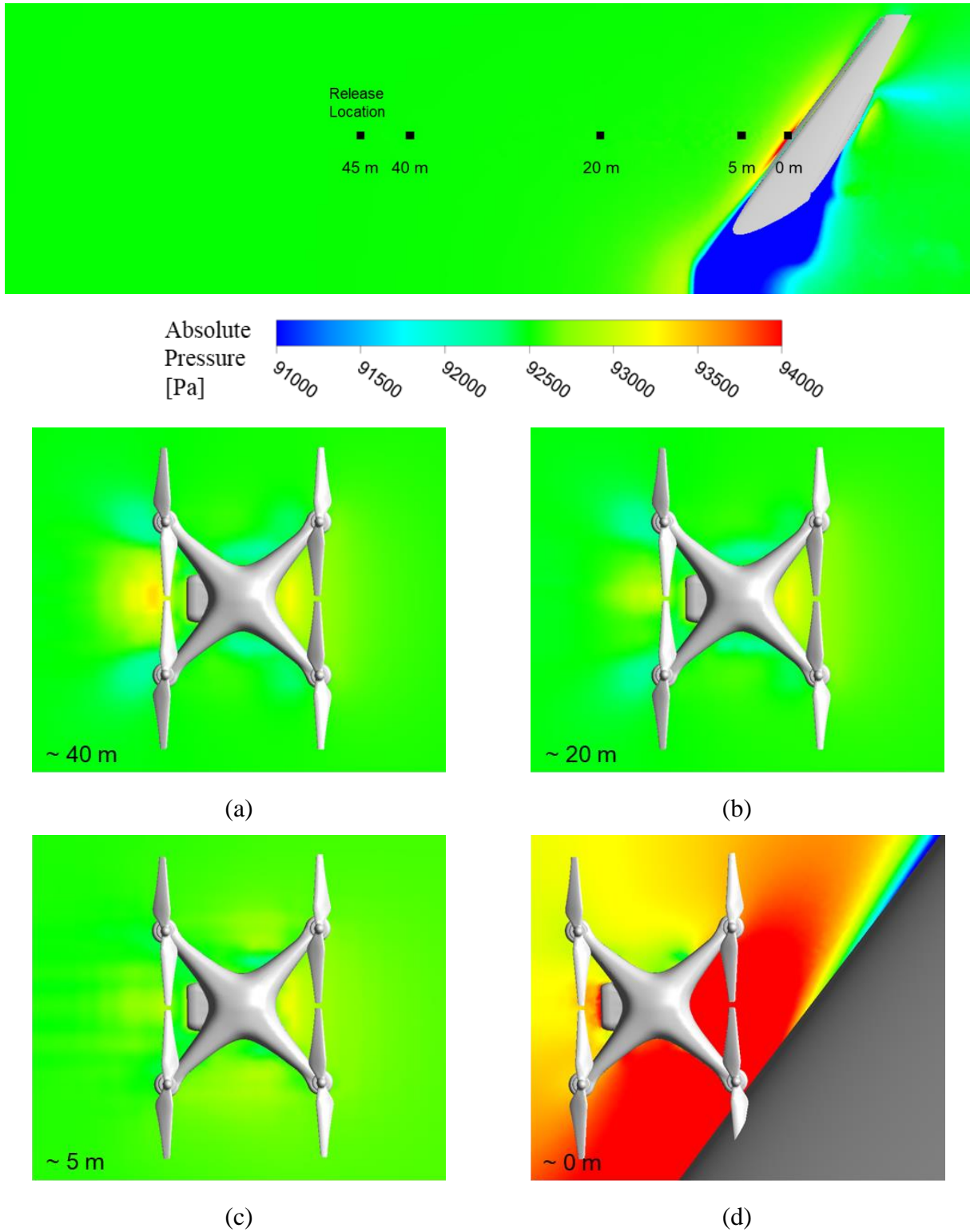


Figure 111. Top view of flow field development over the drone as it approaches the HL-CRM Aircraft in impact scenario IC5-IL1 at relative distances of approximately (a) 40 m (b) 20 m (c) 5 m and (d) 0 m.

### C.3.6 Impact Scenario 6 – IC3-IL2

The results were obtained for the impact scenario IC3-IL2 based on releasing the drone in the domain with the CRM aircraft. Since the drone was released at impact location 2, near the fuselage, the CRM geometry with the fuselage and tail was used for this impact scenario. The drone was released 75 m ahead of the wing's leading-edge at 4.89 m from the fuselage symmetry plane. Once released, the drone was allowed to move without the influence of forces and moments for 20 m. The steady-state force and moment values used as external forces and moments in the UDF were calculated from the last 5 m of the 20 m of prescribed motion.

The forces experienced by the aircraft during the transient simulation were compared with the forces obtained from the steady-state simulation of the CRM aircraft in the domain. Figure 112 shows an acceptable level of correlation between the steady-state and the transient simulation results for the CRM aircraft.

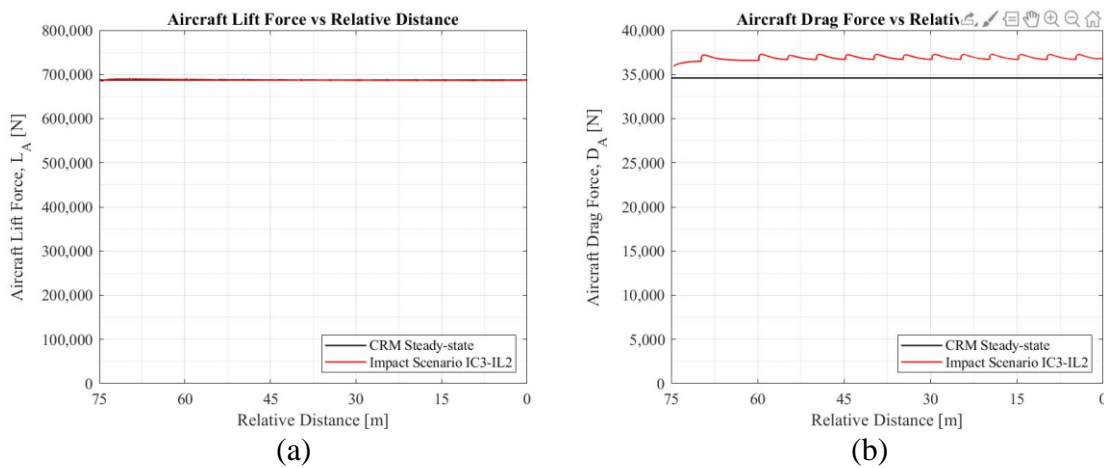


Figure 112. CRM aircraft (a) Drag force and (b) Lift force recorded as the drone approached the aircraft.

The drone forces and moments were plotted with the steady-state forces and moments used in the UDF. As the drone approached the CRM aircraft, the change in forces and moments can be seen in Figure 113 (a) and Figure 113 (b), respectively.

The linear and angular displacements experienced by the drone as it approached the CRM aircraft for impact scenario IC3-IL2 are shown in Figure 114 (a) and Figure 114 (b), respectively. The drone's linear and angular velocities as it approached the CRM aircraft for impact scenario IC3-IL2 are shown in Figure 115 (a) and Figure 115 (b), respectively.

Figure 116 and Figure 117 show the flow field development over the drone at 4 locations away from the CRM aircraft from the side view and top view, respectively. The pressure contour at the initial time of release can be viewed with the CRM aircraft wing. The pressure contour over the drone at relative distances of approximately 40 m, 20 m, 5 m, and 0 m are also provided.

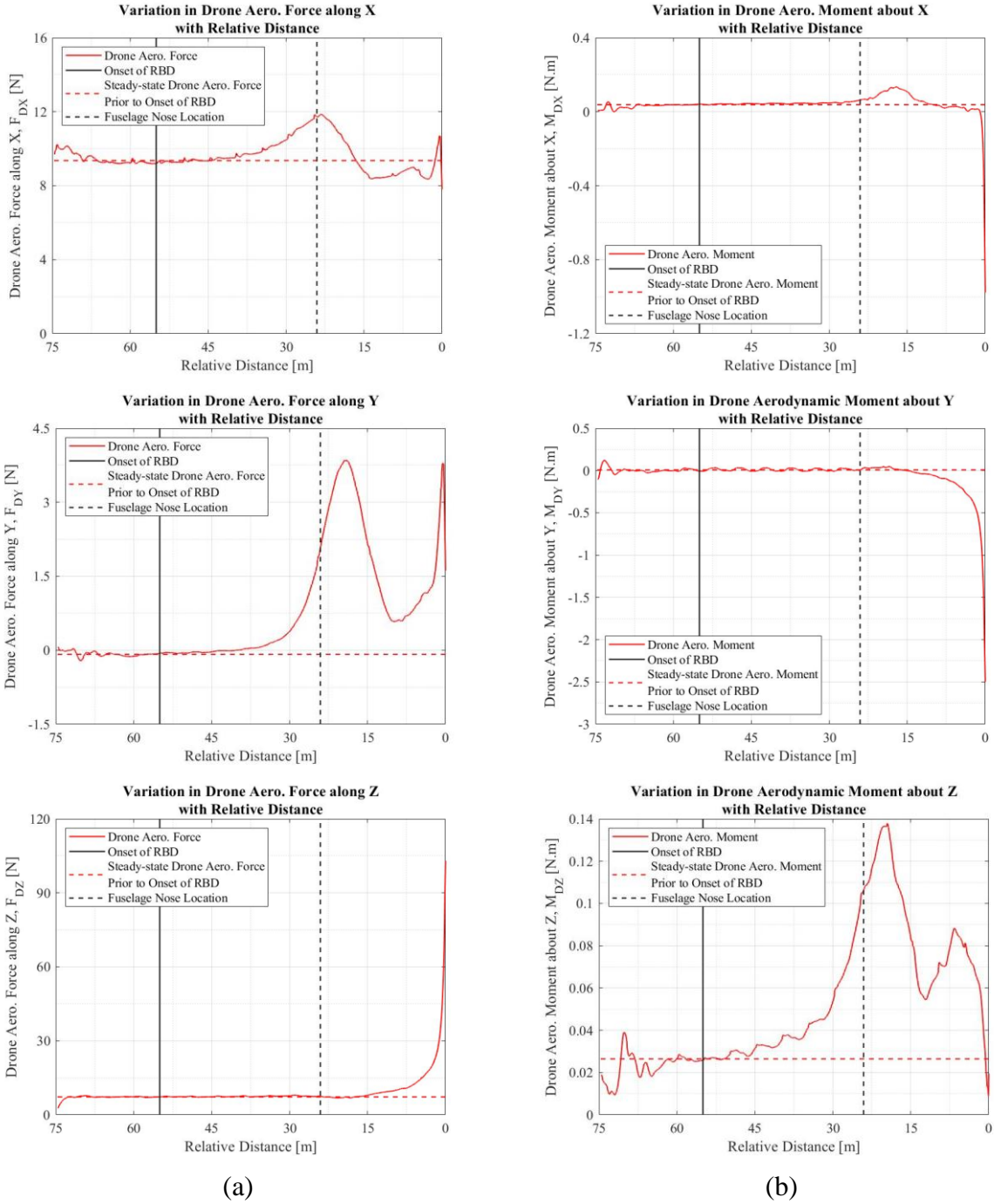


Figure 113. Drone aerodynamic (a) Forces and (b) Moments plotted with respect to relative distance along with average values used in the UDF for impact scenario IC3-IL2.

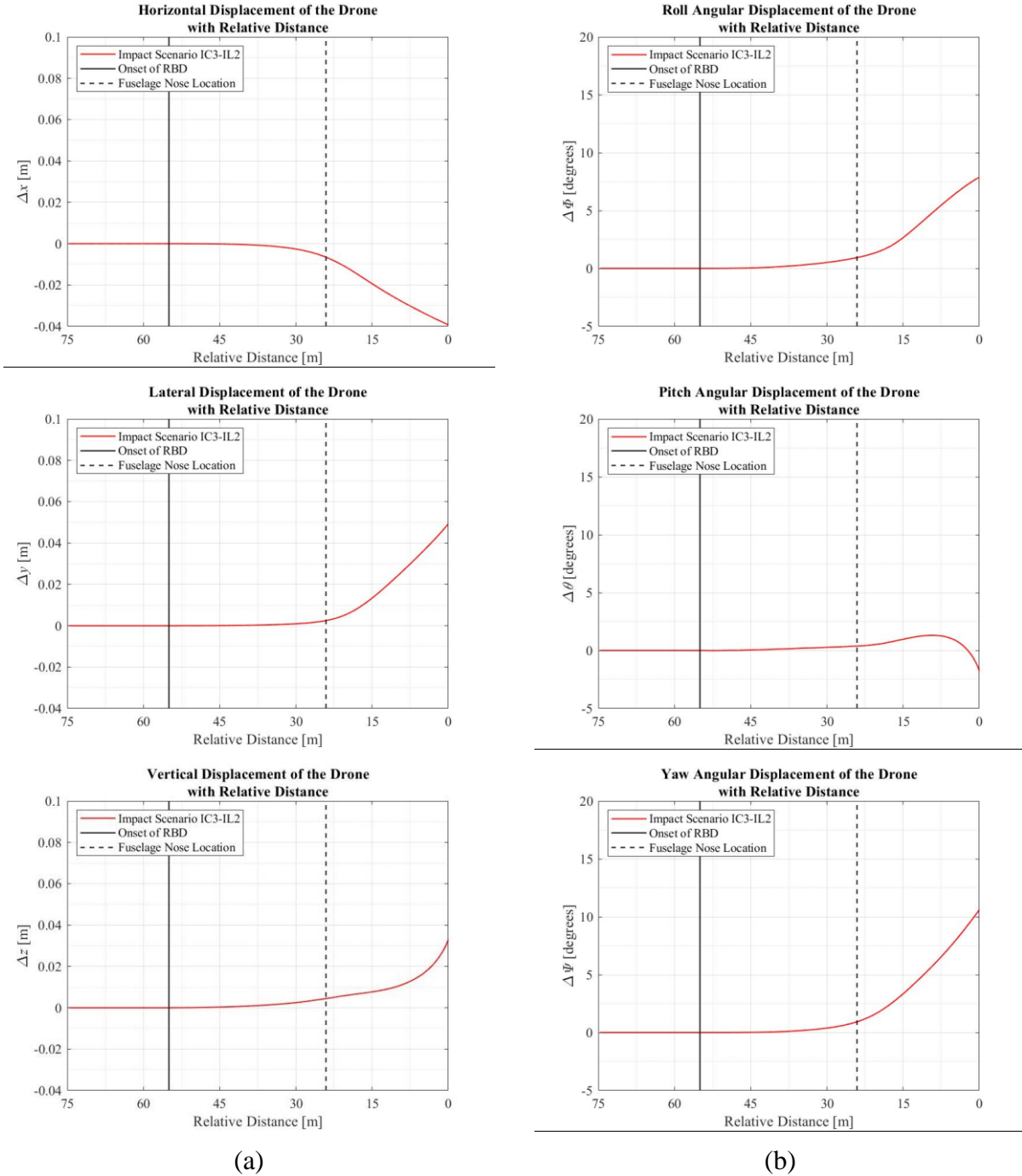


Figure 114. (a) Displacements and (b) Angular displacements experienced by the drone as it traveled towards the CRM aircraft for impact scenario IC3-IL2.

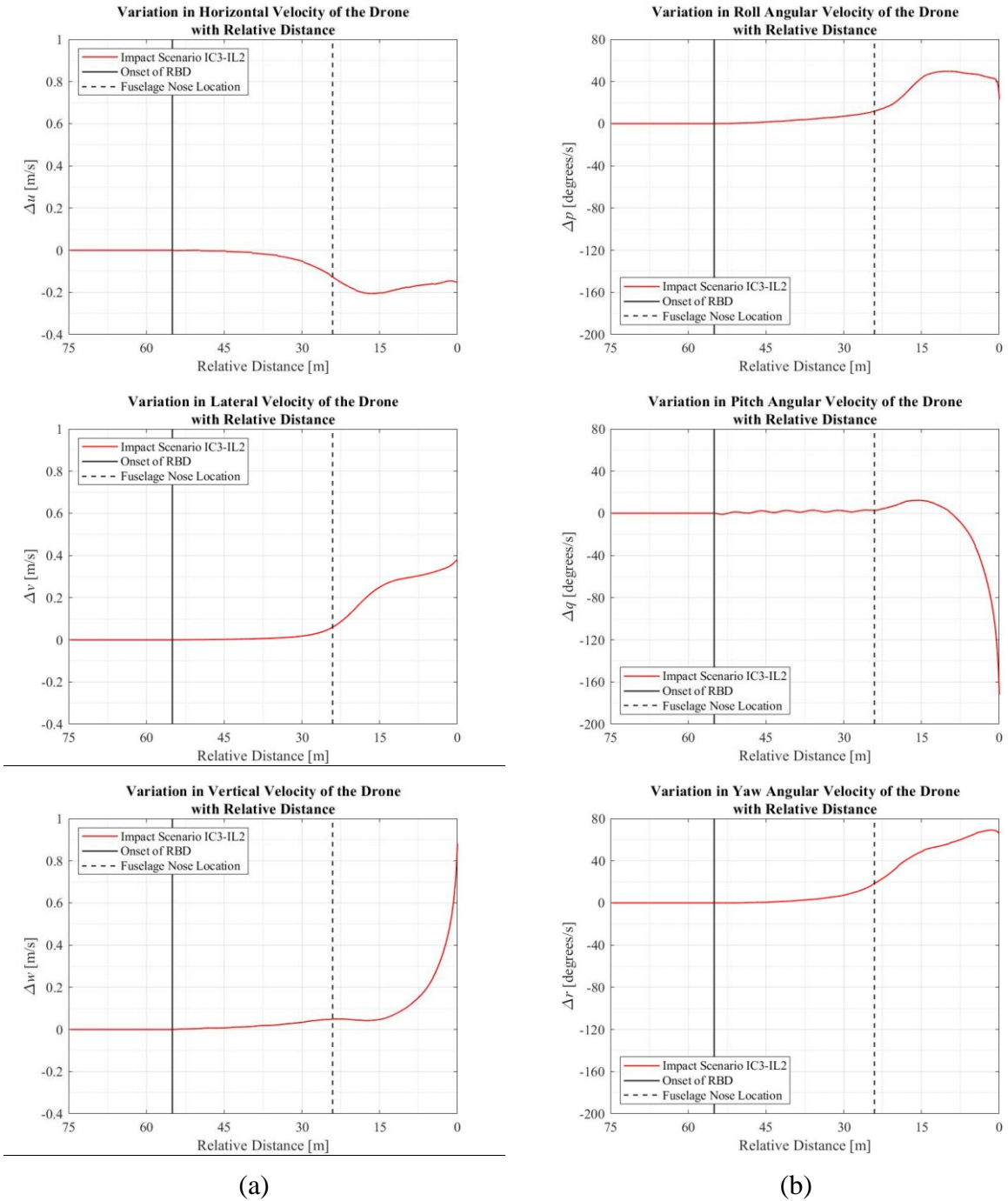


Figure 115. (a) Velocities and (b) Angular velocities experienced by the drone as it traveled towards the CRM aircraft for impact scenario IC3-IL2.

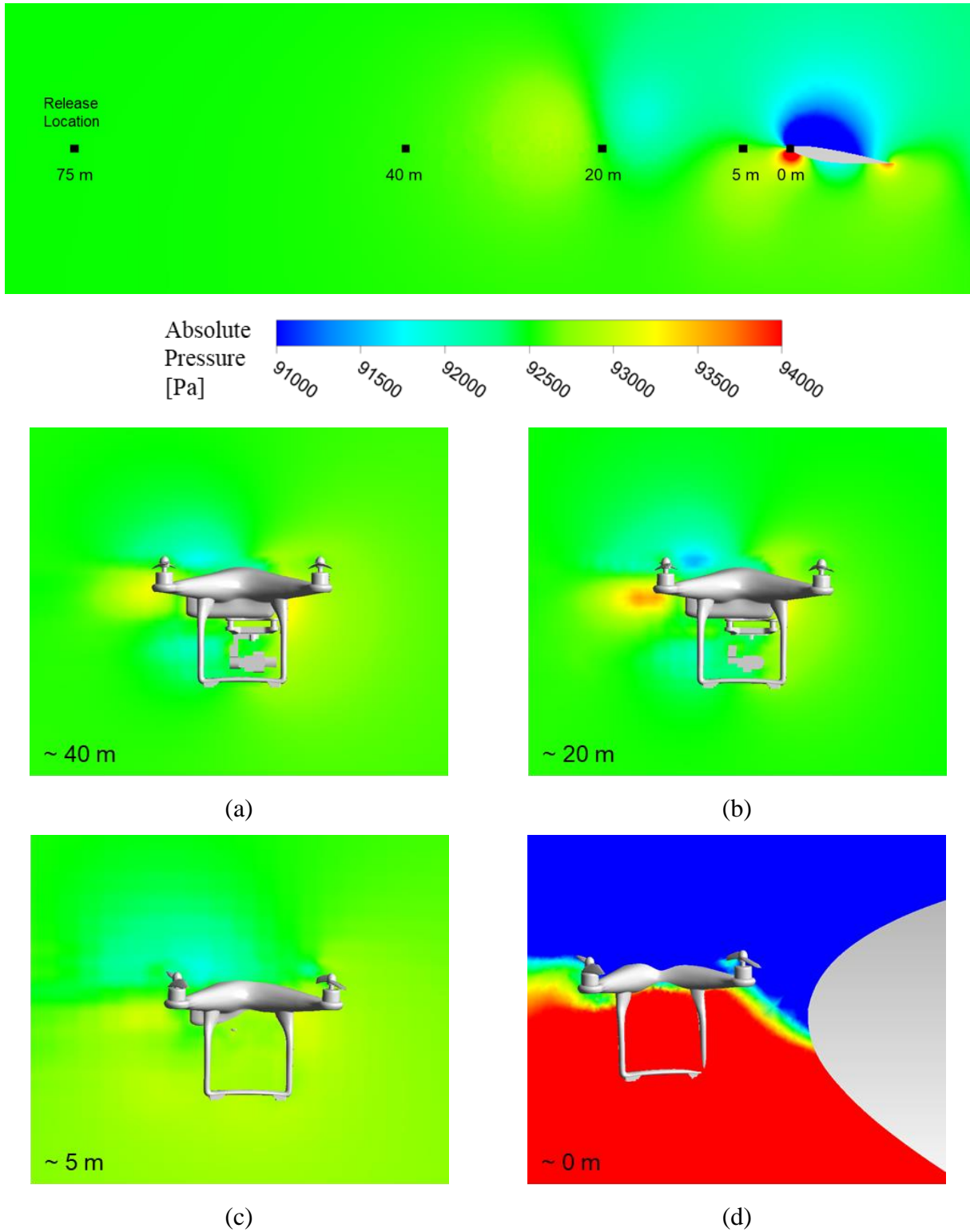


Figure 116. Side view of flow field development over the drone as it approaches the CRM Aircraft in impact scenario IC3-IL2 at relative distances of approximately (a) 40 m (b) 20 m (c) 5 m and (d) 0 m.

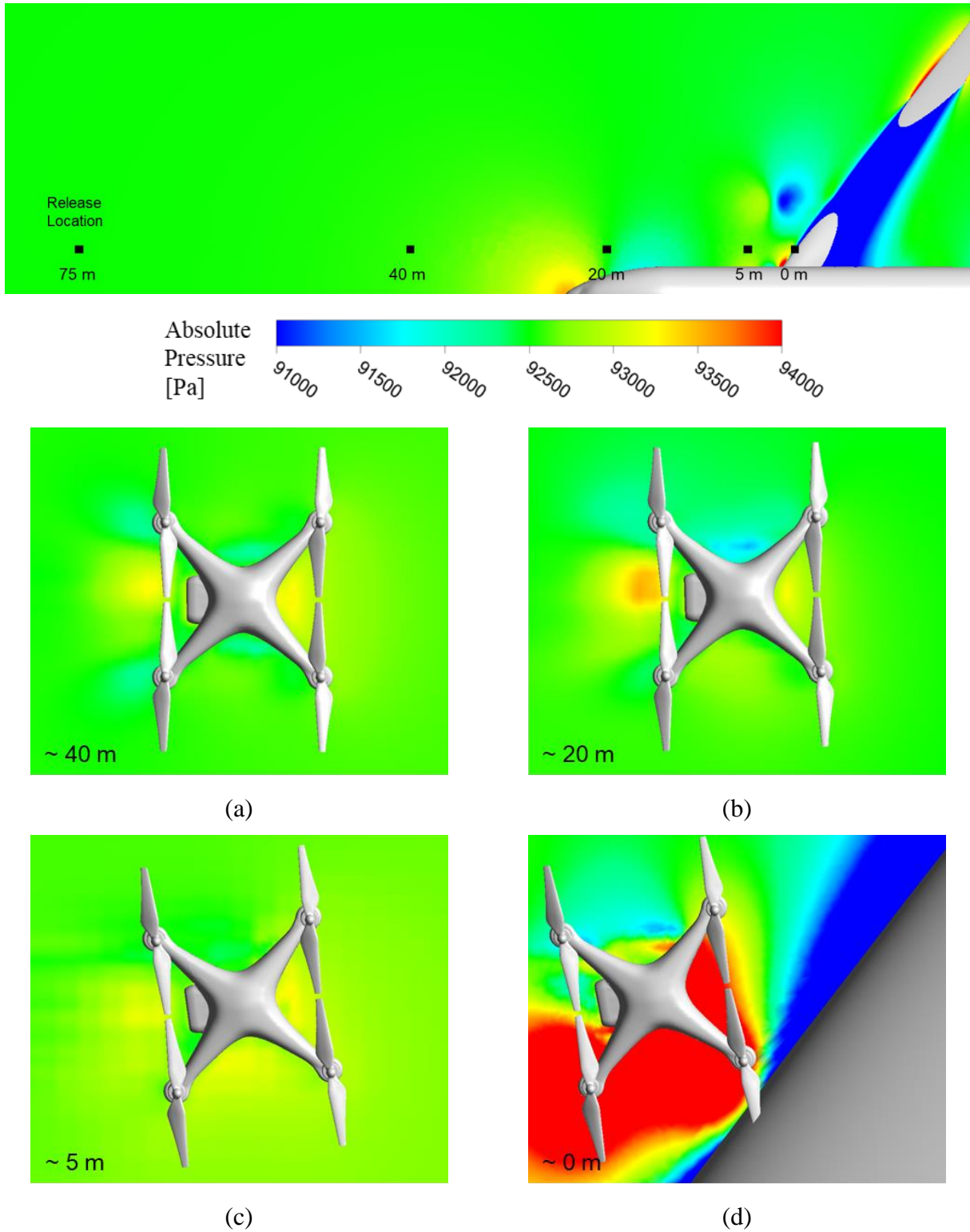


Figure 117. Top view of flow field development over the drone as it approaches the CRM Aircraft in impact scenario IC3-IL2 at relative distances of approximately (a) 40 m (b) 20 m (c) 5 m and (d) 0 m.

### C.3.7 Impact Scenario 7 – IC4-IL2

The results were obtained for the impact scenario IC4-IL2 based on releasing the drone in the domain with the HL-CRM aircraft. For this impact scenario, since the drone was released at impact location 2, near the fuselage, the HL-CRM geometry with the fuselage was used. The drone was released 75 m ahead of the leading-edge of the slat at 4.89 m from the fuselage symmetry plane. Once released, the drone was allowed to move without the influence of forces and moments for 20 m. The steady-state force and moment values used as external forces and moments in the UDF were calculated from the last 5 m of the 20 m of prescribed motion.

The forces experienced by the aircraft during the transient simulation were compared with the forces obtained from the steady-state simulation of the HL-CRM aircraft in the domain. Figure 118 shows an acceptable level of correlation between the steady-state and the transient simulation results for the HL-CRM aircraft.

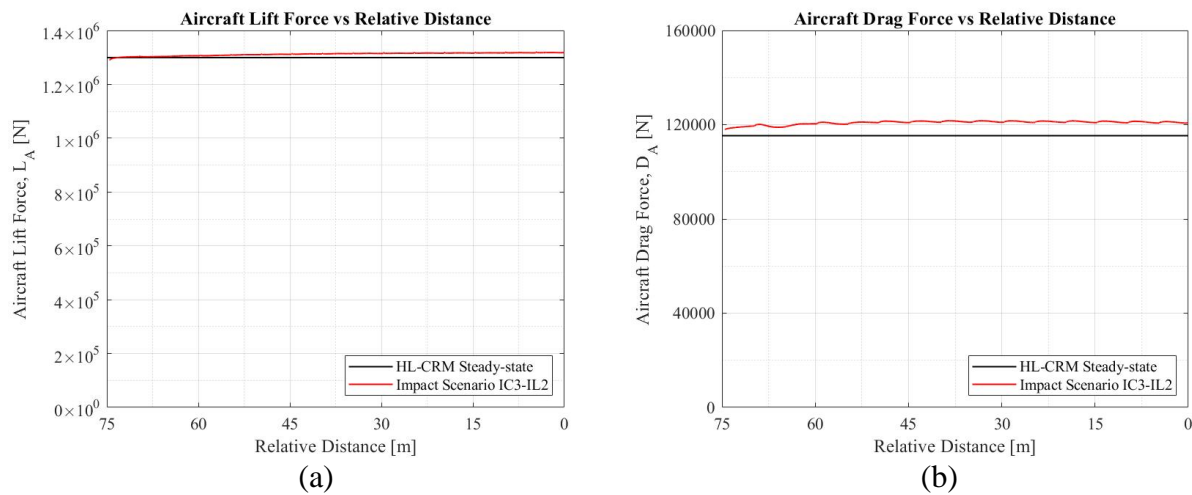


Figure 118. HL-CRM aircraft (a) Drag force and (b) Lift force recorded as the drone approached the aircraft.

The drone forces and moments were plotted with the steady-state forces and moments used in the UDF. As the drone approached the HL-CRM aircraft, the change in forces and moments can be seen in Figure 119 (a) and Figure 119 (b), respectively.

The linear and angular displacements experienced by the drone as it approached the HL-CRM aircraft for impact scenario IC4-IL2 are shown in Figure 120 (a) and Figure 120 (b), respectively. The drone's linear and angular velocities approaching the HL-CRM aircraft for impact scenario IC4-IL2 are shown in Figure 121 (a) and Figure 121 (b), respectively.

Figure 122 and Figure 123 show the flow field development over the drone at 4 locations away from the HL-CRM aircraft from the side view and top view, respectively. The pressure contour at the initial time of release can be viewed with the HL-CRM aircraft slat. The pressure contour over the drone at relative distances of approximately 40 m, 20 m, 5 m, and 0 m are also provided.

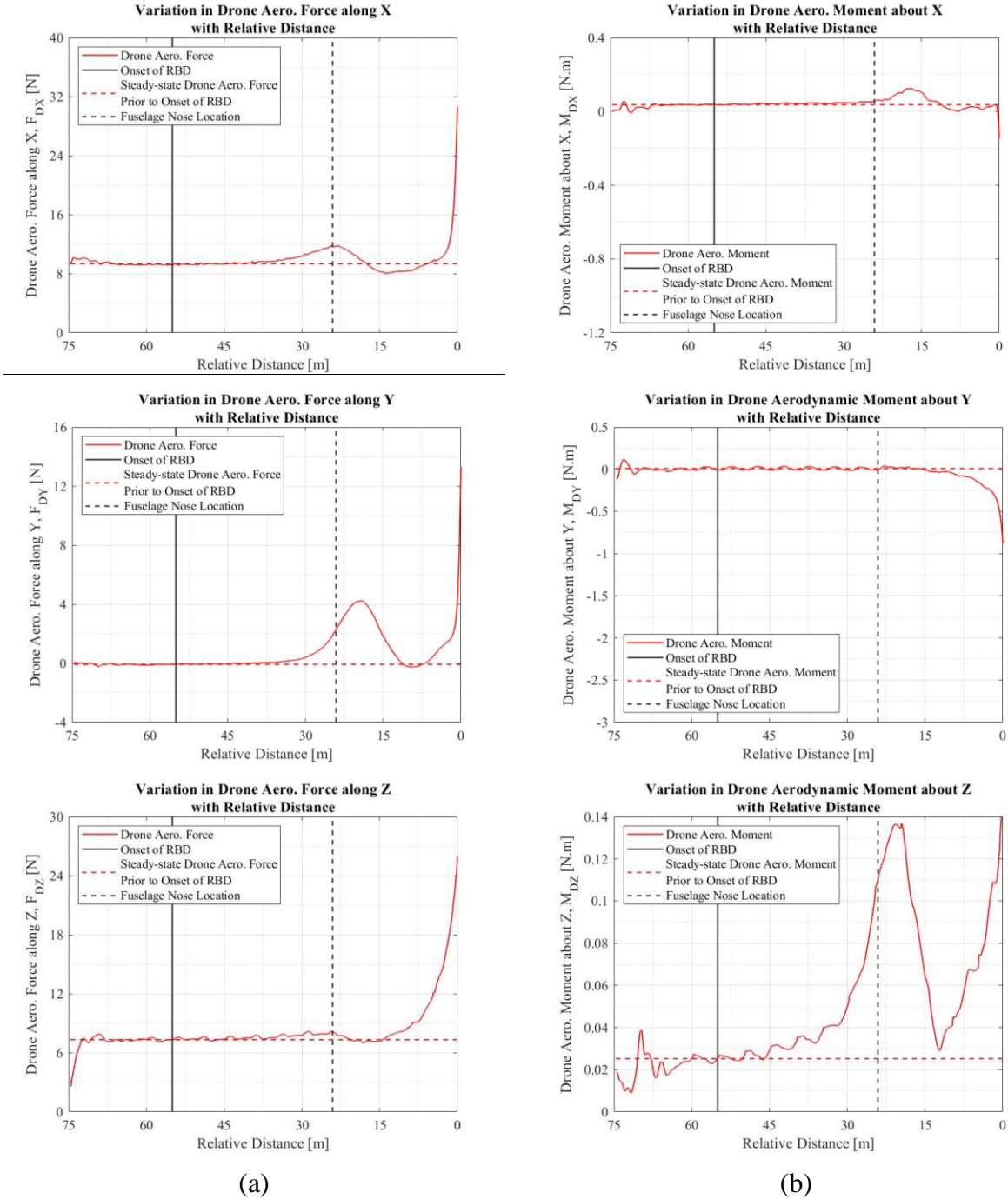


Figure 119. Drone aerodynamic (a) Forces and (b) Moments plotted with respect to relative distance along with average values used in the UDF for impact scenario IC4-IL2.

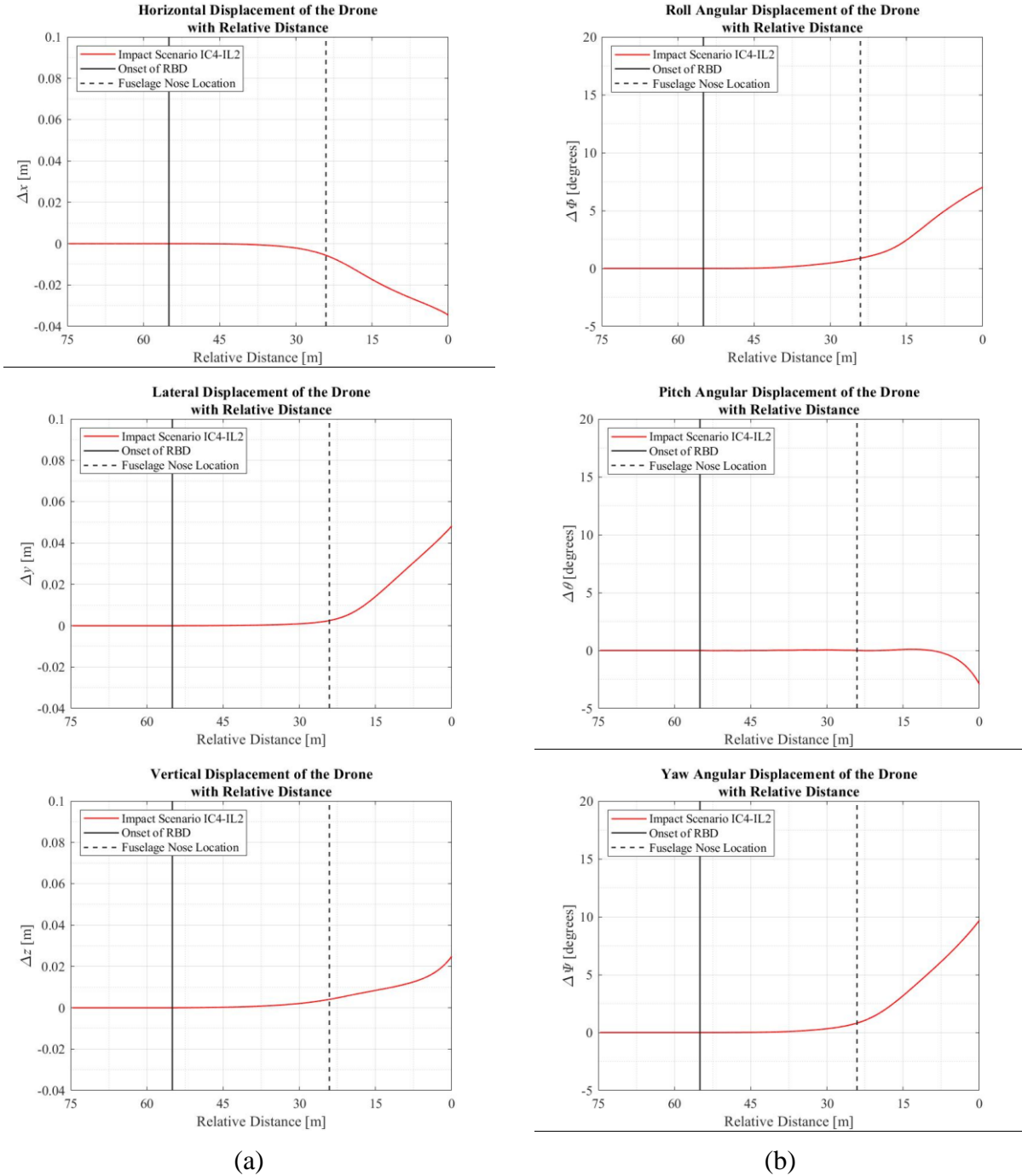


Figure 120. (a) Displacements and (b) Angular displacements experienced by the drone as it traveled towards the HL-CRM aircraft for impact scenario IC4-IL2.

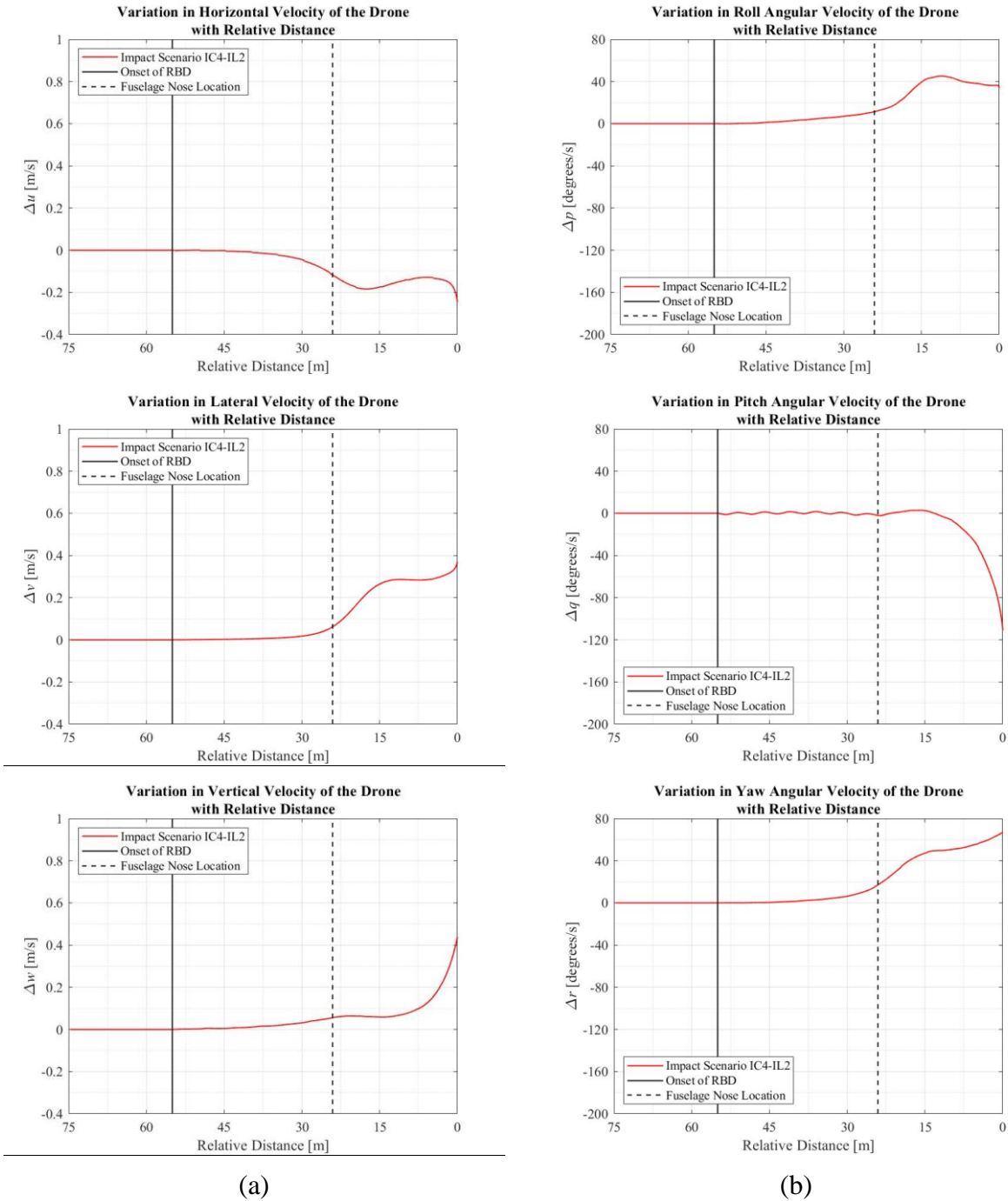


Figure 121. (a) Velocities and (b) Angular velocities experienced by the drone as it traveled towards the HL-CRM aircraft for impact scenario IC4-IL2.

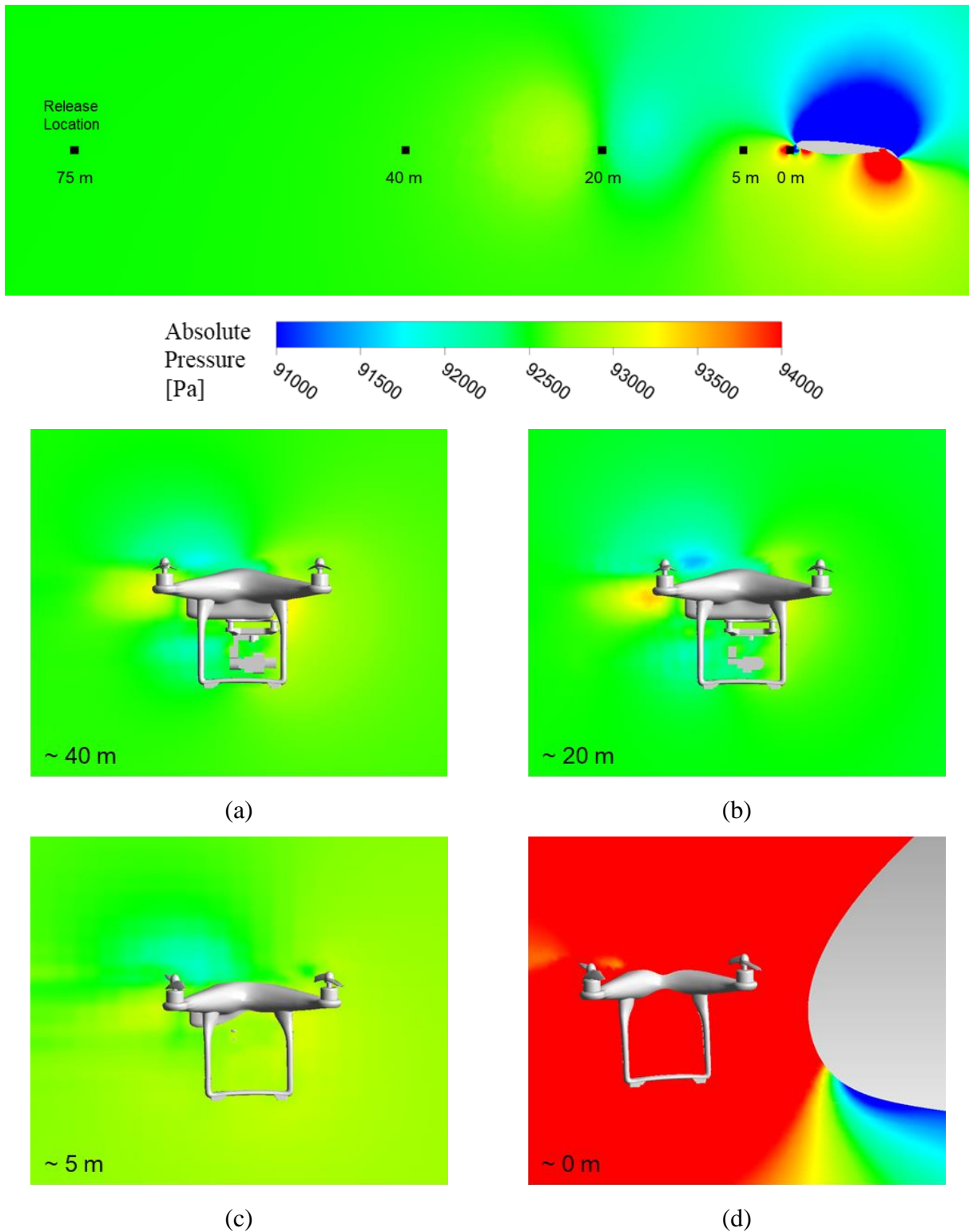


Figure 122. Side view of flow field development over the drone as it approaches the HL-CRM Aircraft in impact scenario IC4-IL2 at relative distances of approximately (a) 40 m (b) 20 m (c) 5 m and (d) 0 m.

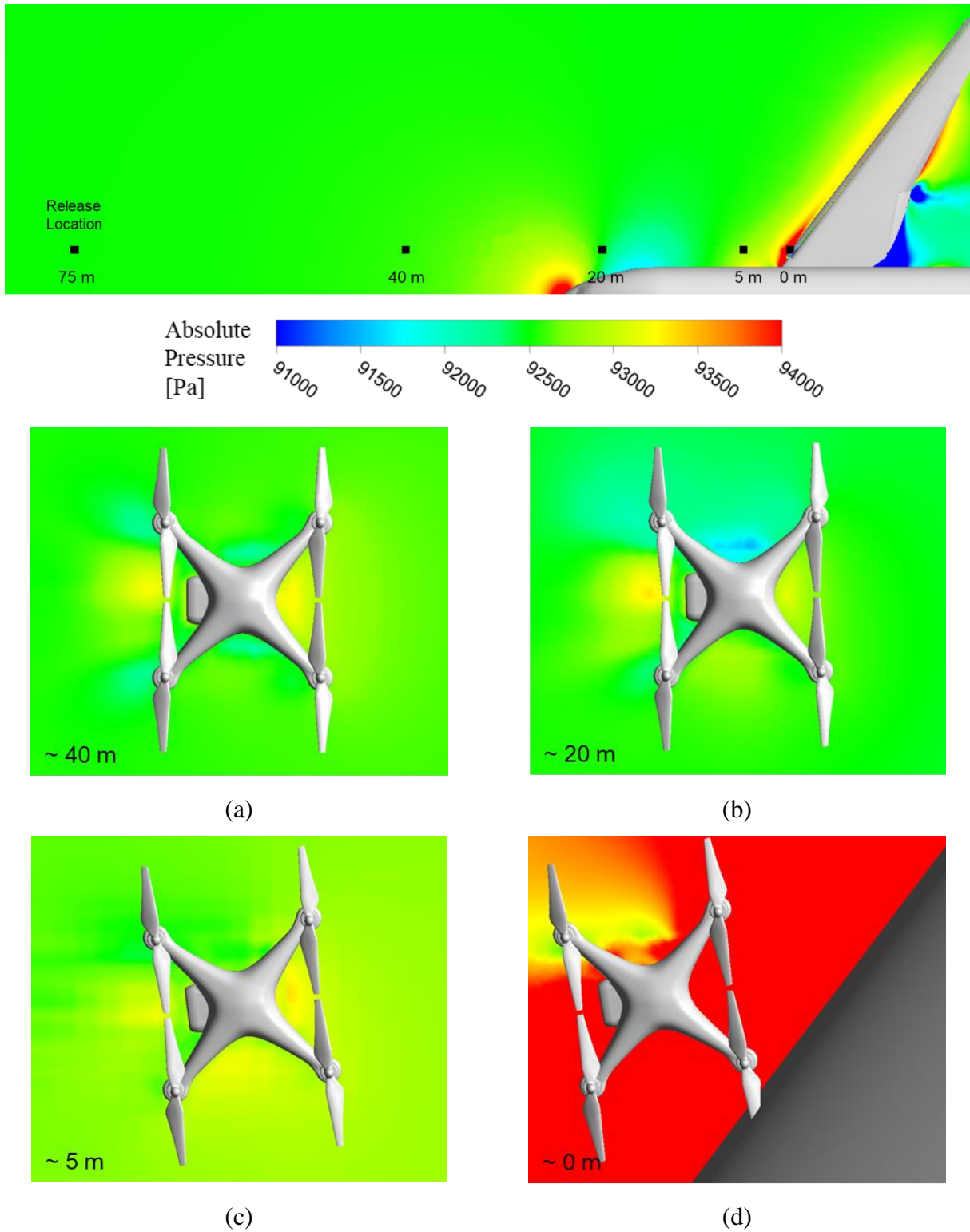


Figure 123. Top view of flow field development over the drone as it approaches the HL-CRM Aircraft in impact scenario IC4-IL2 at relative distances of approximately (a) 40 m (b) 20 m (c) 5 m and (d) 0 m.

## Annex B: ERAU Final Report

Air Traffic Organization  
NextGen & Operations Planning  
Office of Research and  
Technology Development  
Washington, DC 20591



**ERAU**

# **Annex B – UAS Airborne Collision Severity Evaluation: Assessment of sUAS deflections due to aerodynamic interaction with a commercial aircraft**

October 2021

Final Report

This document is available to the U.S. public  
through the National Technical Information  
Services (NTIS), Springfield, Virginia 22161.

This document is also available from the  
Federal Aviation Administration William J. Hughes  
Technical Center at [actlibrary.tc.faa.gov](http://actlibrary.tc.faa.gov).



U.S. Department of Transportation  
**Federal Aviation Administration**

## NOTICE

This document is disseminated under the sponsorship of the U.S. Department of Transportation in the interest of information exchange. The U.S. Government assumes no liability for the contents or use thereof. The U.S. Government does not endorse products or manufacturers. Trade or manufacturers' names appear herein solely because they are considered essential to the objective of this report. The findings and conclusions in this report are those of the author(s) and do not necessarily represent the views of the funding agency. This document does not constitute FAA policy. Consult the FAA sponsoring organization listed on the Technical Documentation page as to its use.

This report is available at the Federal Aviation Administration William J. Hughes Technical Center's Full-Text Technical Reports page: [actlibrary.tc.faa.gov](http://actlibrary.tc.faa.gov) in Adobe Acrobat portable document format (PDF).

**Legal Disclaimer:** The information provided herein may include content supplied by third parties. Although the data and information contained herein has been produced or processed from sources believed to be reliable, the Federal Aviation Administration makes no warranty, expressed or implied, regarding the accuracy, adequacy, completeness, legality, reliability or usefulness of any information, conclusions or recommendations provided herein. Distribution of the information contained herein does not constitute an endorsement or warranty of the data or information provided herein by the Federal Aviation Administration or the U.S. Department of Transportation. Neither the Federal Aviation Administration nor the U.S. Department of Transportation shall be held liable for any improper or incorrect use of the information contained herein and assumes no responsibility for anyone's use of the information. The Federal Aviation Administration and U.S. Department of Transportation shall not be liable for any claim for any loss, harm, or other damages arising from access to or use of data or information, including without limitation any direct, indirect, incidental, exemplary, special or consequential damages, even if advised of the possibility of such damages. The Federal Aviation Administration shall not be liable to anyone for any decision made or action taken, or not taken, in reliance on the information contained herein.

## ACKNOWLEDGEMENTS

The authors would like to thank all the Federal Aviation Administration (FAA) personnel that have been involved in this research project. Additionally, the authors would like to thank the group of researchers at NIAR who collaborated with us and provided insightful feedback throughout the project.

## TABLE OF CONTENTS

Chapter	Page
TABLE OF CONTENTS	VI
LIST OF FIGURES	VIII
LIST OF TABLES	XIII
LIST OF ACRONYMS	XIV
1. INTRODUCTION	1
1.1 Background	1
1.2 Project Scope	2
1.3 Target Definition	2
1.4 Projectile Definition	3
1.5 Impact Scenarios	4
1.5.1 Impact Conditions	4
1.5.2 Impact Location	6
1.5.3 Summary	9
2. NUMERICAL METHODOLOGY	9
2.1 Introduction	9
2.2 Geometry	11
2.3 Mesh	13
2.4 Numerical MODELS	13
2.4.1 Boundary and Operating Conditions	13
2.4.2 Solver Setup	15
2.4.3 Dynamic Fluid Body Interaction	15
2.4.4 Overset Mesh Method	16
2.4.5 Adaptive Mesh Refinement	16
2.4.6 Time Steps	17

2.5 Assumptions	18
2.6 Drone Release Location	19
2.6.1 Release (Vertical) Location	19
2.6.2 Release (Horizontal) Location without Fuselage	23
2.6.3 Release (Horizontal) Location with Fuselage	24
2.7 Relative Distance	26
2.8 Sign Convention	26
2.9 Force and MOment Balancing on the Drone	27
<b>3. RESULTS</b>	<b>29</b>
3.1 CRM Aircraft Validation	29
3.1.1 Introduction	29
3.1.2 Mesh	29
3.1.3 Numerical Model	29
3.1.4 Results	30
3.2 Cross Verification	32
3.2.1 Introduction	32
3.2.2 Mesh	33
3.2.3 Numerical Model	33
3.2.4 Results	33
3.2.5 Primary ERAU Results for All Impact Scenarios	43
<b>4. CONCLUSIONS</b>	<b>50</b>
<b>5. REFERENCES</b>	<b>52</b>
APPENDIX A – MESH SPECIFICATIONS .....	A-1
APPENDIX B – ADDITIONAL RESULTS OF THE CROSS-VERIFICATION .....	B-1
APPENDIX C – ADDITIONAL RESULTS OF IMPACT SCENARIOS .....	C-1

## LIST OF FIGURES

Figure	Page
1. NASA Common Research Model: a) top view, b) side view.	2
2. a) The DJI Phantom 3 model obtained from [15], [16], b) three-dimensional CAD model used in the current computational analysis.	3
3. The dimensions of the DJI Phantom 3 model.	4
4. Side view showing the placement of the drone with respect to (a) CRM aircraft ( $0^\circ$ AoA) (b) CRM aircraft ( $5^\circ$ AoA) (c) HL-CRM aircraft (d) CRM Horizontal Stabilizer ( $0^\circ$ AoA) and (e) CRM Horizontal Stabilizer ( $5^\circ$ AoA).	7
5. Spanwise location of the drone at IL1 as it approaches the CRM aircraft.	8
6. Spanwise location of the drone at IL3 as approaches the CRM horizontal stabilizer.	8
7. The methodology on the possibility of the collision between the DJI drone and CRM aircraft wing.	10
8. The outline of the current numerical study.	10
9. A computational model of the flow domain.	11
10. Computational models of the CRM aircraft.	12
11. Boundary conditions (speed of sound, Mach number, and x-velocity) for analyzing the impact scenarios.	15
12. Overset mesh around the DJI drone.	16
13. Mesh transition between the overset mesh and background mesh using adaptive mesh refinement (AMR).	17
14. A comparison of the forces on the drone for the time steps of $10^{-5}$ s and $10^{-4}$ s.	18
15. Release location of the DJI drone for impact scenario IC6-IL3.	21
16. Distances from the leading edges of the CRM wing and horizontal stabilizer to the top surfaces.	22
17. Mapped geometry of the DJI drone in the computational domain with respect to the origin in the current simulations.	23
18. The distance at release time with 6-DOF enabled.	24
19. Pressure flow field from the release location to downstream of the horizontal stabilizer for IL3.	24
20. Impact of flow forces on the DJI drone at different distances.	25
21. Sign conventions used for (a) displacements experienced by the drone, (b) forces applied on the CRM aircraft.	27
22. The sign convention used for the computation of the angular displacements experienced by the drone.	27

23.	Force balance applied on the DJI drone when the 6-DOF was enabled.	28
24.	The stations used to validate the pressure coefficients on the CRM wing.	29
25.	Pressure coefficients on the CRM aircraft wing at six stations in the spanwise direction. In this figure, $b$ and $c$ are the semi-span length and airfoil's chord length, respectively.	30
26.	(a) Velocity and (b) absolute pressure flow fields around the CRM wing at a Mach number of 0.85 and reference pressure of 1 atm.	32
27.	Cross-verification results of forces for IC1-IL1.	34
28.	Cross-verification results of moments for IC1-IL1.	35
29.	Cross-verification results of displacements for IC1-IL1.	36
30.	Cross-verification results of absolute pressure distribution for IC1-IL1 at the point of collision, obtained by NIAR and ERAU.	37
31.	Displacements of the Drone from the initial directions resulting from the flow forces and moments for IC1-IL1.	38
32.	Cross-verification results of forces for IC2-IL1.	39
33.	Cross-verification results of moments for IC2-IL1.	40
34.	Cross-verification results of displacements for IC2-IL1.	41
35.	Cross-verification results of absolute pressure distribution for IC2-IL1 at the point of collision, obtained by NIAR and ERAU.	42
36.	Displacements of the Drone from the initial directions resulting from the flow forces and moments for IC2-IL1.	43
37.	Vertical (a) and spanwise (b) displacements of the drone at the point of impact for IC2- IL1, IC2-IL1U1, IC2-IL1D1, IC2-IL1U2, and IC2-IL1D2. The unconstrained (6-DOF) rigid body motion was enabled at the distance of 4.5 m relative to the CRM wing leading edge.	45
38.	Vertical (a) and spanwise (b) displacements of the drone at the point of impact for IC2- IL1 with a variety of considerations, including using adaptive mesh refinement (AMR) method and different instantaneous locations for enabling 6-DOF rigid body motion.	45
39.	Vertical and spanwise displacements of the drone at the point of impact for IC2-IL3 with a variety of considerations, including using adaptive mesh refinement (AMR) method and different force balance values when enabling 6-DOF rigid body motion.	46
40.	Displacements of the drone along the X, Y, and Z axes at the point of impact for all cases studied in this section.	48
41.	The angular displacement of the drone about the X, Y, and Z axes at the point of impact for all cases studied in this section.	50
42.	A trimmed mesh used for validation of flow around the CRM wing at a Mach number of 0.85.	A-1

43. A polyhedral mesh used for the analysis of the impact scenarios at a Mach number of 0.3. A-3
44. A polyhedral surface and volume mesh for the DJI drone. A-5
45. An accurate prediction of velocity gradients within the boundary layers of the CRM wing and DJI drone. A-7
46. Zoomed views of flow forces on the DJI drone for IC1-IL1. B-1
47. Zoomed views of moments on the DJI drone for IC1-IL1. B-2
48. Angular displacements of the DJI drone for IC1-IL1; (a) the angular displacements with respect to the relative distance and (b) the final angular displacement of the drone at the point of collision. B-3
49. DJI drone axial (a) and angular (b) velocities for IC1-IL1. B-4
50. Zoomed views of the flow forces on the DJI drone for IC2-IL1. B-5
51. Zoomed views of the moments on the DJI drone for IC2-IL1. B-6
52. Angular displacements of the DJI drone for IC2-IL1; (a) the angular displacements with respect to the relative distance and (b) the final angular displacement of the drone at the point of collision. B-7
53. DJI drone axial (a) and angular (b) velocities for IC2-IL1. B-8
54. CRM aircraft lift and drag forces recorded as the drone approached the aircraft wing. C-1
55. Axis system used for the drone. C-1
56. Drone aerodynamic forces (a) and moments (b) plotted with respect to relative distance along with average values used in the UDF. C-2
57. Displacements (a) and angular displacements (b) experienced by the drone as it traveled towards the CRM aircraft wing. C-3
58. Velocities (a) and angular velocities (b) experienced by the drone as it traveled towards the CRM aircraft wing. C-4
59. CRM aircraft lift and drag forces recorded as the drone approached the aircraft wing. C-5
60. Axis system used for the drone. C-5
61. Drone aerodynamic forces (a) and moments (b) plotted with respect to relative distance along with average values. C-6
62. Displacements (a) and angular displacements (b) experienced by the drone as it traveled towards the CRM aircraft wing. C-7
63. Velocities (a) and angular velocities (b) experienced by the drone as it traveled towards the CRM aircraft. C-8
64. CRM aircraft lift and drag forces recorded as the drone approached the aircraft. C-9
65. Axis system used for the drone. C-9

66. Drone aerodynamic forces (a) and moments (b) plotted with respect to relative distance along with average values. C-10
67. Displacements (a) and angular displacements (b) experienced by the drone as it traveled towards the CRM aircraft wing. C-11
68. Velocities (a) and angular velocities (b) experienced by the drone as it traveled towards the CRM aircraft wing. C-12
69. CRM aircraft lift and drag forces recorded as the drone approached the aircraft. C-13
70. Axis system used for the drone. C-13
71. Drone aerodynamic forces (a) and moments (b) plotted with respect to relative distance along with average values. C-14
72. Displacements (a) and angular displacements (b) experienced by the drone as it traveled towards the CRM aircraft wing. C-15
73. Velocities (a) and angular velocities (b) experienced by the drone as it traveled towards the CRM aircraft wing. C-16
74. CRM aircraft lift and drag forces recorded as the drone approached the aircraft. C-17
75. Axis system used for the drone. C-17
76. Drone aerodynamic forces (a) and moments (b) plotted with respect to relative distance along with average values. C-18
77. Displacements (a) and angular displacements (b) experienced by the drone as it traveled towards the CRM aircraft wing. C-19
78. Velocities (a) and angular velocities (b) experienced by the drone as it traveled towards the CRM aircraft wing. C-20
79. CRM aircraft lift and drag forces recorded as the drone approached the aircraft. C-21
80. Axis system used for the drone. C-21
81. Drone aerodynamic forces (a) and moments (b) plotted with respect to relative distance along with average values. C-22
82. Displacements (a) and angular displacements (b) experienced by the drone as it traveled towards the CRM aircraft. C-23
83. Velocities (a) and angular velocities (b) experienced by the drone as it traveled towards the CRM aircraft. C-24
84. CRM aircraft lift and drag forces recorded as the drone approached the aircraft. C-25
85. Axis system used for the drone. C-25
86. Drone aerodynamic forces (a) and moments (b) plotted with respect to relative distance along with average values. C-26
87. Displacements (a) and angular displacements (b) experienced by the drone as it traveled towards the CRM aircraft. C-27

88. Velocities (a) and angular velocities (b) experienced by the drone as it traveled towards the CRM aircraft horizontal stabilizer. C-28
89. CRM aircraft lift and drag forces recorded as the drone approached the aircraft. C-29
90. Axis system used for the drone. C-29
91. Drone aerodynamic forces (a) and moments (b) plotted with respect to relative distance along with average values. C-30
92. Displacements (a) and angular displacements (b) experienced by the drone as it traveled towards the CRM aircraft. C-31
93. Velocities (a) and angular velocities (b) experienced by the drone as it traveled towards the CRM aircraft horizontal stabilizer. C-32
94. CRM aircraft lift and drag forces recorded as the drone approached the aircraft. C-33
95. Axis system used for the drone. C-33
96. Drone aerodynamic forces (a) and moments (b) plotted with respect to relative distance along with average values used in the UDF. C-34
97. Displacements (a) and angular displacements (b) experienced by the drone as it traveled towards the CRM aircraft. C-35
98. Velocities (a) and angular velocities (b) experienced by the drone as it traveled towards the CRM aircraft horizontal stabilizer. C-36

## LIST OF TABLES

Table	Page
1. Summary of impact conditions	6
2. Summary of impact scenarios.	9
3. Boundary and operating conditions at a Mach number of 0.85.	14
4. Boundary and operating conditions at a Mach number of 0.30.	14
5. Release location of the DJI drone in the vertical direction with respect to the CRM leading edge of the wing or horizontal stabilizer.	20
6. Required vertical displacement of DJI drone to avoid collision with CRM.	22
7. Comparison of the lift coefficients obtained from the wind tunnel experimental and CFD studies done by NIAR and ERAU.	31
8. Comparison of the drag coefficients obtained from the wind tunnel experimental and CFD studies done by NIAR and ERAU.	31
9. A summary of displacements of the drone for all impact scenarios.	47
10. A summary of angular displacements of the drone for all impact scenarios.	49
11. Mesh Specifications for the flow around CRM wing at a Mach number of 0.85.	A-2
12. Mesh Specifications for the analysis of the impact scenarios at a Mach number of 0.3.	A-4
13. Mesh Specifications for the moving DJI drone.	A-6

## LIST OF ACRONYMS

1D	One-Dimensional
2D	Two-Dimensional
3D	Three-Dimensional
AoA	Angle of Attack
AMR	Adaptive Mesh Refinement
CAD	Computer-Aided Design
CFD	Computational Fluid Dynamics
CG	Center of Gravity
CRM	Common Research Model
DFBI	Dynamic Fluid Body Interaction
DOF	Degree of Freedom
ERAU	Embry-Riddle Aeronautical University
FAA	Federal Aviation Administration
FEA	Finite Element Analysis
IC	Impact Condition
IL	Impact Location
IS	Impact Scenario
NASA	National Aeronautics and Space Administration
NIAR	National Institute for Aviation Research
sUAS	small Unmanned Aircraft Systems
UAS	Unmanned Aircraft Systems

## 1. INTRODUCTION

### 1.1 BACKGROUND

The employment of unmanned aircraft systems (UAS) is becoming prominent in the aviation industry. The applications of UAS have been constantly expanded during the last two decades with increasing utilization of such systems in military, security, agricultural operations, and entertainment operations [1]. The UAS and their operating components are also revolutionizing our approaches in flight and global environment explorations. The UAS has benefited the public sector and several organizations. The potential for increasing commercial applications has been noticed, with significant investments estimated in the next few years [2]. It is estimated that the market for UAS can grow significantly to \$82.1 billion by the end of 2025 [3], which could lead to an increase in accidents between aerial vehicles [4].

A broad distinction can be made between the smallest unmanned aircraft flying close to the ground, usually within direct line of sight of the operator, and larger systems that can operate beyond visual range and at higher altitudes. UAS offer the promise of another level in a hierarchy of sampling; by flying at lower elevations than other aircraft and satellites, they would provide visual imagery at a more localized and biologically distinguishable level. The relatively small and low-cost drones can record and store onboard data. These merits make UAS a valuable tool for wildlife management with profound advantages in viewing animals in open habitats. These features potentially reduce errors in the aerial estimation of wildlife populations often caused by variation in survey path, long time over the survey target, and observer fatigue [5]. Also, small UAS (sUAS) offer a reduced potential for disturbance to wildlife populations.

Potential advantages of UAS include lower operating costs, safety for the operator, consistency of flight path, and image acquisition. The easy-to-use feature, uncomplicated launch, and land without runways can lower the barriers to many public and government users [6]. This class of users includes all individuals or groups of citizens operating UAS for recreation, competition, or any other private endeavor. However, the significant growth in the use of UAS can be a considerable concern for the safe operations of airports worldwide [7]. Despite the popularity of UAS, they raise safety concerns to the public and airspace users from airlines, air freight service providers to general aviation pilots. The expansion of UAS applications can lead to the drones trespassing the restricted national airspace, highlighting the UAS operational needs and the significant issues associated with those operations. This technology is still considered far less mature than manned aviation [8], especially with higher potential risks to the pilot and passengers at low altitudes. Despite extensive efforts to improve safety, small aircraft crashes are a leading cause of work-related mortality among wildlife researchers [9]. The Federal Aviation Administration (FAA) recently released proposed rules for unmanned aircraft weighing less than 55 pounds and flown within visual line of sight [10].

The impact of drones has also gained a major attraction in different industries. However, extensive growth in the drones' public use has led to an increase in aerial accidents. This issue has increased the motivation for finite element analysis (FEA) and computational fluid dynamics (CFD) analysis of the collision between drones and manned aircraft. The results from such studies can provide important information regarding the occurrence and severity of the incidents. The objective of the current study is to investigate the trajectory of the drone approaching the National Aeronautics and Space Administration (NASA) Common Research Model (CRM) aircraft. In the current study,

different impact scenarios involving different impact locations and conditions were considered to investigate the collision and deflection of the drone from its initial direction extensively.

## 1.2 PROJECT SCOPE

The airborne collision between a UAS and a manned aircraft is a concern to the public and government, leading to ongoing studies to assure an appropriate level of safety. In this regard, the collision of rigid UASs with aircraft structures and propulsion systems has been investigated in the last decade. This research evaluates the possibility of deflection from the collision between a sUAS with a commercial CRM aircraft under a few impact scenarios. The results presented in this report will focus on the variation in the trajectory of the DJI drone based on reaction forces and moments exerted on the drone. The current analysis was performed in several steps, starting with a validation of the flow parameters such as lift and drag coefficients on the CRM wing compared to the experimental wind tunnel data presented in [11]. In addition, a cross-verification of data obtained for two impact scenarios, investigated by both Embry Riddle Aeronautical University (ERAU) and the National Institute for Aviation Research (NIAR), was done using different CFD codes. Subsequently, additional impact scenarios were studied for different critical locations and flow conditions, focusing on the DJI drone's collision with CRM aircraft wing and horizontal stabilizer. Findings from this research can help understand pressure and velocity flow fields and the displacements of the DJI drone from its prescribe motion (without the influence of flow forces) at the point of collision for different impact scenarios.

## 1.3 TARGET DEFINITION

The NASA CRM was selected for the current study. This model consists of a contemporary supercritical transonic wing and a fuselage representative of a widebody commercial transport aircraft [11]. The CRM is designed for a cruise Mach number of 0.85 and a corresponding design lift coefficient of  $C_L = 0.5$ . The surface area and characteristic lengths of the CRM wing were  $383.69 \text{ m}^2$  and  $7.005 \text{ m}$ . Experimental aerodynamic investigations of the NASA CRM have been conducted in several studies [12], including the NASA Langley National Transonic Facility and the NASA Ames 11-ft wind tunnel [13]. The extensive model description of CRM can be found in [14].

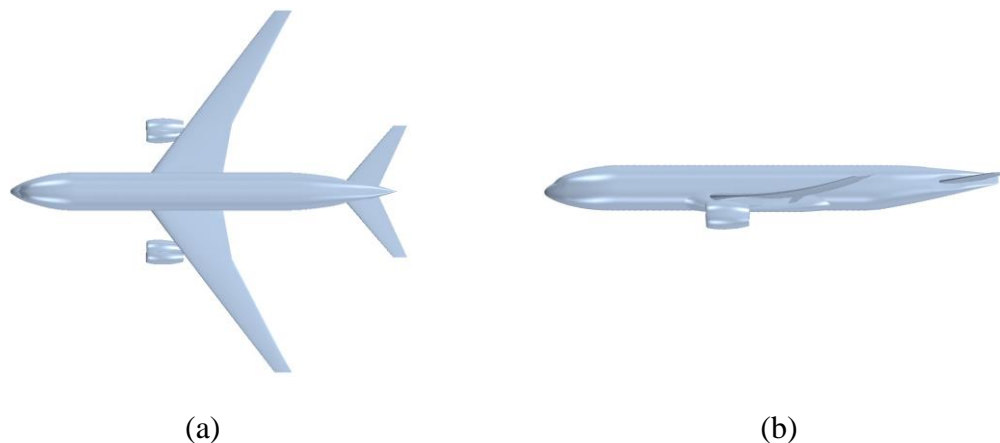


Figure 1. NASA Common Research Model: a) top view, b) side view.

For some preliminary analyses in this study, only the CRM wing was selected as the target, while for the impact scenarios between the DJI drone and CRM horizontal stabilizer, a half model of the CRM was introduced in the simulations. This was due to the interactions, caused by the pressure flow field around the CRM wing and fuselage, with the DJI drone moving towards and colliding with the horizontal stabilizer. Additional information is presented in section 2.2.

#### 1.4 PROJECTILE DEFINITION

The DJI Phantom family was found as one of the most popular UAS, according to an investigation performed by Montana State University [15]. The Phantom 3 Standard is a 1.2 kg (2.7 lb.) quadcopter with a diagonal length of 350 mm (13.8 in) and a maximum horizontal speed of 16 m/s, common in recreational activities and commercial aerial photography [16]. This DJI drone has a maximum service ceiling of 6000 m (19,685 ft), which is the maximum altitude above the mean sea level at which the UAS can operate. Additionally, the DJI Phantom 3 Standard edition is accessible to the public; therefore, it was selected as the UAS DJI drone model for the current study, as shown in Figure 2(a), obtained from [15], [16]. In Figure 2(b), the three-dimensional Computer-Aided Design (CAD) model of the selected DJI drone is shown.

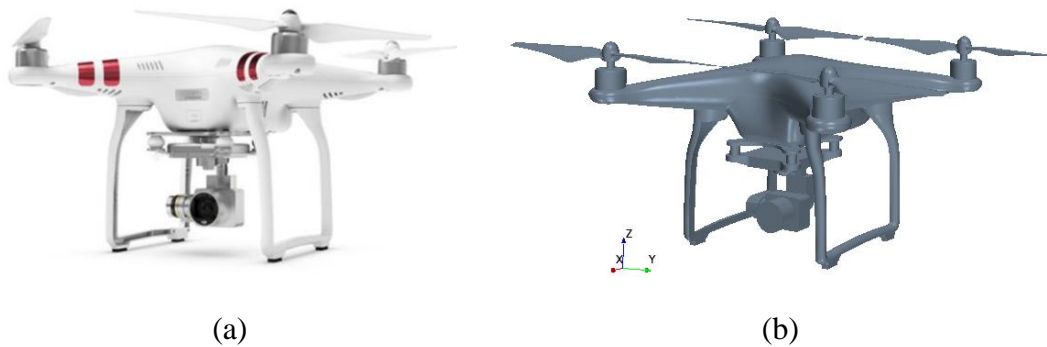


Figure 2. a) The DJI Phantom 3 model obtained from [15], [16], b) three-dimensional CAD model used in the current computational analysis.

A preliminary investigation done by NIAR on 3D vs. 2D flow analysis showed that three-dimensional flow analysis is more appropriate for this study, as it can provide in-depth information about the flow structures in the regions of interest and accurate results of flow-induced forces and moments on the DJI drone. These flow parameters are the key factors that can lead to the deflection of the DJI drone from its trajectory towards the CRM aircraft. In this study, the rotors were aligned and assumed to be stationary. Figure 3 shows the dimensions of the DJI drone used in the current computational analysis.

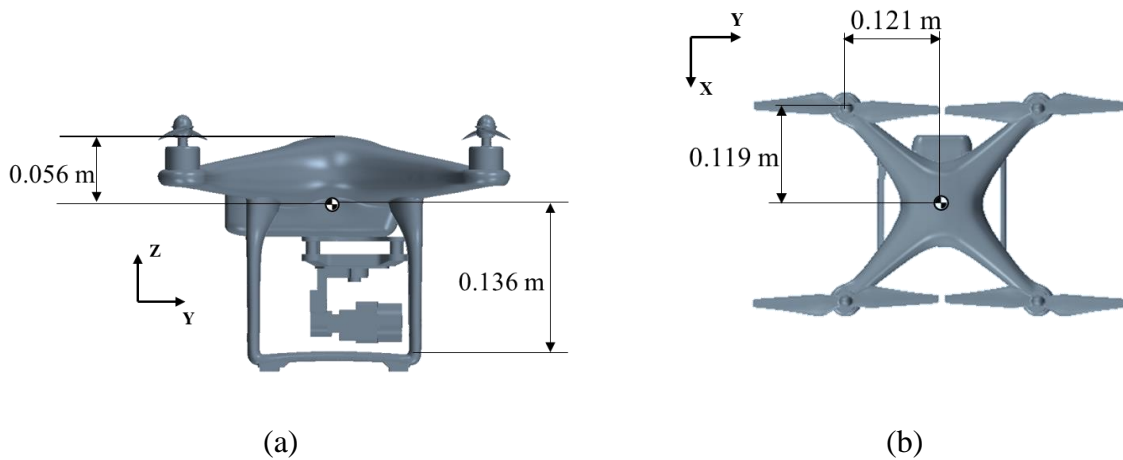


Figure 3. The dimensions of the DJI Phantom 3 model.

## 1.5 IMPACT SCENARIOS

In collaboration with NIAR, several impact scenarios between the DJI drone and CRM aircraft were defined for this study. The focus was to determine the impact conditions that result in higher chances of DJI drone deflection prior to the point of its collision with CRM aircraft wing and horizontal stabilizer. The main differences among the impact scenarios presented in this report were the point of collision (CRM aircraft wing or horizontal stabilizer), the approach speed at the initial distance, and the initial release location of the drone with respect to the point of collision. The approach speed was defined based on two conditions of the DJI drone (a) hovering and (b) moving towards the target, while the effect of the initial release location of the drone was investigated if the drone was aligned with the point of collision.

### 1.5.1 Impact Conditions

All analyses were conducted for a total of four impact conditions, investigating different factors that can influence the trajectory of the DJI drone. It should be noted that, in this list, we skipped the impact conditions 4 and 5, which were the focuses in a parallel study conducted by NIAR. The impact conditions were determined according to the approach speeds, angle of attack (AoA) of the CRM aircraft, and the angle defined for the DJI trajectory towards the point of collision.

#### 1.5.1.1 Impact Condition 1 (IC1):

In this impact condition, the DJI drone was specified at a hovering state with zero velocity, while the CRM aircraft approached the drone at a fixed speed of 102.889 m/s (200 knots) and a 0° angle of attack.

#### 1.5.1.2 Impact Condition 2 (IC2):

In this impact scenario, the effect of the moving condition of the DJI drone on its trajectory was analyzed. The CRM aircraft approached the drone at a fixed speed of 102.889 m/s (200 knots) and 0° angle of attack (AoA), while the drone approached the aircraft at a constant velocity of 25.722 m/s (50 knots).

#### 1.5.1.3 Impact Condition 3 (IC3):

In this impact condition, the effect of the aircraft angle of attack on the flow around the DJI drone close to the region of the collision was investigated. The CRM aircraft approached the drone at a fixed speed of 102.889 m/s (200 knots) and a 5° angle of attack (AoA), while the drone approached the CRM aircraft at a constant velocity of 25.722 m/s (50 knots). This impact scenario studied the effect of the AoA on the forces and moments exerted on the DJI drone leading to potential deflection of the drone from the point of collision.

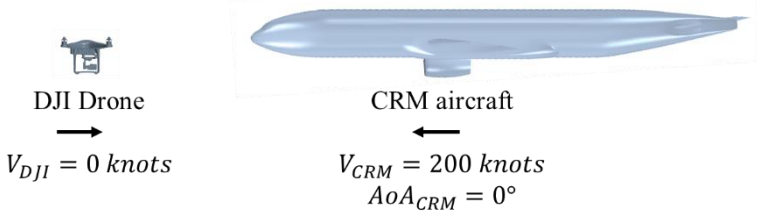
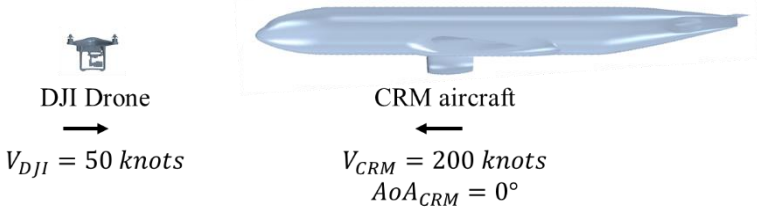
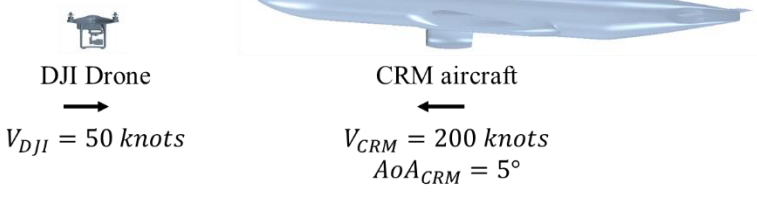
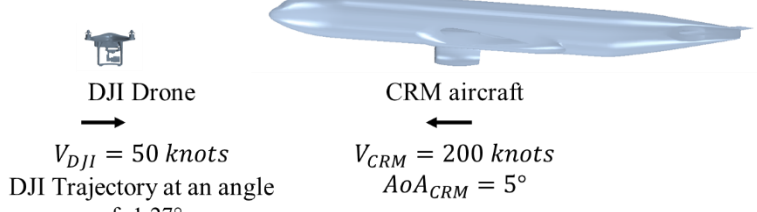
#### 1.5.1.4 Impact Condition 6 (IC6):

Impact Condition 6 also refers to the study of aircraft AoA on the drone trajectory; however, the drone approaches the CRM horizontal stabilizer with an angle. The drone approached the aircraft at 25.722 m/s (50 knots) velocity while it had an initially defined inclined trajectory of 1.27° downward towards the CRM horizontal stabilizer. The aircraft approached the drone with a speed of 102.889 m/s (200 knots) while flying at an AoA of 5°.

#### 1.5.1.5 Summary of the Impact Conditions:

A summary of the impact conditions can be found in Table 2. In this table, detailed information regarding the drone and aircraft velocities, the AoA, and directions of the CRM and DJI motions are provided. The impact conditions were used in combination with impact locations to create the impact scenarios for the current investigations.

Table 1. Summary of impact conditions

Impact Condition (IC)	Depiction
IC1	
IC2	
IC3	
IC6	

### 1.5.2 Impact Location

The CRM aircraft wing and horizontal stabilizer were selected as the locations of the possible impact of the drone on the aircraft. The exact locations were defined by the spanwise distance of the drone away from the symmetry plane at the time of release. Additionally, the center of gravity (CG) of the drone was aligned with the leading edges of the wing (CRM aircraft) or the Horizontal Stabilizer (CRM aircraft), as shown in Figure 4, except in some particular cases that the CG of the DJI drone was placed above or below the CRM wing leading edge. Note that Figure 4 is out of scale to clearly show the prescribed trajectory of the drone to the points of collision.

It should be noted that, in this list of impact locations, we skipped impact location 2, which was the focus in a parallel study conducted by NIAR.

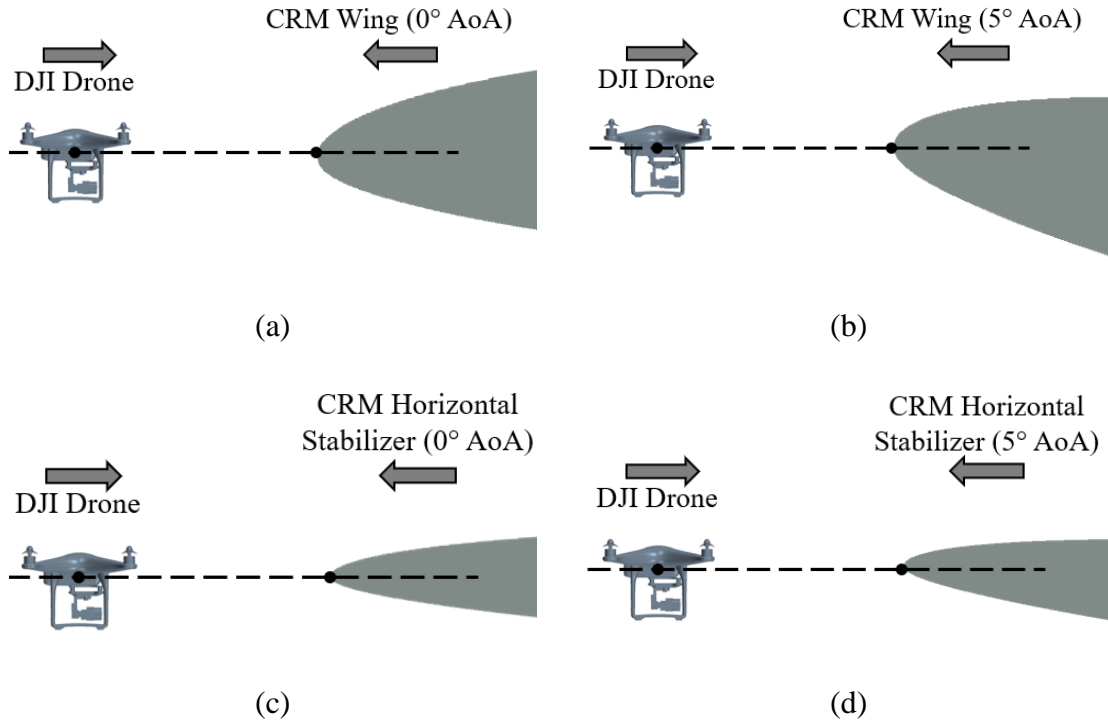


Figure 4. Side view showing the placement of the drone with respect to (a) CRM aircraft (0° AoA) (b) CRM aircraft (5° AoA) (c) HL-CRM aircraft (d) CRM Horizontal Stabilizer (0° AoA) and (e) CRM Horizontal Stabilizer (5° AoA).

### 1.5.2.1 Impact Location 1

The first impact location was based on the critical impact case identified in the previous phase [16]. For the first impact location, the drone was placed at a spanwise distance of 16.8 m (55.12 ft) away from the symmetry plane of the CRM aircraft, Figure 6. Some special cases were also considered for which the DJI drone was initially placed 5 cm (0.164 ft) and 15 cm (0.492 ft) above and below the CRM leading edge. For these special cases, additional notations were added to the definition of impact location as follows: 5 cm above (U1), 5 cm below (D1), 15 cm above (U2), and 15 cm below (D2).

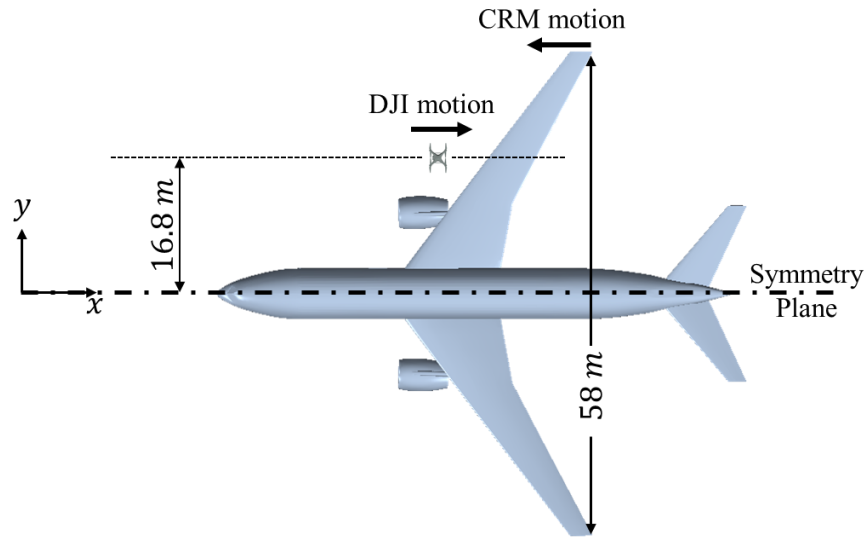


Figure 5. Spanwise location of the drone at IL1 as it approaches the CRM aircraft.

### 1.5.2.2 Impact Location 3

For impact location 3, the drone was placed at a spanwise distance of 6.25 m (20.5 ft) away from the symmetry plane of the CRM aircraft. This spanwise distance was selected to target the middle point of the horizontal stabilizer. As the drone travels towards the point of collision, it passes over the front wing closer to the fuselage. This could increase the chances of the vertical and spanwise displacements before reaching the horizontal stabilizer. Note that the initial vertical location of the drone CG was aligned with the leading edge of the CRM horizontal stabilizer.

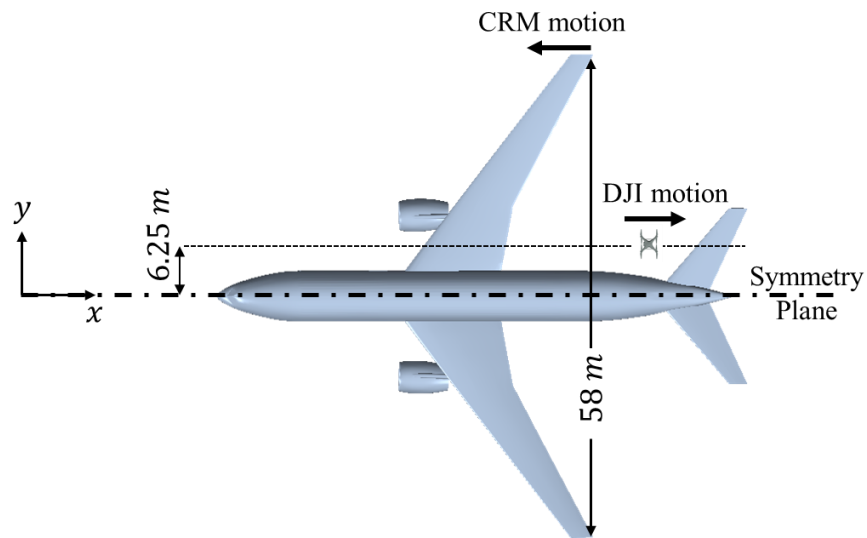


Figure 6. Spanwise location of the drone at IL3 as approaches the CRM horizontal stabilizer.

### 1.5.3 Summary

There were nine impact scenarios investigated in this study as a result of combined impact conditions (ICs) with the impact locations (ILs) discussed in 1.5.1 and 1.5.2. These impact scenarios (ISs) were determined to analyze the trajectory and the possibility of the deflection of the DJI drone. The results of each IS will illustrate whether the predefined impact conditions led to avoiding collision of the DJI drone with the aircraft or it would impact the aircraft. Table 3 provides the details of each impact scenario in this study.

Table 2. Summary of impact scenarios.

<b>Impact Scenario</b>	<b>Impact Scenario Definition</b>	<b>Aircraft Config.</b>	<b>Aircraft Velocity [m/s]</b>	<b>Aircraft Angle of Attack [degrees]</b>	<b>Drone Velocity [m/s]</b>	<b>Impact Location/ Spanwise Distance [m]</b>	<b>Aircraft Area of Interest</b>
1	IC1-IL1	CRM	102.889	0	0	16.80	wing
2	IC2-IL1	CRM	102.889	0	25.722	16.80	wing
3	IC2-IL1U1	CRM	102.889	0	25.722	16.80	wing
4	IC2-IL1D1	CRM	102.889	0	25.722	16.80	wing
5	IC2-IL1U2	CRM	102.889	0	25.722	16.80	wing
6	IC2-IL1D2	CRM	102.889	0	25.722	16.80	wing
7	IC2-IL3	CRM	102.889	0	25.722	6.25	horizontal stabilizer
8	IC3-IL3	CRM	102.889	5	25.722	6.25	horizontal stabilizer
9	IC6-IL3	CRM	102.889	5	25.722	6.25	horizontal stabilizer

## 2. NUMERICAL METHODOLOGY

### 2.1 INTRODUCTION

The goal of the current study was to investigate the possibility of the drone's deflection from the collision point with the aircraft for different impact scenarios. As the drone travels towards the CRM aircraft, the drone interacts with the pressure flow field around the CRM, which can lead to an impact by the flow forces and moments displacing the DJI drone from its prescribed trajectory. The sufficient displacements, especially in the vertical direction from the leading edge of the CRM wing and horizontal stabilizer, is desirable.

Figure 7 shows the possibility of the collision between the DJI drone and CRM aircraft wing. The drone can be deflected in the spanwise and vertical directions due to the flow forces and moments. These deflections of the drone must be larger than specific lengths (collision cone) to completely avoid the collision with the CRM wing. The exact values for the sufficient displacements to avoid collision are illustrated (Table 6).

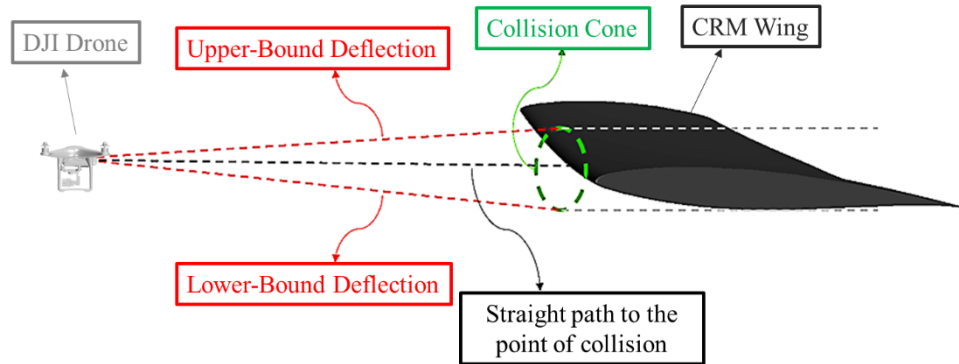


Figure 7. The methodology on the possibility of the collision between the DJI drone and CRM aircraft wing.

In Figure 8, the outline of the current study is illustrated. The current study started with a validation of the computational model using STAR-CCM+ (2020.1.1, CD-Adapco, Siemens PLM, Plano, TX, USA) compared to the wind tunnel experimental data provided in [17]. The impact scenarios were selected by targeting the CRM wing and horizontal stabilizer under different conditions such as at critical locations and speeds, the various initial vertical location of the drone, and angles of attack of  $0^\circ$  and  $5^\circ$ . The results of the two impact scenarios were cross-verified with the results obtained by NIAR to ensure accurate and reliable computational analysis.

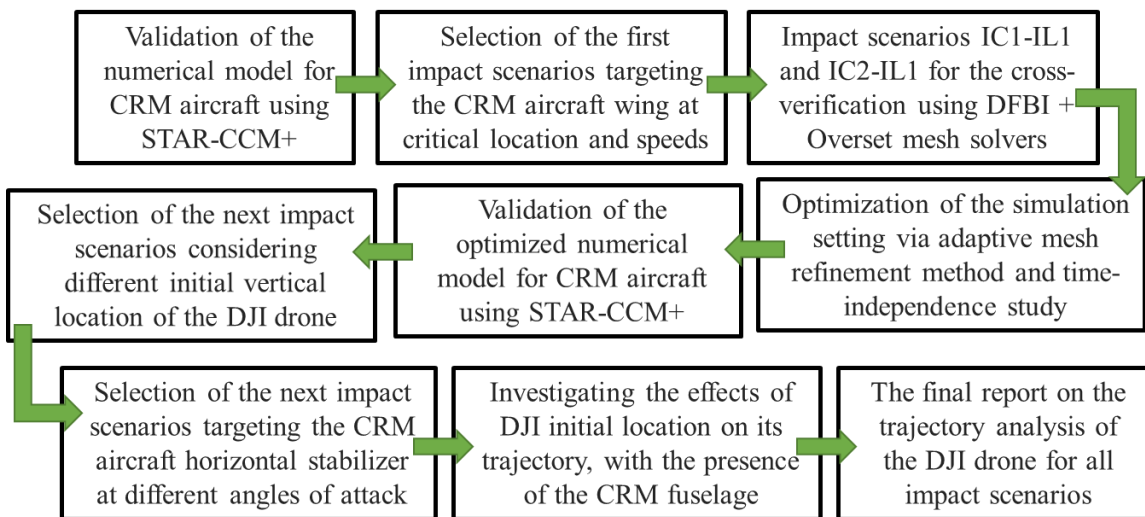


Figure 8. The outline of the current numerical study.

## 2.2 GEOMETRY

The geometry of the computational model in this study consists of a sphere-shaped flow domain with a diameter of 1500 m (4921 ft), the CRM aircraft, and the DJI drone as described in sections 1.3 and 1.4.

Figure 9a shows the computational model of the flow domain. Due to the symmetry of the model, half of the domain was considered with the symmetry X-Z plane. The boundary conditions are illustrated in detail in section 2.4.1.

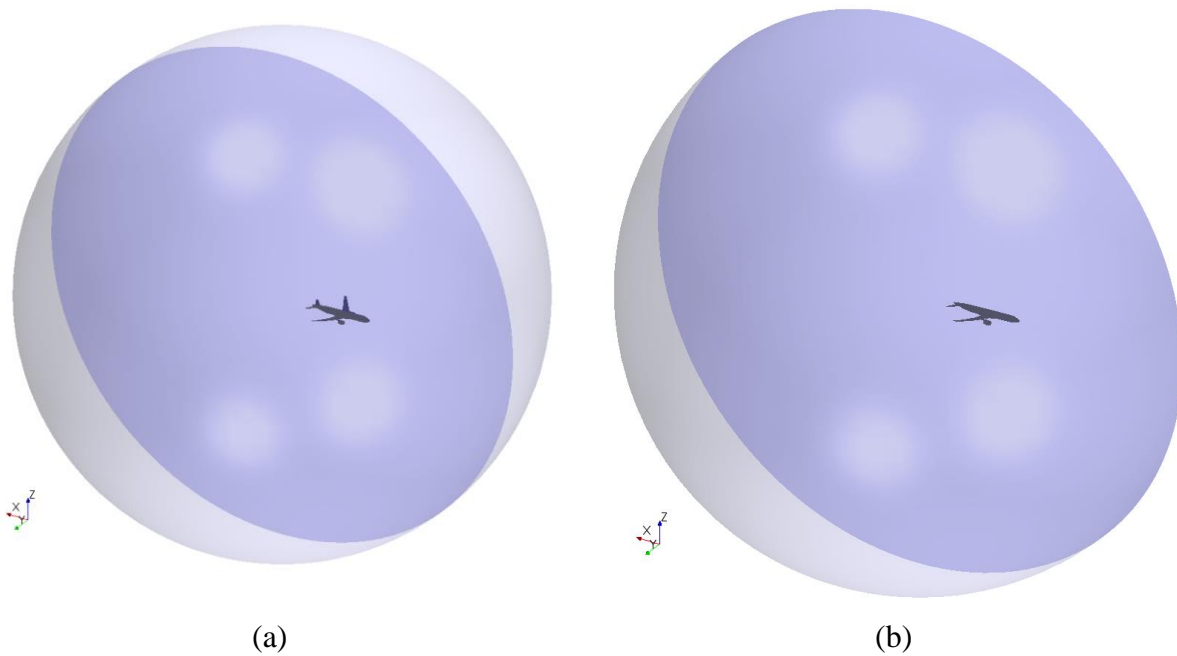
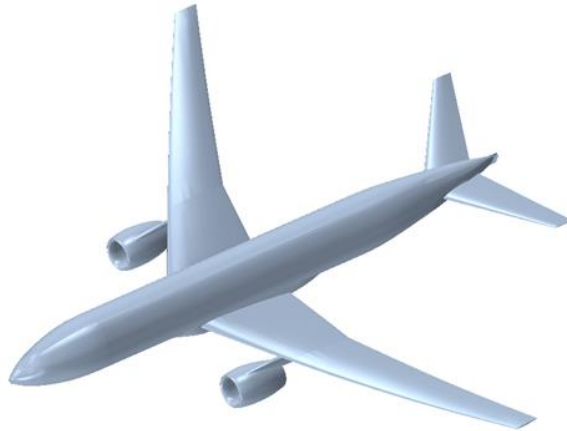


Figure 9. A computational model of the flow domain.

The analysis of deflection and trajectory of the drone for different impact scenarios required high computational resources and collaboration between ERAU and NIAR. To reduce the computation time, CFD studies were conducted for the simplified CRM aircraft models. Figure 10a shows the complete model of the CRM aircraft. For some impact scenarios targeting the collision of the DJI drone with the CRM aircraft wing, the simplified aircraft model consisting of the CRM wing was used in this study, Figure 10a. However, for the validation of the numerical solvers and the impact scenarios targeting the collision of the DJI drone with the CRM horizontal stabilizer, the half-model of the CRM aircraft was used. The half-model was sufficient due to the symmetry of the flow domain.

(a)  
Complete Model of  
CRM Aircraft



(b)  
Simplified CRM  
Aircraft Model



(c)  
A computational  
model of the CRM  
aircraft due to  
Symmetry



Figure 10. Computational models of the CRM aircraft.

## 2.3 MESH

The mesh is a representation of a discretized geometry of the flow domain. STAR-CCM+ solves the flow accurately at the mesh cell centers using the finite volume method (FVM). IN complex geometries with small gaps and curved edges (here, the DJI drone), a high-resolution mesh is required to completely attain the geometry. There are several tools, such as Surface Remesher, to improve the quality of the surfaces. As the accurate solution of pressure in the near-field volume around the DJI drone and CRM and flow forces on the surfaces is essential, a suitable mesh volume growth rate could control the density of the core mesh around them in this study. Mesh should be finer in these regions to increase the accuracy of the flow solution and capture the high flow fluctuations in those areas where high physical gradients are present. In the presence of moving objects (here, the DJI drone), some techniques and solvers such as overset mesh (section 2.4.4), dynamic fluid body interactions (section 2.4.3), and adaptive mesh refinement (section 2.4.5) were used to simulate the motion of the drone and the surrounding mesh precisely.

As a pre-processing step, the surface and volume mesh quality needs to be checked before running the simulations. The information regarding the specifications and quality check of the surface and volume mesh can be found in APPENDIX A.

## 2.4 NUMERICAL MODELS

The Simcenter STAR-CCM+ commercial solver was used to simulate a DJI drone's trajectory approaching a transport category aircraft represented by the CRM aircraft. A  $k-\omega$  SST and  $k-\varepsilon$  realizable two-layer turbulence models were selected for the validation and impact scenarios, resulted in similar conclusions. The governing equations were discretized using a coupled flow model with second-order central discretization in space and second-order implicit discretization in time. The air was modeled as a compressible ideal gas with the material properties described in section 2.4.1.

Additional information on the flow solvers is available in the following sections:

- Dynamic Fluid Body Interactions (DFBI): section 2.4.3.
- Overset Mesh: section 2.4.4.
- Adaptive Mesh refinement (AMR): section 2.4.5.
- Time Step: section 2.4.6.
- Assumptions: section 2.5.

### 2.4.1 Boundary and Operating Conditions

In this study, the flow domain was considered a freestream boundary that allowed us to model free-stream compressible flow conditions at a far-field boundary. It means that the flow at boundaries of the computational domain was under the assumption of irrotational, quasi-1D flow in the boundary-normal direction. This condition is suitable for the external flows with the boundary sufficiently far from the body (here, CRM and DJI drone). Mach number, working pressure, and static temperature were explicitly defined at the boundary using the freestream. In the current study, the analysis was done for two different operating conditions at (1) Mach number of 0.85 and (2) holding condition at a Mach number of 0.3.

### 2.4.1.1 Boundary and Operating Conditions at a Mach number of 0.85

Table 3 contains the information regarding the boundary and operating conditions at Mach number of 0.85, which were used to validate the pressure coefficients on the CRM wing.

Table 3. Boundary and operating conditions at a Mach number of 0.85.

Mach number	0.85	Reynolds number	$5 \times 10^6$
Inlet velocity	300 m/s	Static temperature	311 K
Pressure	4195 Pa	Density	$0.047 \text{ kg/m}^3$
Angle of Attack	$4^\circ$	Altitude	Wind tunnel experiments

### 2.4.1.2 Boundary and Operating Conditions at a Mach number of 0.30

Table 4 contains the information regarding the boundary and operating conditions at Mach number of 0.3, which were used to analyze different impact scenarios.

Table 4. Boundary and operating conditions at a Mach number of 0.30.

Mach number	0.30	Reynolds number (Simplified CRM)	$46.5 \times 10^7$
Inlet velocity	102.889 m/s	Reynolds number (DJI drone)	$4.11 \times 10^5$
Pressure	92500 Pa	Static temperature	283.2 K
Density	$1.138 \text{ kg/m}^3$	Angle of Attack	$0^\circ$ and $5^\circ$
DJI Velocity	102.889 m/s for IC1 128.611 m/s for IC2, IC3, and IC6	Aircraft Velocity	102.889 m/s (200 knots)
Altitude	Holding condition at 2500 ft		

In contrast with the simulations done for the validation, the analysis of the DJI drone trajectory moving towards the CRM aircraft was determined based on CRM velocity (applied to the inlet) and the speed of the moving drone. Therefore, an additional investigation was done to determine the exact Mach number for the known velocity of the CRM aircraft to apply to the boundary. To find the right value of the Mach number at the boundary, a probe line was created on the axial X-

direction from the boundary to the leading edge of the CRM wing. Figure 11 shows the speed of sound, velocity in the axial direction, and Mach number on this probe line. The velocity of 102.889 m/s (the CRM velocity) was obtained at a Mach number of approximately 0.30493, with the speed of sound at 337.418 m/s found at the operating conditions described in Table 4. This Mach number, along with the operating conditions, was set at the freestream boundary for all impact scenarios, analyzing the DJI drone trajectory towards the CRM wing and horizontal stabilizer.

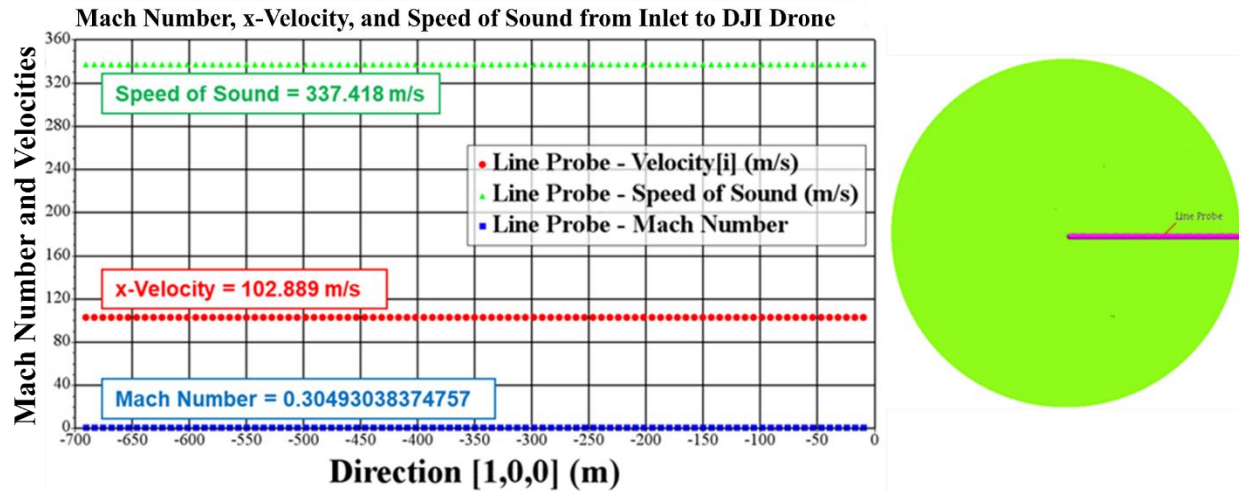


Figure 11. Boundary conditions (speed of sound, Mach number, and x-velocity) for analyzing the impact scenarios.

#### 2.4.2 Solver Setup

#### 2.4.3 Dynamic Fluid Body Interaction

The current analysis was performed by implementing dynamic fluid body interaction (DFBI) with an unconstrained six degree of freedom (6-DOF) rigid body motion. The DFBI module simulates the motion of a rigid body in response to pressure and shear forces the fluid exerts. Any additional forces acting on the moving object can also be defined. This module calculates the resultant forces and moments acting on the body due to all influences and solves the governing equations of rigid body motion to find the new position of the rigid body using a 6-DOF Solver. The 6-DOF Solver computes fluid forces, moments, and gravitational forces and integrates them over the surfaces of the 6-DOF bodies. The positive directions of these forces and moments are shown in Figure 4 and Figure 5. For rigid bodies, here, the DJI drone, it is sufficient to model the motion of the center of gravity (CG) of the moving body alone. The relative motion of any other part of the body can be extrapolated from the CG.

Moreover, it is necessary to know the moments of inertia of the body about a fixed reference point, which is normally the CG, before the translational and rotational motions can be computed. For time integration, the 6-DOF solver employs an implicit scheme with second-order accuracy. This order of accuracy is independent of the order of accuracy of the implicit unsteady solver.

It is important to note that the DFBI 6-DOF solver was frozen at the beginning of the simulation (up to 0.005 s, equivalent to the first 500 iterations) before the drone started to move. Then, the solver was enabled with 1-DOF translational motion in the flow direction without any influences

from the flow forces and moment. This approach helped flow became stable and reduced numerical error when the DJI drone moved. Without this approach, due to high momentums and numerical errors at the beginning of the motion, the unrealistic forces and moments could lead to inaccurate motion of the DJI drone. The DFBI 6-DOF was enabled after 500 iterations until the drone reached the point of collision. During this time, the drone could freely translate, rotate, and react to the forces and moments due to the changes in the pressure flow field around the drone and close to the CRM. For the drone travel distance of 90 m, the travel time differs for IC1 and IC2, is about 0.87 s and 0.73 s, respectively.

#### 2.4.4 Overset Mesh Method

Simulation of the moving objects (here, the DJI drone) was achieved by discretizing the computational domain with two different meshes (the flow domain as a background within a lower priority region and DJI drone as the moving mesh within the higher priority region) that overlap each other, Figure 12. This approach is known as overset mesh, which is the most useful in problems involving moving bodies. The overset mesh around the DJI drone was created using the overset mesh boundary, which is the outer boundary of the overset region that is expected to be coupled with the background mesh.

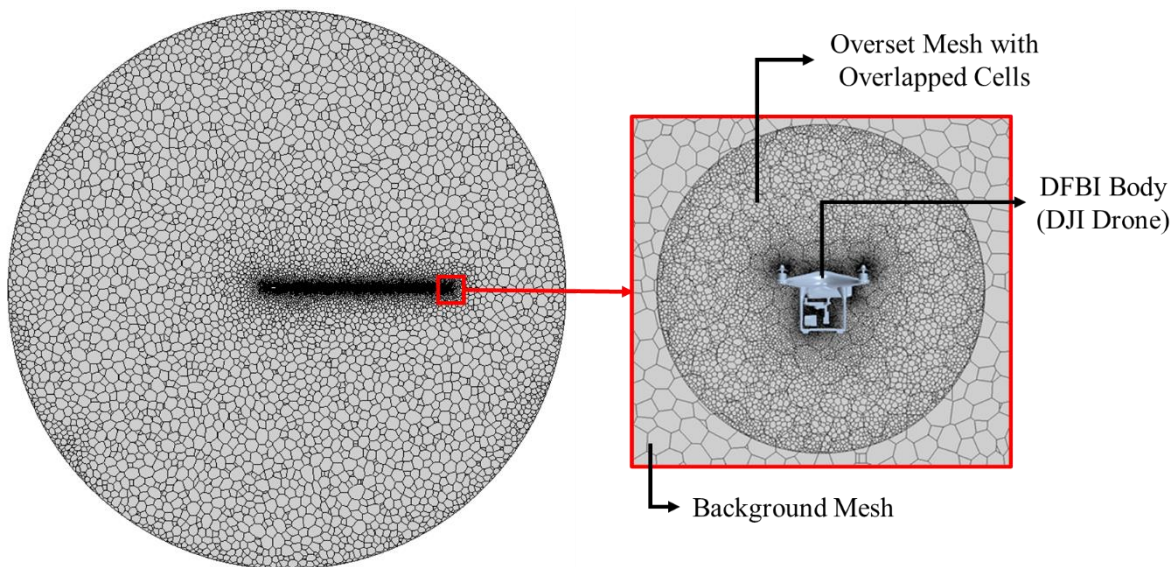


Figure 12. Overset mesh around the DJI drone.

It is essential to generate 4-5 mesh cells between the drone and the overset mesh boundary, common in both background and overset mesh regions. The cell size in the background mesh (flow domain) was adapted to the mesh size around the drone in the overset region within the zone of its motion. The background mesh is coarser than the overset mesh around the drone but sufficient to captures the basic flow characteristics such as velocity and absolute pressure around the CRM wing and horizontal stabilizer.

#### 2.4.5 Adaptive Mesh Refinement

Adaptive Mesh Refinement (AMR) refined the mesh cells around the drone dynamically based on adaptive mesh criteria, and accordingly, it automatically interpolates the flow solution quantities

to the adapted mesh. The refinement occurred during the simulation run and is an integral part of the solution process. In this case, the background mesh in the flow domain is refined according to the overset region around the drone. Overset mesh refinement module was used to adapt the cell size of the lower priority region in the background to the cell size of a higher priority region close to the DJI drone.

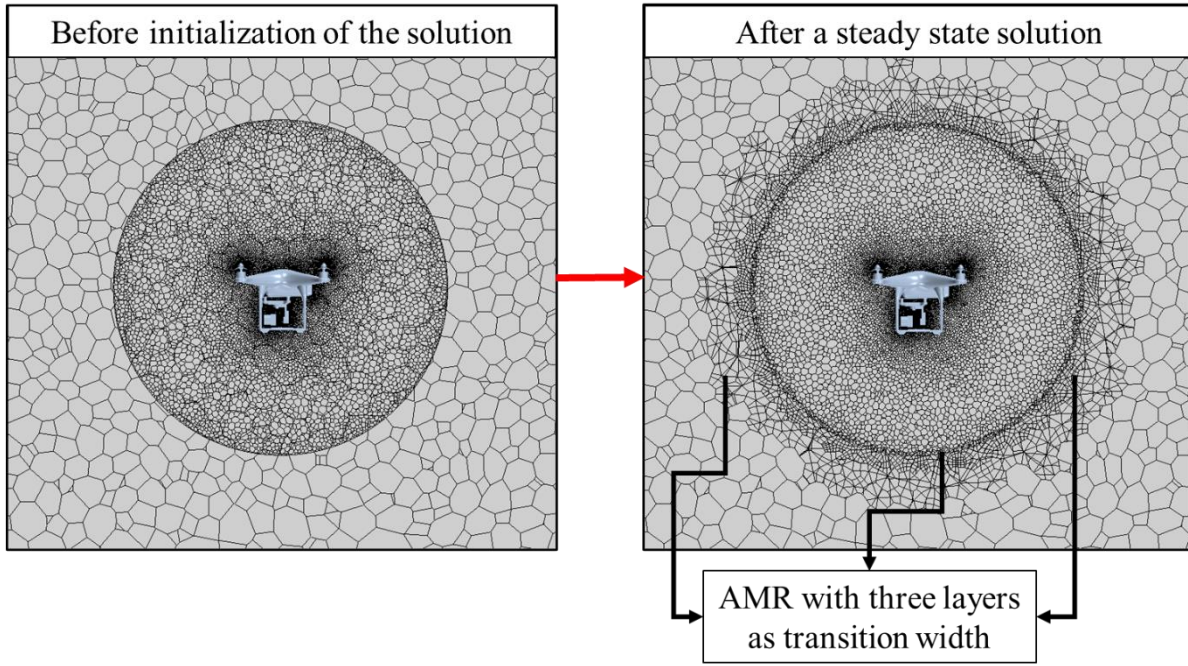


Figure 13. Mesh transition between the overset mesh and background mesh using adaptive mesh refinement (AMR).

Although you can provide a coarser mesh for an AMR simulation, the initial mesh must be able to capture the basic flow characteristics. The adaptive mesh model solver:

- Combines all the calculated adaptive mesh criteria for each cell based on the current flow solution to derive the final adaption request with the priorities described above.
- Applies the mesh adaption by refining the cells according to the final adaption request.
- Repartitions the domain due to the change in the cell connectivity induced by AMR.
- Interpolates the flow solution to the adapted mesh.
- Re-initializes the interfaces.

AMR improves the volume mesh to capture the desired flow features, but it does not eliminate the need for careful initial mesh.

#### 2.4.6 Time Steps

The selection of the right time step can affect the accuracy of the results and convergence of the solution, especially when complex physics such as DFBI and overset mesh modules are used. For second-order implicit time integration, the maximum movement of the overset mesh (DJI drone) should not exceed half the smallest cell size in the overlapping meshes. Additionally, the time step was determined to keep the convective courant number below 1, which helped improve the

stability of the flow solution. In this study, the time step was set to  $10^{-5}$  s to ensure the convergence of the solution. However, the time step was increased to  $10^{-4}$  after implementing the adaptive mesh refinement module. In Figure 14, the results of the forces exerted on the drone were investigated for the impact scenario IC2-IL1 for different time steps of  $10^{-5}$  s and  $10^{-4}$  s. This time-independence study showed that similar results were obtained for the analysis with the time of step of  $10^{-4}$  s.

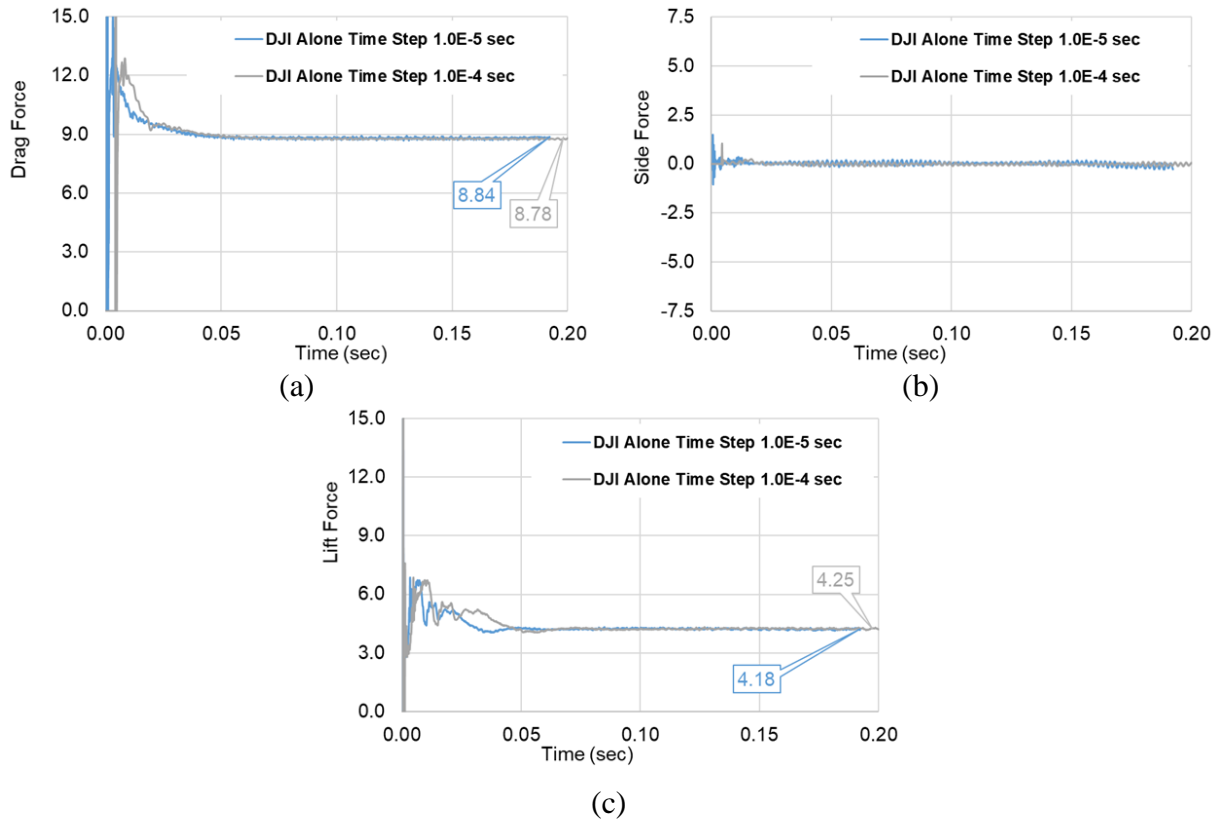


Figure 14. A comparison of the forces on the drone for the time steps of  $10^{-5}$  s and  $10^{-4}$  s.

As a result of implementing the adaptive mesh refinement method in the simulations with a larger time step of  $10^{-4}$  s, a reduction of about 30% and 75% was observed in the number of mesh cells and simulation runtime, respectively. The simulation runtime was reduced from about 90 hours for the drone's horizontal displacement of 15 m to about 122 hours for the horizontal displacement of 90 m. These results remarkably helped NIAR and ERAU increase the speed of the current analysis to investigate several impact scenarios.

## 2.5 ASSUMPTIONS

The assumptions can be categorized into three groups related to the flow domain, the DJI drone, and the CRM aircraft. Here is the list of assumptions in this study:

Air:

- Air was assumed to be an ideal gas.
- Idea gas law expresses that the density of the compressible flow is a function of temperature and pressure.

- Newtonian air flow, which means that the relation between the shear stress and shear rate is linear.
- Air flow was defined as an irrotational, quasi-1D flow in the boundary-normal direction.
- Due to symmetry and reducing computational costs, half of the flow domain and CRM aircraft were included in the studies.
- In some impact scenarios, only the CRM aircraft wing was included in the analysis.

DJI drone:

- The rotors of the drone were aligned and stationary, as shown in Figure 3.
- The DJI drone was assumed to be a rigid-wall moving object.
- Fluid-structure interaction, which could predict the deformations resulting from the collision between the drone and CRM aircraft, was not included in this study.

CRM aircraft:

- The motion of the CRM aircraft was simulated as the airflow speed at the far-field boundary.
- The CRM aircraft was assumed to have rigid walls.
- The CRM turbine engine was not included in this study.
- The CRM speed was constant.
- The impact scenarios were simulated for the holding conditions at an altitude of 2500 ft.
- Due to the high approaching speeds of the CRM and DJI drone, it was assumed that the pilot was not able to react to the interactions and possibility of collision.

## 2.6 DRONE RELEASE LOCATION

The release location of the DJI drone was determined in all three directions. The spanwise release location of the drone with respect to the CRM aircraft wing and horizontal stabilizer were set at 16.8 m and 6.25 m from the symmetry plane, as shown in Figure 6 and Figure 6, respectively. In the following sections, the release locations of the drone in the vertical and horizontal directions are explained.

### 2.6.1 Release (Vertical) Location

The release locations of the drone for different impact scenarios and in a vertical direction with respect to the aircraft wing and horizontal stabilizer are shown in Table 5.

Table 5. Release location of the DJI drone in the vertical direction with respect to the CRM leading edge of the wing or horizontal stabilizer.

	<p>— — — Aligned with CRM Leading Edge</p> <p>- - - Aligned with DJI Drone CM</p>
<p>(a) IC2-IL1</p> <p><math>Y_{\text{Wing-Drone}} = 0 \text{ mm}</math></p>	
<p>(b) IC2-IL1U1</p> <p><math>Y_{\text{Wing-Drone}} = +50 \text{ mm}</math></p>	
<p>(c) IC2-IL1D1</p> <p><math>Y_{\text{Wing-Drone}} = -50 \text{ mm}</math></p>	
<p>(d) IC2-IL1U2</p> <p><math>Y_{\text{Wing-Drone}} = +150 \text{ mm}</math></p>	
<p>(e) IC2-IL1D2</p> <p><math>Y_{\text{Wing-Drone}} = -150 \text{ mm}</math></p>	
<p>(f) IC2-IL3</p> <p><math>Y_{\text{Stabilizer-Drone}} = 0 \text{ mm}</math></p>	
<p>(g) IC6-IL3</p> <p><math>Y_{\text{Stabilizer-Drone}} = 0 \text{ mm}</math></p>	

For IC1-IL1 and IC2-IL1 impact scenarios, the drone was aligned with the CRM aircraft wing; i.e., the vertical distance from the drone CG to the leading edge of the aircraft wing was determined as 0 m. In the special cases of the IC2-IL1, the drone CG was placed at 5 cm and 15 cm below and

above the leading edge of the aircraft wing. This analysis was done to understand the effects of the initial placement of the DJI drone on its trajectory up to the point of collision.

In the other impact scenarios, the collision between the drone and CRM horizontal stabilizer was investigated. In these impact scenarios, IC2-IL3 and IC3-IL3, the drone CG was aligned with the leading edge of the horizontal stabilizer, except for IC6-IL3, for which the drone was initially placed 2 m (6.56 ft) above the leading edge, as shown in Figure 15. It was due to an early collision of the drone and CRM front wing with AoA of  $5^\circ$  before the drone reaches the horizontal stabilizer.

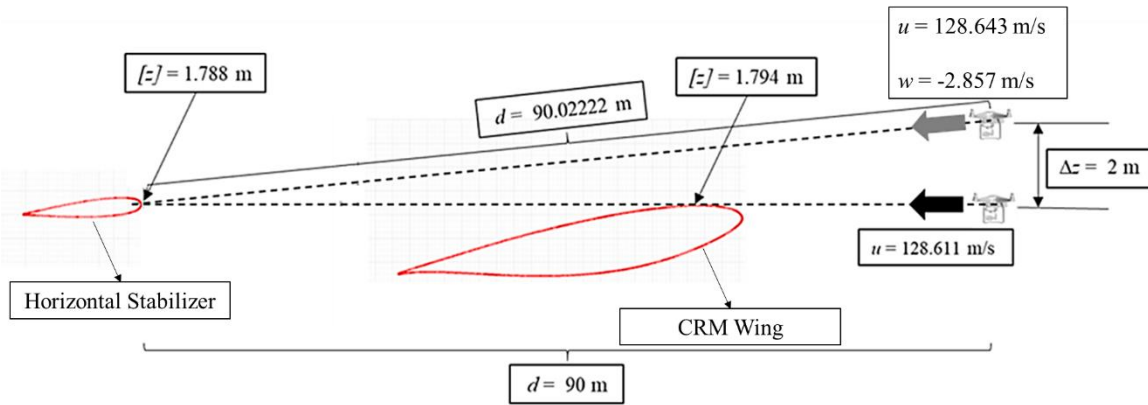


Figure 15. Release location of the DJI drone for impact scenario IC6-IL3.

In Figure 15,  $u$  and  $w$  are the drone velocities in the horizontal and vertical directions, respectively, according to the sign convention described in Figure 4. It can be noted that the  $z$ -coordinates of the top surface of the CRM wing and the leading edge of the horizontal stabilizer are at 1.794 m and 1.788 m, respectively, with respect to the origin in the domain. In IC3-IL3, the drone CG was initially aligned with the leading edge of the horizontal stabilizer with an AoA of  $5^\circ$ ; however, the drone was not impacted significantly to deflect sufficiently and move over the aircraft wing. Therefore, in IC6-IL3, the drone was initially placed 2 m in the positive vertical direction and approached the CRM horizontal stabilizer at different speeds in vertical and horizontal directions, as described in Table 2.

The main focus of this study was on the displacement of the drone in the vertical direction. It should be noted that the displacement of the drone in a horizontal direction represents the distance that the drone travels to the point of collision. Additionally, the displacement in  $Y$ -direction (Figure 4) should be very large, beyond the distance between the point of collision and the wing or horizontal stabilizer tips. Therefore, the displacement of the drone in vertical direction was determined as an indicator to determine sufficient deflection from the point of collision. In Figure 16, the distances from the leading edges of the CRM wing and horizontal stabilizer to the top surfaces are shown. In Table 6, the required vertical displacement of the drone is identified for all impact scenarios to prevent the collision.

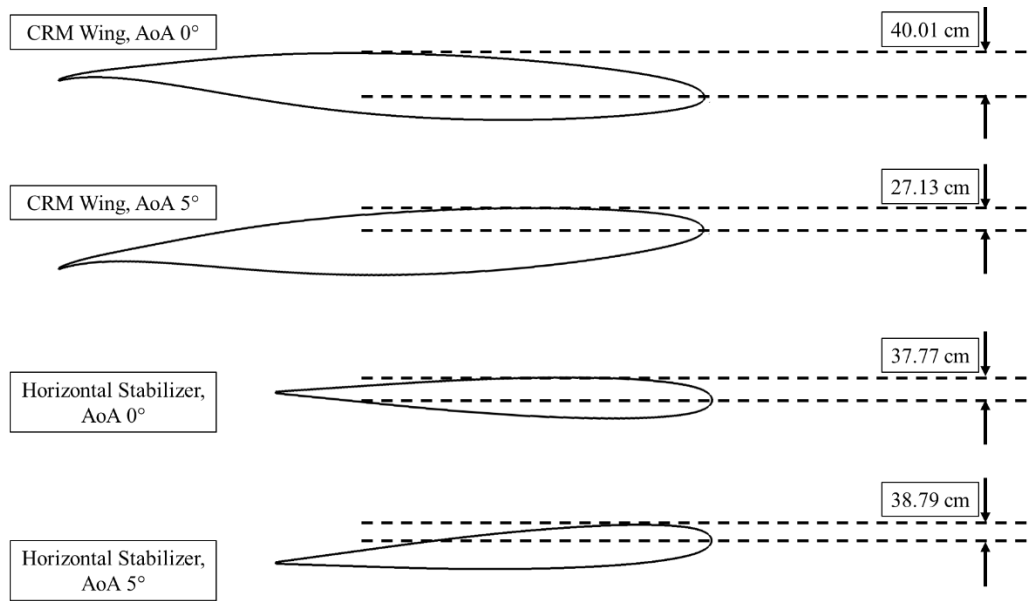


Figure 16. Distances from the leading edges of the CRM wing and horizontal stabilizer to the top surfaces.

Table 6. Required vertical displacement of DJI drone to avoid collision with CRM.

<b>Aircraft Geometry</b>	<b>Impact Scenario</b>	<b>Aircraft Angle of Attack [degrees]</b>	<b>Initial Z-Location Relative to Leading Edge [cm]</b>	<b>Required Vertical Displacement [cm]</b>
CRM	IC1-IL1	0	0	53.61
CRM	IC2-IL1	0	0	53.61
CRM	IC2-IL1U1	0	5.0	48.61
CRM	IC2-IL1D1	0	-5	58.61
CRM	IC2-IL1U2	0	15.0	38.61
CRM	IC2-IL1D2	0	-15	68.61
CRM	IC2-IL3	0	0	51.37
CRM	IC3-IL3	5	0	Early collision with CRM wing
CRM	IC6-IL3	5	200	0 to 186.4 (in negative vertical direction)

In Table 6, the landing gear (legs) were also considered in the calculation that required vertical displacement to avoid the collision. The distance from the drone CG and the lowest point on the landing gear surface of the drone was determined after its geometry was mapped from the computational model, as shown in Figure 17. In IC6-IL3, the initial vertical location of the drone was 2 m above the leading edge of the horizontal stabilizer, while the drone moves downward and towards the horizontal stabilizer. Therefore, the vertical displacements, in the negative direction, smaller than 186.4 cm (6.11 ft), denote no collision.

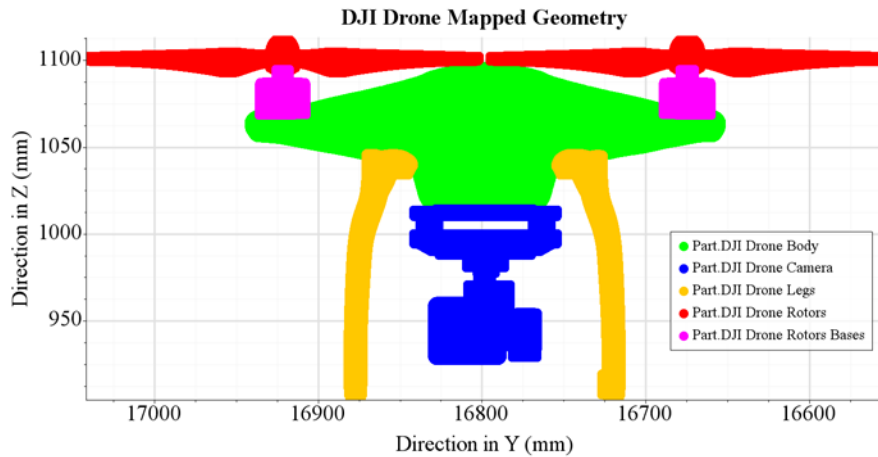


Figure 17. Mapped geometry of the DJI drone in the computational domain with respect to the origin in the current simulations.

### 2.6.2 Release (Horizontal) Location without Fuselage

The initial horizontal location of the drone with respect to the leading edges of the CRM wing and horizontal stabilizer determined the total distance that the drone needed to travel to the point of collision. The trajectory of the drone was influenced by the pressure flow fields around the drone and CRM aircraft at high speeds. Therefore, it was essential to initially place the drone in a region where there was no impact of pressure field or significant variation in the pressure flow field at the release location. For the impact scenarios investigating the collision of the drone and the CRM wing, the CRM wing and the housing of the jet engine were considered. This was determined as the impact location was 16.8 m from the symmetry plane far from the fuselage.

The drone was initially placed at 15 m from the CRM wing leading edge for IC1-IL1, IC2-IL1, IC2-IL1U1, IC2-IL1D1, IC2-IL1U2, IC2-IL1D2, and IC2-IL1AMR. Additionally, the impact scenarios of IC1-IL1 and IC2-IL1 were analyzed, with the purpose of cross-verification, for an initial release location at a distance of 60 m and 45 m, respectively, with 6-DOF enabled, as shown in Figure 18.

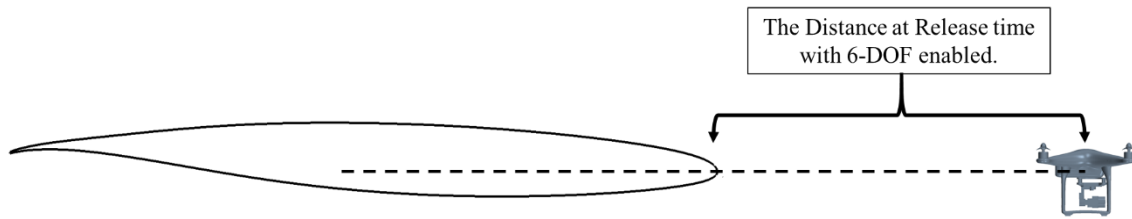


Figure 18. The distance at release time with 6-DOF enabled.

### 2.6.3 Release (Horizontal) Location with Fuselage

For the impact scenarios IC2-IL3, IC2-IL3, and IC2-IL3, the drone was initially placed at a 90 m distance from the leading edge of the CRM horizontal stabilizer, and the DFBI 6-DOF was enabled after 16 m when the flow solution stabilized. The larger distances for these impact scenarios were determined based on the larger region around the CRM aircraft with higher pressure variations in the presence of the CRM fuselage. Figure 19 shows the pressure flow field from the initial location of the drone to the downstream of the horizontal stabilizer. It was observed that the pressure changed significantly closer to the CRM cockpit, impacting the drone.

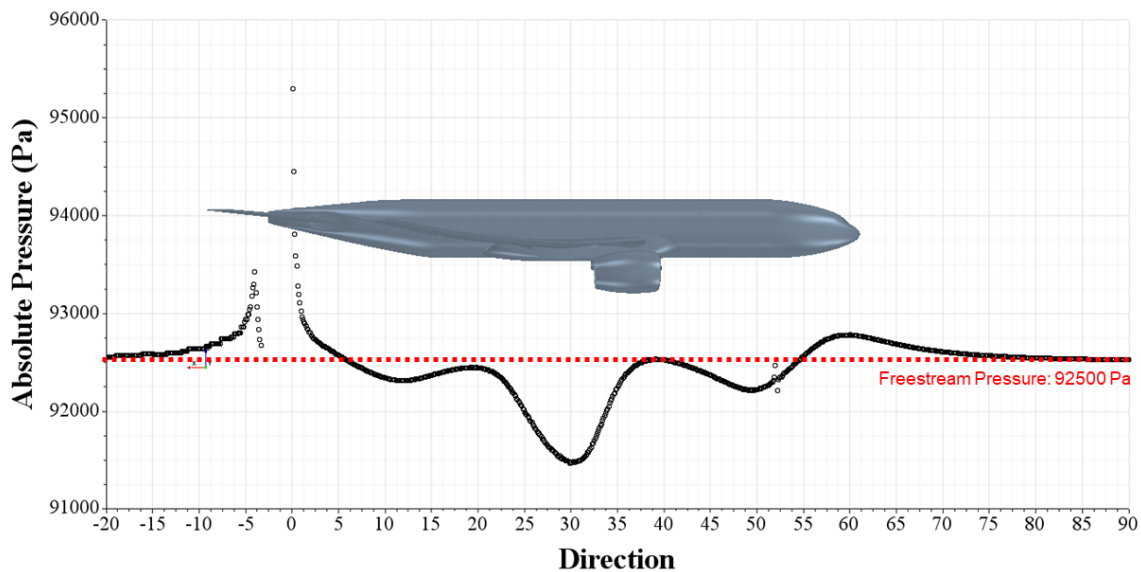
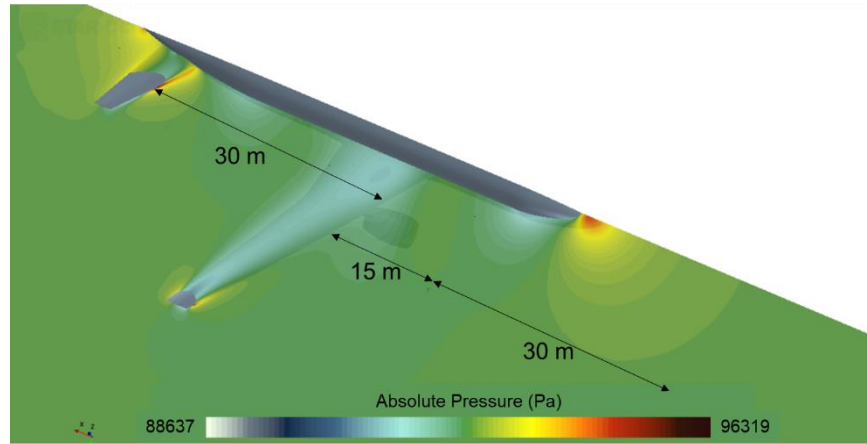
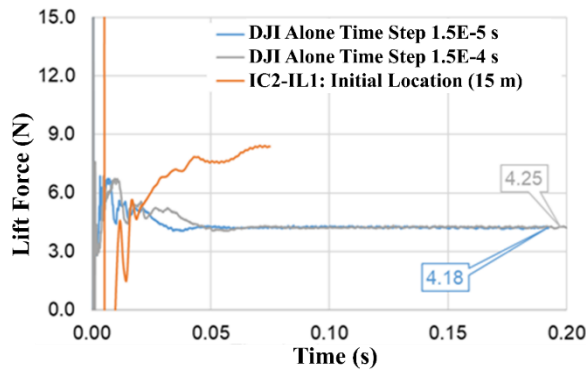


Figure 19. Pressure flow field from the release location to downstream of the horizontal stabilizer for IL3.

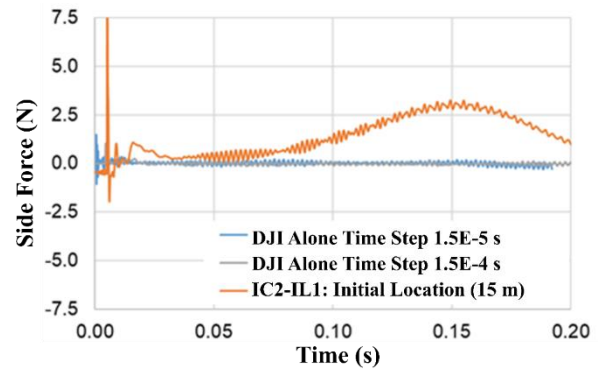
Figure 20a illustrates that the drone's initial location is a key factor in the prediction of the drone's trajectory, especially for the impact scenarios between the drone and CRM horizontal stabilizer. For these impact scenarios, the drone travels over the CRM wing to reach the horizontal stabilizer. The existence of the CRM fuselage can significantly affect the trajectory of the drone by applying larger forces and moments. Figures 20b and c showed that the lift and side forces did not stabilize before the interactions between the drone and CRM aircraft started. The results were compared with the forces obtained from a DJI-alone simulation under the same flow conditions.



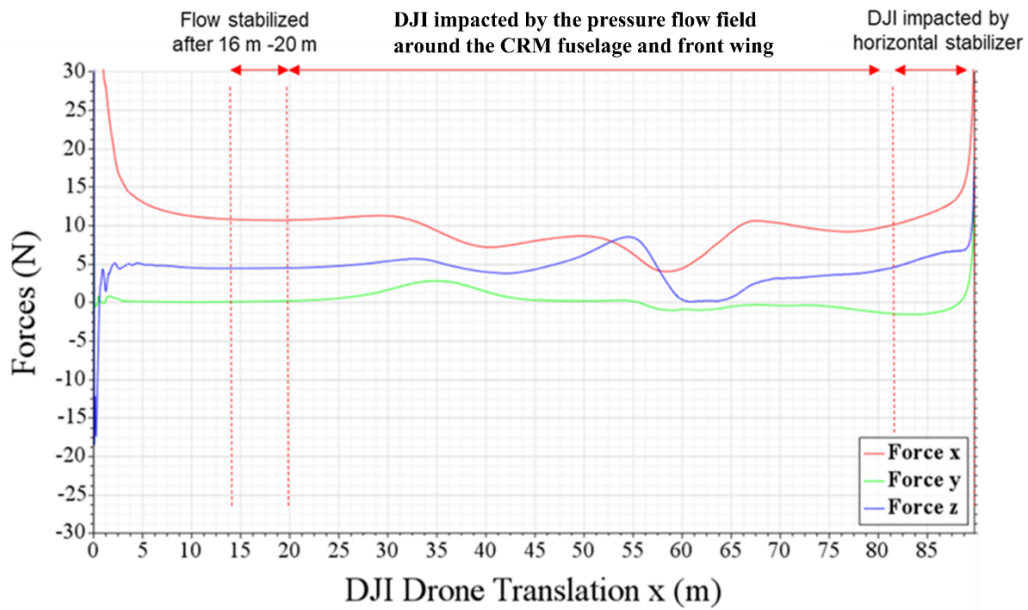
(a)



(b)



(c)



(d)

Figure 20. Impact of flow forces on the DJI drone at different distances.

Figure 20d shows that a distance of about 60 m from the CRM wing (90 from the horizontal stabilizer) led to more realistic and reliable results.

## 2.7 RELATIVE DISTANCE

In this report, all plots indicating the variations of flow forces and moments and the drone's axial and angular displacements and velocities are presented with respect to the relative distance of the drone. The relative distance is the distance between the foremost point on the chassis of the DJI drone to the leading edge point on the wing or horizontal stabilizer. It should be noted that the relative distance is different than the horizontal displacement of the drone. For example, it takes about 0.70 s for the drone to travel a distance of 90 m to the CRM wing leading edge with an initial speed of 128.611 m/s (IC2) and without any impact from the flow forces (prescribed trajectory). However, in the presence of flow forces, the drone may slow down due to the drag forces. Accordingly, the horizontal displacement was computed by comparing the difference between the horizontal location of the drone at each time step with or without the impact of the flow.

## 2.8 SIGN CONVENTION

The consistency in the positive and negative directions of the flow parameters, as well as axial and angular displacements of the drone, allowed an accurate perception and interpretation of the results. Figure 4a shows the sign convention for the drone displacements along all axes. The definition of the prescribed positive and negative displacements experienced by the drone was applied and measured about the drone CG. A negative horizontal displacement indicated that the drone slowed down from its initial speed by the drag forces, whereas, if the drone sped up, it experienced a positive horizontal displacement.

Due to the side forces along the Y-axis, positive spanwise displacements of the DJI drone denoted the drone moved away from the CRM fuselage (toward the wingtip of the aircraft). In contrast, the drone moving towards the fuselage is a negative spanwise displacement. The displacement of the drone in the Z-axis, as one of the main focuses in this study, which at higher scales can indicate a complete deflection of the drone from the point of collision. In the current analysis, the positive vertical drone displacement indicated that the drone would flow over the aircraft wing and horizontal stabilizer. The negative vertical displacement points to an expected trajectory of the drone under the CRM and horizontal stabilizer. The results of the drone displacements along and around all axes were computed with respect to the location of the CG when the influences of the pressure flow field were considered, and six degrees of freedom (6-DOF) were enabled for the DJI drone.

Figure 4b shows the positive directions for the computed forces on CRM aircraft. The forces applied on the aircraft are due to its motion in negative X-direction with a constant velocity describe for impact conditions. These forces can be slightly affected as the drone approaches the aircraft.

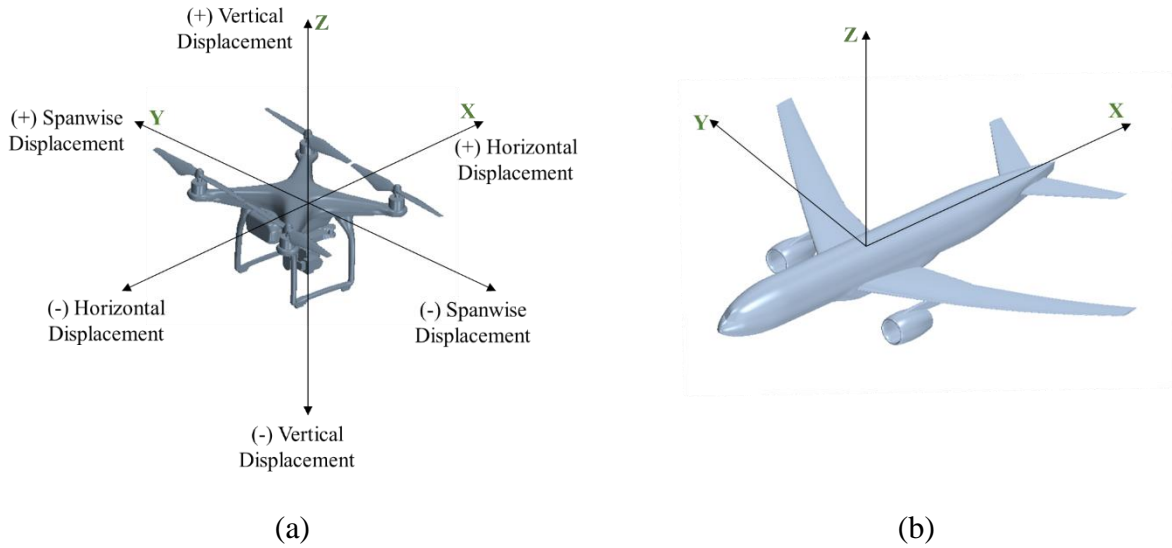


Figure 21. Sign conventions used for (a) displacements experienced by the drone, (b) forces applied on the CRM aircraft.

Figure 5 shows the sign convention for the drone angular displacements and velocities around all axes. The angular displacements and velocities are due to the moments applied on the CG of the drone, as the drone approaches the aircraft. The sign convention is defined by using the right-hand rule.

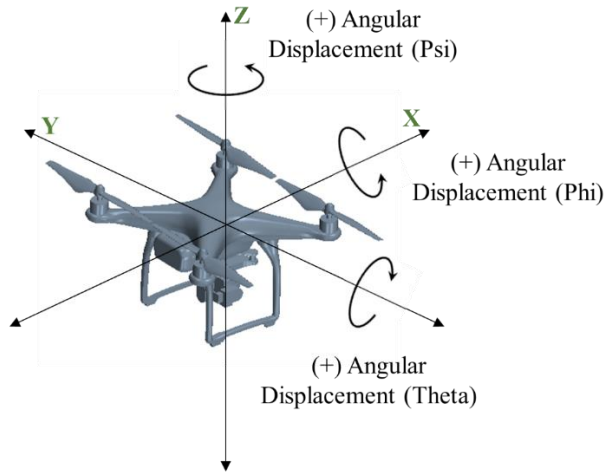


Figure 22. The sign convention used for the computation of the angular displacements experienced by the drone.

## 2.9 FORCE AND MOMENT BALANCING ON THE DRONE

Force and moment balances were applied on the DJI drone. It was essential to maintain the drone's initial configuration; i.e., there should be no change in the displacements and velocities compared to the release time when there is no impact from pressure flow field around the DJI drone and CRM aircraft. For example, for IC1-IL1, the drone remains hovering, and for IC2-IL1, the drone

moves towards the aircraft at a constant velocity while showing no displacement in or around other axes.

The impacts on the drone were computed with respect to the drone CG, so it was necessary to define the moment of inertia tensor to accurately simulate the impacts on the drone, as described in the following equation:

$$\begin{bmatrix} 0.0081 & & \\ -2.38 \times 10^{-5} & 0.0086 & \\ 1.40 \times 10^{-4} & -3.27 \times 10^{-5} & 0.0123 \end{bmatrix} \text{ kg-m}^2$$

In Figure 23, the forces impacting the drone are shown. The total lift on the drone consists of the lift due to the standalone motion of the drone in addition to the lift computed considering the interactions due to the pressure flow field between the drone and CRM aircraft. Similarly, the total drag equals the drags due to the standalone motion of DJI and the interactions. The force balance was applied to eliminate the lift and drag forces due to the standalone motion of the drone, as it should show no changes in the axial and angular displacements and velocities in the absence of the flow impacts. The vertical, horizontal, and side forces used in the force balance were calculated based on the prescribed motion of the drone without any flow impacts. In these analyses, the weight of the drone and gravitational forces were not included to reduce the unnecessary term of additional vertical thrust in the simulation of the rigid body motion.

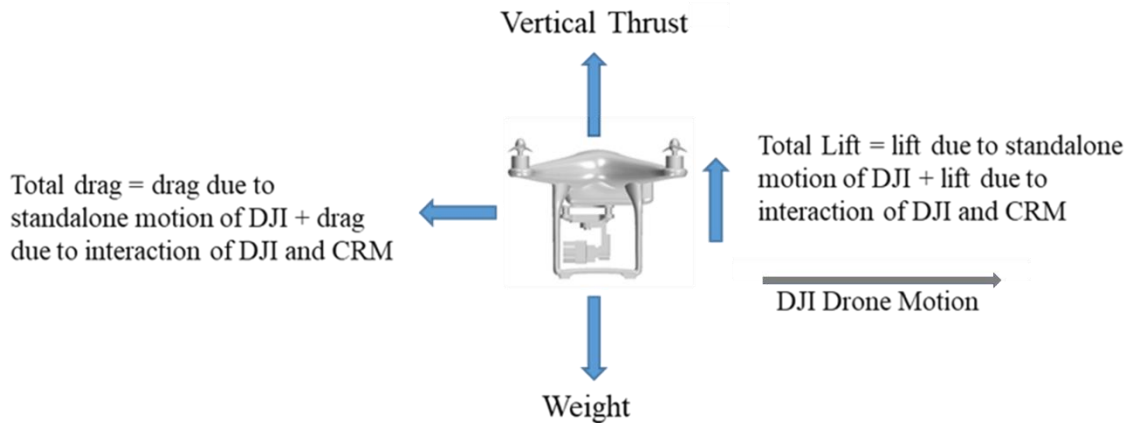


Figure 23. Force balance applied on the DJI drone when the 6-DOF was enabled.

Similarly, the moment balance was applied on the drone to eliminate any initial impacts on the drone in the absence of the interactions. The moment balance consisted of the moments around the X-, Y-, and Z-axis according to the sign conventions, shown in Figure 5. The values of the forces and moments used at the beginning of the analysis, after the 6-DOF was enabled, are shown as the horizontal lines included in the plots in 0.

### 3. RESULTS

#### 3.1 CRM AIRCRAFT VALIDATION

##### 3.1.1 Introduction

The current numerical analysis of the flow around the CRM aircraft, done by ERAU and NIAR in two parallel studies, was validated for the pressure coefficients on the CRM aircraft wing at six stations in the spanwise direction. The results obtained by the two institutions were compared with the wind tunnel experimental data provided in [17]. In this study, the pressure coefficients were recorded for the CRM aircraft with the inclusion of the CRM fuselage, engine nacelle (housing), and horizontal stabilizer. In this model, the engine, vertical stabilizer, and rudder were neglected. Figure 24 shows the six stations where the pressure coefficients on the CRM wing were analyzed. These stations (1 to 6) were located at  $y/b = 0.131, 0.286, 0.502, 0.603, 0.846, 0.950$ , respectively, where  $b$  is the semi-spanwise length for the CRM aircraft.

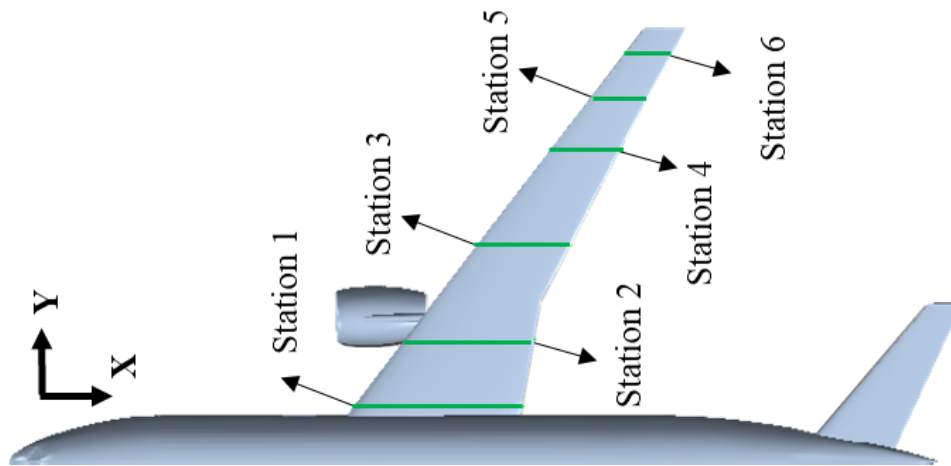


Figure 24. The stations used to validate the pressure coefficients on the CRM wing.

It should be noted that due to the symmetry of the model, half of the flow domain and CRM aircraft were considered for the current validation.

##### 3.1.2 Mesh

The information on the mesh configuration in different flow conditions was presented in APPENDIX A.

##### 3.1.3 Numerical Model

The information on the numerical models as well as initial and boundary conditions for the validation of the pressure coefficients on the CRM wing was presented in 2.4.

### 3.1.4 Results

#### 3.1.4.1 CRM Aircraft Verification

Figure 25 shows the pressure coefficients at six different stations along the CRM aircraft wing. The results compared the experimental results [17] and the computational studies performed by ERAU and NIAR. A good agreement was observed for the coefficient of the pressure analysis. Similar results were concluded in [17] when comparing the experimental data with the computational models with different turbulence models.

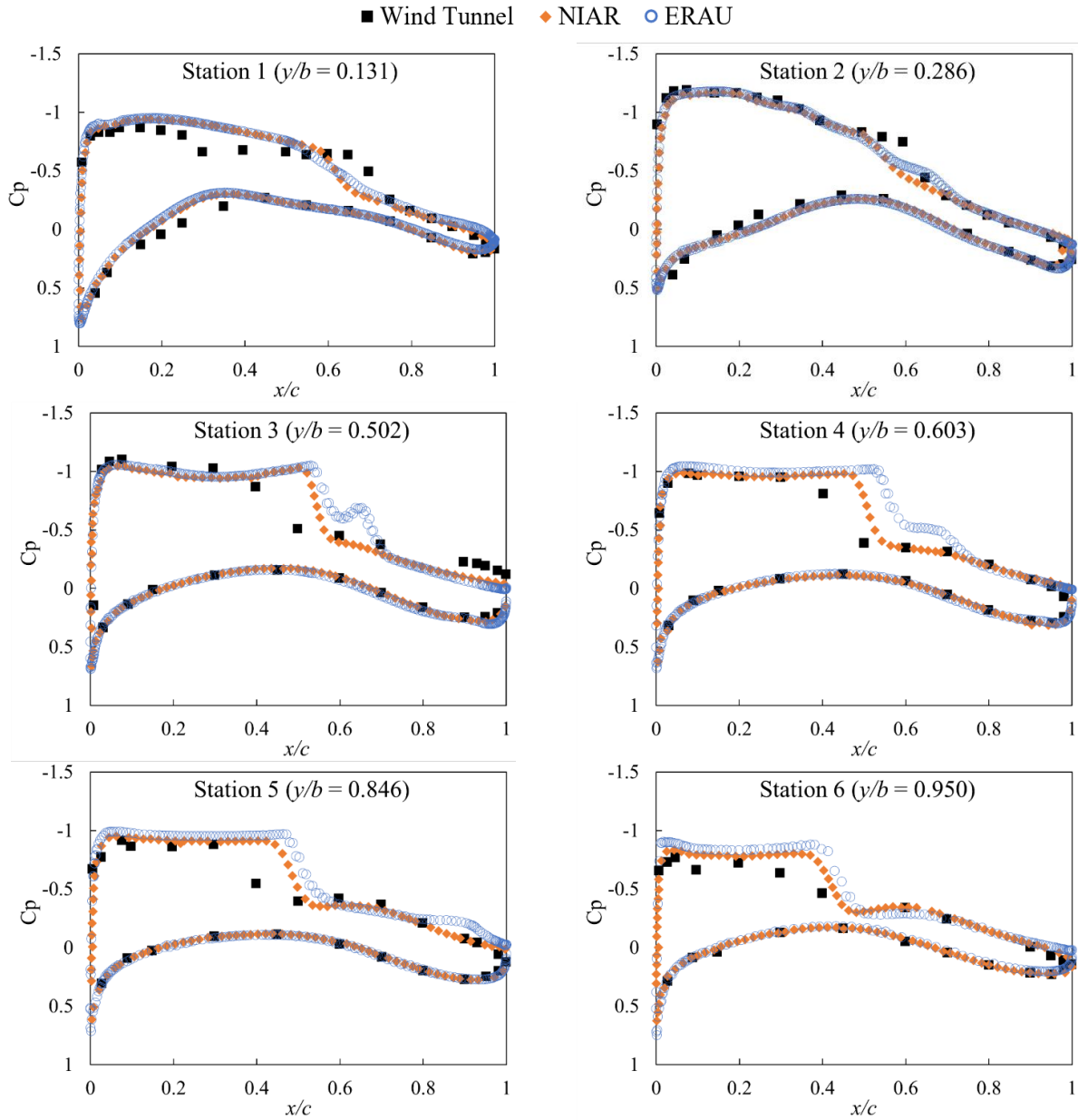


Figure 25. Pressure coefficients on the CRM aircraft wing at six stations in the spanwise direction. In this figure,  $b$  and  $c$  are the semi-span length and airfoil's chord length, respectively.

Table 7 summarizes the results of the CRM wing lift coefficient ( $C_L$ ). The lift coefficient of 0.625 was observed in the experimental study. The  $C_L$  was -1.2% and 2.8%, different from the current computational analysis done by NIAR and ERAU, respectively.

Table 7. Comparison of the lift coefficients obtained from the wind tunnel experimental and CFD studies done by NIAR and ERAU.

Lift Coefficient					
AoA	Wind Tunnel	NIAR Results		ERAU Results	
	$C_L$	$C_L$	$\Delta C_L \%$	$C_L$	$\Delta C_L \%$
4.00	0.625	0.617	-1.2	0.643	+2.8

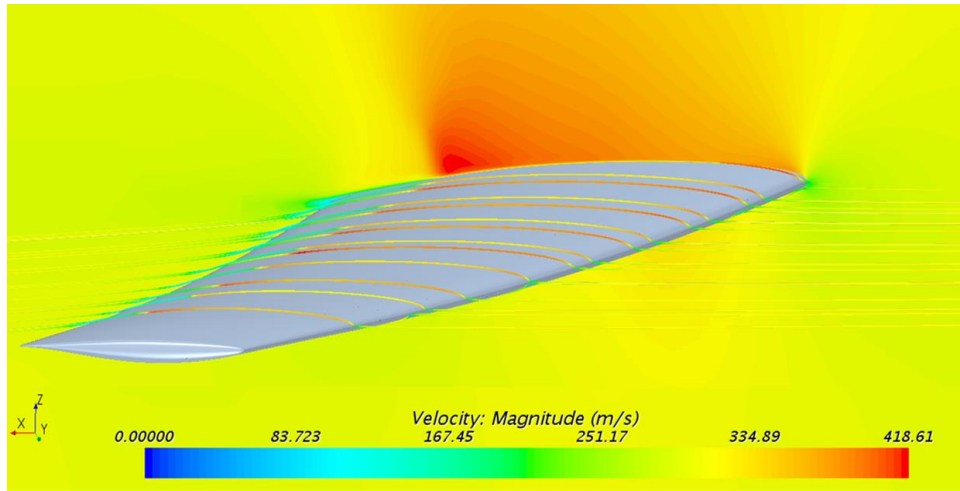
The drag coefficient results on the CRM wing ( $C_D$ ) from the experimental and current computational studies can be found in Table 8. The drag coefficient of 0.046 was found in the experimental study. The  $C_D$  observed by ERAU was found 1.6% smaller relative to the experimental data.

Table 8. Comparison of the drag coefficients obtained from the wind tunnel experimental and CFD studies done by NIAR and ERAU.

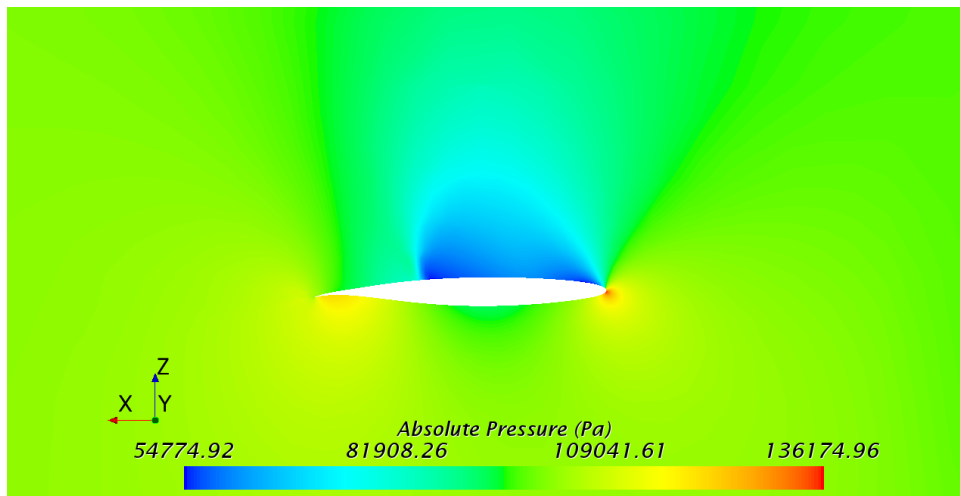
Drag Coefficient					
AoA	Wind Tunnel	NIAR Results		ERAU Results	
	$C_D$	$C_D$	$\Delta C_D \%$	$C_D$	$\Delta C_D \%$
4.00	0.046	0.047	3.6	0.0453	-1.6

#### 3.1.4.2 Flow around the CRM Aircraft

In the validation study, the CRM is subject to a freestream flow at the Mach number of 0.8. This means that the velocity at the inlet of the computational domain was about 300 m/s. Figure 26 shows the velocity distribution around the CRM wing at this Mach number. The magnitude of the velocity increase to about 418 m/s on the top surface of the CRM wing, Figure 26a, leading to a high-pressure gradient between the bottom and top surfaces, as shown in Figure 26b. The flow velocity and pressure results are consistent with findings of the lift coefficient on the wing.



(a)



(b)

Figure 26. (a) Velocity and (b) absolute pressure flow fields around the CRM wing at a Mach number of 0.85 and reference pressure of 1 atm.

## 3.2 CROSS VERIFICATION

### 3.2.1 Introduction

A cross-verification study was performed for the impact scenarios IC1-IL1 and IC2-IL1, between the results obtained from Simcenter STAR-CCM+ (2020.1.1, CD-Adapco, Siemens PLM, Plano, TX, USA) and ANSYS Fluent (Ansys® Fluent, Release 18.2) by ERAU and NIAR, respectively. Due to the lack of experimental data for CRM aircraft at holding condition (at an altitude of 2500

ft), ERAU and NIAR conducted the current analysis using the two different CFD codes and cross-verified the results to ensure an accurate and reliable investigation on the trajectory of DJI drone from the release location to the point of collision with the CRM aircraft. The results shown in this section consist of flow forces and moments exerted on the DJI drone and axial displacement from the drone's initial position. Additional information on the variation of drone's velocity, angular displacement, velocity, etc., can be found in section B.1.

### 3.2.2 Mesh

The information on the mesh configuration in different flow conditions was presented in APPENDIX A.

### 3.2.3 Numerical Model

The information on the numerical models as well as initial and boundary conditions for the analysis of IC1-IL1 and IC2-IL1 were presented in 2.4.

### 3.2.4 Results

#### 3.2.4.1 Impact Scenario IC1-IL1

For the impact scenario IC2-IL1, the DFBI 6-DOF was enabled from a distance of 60 m (ERAU) and 45 m (NIAR) away from the leading edge of the CRM wing. The specifications of this impact scenario were explained in section 1.5. The results were obtained based on releasing the drone in the domain with the CRM aircraft wing without the fuselage and tail. In the current analysis done by ERAU, when the DJI drone was released, the drone was allowed to move based on a prescribed motion without the influence of forces and moments for 30 m until the flow solution, especially around the drone, stabilized. At the distance of 60 m with 6-DOF enabled, the average aerodynamic forces and moments were used as external forces and moments in the force balance, as described in section 2.9. The forces experienced by the drone during the transient simulation were compared with the averaged forces obtained for the prescribed trajectory analysis without the influence of the flow on the drone and the results provided by NIAR. Figure 27 shows a good agreement between the results of forces in all three directions between NIAR and ERAU. A zoomed-view of the plots is shown in section B.1.

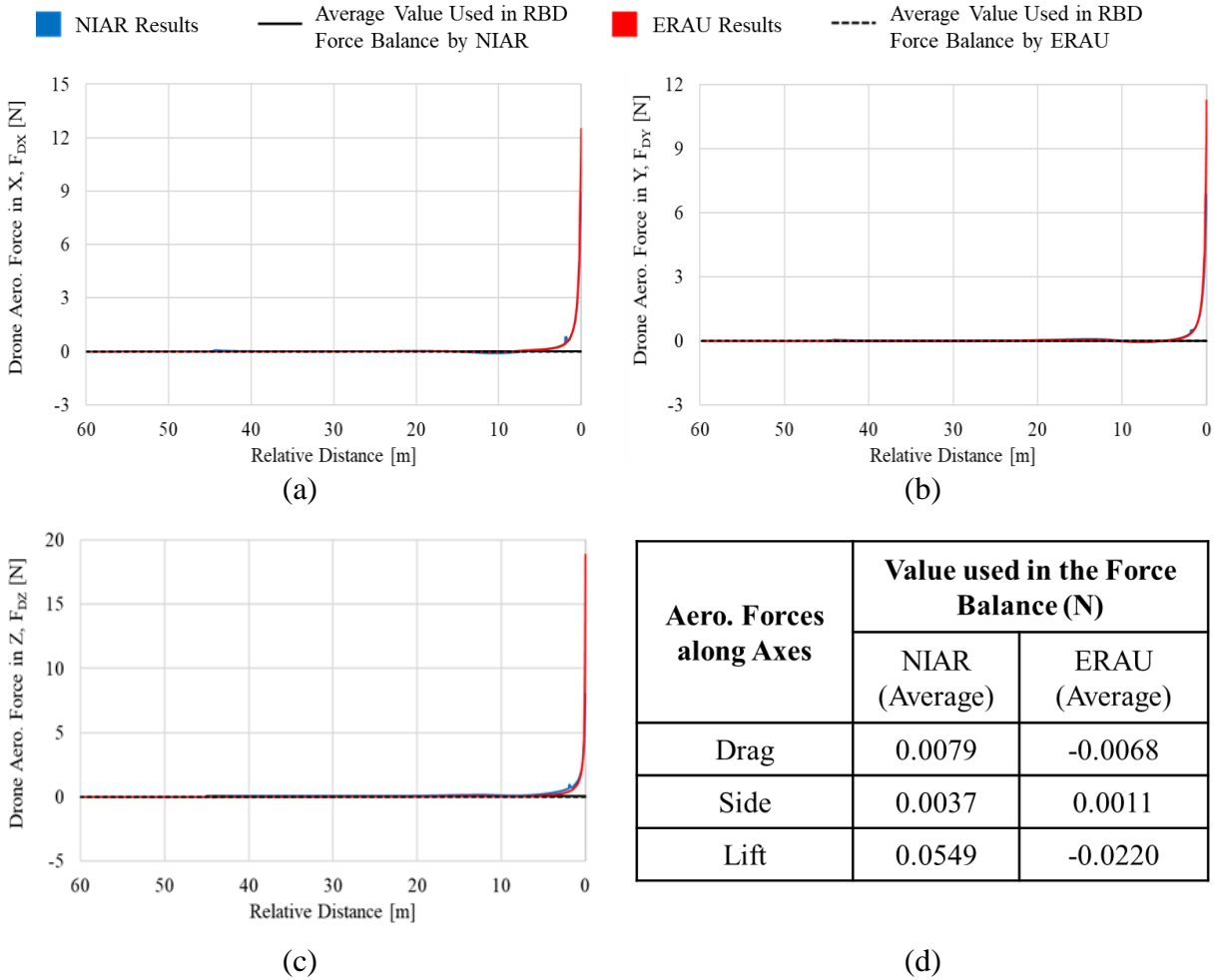


Figure 27. Cross-verification results of forces for IC1-IL1.

As a note, in 1.5.2.1, for this impact location, the drone was placed at a spanwise distance of 16.8 m (55.12 ft) away from the symmetry plane of the CRM aircraft. In this impact condition (IC1-IL1), the DJI drone was specified with zero velocity, while the CRM aircraft approached the drone at a fixed speed of 102.889 m/s (200 knots) and  $0^\circ$  angle of attack. Therefore, the pressure flow field around the CRM wing had the highest impact on the trajectory of the drone, leading to angular velocities and displacements due to the moments exerted on the drone. The moments experienced by the drone around each axis, as described in Figure 23, were compared with the moments obtained from the averaged forces obtained for the prescribed trajectory analysis without the influence of the flow on the drone and the results provided by NIAR. Figure 28 shows a good agreement between the results of moments obtained by NIAR and ERAU. A zoomed-view of the plots is included in section B.1.

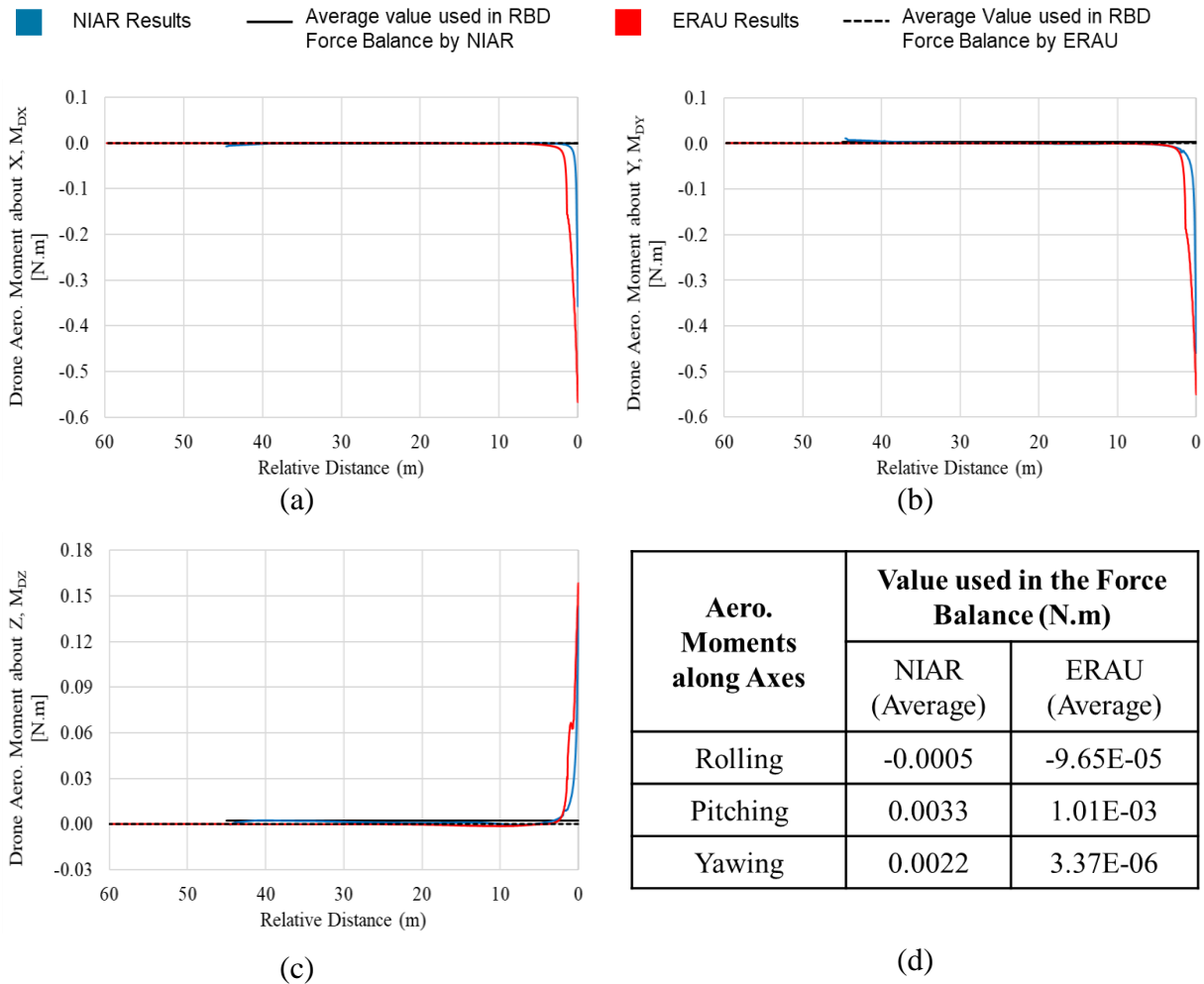


Figure 28. Cross-verification results of moments for IC1-IL1.

As the main focus of the current study, displacements of the drone from the initial direction were examined and cross-verified carefully to ensure reliable results obtained from each CFD code. For Impact scenario IC1-IL1, the drone was considered hovering condition; hence, it showed smaller interactions with the pressure flow field around the CRM aircraft compared to the other impact scenarios. Figure 29 shows the displacements of the DJI drone in the spanwise (Y) and vertical (Z) directions with respect to the relative distance of the drone up to the point of collision. The results obtained from NIAR and ERAU showed small deflections of less than 1 mm and 2 mm in Y- and Z-directions, respectively. It should be noted that the small differences in the results raised from the flow solved using different CFD codes; however, these differences are acceptable and do not affect the final conclusions for each impact scenario. As described in Table 6, these deflections are insufficient to prevent the collision between the CRM aircraft and the DJI drone.

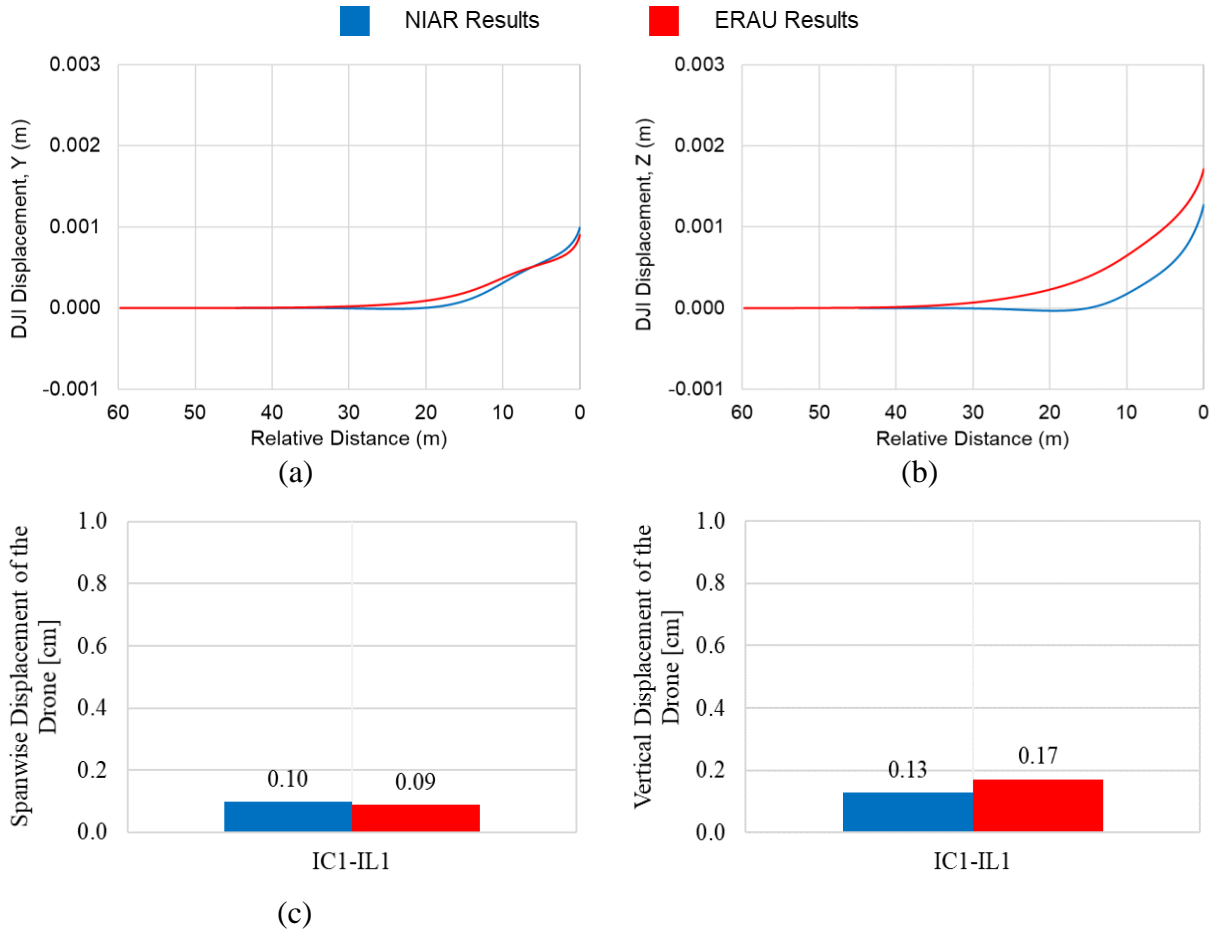


Figure 29. Cross-verification results of displacements for IC1-IL1.

Figure 30 shows absolute pressure distribution around the CRM aircraft and DJI drone at the point of collision from the side and top views, comparing the results obtained by ERAU and NIAR. The pressure contours were obtained about planes created along the XZ-plane (side view) and the XY-plane (top view) passing through the drone CG at the times of release. As described in section 2.4.1, the reference pressure at holding condition (altitude of 2500 ft) was set to 92500 Pa. This means that as the drone approached the leading edge of the CRM wing, the pressure and interactions between them increased significantly.

As it can be seen in this figure, the pressure distribution was not symmetric around the drone CG, leading to different displacement and velocity variations through and around all axes. It should be noted that the point of collision was determined based on the front point of the drone (here, drone's rotor or chassis), colliding with the CRM wing, before the drone CG reached this point. The results of pressure distribution around the CRM wing and drone were also consistent with forces and moments exerted on the drone with respect to the relative distance, shown in Figure 27 and Figure 28.

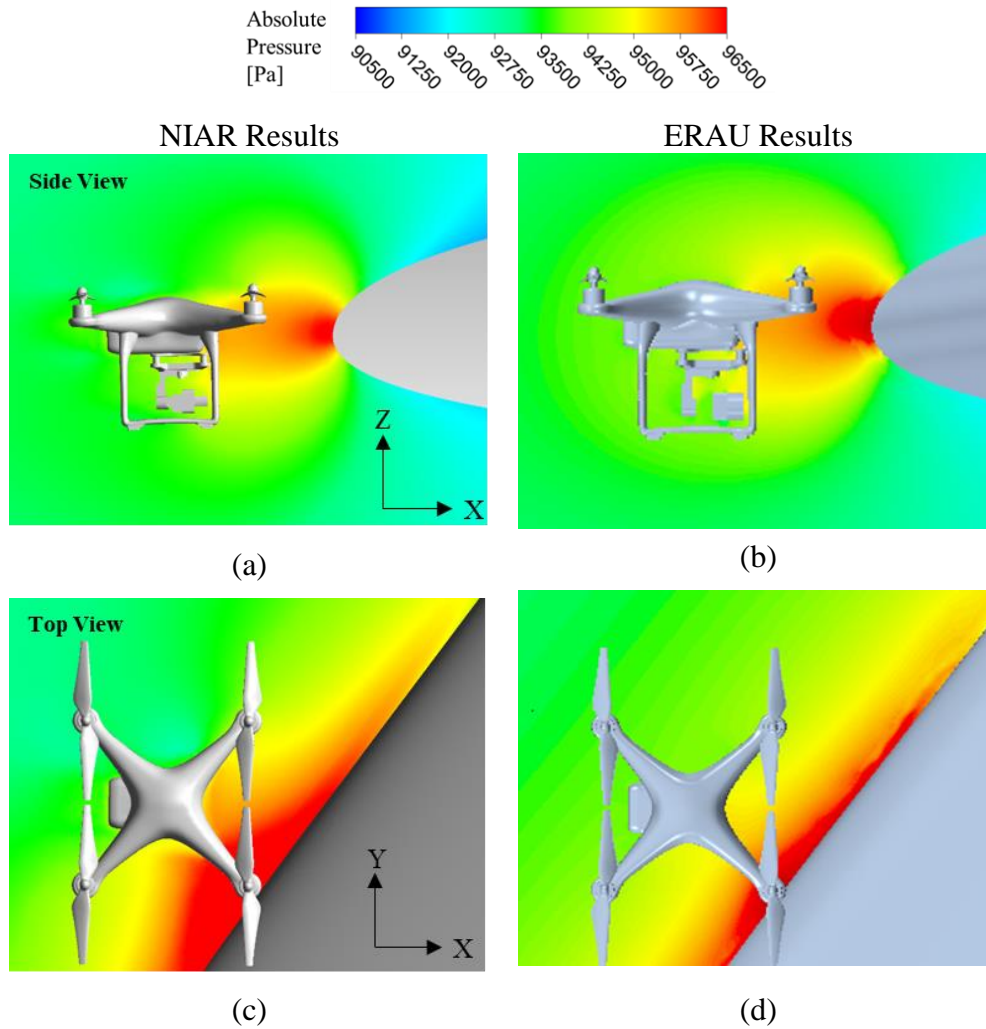


Figure 30. Cross-verification results of absolute pressure distribution for IC1-IL1 at the point of collision, obtained by NIAR and ERAU.

Figure 31 shows displacements of the drone at the point of collision from two different back and side views, compared to the initial location of the drone CG. The forces and moments, and impacts on the drone were very insignificant up to a point close to collision. At a distance of about 4 m, the forces and moments exerted on the drone started to increase; however, these variations in the flow parameters occurred in a very short time (less than 0.1 s), which did not lead to large axial and angular displacements.

It can be concluded that, due to small impacts on the DJI drone, the drone did not deflect sufficiently to prevent the collision with the CRM wing. However, the goal of cross-verification was accomplished, based on the results obtained by NIAR and ERAU using different codes, to ensure that reliable results are included in this report, while there were no experimental results for the CRM at holding conditions.

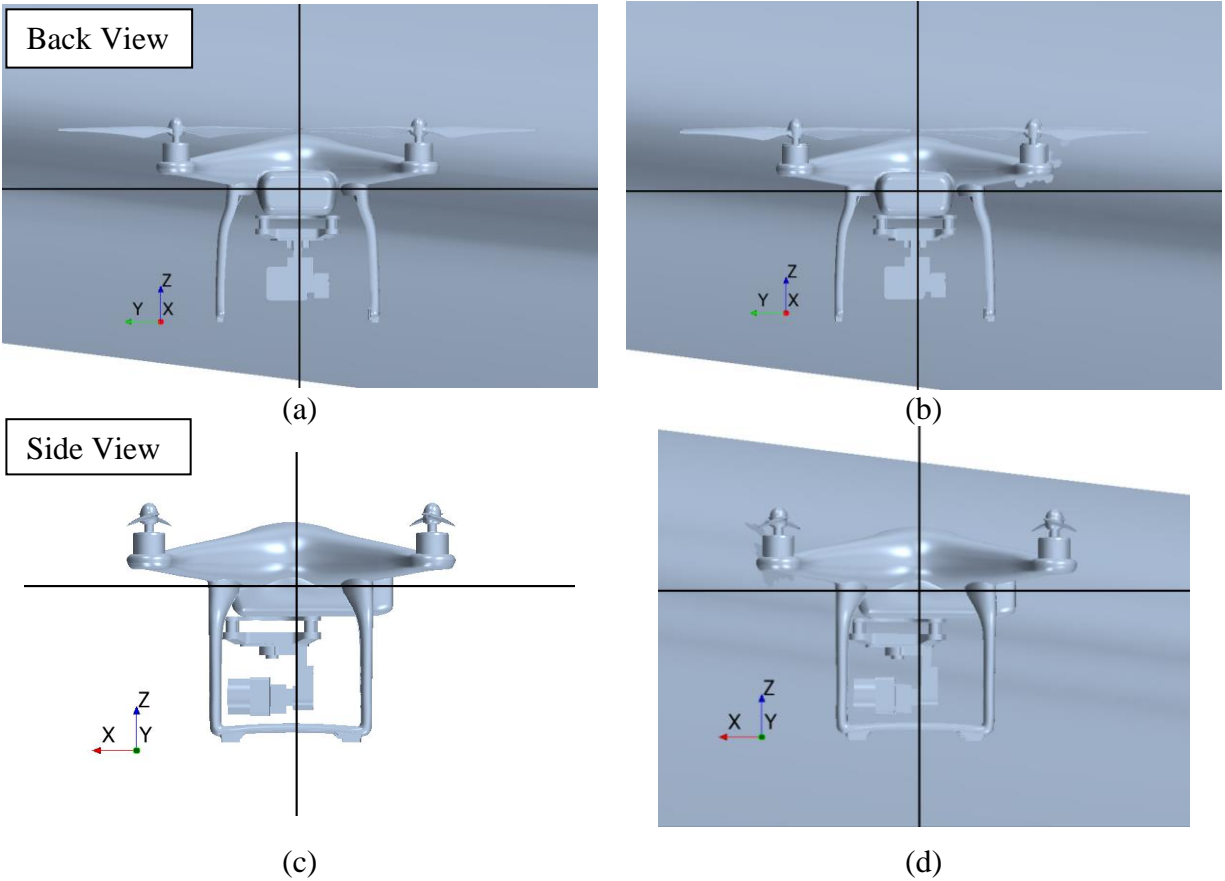


Figure 31. Displacements of the Drone from the initial directions resulting from the flow forces and moments for IC1-IL1.

#### 3.2.4.2 Impact Scenario IC2-IL1

For the impact scenario IC2-IL1, the DFBI 6-DOF was enabled from a distance of 45 m (for both results obtained by ERAU and NIAR) away from the leading edge of the CRM wing. The specifications of this impact scenario were explained in section 1.5. The results were obtained based on releasing the drone in the domain with the CRM aircraft wing without the fuselage and tail. In the current analysis done by ERAU, when the DJI drone was released, the drone was allowed to move based on a prescribed motion without the influence of forces and moments for 45 m until the flow solution, especially around the drone, stabilized. This initial distance, before enabling 6-DOF was larger compared to IC1-IL1 because of the higher inertial and impacts of the moving drone. At the distance of 45 m with 6-DOF enabled, the instantaneous aerodynamic forces and moments were used as external forces and moments in the force balance, as described in section 2.9. The forces experienced by the drone during the transient simulation were compared with the forces obtained from the prescribed trajectory analysis without the influence of the flow on the drone and the results provided by NIAR. Figure 32 shows a good agreement between the results of forces in all three directions between NIAR and ERAU. It should be noted that NIAR used average values in the force balance. A zoomed-view of the plots is shown in section B.1.

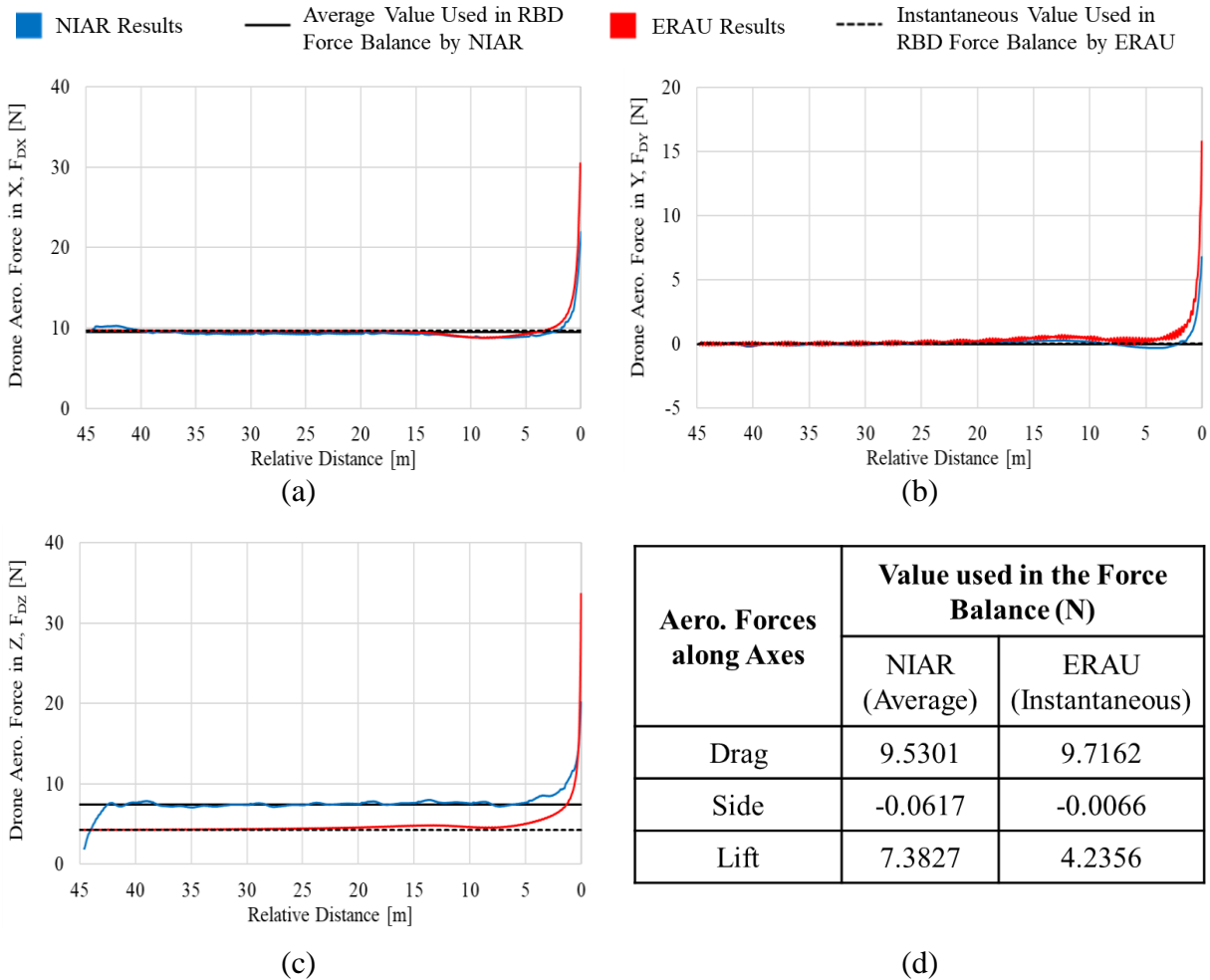


Figure 32. Cross-verification results of forces for IC2-IL1.

As a note in 1.5.2.1, for this impact location, the drone was placed at a spanwise distance of 16.8 m (55.12 ft) away from the symmetry plane of the CRM aircraft. In this impact condition (IC2-IL1), the DJI drone was specified with a velocity of 25.722 m/s, while the CRM aircraft approached the drone at a fixed speed of 102.889 m/s (200 knots) and 0° angle of attack. Therefore, the impacts on the trajectory of the drone were significantly higher than the impact scenario IC1-IL1, leading to higher linear and angular velocities and displacements of the drone as a result of the forces and moments applied on the drone.

The moments experienced by the drone around each axis, as described in Figure 33, were compared with the moments obtained from the the prescribed trajectory analysis without the influence of the flow on the drone and the results provided by NIAR. Figure 28 shows a good agreement between the results of moments obtained by NIAR and ERAU. A zoomed-view of the plots is included in section B.1.

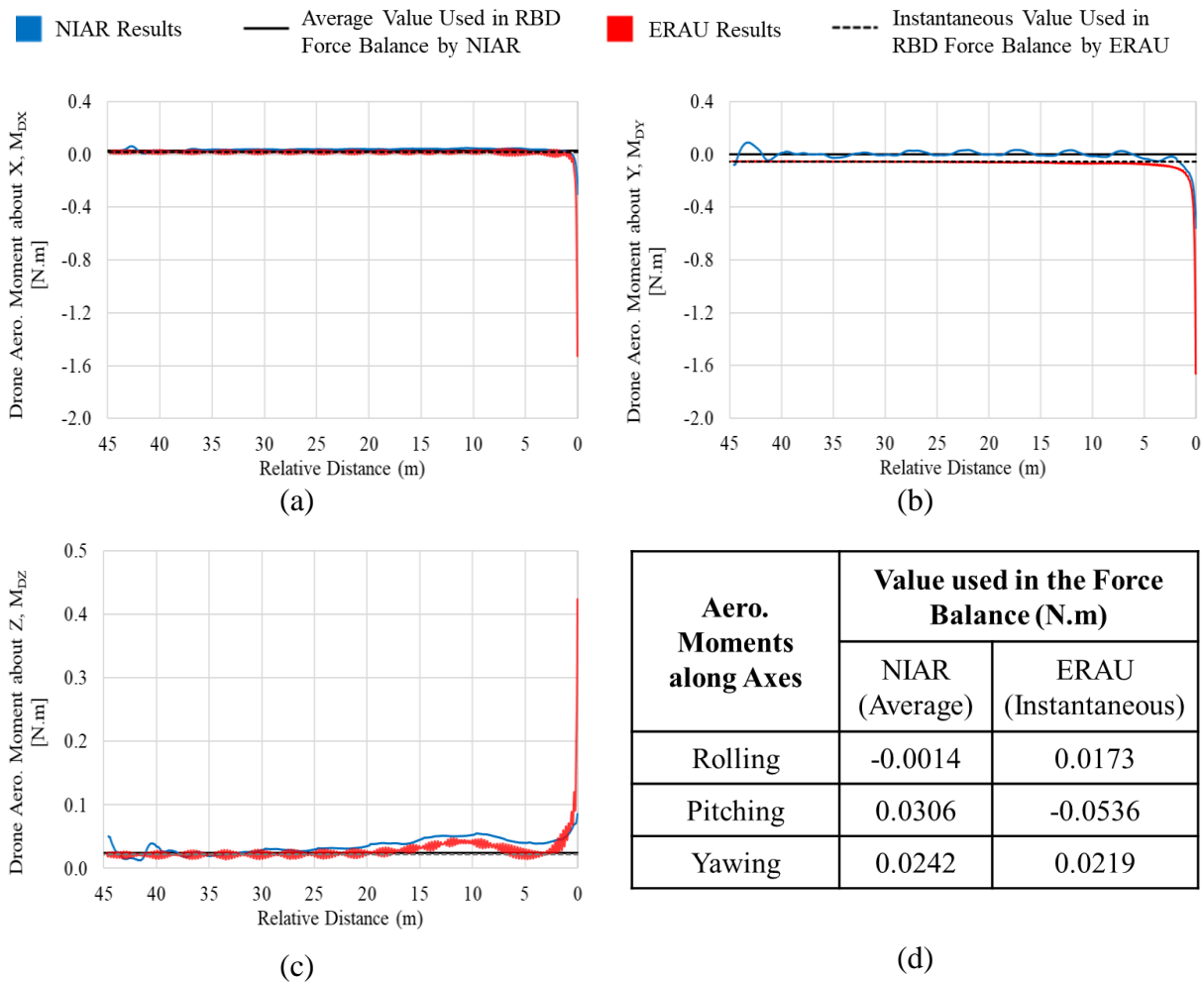


Figure 33. Cross-verification results of moments for IC2-IL1.

The results were expected to show higher displacements of the drone due to the higher impacts from the moving drone approaching the CRM wing. Similar to the results shown in section 3.2.4.1 for IC1-IL1, the displacements of the drone from the initial direction were examined and cross-verified carefully for the results obtained from each CFD code. Figure 34 shows the displacements of the DJI drone in the spanwise (Y) and vertical (Z) directions with respect to the relative distance of the drone up to the point of collision. In the spanwise direction, small deflections of less than 0.3 and 0.6 cm resulted in the studies done by NIAR and ERAU, respectively. In the vertical direction, deflections of less than 0.3 and 0.9 cm were provided by NIAR and ERAU, respectively.

It should be noted that the small differences in these results raised from the flow solved using different CFD codes. These minor differences are acceptable and do not affect the final conclusions for each impact scenario. As described in Table 6, these deflections are insufficient to prevent the collision between the CRM aircraft and the DJI drone.

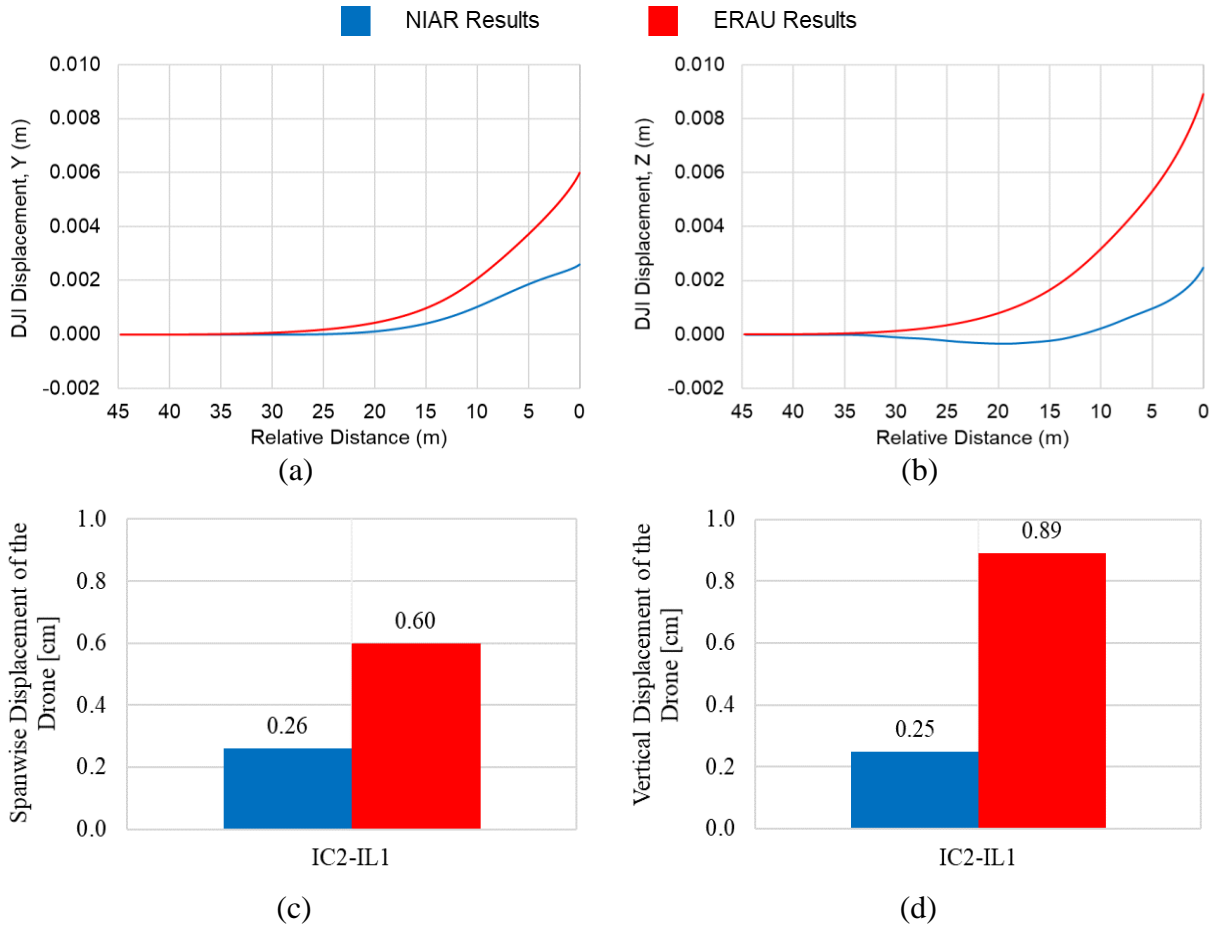


Figure 34. Cross-verification results of displacements for IC2-IL1.

Figure 35 shows absolute pressure distribution around the CRM aircraft and DJI drone at the point of collision from the side and top views, with a comparison between the results obtained by ERAU and NIAR. The pressure contours were obtained about planes created along the XZ-plane (side view) and the XY-plane (top view) passing through the drone CG at the times of release. The pressure and interactions between the CRM wing and the DJI drone increased significantly as the drone approached the leading edge of the CRM wing. As described in section 2.4.1, the reference pressure at holding condition of CRM aircraft (altitude of 2500 ft) was set to 92500 Pa, which increased to about 96500 Pa at the point of collision.

It was observed that different displacements and velocities were obtained for the drone due to the asymmetric distribution of the pressure around the drone CG. It should be noted that the point of collision was determined based on the front point of the drone (here, drone's rotor or chassis), colliding with the CRM wing, before the drone CG reached this point. The results of pressure distribution around the CRM wing and drone were also consistent with forces and moments exerted on the drone with respect to the relative distance, shown in Figure 32 and Figure 33.

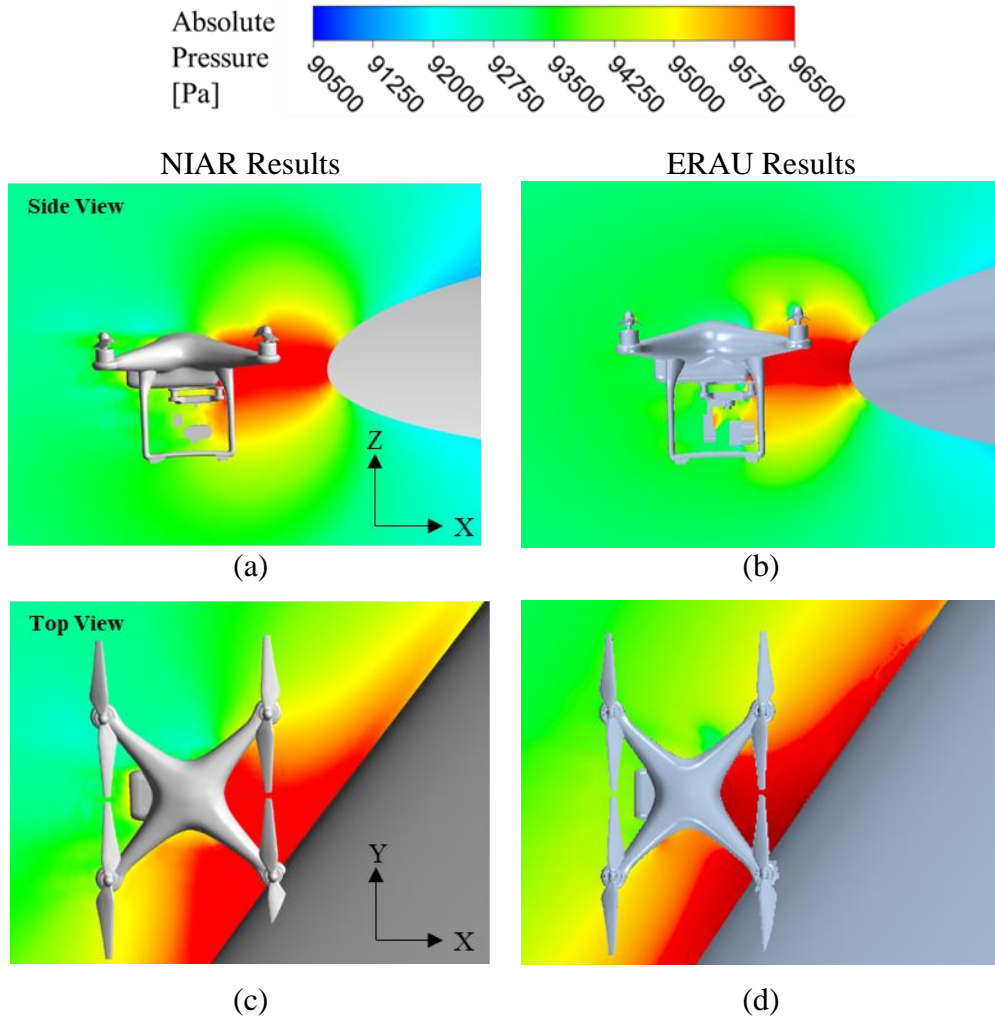


Figure 35. Cross-verification results of absolute pressure distribution for IC2-IL1 at the point of collision, obtained by NIAR and ERAU.

Figure 36 shows the displacements of the drone at the point of collision from two different back and side views, compared to the initial location of the drone CG. The forces and moments, and impacts on the drone were very insignificant up to a point close to collision. At about 4 m, the forces and moments exerted on the drone started to increase; however, these variations in the flow parameters occurred in a very small time (less than 0.1 s), which did not lead to large linear and angular displacements.

It can be concluded that, due to small impacts on the DJI drone from the variation of the pressure flow field along drone's trajectory towards the CRM, the drone did not deflect sufficiently to prevent the collision with the CRM wing. However, the goal of cross-verification was accomplished, based on the results obtained by NIAR and ERAU using different codes, to ensure that reliable results are included in this report, while there were no experimental results for the CRM at holding conditions.

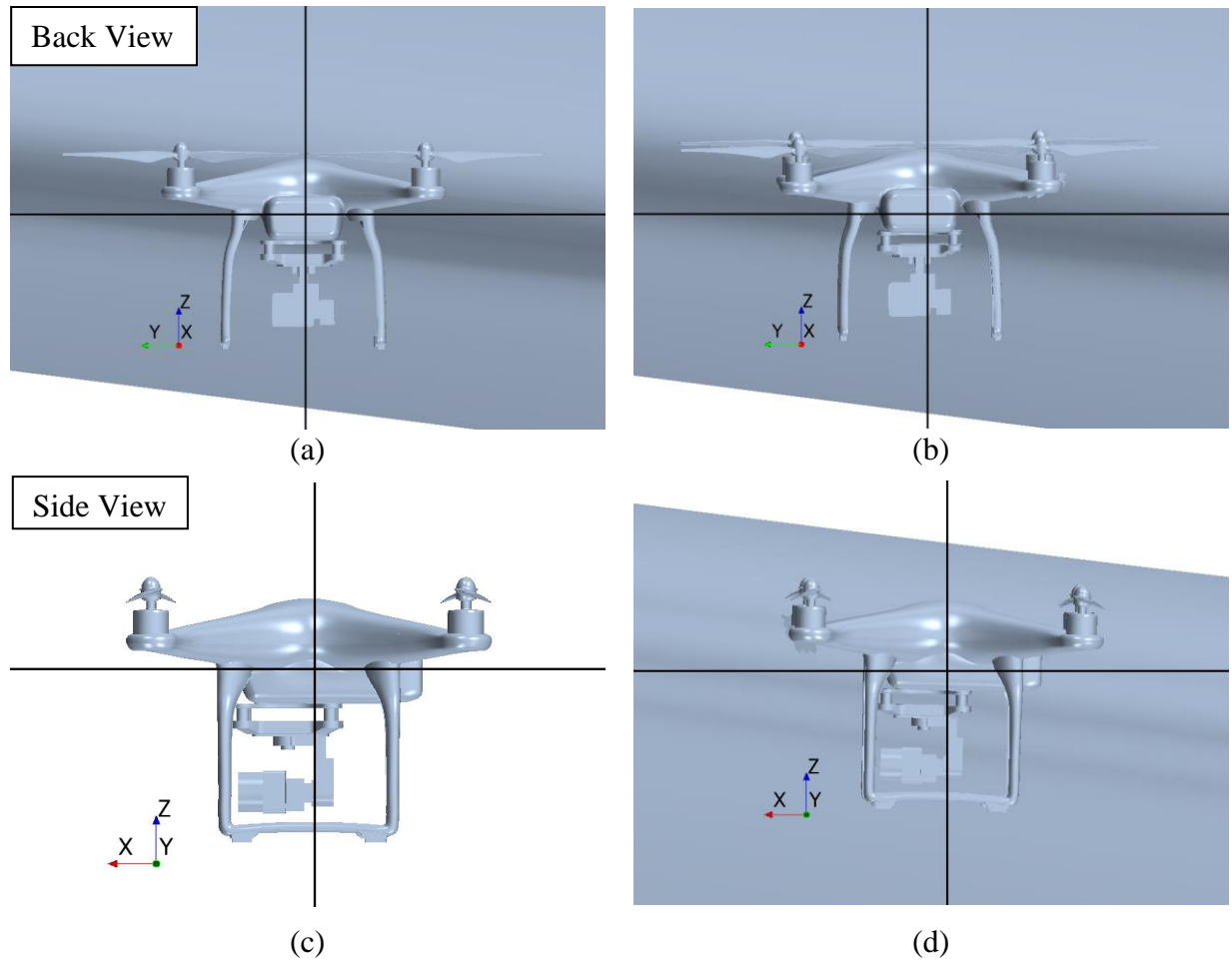


Figure 36. Displacements of the Drone from the initial directions resulting from the flow forces and moments for IC2-IL1.

### 3.2.5 Primary ERAU Results for All Impact Scenarios

The goal of the current study was to investigate the trajectory of the drone up to the point of collision with the aircraft at specific impact conditions and locations. The trajectory of the drone to the aircraft was obtained for different impact scenarios with the combinations of four different impact conditions, at two separate impact locations, with special cases with four different initial vertical placements of DJI drone relative to CRM wing and horizontal stabilizer. The results for the total of all impact scenarios are presented in this section in terms of the relative displacements: horizontal (over X), spanwise (over Y), and vertical (over Z), and the angular displacements about the X-axis ( $\Phi$ ), about the Y-axis ( $\Theta$ ), and the Z-axis ( $\Psi$ ). The results displaying forces and moments exerted on the DJI drone due to the impact of pressure flow field and the DJI drone velocity change are included in APPENDIX B. An additional case comparing the results of the simulations with original mesh configuration and adaptive mesh refinement method was performed to investigate the effects of optimized mesh configuration and higher time steps. This comparison was made for the impact scenario IC2-IL1, described in Table 3.

The vertical displacement of the drone determined the deflection of the drone from the leading edges of the aircraft wing and horizontal stabilizer at the time of impacts. The point of collision in the results was determined when the distance between the foremost point on the drone's rotors or chassis and the aircraft wing or horizontal stabilizer was approximately 0 m. It means that when the drone experienced greater angular displacements, the propeller was seen to impact the wing before the chassis was close enough.

The information regarding the definitions of linear and angular displacements experienced by the drone about its CG, and the selected sign conventions, defined by using the right-hand rule, is given in Figure 4 and Figure 5. The relative displacement of the DJI drone along the direction of the motion (X-axis), as described in section 2.7, was computed considering the difference between the location of the CG at any physical time and the location of the CG if the drone had been moving along a prescribed trajectory toward the impact location influenced by no forces. On the other hand, spanwise (i.e., relative to the wingtip of the aircraft) and vertical (i.e., relative to the centerline of the CRM wing or horizontal stabilizer leading edges) displacements indicated that the DJI drone moved from its initial coordinates along the Y- and Z-axis, respectively.

The DJI drone was required to sufficiently displace vertically (in Z-axis) relative to the point aligned with the leading edge of the CRM wing or horizontal stabilizer to avoid the collision. This vertical deflection varied for different impact scenarios analyzed in this section. Table 6 illustrates the required vertical displacements of the DJI drone for each impact scenario. It should be noted that for the special cases with the same impact condition and location similar to IC2-IL1, also explained in 1.5.2.1, the required vertical displacement to avoid collision with CRM wing was different compared to IC2-IL1. Additionally, the required vertical displacement for impact scenarios IC2-IL3, IC3-IL3, IC6-IL3 was calculated relative to the leading edge of the CRM horizontal stabilizer as the point of impact. For IC6-IL3, an inclined trajectory was also considered for the DJI drone towards the horizontal stabilizer to avoid an early collision with the CRM wing. In this specific case, which was a "modified IC3-IL3", due to 5° AoA of CRM, the DJI drone collided with the CRM wing before reaching the leading edge of the horizontal stabilizer.

The final displacements of the drone in the vertical and spanwise directions for impact scenarios impact scenario 1 are provided in Figure 37. The maximum vertical displacement was observed to be 0.045 cm (0.018 in) for IC2-IL1D1 and IC2-IL1D2. The maximum spanwise displacement of 0.088 cm (0.035 in) resulted in the impact scenario IC2-IL1U1. According to Table 6, these displacements are not sufficient to prevent the collision. It should be noted that, in order to be consistent in the presentation of the results, the results are shown for IC2-IL1, when the DFBI 6-DOF was enabled at a 4.5 m distance from the CRM wing leading edge (the distance between the drone CG and wing leading edge was 15 m at the time of release). A similar analysis for IC2-IL1 with an initial distance of 45 m was shown in sections 3.2.4.2 and B.2. The minor difference between the results obtained for IC2-IL1 with initial distances of 4.5 m and 45 m resulted from the force balance and additional time required for the drone to travel to the point of collision. The final conclusion was not affected by these differences. Additional details of the time history of the forces, moments, displacements, and velocities experienced by the drone as it moved through the domain can be found in APPENDIX C.

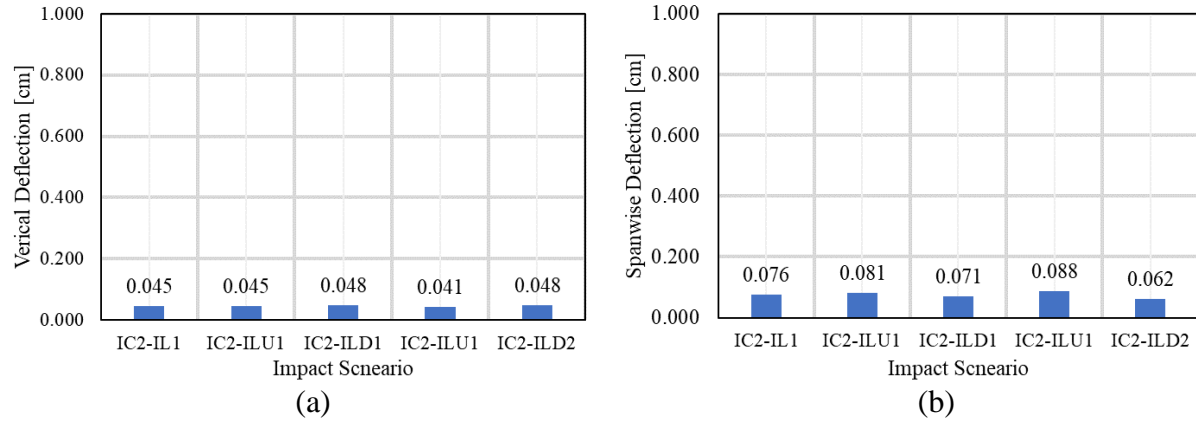


Figure 37. Vertical (a) and spanwise (b) displacements of the drone at the point of impact for IC2-IL1, IC2-IL1U1, IC2-ILD1, IC2-IL1U2, and IC2-ILD2. The unconstrained (6-DOF) rigid body motion was enabled at the distance of 4.5 m relative to the CRM wing leading edge.

To study the effects of the original mesh configuration (section 2.3) and the adaptive mesh refinement method (section 2.4.5), as well as different time steps on the flow solution (section 2.4.6), further investigations were performed on the impact scenario IC2-IL1. Figure 38 show the results of impact scenario IC2-IL1 for the following conditions: (1) original mesh, a time step of  $10^{-5}$ , and 6-DOF enabled at 4.5 m distance, (2) adaptive mesh refinement, a time step of  $10^{-4}$ , and 6-DOF enabled at 4.5 m distance, and (3) adaptive mesh refinement, a time step of  $10^{-4}$ , and 6-DOF enabled at 45 m distance. Although the results from the third condition show small differences in the vertical and spanwise displacements, these minor differences are acceptable and did not affect the conclusion of the current investigation.

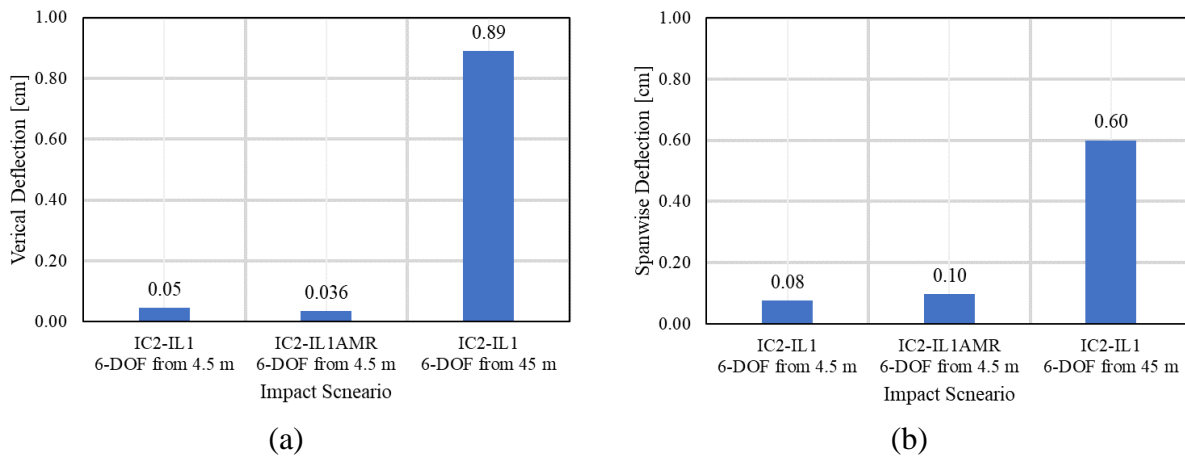


Figure 38. Vertical (a) and spanwise (b) displacements of the drone at the point of impact for IC2-IL1 with a variety of considerations, including using adaptive mesh refinement (AMR) method and different instantaneous locations for enabling 6-DOF rigid body motion.

Moreover, additional initial conditions for DFBI 6-DOF were investigated to ensure that the changes and uncertainties in the numerical solvers and initial conditions do not affect the outcomes

of the current study. Therefore, for the impact scenario IC2-IL3, described in section 1.5, different inputs to the force balance were analyzed to better understand the trajectory of the DJI with respect to the displacements of the drone approaching the horizontal stabilizer. These initial conditions of the force balance were: (1) instantaneous forces and moments obtained at the time step before enabling the 6-DOF solver and (2) averaged values of forces and moments in the last 5 m of drone’s motion before enabling the 6-DOF solver. These results are shown in Figure 39. The vertical displacements of the drone for this impact scenario were 0.089 cm and 0.094 cm for the force balance conditions with instantaneous and averaged values, respectively. The difference in the spanwise displacement was also very small, about 0.013 cm between the two force balance conditions. It should be noted that the drone was released at a distance of 74 m from the horizontal stabilizer and showed negligible differences with the two force balance conditions. Therefore, we concluded that the use of each condition could result in reliable and accurate results.

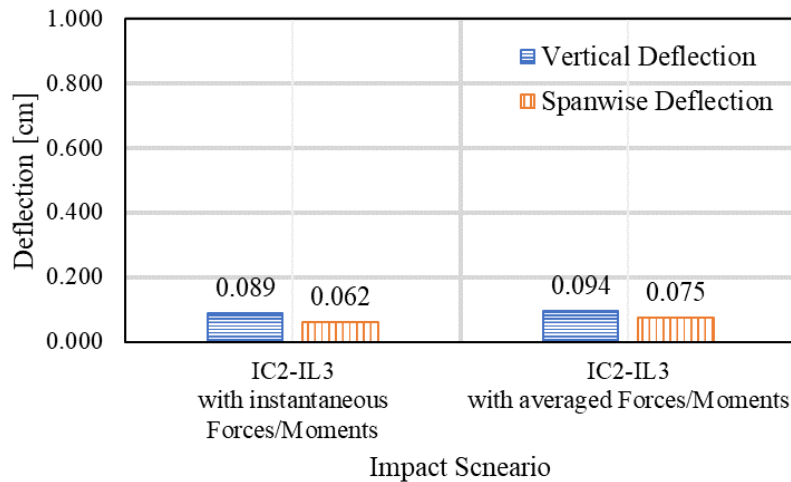


Figure 39. Vertical and spanwise displacements of the drone at the point of impact for IC2-IL3 with a variety of considerations, including using adaptive mesh refinement (AMR) method and different force balance values when enabling 6-DOF rigid body motion.

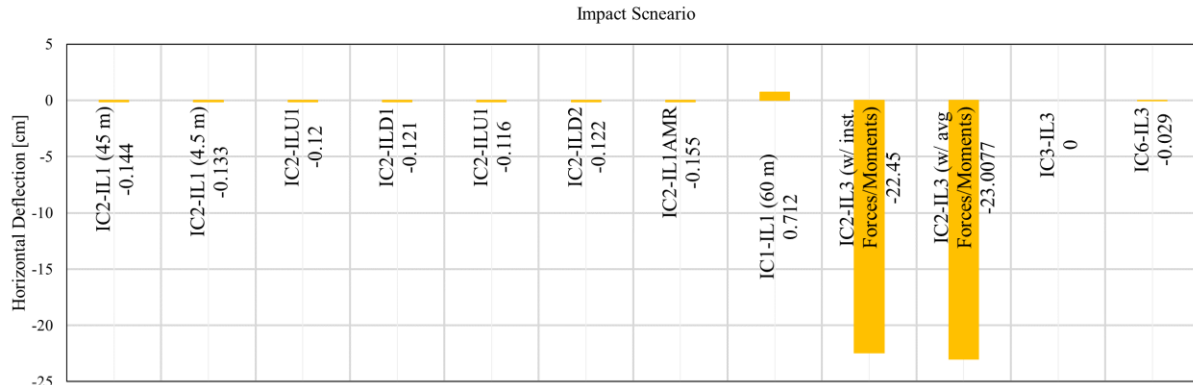
Table 9 summarizes the horizontal, spanwise, and vertical displacements of the drone for each impact scenario at the point of impact. In these results, the negative horizontal displacement indicates that the drone slowed down as it approached the aircraft due to the drag forces. There are other factors such as initial forces and moments used in the force balance and inclusion of the CRM fuselage that also affected the displacements of the drone between the impact scenarios. The largest horizontal displacements were for the impact scenarios between the drone and CRM horizontal stabilizer in the presence of the drag forces caused by the CRM fuselage and wing before the drone reached the point of collision.

The largest relative vertical displacements were observed for IC6-IL3, IC2-IL1 (45 m), and IC1-IL1 (60 m), respectively. The drone experiences the highest lift forces from the CRM fuselage and wing as it approached the horizontal stabilizer with an inclined prescribed trajectory for impact scenario IC6-IL3. It should be noted that for this impact scenario, the CRM aircraft was at an angle of attack of 5°. In addition, the largest spanwise displacement was also observed for the same impact scenario where the CRM fuselage could significantly affect the trajectory of the drone. It should be noted that for impact scenario IC3-IL3, no data was observed as the drone collided with

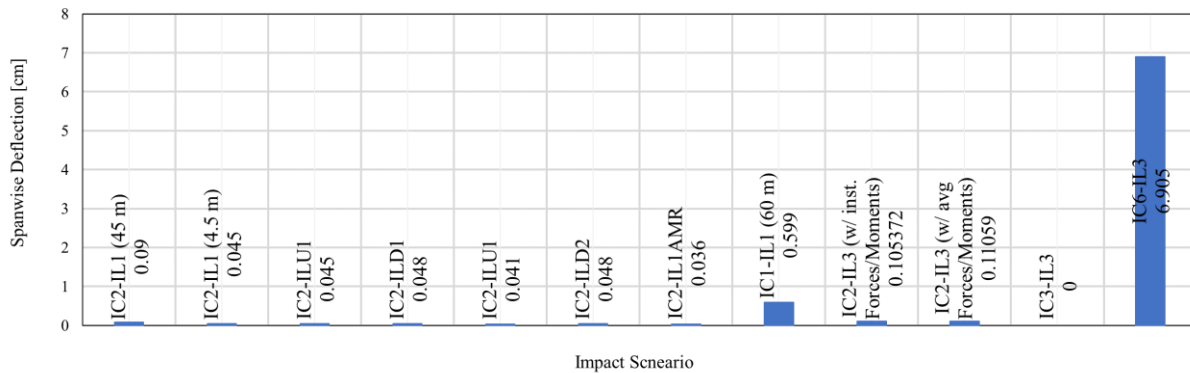
the CRM wing at an angle of attack of 5° before it reached the horizontal stabilizer. The same results are represented in Figure 40 to clearly compare the axial displacements of the drone for all impact scenarios.

Table 9. A summary of displacements of the drone for all impact scenarios.

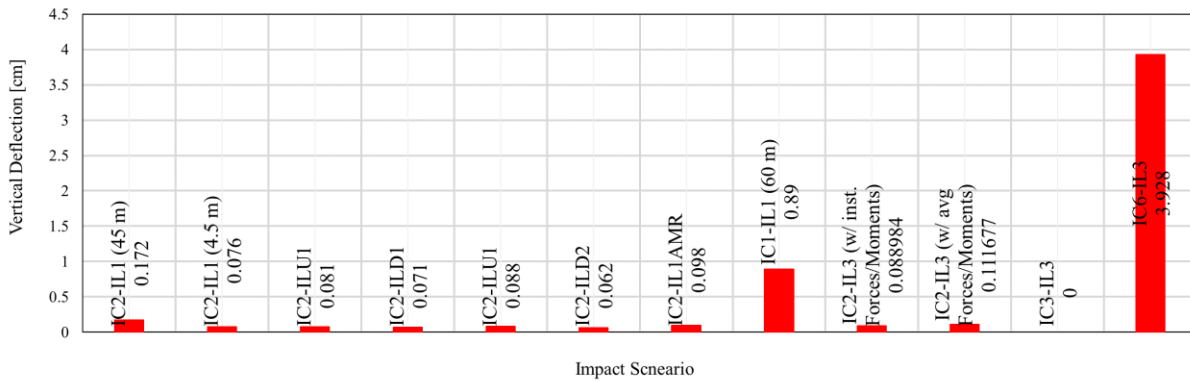
Impact Scenario	Drone Displacement [cm]		
	X	Y	Z
IC1-IL1 (60 m)	-0.144	0.090	0.172
IC2-IL1 (4.5 m)	-0.133	0.045	0.076
IC2-ILU1	-0.120	0.045	0.081
IC2-ILD1	-0.121	0.048	0.071
IC2-ILU1	-0.116	0.041	0.088
IC2-ILD2	-0.122	0.048	0.062
IC2-IL1AMR	-0.155	0.036	0.098
IC2-IL1 (45 m)	0.712	0.599	0.890
IC2-IL3 (w/ inst. Forces/Moments)	-12.974	0.089	0.062
IC2-IL3 (w/ avg Forces/Moments)	-13.077	0.094	0.075
IC3-IL3	Early collision of drone with CRM wing		
IC6-IL3	-0.029	6.905	3.928



(a)



(b)



(c)

Figure 40. Displacements of the drone along the X, Y, and Z axes at the point of impact for all cases studied in this section.

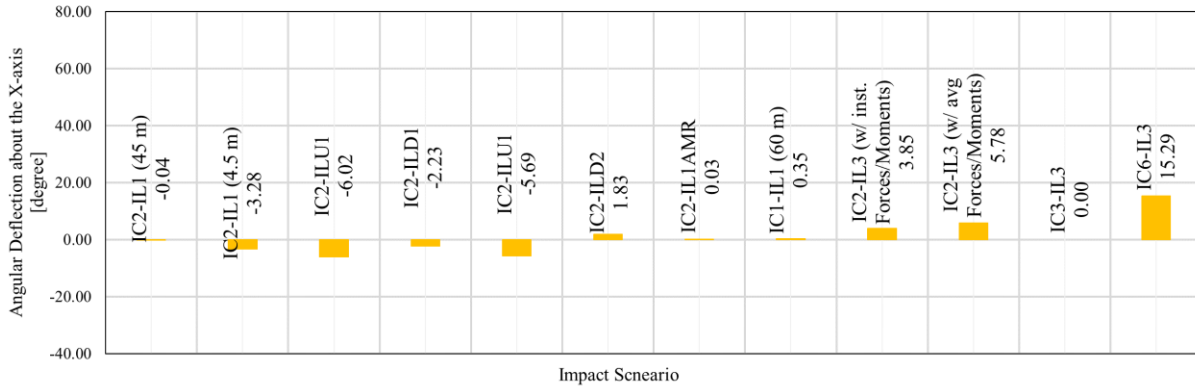
Table 10 summarizes the angular displacements of the drone around all axis for each impact scenario at the point of impact. The results are shown according to the sign convention described in section Sign Convention 2.8. The results of the angular displacements showed the highest uncertainties as they are influenced by the moments. Small variations in the moments resulted in differences in the orientation of the drone in all impact scenarios. This was also affected by the values used in the force balance. It should be noted that the orientation of the drone did not affect the conclusion of this report which was main focused on the required vertical deflection from the

point of collision. Therefore, the following information are included in this report to show that the orientation of the drone can change significantly due to the high impacts of the moments applied by the CRM. In most of the scenarios with the addition of the CRM fuselage, the change in the orientation of the drone was maximum. The largest angular displacement around the X-axis (Phi) was for the impact scenarios between the drone and CRM horizontal stabilizer in the presence of the moment by the CRM fuselage and wing before the drone reached the point of collision.

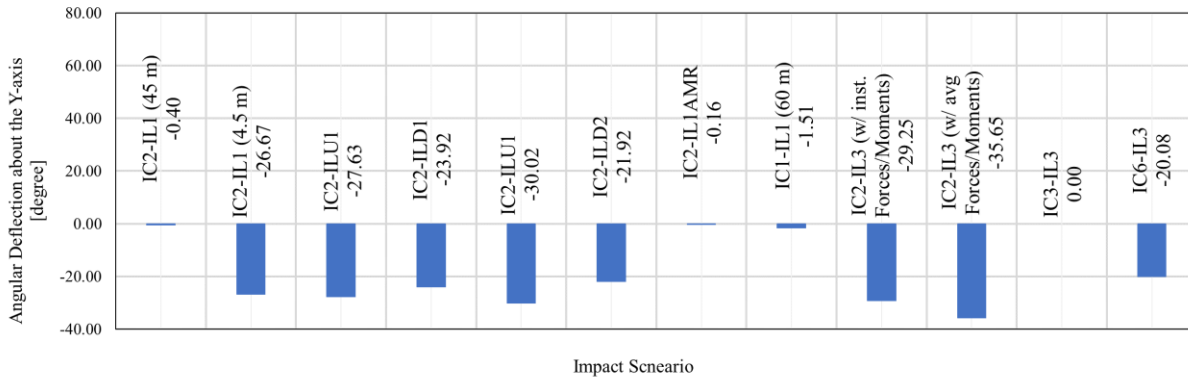
Similar results were observed for the angular displacement of the drone around the Y- (Theta) and Z- (Psi) axis. Figure 41 clearly shows the differences in the angular displacements of the drone for all impact scenarios.

Table 10. A summary of angular displacements of the drone for all impact scenarios.

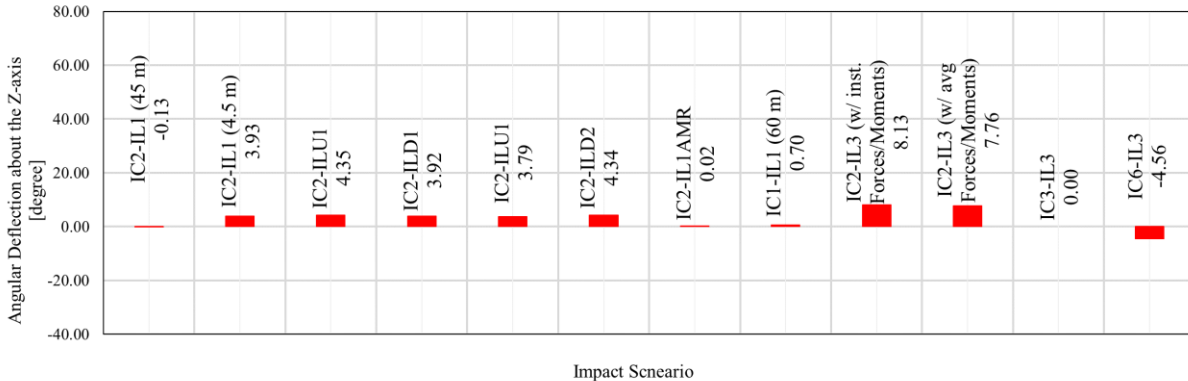
Impact Scenario	Drone Angular Displacement [degrees]		
	Phi	Theta	Psi
IC1-IL1 (60 m)	-0.04	-0.40	-0.13
IC2-IL1 (4.5 m)	-3.28	-26.67	3.93
IC2-IL1U1	-6.02	-27.63	4.35
IC2-IL1D1	-2.23	-23.92	3.92
IC2-IL1U1	-5.69	-30.02	3.79
IC2-IL1D2	1.83	-21.92	4.34
IC2-IL1AMR	0.03	-0.16	0.02
IC2-IL1 (60 m)	0.35	-1.51	0.70
IC2-IL3 (w/ inst. Forces/Moments)	2.47	-20.73	7.44
IC2-IL3 (w/ avg Forces/Moments)	3.83	-24.74	7.45
IC3-IL3	Early collision of drone with CRM wing		
IC5-IL3	15.29	-20.08	-4.56



(a)



(b)



(c)

Figure 41. The angular displacement of the drone about the X, Y, and Z axes at the point of impact for all cases studied in this section.

#### 4. CONCLUSIONS

This study investigated the trajectory of a Phantom 3 DJI drone and deflection from the point of collision with a CRM aircraft wing and horizontal stabilizer. The main focus was on the vertical displacement of the drone with respect to the initial direction and its prescribed motion. The sufficient vertical displacement of the drone could lead to the possible deflection from the

collision. Therefore, several impact scenarios involving different impact locations and conditions were analyzed in parallel studies done by ERAU and NIAR. The results presented in this report showed the variation in the trajectory of the DJI drone based on the reaction forces and moments exerted on the drone. The validation of the flow around the CRM aircraft and the cross-verification between the results obtained by ERAU and NIAR using different CFD codes ensured that the results were sufficiently accurate and reliable.

Findings from this research can be used to help understand the interactions due to the pressure flow fields around the drone and CRM at high speeds for different impact scenarios. Due to these interactions, the drone experienced a maximum vertical deflection of less than 1 cm and 4 cm for the impacts at the CRM wing and horizontal stabilizer, respectively. A maximum spanwise deflection of 0.6 cm and 7 cm was also obtained from the analysis of the DJI drone trajectory towards the CRM wing and horizontal stabilizer, respectively. The larger vertical and spanwise displacements were expected for the impact scenarios with the horizontal stabilizer as the presence of the CRM fuselage created a larger region with stronger pressure flow field impacting the moving drone. A complementary analysis of the forces, moments, angular displacement (orientation of the drone), and linear and angular velocities were also included in this report. The deflection, especially in the vertical direction, was not sufficient in any of the impact scenarios to prevent the collision between the DJI drone and CRM aircraft.

## 5. REFERENCES

- [1] J. Gundlach, “Overview of Unmanned Aircraft Systems,” in *Designing Unmanned Aircraft Systems*, 2012.
- [2] C. A. Wargo, G. C. Church, J. Glaneueski, and M. Strout, “Unmanned Aircraft Systems (UAS) research and future analysis,” 2014, doi: 10.1109/AERO.2014.6836448.
- [3] D. Jenkins and B. Vasigh, “The Economic Impact of Unmanned Aircraft Systems Integration in the United States,” 2013.
- [4] X. Lu, X. Liu, Y. Li, Y. Zhang, and H. Zuo, “Simulations of airborne collisions between drones and an aircraft windshield,” *Aerosp. Sci. Technol.*, 2020, doi: 10.1016/j.ast.2020.105713.
- [5] M. J. Conroy *et al.*, “Sources of variation in detection of wading birds from aerial surveys in the Florida everglades,” 2008. doi: 10.1525/auk.2008.07134.
- [6] G. P. JONES, L. G. PEARLSTINE, and H. F. PERCIVAL, “An Assessment of Small Unmanned Aerial Vehicles for Wildlife Research,” *Wildl. Soc. Bull.*, 2006, doi: 10.2193/0091-7648(2006)34[750:aaosua]2.0.co;2.
- [7] N. Zhang, H. Liu, B. F. Ng, and K. H. Low, “Collision probability between intruding drone and commercial aircraft in airport restricted area based on collision-course trajectory planning,” *Transp. Res. Part C Emerg. Technol.*, 2020, doi: 10.1016/j.trc.2020.102736.
- [8] K. Dalamagkidis, K. P. Valavanis, and L. A. Piegl, “On unmanned aircraft systems issues, challenges and operational restrictions preventing integration into the National Airspace System,” *Progress in Aerospace Sciences*. 2008, doi: 10.1016/j.paerosci.2008.08.001.
- [9] D. A. Wiegmann and N. Taneja, “Analysis of injuries among pilots involved in fatal general aviation airplane accidents,” *Accid. Anal. Prev.*, 2003, doi: 10.1016/S0001-4575(02)00037-4.
- [10] FAA, “Overview of Small UAS Notice of Proposed Rulemaking,” [http://www.faa.gov/regulations\\_policies/rulemaking/media/021515\\_sUAS\\_Summary.pdf](http://www.faa.gov/regulations_policies/rulemaking/media/021515_sUAS_Summary.pdf), 2015.
- [11] M. B. Rivers and A. Dittberner, “Experimental investigations of the NASA common research model,” 2014, doi: 10.2514/1.C032626.
- [12] S. Keye and R. Rudnik, “Validation of wing deformation simulations for the NASA CRM model using fluid-structure interaction computations,” 2015, doi: 10.2514/6.2015-0619.
- [13] M. B. Rivers, C. A. Hunter, and R. L. Campbell, “Further investigation of the support system effects and wing twist on the NASA common research model,” 2012, doi: 10.2514/6.2012-3209.
- [14] M. B. Rivers, “NASA Common Research Model,” 2018. <https://commonresearchmodel.larc.nasa.gov/home-2/high-speed-crm/experimental-approach/model-description/>.
- [15] D. S. Cairns, G. Johnson, M. Edens, and F. Arnold, “Volume I – UAS Airborne Collision Severity – Projectile and Target Definitions.” [Online]. Available:

[https://www.assureuas.org/projects/deliverables/a3/Volume I UAS Airborne Collision Severity Projectile and Target Definition.pdf](https://www.assureuas.org/projects/deliverables/a3/Volume%20I%20UAS%20Airborne%20Collision%20Severity%20Projectile%20and%20Target%20Definition.pdf).

- [16] G. Olivares, L. Gomez, J. E. de los Monteros, R. J. Baldrige, C. Zinzuwadia, and T. Aldag, "Volume II – UAS Airborne Collision Severity Evaluation – Quadcopter."
- [17] E. N. Tinoco *et al.*, "Summary data from the sixth AIAA CFD drag prediction workshop: CRM cases," 2018, doi: 10.2514/1.C034409.

## APPENDIX A– MESH SPECIFICATIONS

The determination of a valid mesh depends on the mesh quality and the physics models used for the simulation, especially in cases with high flow gradients and complex models. In this study, a trimmed mesh was initially used for the validation of the flow over the CRM wing at a Mach number of 0.85, as shown in Figure 42. Careful attention was paid to the regions with small and sharp surfaces that were subject to higher pressure and velocity gradients, such as the CRM wing leading edge, trailing edge, and the fuselage nose. The mesh size increases gradually in the far-field region to reduce the computational costs. Therefore, the fine mesh around the CRM and the coarse mesh in the far-field region could accurately solve the flow.

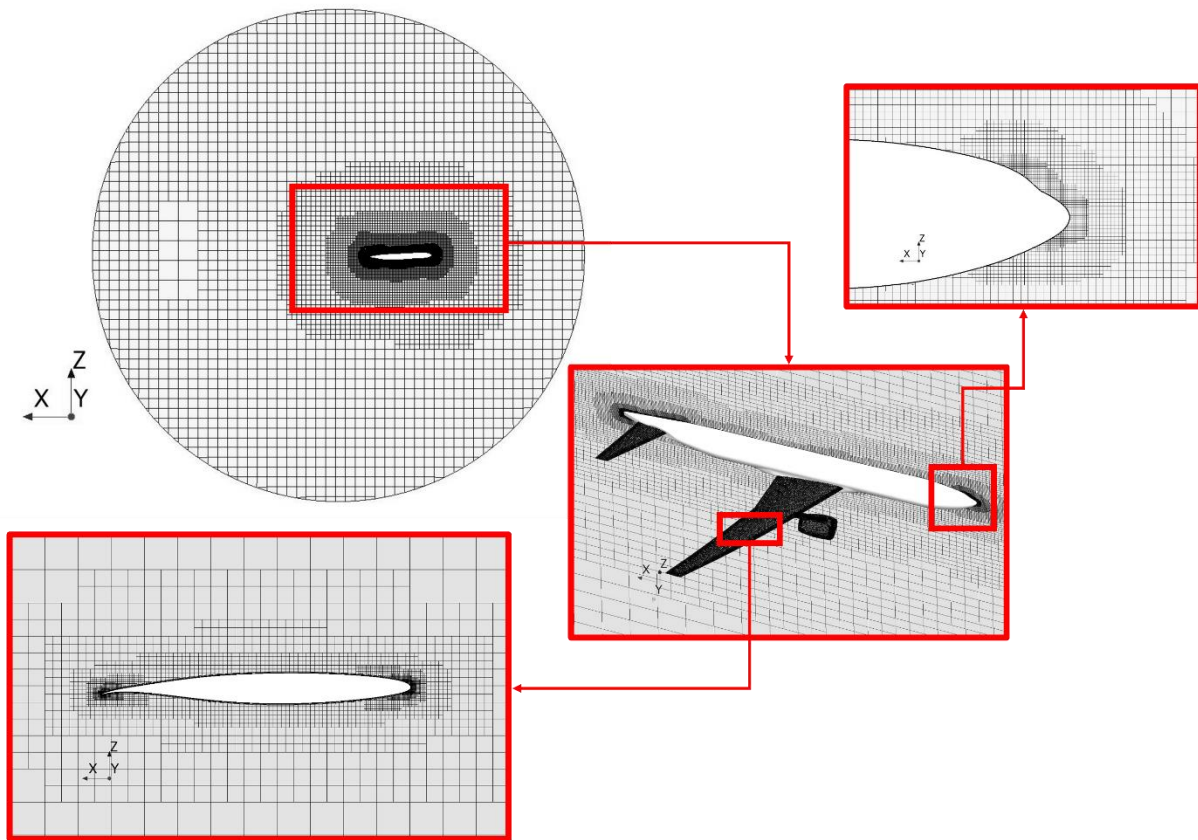


Figure 42. A trimmed mesh used for validation of flow around the CRM wing at a Mach number of 0.85.

Table 11 illustrates the mesh specifications for the flow over the CRM wing at a Mach number of 0.85. A high-quality surface mesh, especially around the trailing and leading edges of the CRM wing, is crucial for a suitable volume mesh. Therefore, the face quality of the surface mesh was checked and refined where necessary. Although the flow solution can be initialized on a valid mesh, a poor-quality mesh can negatively affect the solution; therefore, a detailed diagnosis of the volume mesh quality was performed to ensure the mesh generated for the current simulations resulted in accurate and reliable solutions. The percentage of the mesh elements that failed the quality criteria are also included in Table 11, which were mostly in the far-field region of the domain with coarser mesh cells. A wall  $y^+$  value of about one was achieved.

Table 11. Mesh Specifications for the flow around CRM wing at a Mach number of 0.85.

<b>Mesh Specifications (CRM Wing and Flow Domain)</b>		
<b>Total number of 3D elements</b>	<b>25,394,410</b>	
<b>Total number of Interior Faces</b>	<b>74,264,586</b>	
<b>Surface / Volume Mesh</b>		
Minimum Surface Size (trailing and leading Edges)	0.003 m	
Minimum Surface Size (wing, horizontal stabilizer, and engine)	0.005 m	
Surface Growth Rate	1.1	
Surface Curvature (# of points/circle)	76	
Surface Proximity (# of points in gaps)	2	
Edge Proximity (# of face)	3	
Perform Curvature/Proximity/Compatibility Refinement	Yes	
Volume Growth Rate	Slow	
Run Post Mesh Optimizer	Yes	
<b>Prism Layers</b>		
Number of Prism Layers	15	
Prism Layer Near Wall Thickness	$1.2 \times 10^{-6}$ m	
Total Thickness (Hyperbolic Stretching)	0.03 m	
Boundary March Angle	85.0°	
Minimum Thickness Percentage	0.01	
<b>Surface / Volume Mesh Quality</b>		
<b>Quality Criteria</b>	<b>Target</b>	<b>% Elements Failed</b>
Face Validity	1	0.000012
Cell Quality	$> 10^{-5}$	0.000004
Volume Change	$> 0.01$	0.00081
Skewness Angle	$< 85^\circ$	0.029
Cell Warpage Quality	$> 0.15$	0.000035
Zero or Negative Cell Volumes	0	0

The computational costs, including the simulation runtime and a need for more powerful computer resources, critically increase when the drone was added to the simulation. With the inclusion of the drone, additional refined meshes were required around the drone, with a smaller size relative to the CRM and along the trajectory of the drone moving towards the CRM wing and horizontal stabilizer. Therefore, an optimized polyhedral mesh was used for the analysis of the impact scenarios. It should be noted that the validation of the flow around the CRM wing at a Mach number of 0.85 was also done for the polyhedral mesh, which led to the same results described in 3.1.4.1. Figure 43 shows an example of the polyhedral mesh in the flow domain with a refined region around the CRM wing and the drone. The mesh specifications can be found in Table 12.

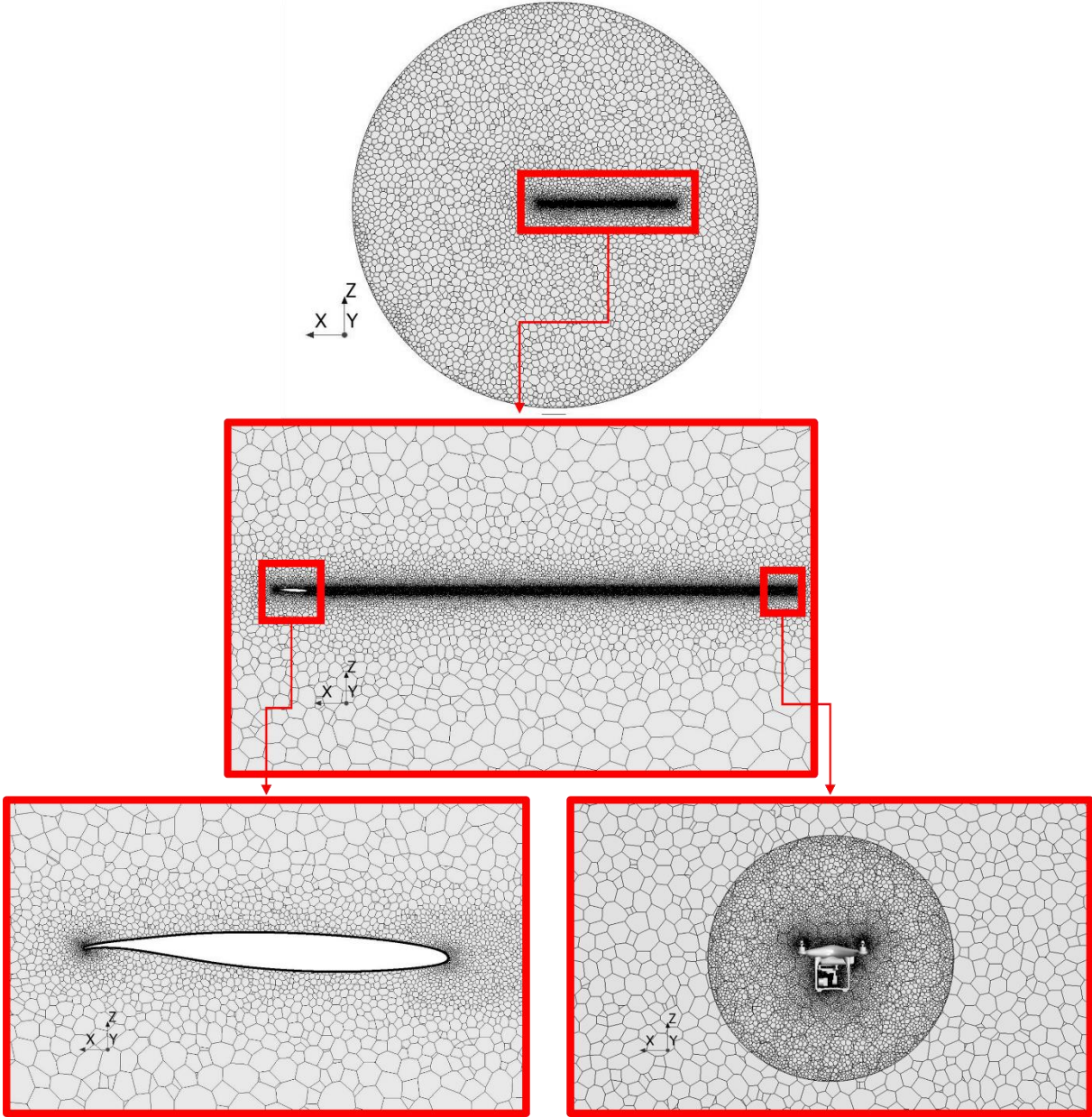


Figure 43. A polyhedral mesh used for the analysis of the impact scenarios at a Mach number of 0.3.

Table 12. Mesh Specifications for the analysis of the impact scenarios at a Mach number of 0.3.

<b>Mesh Specifications (CRM and Flow Domain)</b>		
<b>Total number of 3D elements</b>	<b>9,590,070</b>	
<b>Total number of Interior Faces</b>	<b>48,249,907</b>	
<b>Surface / Volume Mesh</b>		
Minimum Surface Size (trailing and leading Edges)	0.003 m	
Minimum Surface Size (wing, horizontal stabilizer, and engine)	0.005 m	
Minimum Surface Size (CRM fuselage)	0.05 m	
Surface Growth Rate	1.05	
Surface Curvature (# of points/circle)	76	
Surface Proximity (# of points in gaps)	2	
Perform Curvature/Proximity/Compatibility Refinement	Yes	
Volume Growth Rate	1.2	
Run Post Mesh Optimizer	Yes	
<b>Prism Layers</b>		
Number of Prism Layers	10	
Prism Layer Near Wall Thickness	0.0014	
Total Thickness (Hyperbolic Stretching)	0.03 m	
Boundary March Angle	85.0°	
Minimum Thickness Percentage	0.01	
<b>Surface / Volume Mesh Quality</b>		
<b>Quality Criteria</b>	<b>Target</b>	<b>% Elements Failed</b>
Face Validity	1	0.0
Cell Quality	$> 10^{-5}$	0.0
Volume Change	$> 0.01$	0.0
Skewness Angle	$< 85^\circ$	0.0
Cell Warpage Quality	$> 0.15$	0.0
Zero or Negative Cell Volumes	0	0.0

It should be noted that the surface and volume mesh for the CRM and the flow domain perfectly met the quality criteria as no mesh element failed the assessments. The wall  $y^+$  for the current mesh confirmation was about 300. Therefore, a Two-Layer All  $y^+$  solver that uses a blended wall function was added to accurately resolve the boundary layer with different mesh sizes when achieving a consistent wall  $y^+$  value is difficult due to varying geometrical and velocity scales.

Due to the smaller size of the DJI drone relative to the CRM, the mesh cell size was smaller on the drone's surface and within the overset mesh around it. This led to a higher mesh density from the initial location of the drone up to the point of collision along the trajectory. Figure 44 shows the fine mesh generated for the drone. Careful attention was paid to guarantee a high-quality surface mesh to precisely capture the complex geometry of the drone with small gaps and curvy surfaces, leading to accurate discretization and flow solutions.

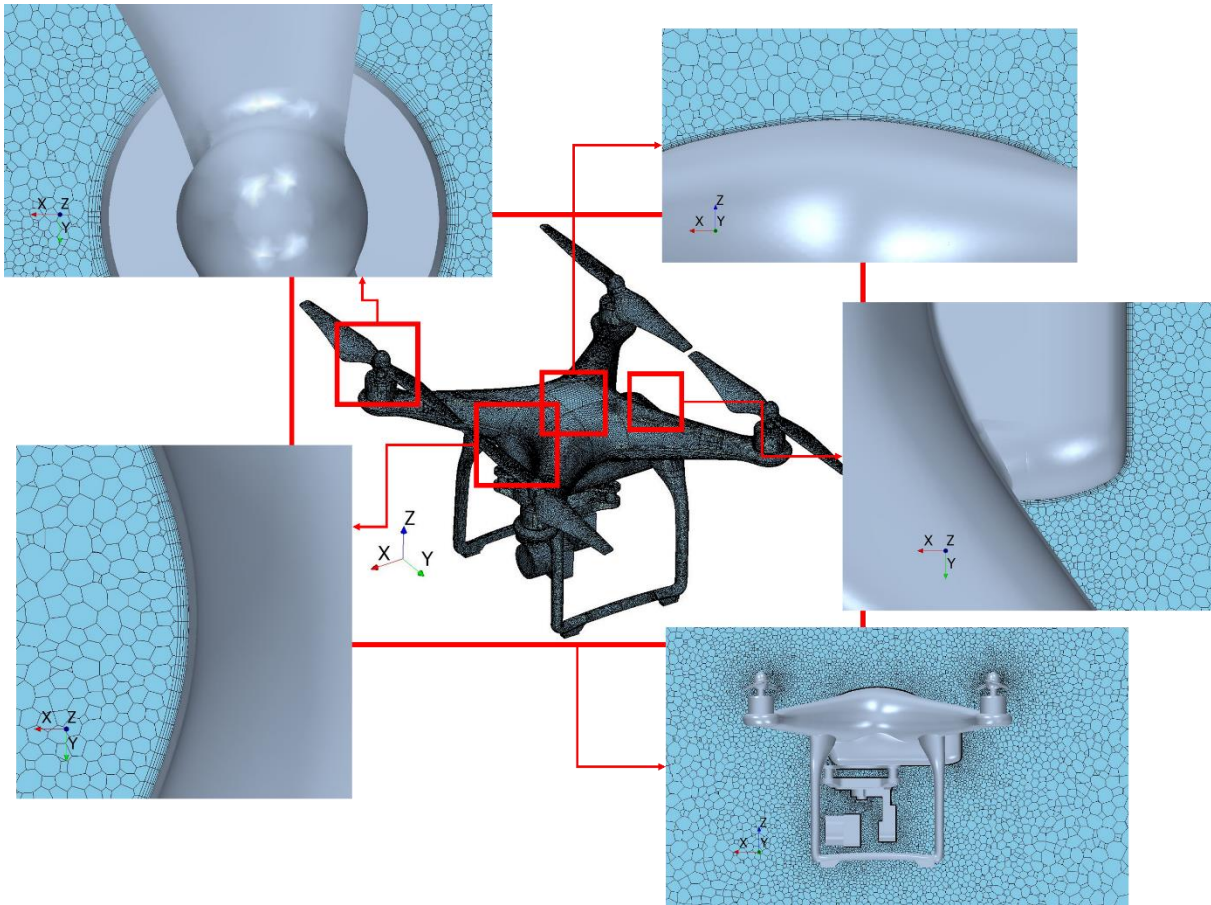


Figure 44. A polyhedral surface and volume mesh for the DJI drone.

Table 13 illustrates the mesh specifications for the flow over the DJI drone at a Mach number of 0.3. A high-quality surface mesh was essential to accurately capture the flow forces and moments on the drone. Therefore, the quality of the mesh was assessed and refined to successfully meet all the requirements. The percentage of the mesh elements that failed the quality criteria are also included in Table 13. The techniques used to create an overset mesh around the drone and optimize the mesh at larger time steps using the adaptive mesh refinement method were described in sections 2.4.4 and 2.4.5.

Table 13. Mesh Specifications for the moving DJI drone.

<b>Mesh Specifications (CRM and Flow Domain)</b>		
<b>Total number of 3D elements</b>	<b>3,967,724</b>	
<b>Total number of Interior Faces</b>	<b>24,158,567</b>	
<b>Surface / Volume Mesh</b>		
Minimum Surface Size	0.001 m	
Surface Growth Rate	1.05	
Surface Curvature (# of points/circle)	76	
Surface Proximity (# of points in gaps)	2	
Perform Curvature/Proximity/Compatibility Refinement	Yes	
Volume Growth Rate	1.05	
Run Post Mesh Optimizer	Yes	
<b>Prism Layers</b>		
Number of Prism Layers	5	
Prism Layer Stretching (Hyperbolic Stretching)	1.2	
Total Thickness (Hyperbolic Stretching)	0.001 m	
Boundary March Angle	85.0°	
Minimum Thickness Percentage	0.01	
<b>Surface / Volume Mesh Quality</b>		
<b>Quality Criteria</b>	<b>Target</b>	<b>% Elements Failed</b>
Face Validity	1	0.00088
Cell Quality	$> 10^{-5}$	0.0
Volume Change	$> 0.01$	0.0013
Skewness Angle	$< 85^\circ$	0.0015
Cell Warpage Quality	$> 0.15$	0.000025
Zero or Negative Cell Volumes	0	0

It should also be noted that an accurate prediction of the pressure drop in the flows with separation depends on resolving the velocity gradients normal to the wall. Prism layers allow the solver to resolve the near-wall flow more accurately. The information of the prism layers in boundary layers

of the CRM wing and DJI drone are described in this section. Figure 45 shows the vectors representing the velocity gradients in the boundary layers.

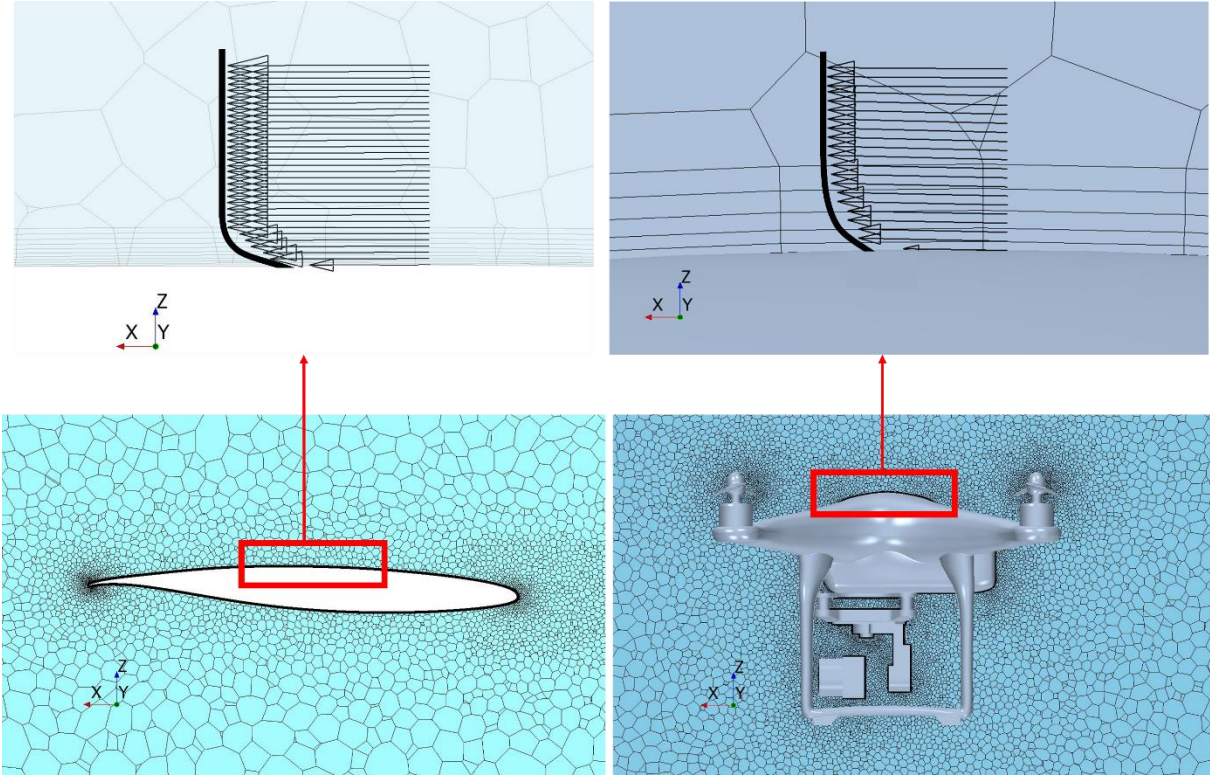


Figure 45. An accurate prediction of velocity gradients within the boundary layers of the CRM wing and DJI drone.

APPENDIX B- ADDITIONAL RESULTS OF THE CROSS-VERIFICATION

B.1 IMPACT SCENARIO IC1-IL1

A cross-verification study between the results obtained by NIAR and ERAU was required to ensure that (a) the two CFD codes used by the two institution provide consistent results for all impact scenarios and (b) due to the absence of experimental (wind tunnel) data of the CRM aircraft operation at holding condition (2500 ft), the results from the computational analysis are reliable. Therefore, the impact scenario IC1-IL1 was selected as the first case for cross-verification. These results are presented in section 3.2.4.1. The results shown in this section consist of zoomed views of flow forces and moments exerted on the DJI drone, angular displacement, and the axial and angular velocity of the drone with respect to the relative distance. Figure 46 shows the zoomed views of flow forces on the DJI drone with respect to the relative distance. In Figure 46(d), the initial forces used in the force balance are included. The forces experienced by the drone during the transient simulation were compared with the forces obtained from the prescribed trajectory analysis without the influence of the flow on the drone and the results provided by NIAR.

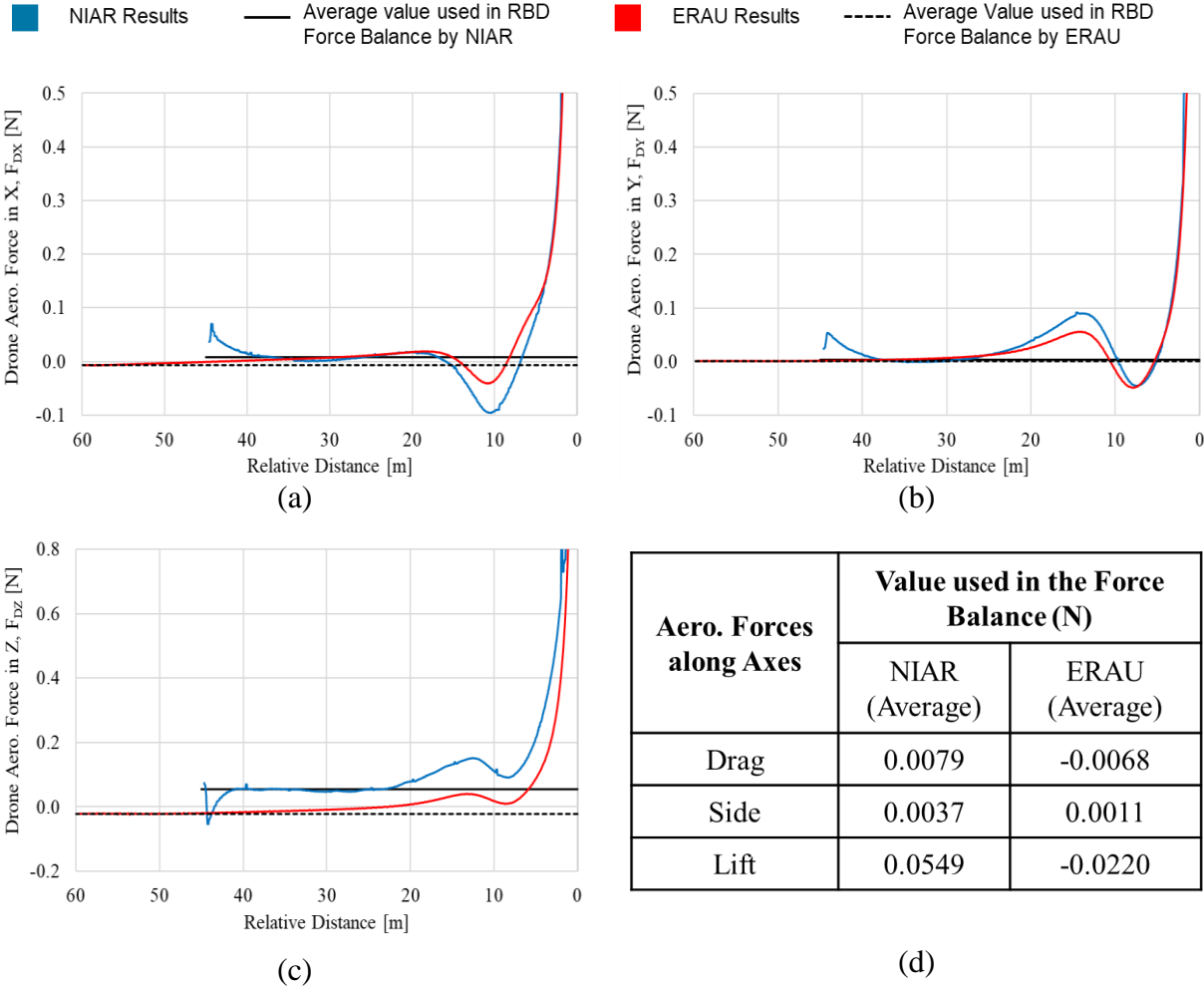


Figure 46. Zoomed views of flow forces on the DJI drone for IC1-IL1.

In the analysis done by ERAU, for the impact scenario IC1-IL1, the DJI drone was released at a distance of 90 m from the CRM leading edge, and the drone was allowed to move based on a prescribed motion without the influence of flow forces and moments for 30 m until the flow solution, especially around the drone, stabilized. Then, the DFBI 6-DOF was enabled from a distance of 60 m away from the leading edge of the CRM wing. Instantaneous aerodynamic forces and moments were used as external forces and moments in the force balance, as verified in Figure 39. The specifications of this impact scenario were explained in section 1.5. In this impact scenario, the results were obtained based on releasing the drone in the domain with the CRM aircraft wing without the fuselage and tail. Figure 47 shows the zoomed views of moments acting on the DJI drone with respect to the relative distance. In Figure 47(d), the initial moments used in the force balance are included. The moments experienced by the drone during the transient simulation were compared with the moments obtained from the prescribed trajectory analysis without the influence of the flow on the drone and the results provided by NIAR.

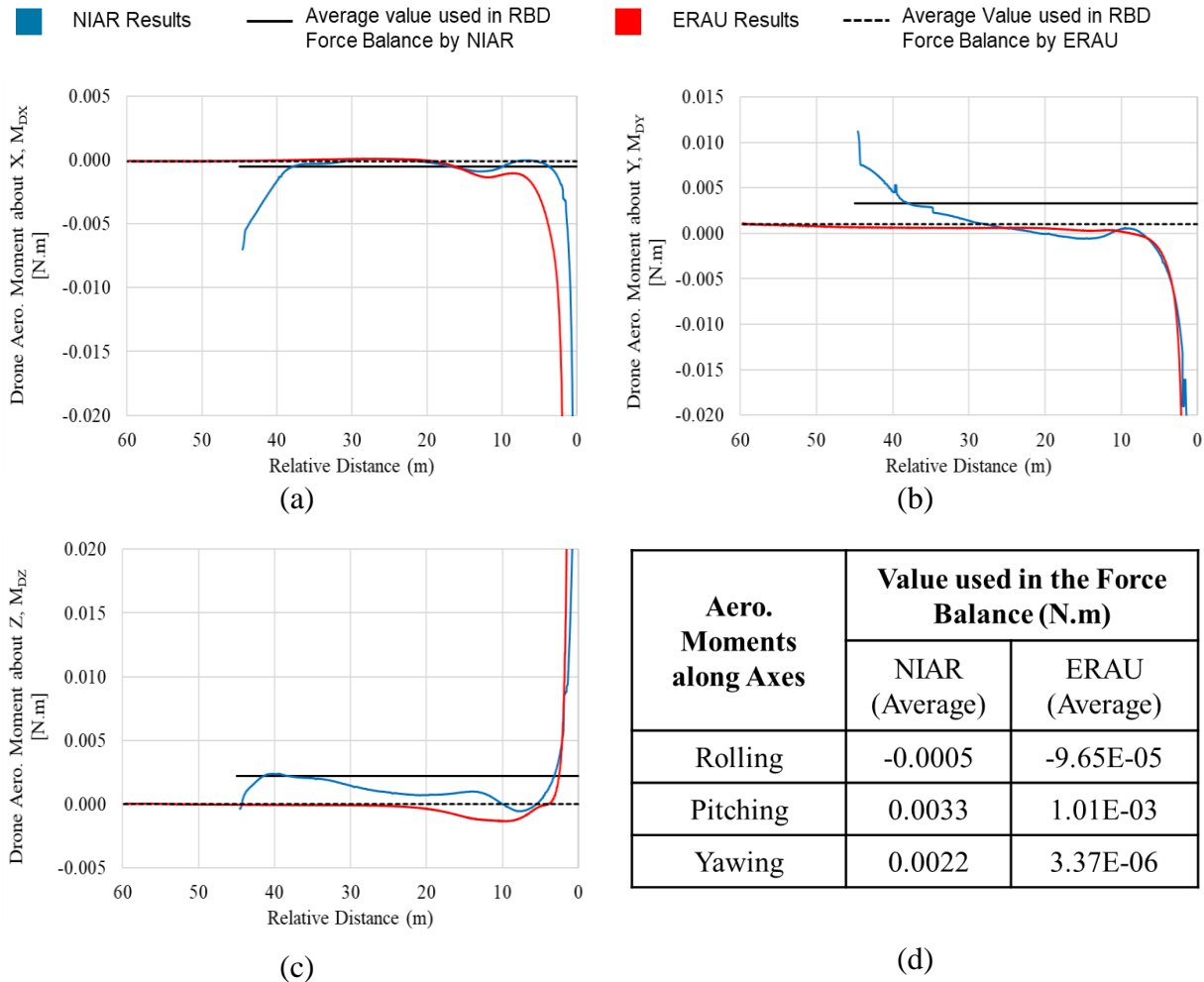


Figure 47. Zoomed views of moments on the DJI drone for IC1-IL1.

As the main focus of the current study, displacements of the drone from the initial direction were examined and cross-verified carefully to ensure reliable results obtained from each CFD code.

These results can be found in section 3.2.4.1. Figure 48 shows the angular displacements of the DJI drone around all axes with respect to the relative distance of the drone and the final angular displacements at the point of collision.

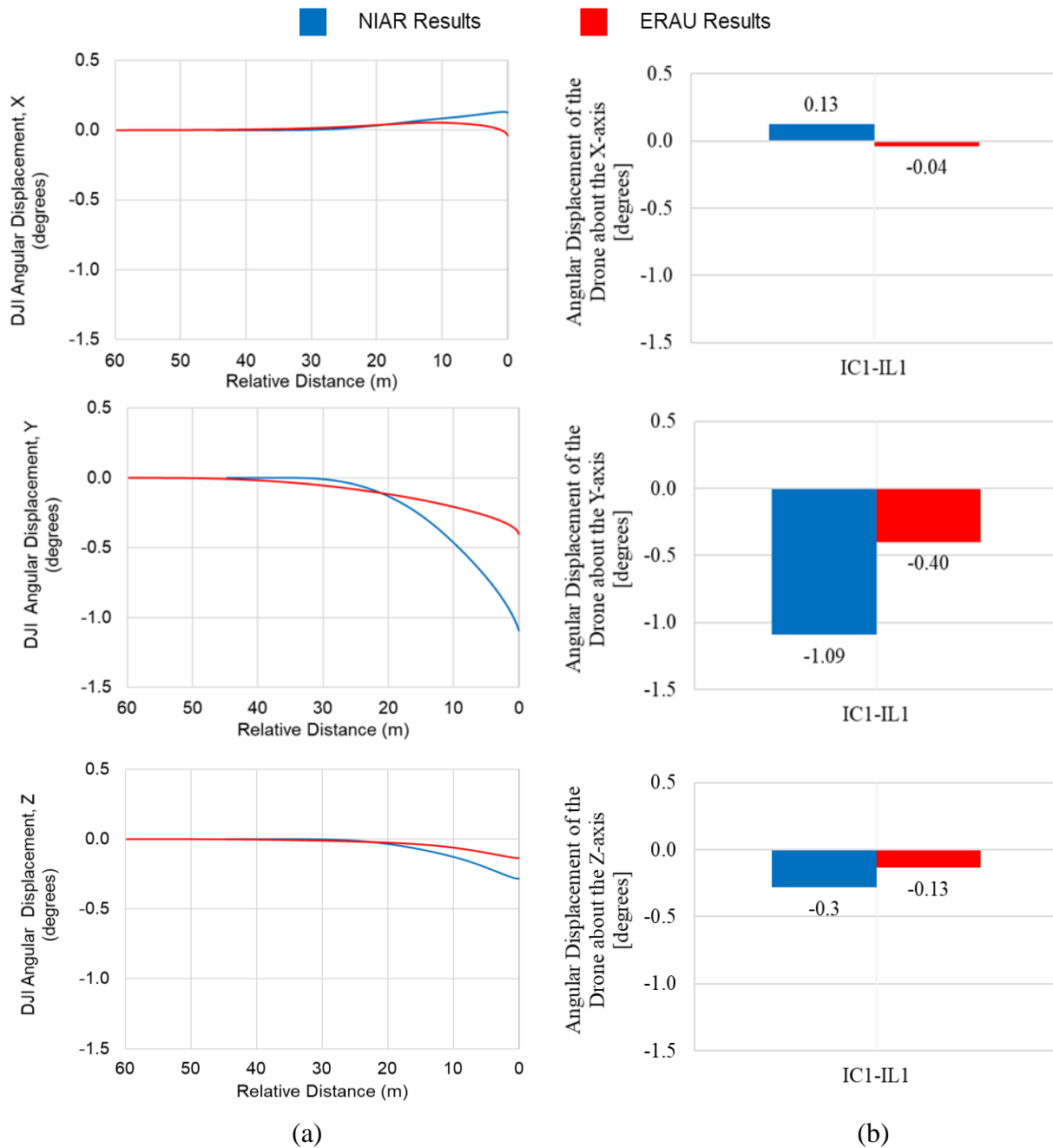


Figure 48. Angular displacements of the DJI drone for IC1-IL1; (a) the angular displacements with respect to the relative distance and (b) the final angular displacement of the drone at the point of collision.

The results obtained from NIAR and ERAU showed small angular displacements of less than one degree about all axes. It should be noted that the small differences in the results raised from the

flow solved using different CFD codes; however, these differences are acceptable and do not affect the final conclusions for each impact scenario. The velocities and angular velocities experienced by the drone as it approached the CRM aircraft wing for impact scenario IC1-IL1 are shown in Figure 49(a) and Figure 49(b), respectively.

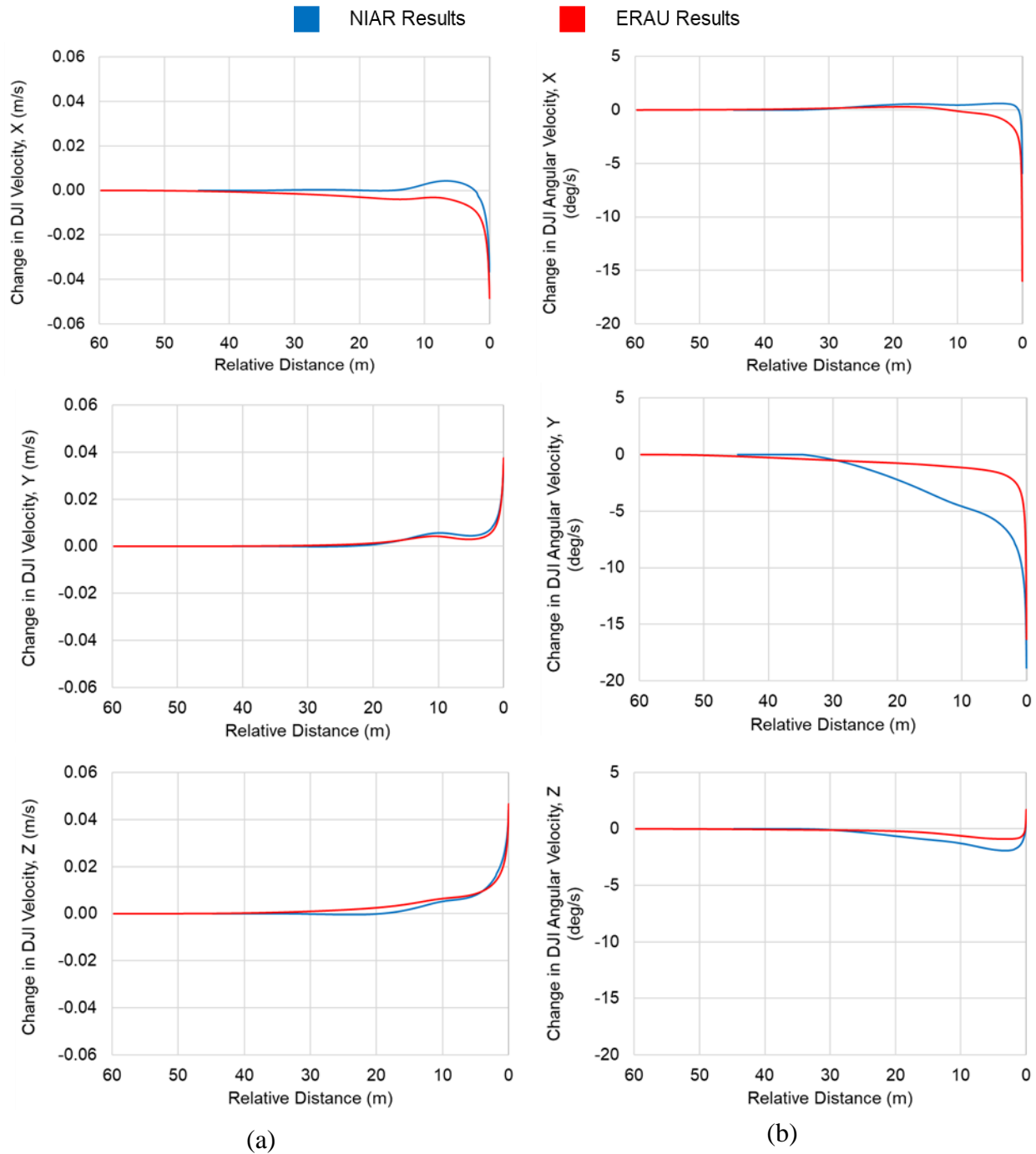


Figure 49. DJI drone axial (a) and angular (b) velocities for IC1-IL1.

## B.2 IMPACT SCENARIO IC2-IL1

A cross-verification study between the results obtained by NIAR and ERAU was also required to ensure that consistent results can be achieved using the two CFD codes for impact scenarios with higher momentums and inertial of the moving drone. This step was essential, especially due to the absence of experimental (wind tunnel) data of the CRM aircraft operation at holding condition (2500 ft). Therefore, the impact scenario IC2-IL1 was also selected for cross-verification. The main results of forces and displacements of the drone are presented in section 3.2.4.2. The results shown in this section consist of zoomed views of flow forces and moments exerted on the DJI drone, angular displacement, the axial and angular velocity of the drone with respect to the relative distance. Figure 50 shows the zoomed views of flow forces on the DJI drone with respect to the relative distance. In Figure 50d, the initial forces used in the force balance are included. The forces experienced by the drone during the transient simulation were compared with the forces obtained from the prescribed trajectory analysis without the influence of the flow on the drone and the results provided by NIAR. It should be noted that some oscillations were observed in the flow forces experienced by the drone. These oscillations can be filtered, as shown in the results provided by NIAR.

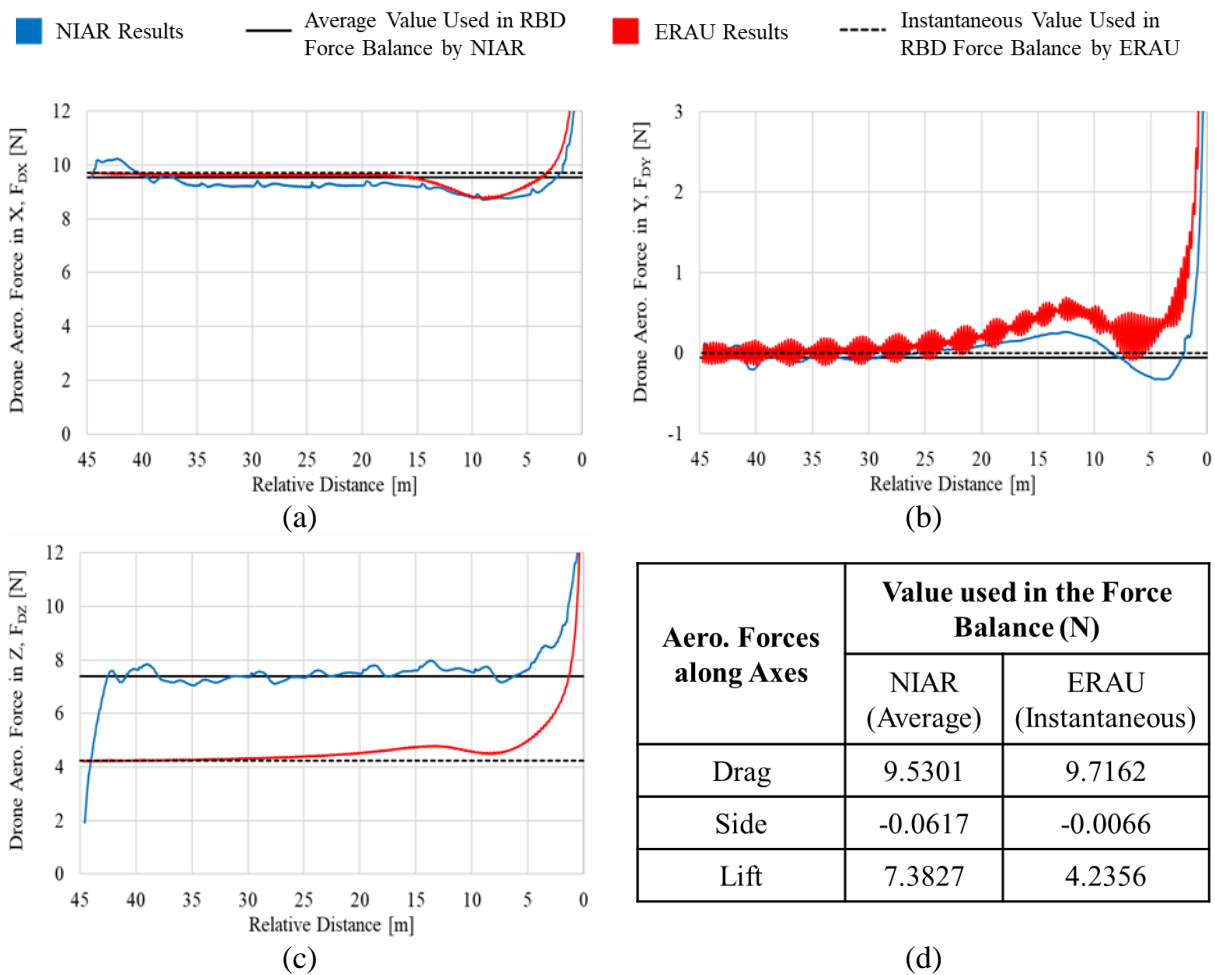


Figure 50. Zoomed views of the flow forces on the DJI drone for IC2-IL1.

In the analysis done by ERAU, for the impact scenario IC2-IL1, the DJI drone was released at a distance of 90 m from the CRM leading edge, and the drone was allowed to move based on a prescribed motion without the influence of flow forces and moments for 45 m until the flow solution, especially around the drone, stabilized. This distance was larger compared to IC1-IL1 due to an additional simulation time required for the flow to stabilize. Then, the DFBI 6-DOF was enabled from a distance of 45 m away from the leading edge of the CRM wing. Instantaneous aerodynamic forces and moments were used as external forces and moments in the force balance, as verified in Figure 39. The specifications of this impact scenario were explained in section 1.5. Figure 51 shows the zoomed views of moments acting on the DJI drone with respect to the relative distance. In Figure 51d, the initial moments used in the force balance are included. The moments experienced by the drone during the transient simulation were compared with the moments obtained from the prescribed trajectory analysis without the influence of the flow on the drone and the results provided by NIAR. It should be noted that some oscillations were observed in the moments experienced by the drone. These oscillations can be filtered, as shown in the results provided by NIAR.

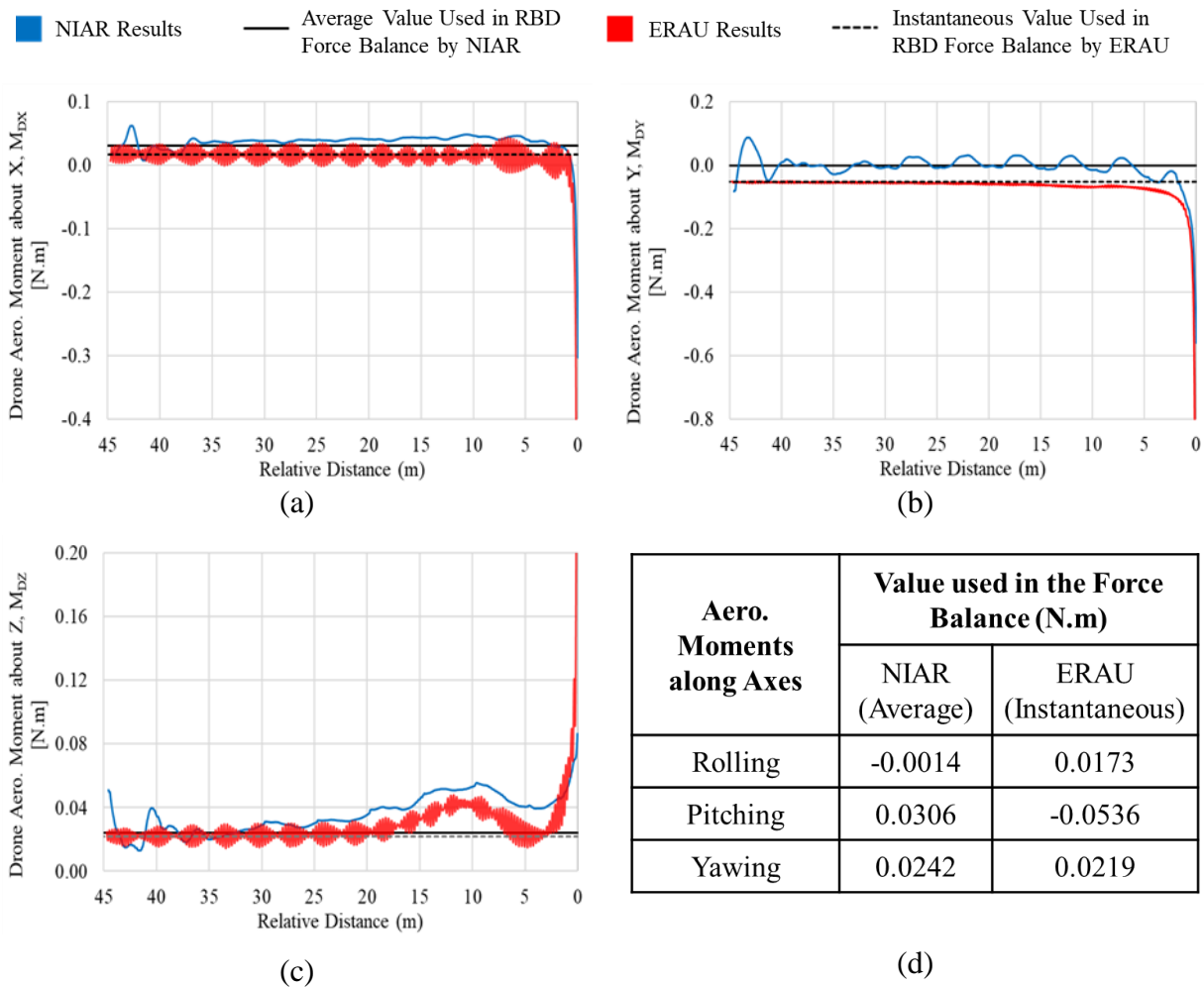


Figure 51. Zoomed views of the moments on the DJI drone for IC2-IL1.

As the main focus of the current study, displacements of the drone from the initial direction were examined and cross-verified carefully to ensure reliable results obtained from each CFD code. These results can be found in sections 3.2.4.1 and 3.2.4.2. Figure 52 shows the angular displacements of the DJI drone around all axes with respect to the relative distance of the drone and the final angular displacements at the point of collision.

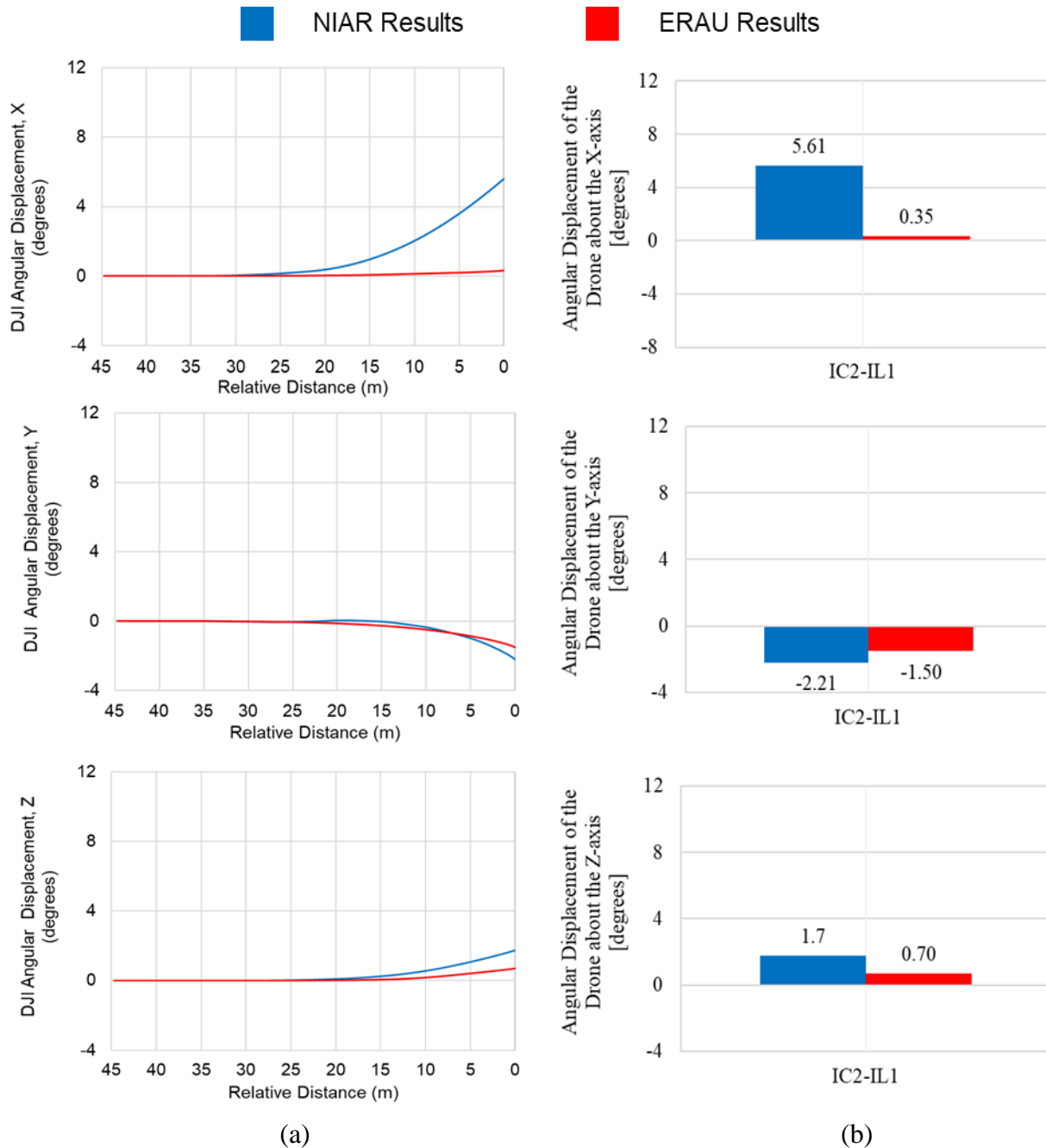


Figure 52. Angular displacements of the DJI drone for IC2-IL1; (a) the angular displacements with respect to the relative distance and (b) the final angular displacement of the drone at the point of collision.

The results obtained from NIAR and ERAU showed small angular displacements of less than 5 degrees about all axes. It should be noted that the small differences in the results raised from the flow solved using different CFD codes; however, these differences are acceptable and do not affect the final conclusions for each impact scenario. The velocities and angular velocities experienced by the drone as it approached the CRM aircraft wing for impact scenario IC2-IL1 are shown in Figure 53(a) and Figure 53(b), respectively. The changes in the axial and angular velocities are very small and did not contribute to the deflection of the drone from the point of collision.

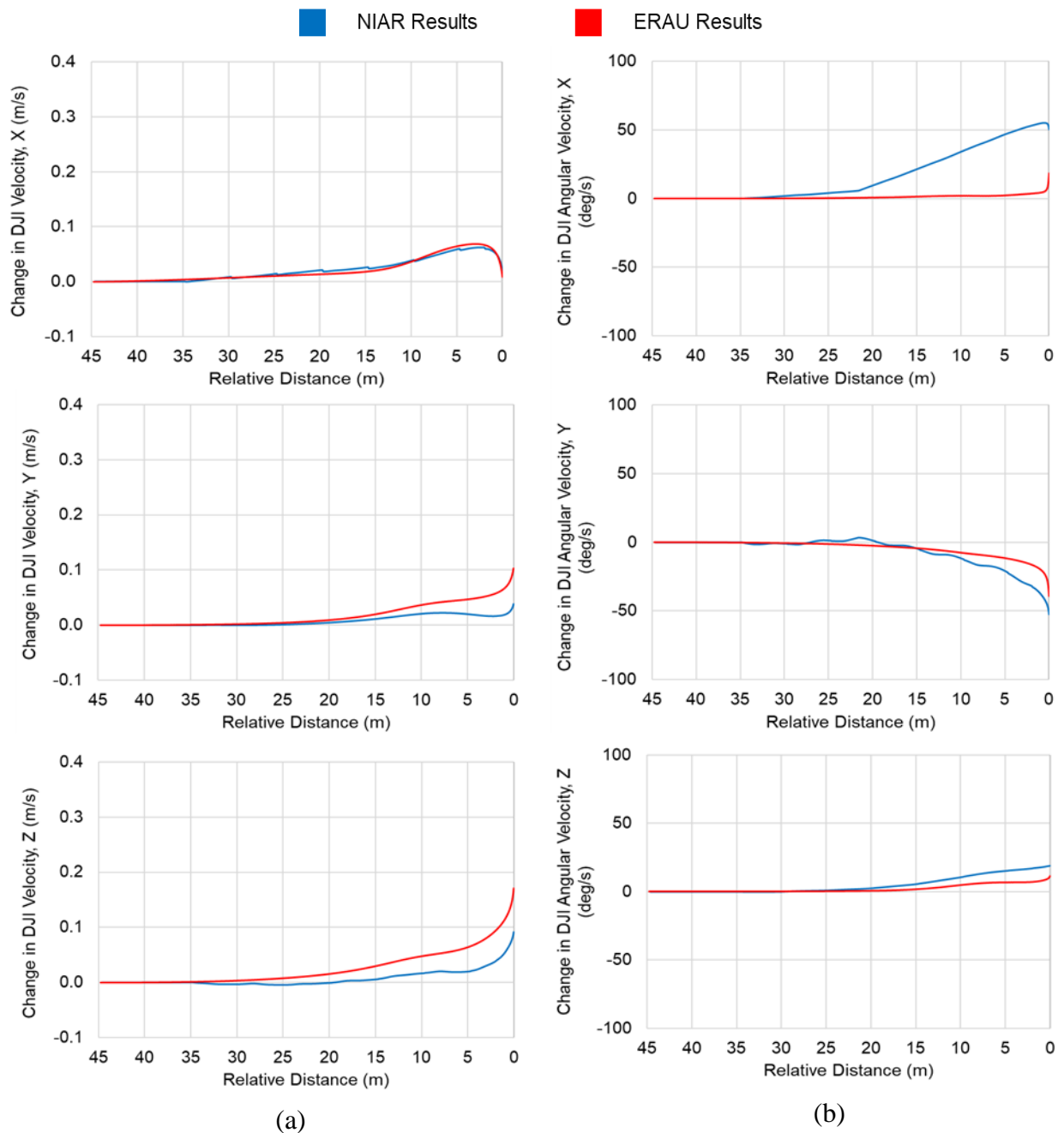


Figure 53. DJI drone axial (a) and angular (b) velocities for IC2-IL1.

APPENDIX C- ADDITIONAL RESULTS OF IMPACT SCENARIOS

C.1 IMPACT SCENARIO 1

For the special case of impact scenario IC2-IL1U1, the results were obtained based on releasing the drone in the domain with the CRM aircraft wing without the fuselage and tail. The drone was released from a distance of 15 m away from the leading edge of the wing at a plane located at a distance of 16.80 m (55.12 ft) in the spanwise direction from the symmetry plane. Once released, the drone was allowed to move, without the influence of forces and moments, for about 10.5 m to ensure a stable flow solution before enabling the 6-DOF. The instantaneous aerodynamic forces and moments were used as external forces and moments in the UDF.

The forces experienced by the aircraft during the transient simulation were compared with the forces obtained from the steady-state simulation of the CRM aircraft in the domain. Figure 54 shows good agreement between the steady-state and the transient simulation results for the CRM aircraft wing.

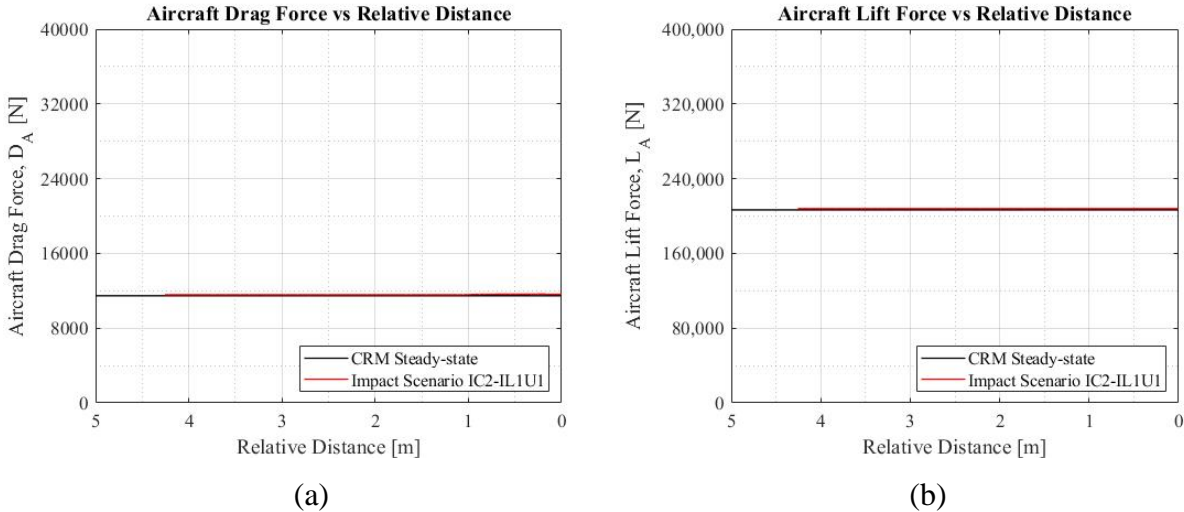


Figure 54. CRM aircraft lift and drag forces recorded as the drone approached the aircraft wing.

The drone forces and moments were plotted with the instantaneous values of the forces used to balance the drone independent of aerodynamic forces. The change in forces and moments as the drone approaches the CRM aircraft can be seen in Figure 56(a) and Figure 56(b), respectively. Figure 55 provides a reference for the axis systems used in the plots.

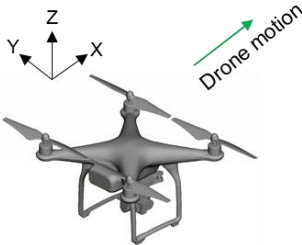
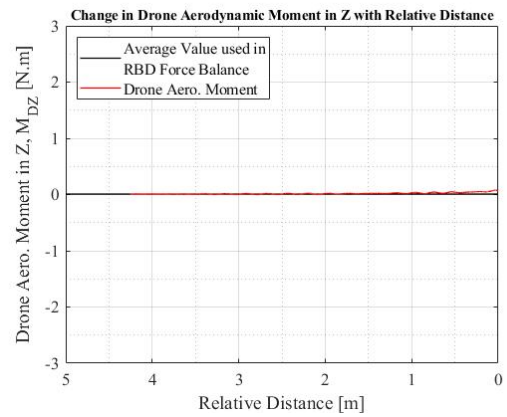
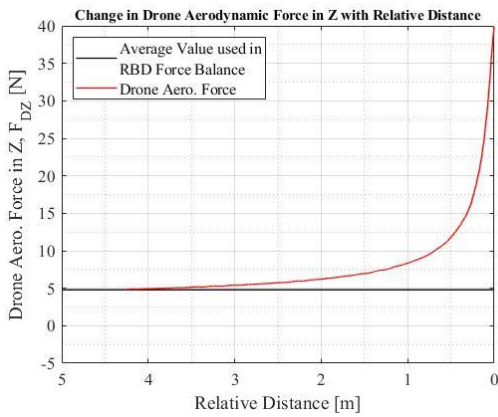
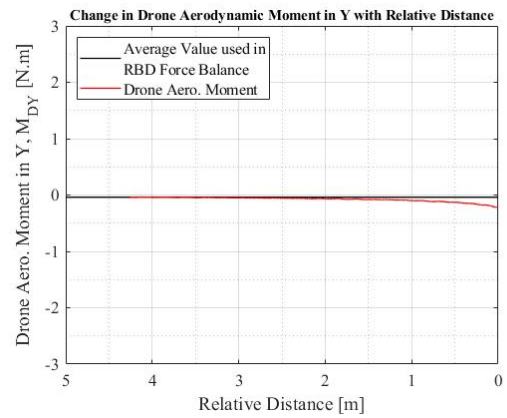
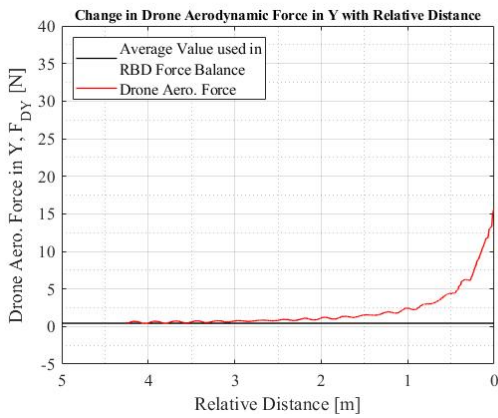
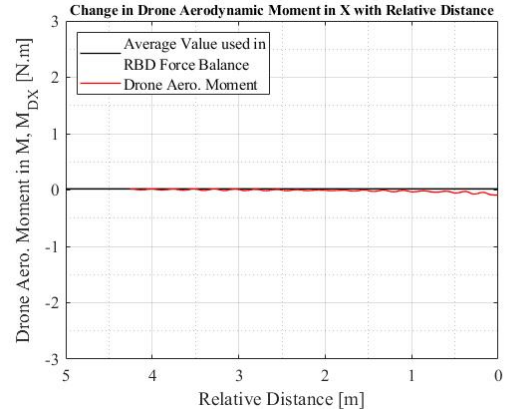
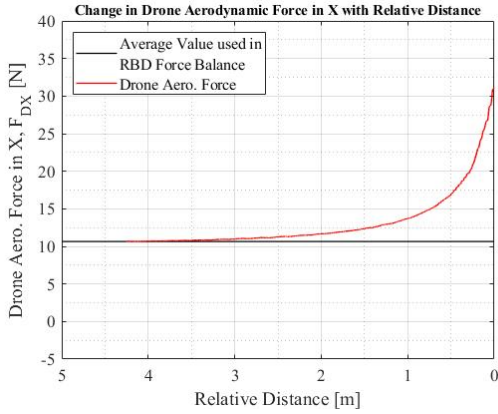


Figure 55. Axis system used for the drone.

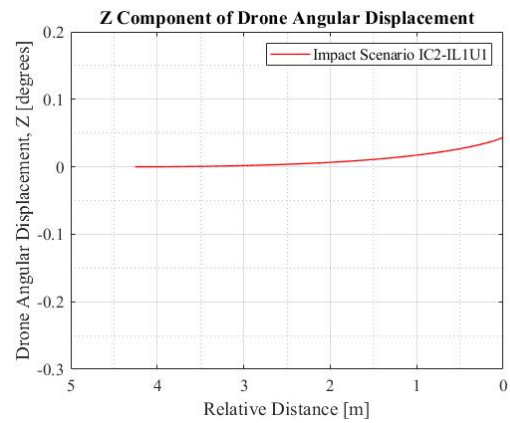
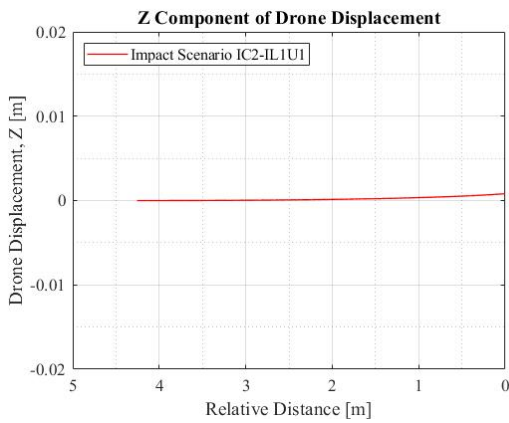
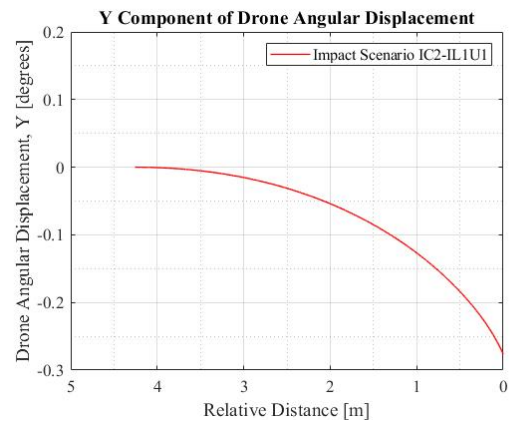
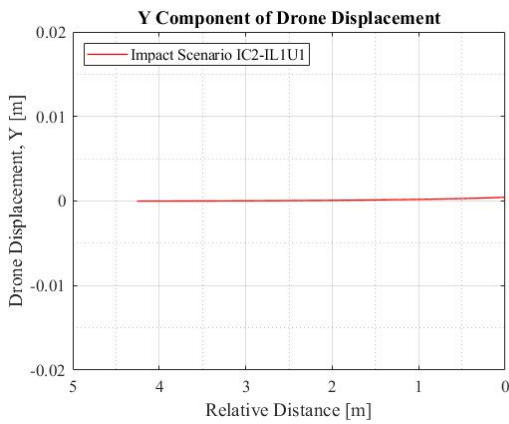
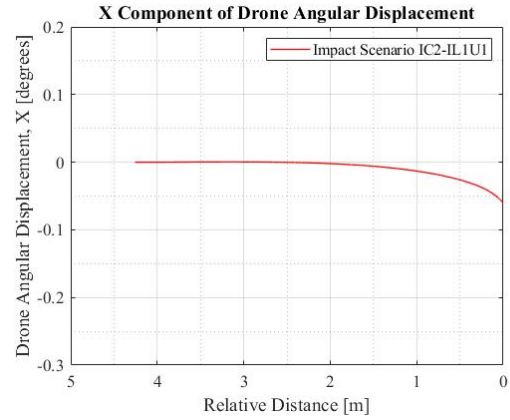
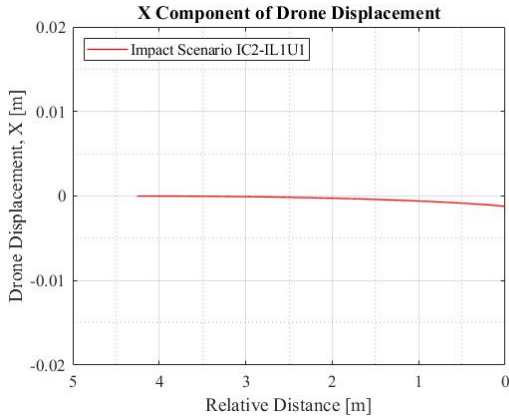


(a)

(b)

Figure 56. Drone aerodynamic forces (a) and moments (b) plotted with respect to relative distance along with average values used in the UDF.

The displacements and angular displacements experienced by the drone as it approached the CRM aircraft wing for impact scenario IC2-IL1U1 are given in Figure 57(a) and Figure 57(b), respectively.

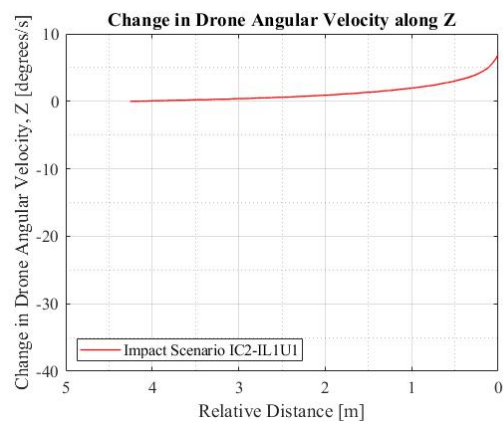
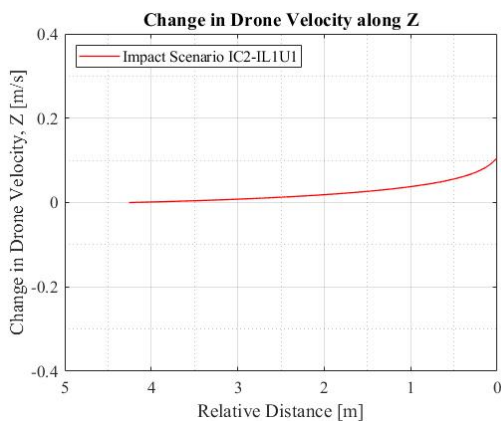
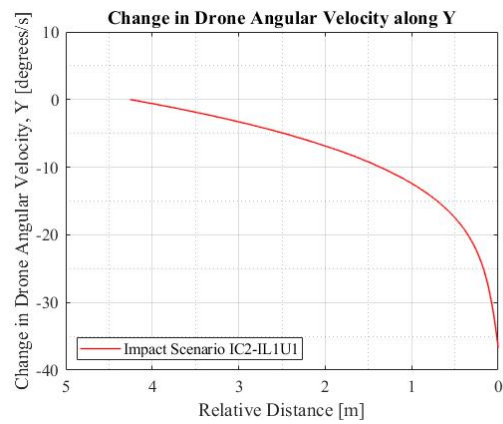
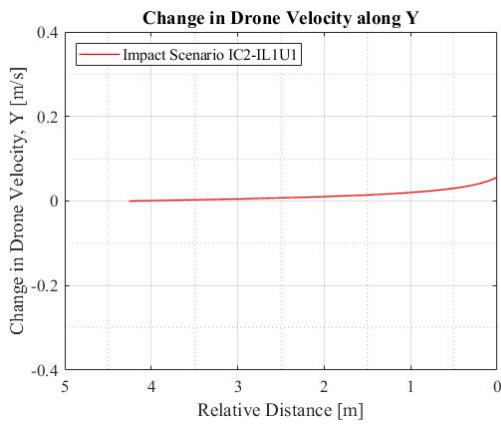
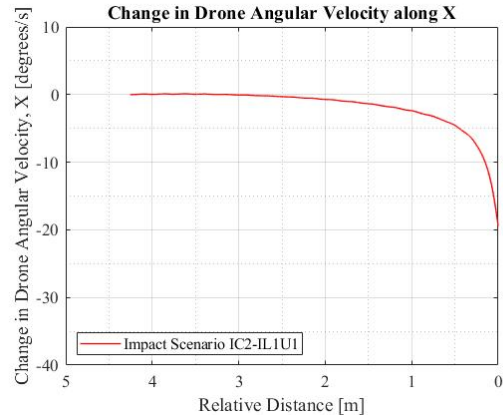
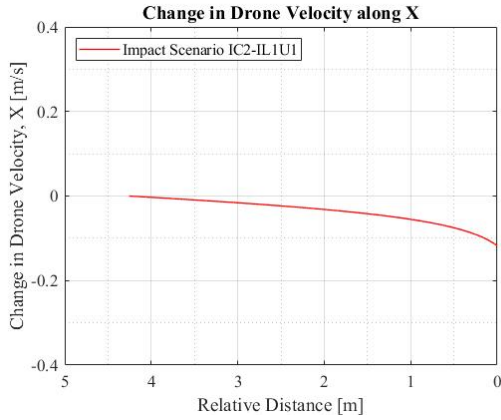


(a)

(b)

Figure 57. Displacements (a) and angular displacements (b) experienced by the drone as it traveled towards the CRM aircraft wing.

The velocities and angular velocities experienced by the drone as it approached the CRM aircraft wing for impact scenario IC2-IL1U1 are given in Figure 58(a) and Figure 58(b), respectively.



(a)

(b)

Figure 58. Velocities (a) and angular velocities (b) experienced by the drone as it traveled towards the CRM aircraft wing.

## C.2 IMPACT SCENARIO 2

For the special case of impact scenario IC2-IL1D1, the results were obtained based on releasing the drone in the domain with the CRM aircraft wing without the fuselage and tail. The drone was released from a distance of 15 m from the leading edge of the wing at a plane located at a distance of 16.80 m (55.12 ft) in the spanwise direction from the symmetry plane. Once released, the drone was allowed to move without the influence of forces and moments for 10.5 m. The Instantaneous aerodynamic forces and moments were used as external forces and moments in the UDF.

The forces experienced by the aircraft during the transient simulation were compared with the forces obtained from the steady-state simulation of the CRM aircraft in the domain. Figure 59 shows good agreement between the steady-state and the transient simulation results for the CRM aircraft wing.

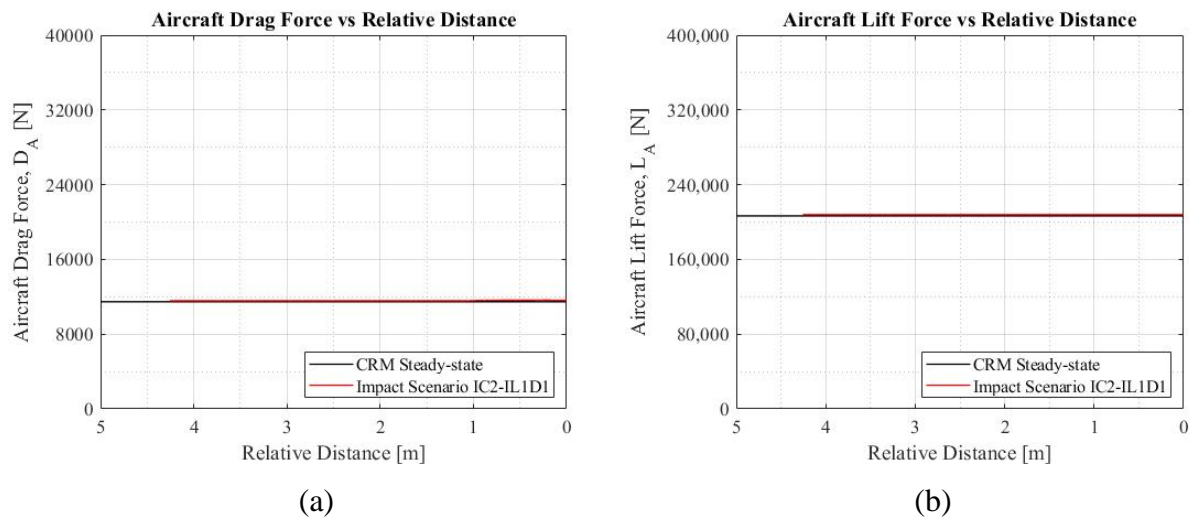


Figure 59. CRM aircraft lift and drag forces recorded as the drone approached the aircraft wing.

The drone forces and moments were plotted with the instantaneous values of the forces used to balance the drone independent aerodynamic forces. The change in forces and moments as the drone approaches the CRM aircraft can be seen in Figure 61(a) and Figure 61(b), respectively. Figure 60 provides a reference for the axis systems used in the plots.

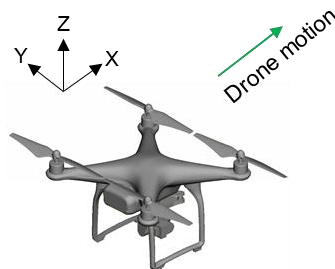
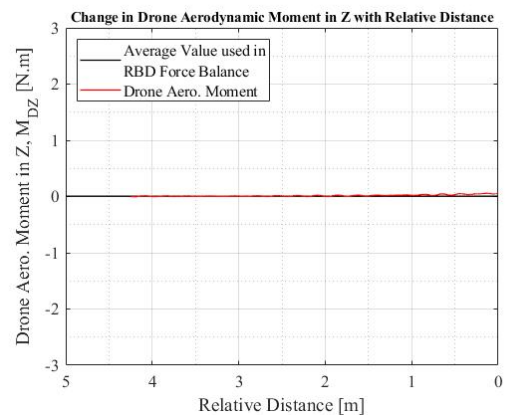
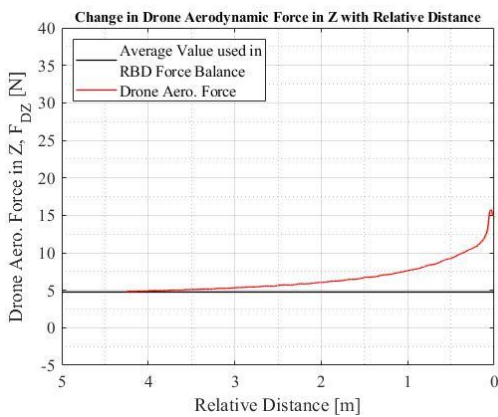
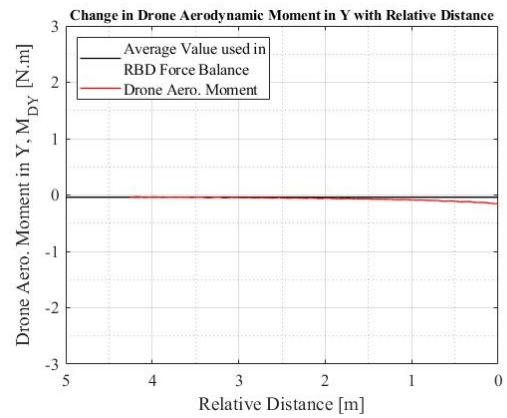
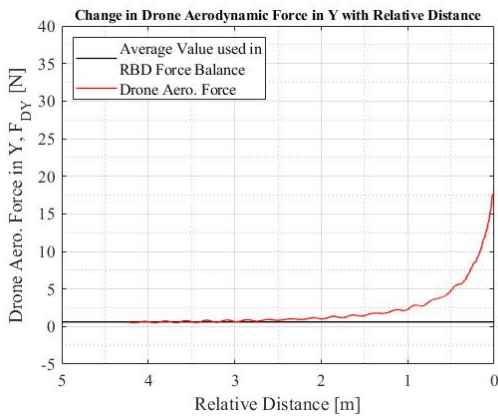
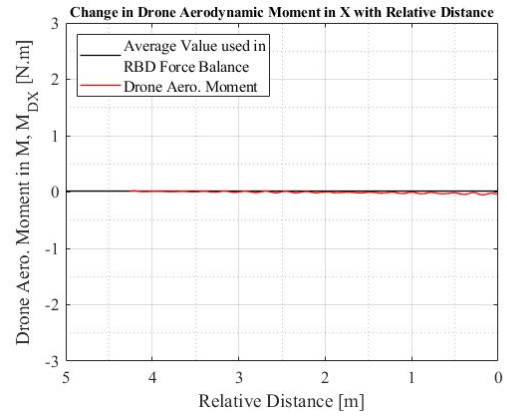
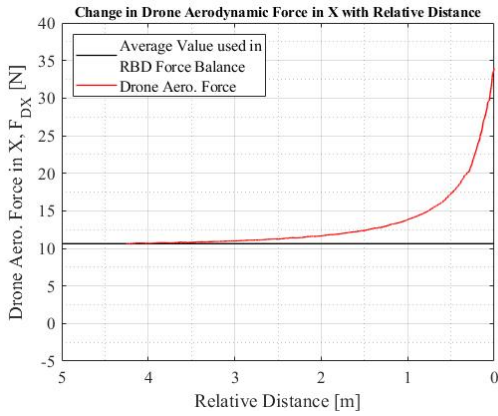


Figure 60. Axis system used for the drone.

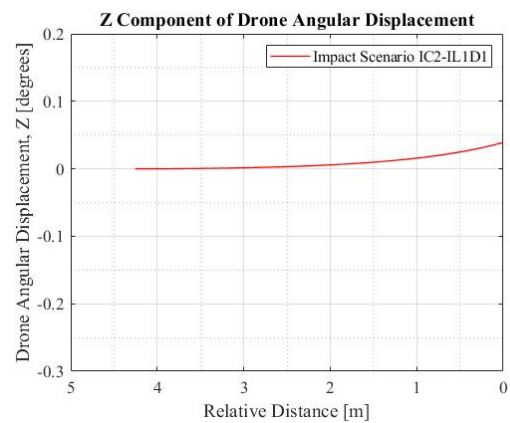
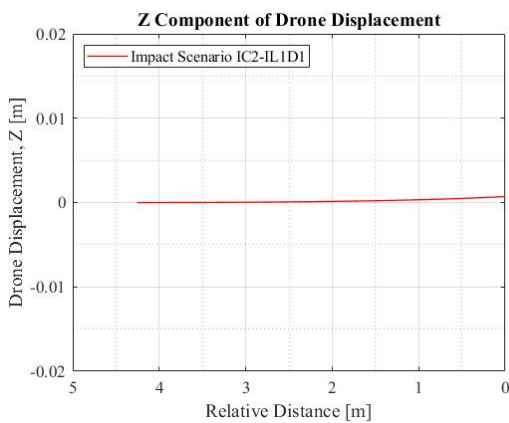
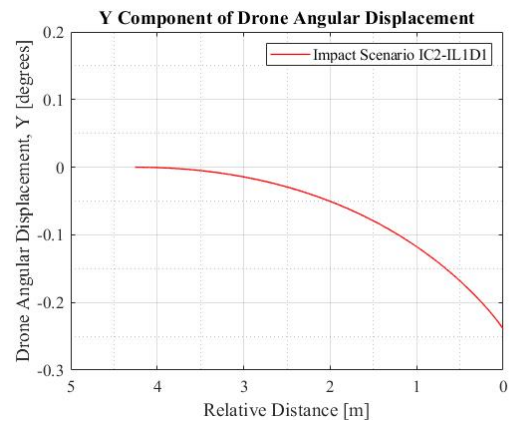
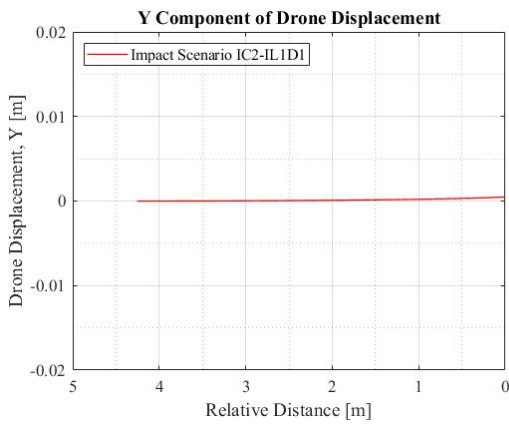
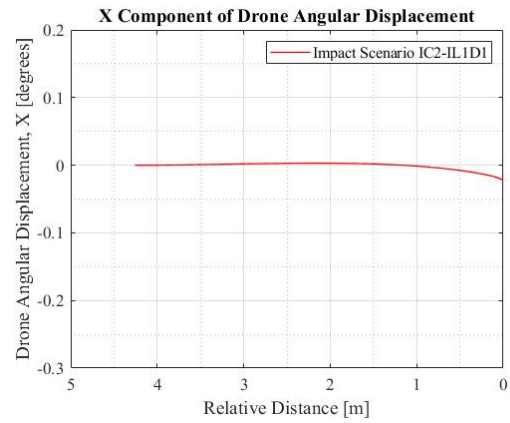
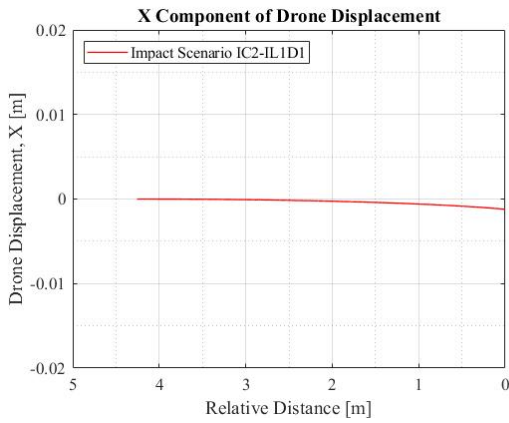


(a)

(b)

Figure 61. Drone aerodynamic forces (a) and moments (b) plotted with respect to relative distance along with average values.

The displacements and angular displacements experienced by the drone as it approached the CRM aircraft wing for impact scenario IC2-IL1D1 are given in Figure 62(a) and Figure 62(b), respectively.

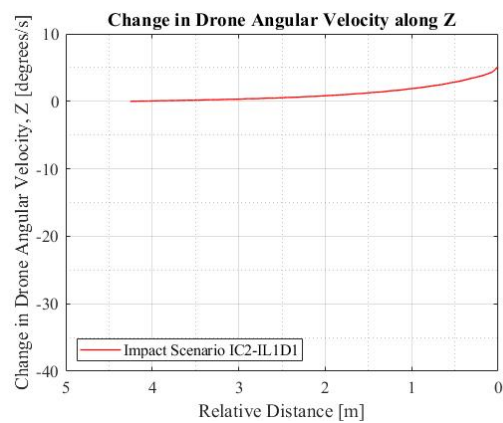
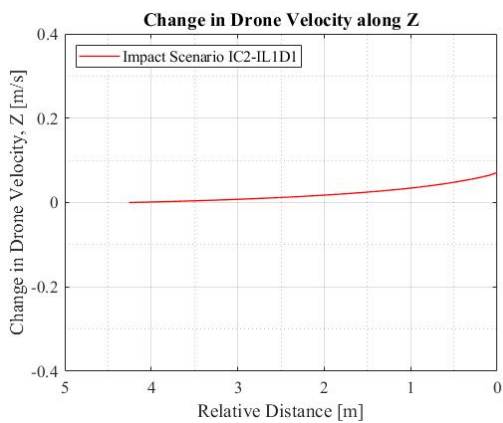
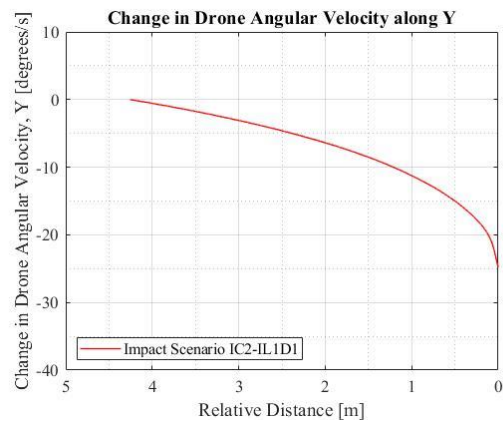
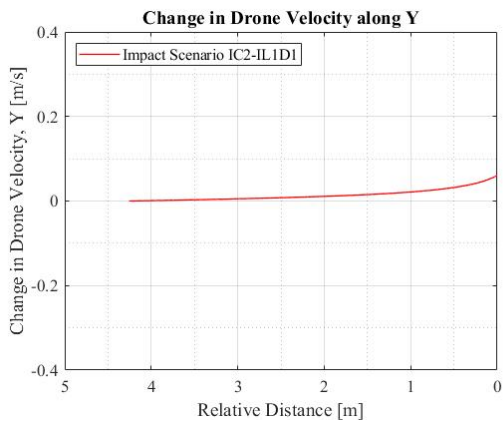
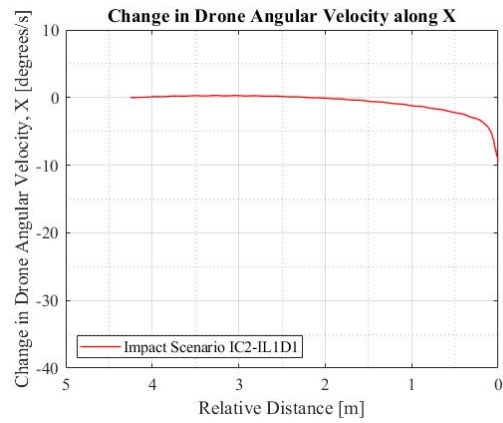
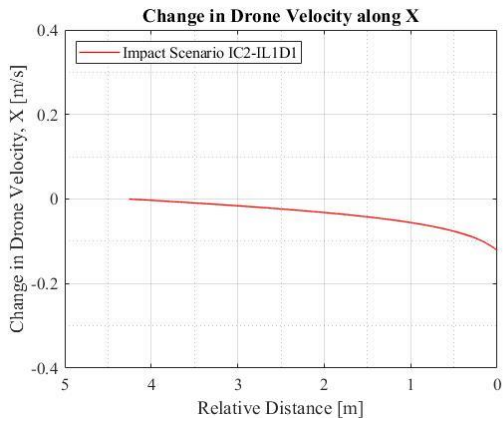


(a)

(b)

Figure 62. Displacements (a) and angular displacements (b) experienced by the drone as it traveled towards the CRM aircraft wing.

The velocities and angular velocities experienced by the drone as it approached the CRM aircraft wing for impact scenario IC2-IL1D1 are given in Figure 63(a) and Figure 63(b), respectively.



(a)

(b)

Figure 63. Velocities (a) and angular velocities (b) experienced by the drone as it traveled towards the CRM aircraft.

### C.3 IMPACT SCENARIO 3

For the special case of impact scenario IC2-IL1U2, the results were obtained based on releasing the drone in the domain with the CRM aircraft wing without the fuselage and tail. The drone was released from a distance of 15 m from the leading edge of the wing at a plane located at a distance of 16.80 m (55.12 ft) in the spanwise direction from the symmetry plane. Once released, the drone was allowed to move without the influence of forces and moments for 10.5 m. The instantaneous aerodynamic forces and moments were used as external forces and moments in the UDF.

The forces experienced by the aircraft during the transient simulation were compared with the forces obtained from the steady-state simulation of the CRM aircraft in the domain. Figure 64 shows good agreement between the steady-state and the transient simulation results for the CRM aircraft wing.

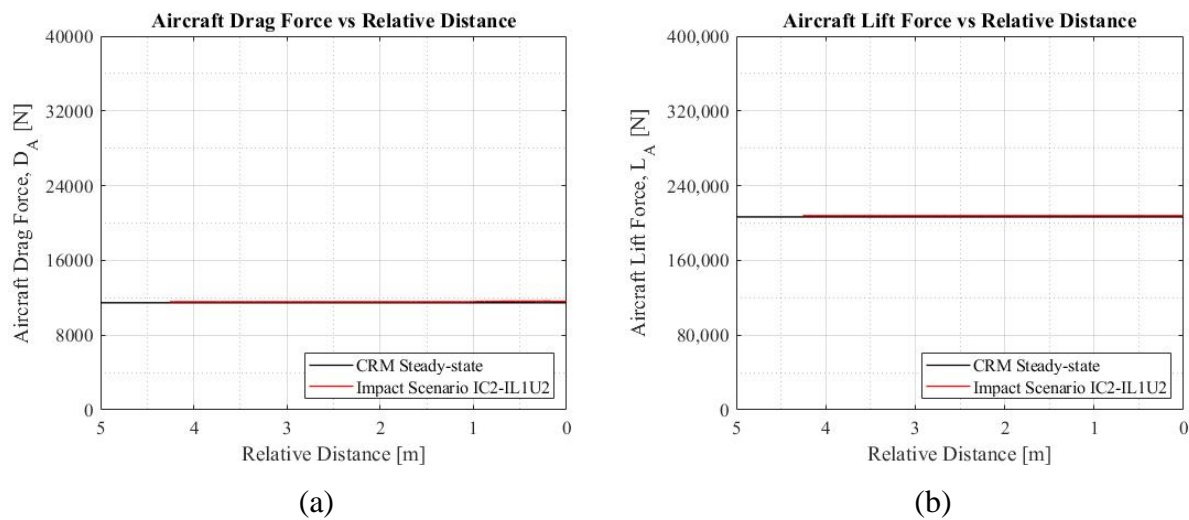


Figure 64. CRM aircraft lift and drag forces recorded as the drone approached the aircraft.

The drone forces and moments were plotted with the instantaneous value of the forces used to balance the drone independent aerodynamic forces. The change in forces as the drone approaches the CRM aircraft wing can be seen in Figure 66(a) and Figure 66(b), respectively. Figure 65 provides a reference for the axis systems used in the plots.

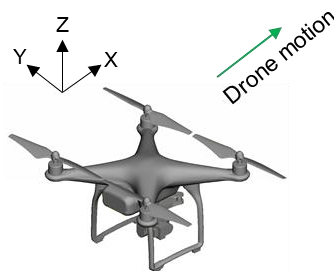
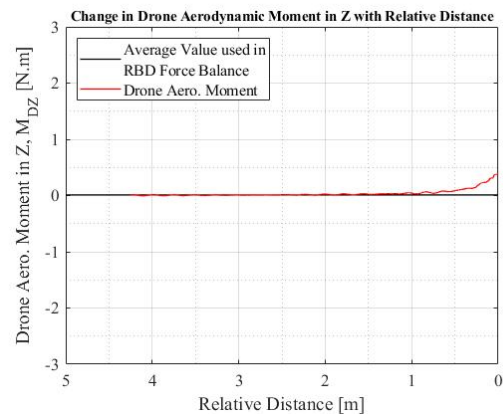
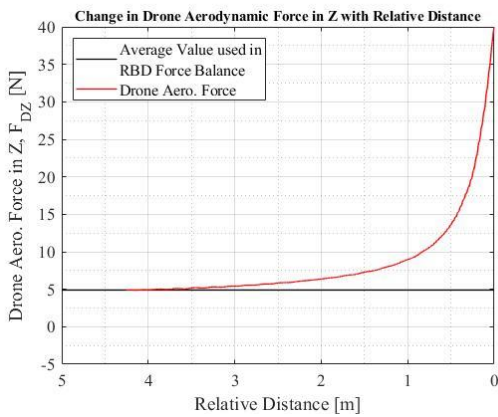
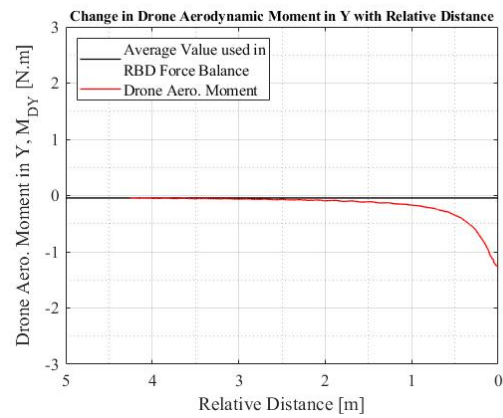
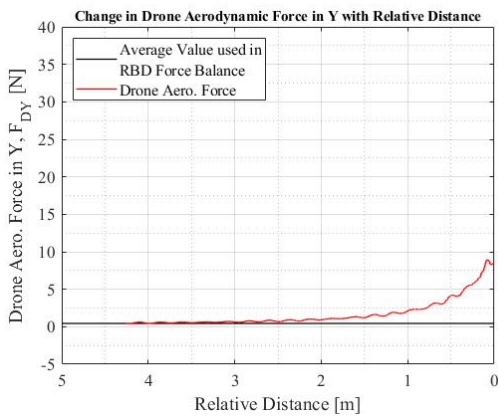
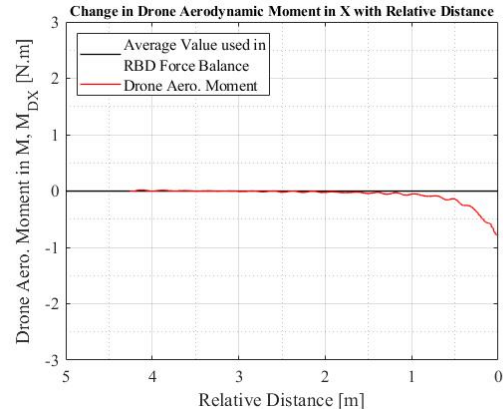
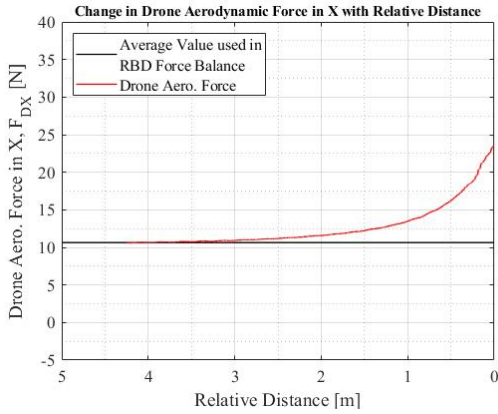


Figure 65. Axis system used for the drone.

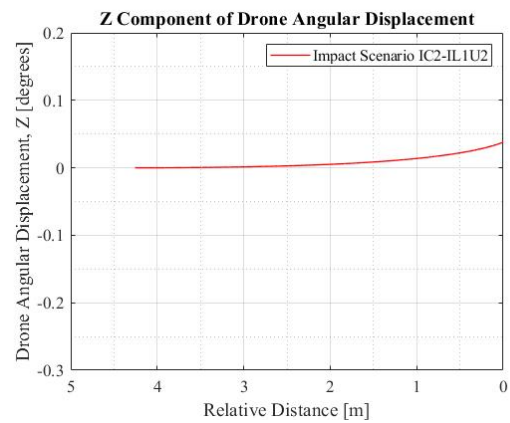
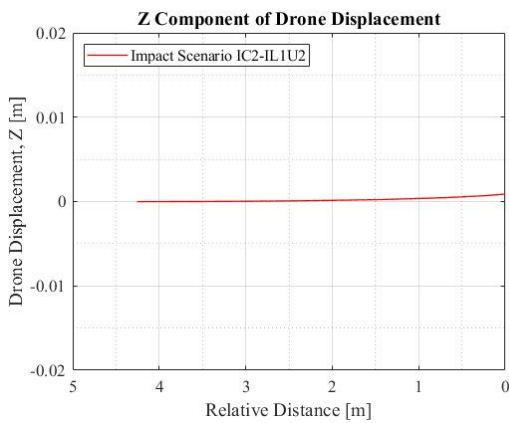
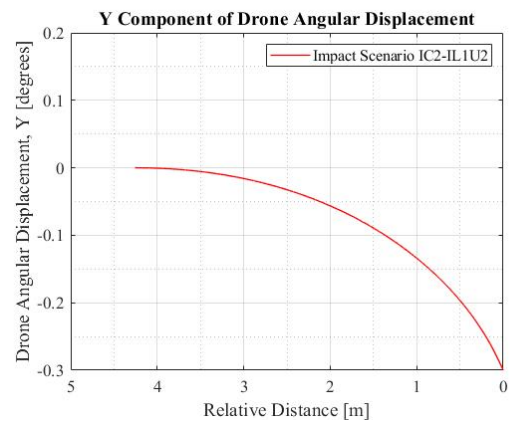
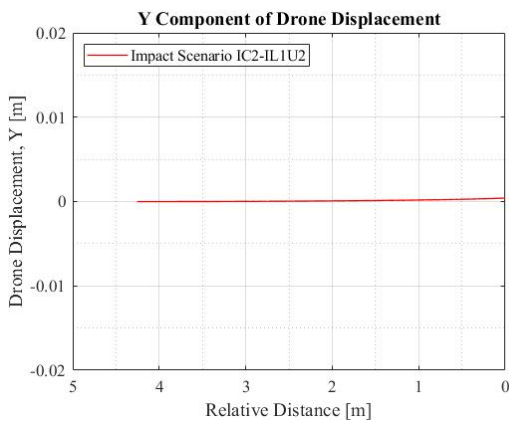
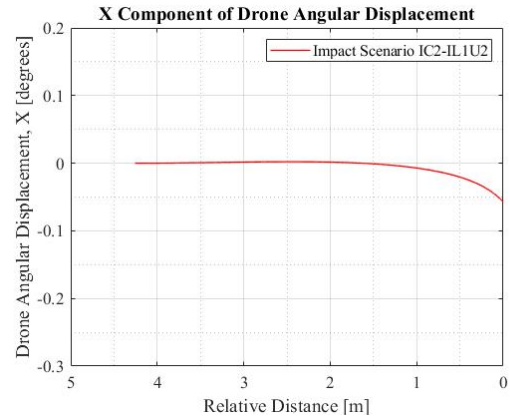
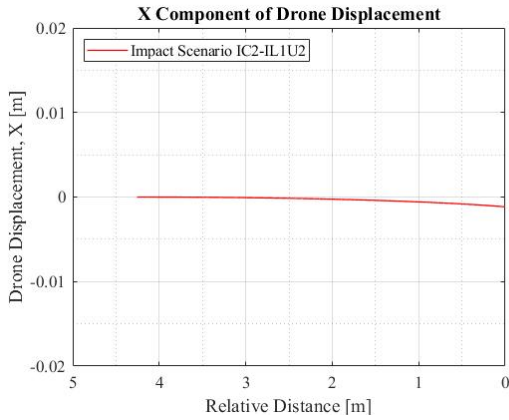


(a)

(b)

Figure 66. Drone aerodynamic forces (a) and moments (b) plotted with respect to relative distance along with average values.

The displacements and angular displacements experienced by the drone as it approached the CRM aircraft wing for impact scenario IC2-IL1U2 are given in Figure 67(a) and Figure 67(b) respectively.

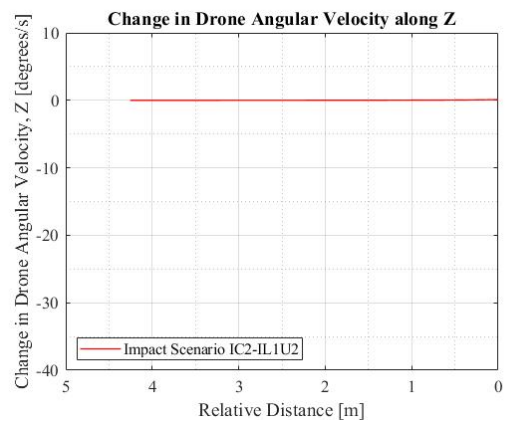
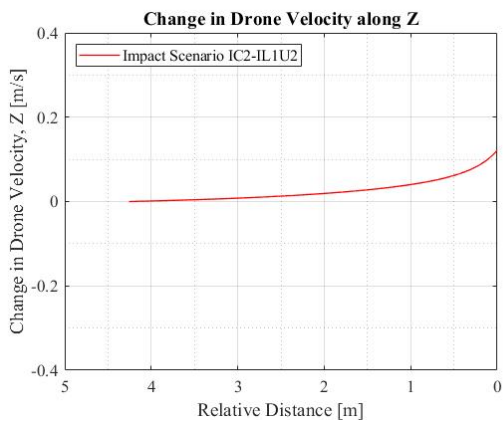
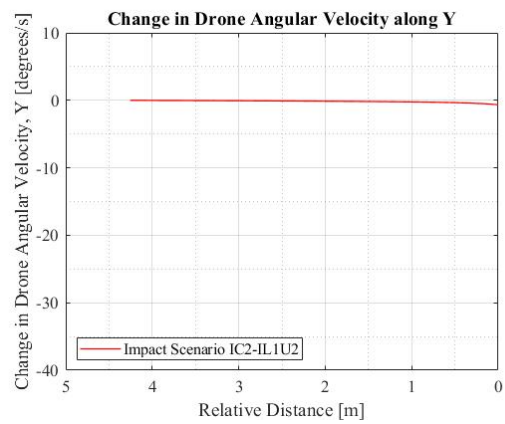
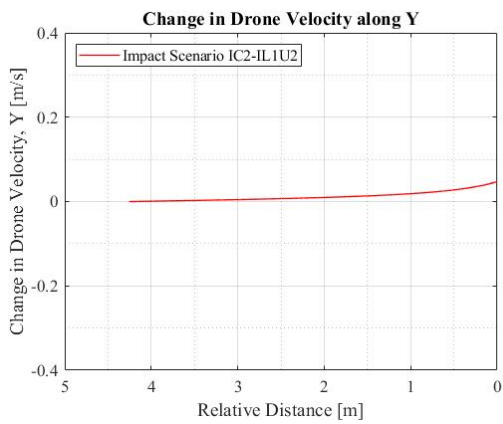
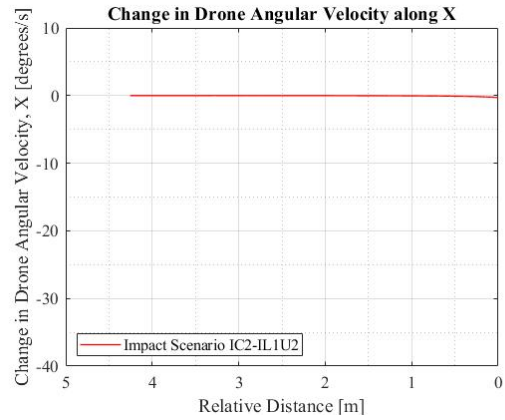
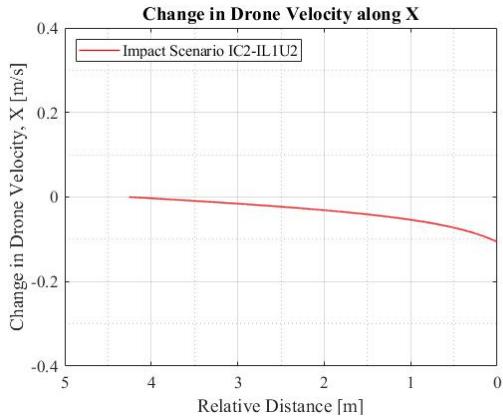


(a)

(b)

Figure 67. Displacements (a) and angular displacements (b) experienced by the drone as it traveled towards the CRM aircraft wing.

The velocities and angular velocities experienced by the drone as it approached the CRM aircraft wing for impact scenario IC2-IL1U2 are given in Figure 68(a) and Figure 68(b), respectively.



(a)

(b)

Figure 68. Velocities (a) and angular velocities (b) experienced by the drone as it traveled towards the CRM aircraft wing.

#### C.4 IMPACT SCENARIO 4

For the special case of impact scenario IC2-IL1D2, the results were obtained based on releasing the drone in the domain with the CRM aircraft wing without the fuselage and tail. The drone was released from a distance of 15 m from the leading edge of the wing at a plane located at a distance of 16.80 m (55.12 ft) in the spanwise direction from the symmetry plane. Once released, the drone was allowed to move without the influence of forces and moments for 10.5 m. The Instantaneous aerodynamic forces and moments were used as external forces and moments in the UDF.

The forces experienced by the aircraft during the transient simulation were compared with the forces obtained from the steady-state simulation of the CRM aircraft in the domain. Figure 69 shows good agreement between the steady-state and the transient simulation results for the CRM aircraft wing.

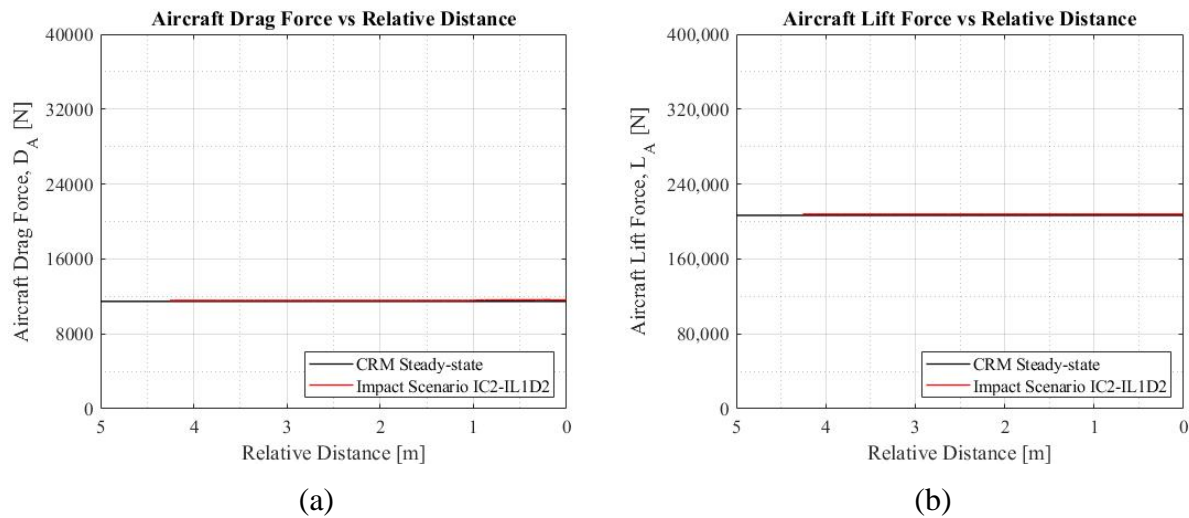


Figure 69. CRM aircraft lift and drag forces recorded as the drone approached the aircraft.

The drone forces and moments were plotted with the instantaneous value of the forces used to balance the drone independent aerodynamic forces. The change in forces and moments as the drone approaches the CRM aircraft can be seen in Figure 71(a) and Figure 71(b), respectively. Figure 70 provides a reference for the axis systems used in the plots.

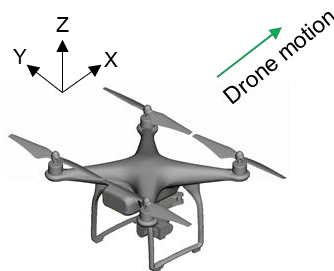
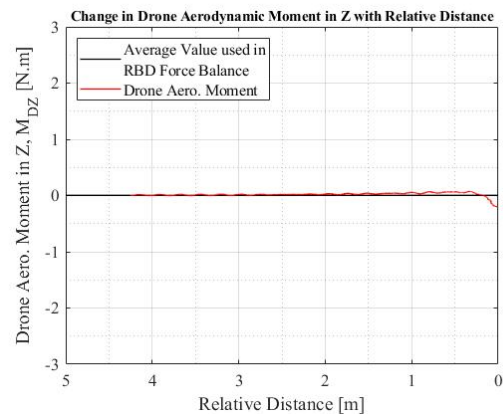
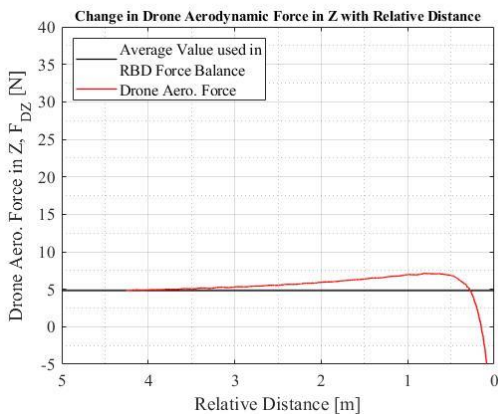
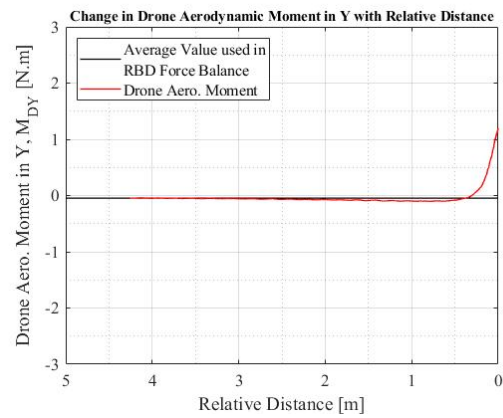
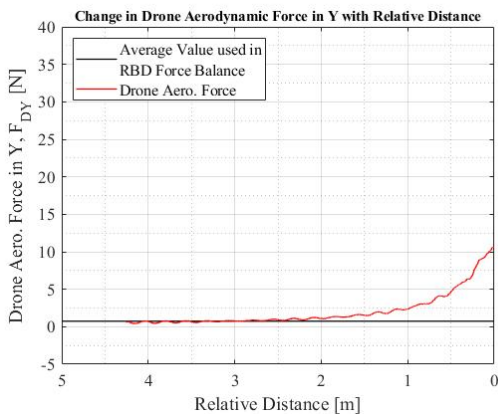
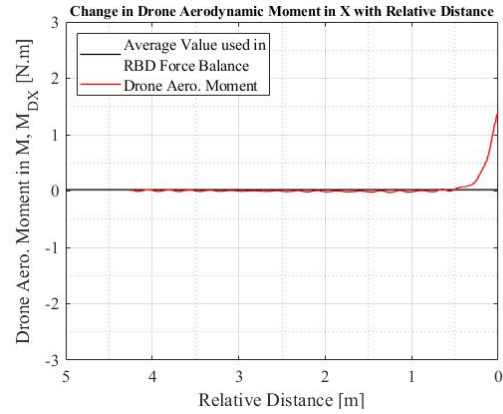
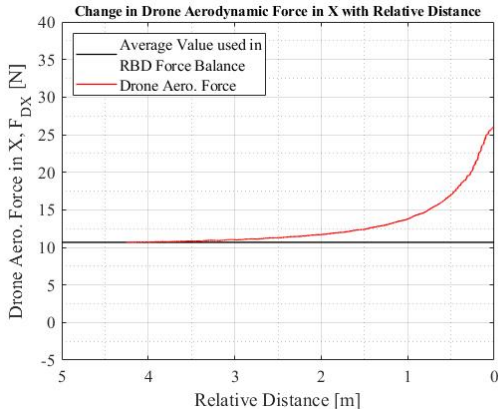


Figure 70. Axis system used for the drone.

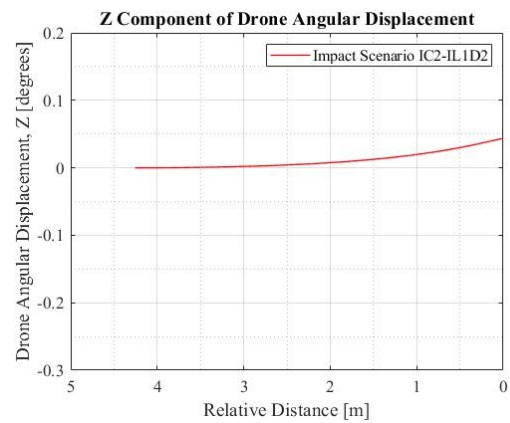
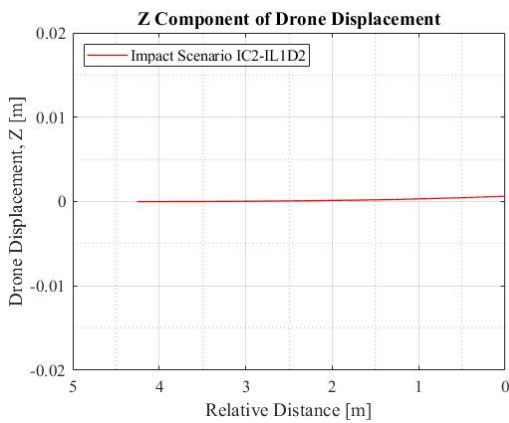
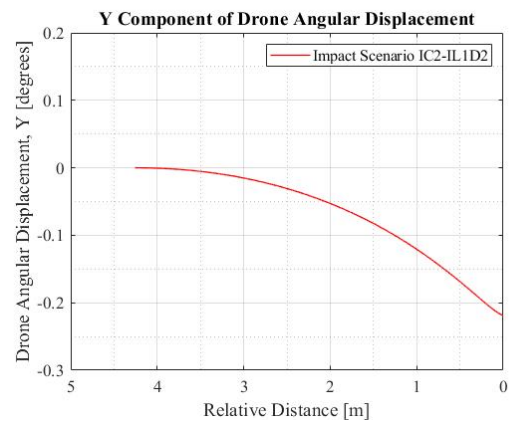
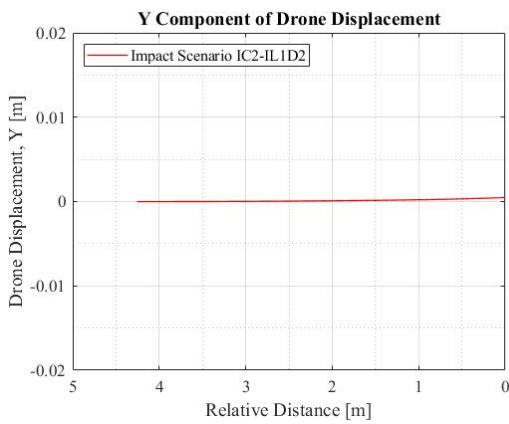
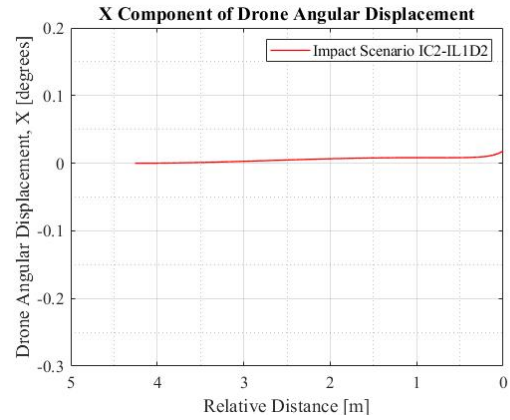
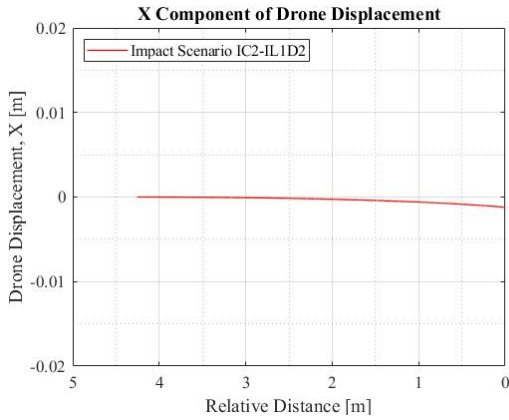


(a)

(b)

Figure 71. Drone aerodynamic forces (a) and moments (b) plotted with respect to relative distance along with average values.

The displacements and angular displacements experienced by the drone as it approached the CRM aircraft wing for impact scenario IC2-IL1D2 are given in Figure 72(a) and Figure 72(b), respectively.

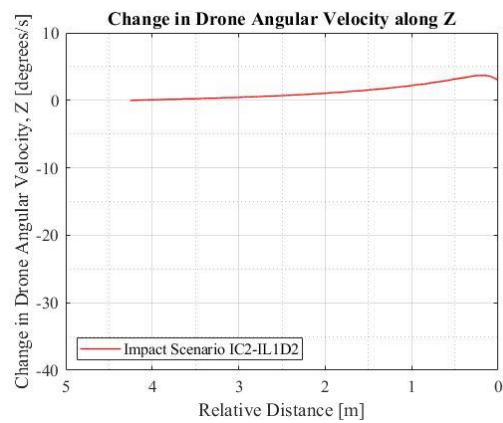
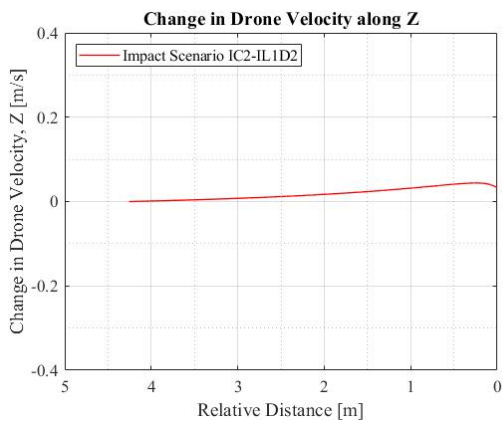
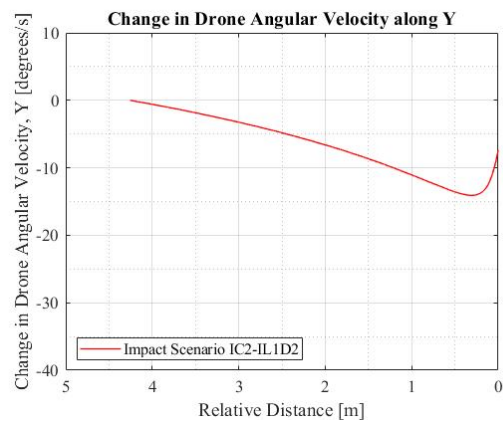
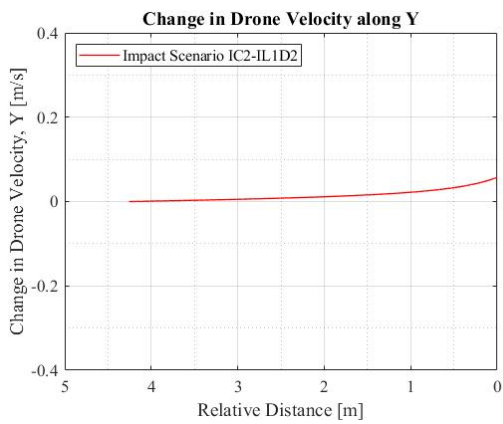
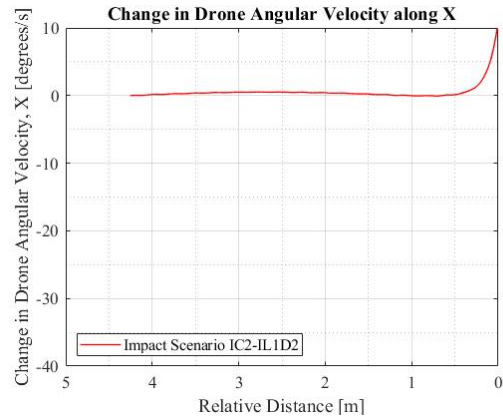
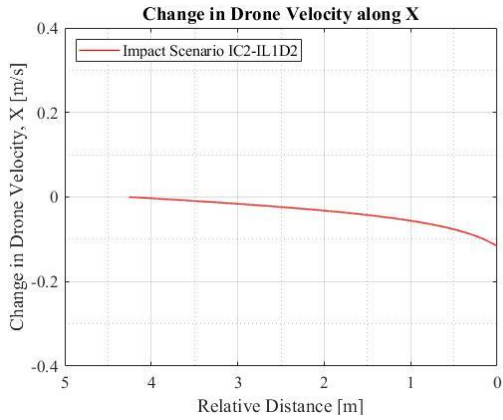


(a)

(b)

Figure 72. Displacements (a) and angular displacements (b) experienced by the drone as it traveled towards the CRM aircraft wing.

The velocities and angular velocities experienced by the drone as it approached the CRM aircraft wing for impact scenario IC2-IL1D2 are given in Figure 73(a) and Figure 73(b), respectively.



(a)

(b)

Figure 73. Velocities (a) and angular velocities (b) experienced by the drone as it traveled towards the CRM aircraft wing.

## C.5 ADDITIONAL ANALYSIS ON IMPACT SCENARIO 4

For the special case of impact scenario IC2-IL1AMR, the results were obtained based on releasing the drone in the domain with the CRM aircraft wing without the fuselage and tail. This analysis was performed with the purpose of comparison between an optimized mesh configuration using adaptive mesh refinement (AMR) method with higher time steps and the original simulation setup done for the impact scenario IC2-IL1 by ERAU. The drone was released from a distance of 15 m from the leading edge of the wing at a plane located at a distance of 16.80 m (55.12 ft) in the spanwise direction from the symmetry plane. Once released, the drone was allowed to move without the influence of forces and moments for 10.5 m. The instantaneous aerodynamic forces and moments were used as external forces and moments in the UDF.

The forces experienced by the aircraft during the transient simulation were compared with the forces obtained from the steady-state simulation of the CRM aircraft. Figure 74 shows good agreement between the steady-state and the transient simulation results for the CRM aircraft wing.

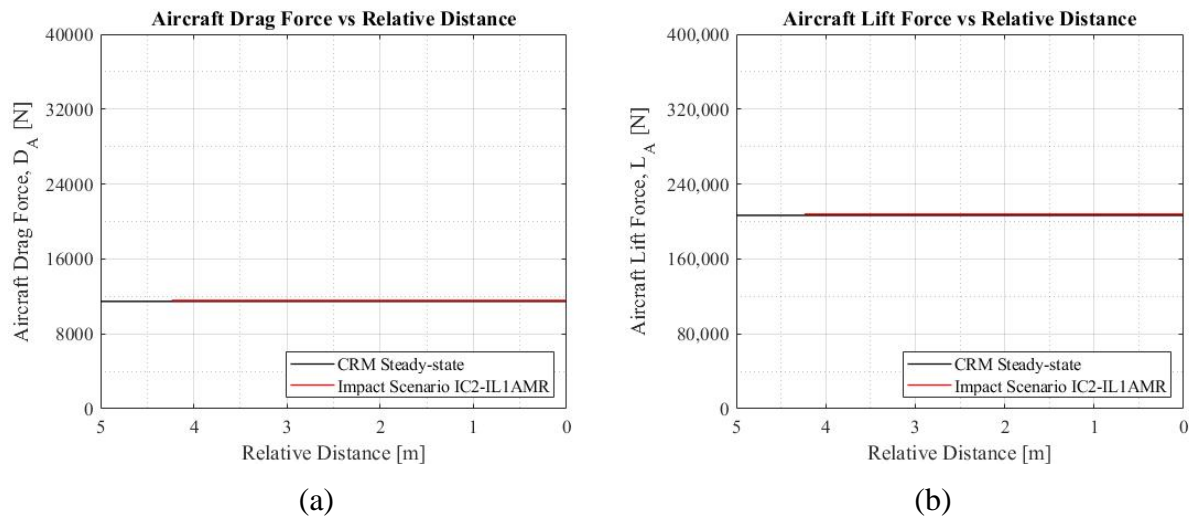


Figure 74. CRM aircraft lift and drag forces recorded as the drone approached the aircraft.

The drone forces and moments were plotted with the instantaneous values of the forces used to balance the drone independent aerodynamic forces. The change in forces and moments as the drone approaches the CRM aircraft can be seen in Figure 76(a) and Figure 76(b), respectively. Figure 75 provides a reference for the axis systems used in the plots.

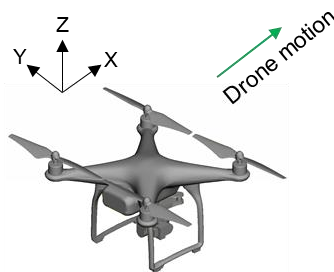
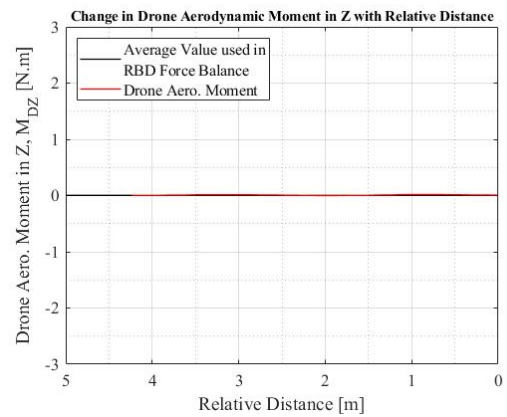
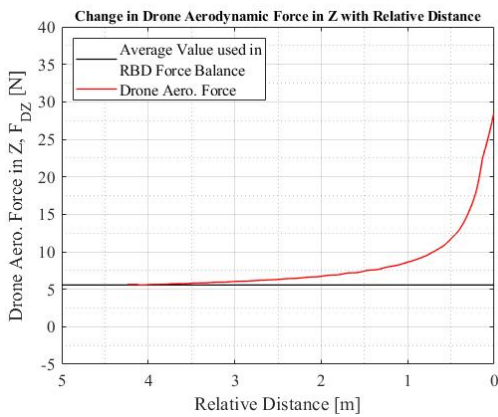
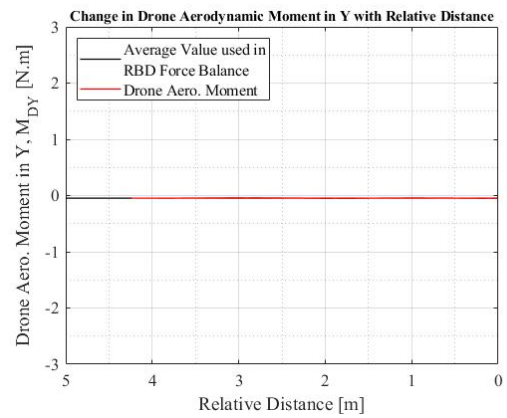
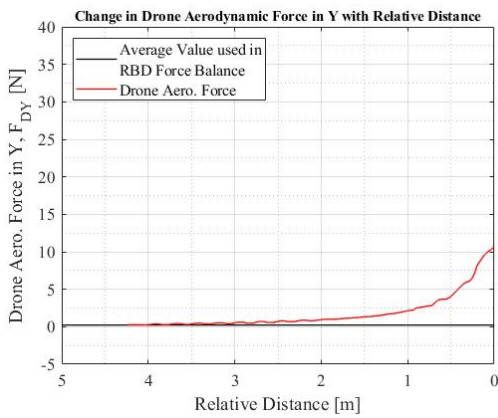
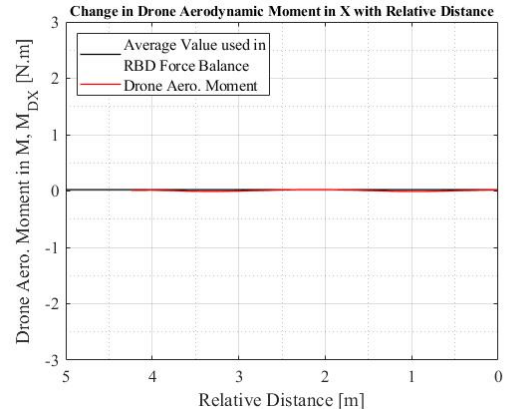
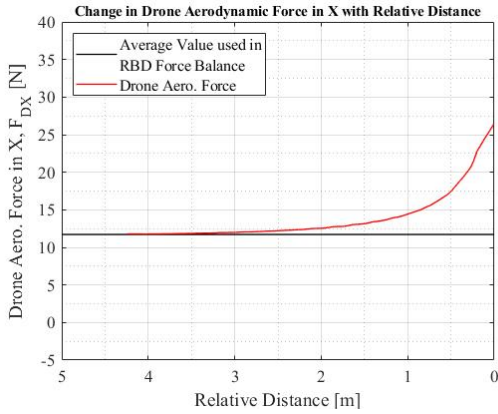


Figure 75. Axis system used for the drone.

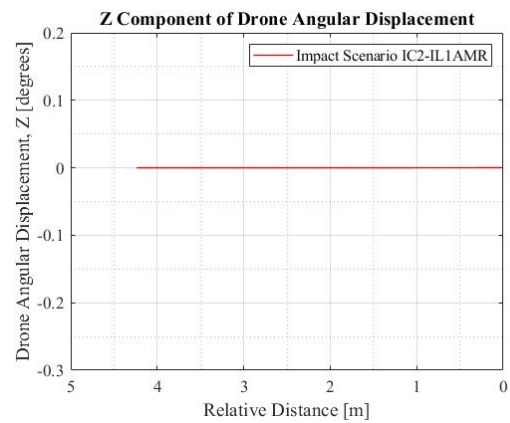
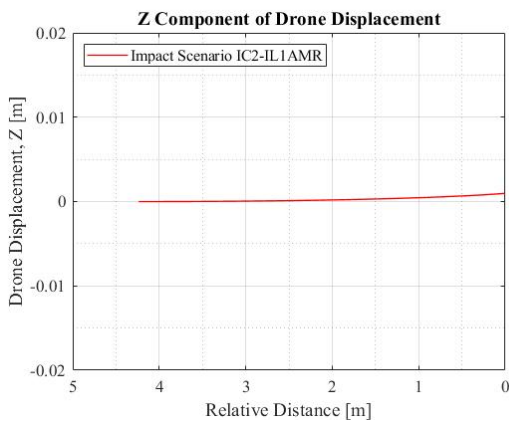
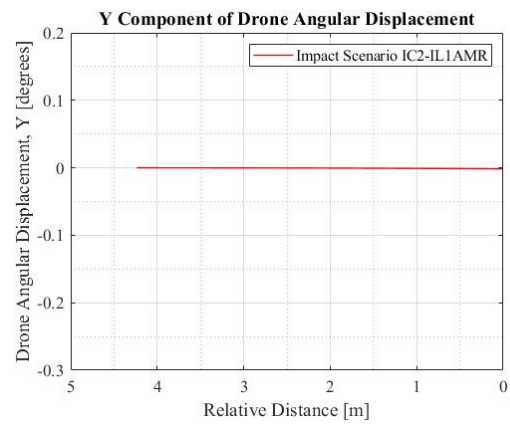
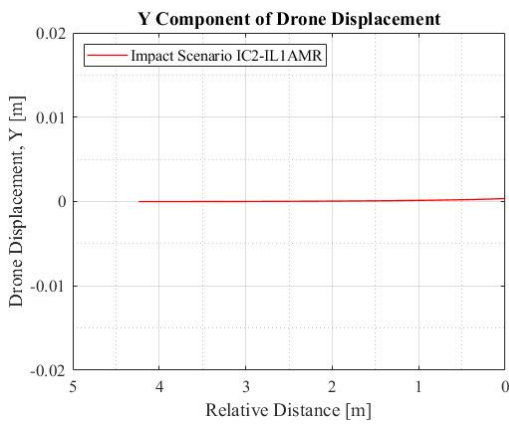
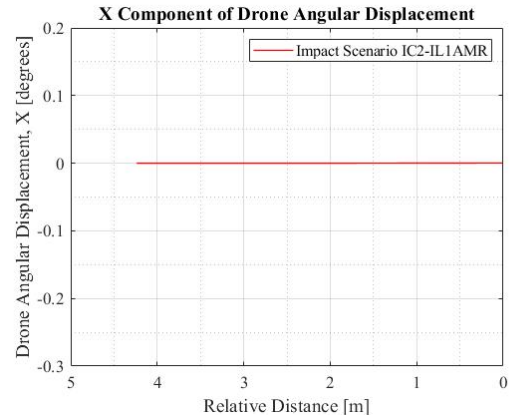
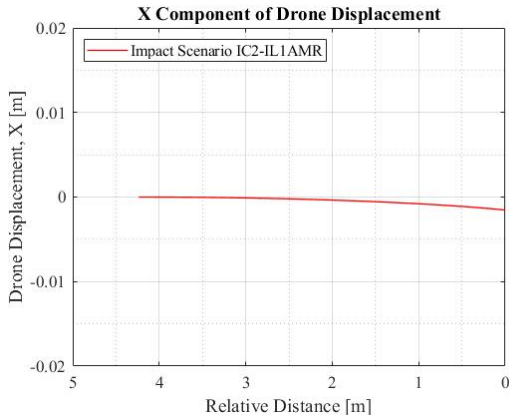


(a)

(b)

Figure 76. Drone aerodynamic forces (a) and moments (b) plotted with respect to relative distance along with average values.

The displacements and angular displacements experienced by the drone as it approached the CRM aircraft wing for impact scenario IC2-IL1AMR are given in Figure 77(a) and Figure 77(b), respectively.

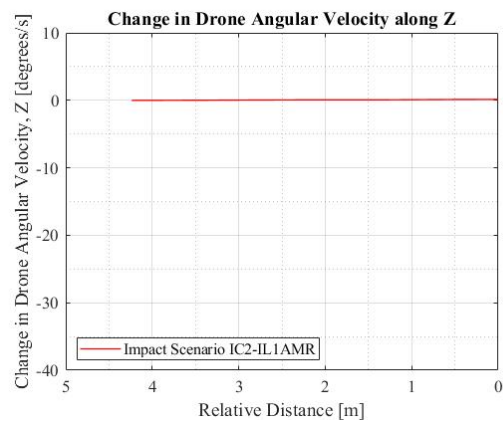
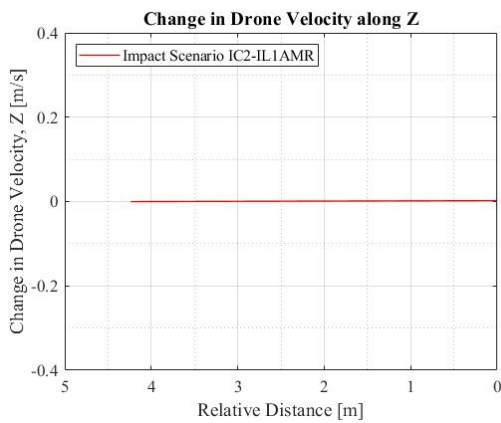
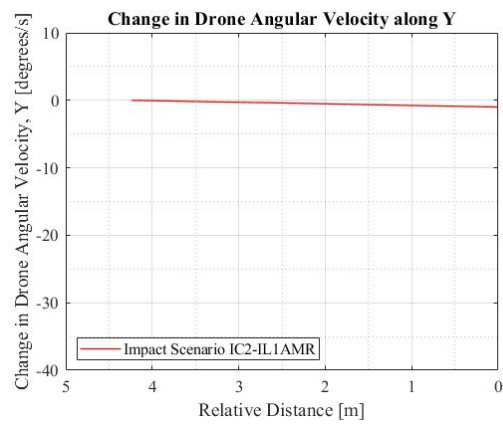
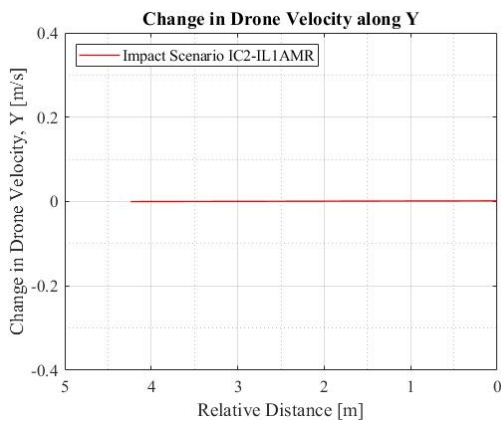
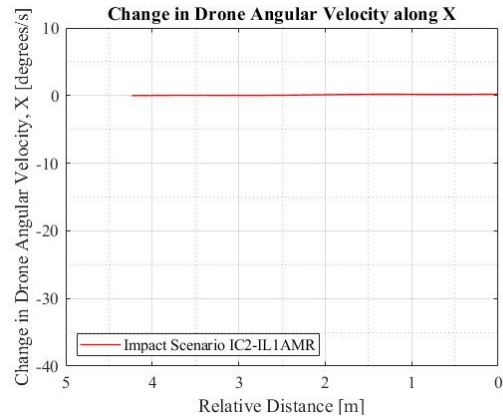
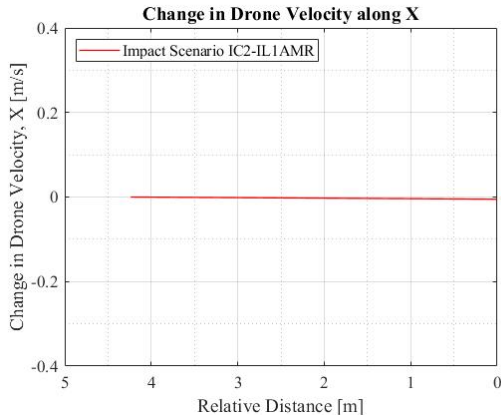


(a)

(b)

Figure 77. Displacements (a) and angular displacements (b) experienced by the drone as it traveled towards the CRM aircraft wing.

The velocities and angular velocities experienced by the drone as it approached the CRM aircraft for impact scenario IC2-IL1AMR are given in Figure 78(a) and Figure 78(b), respectively.



(a)

(b)

Figure 78. Velocities (a) and angular velocities (b) experienced by the drone as it traveled towards the CRM aircraft wing.

### C.6 IMPACT SCENARIO 5 (WITH INSTANTANEOUS FORCE/MOMENTS)

For the impact scenario IC2-IL3, the results were obtained based on releasing the drone in the domain with the CRM aircraft wing with the fuselage, horizontal stabilizer, and tail. The drone

was released from a distance of 90 m from the leading edge of the horizontal stabilizer at a plane located at a distance of 6.24 m (20.47 ft) in the spanwise direction from the symmetry plane. Once released, the drone was allowed to move without the influence of forces and moments for 16 m. The instantaneous aerodynamic forces and moments were used as external forces and moments in the UDF.

The forces experienced by the aircraft during the transient simulation were compared with the forces obtained from the steady-state simulation of the CRM aircraft in the domain. Figure 79 shows good agreement between the steady-state and the transient simulation results for the CRM aircraft wing.

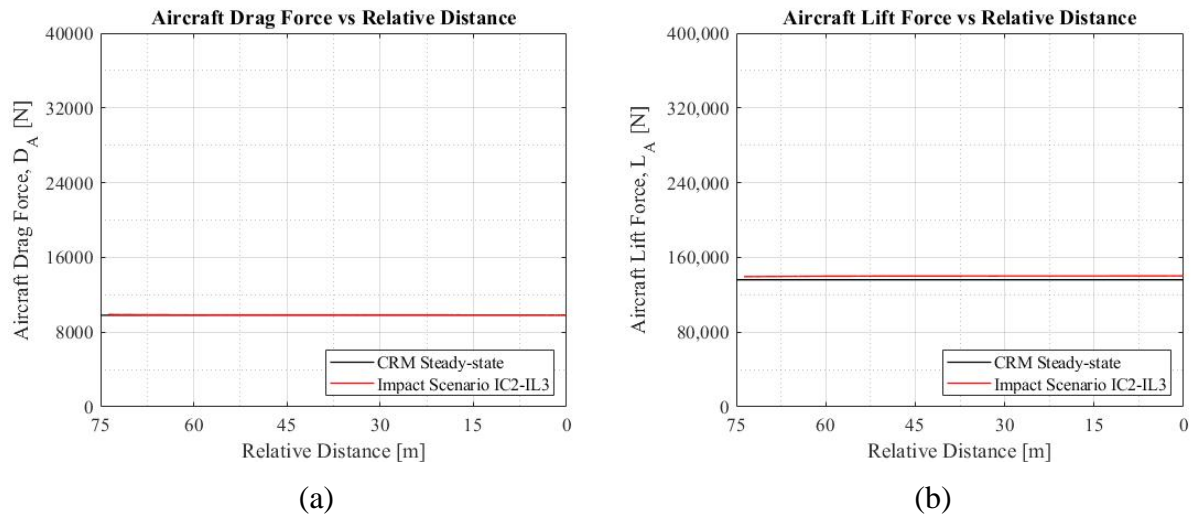


Figure 79. CRM aircraft lift and drag forces recorded as the drone approached the aircraft.

The drone forces and moments were plotted with the instantaneous value of the forces and moments used to balance the drone independent aerodynamic forces and moments. The change in forces and moments as the drone approaches the CRM aircraft horizontal stabilizer can be seen in Figure 81(a) and Figure 81(b), respectively. Figure 80 provides a reference for the axis systems used in the plots.

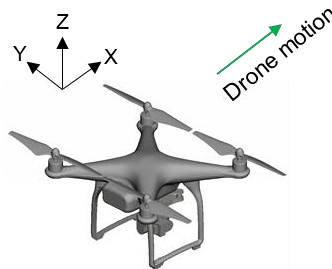
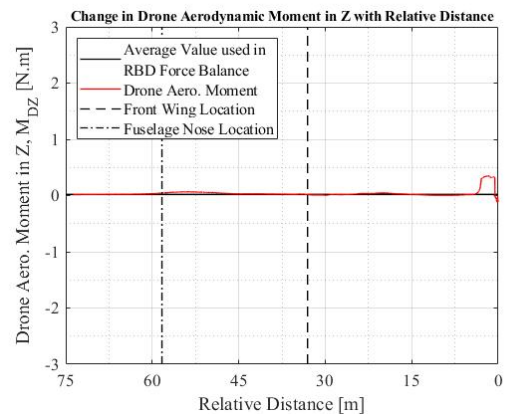
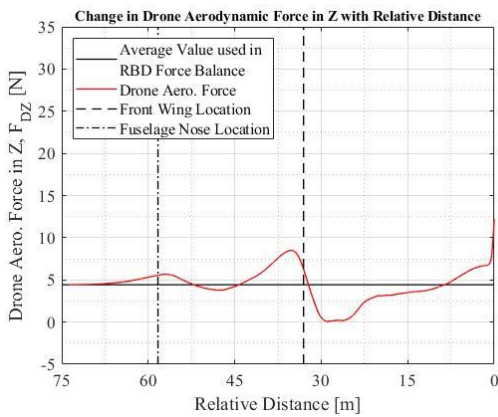
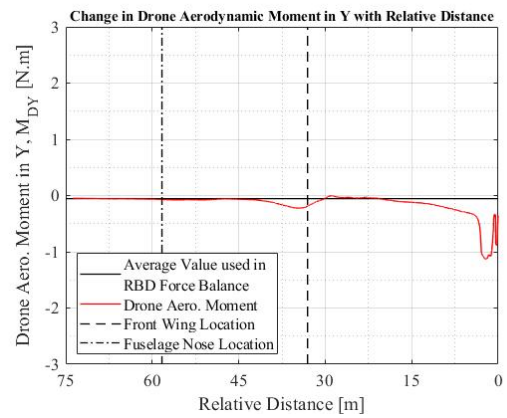
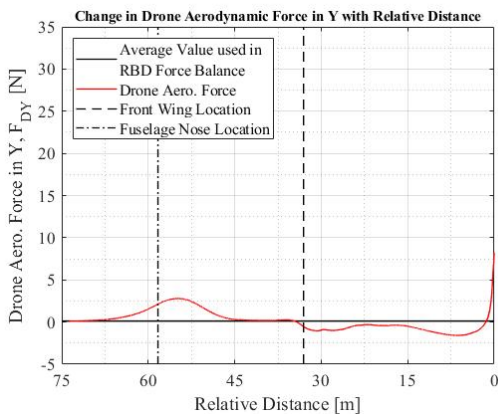
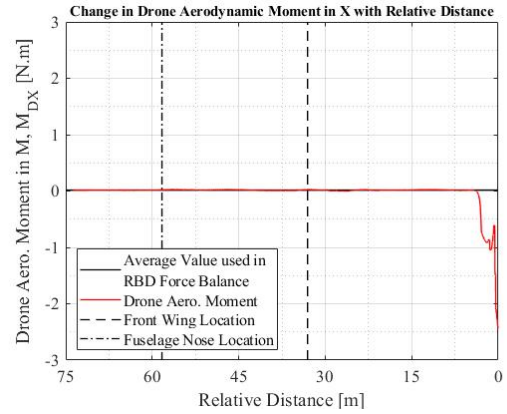
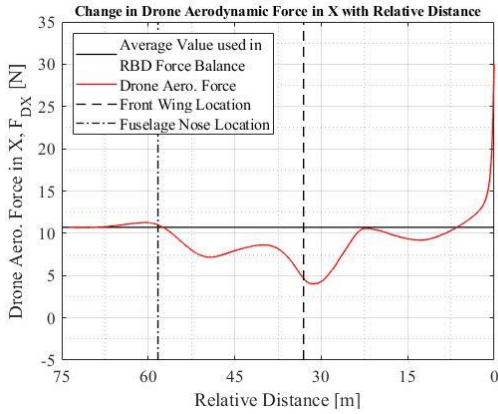


Figure 80. Axis system used for the drone.

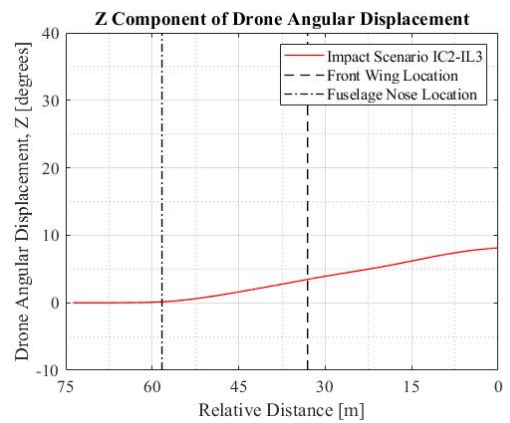
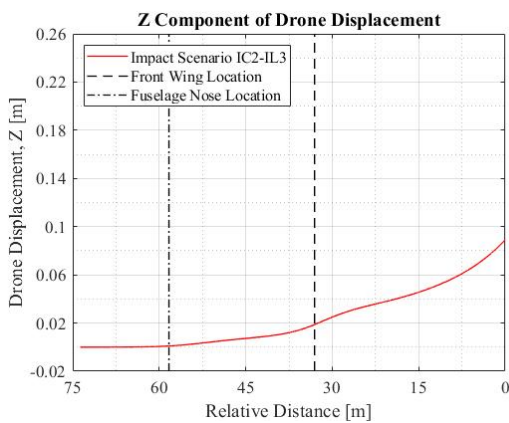
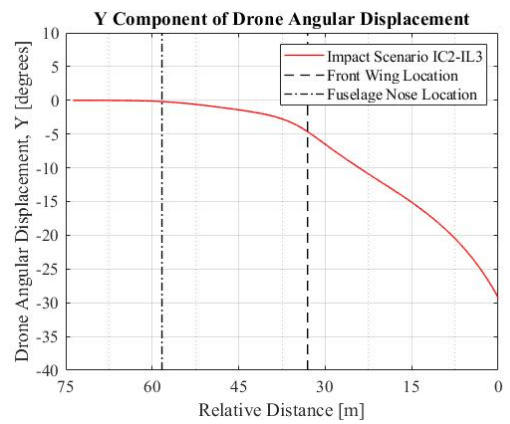
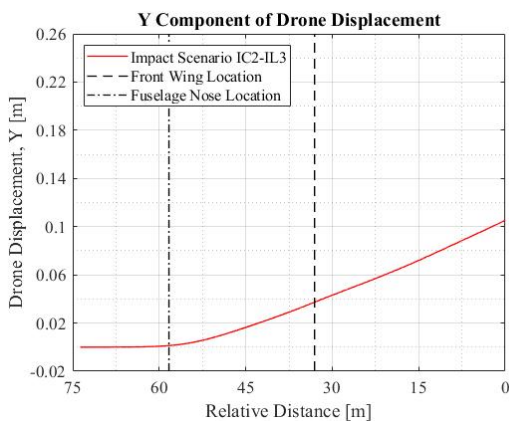
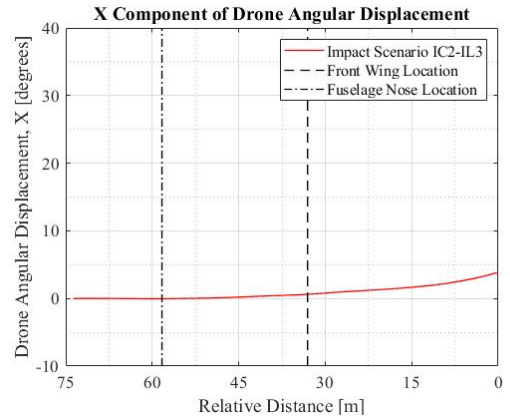
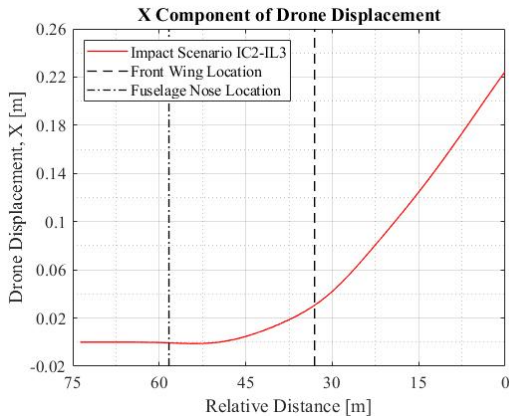


(a)

(b)

Figure 81. Drone aerodynamic forces (a) and moments (b) plotted with respect to relative distance along with average values.

The displacements and angular displacements experienced by the drone as it approached the CRM aircraft horizontal stabilizer for impact scenario IC2-IL3 are given in Figure 82(a) and Figure 82(b), respectively.

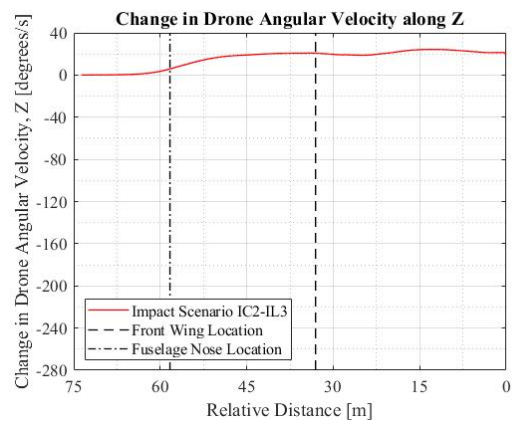
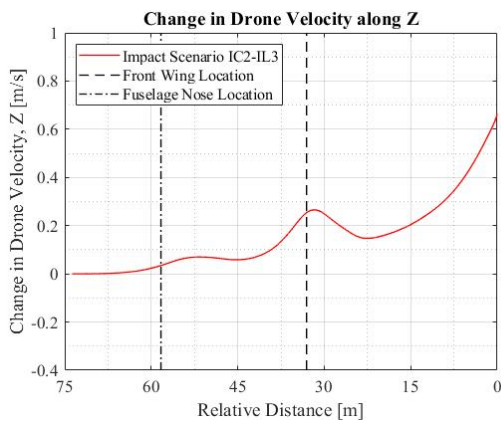
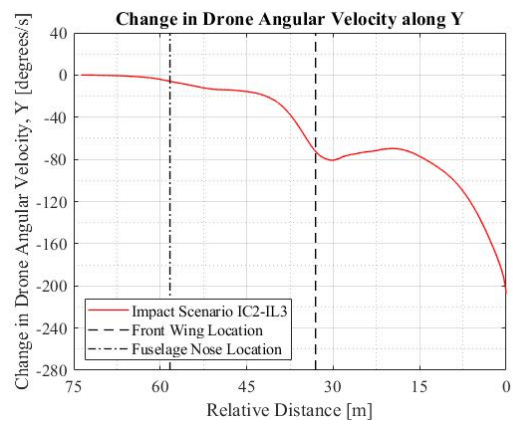
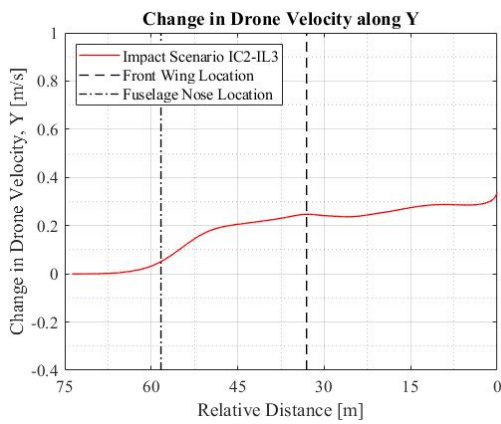
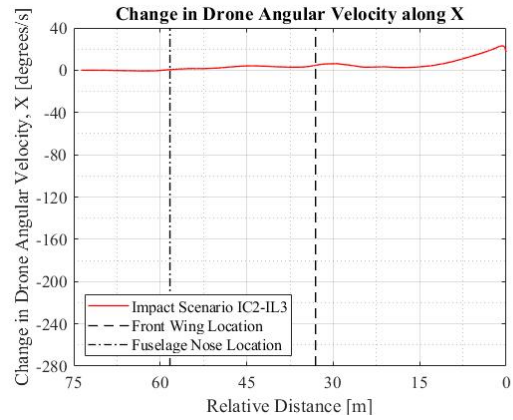
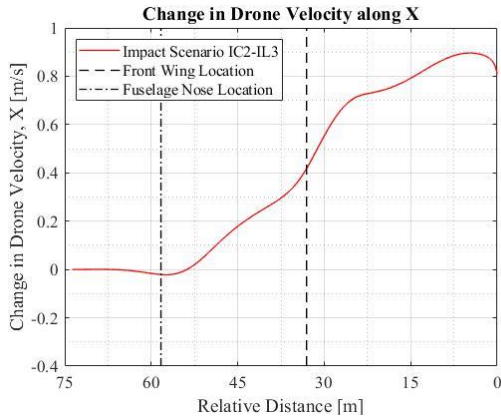


(a)

(b)

Figure 82. Displacements (a) and angular displacements (b) experienced by the drone as it traveled towards the CRM aircraft.

The velocities and angular velocities experienced by the drone as it approached the CRM aircraft horizontal stabilizer for impact scenario IC2-IL3 are given in Figure 83(a) and Figure 83(b), respectively.



(a)

(b)

Figure 83. Velocities (a) and angular velocities (b) experienced by the drone as it traveled towards the CRM aircraft.

### C.7 IMPACT SCENARIO 5 (WITH AVERAGED FORCE/MOMENTS)

For the impact scenario IC2-IL3, the results were obtained based on releasing the drone in the domain with the CRM aircraft wing with the fuselage, horizontal stabilizer, and tail. The drone was released from a distance of 90 m from the leading edge of the horizontal stabilizer at a plane located at a distance of 6.24 m (20.47 ft) in the spanwise direction from the symmetry plane. Once released, the drone was allowed to move without the influence of forces and moments for 16 m. The averaged aerodynamic forces and moments were used as external forces and moments in the UDF.

The forces experienced by the aircraft during the transient simulation were compared with the forces obtained from the steady-state simulation of the CRM aircraft in the domain. Figure 84 shows good agreement between the steady-state and the transient simulation results for the CRM aircraft wing.

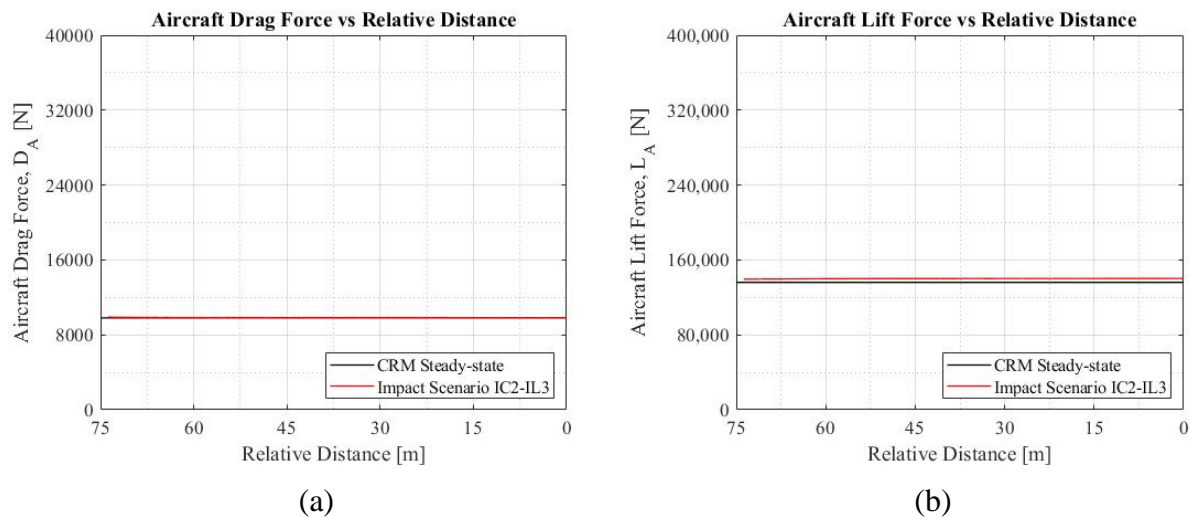


Figure 84. CRM aircraft lift and drag forces recorded as the drone approached the aircraft.

The drone forces and moments were plotted with the average value of the forces and moments used to balance the drone independent aerodynamic forces and moments. The change in forces and moments as the drone approaches the CRM aircraft horizontal stabilizer can be seen in Figure 86(a) and Figure 86(b), respectively. Figure 85 provides a reference for the axis systems used in the plots.

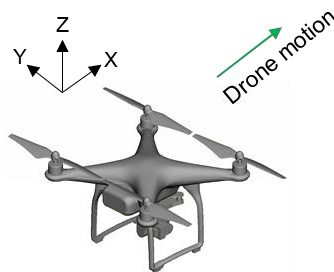
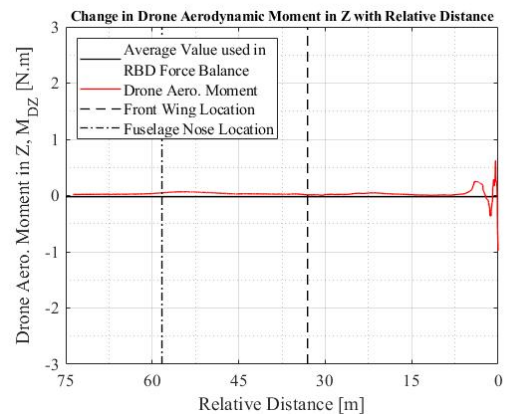
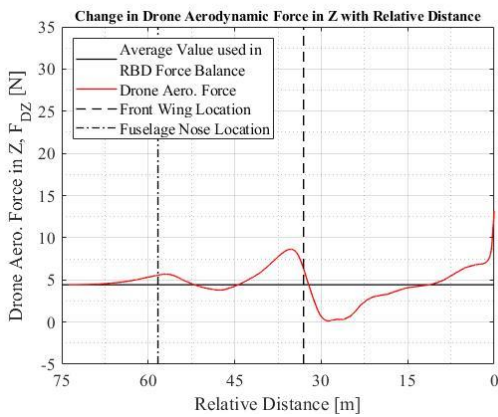
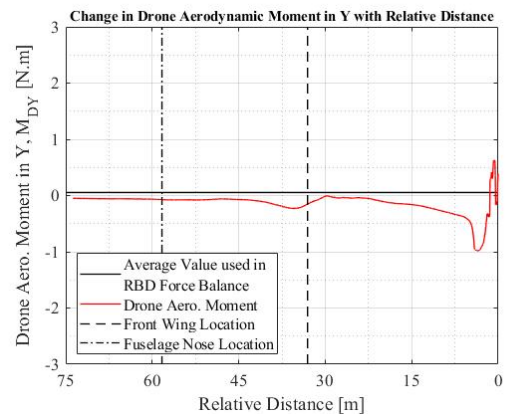
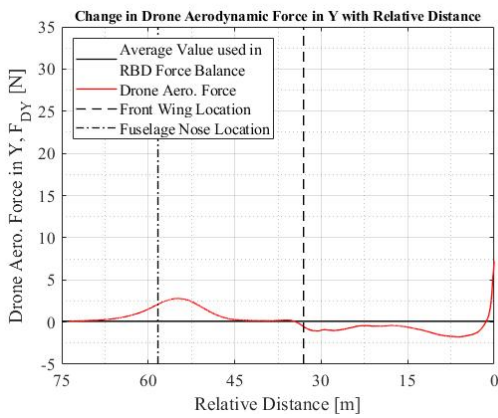
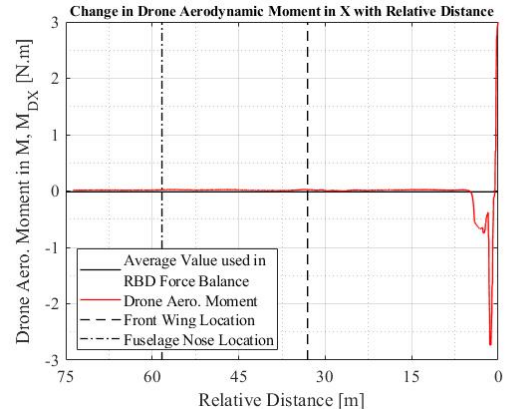
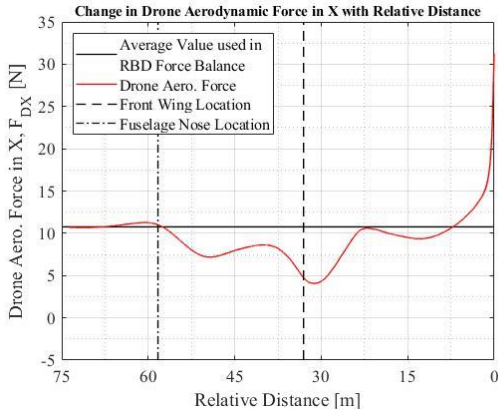


Figure 85. Axis system used for the drone.

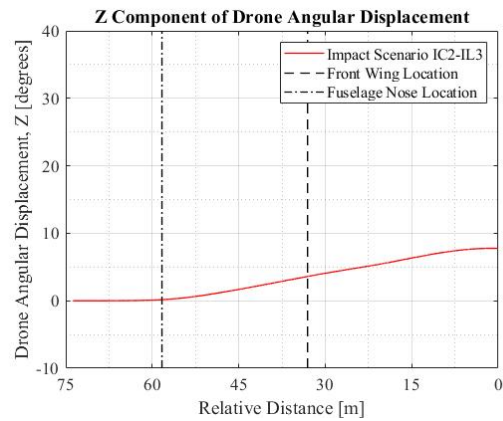
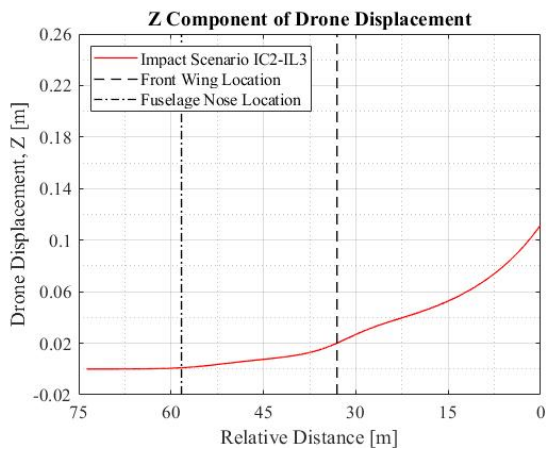
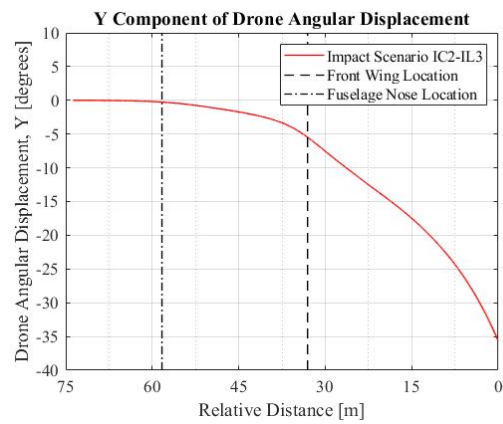
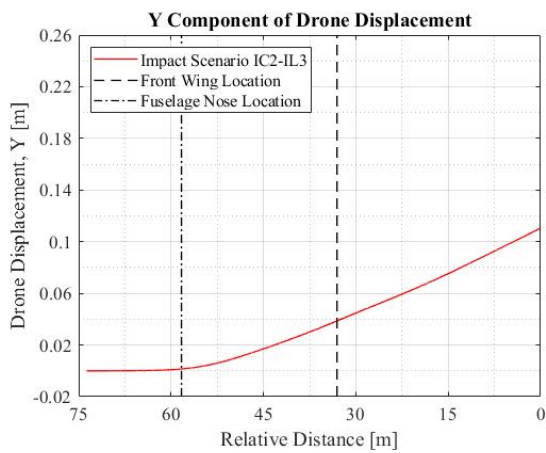
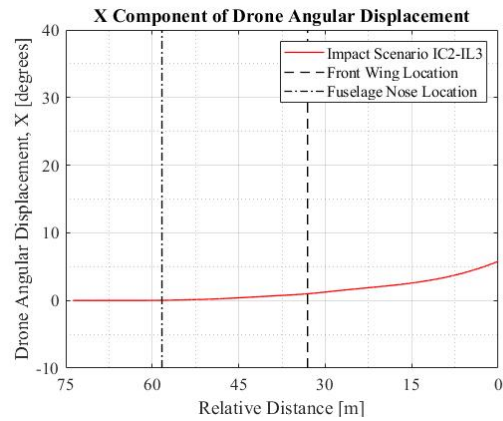
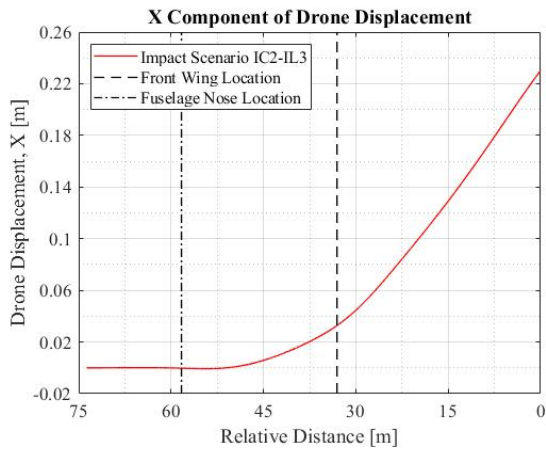


(a)

(b)

Figure 86. Drone aerodynamic forces (a) and moments (b) plotted with respect to relative distance along with average values.

The displacements and angular displacements experienced by the drone as it approached the CRM aircraft horizontal stabilizer for impact scenario IC2-IL3 are given in Figure 87(a) and Figure 87(b), respectively.



(a)

(b)

Figure 87. Displacements (a) and angular displacements (b) experienced by the drone as it traveled towards the CRM aircraft.

The velocities and angular velocities experienced by the drone as it approached the CRM aircraft horizontal stabilizer for impact scenario IC2-IL3 are given in Figure 88(a) and Figure 88(b), respectively.

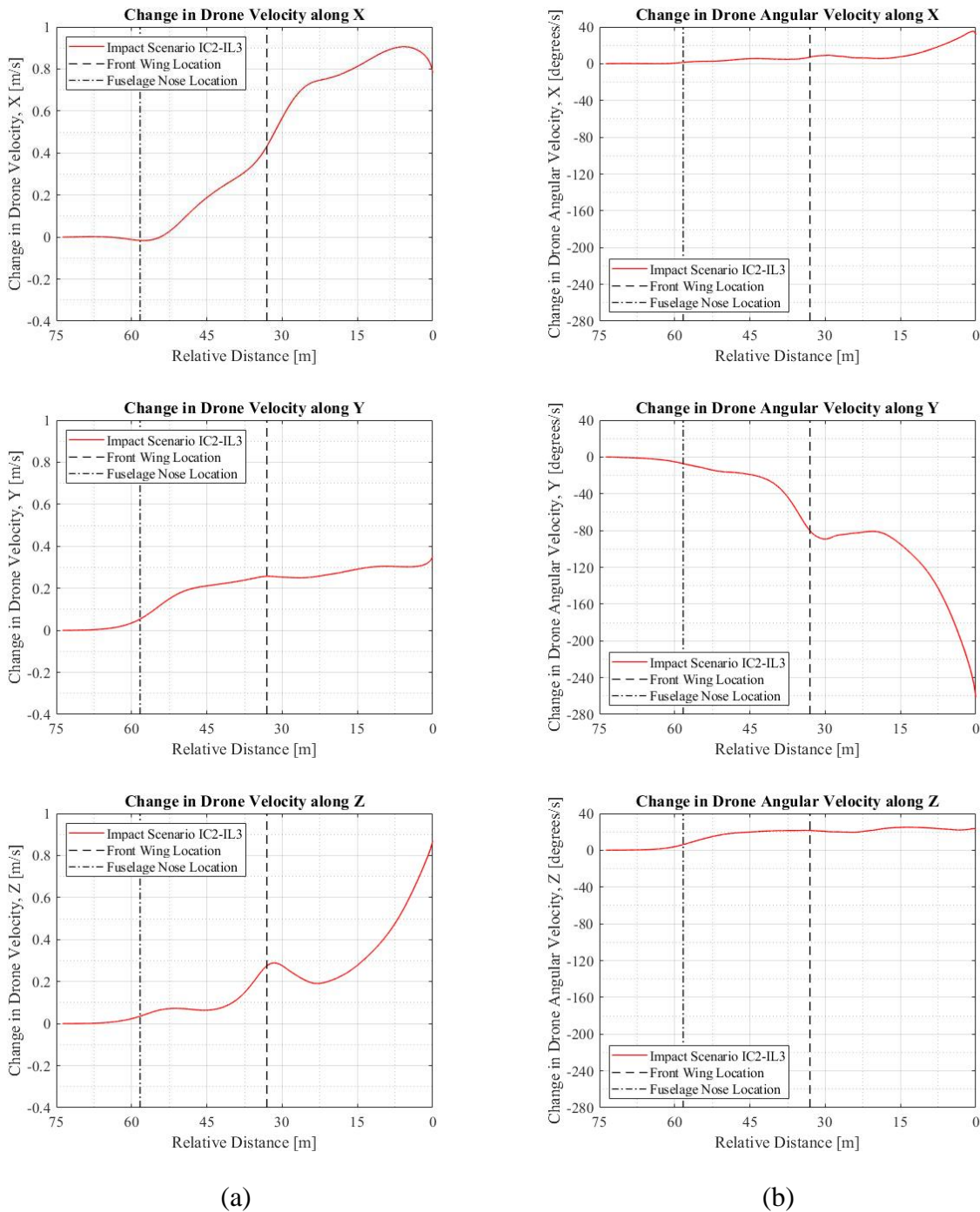


Figure 88. Velocities (a) and angular velocities (b) experienced by the drone as it traveled towards the CRM aircraft horizontal stabilizer.

## C.8 IMPACT SCENARIO 6

For the impact scenario IC3-IL3, the results were obtained based on releasing the drone in the domain with the CRM aircraft wing with the fuselage, horizontal stabilizer, and tail. The drone was released from a distance of 90 m from the leading edge of the horizontal stabilizer at a plane located at a distance of 6.24 m (20.47 ft) in the spanwise direction from the symmetry plane. Once released, the drone was allowed to move without the influence of forces and moments for 16 m. The instantaneous aerodynamic forces and moments were used as external forces and moments in the UDF.

The forces experienced by the aircraft during the transient simulation were compared with the forces obtained from the steady-state simulation of the CRM aircraft in the domain. Figure 89 shows good agreement between the steady-state and the transient simulation results for the CRM aircraft wing.

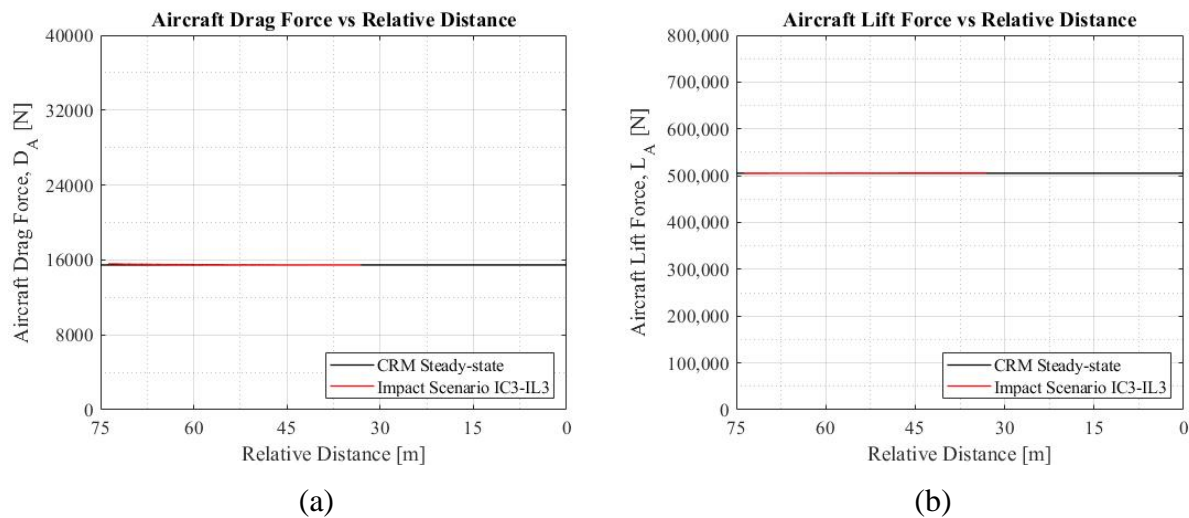


Figure 89. CRM aircraft lift and drag forces recorded as the drone approached the aircraft.

The drone forces and moments were plotted with the instantaneous value of the forces and moments to balance the drone independent aerodynamic forces and moments. The change in forces and moments as the drone approaches the CRM aircraft horizontal stabilizer can be seen in Figure 91(a) and Figure 91(b), respectively. Figure 90 provides a reference for the axis systems used in the plots.

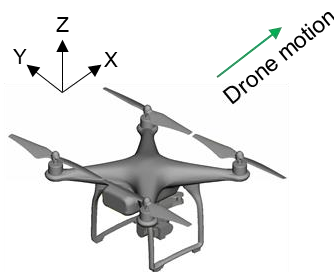
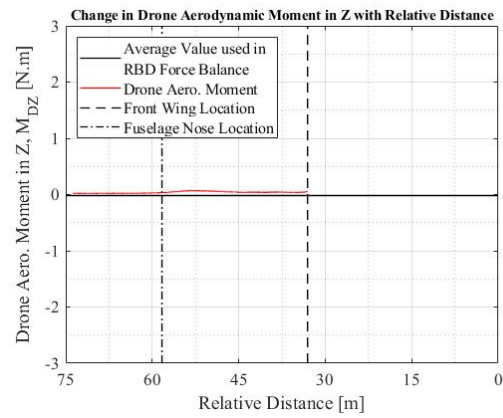
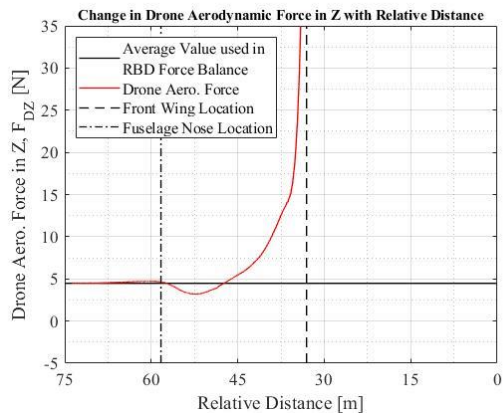
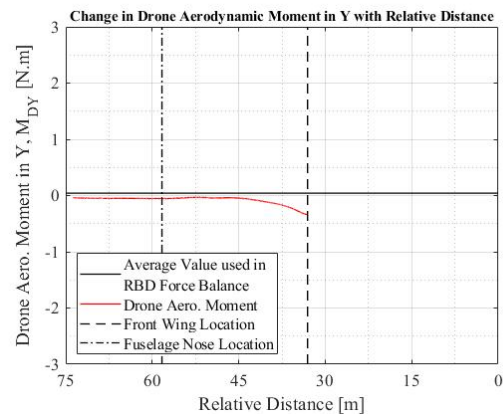
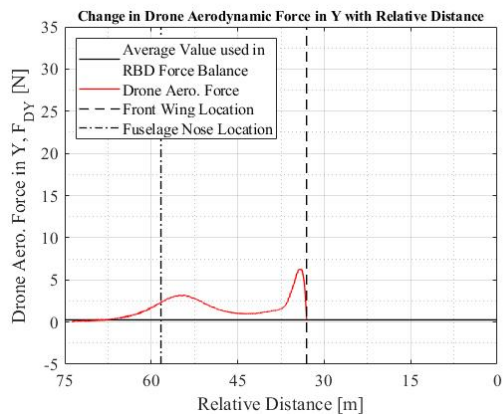
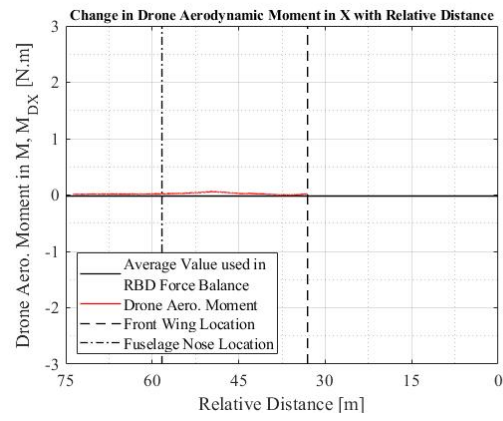
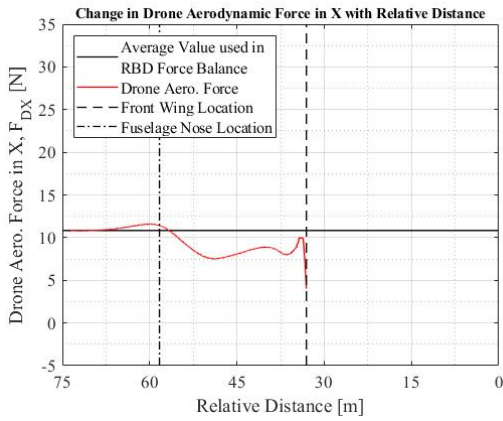


Figure 90. Axis system used for the drone.



(a)

(b)

Figure 91. Drone aerodynamic forces (a) and moments (b) plotted with respect to relative distance along with average values.

The plots presented in this section show the results up to the CRM front wing. This is due to an early collision of the DJI drone with the CRM wing before it reached the CRM horizontal stabilizer. The displacements and angular displacements experienced by the drone as it approached

the CRM aircraft for impact scenario IC3-IL3 are given in Figure 92(a) and Figure 92(b), respectively.

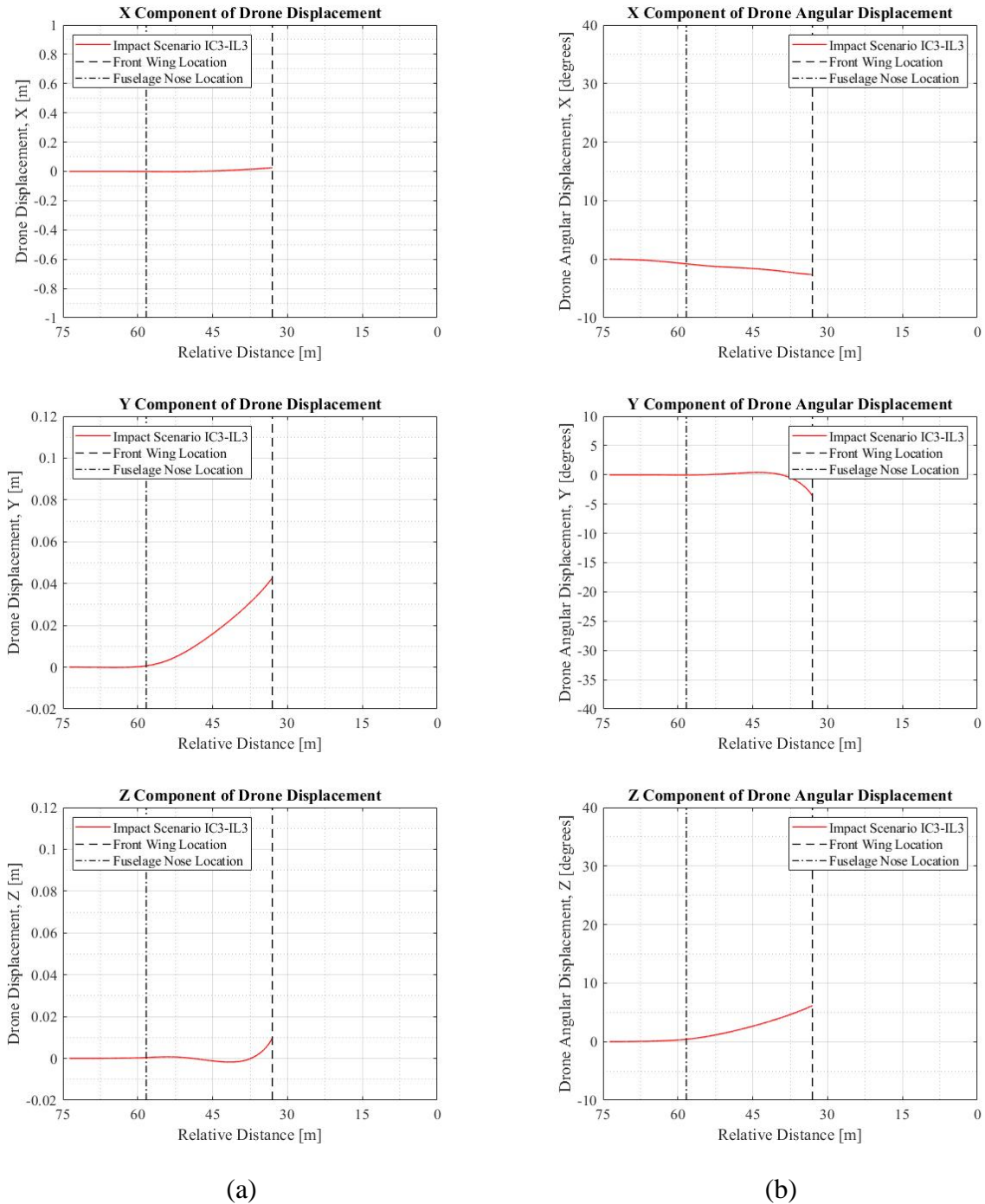


Figure 92. Displacements (a) and angular displacements (b) experienced by the drone as it traveled towards the CRM aircraft.

The velocities and angular velocities experienced by the drone as it approached the CRM aircraft for impact scenario IC3-IL3 are given in Figure 93(a) and Figure 93(b), respectively.

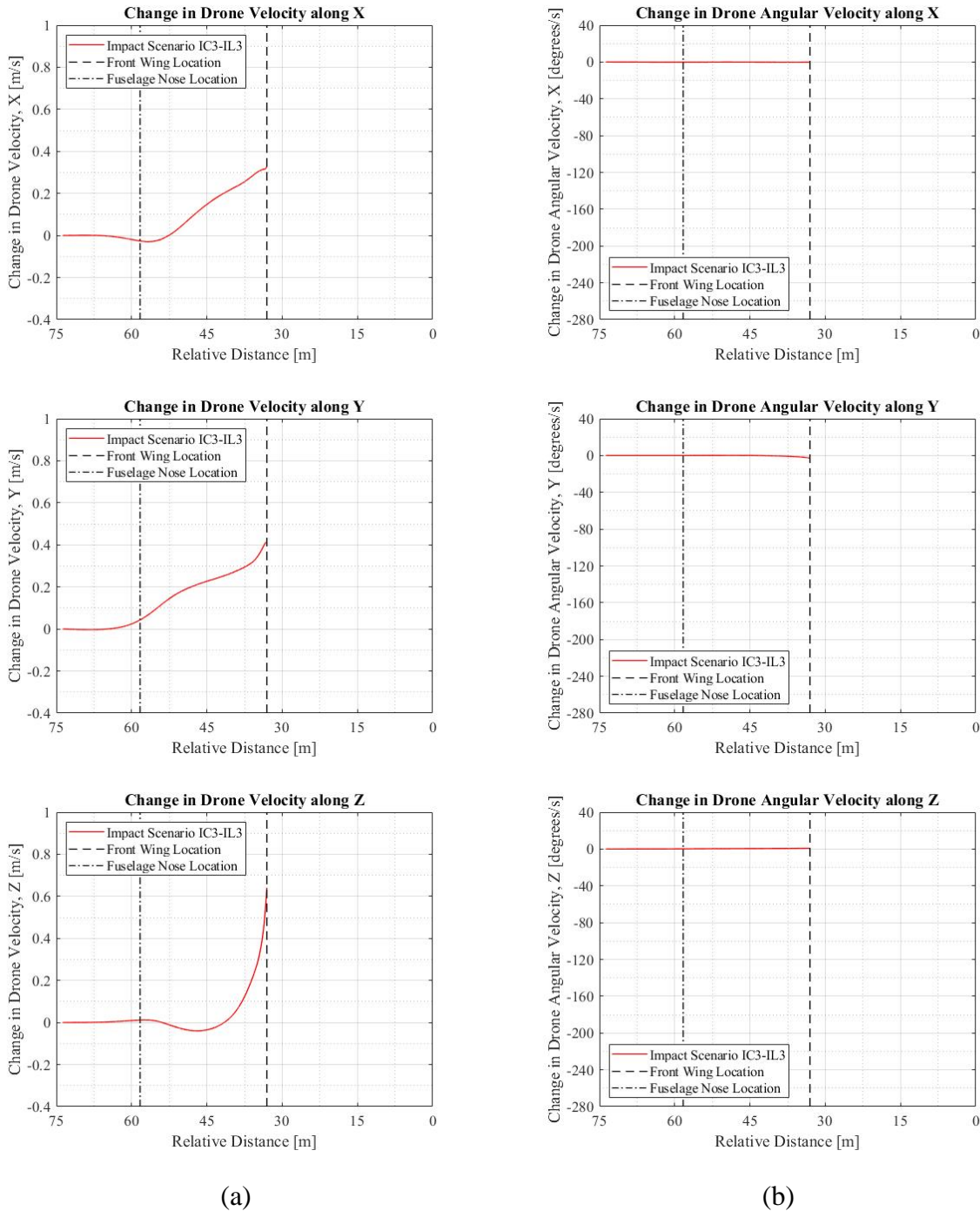


Figure 93. Velocities (a) and angular velocities (b) experienced by the drone as it traveled towards the CRM aircraft horizontal stabilizer.

### C.9 IMPACT SCENARIO 7

For the impact scenario IC3-IL3, the results were obtained based on releasing the drone in the domain with the CRM aircraft wing with the fuselage, horizontal stabilizer, and tail. The drone was released from a distance of 90 m from the leading edge of the horizontal stabilizer at a plane located at a distance of 6.24 m (20.47 ft) in the spanwise direction from the symmetry plane. Once released, the drone was allowed to move without the influence of forces and moments for 16 m. The instantaneous aerodynamic forces and moments were used as external forces and moments in the UDF.

The forces experienced by the aircraft during the transient simulation were compared with the forces obtained from the steady-state simulation of the CRM aircraft in the domain. Figure 94 shows good agreement between the steady-state and the transient simulation results for the CRM aircraft wing.

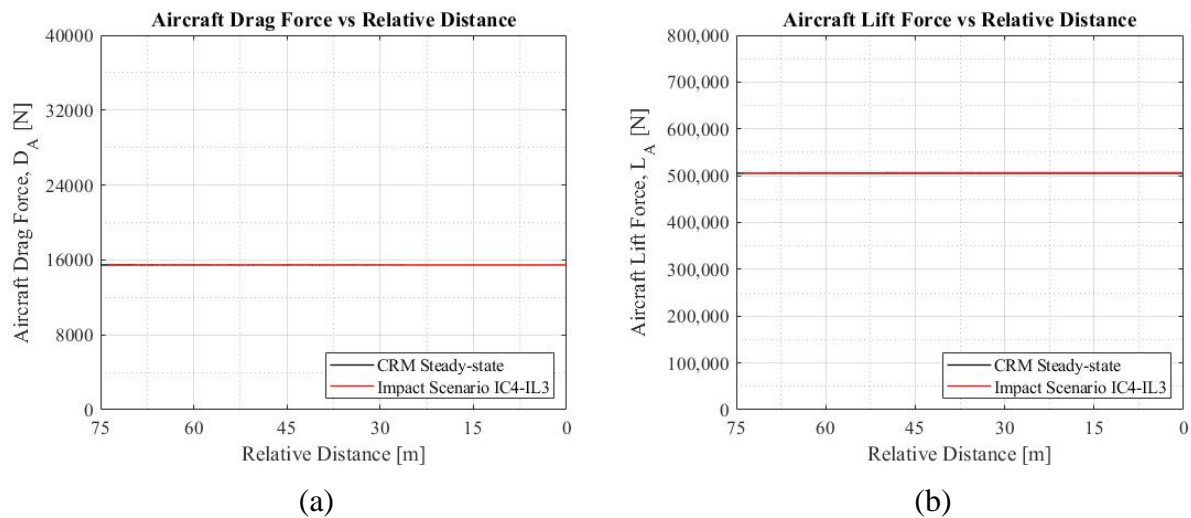


Figure 94 CRM aircraft lift and drag forces recorded as the drone approached the aircraft.

The drone forces and moments were plotted with the instantaneous value of the forces and moments used to balance the drone independent aerodynamic forces and moments. The change in forces and moments as the drone approaches the CRM aircraft horizontal stabilizer can be seen in Figure 96(a) and Figure 96(b), respectively. Figure 95 provides a reference for the axis systems used in the plots.

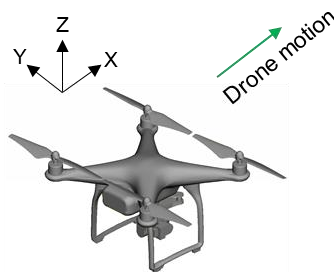


Figure 95. Axis system used for the drone.

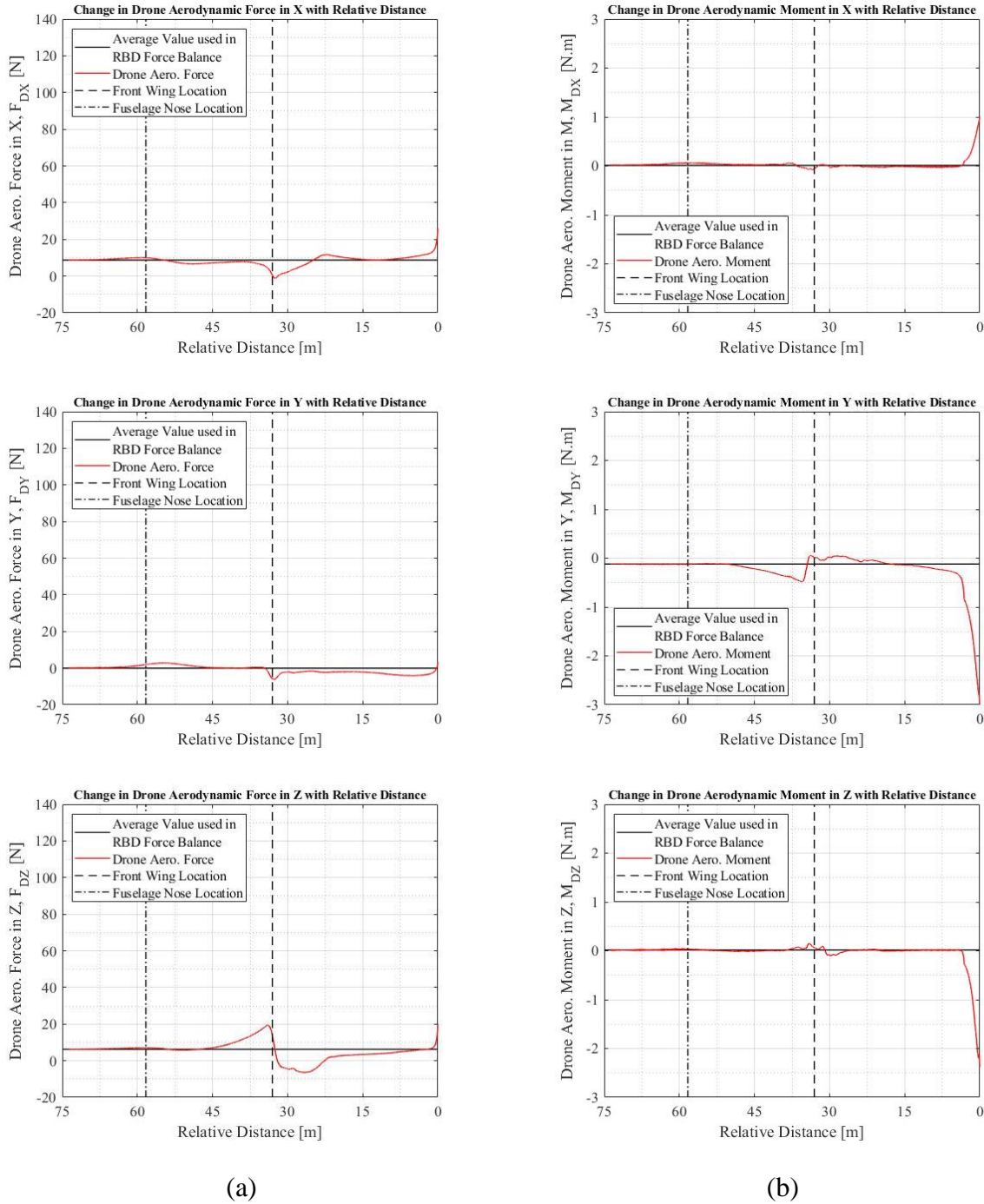


Figure 96. Drone aerodynamic forces (a) and moments (b) plotted with respect to relative distance along with average values used in the UDF.

The plots presented in this section show the results up to the CRM front wing. This is due to an early collision of the DJI drone with the CRM wing before it reached the CRM horizontal stabilizer. The displacements and angular displacements experienced by the drone as it approached

the CRM aircraft for impact scenario IC3-IL3 are given in Figure 97(a) and Figure 97(b), respectively.

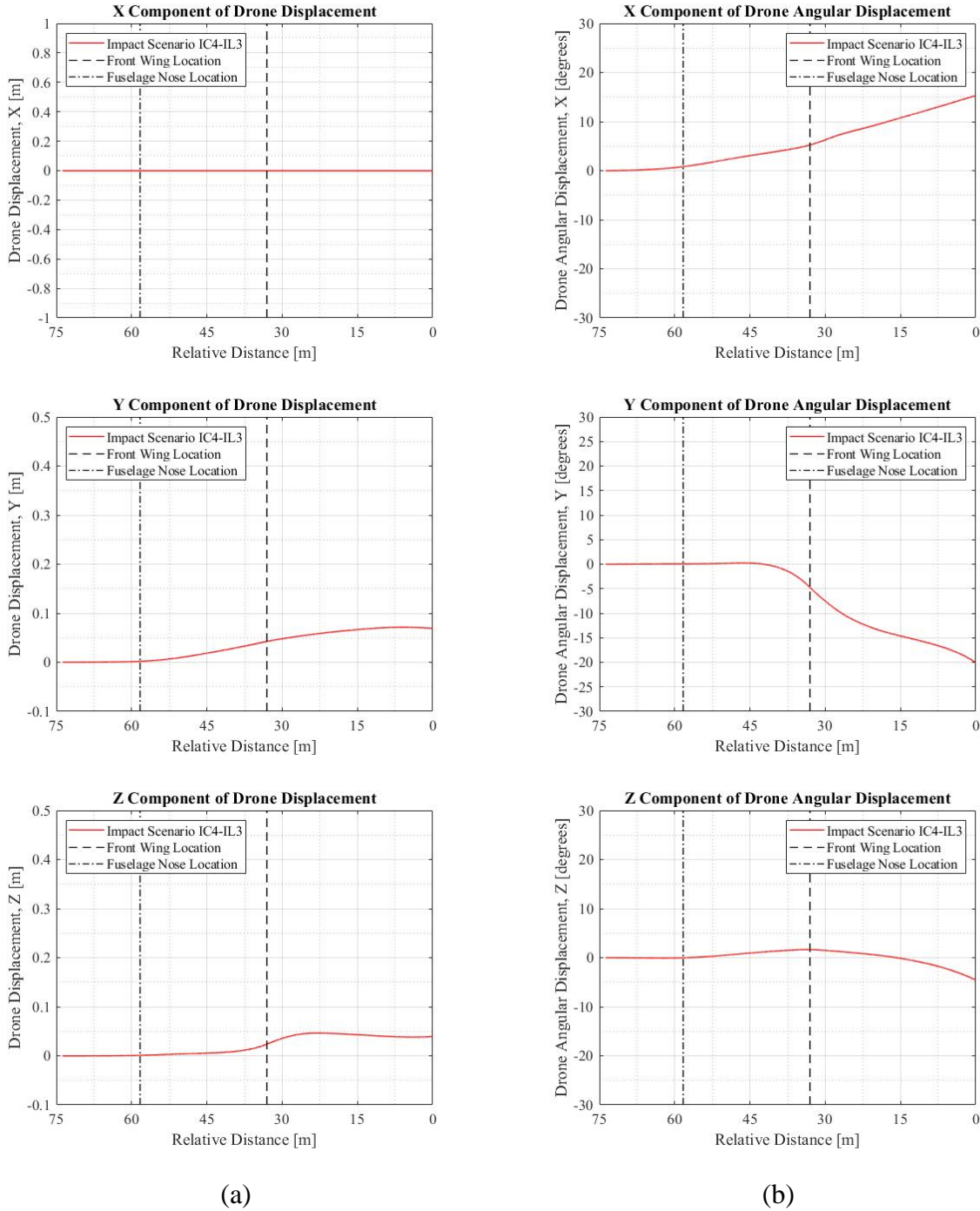
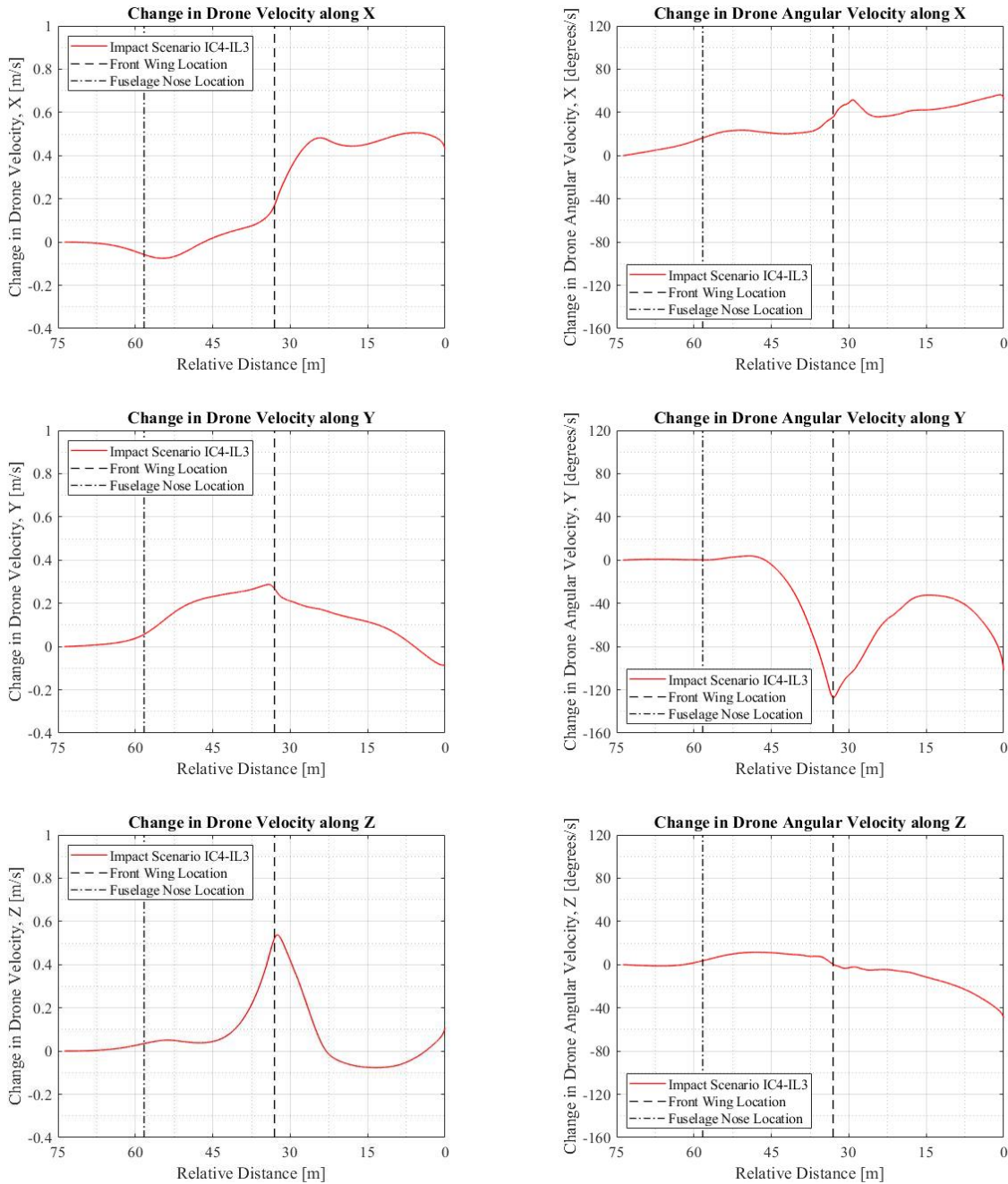


Figure 97. Displacements (a) and angular displacements (b) experienced by the drone as it traveled towards the CRM aircraft.

The velocities and angular velocities experienced by the drone as it approached the CRM aircraft for impact scenario IC3-IL3 are given in Figure 98(a) and Figure 98(b), respectively.



(a)

(b)

Figure 98. Velocities (a) and angular velocities (b) experienced by the drone as it traveled towards the CRM aircraft horizontal stabilizer.